1890

New Frontiers in Stable Isotopic Research: Laser Probes, Ion Probes, and Small-Sample Analysis

U.S. GEOLOGICAL SURVEY BULLETIN 1890

I 19.3:

READEX FICHE best copy available

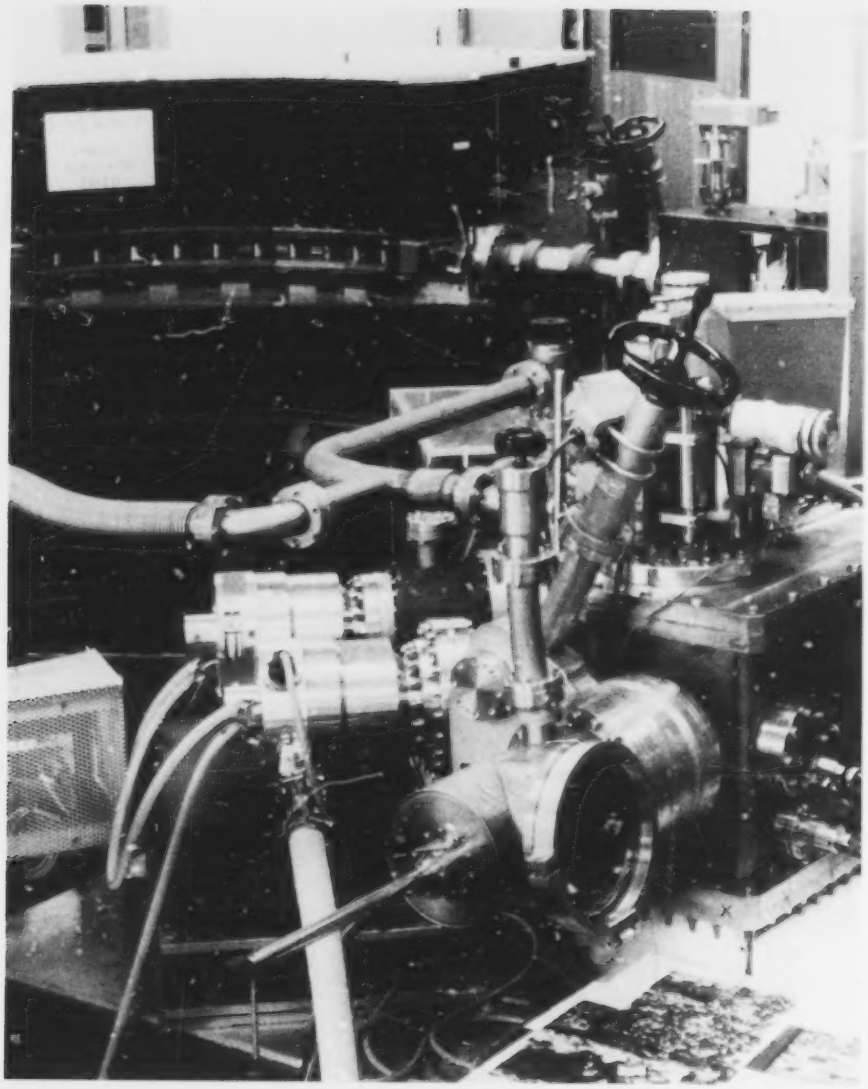

New Frontiers in Stable Isotopic Research: Laser Probes, Ion Probes, and Small-Sample Analysis

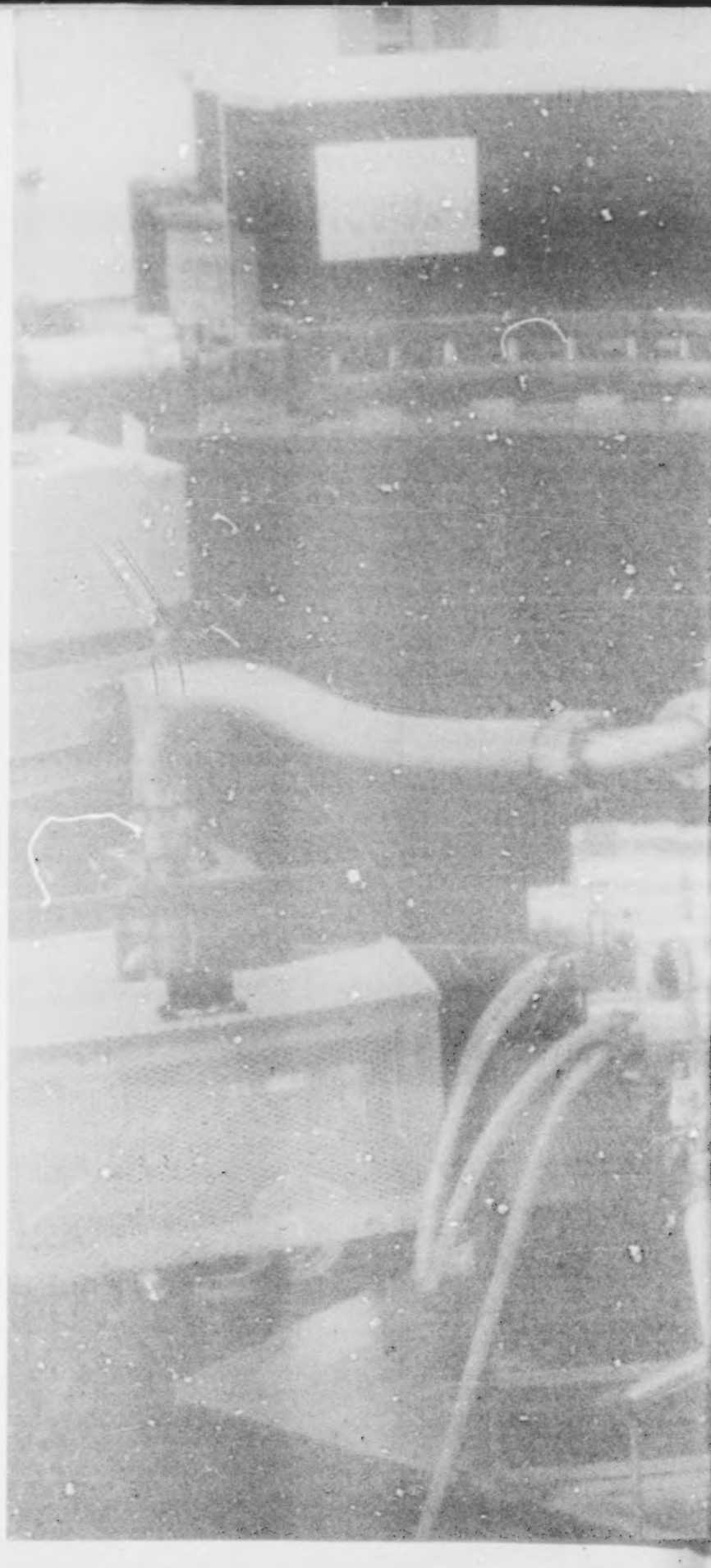

The SHRIMP (Sensitive High mass Resolution Ion Micro Probe) instrument at the Research School of Earth Sciences, The Australian National University. In the right foreground are the duoplasmatron for primary-ion beam generation and the sample chamber where the secondary-ion beam is generated and extracted. The electrostatic sector analyzer is in the right rear of the photo, and the 1-m radius, 6-t magnetic sector analyzer is in the rear center. The ion collector system is in the left rear. See Eldridge and others (p. 163) for details of SHRIMP construction and operation.

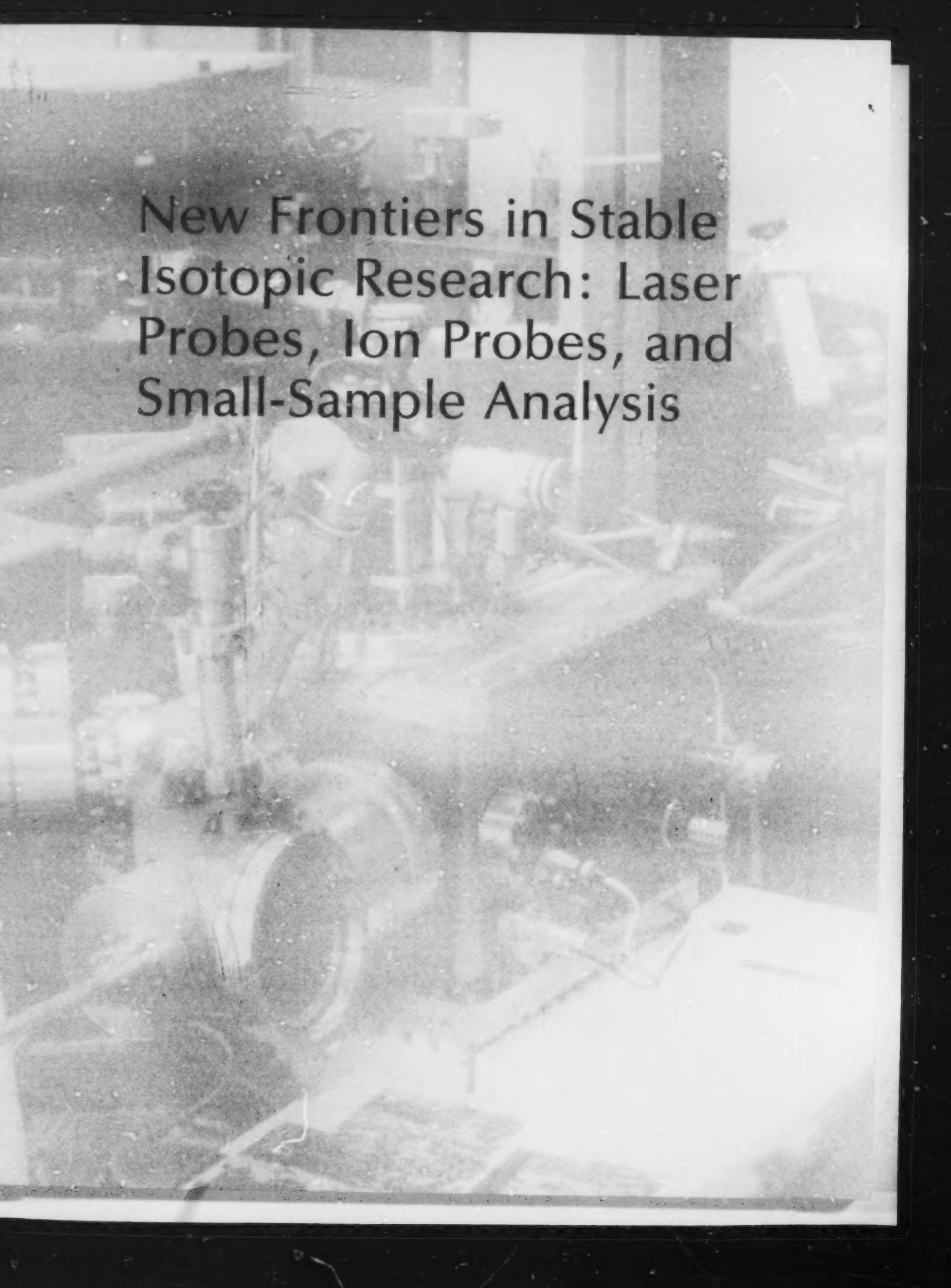

New Frontiers in Stable Isotopic Research: Laser Probes, Ion Probes, and Small-Sample Analysis

New Frontiers in Stable Isotopic Research: Laser Probes, Ion Probes, and Small-Sample Analysis

W.C. SHANKS III and R.E. CRISS, editors

Results of a workshop held in Reston, Va., January 12–13, 1988, on laser microprobe and ion microprobe analysis techniques performed on geological samples for stable and rare gas isotopic ratios

U.S. GEOLOGICAL SURVEY BULLETIN 1890

DEPARTMENT OF THE INTERIOR
MANUEL LUJAN, Jr., Secretary

U.S. GEOLOGICAL SURVEY
Dallas L. Peck, Director

Any use of trade, product, or firm names in this publication is for descriptive purposes only and does not imply endorsement by the U.S. Government

UNITED STATES GOVERNMENT PRINTING OFFICE: 1989

For sale by the Books and Open-File Reports Section,
U.S. Geological Survey, Federal Center,
Box 25425, Denver, CO 80225

Library of Congress Cataloging in Publication Data

New frontiers in stable isotopic research : laser probes, ion probes, and small-sample analysis. W.C. Shanks III and R.E. Criss, editors.
(U.S. Geological Survey bulletin ; 1890)
"Results of a workshop held in Reston, Va., January 12–13, 1988, on laser microprobe and ion microprobe analysis techniques on geological samples for stable and rare gas isotopic ratios."
Bibliography: p.
Supt. of Docs. no. : Supt. of Docs. no. : I 19.3:1890
1. Isotope geology—Congresses. 2. Microprobe analysis—Congresses. I. Shanks, Wayne C. II. Criss, R.E. III. Series.
QE75.B9 no. 1890
[QE501.4.N9]
557.3 s—dc20
[551'.028]

89-600096
CIP

PREFACE

Approximately 70 persons attended a workshop on January 12 and 13, 1988, entitled "New Frontiers in Stable Isotopic Research: Laser Probes, Ion Probes, and Small-Sample Analysis" held at the USGS National Center, Reston, Va. The program (see p. XI) included 16 talks on new methods for performing high-precision stable and rare-gas isotopic analyses on submicrogram quantities of minerals. The workshop was organized by W.C. Shanks III (USGS) and R.E. Criss (USGS) and was sponsored by the USGS Development of Assessment Techniques Program.

Bruce Doe (USGS Assistant Director for Research) presented an introductory address in which he emphasized the USGS commitment to innovative research. I. Lynus Barnes (National Bureau of Standards) led off the workshop by summarizing the current state of the art in conventional mass spectrometry, secondary ion mass spectrometry, and resonance ionization mass spectrometry using thermal vaporization and tunable lasers. Alfred Nier (University of Minnesota, Minneapolis, Minn.) described terrestrial and extraterrestrial applications of small volume, double-focusing mass spectrometers of the type he designed for the Viking lander.

Two predominant themes emerged in the remainder of the workshop: (1) the use of a focused laser beam (laser probe) to vaporize 10- to 100-μm cavities followed by dynamic or static mass spectrometry to analyze resultant gases and (2) the use of a focused ion beam (ion probe) to sputter a 1- to 30-μm spot to produce secondary ions that are analyzed in a large-radius double-focusing mass spectrometer. Both technologies have been successfully employed in certain radiogenic and microanalytical applications but are only now being developed for high-precision stable isotopic analysis. Ian Wright (The Open University, England) discussed $\delta^{13}C$ and $\delta^{18}O$ analysis by static mass spectrometry of very small amounts of gas released by stepped heating of separated minerals. This procedure allows the systematic elimination of contaminants from very small samples. Henryk Herman (BP Research Centre, England) reported complete conversion of calcite to CO_2 with no isotopic fractionation under carefully selected conditions of laser ablation of calcite. Everett Gibson (NASA Johnson Space Center, Houston, Tex.) noted that laser techniques are essentially perfected for $\delta^{15}N$ analyses. He also utilized a laser probe to study fluid inclusions and a number of mineral and rock fragments and made chemical (not isotopic) analyses on the released gas with a quadrupole mass spectrometer. Problems with laser probes discussed by these workers principally relate to inefficient ion production, incomplete conversion to the desired gas, and difficulties in handling very small gas samples. Other applications of laser techniques to microanalytical isotopic problems will be important in future stable isotopic research. For example, David Cole (Oak Ridge National Laboratory, Oak Ridge, Tenn.) discussed possible future stable isotopic analysis by resonance ionization spectroscopy, in which a secondary laser is tuned to selectively ionize specific species in a vapor cloud produced by laser ablation. In addition, Robert Burruss (USGS, Denver, Colo.) discussed the potential for nondestructive analysis of carbon and oxygen isotopes in fluid inclusions by use of laser Raman spectroscopy.

Ion probe techniques also offer great promise for high-precision stable isotopic microanalysis. Stewart Eldridge (Australian National University, Canberra, Australia) reported remarkable success analyzing sulfur isotopic values on 30-μm spots with the SHRIMP (Selective High mass Resolution Ion MicroProbe), attaining a precision of ±2 ‰. Of particular importance are his observations that different generations of

sulfide minerals having radically different $\delta^{34}S$ values can occur in single samples. Nobu Shimizu (M.I.T., Cambridge, Mass.) also reported good success with ion probe determinations of $\delta^{34}S$ and showed that matrix effects, which invariably enrich the light isotopes, depend on the kinetic energy of the secondary ions. The ultimate precision of ion probe analyses on very small volumes ($\leq 1\ \mu m^3$) of material depends directly on the natural abundance of the isotopic species in question. Accordingly, there are large differences in the precision of $\delta^{34}S$ measurements ($^{32}S/^{34}S = 20$) and $\delta^{18}O$ measurements ($^{16}O/^{18}O = 500$ in normal samples), with precise determinations of $\delta^{18}O$ being more difficult. However, Bruno Giletti (Brown University, Providence, R.I.) reported preliminary $\delta^{18}O$ measurements of homogeneous plagioclase from a volcanic rock with a precision of about ± 0.5 ‰, for measurements taken on a single day. He also reviewed a variety of geologic and petrologic problems where microanalytical capability for $\delta^{18}O$ would result in substantial scientific gains. Ernst Zinner (Washington University, St. Louis, Mo.) reported useful $\delta^{18}O$ and $\delta^{17}O$ measurements on small grains from meteorite samples, which commonly have highly variable and extreme oxygen isotopic ratios relative to terrestrial samples, and he also illustrated the versatility of the ion probe by showing useful measurements for Ti, Si, Mg, Ca, and H isotopes in meteorites. Richard Hervig (Arizona State University, Tempe, Ariz.) discussed the current technology of primary ion beams for ion probe measurements and reported on his attempts to eliminate surface charging effects and to measure $\delta^{18}O$ values in thin sections. The authors all discussed difficulties that arise from the insulating nature of most silicate samples, which leads to surface charging, and the additional problem of using inherently unstable electron multipliers to count minor ion beams. Nonetheless, ion probes provide extremely good spatial resolution, are less destructive than laser techniques, and have already permitted many remarkable measurements to be made.

Several talks were scheduled on $^{40}Ar/^{39}Ar$ and other rare-gas studies in hope of adapting the technology that has been so successfully utilized by noble-gas investigators to stable isotopic microanalysis. Brent Dalrymple (USGS, Menlo Park, Calif.) discussed the use of continuous argon-ion lasers for stepped heating of separated mineral grains. He pointed out that this technique offers numerous advantages, such as rapid low-blank analysis of very small samples, over conventional $^{40}Ar/^{39}Ar$ analysis. Ed Spooner (University of Toronto, Ontario, Canada) discussed laser probe $^{40}Ar/^{39}Ar$ dating of fine-grained illites. The above techniques offer potential for stable isotopic work because they are safer (argon laser beam is visible) and contaminants can be eliminated by stepped heating. In addition, Paul Hearn (USGS, Reston, Va.) presented an application of an air abrasion mill for separation of diagenetic rims on potassium feldspar. J.K. Böhlke (Argonne National Laboratory, Argonne, Ill.) presented results of an innovative approach of analyzing chemical and isotopic species in fluid inclusions in which a laser microprobe is used to open fluid inclusions in irradiated samples for noble gas mass spectrometry.

At the workshop, we offered to the authors and to others present the possibility of publishing a symposium volume as a U.S. Geological Survey Bulletin. The response was so positive that we decided to proceed. A target date of April 15, 1988, was set for manuscript submittal. Thirteen manuscripts were received, covering most of the topics discussed at the workshop, and two additional topics: $\delta^{15}N$ analysis of diamonds by use of the laser probe and static mass spectrometry (by I.A. Franchi and others) and laser microprobe microanalysis of coal (by P.C. Lyons and others). All manuscripts were subjected to thorough peer review, including scientific reviews by Shanks or Criss or both and at least one reviewer from outside the USGS.

We are highly impressed with the bright future of stable isotopic microanalytical techniques, which ultimately will permit precise isotopic determinations on a variety of samples that are up to a billion times smaller than those used in conventional analyses. Such techniques will open numerous new avenues of research, will clearly revolutionize current understanding of stable isotopic geochemistry, and will make obsolete the

conventional analysis of certain isotopically heterogeneous geologic materials. As an example of the many possible future applications that the conference portends, we point out that there is immediate potential for laser application to δD analyses of small samples that require only heating to release structural or included water. We feel certain that future research using ion probes and laser probes will lead to routine microanalysis of the isotopic ratios of carbon, oxygen, and sulfur and many other elements in ordinary samples, with accuracies and precisions similar to conventional macroanalysis techniques.

We wish to acknowledge the helpful assistance of Irene Harrel, who organized registration, Jeffrey Thole, who operated the projection facilities, Susan Socks, who translated manuscripts on a wide variety of digital formats into the USGS computer system, Linda Shanks, who allowed 70 scientists to invade her house, and John Watson, who did an outstanding job of technical editing on the manuscripts.

W.C. Shanks III
R.E. Criss

PROGRAM

National Center Auditorium

TUESDAY, JANUARY 12, 1988

8:30–8:45 AM — INTRODUCTORY ADDRESS. Bruce Doe, Assistant Director for Research, U.S. Geological Survey, Reston, Va.

8:45–9:30 AM — "RIMS, SIMS, and 23°: Recent advances in mass spectrometry." I. Lynus Barnes, National Bureau of Standards, Washington, D.C.

9:35–9:50 AM — COFFEE BREAK

9:50–10:35 AM — "Isotope analyses with small-volume mass spectrometers." Alfred O. Nier, Department of Physics, University of Minnesota, Minneapolis, Minn.

10:40–11:25 AM — "Applications of static mass spectrometry to stable isotope studies." I.P. Wright, Department of Earth Sciences, The Open University, Milton Keynes, England

11:30–1:00 PM — LUNCH

1:00–1:45 PM — "Laser ablation in microsampling for geological applications and stable isotope analysis." Henryk Herman, BP Research Centre, Sunbury-on-Thames, England

1:50–2:20 PM — "A quadrupole mass spectrometer laser microprobe system for analysis of gases released from geological samples." Everett K. Gibson, Jr., NASA Johnson Space Center, Houston, Tex.

2:25–2:40 PM — COFFEE BREAK

2:40–3:00 PM — "USGS laser Raman spectroscopy laboratory: Introduction to the technique, hardware, and opportunities for stable isotope studies of individual fluid inclusions." Robert C. Burruss, U.S. Geological Survey, Denver, Colo.

3:05–3:20 PM — "Geological applications of resonance ionization spectroscopy." David R. Cole (with N. Thonnard), Oak Ridge National Laboratory, Oak Ridge, Tenn.

3:25–4:00 PM — GROUP DISCUSSION of laser probe techniques in stable isotope research.

WEDNESDAY, JANUARY 13, 1988

8:30–9:15 AM — "SHRIMP ion microprobe analysis of sulfur isotope values in minerals." C.S. Eldridge (with W. Compston, I.S. Williams, and R.A. Both), Geology Department, Australian National University, Canberra, Australia

9:20–9:30 AM — "Analysis of sulfur isotopes in sulfides with a Cameca IMS 3f." A. MacFarlane and Nobu Shimizu, Department of Earth, Atmospheric, and Planetary Science, Massachusetts Institute of Technology, Cambridge, Mass.

9:35–9:50 AM — COFFEE BREAK

9:50–10:35 AM — "Use of ion microprobes to measure natural oxygen isotope abundances in minerals." Bruno J. Giletti, Department of Geology, Brown University, Providence, R.I.

10:40–11:25 AM — "Ion probe isotopic analysis of extraterrestrial materials." Ernst Zinner, McDonnell Center for the Space Sciences, Washington University, St. Louis, Mo.

11:30–1:00 PM — LUNCH

1:00–1:30 PM — "Charge neutralization and ion microprobe analysis of oxygen isotopes in insulating phases." Richard L. Hervig, Department of Chemistry, Arizona State University, Tempe, Ariz.

1:35–2:30 AM — GROUP DISCUSSION of future developments in ion probe analyses.

2:30–2:45 PM — COFFEE BREAK

2:45–3:05 PM — "$^{40}Ar/^{39}Ar$ dating of submicrogram samples with a continuous laser." G. Brent Dalrymple, U.S. Geological Survey, Menlo Park, Calif.

3:10–3:30 AM — "Continuous laser probe $^{40}Ar/^{39}Ar$ and conventional K/Ar dating of illites associated with U mineralization, N. Saskatchewan, Canada: Comparison of results, and comparison with pitchblende U-Pb dates." Ed Spooner and Colin Bray, Department of Geology, University of Toronto, Ontario, Canada.

3:35–3:45 PM — "$^{40}Ar/^{39}Ar$ dating of secondary overgrowths using quantitative separation via air abrasion and gravity settling techniques." Paul P. Hearn, Jr., U.S. Geological Survey, Reston, Va.

3:50–4:10 PM — "Simultaneous analyses of noble gas isotopes and halogens in irradiated fluid inclusions using a laser microprobe noble gas mass spectrometer." J.K. Böhlke, C. Kirschbaum, and J. Irwin, Argonne National Laboratory, Argonne, Ill.

4:15–5:00 PM — SUMMARY DISCUSSION

CONTENTS

Preface **VII**

Program **XI**

Isotope analyses with small-volume mass spectrometers—by Alfred O. Nier **1**

Carbon isotopic analysis of small samples by use of stepped-heating extraction and static mass spectrometry—by I.P. Wright and C.T. Pillinger **9**

Laser microprobe–quadrupole mass spectrometer system for the analysis of gases and volatiles from geologic materials—by Everett K. Gibson, Jr., and Robert H. Carr **35**

Application of lasers in small-sample stable isotopic analysis—by I.A. Franchi, S.R. Boyd, I.P. Wright, and C.T. Pillinger **51**

Simultaneous analyses of noble-gas isotopes and halogens in fluid inclusions in neutron-irradiated quartz veins by use of a laser-microprobe noble-gas mass spectrometer—by J.K. Böhlke, C. Kirschbaum, and J. Irwin **61**

The GLM Continuous Laser System for $^{40}Ar/^{39}Ar$ dating: Description and performance characteristics—by G. Brent Dalrymple **89**

Application of the laser microprobe (LAMMA 1000) to the microanalysis of coal constituents—by Paul C. Lyons, John J. Morelli, and David M. Hercules **97**

Quantitative separation or authigenic overgrowths from mineral grains by air-abrasion and gravity settling techniques—by Paul P. Hearn, Jr., Jerry D. Gandy, John N. Aleinikoff, and Raymond W. Werre **111**

Resonance ionization spectroscopy and its potential application in geosciences—by Robert D. Willis, Norbert Thonnard, and David R. Cole **117**

Use of the ion microprobe to measure natural abundances of oxygen isotopes in minerals—by Bruno J. Giletti and Nobu Shimizu **129**

Charge neutralization and oxygen isotopic analysis of insulators with the ion microprobe—by Richard L. Hervig, Robert M. Thomas, and Peter Williams **137**

Isotopic measurements with the ion microprobe—by Ernst Zinner **145**

Sulfur isotopic analyses on the SHRIMP ion microprobe—by C.S. Eldridge, W. Compston, I.S. Williams, and J.L. Walshe **163**

Isotope Analyses with Small-Volume Mass Spectrometers

By Alfred O. Nier[1]

Abstract

Accurate isotope abundance measurements by mass spectroscopy became practical in the 1930's after the invention of the electrometer vacuum tube and the transverse electron-beam ion source. The introduction of magnetic sector mass analyzers greatly reduced the weight and power requirements of instruments and made practical the wide use of mass spectrometers for isotope and gas analyses. The advent of the space age stimulated the development of high-performance miniaturized instruments carried on sounding rockets, Earth satellites, and space probes. The techniques that were developed have been transferred to laboratory instrumentation. Among applications that have been made are the isotopic analysis of traces of mercury found in meteorites and the isotopic analysis of the helium extracted from small samples of extraterrestrial dust and from processed and native metals.

INTRODUCTION

Isotope analysis by mass spectroscopy had its practical beginning in the early 1930's, although measurements had been made before that time. Dempster (1918), after constructing the first magnetic deflection mass spectrometer, analyzed a number of elements, as did a few others who used instruments based on his design. Aston (1919), with his mass spectrograph, as he called it, and with later improved versions of the instrument, measured both masses and abundances of a large number of elements. Because Aston's abundances were determined from the blackening of photographic plates, the precision was not high. A few investigators, using thermal ionization for the production of ions, studied the isotopic constitution of elements such as lithium, potassium, and rubidium. Smythe and Mattauch (1932), by using a mass separator based on a radio-frequency filter array, studied the isotopic constitution of oxygen.

The development of techniques for making accurate isotopic analyses on a routine basis had to wait for two important innovations: (1) the invention of the electrometer tube and (2) the introduction of the transverse electron-beam ion source. The former, a vacuum tube having an extremely high input impedance, made possible the measurement of very small ion currents—below 10^{-16} A. It replaced the quadrant electrometer, whose operation was an art in itself. The transverse electron-beam ion source, introduced by Bleakney (1930, 1932), made possible the design of mass spectrometers having improved resolution and other desirable characteristics. The stage was set for measurement of precise isotopic abundances including, of course, variations in abundance ratios.

The mass spectrometers of the 1930's that were employed for measurement of isotopic abundances mainly used 180° magnetic deflection of the ions to create mass spectra. It was realized that by building larger instruments, higher resolution and better performance could be obtained. The ratio of energy spread of the ions leaving the ion source compared to the ion accelerating voltage would be reduced, as would the ratio of slit widths to the radius of curvature of the ion trajectories in the magnetic analyzers. As instruments grew so did their magnets, with the result that by 1940 successful isotopic analysis instruments employing 2-t magnets were in use. These were powered by 5-kW generators whose output voltages had to be stabilized by ingenious electronic devices.

A drastic reduction in the weight and power requirement of the electomagnet resulted when a principle published independently by Barber (1933) and Stephens (1934) made possible the construction of magnetic sector mass spectrometers (Nier, 1940). During World War II, many sector instruments were employed for measuring the enrichment achieved in the uranium isotope separation plants, for analyzing the process stream in the large gaseous diffusion plant in Oak Ridge, Tenn. (Nier and others, 1948), and for hunting vacuum leaks in such plants (Nier and others, 1947).

Following World War II, as scientists returned to civilian life, there was a surge of interest in mass spectrometry—particularly in the application of isotope studies to geological and cosmological problems. The do-it-yourself era of construction of mass spectrometers largely came to an end as commercial instruments became available, and mass spectrometers became tools available to many more investigators. As the drive for higher performance and precision grew, so did the size of the instruments. Ninety-degree magnetic sector mass spectrometers having radii of 30 cm became standard in many laboratories. In such instruments, the ion path length from ion source to collector exceeded 1 m.

An interesting modification of the sector geometry was proposed by Cross (1951). In this geometric configuration, the ions enter and leave the magnetic sector at a

Manuscripts approved for publication March 3, 1989.

[1] School of Physics and Astronomy, University of Minnesota, Minneapolis, MN 55455.

suitably chosen angle rather than at right angles as in the usual application, and one obtains higher dispersion as well as a desirable focusing of the individual beams in the z direction, perpendicular to the x-y plane of the trajectories. Successful commercial instruments have been built on the basis of this principle.

While the determination of isotopic abundances was proceeding, a parallel effort was being made in the measurement of precise isotopic masses. Here, much higher resolution and stability were required, and, as a result, the instruments were more complex. In a typical case, the ions, after leaving the source, traveled through an electric sector analyzer in tandem with a magnetic sector analyzer. The combination produced what is called double focusing and insured that ions of a given mass leaving the ion source with a spread in energy as well as angle would focus sharply at a single position along the focal plane. The single-focusing instruments previously described provide only angle focusing.

Among the double-focusing geometries employed in the pre-World War II era were those of Aston (1919), Dempster (1935), and Bainbridge and Jordan (1936). In these instruments, ions were detected by the blackening of photographic plates mounted along the focal planes. Through precise calibration, masses were related to position along the photographic plate. Such instruments were called mass *spectrographs* to distinguish them from mass *spectrometers*, where ions were detected electrically.

MINIATURIZED MASS SPECTROMETERS

When the space age arrived and rockets and space probes became available for conducting research in the Earth's upper atmosphere, or in the atmospheres of other planets, it was natural that mass spectrometry would be employed for studying the composition of atmospheric gases. In such investigations, in addition to magnetic deflection analyzers, a number of other mass analysis systems were successfully employed (Bennett, 1950; Paul and others, 1958).

Weight, physical size, and power consumption are of minor consequence in laboratory instrumentation, but in space applications, this is not the case. Instruments must be small, light, and consume a minimum of power. In addition, they must be rugged so they can withstand the severe vibrational environment encountered in rocket launches and maneuvers. These requirements must be met without too much degradation of the performance found in laboratory instrumentation.

For our laboratory investigations involving space flights, these factors led to the adoption of the Mattauch-Herzog geometry (Mattauch and Herzog, 1934), because it appeared best able to meet the requirements without seriously compromising performance and versatility. Figure 1

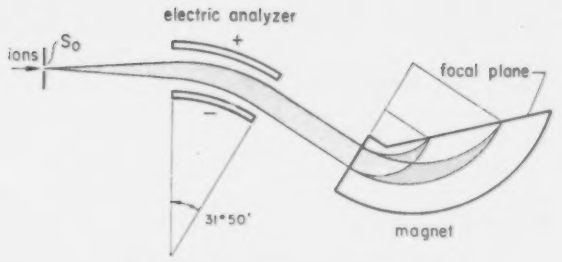

Figure 1. Schematic diagram showing the angular focusing properties of the Mattauch-Herzog double-focusing mass spectrometer. A diverging beam leaving the ion source through slit S_o, located at the focus of the electric sector analyzer, emerges from this sector as a parallel beam. In the magnetic analyzer, the trajectories are such that the parallel beam focuses on a focal plane, the position along the plane being proportional to the square root of the ratio of mass to charge of the ions. Ions having two different mass-to-charge ratios are shown for illustration. A beam leaving the ion source and having a spread in velocities (not shown here) also emerges from the electric analyzer as a parallel beam that, for a given mass-to-charge ratio, focuses at the same point as the ions that have an angular spread. Hence the expression double focusing. Convergence is to first order only. A diaphragm placed near the exit of the electric analyzer limits the angular and velocity spread sufficiently so that the first-order approximation pertains. At one point along the focal plane (and closely aprroximated for nearby points) second-order angular focusing exists (Johnson and Nier, 1953) and permits a larger angular spread than would otherwise be the case. It is this feature that provides sharper peaks (see figs. 4 through 8) and hence better effective resolution than found in conventional sector instruments.

is a schematic drawing showing the essential features of the Mattauch-Herzog geometry. Ions leave the ion source through a grounded defining slit, S_o, and pass between the plates of a cylindrical capacitor sector before entering the space between the poles of a magnet. Ions of different mass focus along a focal plane as shown. The existence of the well-defined focal plane lends itself to the use of multiple collectors for the simultaneous measurement of several masses of ions.

As in all magnetic deflection instruments, spectra can be swept by changing either the ion accelerating potential or the magnetic field. In the flight instruments, a permanent magnet was employed to conserve weight and power. The use of several collectors made it possible to cover an extended mass range without employing either excessively high or low ion accelerating potentials. In laboratory instruments, an electromagnet can be employed to give additional flexibility.

In the flight programs, several sizes of instruments were employed. The radii of curvature of the outermost ion beams used were 1 in (2.54 cm), 1.5 in (3.81 cm), and 2.5

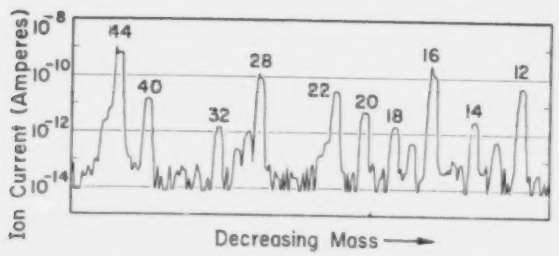

Figure 2. Mass spectrum of atmosphere obtained at an altitude of 135 km during the descent of the Viking Lander to the surface of Mars on July 20, 1976. From laboratory calibration of the instrument before the flight, the principal peaks are related to atmospheric species as follows: 44, CO_2; 40, Ar; 32, O_2; 28, CO_2 fragment, N_2, and CO; 22 and 20, doubly charged CO_2 and Ar, respectively; 18, residual instrument H_2O; 16, CO_2, CO and O_2 fragments, and O; 14, N_2 fragments; 12, CO_2 and CO fragments. Other smaller peaks are produced by species containing minor abundance isotopes. A careful analysis of the 30, 29, and 28 peaks led to the conclusion that NO was present and that the isotopic ratio for nitrogen is differerent than on the Earth (Nier and McElroy, 1977).

in (6.35 cm), depending on the resolution requirements and weight restrictions of the particular program.

Instruments based on this geometry were used in a number of rocket flights to the Earth's upper atmosphere, in the Atmosphere Explorer–C, –D, and –E satellites (Nier and others, 1973), in the Viking Mars Project (Nier and Hayden, 1971), the Pioneer-Venus program (von Zahn and others,1979), and in balloon flights to the Earth's stratosphere to study ozone and other minor constituents (Mauersberger and Finstad, 1979; Murphy and Mauersberger, 1985).

Figure 2 shows the mass spectrum of the Martian atmosphere obtained as the first Viking Lander spacecraft descended to the surface of the planet on July 20, 1976 (Nier and others, 1976a). The resolution was rather low because of the small size of the instrument and the fact that the slits had been made relatively wide to insure stability in the measurements (the cruise to Mars took 10 months, and the instrument had to be released for integration in the spacecraft some months before launch). In spite of the relative crudeness of the measurements, some significant discoveries were made. The composition of the atmosphere was studied, and the amounts of Ar, N_2, O_2, CO, and NO were determined quantitatively in the presence of the much more abundant CO_2. Carbon and oxygen were shown to have isotopic constitutions similar to terrestrial constitutions. A careful analysis of the spectrum gave convincing evidence that the $^{15}N/^{14}N$ ratio in the Martian atmosphere is approximately 60 percent higher than in the Earth's atmosphere, an observation which may provide important clues about the history of the planet's atmosphere (Nier and others,1976b ; McElroy and others, 1976; Nier and McElroy, 1977).

LABORATORY APPLICATIONS OF MINIATURIZED MASS SPECTROMETERS

It became obvious that techniques learned in building high-performance miniaturized instruments for flight would also be applicable to laboratory investigations. Application of the techniques led to the development of a versatile high-performance laboratory instrument suitable for precise isotope and gas analyses.

A schematic drawing of a somewhat larger laboratory instrument having an outermost radius of 3.75 in (9.53 cm) (Nier and Schlutter, 1985) and employing an electron bombardment ion source is shown in figure 3. It was initially designed primarily for the study of $^3He/^4He$ ratios in the low parts per million range but has been used for other isotopic investigations as well. The collector slits are spaced for collecting masses 2, 3, and 4 simultaneously. For the $^3He/^4He$ measurements, the mass 4 collector has a relatively wide slit, and an electrometer amplifier is used for measuring the ^4He ion current. The mass 3 ion collector slit is relatively narrow so that it can resolve ^3He from HD and H_3. For this collector, an ion-counting electron multiplier is employed.

Figure 4 is a mass spectrum for xenon obtained with the instrument shown in figure 3. The intermediate collector was employed in this case. It is interesting to note that the valleys between the peaks, when compared to the peaks, are down by four orders of magnitude. The small peaks in the odd mass positions are the result of hydrocarbon impurities that were present at the time the spectrum was run.

For a different research program, an instrument was constructed that employed a thermal ion source rather than the electron bombardment source shown in figure 3. It was used for isotopic studies of neodymium (Nier and others, 1983). A typical spectrum is shown in figure 5. The "tailing" of peaks was so small that, for all practical purposes, interference between adjacent peaks was negligible.

Because the instruments can be thoroughly baked, have a relatively small internal surface and volume, and employ gold wire gaskets, inleakage is negligible and outgassing is low. The instruments can thus be used in the static mode and are ideal for the analysis of small gas samples. Two examples follow.

Isotope Analysis of Small Samples of Mercury

Neutron activation experiments performed on Allende and several other meteorites (Jovanovic and Reed,

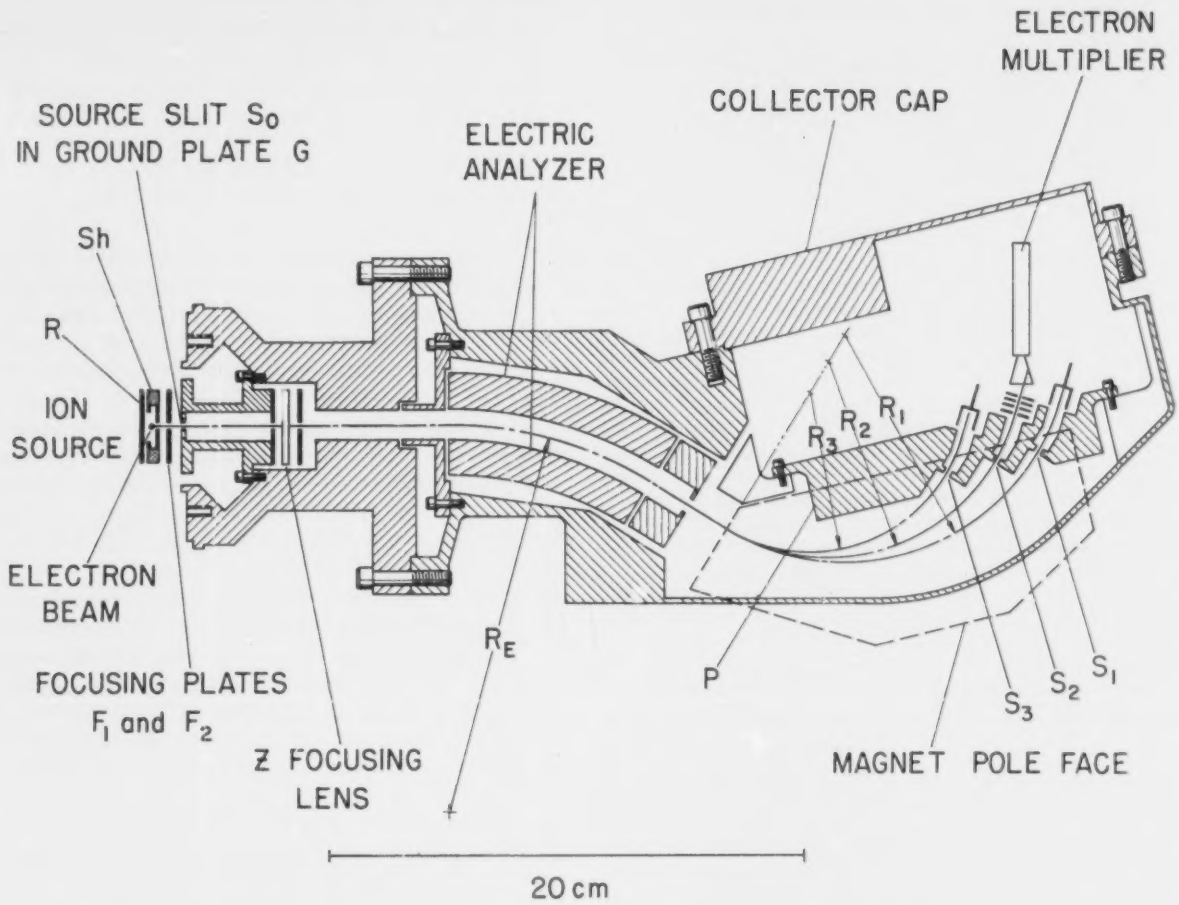

Figure 3. Cross-sectional schematic of prototype laboratory instrument (Nier and Schlutter, 1985) similar to that employed for most of the present research. In the prototype instrument, R_E, R_1, R_2, and R_3 were 16.03, 9.53, 8.25, and 6.74 cm, respectively. Slits S_0, S_1, S_2, and S_3 had widths of 0.0076, 0.051, 0.013, and 0.051 cm, respectively. The perfect second-order focusing occurs for the ions reaching the outermost collector. In the present version of the instrument, the outer collector is used for most of the measurements for which high resolution is required, and slits S_1 and S_2 have widths of 0.015 and 0.051 cm, respectively. R, repeller; Sh, shield; P, plate for holding exit slits and collector assemblies.

1976a,b) suggested that the $^{196}Hg/^{202}Hg$ abundance ratio in the mercury found in some meteorites may be anomalous. An attempt to verify this effect was made by extracting the mercury from samples of the Allende meteorite, purifying it, and introducing it into an instrument such as shown in figure 3, operated in the static mode (Nier and Schlutter, 1986). Figure 6 shows the mass spectrum obtained when 12 ng (1.3×10^{-6} cm^3 at STP) of normal laboratory mercury are introduced. Note that the ion currents for the principal isotopes are of the order of 10^4 ions per second.

As is to be expected, the peaks drop with time because the mercury is absorbed on the gaskets and probably on the very clean surfaces of the walls of the instrument housing. Since measurements are made by peak stepping and the data are fed into a computer, allowance can be made for the decay of the peaks with time when the isotope ratios are calculated. "Memory" (cross-contamination that is due to desorption) between samples was a matter of some concern. Through the use of mercury having a drastically different isotopic composition, it was demonstrated that, with the baking techniques used between samples, memory was not a problem.

The mass spectrometric measurements did not confirm anomalous mercury isotopic abundances in the meteorite studied. The reason for this apparent contradiction is not clear but could be that an error occurred in the neutron activation experiments of Jovanovic and Reed (1976a,b). Another possible explanation may be found in the difference in mercury extraction techniques used in the two methods of analysis.

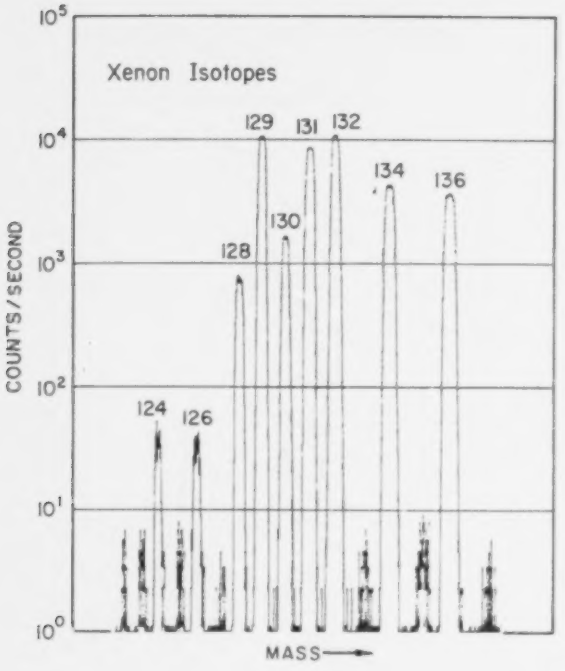

Figure 4. Mass spectrum of commercial atmospheric xenon obtained with the prototype instrument shown in figure 3. Individual ions were counted by an electron multiplier, and the count rate is plotted on a logarithmic scale.

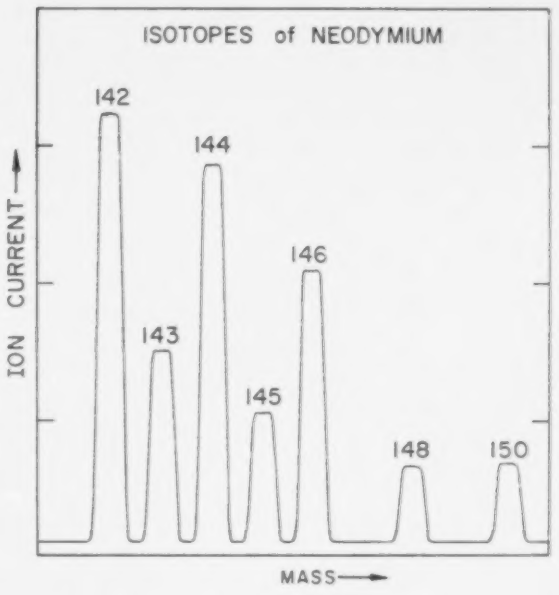

Figure 5. Typical mass spectrum for normal neodymium obtained with a modified instrument having a thermal ion source in place of the electron bombardment source shown in figure 3. In this case, the slits S_0 and S_1 were 0.0076 and 0.023 cm, respectively, and a vibrating reed electrometer was employed for measuring the ion currents that are plotted on a linear scale with arbitrary units.

Helium in Extraterrestrial Dust Particles

Helium extracted from particles found in the deep Pacific has been observed to have a $^3He/^4He$ ratio of 10^{-4}, or more, as contrasted with 1.4×10^{-6} for normal atmospheric helium (Merrihue, 1964; Amari and Ozima, 1985; Fukumoto and others, 1986). This information, together with other evidence, has led to the assumption that the particles are of extraterrestrial origin. The precise reason for the anomaly is not clear and has been attributed to the solar wind or solar flare bombardment of particles in the interplanetary medium, to spallation by cosmic rays, or to the possibility that it is of primordial origin.

Rajan and others (1977) examined single stratospheric particles of mass in the low nanogram range and showed they contained ^4He. Their experiments could not measure ^3He. Determination of the isotopic ratio of ^3He to ^4He for such particles appeared to be an appropriate task for the instrument described in the present paper. With the slit widths and operating conditions chosen for the work described here, the sensitivity in the static mode of operation was such that 3×10^6 atoms of helium were required to produce a count rate of 1 count per second at the output of the ion counting system. The background counting rate, at positions in the spectrum where ions are not expected, is typically less than 0.005 counts per second. To gain experience in working with small samples, experiments were carried out with single grains of lunar soil as well as deep Pacific magnetic fines.

A small square (approximately $5 \times 5 \times 0.025$ mm) of previously outgassed tantalum foil was folded around the material to be tested and mounted in a manifold attached to the mass spectrometer. The foil was heated by passing an electric current directly through it. Temperatures of up to 1600 °C were employed. The gas released was passed through two liquid-nitrogen-cooled charcoal traps in tandem before it was admitted to the mass spectrometer. The mass spectrometer had attached to it an additional charcoal trap as well as a liquid-nitrogen-cooled cell, on the wall of which a fresh film of titanium had been evaporated to reduce the hydrogen background in the instrument. While the mass spectrometer separates ^3He from HD, it is obviously advantageous to reduce the HD peak as much as possible.

In the course of the work, it was found that in running instrument blanks (that is, heating the foil and the electrical attachment leads without a sample), the small amount of helium released sometimes had a higher $^3He/^4He$ ratio than found in atmospheric helium. H. Craig (personal commun.,

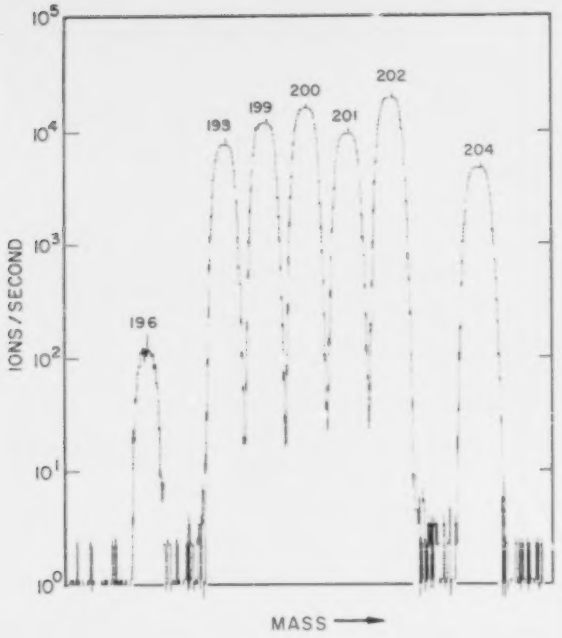

Figure 6. Mass spectrum of normal laboratory mercury.

1988) reports that he and colleagues observed high $^3He/^4He$ in tantalum used for extraction furnaces. They attributed the effect to tritium diffusion studies in metals which were subsequently reprocessed and sold by distributors. Mamyrin and Tolstikhin (1984) reported a similar effect.

Our observation led to a study of the helium content of various metals, including specimens of native metals. It was found that many of the common metals used in the construction of apparatus exhibited anomalous $^3He/^4He$ ratios in the helium released upon heating. The same was true of samples of some native metals. Figure 7 shows the spectrum for the mass 3 region for a 2.8-mg sample from the surface of a piece of native copper from the upper peninsula of Michigan. Here the $^3He/^4He$ ratio is unusually high—4.2×10^{-3}. Other small samples from the same piece did not show the effect. A random study of milligram-sized samples removed from larger specimens of other native metals such as gold, $FeNi_3$, and iron also showed anomalies in the helium isotopic ratio in some cases. At present, we do not have a good explanation for the phenomenon. It has been surmised that in the case of the native metals this anomaly may be due to the diffusion of hydrogen into metal and the subsequent decay of its tritium into ^3He that is trapped. Effects of cosmic rays, such as observed by Kurz (1986) and Craig and Poreda (1986), might also be responsible. ^3He could be much more abundant in the Earth than is generally appreciated. Clearly, it is an interesting subject worthy of more systematic investigation.

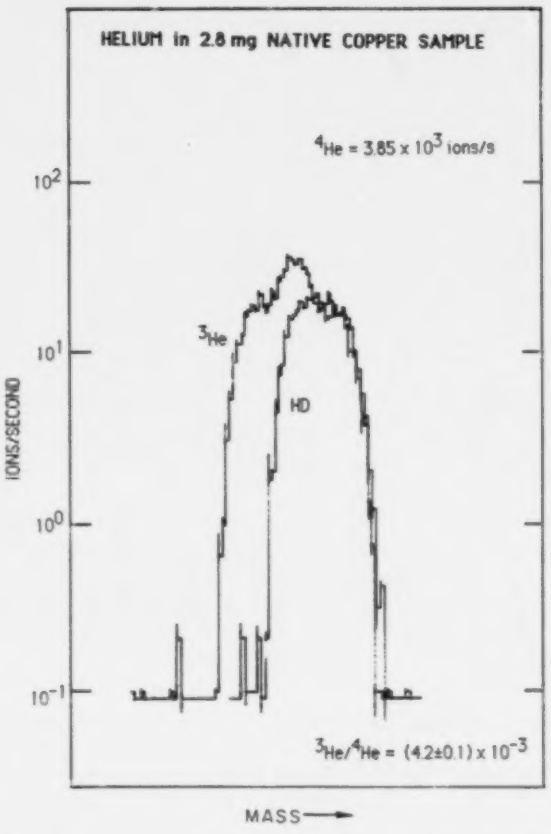

Figure 7. Mass spectrum of mass 3 region showing ^3He extracted from a sample of native copper along with the residual HD in the instrument. Superimposed is the spectrum remaining when the helium is pumped away. Ten-second integrations were used in obtaining data points.

For comparison, figure 8 shows the spectrum obtained for the mass 3 region for the helium extracted from 1.5×10^{-3} cm^3 at STP of air. The ^3He in this amount of air is approximately 10^{-14} cm^3 at STP. The instrument blank accounts for approximately one-third of the ^3He peak. When correction is made for this residual, the calculated $^3He/^4He$ is $(1.6\pm0.4)\times10^{-6}$, in excellent agreement, considering the small size of the sample, with 1.4×10^{-6}, the accepted value for the ratio. The amount of air used in the test was deliberately chosen to be small so that the ^3He would be comparable to the amount that is seen in some of the smallest samples used in our investigations.

SUMMARY

The availability of rockets and other space vehicles stimulated the development of high-performance, miniaturized mass spectrometers for the study of the composition of the Earth's upper atmosphere and the atmospheres of other

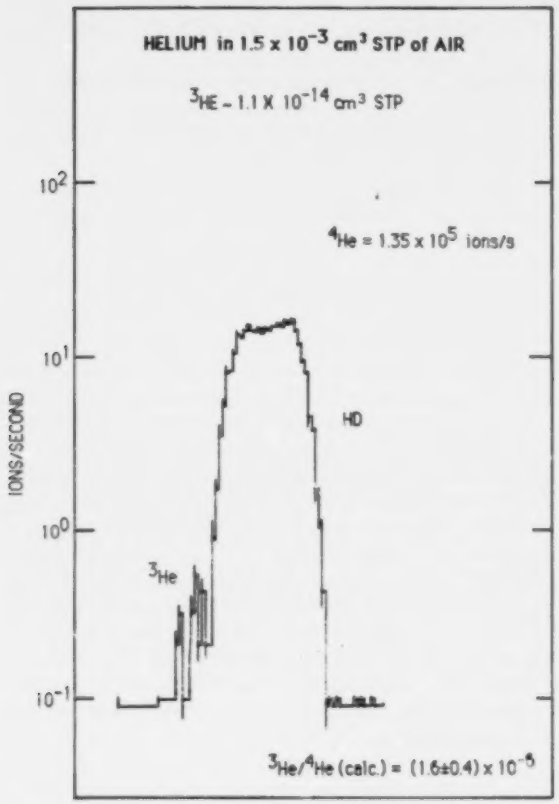

Figure 8. Mass spectrum of mass 3 region showing ^{3}He together with the residual HD in the mass spectrometer after the helium extracted from 10^{-3} cm^3 of air at STP is introduced. In practice, a spectrum such as this is used only for illustration. In making ^{3}He/^{4}He determinations on small samples, many readings are obtained at the ^{3}He mass "position" to average out statistical fluctuations that appear in the counting rates of single determinations. Blanks are always run, and peak shapes are carefully studied. With the slits employed in the present work, the HD contribution at the ^{3}He position is less than 1 percent of the height of the HD peak. Over many months of running, the peak shapes have been found to be remarkably reproducible. If narrower slits were employed, the ^{3}He and HD would naturally be better resolved, but at the expense of sensitivity and "flatness" of peak tops. In view of the high stability and reproducibility of the apparatus in its present form, we felt that from the standpoint of ultimate accuracy, retaining sensitivity and flat-top peaks was more important than having sharp peaks with valleys between them.

planets. The technology that evolved is transferable to laboratory instrumentation and has particular application to analysis of small samples. High-performance, miniaturized mass spectrometers are capable of making precision measurements of isotope abundances. The small volume and surface area insure high sensitivity with a minimum of residual background. An instrument employing the Mattauch-Herzog geometry, with a radius of 9.53 cm in the magnetic field, had a sensitivity sufficient to detect less than 10^{-14} cm^3 at STP of ^{3}He in the presence of a much larger HD instrument residual from which it was resolved. The mass spectrometer is applicable to isotopic studies as diverse as those of the helium in cosmic dust particles or of traces of mercury in meteorites.

ACKNOWLEDGMENTS

The instrument used in the investigation was made possible by grants from the Planetary Atmosphere Program of the National Aeronautics and Space Administration (NASA) and from the Geochemistry Program of the National Science Foundation (NSF). The research itself was supported by a grant from the Planetary Materials and Geochemistry Program of NASA. I am indebted to my associate, Dennis Schlutter, for some of the measurements reported here and to Dr. E.J. Olsen of the Field Museum of Natural History of Chicago for samples of native metals used in the research. Samples of the Allende meteorite used for the mercury studies were kindly provided by Dr. George Reed of the Argonne National Laboratory.

REFERENCES CITED

Amari, S., and Ozima, M., 1985, Search for the origin of exotic helium in deep-sea sediments: Nature, v. 317, p. 520–522.

Aston, F.W., 1919, A positive ray spectrograph: Philosophical Magazine, v. 38, p. 707–714.

Bainbridge, K.T., and Jordan, E.B., 1936, Mass spectrum analysis: Physical Review, v. 50, p. 282–296.

Barber, N.F., 1933, Note on the shape of an electron beam bent in a magnetic field: Leeds Philosophical and Literary Society Proceedings, v. 2, p. 427–434.

Bennett, W.H., 1950, Radiofrequency mass spectrometer: Journal of Applied Physics, v. 21, p. 143–149.

Bleakney, W., 1930, Probability and critical potentials for the formation of multiply-charged ions in mercury vapor by electron impact: Physical Review, v. 35, p. 139–148.

———1932, The ionization potential of molecular hydrogen: Physical Review, v. 40, p. 496–501.

Craig, H., and Poreda, R.J., 1986, Cosmogenic ^{3}He in terrestrial rocks: The summit lavas of Maui: Proceedings of the National Academy of Sciences, v. 83, p. 1970–1974.

Cross, W.G., 1951, Two-directional focusing of charged particles with a sector-shaped, uniform magnetic field: Review of Scientific Instruments, v. 22, p. 717–722.

Dempster, A.J., 1918, A new method of positive ray analysis: Physical Review, v. 11, p. 316–325.

———1935, New methods in mass spectroscopy: Proceedings of the American Philosophical Society, v. 75, p. 755–767.

Fukumoto, H., Nagao, K., and Matsuda, J., 1986, Noble gas studies on the host phase of high ^{3}He/^{4}He ratios in deep-sea

sediments: Geochimica et Cosmochimica Acta, v. 50, p. 2245–2253.

Johnson, E.G., and Nier, A.O., 1953, Angular aberrations in sector shaped electromagnetic lenses for focusing beams of charged particles: Physical Review, v. 91, p. 10–17.

Jovanovic, S., and Reed, G.W., 1976a, ^{196}Hg and ^{202}Hg isotopic ratios in chondrites: Revisited: Earth and Planetary Science Letters, v. 31, p. 95–100.

———1976b, Interrelations among isotopically anomalous mercury fractions from meteorites and possible cosmological inferences: Science, v. 193, p. 888–891.

Kurz, M.D.,1986, Cosmogenic helium in a terrestrial igneous rock: Nature, v. 320, p. 435–439.

Mamyrin, A., and Tolstikhin, I.N., 1984, Helium isotopes in nature: Amsterdam, Elsevier, p. 15.

Mattauch, J., and Herzog, R., 1934, Uber einen neuen Massenspektrographen: Zeitschrift für Physik, v. 89, p. 786–795.

Mauersberger, K., and Finstad, R., 1979, Further laboratory studies and stratospheric flight of a mass spectrometer beam system: Review of Scientific Instruments, v. 50, p. 1612–1617.

McElroy, M.B., Yung, Y.L., and Nier, A.O., 1976, Isotopic composition of nitrogen: Implications for the past history of Mars' atmosphere: Science, v. 194, p. 70–72.

Merrihue, C., 1964, Rare gas evidence for cosmic dust in modern Pacific red clay: Annals of the New York Academy of Sciences, v. 119, p. 351–367

Murphy, D.M., and Mauersberger, K., 1985, Operation of a microchannel plate counting system in a mass spectrometer: Review of Scientific Instruments, v. 56, p. 220–226.

Nier, A.O., 1940, A mass spectrometer for routine isotope abundance measurements: Review of Scientific Instruments, v. 11, p. 212–216.

Nier, A.O., and Hayden, J.L., 1971, A miniature Mattauch-Herzog mass spectrometer for the investigation of planetary atmospheres: International Journal of Mass Spectrometry and Ion Processes, v. 6, p. 339–346.

Nier, A.O., and McElroy, M.B., 1977, Composition and structure of Mars' upper atmosphere: Results from the neutral mass spectrometers on Viking 1 and 2: Journal of Geophysical Research, v. 82, p. 4341–4349.

Nier, A.O., and Schlutter, D.J., 1985, High-performance double-focusing mass spectrometer: Review of Scientific Instruments, v. 56, p. 214–219.

———1986, Mass spectrometric study of the mercury isotopes in the Allende meteorite: Proceedings of the 17th Lunar and Planetary Science Conference, pt. 1, Journal of Geophysical Research, v. 91, p. E124–E128.

Nier, A.O., Stevens, C.M., Hustrulid, A., and Abbott, T.A., 1947, Mass spectrometer for leak detection: Journal of Applied Physics, v. 18, p. 30–33.

Nier, A.O., Abbott, T.A., Pickard, J.K., Leland, W.T., Taylor, T.I., Stevens, C.M., Drukey, D.L., and Goertzel, G., 1948, Recording mass spectrometer for process analysis: Analytical Chemistry, v. 20, p. 188–192.

Nier, A.O., Potter, W.E., Hickman, D.R., and Mauersberger, K., 1973, The open-source neutral mass spectrometer on Atmosphere Explorer-C, -D, and -E : Radio Science, v. 8, p. 271–276.

Nier, A.O., Hanson, W.B., Seiff, A., McElroy, M.B., Spencer, N.W., Duckett, R.J., Knight, T.C.D., and Cook, W.S., 1976a, Composition and structure of the Martian atmosphere: Science, v. 193, p. 786–788.

Nier, A.O., McElroy, M.B., and Yung, Y.L., 1976b, Isotopic composition of the Martian atmosphere: Science, v. 194, p. 68–70.

Nier, A.O., Murthy, V.R., and Dosso, L., 1983, Minmass: A small double focusing mass spectrometer for geochemical research: EOS, Transactions of the American Geophysical Union, v. 64., p. 334.

Paul, W., Reinhard, H.P., and von Zahn, U., 1958, Das Elektrische Massenfilter als Massenspektrometer und Isotopentrenner: Zeitschrift für Physik, v. 152, p. 143–182.

Rajan, R.S., Brownlee, D.E., Tomandl, D., Hodge, P.W., Farrar, H., and Britten, R.A., 1977, Detection of ^{3}He in stratospheric particles gives evidence of extraterrestrial origin: Nature, v. 267, p. 133–134.

Smythe, W.R., and Mattauch, J., 1932, A new mass spectrometer: Physical Review, v. 40, p. 429–433.

Stephens, W.E., 1934, Magnetic refocussing of electron paths: Physical Review, v. 45, p. 513–518.

von Zahn, U., Krankowsky, D., Mauersberger, K., Nier, A.O., and Hunten, D.M., 1979, Venus thermosphere: In situ composition measurements, the temperature profile, and the homopause altitude: Science, v. 203, p. 768–769.

Carbon Isotopic Analysis Of Small Samples by Use of Stepped-Heating Extraction and Static Mass Spectrometry

By I.P. Wright[1] *and* C.T. Pillinger[1]

Abstract

Highly sensitive static-vacuum mass spectrometry has been developed for the determination of the stable isotopic compositions of extremely small samples of gaseous carbon-bearing species. The small sample capability of instruments of this type complements extraction procedures that are able to produce small amounts of unionized material in an appropriate gaseous form (which in the case of carbon is CO_2). One such technique is stepped heating, which can be performed either under vacuum conditions (pyrolysis) or in the presence of pure oxygen (combustion). Stepped pyrolyses are used to liberate trapped CO_2 gas, while stepped combustion enables carbonaceous components of different sorts to be separated according to the temperature at which the material is oxidized to form CO_2 gas. In order to obtain the most useful information from stepped-heating experiments, it is necessary to appreciate some of the problems that can arise either during the experiment or during interpretation of the results. These problems are discussed at some length and include (1) the practical difficulties associated with the use of pyrolyses for carbonaceous samples, (2) dependence of the combustion temperature on the grain size of diamond and on the C/H ratio of organic materials, (3) the effect of oxygen pressure or sample size (that is, the O/C ratio) on the nature of the release profile, (4) the use of repeat combustions at specific temperature steps to ensure more complete resolution of two components, (5) problems associated with the use of equal and unequal temperature increments and the implementation of a normalization procedure to correct for unequal step sizes, and (6) the effects of poor control of temperature and (or) time during the experiment, for which a simple mathematical procedure is presented that can be used to diminish the resultant artifacts in the acquired stepped-heating profile. The data acquired from the analyses of meteorite samples are used to demonstrate some of the techniques that can be used during interpretation of stepped-heating results.

INTRODUCTION

Measurement of carbon stable isotopic compositions of samples of geological interest has the potential to provide information about the source of the constituents (for example, in sedimentary geochemical studies) and has at least limited utility in determining temperatures of formation (for example, from an appraisal of carbon isotopic fractionation between (1) CO_2 and CH_4 in well gases and (2) calcite and graphite in metamorphic rocks). Carbon isotopic studies have been applied to all areas of geology, including research on igneous, sedimentary, and metamorphic rocks, ore deposits, oil and gas reserves, and oceanography (Faure, 1986; Valley and others, 1986; Hoefs, 1987; Kyser, 1987). In addition, the carbon isotopic compositions of various extraterrestrial materials have been studied extensively in order to improve the understanding of pre-, syn-, and postsolar system formational processes (Pillinger, 1984; Kerridge, 1985).

Conventionally, carbon isotopic measurements are made by converting the sample of interest to CO_2 gas, prior to determination by dynamic mass spectrometry. (See figure 1. The instrument, which is continuously pumped, is referred to as dynamic because sample and reference gases alternately enter the mass spectrometer by viscous flow.) The isotopic composition of the sample gas is calculated as a $\delta^{13}C$ value (Craig, 1957) relative to an internationally recognized standard known as PDB (Peedee belemnite), the difference being expressed as parts per thousand (per mil, ‰) Some geological studies might require highly precise $\delta^{13}C$ values (±0.1 to ±0.05 ‰), but, on the other hand, many interesting studies can be carried out successfully with somewhat larger errors (<±1 ‰). Up until about 1983, carbon isotopic measurements of the desired precision were made by use of dynamic gas-source mass spectrometers of the type pioneered in the late 1940's (Nier, 1947; McKinney and others, 1950). However, even with the advent of improved commercial equipment, it was still necessary to use microgram amounts of carbon for isotopic analyses. This requirement proved to be prohibitive for some studies, and thus from the early 1970's onward, many studies were devoted to exploring ways of decreasing sample size requirements. One technique uses a variant of a noble-gas-type mass spectrometer. (See figure 2. The instrument, referred to as static, differs from the dynamic version in that it is not pumped during the analysis.) By 1983, the first carbon isotopic studies were undertaken by use of static mass spectrometry: these initially concentrated on isotopically anomalous materials in meteorites (Carr and

[1] Planetary Sciences Unit, Department of Earth Sciences, The Open University, Walton Hall, Milton Keynes, MK7 6AA, England.

Table 1. Some attempts to make small-sample $\delta^{13}C$ measurements

Reference	Size (nanomole)	$\delta^{13}C$ (‰)	Comments
Bridger and others, 1974	300	±0.1	Conventional dynamic mass spectrometry.
Schoeller and Hayes, 1975	25	±.5	Computer control, ion-counting, He dilution.
Matthews and Hayes, 1978	20	±5	Gas chromatography–mass spectrometry.
Fallick and others, 1980	1	±2	Static mass spectrometry (CD_4).
Wada and others, 1982	45	±.04	Conventional mass spectrometry.
Halas and Krouse, 1983	50	±.2	Variation of flow injection.
Swart and others, 1983b	8	±10	Gas mixing ("isotope dilution").
Wright and others, 1983	1	±.25	Static mass spectrometry (CD_4).
Carr and others, 1986	1	±1	Static mass spectrometry (CO_2).
Zinner and Epstein, 1987	~.00001	±10	Ion probe.
Prosser and others, 1988	.001	±2.5	Static mass spectrometry (CO_2).

others, 1983), and so the high levels of precision alluded to above were not needed. The technique rapidly improved and by 1984 was applied to problems of terrestrial geochemistry where precisions of ±1 ‰ or better were necessary (Mattey and others, 1984). The instrument and extraction system have subsequently evolved to the point where they have become a facility that can be used routinely for a wide variety of investigations.

One method able to provide small quantities of CO_2 for analysis by static mass spectrometry is laser-probe extraction. The potential of this technique was originally demonstrated for isotopic analyses of noble gases by Megrue (1967). Subsequently, laser probes have been used for extracting light elements in the form of CO_2, H_2O, SO_2, N_2, and such (Norris and others, 1981; Shankai and others, 1984; Franchi and others, 1985; Sommer and others, 1985; Jones and others, 1986). Franchi and others (1986; this volume) have described a laser-probe system capable of making isotopic determinations of carbon, oxygen, and nitrogen by use of static mass spectrometry. The technique, which offers the chance to make isotopic measurements of solid target materials at spatial resolutions of about 50 μm, is successful because extremely low blanks can be obtained. It is highly probable that analytical instrumentation of this type will play a significant role in future light-element studies. However, there are a number of problems that need to be solved (Franchi and others, 1986; this volume) before laser-probe extraction becomes a routine procedure for light-element isotopic analyses.

A more generally applicable technique for preparing carbon for analysis by static mass spectrometry is one of stepped heating, either in vacuo (stepped pyrolysis), or in an atmosphere of pure oxygen (stepped combustion). Despite their apparent simplicity, these procedures are less than straightforward and require a certain amount of skill and experience in order to produce high-quality data. For this reason, a detailed account of some of the problems associated with stepped heating is given herein.

SMALL-SAMPLE ANALYSIS FOR CARBON

Over the years, numerous attempts have been made to determine the isotopic composition of progressively smaller amounts of carbon. Most efforts have generally involved modification of existing equipment; table 1 shows the sample sizes and precisions in $\delta^{13}C$ obtained by these techniques. Additional studies, which have described either modifications to instruments or attempts to fully understand instrumental effects, with a view to improving precision or decreasing sample size requirements, are given by Shackleton (1965), Deines (1970), Coplen (1973), Mook and Grootes (1973), Fallick and Baxter (1977), and Fallick (1980; 1983).

Prior to the advent of commercially available mass spectrometers, instruments such as that described by Nier (1947), and subsequently modified by McKinney and others (1950), were able to measure $\delta^{13}C$ to precisions of ±0.1 ‰ on samples of about 0.4×10^{-3} mol of carbon (McCrea, 1950). By the early 1970's, instrument companies were producing equipment able to perform $\delta^{13}C$ measurements to ±0.1 ‰ on 0.3×10^{-6} mol of carbon (Bridger and others, 1974), but they were very infrequently operated at this level of sensitivity. The smallest samples that commercial mass spectrometers can accommodate have remained at about this level, although precision has improved (±0.02 ‰, Brunnée and others, 1977).

Schoeller and Hayes (1975) and Hayes and others (1978) describe a technique that utilized a single collector, gas-source, dynamic mass spectrometer fitted with a pulse-counting electron multiplier to increase sensitivity. The three ion beams (produced from CO_2) were focused sequentially onto the detector, by computer control of the accelerating voltage (this in itself was an innovation at the time). In order to prevent isotopic fractionation of the small amounts of CO_2, the gas was diluted with helium. This action ensured preservation of high pressures in the inlet and thus viscous flow through the capillaries into the mass spectrometer. Isotopic values to a precision of ±0.5 ‰ were obtained on samples of about 25×10^{-9} mol of CO_2,

although measurement times of an hour were needed. Analyses of smaller samples (8×10^{-9} mol) were possible, although without correspondingly increased measurement times, levels of precision became somewhat poorer. Des Marais (1978, 1983) successfully applied the helium-dilution technique to the analysis of small amounts of carbon from lunar samples.

Using a combination of gas chromatography and mass spectrometry, Matthews and Hayes (1978; 1979) demonstrated the potential of this arrangement to analyze samples of CO_2 as small as 20×10^{-9} mol. By tuning the single-collector mass spectrometer to monitor selectively the masses of interest, they obtained precisions of ±5 ‰, a level considered adequate for the isotopic-labeling studies that were undertaken by use of the equipment.

Undoubtedly, it is possible to use conventional instrumentation to determine carbon and oxygen isotopic compositions of samples smaller than the manufacturers recommend. Indeed, in this laboratory, by use of the SIRA 24 mass spectrometer (V.G. Isogas, Winsford, U.K.) it has proved possible to make $\delta^{13}C$ measurements on samples as small as 20×10^{-9} mol of CO_2, with acceptable levels of precision (±0.5 ‰). Wada and others (1982), using modified proprietary equipment (MAT–250, Finnigan, Bremen, West Germany), claim to be able to make $\delta^{13}C$ measurements to precisions of ±0.04 ‰ on samples as small as 45×10^{-9} mol of CO_2. This claim has been substantiated by a study of microzoning in $\delta^{13}C$ of graphite and calcite isolated from marble by a combination of microtome cutting and exfoliation procedures (Wada, 1988). However, in the conventional system, pressures of sample and reference gases need accurate balancing, a procedure which, while not difficult, is time consuming if the instrument has been set up to perform automatic analyses of normal-sized samples. In addition, the effects of any contaminant gases become increasingly significant with smaller samples, so it is extremely important to produce samples of the highest purity. Failure to control such factors conspires to produce spurious $\delta^{13}C$ values. From experience of ultrasmall sample analysis in which dynamic mass spectrometry is used, reliable results are generally obtained only when pure CO_2 is produced and a limited range in $\delta^{13}C$ values can be anticipated (erroneous values can thereby be identified). This situation arises, for instance, in carbonate analyses. The use of commercially available equipment for ultrasmall-sample analyses of complicated samples (organic materials) or complete unknowns (some extraterrestrial materials) seems unwise at present.

To avoid the problems of admitting extremely small quantities of CO_2 into a dynamic mass spectrometer, Swart and others (1983b) utilized a technique of gas mixing (described fully in Wright and others, 1984). The procedure, which was developed for elucidating the nature of isotopically unusual carbon-bearing materials in meteorites ($\delta^{13}C$ up to +1,100 ‰), involved mixing small amounts of the ^{13}C-rich sample gas with larger quantities of isotopically normal reference gas in the inlet of a conventional dynamic mass spectrometer. The resultant gas mixture, which may have been up to 10 times the size of the original sample, was then admitted to the mass spectrometer and analyzed in the normal way. It was possible to calculate $\delta^{13}C$ of the sample (albeit with errors of approximately ±10 ‰, which was adequate for the meteorite investigation) because the relative amounts of sample and reference gases, the $\delta^{13}C$ of the reference gas, and the measured $\delta^{13}C$ value of the mixed gases were known.

Halas and Krouse (1983) and Halas (1985) used a system whereby CO_2 sample gas was transferred into a capillary close to the ion source of a normal dynamic mass spectrometer and subsequently forced into the instrument by a second ("pusher") gas. The technique is similar in some respects to flow-injection analysis used in gas chromatography (Stewart, 1981) and proceeds by the sample gas becoming compressed to the same pressure as the pusher gas. At high pressures in the capillary, mixing is limited to the very interface of the two gases, and so a column of sample gas (considerably longer than wide) is slowly forced into the mass spectrometer. In using this technique, all of the sample gas is admitted to the instrument for analysis. Halas and Krouse tested a variety of pusher gases, with the most suitable arrangement for carbon analyses being the use of reference CO_2 to force sample CO_2 into the mass spectrometer. In theory, $\delta^{13}C$ measurements can be made by a comparison of ion-beam intensity ratios recorded from the sample gas, with those from the reference gas flowing through the same inlet some time later. Precisions of about ±0.2 ‰ are possible on samples as small as 50×10^{-9} mol of carbon.

The static mass spectrometers and associated gas-handling systems developed by Fallick and others (1980), Wright and others (1983), Carr and others (1986), and Prosser and others (1988) have been used extensively for small-sample analyses. The most successful carbon instrument constructed thus far, that described by Carr and others (1986), has to date performed around 7,500 individual isotopic analyses and has the capability to routinely determine $\delta^{13}C$ of nanomole samples of carbon with precisions of $<\pm1$ ‰ (samples as small as 40×10^{-12} mol can be determined with somewhat larger errors of ±10 ‰).

The ion probe has great potential in the analysis of extremely small amounts of carbon in solid specimens (grains, polished sections, and such) at high spatial resolution (~1 μm). Thus far, this device has been used to make $\delta^{13}C$ measurements only of extremely small grains extracted from meteorites (Niederer and others, 1985; Zinner and Epstein, 1987; Zinner and others, 1987). Precisions in $\delta^{13}C$ for isotopically anomalous meteoritic materials range from ±10 to ±140 ‰ (Zinner and Epstein, 1987), but it should be possible under optimum conditions to achieve ±3 ‰.

STATIC MASS SPECTROMETRY

History of Development for Stable Isotopic Analyses of Active Gases

The concept of static mass spectrometry as a highly sensitive method of making isotopic measurements of gaseous species was first demonstrated by Reynolds (1956) for noble-gas analysis, although somewhat earlier, Aldrich and Nier (1948) had used a more complicated approach for $^3He/^4He$ measurement, whereby the gas removed by pumping from a dynamic mass spectrometer was recycled. Further developments in noble-gas static mass spectrometry have been documented by, among others, Schaeffer and Zähringer (1958), Merrill (1974), Clarke and others (1976), Hohenberg (1980), and Stacey and others (1981). Such instruments are used routinely in most investigations of noble-gas geochemistry (Böhlke and others, this volume) and potassium-argon and $^{40}Ar/^{39}Ar$ geochronology (Dalrymple, this volume).

The potential for a static mass spectrometer to carry out quantitative measurements of active gases was first investigated by Irako and others (1975) and independently by Gardiner and others (1978) and Gardiner and Pillinger (1979). The instrument used in the study of Irako and others was an all-glass mass spectrometer equipped with a Faraday cup detector. Two different ionization sources were appraised: a hot filament (conventional electron impact) and a cold cathode discharge. Irako and others (1975) demonstrated that N_2, CO, and CH_4 could be analyzed by use of a hot filament for ionization but that H_2, O_2, and CO_2 were too unstable under such conditions, and the use of a cold cathode was required for their analysis. Degradation of gases by thermal cracking on a hot filament (sometimes referred to as "pumping") was also investigated by Gardiner and Pillinger (1979) by use of an all-metal mass spectrometer fitted with an electron multiplier to increase the instrument's sensitivity. In order to reduce thermal decomposition as far as possible, a low work function LaB_6 filament was used at low trap current (4 μA; operating temperature ~700 °C). It was concluded that reliable measurements of CO_2 by static mass spectrometry would be extremely difficult, while N_2 incurred problems associated with mass spectrometer background. However, CH_4, and more particularly its deuterated analog, CD_4, were found to be sufficiently stable in the mass spectrometer (half-life of >11 hours, under the conditions used) for consideration as analysis gases for carbon isotopic measurements, and the long-duration measurement times gave rise to high levels of precision.

Gardiner and others (1978) attempted to measure the $\delta^{13}C$ of so-called hydrolyzable carbon, in the form of CD_4, liberated by the action of DCl on lunar soils. Unfortunately, the analyses suffered from the effects of hydrogen partial labeling manifested as a large contribution at mass to charge (m/z) 19 from $^{12}CD_3H^+$ ($^{12}CD_4^+/^{12}CD_3H^+ \approx 2$ to 10). This uncontrollable effect precluded isotopic measurements because of the associated $^{13}CD_3H^+$ interference at m/z 20. However, it was demonstrated that carbon isotopic measurements of a pure reference gas were relatively reliable.

Following the work of Gardiner and others (1978), a further investigation by Fallick and others (1980) demonstrated that the molecular dissociation of CD_4 under electron impact did not cause isotopic fractionation. As such, use of a higher trap current was advocated (100 μA), with concomitant increases in ion beam currents, and improved stability and sensitivity, which in turn permitted replacement of the electron multiplier by a more reliable Faraday collector. It was concluded that $\delta^{13}C$ measurements having precisions of ±2 ‰ should be possible, provided that pure CD_4 was available for analysis.

In order to derive a generally applicable extraction technique capable of producing CD_4 from a variety of carbonaceous materials, Abell and others (1979) and McNaughton and others (1983) investigated the possibilities of forming CD_4 directly from CO_2. The philosophy was that CO_2 that formed by combustion of a range of carbon components could be subsequently reduced to CD_4 for analysis by high-sensitivity mass spectrometry. The method was based on the so-called Sabatier reaction (Sabatier and Senderens, 1902):

$$CO_2 + 4D_2 \xrightarrow[400\ ^\circ C]{\text{catalyst}} CD_4 + 2D_2O$$

Sample CO_2 was transferred to a small-volume vessel containing a suitable catalyst (nickel or ruthenium) and subsequently pressurized with pure deuterium gas. The catalyst was then heated to about 400 °C for 20 min, after which time excess D_2, and any D_2O formed during the conversion, was selectively removed by use of a Zr/Al getter. Deuteromethane was then admitted to the static mass spectrometer (Wright and others, 1983). Although many problems were encountered with this technique, some successes were obtained with nanomole quantities of carbon (McNaughton and others, 1983). However, the method was found to be inapplicable because of an intermittent and uncontrollable blank/memory problem. Regardless, the dual-Faraday-collector static mass spectrometer constructed for the analyses (Wright and others, 1983) was found to be capable of making $\delta^{13}C$ measurements of nanomole amounts of a pure CD_4 reference gas to precisions of $<\pm 0.25$ ‰.

The experience gained in the interval between the studies of Gardiner and others (1978) (who state that "...the behaviour of CO_2 in the static mass spectrometer is found to be very unstable and obviously would be unsuitable for isotopic studies....") and Wright and others (1983) allowed

the construction of a static mass spectrometer for isotopic analysis of CO_2. The features of the mass spectrometer and associated inlet system (described fully by Carr and others, 1986), which allow $\delta^{13}C$ and $\delta^{18}O$ measurements of nanomole amounts of CO_2 to precisions of approximately ± 1 ‰, are the use of three Faraday collectors for simultaneous ion-beam detection and a strict protocol of equalizing ion source pressures of reference and sample gases. The mass spectrometer is a 90° magnetic sector instrument that has a normal entrance and exit angle for the ion beams. The volume of the instrument is estimated to be about 1 L; typical source pressures are 1×10^{-5} torr. The sensitivity of the mass spectrometer (which is about 1×10^{-5} A torr^{-1}) is maximized by use of a wide source-exit slit of about 0.5 mm; the central (m/z 45) collector also has a slit of about 0.5 mm, so the resulting resolution ($m/\Delta m$) for this collector is ~100. The three collectors are arranged in a straight line rather than at the points of focus for the ion beams, but wide slits on the m/z 44 and 46 collectors negate the necessity for accurate alignment. The dispersion of the ion beams at the collectors is about 2 mm. The abundance sensitivity of the instrument is poor compared to a conventional instrument because of the relatively higher source pressures used, being 370 ppm and 100 ppm for the proportions of m/z 44 at the 45 and 46 collectors, respectively. The stability of the instrument is considerably improved over those used in previous work (that is, Gardiner and others, 1978; Gardiner and Pillinger, 1979; Fallick and others, 1980; Wright and others, 1983) by substitution of the LaB_6 filament with one of tungsten, which has a considerably longer operating lifetime and improved ionization efficiency. The elimination of regular filament replacement enables the mass spectrometer to remain under static conditions for long periods of time. The effect of this substitution is to improve the background in the region of the mass spectrum where CO_2 is analyzed. The success of the analytical procedure lies in its associated extraction system (Carr and others, 1986), which is capable of performing incremental heating with acceptably low blank levels (see below). A second, more advanced triple-collector static mass spectrometer has subsequently been constructed by Prosser and others (1988) and is able to determine $\delta^{13}C$ and $\delta^{18}O$ on samples down to 1×10^{-12} mol to a precision of ± 2.5 ‰.

In addition to carbon isotopic measurements, static mass spectrometers have been used for the determination of nitrogen isotopic compositions (Brown and Pillinger, 1981; Frick and Pepin, 1981; Murty and Marti, 1985). Descriptions of the nitrogen isotope ratio mass spectrometers and associated extraction systems currently in use in our laboratory are given by Wright and others (1988) and Boyd and others (1988), respectively. Some effort has also been given to the assessment of using static mass spectrometry to make δD determinations (Wright and Pillinger, 1983).

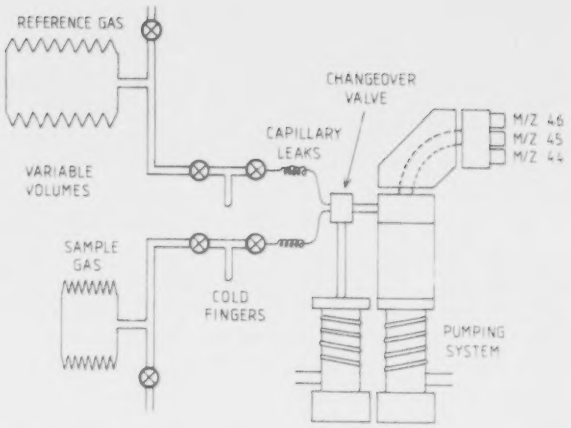

Figure 1. Schematic diagram showing the triple-collector dynamic mass spectrometer. Instrument is shown collecting the three ion beams pertinent to the isotopic analysis of CO_2 (namely, m/z 44, 45, and 46). Dynamic mass spectrometers permit rapid alternation of sample and reference gases, but rather large samples are required to ensure accurate balancing of the inlet pressures, viscous flow in the capillary leaks, and continuous pumping of the analyzer tube. m/z, mass to charge ratio.

Nature of Operation of Static Mass Spectrometry

The static, gas-source mass spectrometer differs from the conventional dynamic isotopic ratio instrument (fig. 1) in a number of ways (see Wright, 1984). In the latter, the sample and reference gases, contained within different parts of a dual-inlet system, continuously flow (hence dynamic) through capillary tubing to a changeover valve (Murphey, 1947; Begbie and others, 1972; Halas, 1979); this device allows either of the two gases to be directed to the ion source of a continuously pumped mass spectrometer while the other is removed through a separate pumping system. The nature of this operation ensures that differential isotopic fractionation effects are avoided and that pressure changes in the ion source are minimized when changing between one gas and the other. However, three areas of sample wastage can be identified. First, large amounts of sample and reference gas, located in reservoirs of adjustable volumes to allow equivalent flow rates through the changeover valve, are required to ensure nonfractionating viscous flow through the capillaries (for example, see Halsted and Nier, 1950). For small-sample analysis, CO_2 may be transferred cryogenically to a low-volume cold finger located in proximity to the end of the capillary, but only a small fraction of the gas is used for isotopic measurements since it is necessary to retain a high gas pressure at the inlet end of the capillary. Second, while the reference gas is being analyzed in the mass spectrometer, the sample gas is bled to waste through a pump connected to one of the outlets of the

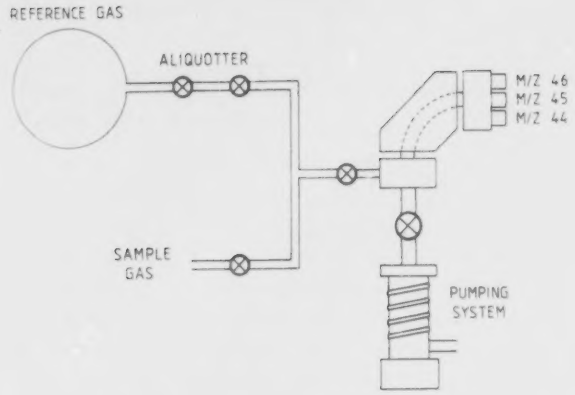

Figure 2. Schematic diagram showing the triple-collector static mass spectrometer. Instrument is shown collecting the three ion beams pertinent to the isotopic analysis of CO_2 (namely, m/z 44, 45, and 46). Because the mass spectrometer is not pumped during an analysis, this type of instrument is extremely sensitive. m/z, mass to charge ratio.

Table 2. Mass spectrum in the region pertinent to isotopic analysis of CO_2

[Interferences can take the form of those species occurring at the same masses. In addition, there are problems with gases such as SO_2 and H_2O, which do not interfere directly]

m/z 44	m/z 45	m/z 46
$^{12}C^{16}O^{16}O^+$	$^{13}C^{16}O^{16}O^+$ $^{12}C^{16}O^{17}O^+$	$^{13}C^{16}O^{17}O^+$ $^{12}C^{16}O^{18}O^+$ $^{12}C^{17}O^{17}O^+$
	Direct interferences	
$^{12}C_3H_8^+$ $^{12}C_3H_6D^+$ and so on	$^{12}C_2{}^{13}CH_8^+$ $^{12}C_3H_7D^+$ and so on	$^{12}C^{13}C_2H_8^+$ $^{12}C_3H_6D_2^+$ and so on
$^{12}C^{32}S^+$	$^{13}C^{32}S^+$ $^{12}C^{33}S^+$	$^{13}C^{33}S^+$ $^{12}C^{34}S^+$

changeover valve. Third, the efficiency of a typical ion source is about 5×10^{-4} ions per molecule (Beckinsale and others, 1973); that is, for every 2,000 gas molecules flowing through the source, only 1 is ionized and thus has the potential to contribute to the measurement.

The operation of a static mass spectrometer is somewhat more straightforward (fig. 2). Sample gas is admitted through a single, wide-bore inlet into the static volume of the mass spectrometer (static implies that the instrument is isolated from the pumping system). After a period of gas equilibration, the inlet valve is closed and the analysis proceeds. Following the measurement period, the valve to the pumping system is opened and the residual gas removed from the system. When base pressure is achieved ($<1\times10^{-9}$ torr), an equivalent amount of reference gas, metered out by use of a variable volume and a capacitance manometer, is introduced and analyzed in an analogous fashion. $\delta^{13}C$ and $\delta^{18}O$ values are then determined from a comparison of ion-beam intensity ratios recorded from the sample and reference gases.

The improvement in sensitivity over the conventional technique is achieved since almost all of the sample gas is admitted to the mass spectrometer and thus has the potential to contribute to the measurement. For carbon dioxide analyses, the mass spectrometer is similar to that employed conventionally (identical construction materials, same magnetic sector, and so on). However, there are some important differences. For instance, because of the high source pressures used in static mass spectrometry, the ion source configuration needs to be of a "nude" design in order to prevent localized high-pressure regions that would result in a number of unwanted ion-molecule reactions and accompanying isotopic-fractionation effects. Another difference between static and dynamic mass spectrometry is that in the former technique the thermal degradation half-life of CO_2 is 30 to 60 s, so ion-beam intensity ratios must be measured rapidly and simultaneously by multiple collection.

A problem common to both dynamic and static mass spectrometry is the need to have pure CO_2 gas for analysis. Table 2 shows some of the species that occur in the region of the mass spectrum of interest for CO_2 (m/z 44–46) and cause direct interference (for example, CS^+ and hydrocarbons, such as $C_3H_8^+$). Other species (not shown) may have an indirect effect (for example, the tailing of Ar^+ or SO^+ and the presence of H_2O, which has a tendency to crack and form reactive ionic fragments). In a conventional isotopic ratio mass spectrometer, following admission of an impure gas sample, it is possible to perform a mass scan in order to assess the purity of the CO_2; a contaminated sample may be recovered and treated to chemical/cryogenic purification procedures in order to remove the interfering species. In the case of static mass spectrometry, because of the small amounts of gas encountered, it is often necessary to admit the entire CO_2 sample to the instrument for analysis (larger samples can be split and conserved in the inlet but if left for long periods of time may become contaminated by outgassed species). Because of the short half-life of CO_2 in a static mass spectrometer, the primary objective following admission of gas is to make isotopic measurements. The presence of impurities is often recognized by changeable ion-beam intensity ratios during the analysis because of interferences in the mass spectrum at m/z 44 to 46. In severe cases of contamination, there will be a disagreement between the measured and expected ion-beam intensities because, having established the relationship for pure reference gas between quantity of CO_2 (measured in the inlet via

a capacitance manometer) and m/z 44 ion-beam intensity, one can infer the presence of contaminants in sample gases by an unexpectedly low measured peak height. Unfortunately, a mass scan after isotopic measurement is not informative, because active gases in a static vacuum environment often suffer from the effects of thermal cracking and (or) reaction of ionic radicals to produce other (sometimes stable) species, from adsorption onto clean surfaces, from reactions with the filament, and so on. Ideally, the process used to prepare carbon for analysis (see next section) should result in the production of pure CO_2. The instrument described by Prosser and others (1988) incorporates an analytical quadrupole mass spectrometer to assess the purity of the sample gas before it is admitted to the isotopic ratio mass spectrometer.

STEPPED HEATING

Principle of Operation

In the technique of evolved-gas analysis, geological samples are subjected to an increasing temperature ramp; gaseous products are continuously removed and analyzed by a detector such as a quadrupole mass spectrometer (Gibson and Johnson, 1972). Unfortunately, because of the nature of isotopic ratio mass spectrometry, it is not possible to perform this type of experiment and measure the $\delta^{13}C$ of CO_2 released from samples undergoing linear heating. Rather, it is necessary to allow CO_2 to accumulate until there is a sufficient amount to permit isotopic measurements. It is thus appropriate to incrementally increase the temperature of the sample, leave it for a certain length of time without further adjustment of the temperature, and collect the evolved gases; this process is referred to as stepped heating. (In principle, if the temperature increments were made infinitely small, the heating/combustion extraction could be considered as having been carried out by use of a linear heating profile, but experiments of this nature await development.)

The analysis of small samples of geological materials by use of stepped heating offers the advantages of contaminant removal and selective volatilization/combustion of different carbonaceous materials. During stepped pyrolysis, a sample is heated under vacuum at progressively higher temperatures (generally from room temperature to ~1,300 °C). Gases evolved from a discrete temperature increment are collected and purified prior to admission of pure CO_2 to the mass spectrometer. Stepped combustion is similar except that the sample is heated in an atmosphere of pure oxygen. In the absence of oxygen, organic materials (including biological contaminants) break down to low-molecular-weight volatile species (CH_4, C_2H_6, C_2H_6, CO, CO_2, and so on). As such, it is customary to perform a combustion extraction up to about 500 °C regardless of the investigation. This procedure ensures that all organic material is converted to CO_2 and subsequently removed. Failure to do this can result in spurious isotopic results at higher temperatures because of interferences in the mass spectrum (m/z 44 to 46) from various contaminant ions. Above 500 °C, combustion can be continued, or, alternatively, the sample can be pyrolyzed in order to release trapped gases from fluid inclusions, vesicles, and such. During pyrolysis, carbonaceous gases such as CH_4, CO, and CO_2 may be evolved. It is possible to separate these gases prior to conversion of each species to CO_2 for isotopic analysis (Sakai and others, 1976). However, the relationship of the carbon-bearing species originally present in the sample to the gas that is subsequently evolved on heating is not always straightforward. For instance, finely divided carbon (from graphite or organic materials) may react with oxygen in silicates to produce CO and CO_2. Furthermore, the presence of hydrated minerals may cause carbon to be liberated as CH_4. Thus, it cannot always be assumed that an evolved gas was originally present in the sample as the trapped species.

Stepped-heating techniques for carbon have been used and (or) described by, amongst others, Briggs and Kitto (1962), Des Marais (1978), Swart and others (1983a), Carr and others (1986), and Halbout and others (1986). The procedures used in our laboratory (Swart and others, 1983a; Carr and others, 1986) involve heating schedules of 30-min steps in which the temperature is increased as quickly as possible at the start of each step. Thus, there may be a time period of up to 5 min while the temperature is adjusted, with the balance of the 30 min at the nominal step temperature.

Common to all combustion techniques is the need to generate a supply of oxygen. An additional constraint for small carbon-sample analyses is that the blank from this oxygen must be <0.5 ng C. A convenient way to generate oxygen is via the thermal decomposition of copper(II) oxide ($CuO_{(1-x)}$, where $x = 0$ in the case of stoichiometric Cu(II)O and 0 to 0.5 for copper oxide that has been pretreated); changing the temperature of the $CuO_{(1-x)}$ allows control of the oxygen pressure. Any $CuO_{(1-x)}$ used in a stepped-combustion apparatus needs to be able to generate a suitable pressure of oxygen repetitively (up to 20 steps per day). Furthermore, once the copper oxide is pretreated and the carbon blank removed, it is desirable to keep the same $CuO_{(1-x)}$ for as long as possible (several months) before replacement (in fact physical replacement is avoided; rather, when the copper oxide becomes oxygen depleted ($x \approx 0.5$), it is usual to resorb oxygen from another source).

Two methods of introducing the oxygen to the sample for combustion have been evaluated. In the techniques of Swart and others (1983a) and Carr and others (1986), chosen to achieve the lowest carbon blanks, oxygen evolved from $CuO_{(1-x)}$ is cryogenically trapped onto a finger containing pellets of a 5-Å molecular sieve. Momentarily

warming the molecular sieve to room temperature desorbs oxygen (at a pressure of ~100–500 torr in the small volume of the extraction system) but leaves any CO_2 from carbon impurities in the $CuO_{(1-x)}$ adsorbed onto the molecular sieve. The purified oxygen can then be admitted to the sample combustion vessel. At the end of the combustion step, oxygen that is surplus to the experiment is removed by resorbing the gas onto the molecular sieve finger, which is immersed in liquid nitrogen (−196 °C), while sample CO_2 is held on a cold finger also at liquid nitrogen temperature. While this method supplies oxygen of the highest purity, its availability in a fixed amount is sometimes unsatisfactory, especially in cases where large amounts of oxidizable materials are present, since the oxygen pressure gradually decreases with time as various components in the sample undergo chemical reactions (for example, hydrogen-, carbon-, and sulfur-bearing species are combusted to H_2O, CO_2, and SO_2, respectively; iron is converted to iron oxide, and so on). A danger of decreasing oxygen pressure is that the carbon will start to be extracted as CO; eventually, combustion may cease altogether. In the case of hydrocarbon-containing samples, graphitization (the transferring of one form of carbon into another) may occur. In any case, the effect of a continuously changing pressure in the oxygen supply is generally undesirable. An additional problem occurs when relatively large amounts of CO_2 are involved, because the procedure used to remove excess oxygen can result in the loss of small, but variable, amounts of CO_2 onto the molecular sieve (this procedure, although resulting in low carbon yields, does not appear to be accompanied by any isotopic fractionation).

As an alternative to using a fixed aliquot of oxygen, it is possible to use a copper oxide furnace within the volume of the combustion vessel. This usage has the advantage that excess oxygen can be resorbed without opening the extraction vessel to another part of the vacuum line, and, more importantly, it is not necessary to use a molecular-sieve trap. Furthermore, by varying the temperature of the copper oxide, oxygen can be made available in a continuous supply at an appropriate pressure (because the equilibrium reaction $CuO_{(1-x)} \rightleftharpoons Cu + O_{(1-x)}$ is temperature dependent). The disadvantage of this method is that prior to its use for combustion of samples, considerable time is required to rid the $CuO_{(1-x)}$ of carbon contaminants that would otherwise contribute to the system blank. To achieve a low blank (<0.5 ng C as CO_2 during the course of a 30-min combustion), the $CuO_{(1-x)}$ is repetitively cycled between 600 and 950 °C to combust any carbon-containing species to CO_2 (with previously untreated $CuO_{(1-x)}$, this process takes several days). In addition, if air is admitted to the previously "blanked-out" $CuO_{(1-x)}$, (because of accidental vacuum failure or when a new sample is loaded into the combustion vessel), the cycling procedure has to be repeated, albeit in a more limited way. To prevent the $CuO_{(1-x)}$ from being exposed to the atmosphere unnecessarily, samples are loaded into an "air-lock" section of the vacuum line that is isolated from the extraction vessel; following evacuation, the sample can be transferred to the combustion vessel through a gate valve (similar to the procedure described by Boyd and others, 1988).

During the combustion interval, a cold trap ensures removal of species such as CO_2, SO_2, and H_2O and thus prevents any possibility of these gases becoming adsorbed onto the copper oxide. A high-temperature platinum surface prevents formation of nitrogen oxide (this problem is dealt with extensively by Boyd and others, 1988). At the end of a combustion step, excess oxygen is resorbed onto $CuO_{(1-x)}$. Following a pyrolysis extraction, carbon-bearing gases may include CO_2, CO, CH_4, and higher hydrocarbons. If the CO_2, CO, and hydrocarbons have different $\delta^{13}C$ values (as result of fractionation during the experiment or because of an inherent property of the sample), it will be impossible to unambiguously comprehend the isotopic data unless each species is converted to CO_2 for isotopic analysis.

Purification of evolved gases is accomplished cryogenically. First, gases that are condensible in liquid nitrogen are separated on a cold finger from noncondensible species (O_2, N_2, and noble gases, and in the case of pyrolyses, CO and CH_4). The temperature of the cold finger is then raised to about −140 °C in order to distill CO_2. SO_2, H_2O, and any higher hydrocarbons from a pyrolysis are left in the trap (the appropriate apparatus and technique are described by Carr and others, 1986). A problem occurs for cryogenic separation if large amounts of H_2O are present, because gases such as CO_2 may become trapped in the ice structure, possibly forming clathrates (which would have an idealized formula of $CO_2 \cdot 5\frac{3}{4}H_2O$; see Davidson, 1973). In water-rich samples, it may be necessary to employ a second cold trap at −90 °C to remove H_2O before cryogenic separation of the remaining gases is attempted. Figure 3 shows that, for a closed volume, when large amounts of gases are handled (that is, high vapor pressures), small changes in temperature can result in very large increases in pressure. Thus, when trying to separate large samples of CO_2 from SO_2, it may become necessary to raise the temperature of the cryogenic trap to as high as −100 °C, an action that has the effect of desorbing some SO_2 (in order to avoid this problem completely, it is sometimes necessary to cryogenically remove the evolved CO_2 into a second cold trap and thus effectively lower the instantaneous vapor pressure). As a general rule, the most effective separations are obtained by monitoring the pressure of the gases liberated from the variable temperature trap; if the onset of SO_2 distillation is detected, the trap can be cooled down again and the process repeated or a second cold trap implemented. On the whole, cryogenic separations are most easily carried out and usually most successful when the smallest possible amounts of gases are handled.

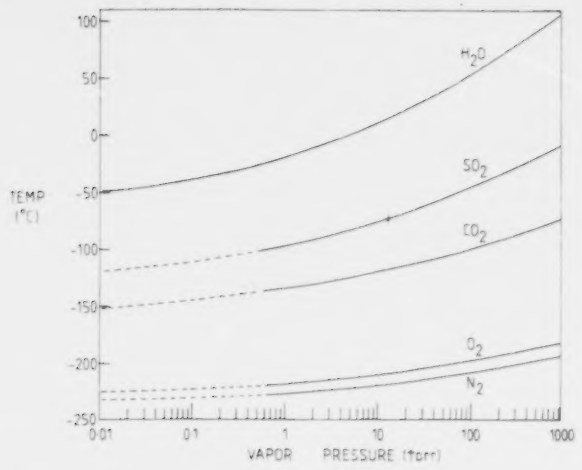

Figure 3. Vapor pressures versus temperature of the gases most commonly encountered during stepped-heating experiments (data from Weast, 1984).

Applications of Stepped Heating

Figure 4 indicates how various carbon-containing species behave during stepped combustion. The kerogen sample (Gilmour and Pillinger, 1985) shows that organic materials burn below about 500 °C. Biological contaminants such as spores, dust, and fibers burn over temperature intervals that are similar to those at which kerogen burns (Des Marais, 1983). Thus, at the very least, stepped combustion can be used for separating high-temperature indigenous carbon from organic contamination. At intermediate temperatures (400–700 °C), amorphous carbon burns (Grady, 1982), and carbonates decrepitate to yield the oxide of the mineral and CO_2 gas (Swart and others, 1982). At higher temperatures, elemental forms of carbon, such as graphite and diamond, combust (Grady and others, 1985), while carbides, such as cementite (Fe_3C, or the meteoritic equivalent cohenite $\{Fe,Ni\}_3C$), burn at temperatures greater than 900 °C (Grady and others, 1986).

When previously unstudied samples are analyzed by stepped combustion, problems may occur when one tries to decide, from an appraisal of the release data, which carbonaceous components are present. It might appear from figure 4 that, when a pure compound is combusted, a single release of carbon is liberated over a diagnostic temperature interval. However, identifications based purely on combustion temperature may be erroneous. Figure 5 shows the combustion temperature of diamonds of different grain sizes (Ash and others, 1987). The finest grain size (~3 nm) combusts at temperatures of 450 to 550 °C, while a single chip of diamond (~100 μm) burns at temperatures greater than 700 °C. Intermediate grain sizes define a trend of increasing combustion temperature with increasing grade (fig. 5). The rate of combustion is presumably dependent on surface area; results from the finest fraction demonstrate that even in the case of a single diamond chip, combustion begins at temperatures as low as 450 °C. However, the relatively low surface to volume ratio would result in an extremely slow combustion rate at these temperatures. At temperatures above approximately 700 °C, combustion rate is considered to be fairly insensitive to temperature.

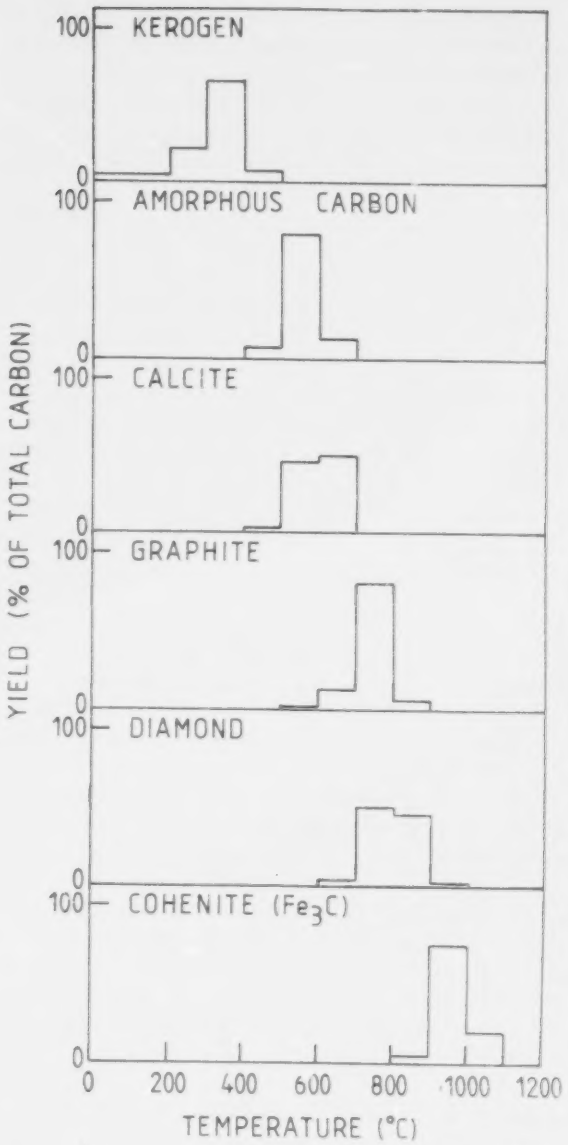

Figure 4. Combustion temperatures of kerogen, amorphous carbon, calcite, graphite, diamond, and cohenite. In each case the yield of carbon from a particular step is expressed as the percentage of the total carbon. Step increments in each example are 100 °C. Grain size (compare fig. 5) may also affect combustion temperature.

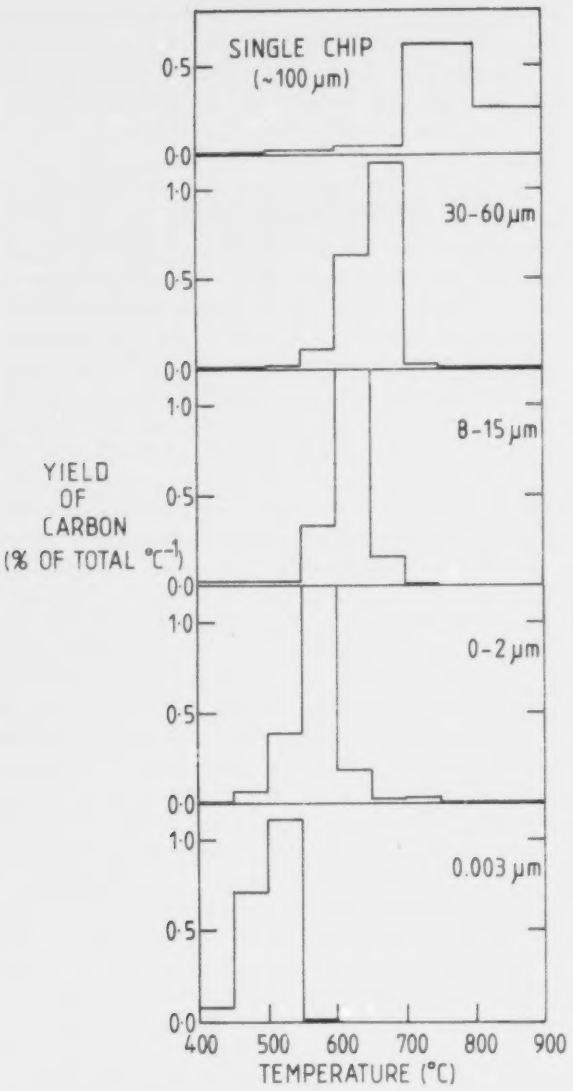

Figure 5. Variation of combustion temperature of diamond with grain size. The single chip is from a natural terrestrial diamond, the three intermediate size fractions are commercially available diamond grits, and the finest fraction is from a carbonaceous chondrite. Yields of carbon are expressed as percent of total carbon $°C^{-1}$; step sizes are generally 50 °C, except for the diamond chip, where they are 100 °C.

In the case of organic materials, the combustion temperature is dependent upon H/C ratio (Gilmour, 1986). Some examples are given in figure 6. Immature kerogens, such as those found in the Green River Shale, have a lower degree of cross-linking and thus have a relatively high hydrogen content. Materials of this nature combust at low temperatures (less than 400 °C). With increasing maturity,

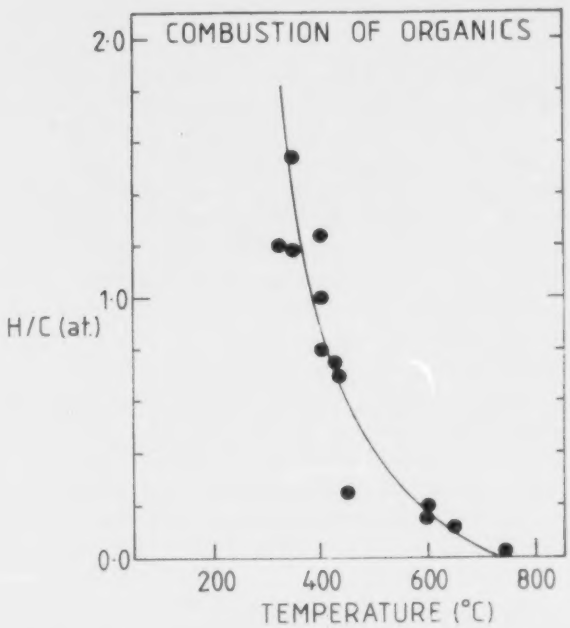

Figure 6. Variation of combustion temperature of organic materials versus atomic (at.) H/C ratio. The combustion temperature is defined as that at which the maximum release is obtained during the stepped-heating extraction. Step sizes are typically 25 to 35 °C.

the concomitant loss of hydrogen leads to the formation of more highly condensed matter and a consequent increase in combustion temperature. In the extreme, when all hydrogen has been lost, the organic material is graphitized and thus combusts at a temperature similar to that of pure graphite (~800 °C; see fig. 4). A good pictoral representation of these maturation processes is given by Hayes and others (1983). Yet a further example of variation in release temperature is demonstrated in the work of Milodowski and Morgan (1980), where it is shown that the temperature of thermal decrepitation of carbonates, in a flowing stream of nitrogen and oxygen, depends on chemical composition. The range in decomposition temperature is from 300 °C (cerussite, $PbCO_3$) to >800 °C (strontianite, $SrCO_3$, and witherite, $BaCO_3$).

The success of static mass spectrometry as applied to the analysis of CO_2 liberated by stepped heating rests on the extraction procedure having a suitably low carbon blank. Figure 7 shows, among other things, a typical blank obtained by stepped combustion; all of the experiments shown in this figure were performed by use of fixed aliquots of oxygen, rather than a continuous supply. Between 200 and 600 °C, the total blank is about 50 ng C, equivalent to about 10 ng C per step when using 100 °C increments. This component arises from a small amount of airborne organic contamination introduced when the extraction system was

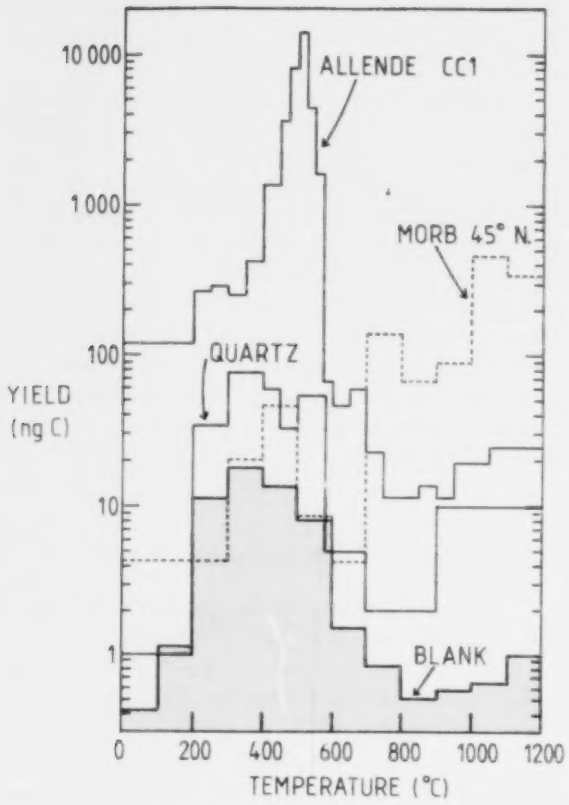

Figure 7. Yield of carbon in nanograms (ng) (log scale) versus temperature, obtainable by the extraction system described by Carr and others (1986). The shaded histogram is the system blank. The plots labeled Allende CC1, MORB 45° N., and Quartz refer to samples of a carbonaceous chondrite, a basaltic glass from the mid-ocean ridge, and a fluid-inclusion-rich sample of quartz, respectively. If sample sizes are chosen properly, the amounts of CO_2 available for analysis are always greater than 50 times the blank at each step; use of a sufficiently large quartz sample is precluded by the extraction vessel's volume.

opened to the atmosphere. Below 200 °C and above 600 °C, the blank, which is <1 ng C as CO_2 per step, is independent of temperature, but proportional to the length of time used for the extraction (30 min). These blank components are from carbon dissolved in the glassware that comprises the extraction line, together with the inherent contamination present in the oxygen.

The three samples shown in figure 7 are typical in the sense that they represent the specimen sizes normally available and that can be manipulated easily and accommodated by the extraction system. Thus, the sample labeled Allende CC1, which is 50 percent carbon, represents a typical amount of material that remains after extensive processing of a primitive meteorite; its weight, 69 μg, can be determined accurately by use of an electronic balance (samples an order of magnitude smaller than this can be weighed but with about ±5 percent errors). The Quartz and MORB 45° N. samples are the largest that can be loaded into the system (at 17.15 and 15.25 mg, respectively).

Allende CC1 (Ash and others, 1987) consists mainly of fine-grained elemental forms of carbon. Although most of the carbon in the sample combusts over a temperature range close to that of the major blank release, yields are considerably above blank levels. No blank correction is therefore necessary, and isotopic measurements are uncompromised. It can be seen that the sample-to-blank ratios are somewhat lower above 600 °C, but again, corrections are not routinely applied.

For the basaltic glass MORB 45° N. (Exley and others, 1986), it can be seen that below 600 °C the amounts of carbon liberated are similar to, or a little larger than, the system blank. The slight enhancement is caused by the presence of a small amount of contaminant organic material on the surface of the sample. Above 600 °C (which in this case represents a stepped pyrolysis), large amounts of indigenous CO_2 are released compared to blank levels.

Carbon released from the quartz sample (Carr, 1985) is liberated in the same temperature range as the blank and only a factor of 3 to 5 in excess of it. The sample was studied in an attempt to acquire data about the isotopic composition of CO_2 in fluid inclusions. However, with such a low sample-to-blank ratio, it is difficult to assess whether the apparent bimodal release is caused by an overlap of (lower temperature) organic contamination and fluid inclusion gas or represents two generations of fluid inclusions superimposed on a release of blank. The true nature of the sample might be elucidated by analysis of a larger amount of material (not possible with this extraction system), but if a large component of the carbon is surficial organic contamination on the sample itself, then this would not necessarily solve the problem. Clearly, stepped-heating extraction is more immediately suitable for some studies than others.

Of importance to isotopic investigations is the question of whether isotopic fractionation accompanies the progressive burning of a sample. Swart and others (1982) demonstrated that stepped combustion of graphite and progressive decrepitation of carbonate did not result in carbon isotopic fractionation. A stepped combustion of a single diamond chip (D.W.McGarvie, unpub. data, 1988), shown in figure 8, demonstrates that no systematic or significant carbon isotopic fractionation was induced (the temperature interval over which the diamond burned is from 650 to 1,000 °C). Some small isotopic variations appear to be outside analytical errors, but these may be due to internal isotopic variations within the diamond, which from other studies are known to be of the order of a few per mil (Swart and others, 1983c; Boyd and others, 1987). Also shown on figure 8 is a line corresponding to a mass-dependent loss of ^{12}C relative to ^{13}C (that is, a Rayleigh distillation with loss

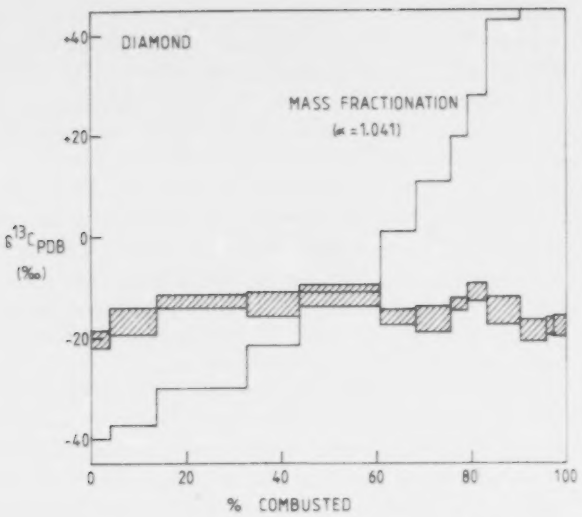

Figure 8. $\delta^{13}C$ versus cumulative release of carbon from a stepped combustion of a single chip of diamond (shaded area). PDB, Peedee belemnite. The temperature interval of the extraction is from about 650 to 1,000 °C (step increments are variable, between 20 and 50 °C). The precision of the isotopic measurements is ±1 to ±2.5 ‰, as indicated by the height of the shaded areas. The line labeled MASS FRACTIONATION represents the result that would be produced by a kinetic isotope effect based on an assumed mass-dependent loss of atomic carbon (for such a process the fractionation factor α, = 1.041; that is, $\sqrt{13/12}$). This line has been calculated so as to correspond to the same percentage yield increments of the sample. Clearly, no systematic or significant isotopic fractionation occurs during stepped combustion.

of atomic carbon assumed). This represents an extreme case but is the only form of isotopic fractionation that can be anticipated from a sample composed of pure carbon. Clearly, stepped combustion of the sample did not produce an isotopic fractionation of this magnitude. It is possible that, during combustion, at the very surface of the diamond $^{12}CO_2$ may be formed at a faster rate than $^{13}CO_2$, or faces of different crystallographic orientation may burn preferentially. However, after a 30-min combustion period a skin of diamond corresponding to between 5 and 10 percent of the total mass would be removed and converted to CO_2 with no net isotopic fractionation.

While combustion of graphite and diamond does not induce any observable carbon isotopic fractionation, it should be noted that progressive combustion of terrestrial kerogen samples does result in a reproducible change in $\delta^{13}C$ value (Gilmour and Pillinger, 1985). This change is not due to kinetic isotope fractionation during combustion but is a result of either (1) ^{12}C enrichment in the more easily combustible side-chain and aliphatic materials compared to the relatively stable aromatic core of the kerogen (a result of kinetic isotopic fractionation during kerogen formation) or (2) the resolution of marine and terrigenous components of different $\delta^{13}C$ values.

Although isotopic fractionation during combustion does not appear to be a problem, fractionation might be expected to occur in pyrolysis experiments where diffusive release of CO_2 is encountered. However, no such effect was observed during studies of MORB (mid-ocean ridge basalt) glasses (Mattey and others, 1984; Exley and others, 1986). Presumably, over a specific, narrow temperature interval, the samples either melted (thereby liberating gases from vesicles or from within the structure of the glass) or the confining pressure of fluid inclusions was exceeded, and fracturing of the sample and nonfractionating loss of gas resulted. In either case, diffusive loss prior to melting was of limited significance.

Inherent Artifacts in Stepped-Heating Profiles

In order to ascertain what information can be derived from a stepped-combustion plot, it is necessary to understand fully some of the problems inherent in the technique. These vagaries are manifested as artifacts on stepped-combustion plots that can be recognized and accounted for. Figures 9 and 10 illustrate examples of common problems. The plots are schematic but based on observations. For various reasons, not least of all because of difficulties associated with cryogenic purification of CO_2 (discussed above), problems of oxygen access or depletion, localized hot spots in the furnaces, and so on, it is desirable to use the smallest sample compatible with good precision in $\delta^{13}C$ and representative of the material under investigation. Of importance here is the ratio of available oxygen, O, to the amount of combustible and oxidizable materials, CM, present in the sample. In systems containing pure carbon, the O/CM is equivalent to the O/C ratio. Figure 9*A* shows an example of a stepped combustion under a relatively low O/CM ratio, that is, a large sample under normal conditions or a small sample under low oxygen pressure. The release profile is broad and positively skewed (relative to the low-temperature part of the release, which rises sharply, the profile at high temperature has a more shallow appearance and is possibly an exponential decay). The extended nature of the release is a result of the inability of oxygen gas to gain access to the whole of the sample and complete that part of the reaction for which the activation energy has been reached; furthermore, CO_2 produced by the combustion may not be removed effectively. Such effects are undesirable in situations where multicomponent samples are being analyzed, since the releases of carbon from individual components will overlap and poor resolution will result. Figure 9*B* shows the effect of using a much higher O/CM

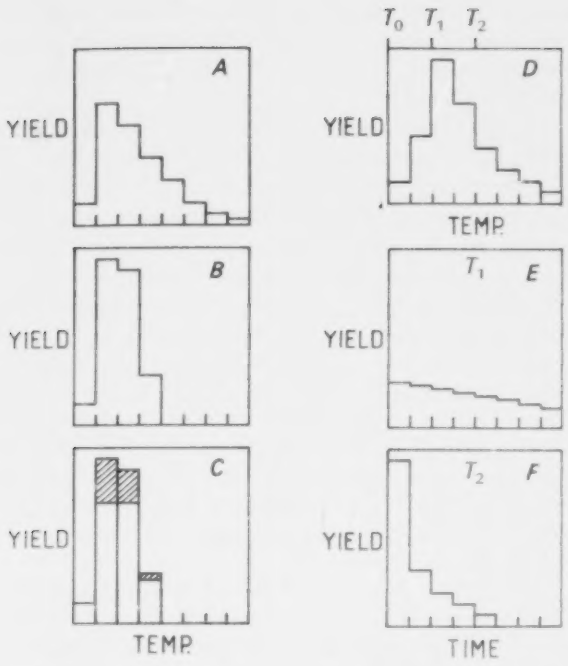

Figure 9. Schematic diagrams showing the effect of the ratio of oxygen pressure to sample size on stepped combustion profiles (*A* through *D*) and the use of repeat combustions at discrete temperature steps (*E*, *F*). *A* represents combustion of a large sample under normal conditions or a small sample under low oxygen pressure. Note the exponential tail on the high-temperature part of the release. *B* shows the same sample combusted under conditions of high oxygen pressure or a small sample under normal conditions. *C* shows that multiple combustions at individual temperature steps may help in confining the release from a large sample to a narrow temperature interval (the shaded region of a particular step demonstrates that additional carbon is released by simply keeping the temperature constant). *D* shows a typical stepped-heating profile for a single component; T_1 and T_2 represent two arbitrary temperatures, one lower and one higher than the maximum release. *E* and *F* show the effect of repeat combustions at T_1 and T_2, respectively.

ratio, that is, a small amount of the same sample under a relatively high pressure of oxygen. The release now occurs over a narrow temperature interval, and the sample burns at a uniform rate, so the indication is that all the constituent grains have access to oxygen, and CO_2 is able to escape. This type of release is more desirable for stepped-combustion analysis, as it may allow components of broadly similar combustion temperature to be resolved. Because multicomponent samples can consist of several carbonaceous materials of widely differing concentrations, it may be necessary to use quite a large sample in order for there to be enough of a minor component to allow measurement. Thus, to avoid the situation depicted in figure 9*A*, it may be necessary to employ multiple combustions at a particular temperature when analyzing large samples. Figure 9*C* is an attempt to demonstrate this effect, although data would probably not be plotted like this in practice (instead, the results from multiple combustions would be compounded). Swart and others (1983b) and Ash and others (1988) have used this procedure to try to resolve minor entities, with slightly higher combustion temperatures, from a major component. The latter authors have taken the procedure to extreme, with the low-temperature combustions enduring many hours before being advanced to higher temperatures. Clearly, the exact temperature program cannot be determined before an unknown sample is analyzed. It is necessary to perform a series of trial experiments to assess the best course of action. Manual stepped combustions as a preliminary to long-duration automated extractions would seem to be a route for future developments in technique.

The use of multiple combustions at discrete temperatures is complicated by the dependence of oxidation rate on temperature. Figure 9*D* shows a stepped-combustion profile for a hypothetical carbon-bearing component. If another aliquot of the same sample was subjected to a temperature increment of T_1-T_0, followed by multiple combustions at this relatively low temperature, then it may take many repeat steps in order to burn all of the component (fig. 9*E*), since the combustion rate is slow at low temperatures. A temperature increment of T_2-T_0 followed by repetitive combustions at T_2 may result in the sample burning completely in just a few repeat steps because of the faster reaction rate (fig. 9*F*). Differences in combustion rates might be used to try to separate components of similar combustion temperatures.

The selection and control of the temperature increments used in stepped-heating experiments can have a profound effect on the nature of the release profiles. To illustrate this, figure 10*A* depicts the release of CO_2 that might be expected when a hypothetical component is treated to a linear-heating extraction (examples of CO_2 release from various samples can be found in Gibson and others, 1974). For the purposes of the following discussion, the *x* axis of figure 10*A* is considered to represent temperature; however, it should be appreciated that a linear-heating schedule implies a temperature ramp directly proportional to time (and thus, the *x* axis in this example may equally well represent time instead of temperature). As stated above, it is not possible to perform a linear-heating extraction by use of the stepped-combustion apparatus, so in reality the sample in figure 10*A* would have to be heated in discrete temperature increments. When these temperature increments are equal (corresponding to the vertical lines in fig. 10*A*), a reasonable representation of the actual release is obtained (fig. 10*B*). However, in figure 10*C*, the same release is depicted if it is assumed that the temperature of one of the steps were underestimated. The nature of the profile is now

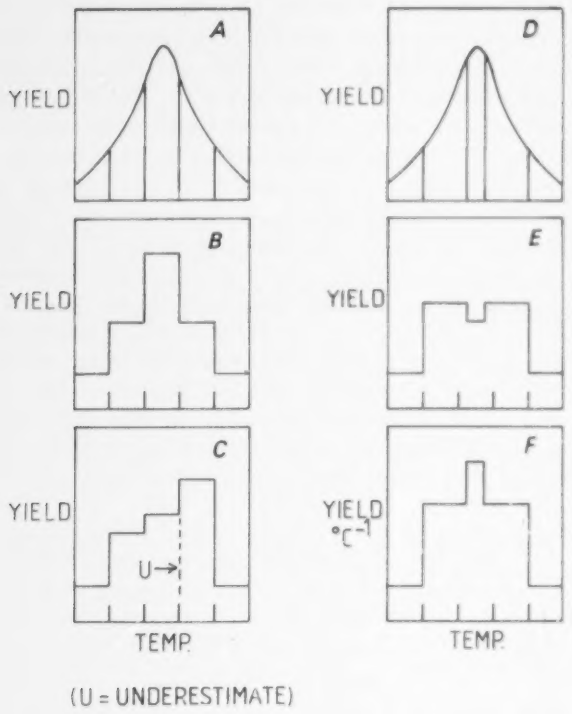

Figure 10. Comparison of stepped-heating data acquired in equal and unequal temperature increments and the effect of normalizing yield data to a $°C^{-1}$ interval. *A* shows a gas release obtained by use of linear heating. The vertical bars, which are equally spaced, represent constant temperature increments. *B* shows the stepped-heating profile that would be obtained. C shows the effect of underestimating the temperature of the third step. *D* shows a gas release obtained by use of linear heating. The vertical bars, which are unequally spaced, represent temperature increments of different sizes. *E* shows the stepped-heating profile that would be obtained. *F* shows the same data but with yield normalized to a $°C^{-1}$ interval.

less straightforward and could even be interpreted as two closely overlapping releases (in practice, additional information would be gained from the isotopic data, and a single release may have been inferred). Temperatures are measured erroneously in a number of ways, but four of the most commonly encountered problems are (1) physical movement of the temperature-measuring device (thermocouple) with respect to the sample during the extraction, (2) the tendency for an operator to log constant temperature increments in order to produce an apparently regular heating schedule, since stepped-heating extractions require adjustment of temperature to successively higher values, (3) the temperature of a resistance-wire furnace may often momentarily exceed the step temperature because of the use of an increased current in order to change temperature as rapidly as possible, and (4) temperatures may drift during the course of the experiment (because of fluctuations in voltage, drafts, operator distraction). The combination of these effects might result in errors of measured temperatures of ±5 to ±10 °C.

In trying to obtain an accurate representation of the temperature increments experienced by a sample during a stepped-heating experiment, one may find it appropriate to record a value considered to represent the mean temperature for the step as a whole. This can often be quite a subjective exercise, but, in principle, if done accurately, the readings correspond to a stepped extraction in unequal temperature increments (the vertical lines in fig. 10*D*). If the yield versus temperature relationship is plotted (fig. 10*E*), a rather misleading representation is obtained, one that suggests a bimodal release. For this reason, it is advisable to normalize yield data to a constant step interval. The most convenient normalization technique is to recalculate the data to a yield $°C^{-1}$ basis. It can be seen from figure 10*F* that, when normalized data are plotted, a fair representation of the real situation is achieved.

During analyses of unknown samples, it is often desirable to perform stepped extractions in temperature increments of ≤25 °C; experiments of this nature are referred to as high-resolution extractions. It is noteworthy that stepped combustions undertaken in small increments are often less reproducible than those performed in temperature increments of 100 °C, undoubtedly because of an inability to reproduce and control the temperature in small increments. The absolute accuracy of an individual measurement is probably ±25 °C, although under optimum conditions the internal error during each experiment may be approximately ±5 to ±10 °C.

In addition to controlling the temperature accurately during a stepped-heating experiment, reproducing the time period for each extraction is also necessary. A computer-controlled stepped-heating extraction could be expected to give the best reproducibility of time and temperature and thereby minimize the incidences of operator error. However, for data already acquired, it is possible to suppress the effects of poor experimental control by subjecting raw data to an appropriate mathematical correction procedure. The results from a stepped-heating experiment may be treated to a form of digital smoothing, in the same way that low abundance peaks can be resolved from "noisy" mass-spectral data (Trott and Beynon, 1979). An even simpler approach to removing spurious irregularities in the yield profile is *reforming* the data, a process (see fig. 11) that is carried out in two stages. First, the raw yield data for each pair of adjacent steps are used to calculate the hypothetical yield for a step that would have been obtained over a temperature interval extending between the midpoints of adjacent steps. Second, the revised yield data are recalculated in the same manner to coincide with the original, measured temperature increments (this is an iteration of the above calculation). An example of the complete operation is

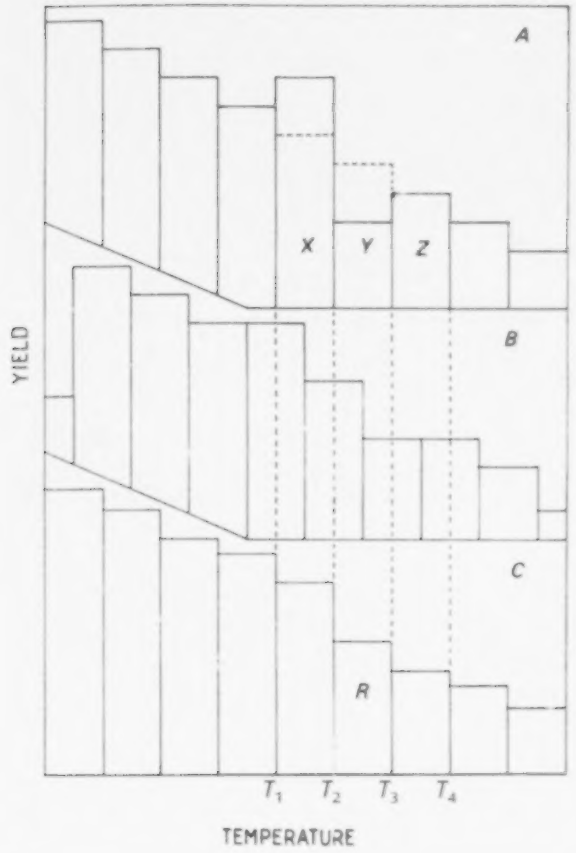

Figure 11. Example of how to reform stepped-yield data. *A* shows a release profile containing inconsistencies in two adjacent steps, such as might be experienced from an erroneous temperature measurement. *B* and *C* show the intermediate and final results of mathematical processing, respectively. *X*, *Y*, and *Z* are the yields of three consecutive temperature steps. *R* shows step *Y*, after having been reformed. T_1-T_2, arbitrary temperatures.

shown in figure 11. Here, figure 11*A* represents a release profile containing inconsistencies in two adjacent steps (of yields *X* and *Y*), of the type that might be experienced from an erroneous temperature measurement. Figures 11*B* and 11*C* show the intermediate and final results of mathematical processing, respectively. The equation that describes the whole operation is given by

$$R=\left(\left(\frac{X+Y}{T_3-T_1}\right)+\left(\frac{Y+Z}{T_4-T_2}\right)\right)\times\left(\frac{T_3-T_2}{2}\right)$$

The notation is consistent with that in figure 11. *X*, *Y*, and *Z* are the yields (in absolute units, meaning parts per million or nanograms carbon rather than $°C^{-1}$-normalized data) from three consecutive temperature steps of temperatures T_2, T_3, and T_4, respectively. *R* is the reformed yield corresponding to the original step, *Y*.

In the special case of the first temperature step where, in effect, step *X* is missing, the reformed yield is calculated from *Y* and *Z* only (*R* corresponding to the same temperature interval as *Y*):

$$R=\frac{Y}{2}+\left(\left(\frac{Y+Z}{T_4-T_2}\right)\times\left(\frac{T_3-T_2}{2}\right)\right)$$

Similarly for the last temperature step:

$$R=\frac{Y}{2}+\left(\left(\frac{X+Y}{T_3-T_1}\right)\times\left(\frac{T_3-T_2}{2}\right)\right)$$

Following calculation of the reformed yields, the data can then be normalized to a $°C^{-1}$ basis.The technique is suitable for application where errors in temperature measurement are greater than 50 percent of the step size. Because the temperature errors may be as great as ±25 °C, the technique is suitable for stepped extractions undertaken in steps of less than 50 °C.

In addition to smoothing the yield profile, it is possible to calculate the $\delta^{13}C$ values for the reformed data as well:

$$^{13}C_R=\frac{\delta^{13}C_X X+2\delta^{13}C_Y Y+\delta^{13}C_Z Z}{X+2Y+Z}$$

Where $\delta^{13}C_R$ is the reformed $\delta^{13}C$ value from the middle of three consecutive steps having yields and $\delta^{13}C$ values of *X*, $\delta^{13}C_X$; *Y*, $\delta^{13}C_Y$; and *Z*, $\delta^{13}C_Z$.

For the initial step of an experiment (step *X* missing)

$$\delta^{13}C_R=\frac{3\delta^{13}C_Y Y+\delta^{13}C_Z Z}{3Y+Z}$$

and for the ultimate step

$$\delta^{13}C_R=\frac{3\delta^{13}C_Y Y+\delta^{13}C_X X}{3Y+X}$$

Mathematical smoothing of stepped-combustion data should be restricted to the process of interpreting the sample under investigation. Some examples of this procedure are given later on.

Interpretations of Stepped-Heating Data

In simple materials (pure compounds) there may be few, if any, problems associated with the interpretation of stepped-heating data. However, in multicomponent samples, such as meteorites, the data may be complicated by the presence of different materials having similar combustion

temperatures, and so on. Furthermore, during a stepped-combustion experiment, carbon in different locations may burn at temperatures that are governed by the nature of the site rather than the form of the carbon. For instance, some carbonaceous chondrites contain carbon both finely dispersed in the matrix and also enclosed within spinel grains (Tang and others, 1988). The carbon in spinel is referred to as "protected" and may not burn until the host mineral begins to crack, melt, or otherwise allows access of oxygen gas; this burning usually occurs at temperatures greater than that at which the unprotected component burns.

There are two ways in which the interpretation of stepped-heating data can be expedited. The first involves the preparation of a suite of chemical or physical separates from the parent sample. For example, whole-rock samples could be treated with (1) organic solvents, or water, (2) various mineral acids, (3) progressively stronger acids, (4) wet-chemical oxidizing agents, or (5) gas-phase oxidation at preselected temperatures. The residues produced during these procedures can be further subdivided by physical separation (magnetic properties, grain-size, density). Stepped-combustion analyses of the whole suite may then elucidate the carbon inventory of the sample under investigation. A comprehensive study of this type can be found in Tang and others (1988).

Much simpler applications of the process can still give useful information; for example, if a whole-rock sample is treated with acid, then both the whole rock and insoluble residue can be analyzed by stepped combustion and the data compared. In a hypothetical case (fig. 12), consisting of a major acid-soluble component that has a broad release, and a small acid-insoluble component combusting at higher temperatures, the release profile is the sum of the insoluble and soluble components (fig. 12*C*). In the ideal case, stepped heating of the acid-insoluble sample (fig. 12*D*) will produce a release profile identical to the hypothetical case. Comparison of the data acquired from both the whole sample and the acid residue then allows one profile to be subtracted from the other, with the result that two components can be deconvolved. In practice, such a situation rarely exists, the acid treatment producing instead a somewhat different effect than might have been anticipated. Figure 12*E* shows a common problem; treatment with acid may result in the removal of a large amount of silicate matrix or a mantle of a "protecting" mineral that, in turn, may allow the acid-insoluble component to burn at a lower temperature. This effect is often accompanied by the combustion interval spanning a narrower temperature range. Clearly, the profile in figure 12*E* cannot now simply be subtracted from the measured release to allow deconvolution into the two components. Further complications may arise (fig.12*F*) if not all of the acid-soluble component is removed by the acid and (or) some of the acid-insoluble component is lost during handling (a serious problem for fine-grained material). Again, comparison of the two measured profiles produces a less than straightforward insight into the nature of the sample. Finally, in figure 12*G*, the release temperature of the acid-insoluble component is shown as occurring at a higher temperature than expected. This situation might occur if a number of fine particles physically aggregate during acid treatment or are otherwise chemically altered. Involatile products of the acid treatment may coat the acid-insoluble component and raise its apparent combustion temperature. In practice, a combination of all these illustrative effects may occur and make interpretation of the sample very difficult without an appreciation of how chemical/physical separations may affect the nature of stepped-heating profiles.

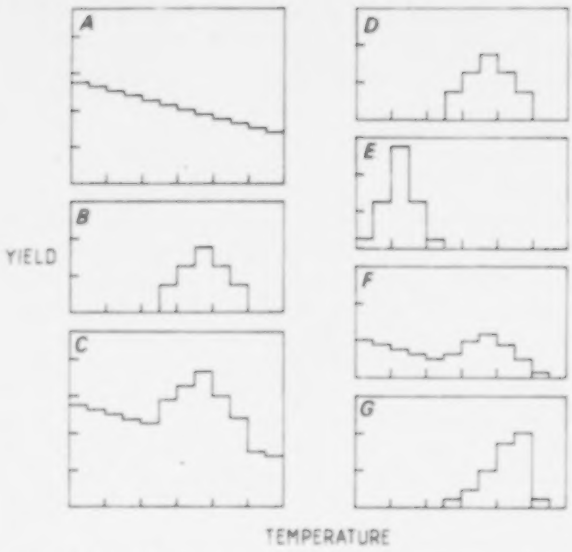

Figure 12. The effects of preparing acid-resistant residues from complex samples. The three plots on the left-hand side show the combustion characteristics of two hypothetical components, one acid soluble (*A*) and the other acid insoluble (*B*). During a stepped-combustion extraction of a sample containing both these components, plot C would be obtained. The plots on the right-hand side (*D* through *G*) illustrate four possible end results following acid dissolution of the sample. *D*, Stepped heating of acid-insoluble sample in an ideal case. *E*, Stepped heating of an acid-treated sample when the treatment caused removal of a silicate matrix or "protecting" mineral, allowing the acid-insoluble component to burn at a lower temperature. *F*, Complications that arise if not all of the acid-soluble component is removed by the acid and (or) some of the acid-insoluble component is lost during handling. *G*, Release temperature of acid-insoluble component occurring at a higher temperature than expected.

In addition to the use of chemical and physical separates, the carbon components of a particular specimen can be deconvolved by detailed appraisal of an individual stepped-heating profile. Halbout and Robert (1986) have attempted to undertake this task by using a mathematical

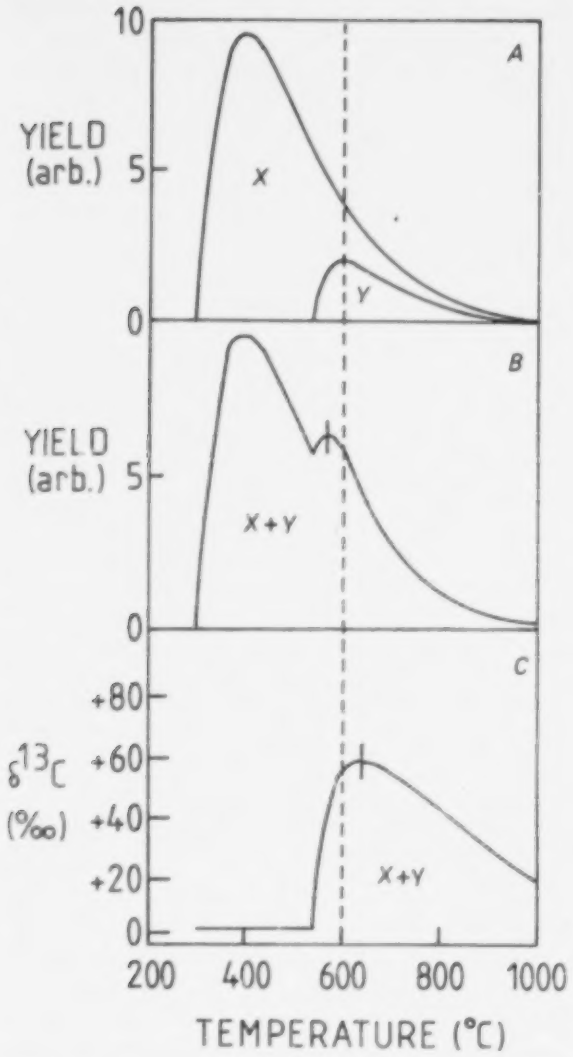

Figure 13. Theoretical effect of mixing two gas releases (redrawn from Halbout and Robert, 1986) (yield in arbitrary units). *A*, Two idealized releases, *X* and *Y*, with the maximum yield of the minor component, *Y*, occurring at 600 °C. *B*, The yield profile obtained by summing together the releases *X* and *Y*. Note that the apparent maximum release of the minor component is displaced toward a lower temperature than 600 °C. *C*, The isotopic profile obtained with *X* and *Y* assumed to have $\delta^{13}C$ values of 0 ‰ and +150 ‰, respectively. The maximum measured $\delta^{13}C$ value occurs at a higher temperature than 600 °C and is considerably lower than the actual value of component *Y*.

approach based on temperature-related diffusion (expounded in detail for the case of stepped pyrolysis by Albarede, 1978). Figure 13*A* shows the apparent combustion behavior of two hypothetical components, *X* and *Y* (each assumed to be in a pure state). *X* is considered to be in the higher abundance and is released to the maximum extent at 400 °C, whereas the release of *Y* is centered on 600 °C. Figure 13*B* shows the combustion release profile obtained when the two components are summed together; the apparent release of the minor component is displaced to a temperature lower than 600 °C. Figure 13*C* shows the measured $\delta^{13}C$ values, assuming component *X* to have a "normal" isotopic composition ($\delta^{13}C = 0$ ‰) and component *Y* to be ^{13}C enriched ($\delta^{13}C = +150$ ‰). The maximum measured $\delta^{13}C$ value is considerably attenuated from the true value because of mixing and occurs at a higher temperature than 600 °C.

A consequence of the Halbout and Robert modeling is that relatively high $\delta^{13}C$ values are obtained over large temperature ranges because of the shallow exponential decay assumed for a minor component (for example, component *Y* in fig. 13). This observation would seem to be corroborated by stepped-combustion analyses of meteorite samples, where high $\delta^{13}C$ values are encountered over the temperature range of ~500 to 1,300 °C. However, Carr and others (1983) and Swart and others (1983b) have shown that, in fact, there are several different ^{13}C-rich components that combust at high temperature. Applying the Halbout and Robert model to meteorite data could therefore be misleading. It is considered that, in contrast to the Halbout and Robert model, the combustion interval of minor components that burn at high temperature are rather narrow because of rapid oxidation rates (this is certainly true for the system described herein that uses small samples and relatively high oxygen pressures). Thus, the high-temperature (exponential) part of a release will have a considerably steeper decay than that shown for component *Y* in figure 13. Indeed, the release of a minor high-temperature component can probably be approximated by a Gaussian profile (the high-temperature profiles of major components are unquestionably described by relatively shallow exponential decays—see next section).

If a Gaussian profile is assumed for a minor high-temperature component, effects similar to those proposed by Halbout and Robert (1986) are still observed when mixtures are modeled. To illustrate this, figure 14*A* shows the exponential tail of a hypothetical major component with $\delta^{13}C$ of 0 ‰; the effects of a superimposed minor component ($\delta^{13}C$ of +100 ‰) with a release temperature of progressively higher values are shown in figures 14*B–E*. In figure 14*B* the minor release occurs in a very steep part of the exponential decay, and, thus, the measured yield profile does not give a clear indication of a second component. As the release of the minor component is progressively shifted to more shallow parts of the exponential decay (figs. 14*C–E*), the yield profile reflects more accurately its existence. In all cases the $\delta^{13}C$ values show the presence of more than one component; however, even in figure 14*E* the measured $\delta^{13}C$ value of the minor component is compromised because of mixing. Note that in figures 14*C–E* the maximum $\delta^{13}C$ value occurs in the step following the

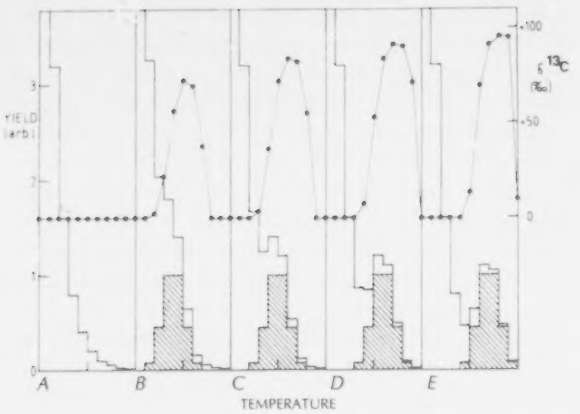

Figure 14. The effect on the measured release (yield in arbitrary units, left-hand axis) and isotope profiles ($\delta^{13}C$, right-hand axis) of a minor component, depicted as a symmetrical Gaussian profile (shaded region) being liberated on the exponential part of a major release. *A* shows the major release only; *B* through *E* show the effects of the minor release occurring in progressively more shallow parts of the exponential tail of the major component. Note that the minor component becomes better resolved in the progression *B* through *E* but that the measured $\delta^{13}C$ values are always lower than the true value of the minor component (+100 ‰). As in the Halbout and Robert modeling, the maximum measured $\delta^{13}C$ occurs at a higher temperature than that which appears to represent the release of the minor component.

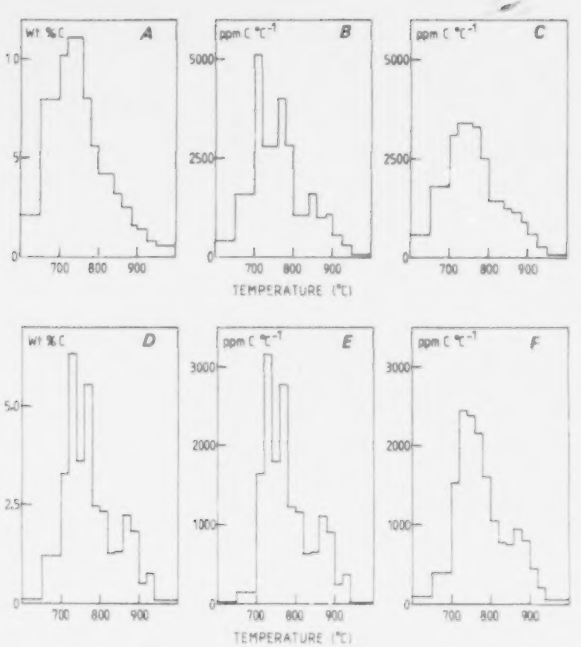

Figure 15. Stepped combustion of diamond by use of small temperature increments. The measured carbon-yield data, in weight percent carbon (wt % C), in *A* were acquired by use of unequal step sizes. *B* shows the effects of normalizing the data to a $°C^{-1}$ interval, and *C* shows the data after being subjected to a mathematical smoothing procedure. *D*, *E*, and *F* show measured, $°C^{-1}$-normalized, and smoothed data, respectively, for a diamond combusted in equal temperature increments.

maximum in yield. It is important to appreciate this effect when interpreting complicated stepped-combustion profiles; otherwise, the release temperature of a minor component may be overestimated.

Some Examples

If the necessity for accurate and reproducible control of temperature and time is fully appreciated, the results of high-resolution stepped-heating experiments can be informative. Well-controlled experiments should be the norm rather than the exception. However, an inexperienced or inattentive operator may produce poor-quality data. The problems associated with high-resolution stepped combustions are exemplified by data acquired from individual diamond fragments (fig. 15). The experiment shown in figure 15*A* was conducted by use of unequal temperature increments (an attempt to document accurately the temperature of each step); the yield versus temperature relationship conforms to a single broad release of carbon between 650 and 950 °C (analogous to the temperature range for diamond shown in fig. 4). The nature of the carbon release, which gradually decays with each consecutive step from 750 °C onwards, suggests that the oxidation rate of diamond at elevated temperatures is not highly temperature dependent (if the extent of combustion had been related to the temperature, the unequal step sizes would have produced a far more irregular profile). Thus, in this case, carbon combustion appears to be controlled by the timing of each step rather than by the temperature (and so the *x* axis could be replaced by one calibrated in time, rather than temperature). When the data are normalized to account for the different step increments (parts per million carbon per °C, fig. 15*B*), the release profile becomes apparently complex (correction of the yield data to account for different temperature increments is erroneous if the combustion reaction is dependent on time rather than temperature). However, the effects of poor temperature control may also produce the complicated $°C^{-1}$-normalized plot. Indeed, applying a ±5 °C error to each temperature step can explain the ostensibly complex normalized yield data. It can be seen that subjecting the yield data to the mathematical smoothing procedure described earlier (fig. 15*C*, dealt with in more detail below) has helped to portray the simplicity of the release.

The profile shown in figure 15*D* represents an attempt to analyze the sample in constant (20 °C) increments in order to avoid some of the problems encountered in the

previous experiment. The use of constant temperature increments results in a $°C^{-1}$-normalized profile (fig. 15*E*) that is similar in appearance to the yield plot (except for the steps below 700 °C and above 940 °C, which are not 20 °C increments). However, the experiment has not produced a single release of carbon. As in the previous example, it is difficult to divorce problems associated with poor control of temperature or time. If it is assumed that diamond exhibits an oxidation rate that is independent of combustion temperature, then figure 15*D* is explained if time intervals of unequal duration were used (although, it would be necessary to accept that perfectly accurate temperature control was achieved, a situation that seems unlikely). On the face of it, problems associated with reproducing the duration of steps might seem to be trivial compared to problems associated with controlling the temperature. However, it should be stressed that high-resolution stepped-combustion experiments may take typically 10 to 15 hours to conduct; as such, it is often a tedious burden on the operator to adhere rigorously to the time schedule. Assuming that the yield of carbon is directly proportional to the extraction time and applying an error of ±7 min to each step of the experiment could produce a yield profile that conforms to the expected single broad release. However, as in the case of the previous example, the effects of poor temperature control must also be considered.

The application of the smoothing procedure to diamond data is shown in figures 15*C* and 15*F*. When the irregularities that are due to experimental conditions have been suppressed, it is possible to appraise the combustion data more critically. It is interesting to note that in figure 15*F* there is a small but distinct release of carbon at about 850 to 900 °C. This effect can also be noted as a distinct shoulder on the release shown in the reformed data of figure 15*C* (this was not necessarily obvious in the yield versus temperature profiles of the raw data). The agreement between the two experiments suggests that the small release is not an experimental artifact but may instead represent the combustion of a relatively more stable part of the diamond (a core of different crystal habit, perhaps). Clearly, this property should be explored to obtain further information about diamond, but thus far the investigation has not been pursued.

An example of the reforming process as applied to the yields and isotope measurements of a meteorite sample (a carbonaceous chondrite, Y82042, McGarvie and others, 1987) is shown in figure 16. The raw data describe a seemingly complicated release pattern that would have several different components burning. When the data are reformed, it can be seen that there are three major releases of carbon with perhaps a further minor component at about 700 °C (the carbon burning from 600 to 700 °C results from the "tail" of a more major release of organic materials). The $\delta^{13}C$ values show that the 3 or 4 releases of carbon are all isotopically light, having $\delta^{13}C$ values of about −20 ‰. At

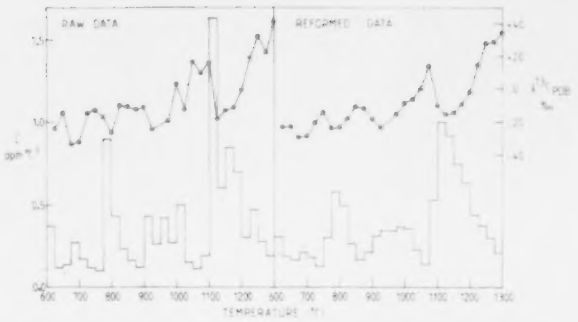

Figure 16. Raw and reformed data for the high-temperature combustion of an HCl-resistant residue from the carbonaceous chondrite Y82042. The yield is plotted as the histogram (left vertical scale) and $\delta^{13}C$ data as solid dots (right vertical scale). (PDB, Peedee belemnite.)

temperatures between the releases of light carbon, $\delta^{13}C$ values increase. The reformed data can be interpreted as several discrete releases of light carbon superimposed on an an overall low abundance of isotopically heavy carbon components. An understanding of the carbon components in this sample is considerably facilitated by the use of a smoothing procedure.

Before attempting to interpret the components present in a complicated meteorite sample, it is necessary to first appreciate the extent to which combustion of a major component may overlap with the release of higher temperature materials. This consideration is especially important in studies of meteorites such as carbonaceous chondrites, where high-temperature minor components (present at the parts per million level) may become obscured by the tail from indigenous organic materials (with a carbon content of 2 to 5 weight percent). Figure 17 shows those parts of the release profiles that are approximately exponential for two chemical separates of the Murray meteorite, an HCl residue of the Y791824 meteorite, and also a terrestrial diamond. The sample named Murray AY shows an exponential decrease in the yield that covers more than 3 orders of magnitude. It would seem impossible to derive an effect like this during a stepped-heating extraction from anything other than the extended combustion of a single component (for the purposes of this example, complex meteoritic organic materials are considered as a single component). Thus, when evaluating stepped-heating data of unknown samples, it is important to consider that low-temperature components may continue to burn and thus produce exponentially decreasing amounts of carbon with increasing temperature.

Figure 18 shows reformed stepped-combustion data (T>800 °C) for an HCl residue of a CM2 carbonaceous chondrite, Pollen (D.W.McGarvie, unpub. data, 1988). A casual inspection shows there to be an exponential tail from organic materials with $\delta^{13}C$ of about −20 ‰, superimposed

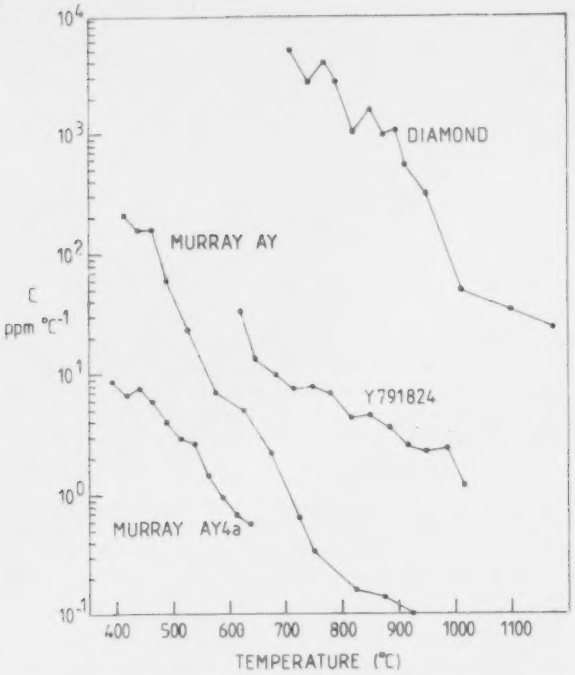

Figure 17. Yields of carbon (log scale) versus temperature for a number of samples. Murray AY and AY4a are chemical and physical separates of the CM2 carbonaceous chondrite Murray, Y791824 is an HCl-resistant residue of a whole-rock sample of another CM2 carbonaceous chondrite, and the diamond is a type II sample from an unknown locality. Only those parts of each release that conform to an exponential decay are shown.

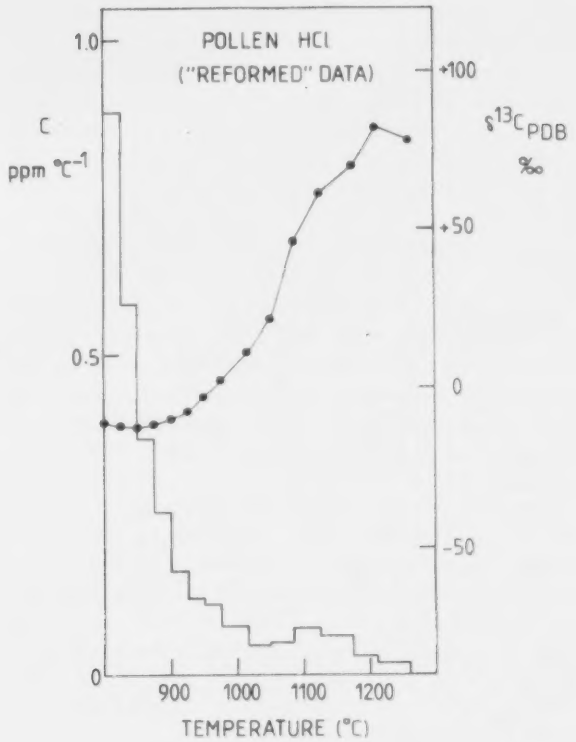

Figure 18. Stepped-combustion plot (800 to 1,260 °C) of an HCl residue prepared from the Pollen CM2 carbonaceous chondrite. Yield (histogram, left vertical scale) and $\delta^{13}C$ data (solid dots, right vertical scale) have been reformed to remove any inconsistencies in the measured profile. (PBD, Peedee belemnite.)

on which is a high-temperature release (~1,100–1,200 °C) of carbon having a $\delta^{13}C$ value of more than +80 ‰. The release profile thus has the appearance of a sample that contains just two components; intermediate $\delta^{13}C$ values between 900 and 1,100 °C reflect overlapping combustion. Inspection of the data reveals that the maximum $\delta^{13}C$ value occurs at a higher temperature than the carbon release discernible at about 1,100 °C. At first sight, this would appear to be compatible with the modeling of Halbout and Robert (1986), discussed previously. However, when the yield data are replotted on a log scale (fig. 19), it is immediately apparent that above 950 °C there are at least two high-temperature minor carbon components (the dashed line, which is a best-fit exponential through the six points that correspond to the lowermost temperatures of the experiment, represents the release of carbon from organic materials). Since the yield data do not return to the exponential decay at the highest temperatures, additional components may be present. If the nature of the release is explained as a mixture of carbon from the tail that is due to organic materials ($\delta^{13}C \approx -20$ ‰) and other minor components, then calculation of the "true" $\delta^{13}C$ values for the minor amounts of high-temperature carbon shows them to be not significantly higher than the measured values (because of the steep slope of the exponential release). However, it is already known from stepped-combustion studies of chemical and physical separates of CM2 carbonaceous chondrites such as Murchison and Murray (Swart and others, 1983b; Tang and others, 1988) and HCl-resistant residues of other CM2 meteorites (McGarvie and others, 1987) that the $\delta^{13}C$ values of high-temperature carbon components are in the range +500 to +1,500 ‰. Thus, a simple mixing calculation is not effective in describing the components in Pollen.

An alternative approach in explaining the Pollen data is to fit a more complicated decay profile to the lower temperature major component (such as that labeled A+B in fig. 19). Curve A+B has been calculated with an assumed mixture of an exponential decay from meteoritic organics ($\delta^{13}C \approx -20$ ‰) and a constant offset, for example from a blank contribution (also with $\delta^{13}C \approx -20$ ‰). Lines A and B have been chosen such that their combined effect when summed together intersects the final measured point

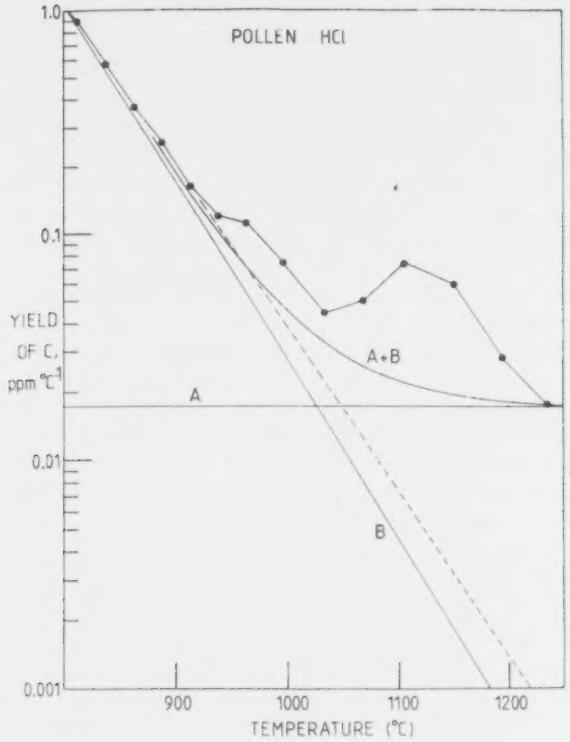

Figure 19. Measured yield of carbon (solid dots, log scale) versus temperature for the Pollen HCl residue shown in figure 18. The dashed line represents a best fit through the part of the release that defines an exponential decay. The line labeled A represents an offset, as might be expected to arise from a constant blank contribution. Line B represents a theoretical exponential decay, selected such that the cumulative effect of adding A and B together is to intersect the yield point measured at the highest temperature. Actual yields, therefore, indicate the presence of two minor components: one between 1,025 and 1,200 °C and a second, less obvious than the first, from about 900 to 1,025 °C.

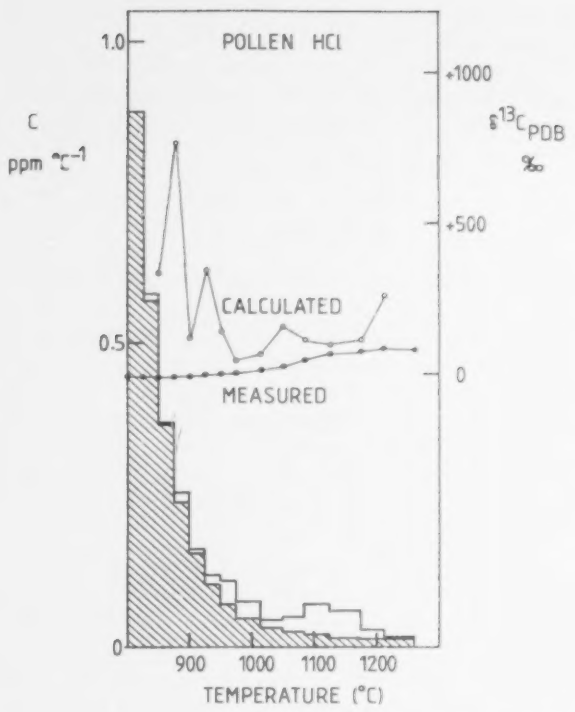

Figure 20. Measured and calculated results for Pollen HCl residue in which mixing of a tail from a major organic component is assumed. The shaded histogram corresponds to the tail component (derived from curve A+B in fig. 19; note that the histogram has been calculated so as to match the temperature increments of the sample). The nonshaded histogram shows the measured yield data. The measured $\delta^{13}C$ values (solid dots) are shown and compared to those calculated for the minor component (open circles), assuming that the major organic component has $\delta^{13}C \approx -20$ ‰, PDB, Peedee belemnite.

(0.017 ppm C °C^{-1} at 1,210–1,260 °C). The line describing the offset (*A*, fig. 19) is about five times higher than that which would be expected for a normal system blank; thus, at very least, this detailed appraisal of the Pollen data appears to have demonstrated an abnormally high blank during the analysis. Regardless, the $\delta^{13}C$ data can now be corrected under the assumption that mixing took place with a component that conforms to the release labeled A+B. The component has a $\delta^{13}C$ of −20 ‰. The calculated $\delta^{13}C$ data are shown in figure 20, along with the exponentially decreasing release ascribed to organic materials plus constant blank (shaded histogram). The calculated isotopic values at low temperatures (*T* about 900 °C) appear to show high degrees of ^{13}C enrichment; this enrichment is largely due to the positioning of the exponential release (the location of line B in fig. 19). Of more importance is that, between 850 and 1,200 °C, three releases of minor amounts of carbon can be discerned, and, perhaps somewhat unexpectedly, the calculated $\delta^{13}C$ values of these components are seen to be relatively ^{13}C poor.

Thus, the Pollen data are in some ways similar to those acquired for Y82042 (fig. 16) because of the observation of both isotopically light and heavy high-temperature carbon components. There is every indication that in carbonaceous chondrites, between four and seven different components burn at high temperatures. The mathematical modeling used to derive this conclusion offers a very different view from that which may have been attained by use of a more simplistic outlook of the type advocated by Halbout and Robert (1986). However, it needs to be stressed that modeling of this nature should be used only to gain an insight into the potential carbon inventory of a

particular sample (calculated yields and $\delta^{13}C$ values of each putative component are, of course, model dependent). Following this process, it should then be possible to devise appropriate separation schemes, or stepped-heating schedules, that can further elucidate the sample under investigation.

CONCLUDING REMARKS

High-sensitivity static mass spectrometry allows isotopic measurements to be made on subnanomole amounts of carbon as CO_2; current instrumentation produces precisions of $< \pm 1$ ‰ for $\delta^{13}C$ ($\delta^{18}O$ measurements are also possible of course, but with somewhat poorer levels of precision of about ± 2.5 ‰; however, thus far no attempts have been made to exploit, or indeed improve, this capability). An instrument being tested appears to be capable of making $\delta^{13}C$ and $\delta^{18}O$ measurements on picomole quantities of CO_2 with precisions of ± 2.5 ‰.

In order for carbon to be extracted in the form of CO_2, samples can be submitted to incremental heating either with oxygen (combustion) or without (pyrolysis). Stepped combustion allows separation of carbon-bearing components on the basis of oxidation temperature. In many favorable instances, different materials can be successfully resolved in carefully controlled experiments. In particular, indigenous high-temperature carbon components are easily distinguished from organic contaminants. Small samples give the best results for stepped-combustion experiments, since materials are able to burn, or degrade, at a more uniform rate and over more tightly constrained temperature intervals, two factors that lead to improved separation of components. Furthermore, low-volume extraction systems can be employed, resulting in reduced system blanks. Because small samples give lower amounts of CO_2 for analysis, the stepped-combustion approach is more suited to static mass spectrometry than the conventional dynamic procedures.

For its full potential to be realized, stepped combustion needs to be performed under the most carefully controlled conditions of temperature, time, oxygen, pressure, and so on. Up to now, these factors have not always been carefully controlled; therefore, a carbon release profile can exhibit features that experience has shown are artifacts of poor technique. A number of vagaries associated with stepped combustion have been dealt with herein. One of the main problems is that in order to resolve components, it is often desirable to employ a high-resolution heating schedule (that is, temperature steps ≤ 25 °C); while it is possible to make measurements of relative increments in temperature to accuracies of $\leq \pm 5$ °C, the absolute temperature of the sample may be in error by ± 25 °C. Thus, with step sizes of ≤ 25 °C it becomes increasingly difficult to compare data from replicate analyses or from measurements of different elements (carbon and nitrogen, for instance, which for technical reasons, have to be measured on separate instruments and thus different aliquots of the same sample). Poor control of either the temperature or the length of time used for an individual step during an experiment may result in release profiles that appear (erroneously) complex. However, data already acquired may be mathematically reformed to smooth out errors of this nature.

The combustion process lends itself ideally to mathematical modeling so that small components overlapped by a major one may be resolved if an exponential tailing effect is assumed. So far, only the very simplest and most easily recognized variables have been considered in modeling. Parameters such as the grain size of the sample and oxygen pressure have yet to be taken into account. The temperature regime experienced by a sample could be much more thoroughly monitored and time averaged. However, even with absolutely perfect temperature control of a furnace there are still problems to be considered, such as (1) temperature gradients within the extraction vessel, (2) positioning of the sample with respect to the temperature measurement device, (3) exothermic or endothermic reactions or changes of state involving various materials (not necessarily carbonaceous) in a multicomponent sample that causes localized temperature variations, and (4) the presence within a particular sample of catalysts, surface poisoning agents, or protecting materials that can cause materials to combust at unexpected temperatures or affect the gas-phase chemistry.

In carbon isotopic studies, as stepped-combustion processes become more fully understood, it should become possible to perform reproducible experiments to smaller temperature increments. If heating schedules can be tailored so as to approximate linear temperature ramps, mathematical modeling of the data will become straightforward and indeed more informative. Extremely small-temperature-increment (ultrahigh resolution) stepped-combustion extractions will undoubtedly require the use of a new generation of high-sensitivity static mass spectrometers. True linear heating may require completely new developments in mass spectrometry. The highest levels of sensitivity for carbon isotopic studies may be found eventually in a combination of ion- or laser-probe extraction followed by resonance ionization mass spectrometry. However, in the meantime stepped heating followed by carbon isotopic analysis in which static mass spectrometry is used will continue to provide valuable information in new and previously studied areas of geochemistry and cosmochemistry, particularly when all the vagaries associated with the technique are taken into account.

ACKNOWLEDGMENTS

The development of the stepped-heating techniques and static mass spectrometers has been made possible by

grants from the Nuffield and Wolfson Foundations and the Science and Engineering Research Council. We acknowledge all those members of the Planetary Sciences Unit past and present whose unpublished data have been included in this paper. The manuscript has been improved by a critical appraisal from Monica Grady and thoughtful reviews by Pat Shanks and Bob Criss. I.P. Wright thanks the USGS and the organizers of the "New Frontiers in Stable Isotopic Research" workshop for providing funds to allow attendance at the meeting.

REFERENCES CITED

Abell, P.I., Fallick, A.E., and Pillinger, C.T., 1979, Microreduction techniques for conversion of CO_2 to CD_4 and their potential application for high sensitivity, precise stable carbon isotope measurements, *in* Douglas, A.R., and Maxwell, J.R., eds., Advances in organic geochemistry: Oxford, Pergammon, p. 689–696.

Albarede, F., 1978, The recovery of spatial isotope distributions from stepwise degassing data: Earth and Planetary Science Letters, v. 39, p. 387–397.

Aldrich, L.T., and Nier, A.O., 1948, The occurrence of He^3 in natural sources of helium: Physical Review, v. 74, p. 1590–1594.

Ash, R.D., Arden, J.W., Alexander, C.O., Grady, M.M., Wright, I.P., and Pillinger, C.T., 1988, Isotopically heavy carbon in the Allende meteorite—New or previously recognised phases?: Lunar and Planetary Science, v. 19, p. 15–16.

Ash, R.D., Wright, I.P., Grady, M.M., Pillinger, C.T., Lewis, R.S., and Anders, E., 1987, An investigation of carbon and nitrogen isotopes in Cô and the effects of grain size upon combustion temperature: Meteoritics, v. 22, p. 319.

Beckinsale, R.D., Freeman, N.J., Jackson, M.C., Powell, R.E., and Young, W.A.P., 1973, A 30 cm radius 90° sector double collecting mass spectrometer with a capacitor integrating detector for high precision isotopic analysis of carbon dioxide: International Journal of Mass Spectrometry and Ion Physics, v. 12, p. 299–308.

Begbie, P.J., Beckinsale, R.D., Freeman, N.J., and Powell, R.E., 1972, A bakable changeover valve for high precision mass spectrometric comparison of the isotopic composition of gases: Review of Scientific Instruments, v. 43, p. 1454–1455.

Boyd, S.R., Mattey, D.P., Pillinger, C.T., Milledge, H.J., Mendelssohn, M., and Seal, M., 1987, Multiple growth events during diamond genesis: An integrated study of carbon and nitrogen isotopes and nitrogen aggregation state in coated stones: Earth and Planetary Science Letters, v. 86, p. 341–353.

Boyd, S.R., Wright, I.P., Franchi, I.A., and Pillinger, C.T., 1988, Preparation of sub-nanomole quantities of nitrogen gas for stable isotopic analysis: Journal of Physics E: Scientific Instruments, v. 21, p. 876–885 .

Bridger, N.I., Craig, R.D., and Sercombe, J.S.F., 1974, New mass spectrometer for isotopic analysis of small gas samples: Advances in Mass Spectrometry, v. 6, p. 365–375.

Briggs, M.H., and Kitto, G.B., 1962, Complex organic microstructures in the Mokoia meteorite: Nature, v. 193, p.1126–1127.

Brown, P.W., and Pillinger, C.T., 1981, Nitrogen concentrations and isotopic ratios from separated lunar soils: Meteoritics, v. 16, p. 298.

Brunnée, C., Laser, B., Rache, H., and Seiler, E.U., 1977, A new automated mass spectrometer for high precision isotope ratio determinations of gases: 25th Annual Conference on Mass Spectrometry, Washington, D.C., p. 95–97.

Carr, R.H., 1985, High sensitivity stable carbon isotope ratio mass spectrometry: Instrument development and applications: Ph.D. thesis, University of Cambridge, 252 p.

Carr, R.H., Wright, I.P., Pillinger, C.T., Lewis, R.S., and Anders, E., 1983, Interstellar carbon in meteorites: Isotopic analysis using static mass spectrometry: Meteoritics, v. 18, p. 277.

Carr, R.H., Wright, I.P., Joines, A.W., and Pillinger, C.T., 1986, Measurement of carbon stable isotopes at the nanomole level: A static mass spectrometer and sample preparation technique: Journal of Physics E: Scientific Instruments, v. 19, p. 798–808.

Clarke, W.B., Jenkins, W.J., and Top, Z., 1976, Determination of tritium by mass spectrometric measurement of ^3He: International Journal of Applied Radiation and Isotopes, v. 27, p. 515–522.

Coplen, T.B., 1973, A double-focusing double-collecting mass spectrometer for light stable isotope ratio analysis: International Journal of Mass Spectrometry and Ion Physics, v. 11, p. 37–40.

Craig, H., 1957, Isotopic standards for carbon and oxygen and correction factors for mass-spectrometric analysis of carbon dioxide: Geochimica et Cosmochimica Acta, v. 12, p. 133–149.

Davidson, D.W., 1973, Clathrate hydrates, *in* Franks, F., ed., Water—A comprehensive treatise, v. 2: New York, Plenum Press, p. 115–234.

Deines, P., 1970, Mass spectrometer correction factors for the determination of small isotopic composition variations of carbon and oxygen: International Journal of Mass Spectrometry and Ion Physics, v. 4, p. 283–295.

Des Marais, D.J., 1978, Carbon, nitrogen and sulfur in Apollo 15, 16 and 17 rocks: Proceedings of the 9th Lunar and Planetary Science Conference, Houston, Texas, p. 2451–2467.

———1983, Light element geochemistry and spallogenesis in lunar rocks: Geochimica et Cosmochimica Acta, v. 47, p. 1769–1781.

Exley, R.A., Mattey, D.P., Clague, D.A., and Pillinger, C.T., 1986, Carbon isotope systematics of a mantle "hotspot": A comparison of Loihi Seamount and MORB glasses: Earth and Planetary Science Letters, v. 78, p. 189–199.

Fallick, A.E., 1980, On the measurement of the valve-mixing correction of the changeover valve of a dual-inlet gas source mass spectrometer: International Journal of Mass Spectrometry and Ion Physics, v. 36, p. 47–55.

———1983, The ion beam profile and abundance sensitivity corrections for carbon dioxide in a gas source mass spectrometer: International Journal of Mass Spectrometry and Ion Physics, v. 46, p. 59–62.

Fallick, A.E., and Baxter, M.S., 1977, The pressure effect and peak broadening in gas source stable isotope mass spectrometry: International Journal of Mass Spectrometry and Ion Physics, v. 25, p. 155–165.

Fallick, A.E., Gardiner, L.R., Jull, A.J.T., and Pillinger, C.T., 1980, Instrumental effects in the application of static mass spectrometry to high sensitivity carbon isotope measurements: Advances in Mass Spectrometry, v. 8A, p. 309–317.

Faure, G., 1986, Principles of isotope geology: New York, Wiley and Sons, 589 p.

Franchi, I.A., Gibson, E.K., Wright, I.P., and Pillinger, C.T., 1985, Nitrogen isotopes by laser probe extraction: Lunar and Planetary Science, Houston, Texas, v. 14, p. 248–249.

Franchi, I.A., Wright, I.P., Gibson, E.K., and Pillinger, C.T., 1986, The laser microprobe: A technique for extracting carbon, nitrogen, and oxygen from solid samples for isotopic measurements: Journal of Geophysical Research, v. 91, no. B4, p. D514–D524.

Frick, U., and Pepin, R.O., 1981, Microanalysis of nitrogen isotope abundances: Association of nitrogen with noble gas carriers in Allende: Earth and Planetary Science Letters, v. 56, p. 64–81.

Gardiner, L.R., and Pillinger, C.T., 1979, Static mass spectrometry for the determination of active gases: Analytical Chemistry, v. 51, p. 1230–1236.

Gardiner, L.R., Jull, A.J.T., and Pillinger, C.T., 1978, Progress towards a direct measurement of $^{13}C/^{12}C$ ratios for hydrolysable carbon in lunar soil by static mass spectrometry: Proceedings of the 9th Lunar and Planetary Science Conference, Houston, Texas, p. 2149–2165.

Gibson, E.K., and Johnson, S.M., 1972, Thermogravimetric-quadrupole mass-spectrometric analysis of geochemical samples: Thermochimica Acta, v. 4, p. 49–56.

Gibson, E.K., Moore, G.W., and Johnson, S.M., 1974, Summary of analytical data from gas release investigations, volatilization experiments, elemental abundance measurements on lunar samples, meteorites, minerals, volcanic ashes and basalts: Houston, Texas, NASA Preprint, L.B. Johnson Space Center, 201 p.

Gilmour, I., 1986, The distribution of carbon stable isotopes within sedimentary organic matter: University of Cambridge, Ph.D. thesis, 240 p.

Gilmour, I., and Pillinger, C.T., 1985, Stable carbon isotopic analysis of sedimentary organic matter by stepped combustion: Organic Geochemistry, v. 8, p. 421–426.

Grady, M.M., 1982, The content and isotopic composition of carbon in stony meteorites: University of Cambridge, Ph.D. thesis, 216 p.

Grady, M.M., Swart, P.K., Wright, I.P., and Pillinger, C.T., 1985, The carbon and nitrogen isotopic composition of ureilites: Implications for their genesis: Geochimica et Cosmochimica Acta, v. 49, p. 903–915.

Grady, M.M., Wright, I.P., Carr, L.P., and Pillinger, C.T., 1986, Compositional differences in enstatite chondrites based on carbon and nitrogen stable isotope measurements: Geochimica et Cosmochimica Acta, v. 50, p. 2799–2813.

Halas, S., 1979, An automatic inlet system with pneumatic changeover valves for isotope ratio mass spectrometer: Journal of Physics E: Scientific Instruments, v. 12, p. 418–420.

———1985, Isotope analysis on nanomole gas samples: Isotopenpraxis, v. 21, p. 86–87.

Halas, S., and Krouse, H.R., 1983, Isotopic analysis of nanomole gas samples by means of dynamic flow mass spectrometry: Review of Scientific Instruments, v. 54, p. 437–443.

Halbout, J., and Robert, F., 1986, Numerical simulations of stable isotope results of progressive heating experiments: Meteoritics, v. 21, p. 384–386.

Halbout, J., Mayeda, T.K., and Clayton, R.N., 1986, Carbon isotopes and light element abundances in carbonaceous chondrites: Earth and Planetary Science Letters, v. 80, p. 1–18.

Halsted, R.E., and Nier, A.O., 1950, Gas flow through the mass spectrometer viscous leak: Review of Scientific Instruments, v. 21, p. 1019–1021.

Hayes, J.M., Des Marais, D.J., Peterson, D.W., Schoeller, D.A., and Taylor, S.P., 1978, High precision stable isotope ratios from microgram samples: Advances in Mass Spectrometry, v. 7A, p. 475-480.

Hayes, J.M., Kaplan, I.R., and Wedeking, K.W., 1983, Precambrian organic geochemistry, preservation of the record, *in* Schopf, J.W., ed., Earth's earliest biosphere: Its origin and evolution: Princeton University Press, New Jersey, p. 93–134.

Hoefs, J., 1987, Stable isotope geochemistry: Berlin, Springer-Verlag, 241 p.

Hohenberg, C.M., 1980, High sensitivity pulse-counting mass spectrometer system for noble gas analysis: Review of Scientific Instruments, v. 51, p. 1075–1082.

Irako, M., Oguri, T., and Kanomata, I., 1975, The static operation mass spectrometer: Japanese Journal of Applied Physics, v. 14, p. 533–543.

Jones, L.M., Taylor, A.R., Winter, D.L., Hurst, S.D., and Keen, G.W., 1986, The use of the laser microprobe for sample preparation in stable isotope mass spectrometry: TERRA cognita, v. 6, p. 263.

Kerridge, J.F., 1985, Carbon, hydrogen and nitrogen in carbonaceous chondrites: Abundances and isotopic compositions in bulk samples: Geochimica et Cosmochimica Acta, v. 49, p. 1707–1714.

Kyser, T.K., ed., 1987, Stable isotope geochemistry of low temperature fluids: Saskatoon, Mineralogical Society of Canada Short Course 13, 452 p.

Mattey, D.P., Carr, R.H., Wright, I.P., and Pillinger, C.T., 1984, Carbon isotopes in submarine basalts: Earth and Planetary Science Letters, v. 70, p. 196–206.

Matthews, D.E., and Hayes, J.M., 1978, Isotope-ratio-monitoring gas chromatography-mass spectrometry: Analytical Chemistry, v. 50, p. 1465–1473.

———1979, Isotope-ratio-monitoring gas chromatography-mass spectrometry, *in* Klein, E.R., and Klein, P.D., eds., Stable isotopes: Proceedings of the Third International Conference: New York, Academic Press, p. 95–100.

McCrea, J.M., 1950, On the isotopic chemistry of carbonates and a paleotemperature scale: Journal of Chemical Physics, v. 18, p. 849–857.

McGarvie, D.W., Wright, I.P., Grady, M.M., Pillinger, C.T., and Gibson, E.K., 1987, A stable carbon isotopic study of types 1 and 2 carbonaceous chondrites: Memoirs of the National Institute of Polar Research, Special Issue, v. 46, p. 179–195.

McKinney, C.R., McCrea, J.M., Epstein, S., Allen, H.A., and Urey, H.C., 1950, Improvements in mass spectrometers for the measurement of small differences in isotope abundance ratios: Review of Scientific Instruments, v. 21, p. 724–730.

McNaughton, N.J., Abell, P.I., Wright, I.P., Fallick, A.E., and Pillinger, C.T., 1983, Preparation of nanogram quantities of deuteromethane for stable carbon isotope analysis: Journal of Physics E: Scientific Instruments, v. 16, p. 505–511.

Megrue, G.H., 1967, Isotopic analysis of rare gases with a laser microprobe: Science, v. 157, p. 1555–1556.

Merrill, G.L., 1974, A static mode mass spectrometer for the measurement of noble gases: International Journal of Mass Spectrometry and Ion Physics, v. 13, p. 281–290.

Milodowski, A.E., and Morgan, D.J., 1980, Identification and estimation of carbonate minerals at low levels by evolved CO_2 analysis: Nature, v. 286, p. 248–249.

Mook, W.G., and Grootes, P.M., 1973, The measuring procedure and corrections for the high-precision mass-spectrometric analysis of isotopic abundance ratios, especially referring to carbon, oxygen and nitrogen: International Journal of Mass Spectrometry and Ion Physics, v. 12, p. 273–298.

Murphey, B.F., 1947, The temperature variation of the thermal diffusion factors for binary mixtures of hydrogen, deuterium, and helium: Physical Review, v. 72, p. 834–837.

Murty, S.V.S., and Marti, K., 1985, Nitrogen abundances in individual chondrules: Lunar and Planetary Science, Houston, Texas, v. 16, p. 605–606.

Niederer, F.R., Eberhardt, P., Geiss, J., and Lewis, R.S., 1985, Carbon isotope abundances in Murchison residue 2C10c: Meteoritics, v. 4, p. 716–718.

Nier, A.O., 1947, A mass spectrometer for isotope and gas analysis: Review of Scientific Instruments, v. 18, p. 398–411.

Norris, S.J., Brown, P.W., and Pillinger, C.T., 1981, Laser pyrolysis for light element and stable isotope studies: Meteoritics, v. 16, p. 369.

Pillinger, C.T., 1984, Light element stable isotopes in meteorites—From grams to picograms: Geochimica et Cosmochimica Acta, v. 48, p. 2739–2766.

Prosser, S.J., Wright, I.P., and Pillinger, C.T., 1988, A gas source, static vacuum mass spectrometer for determination of carbon stable isotopes at the picomole level [abs.]: 11th International Mass Spectrometry Conference, Bordeaux.

Reynolds, J.H., 1956, High sensitivity mass spectrometer for noble gas analysis: Review of Scientific Instruments, v. 27, p. 928–934.

Sabatier, P., and Senderens, J-B., 1902, Nouvelles syntheses du methane: Comptes Rendus, v. 134, p. 514–516.

Sakai, H., Smith, J.W., Kaplan, I.R., and Petrowski, C., 1976, Micro-determinations of C, N, S, H, He, metallic Fe, $\delta^{13}C$, $\delta^{15}N$ and $\delta^{34}S$ in geologic samples: Geochemical Journal, v. 10, p. 85–96.

Schaeffer, O.A., and Zähringer, J., 1958, High-sensitivity mass spectrometric measurement of stable helium and argon isotopes produced by high-energy protons: Physical Review, v. 113, p. 674–678.

Schoeller, D.A., and Hayes, J.M., 1975, Computer controlled ion counting isotope ratio mass spectrometer: Analytical Chemistry, v. 47, p. 408–415.

Shackleton, N.J., 1965, The high-precision isotopic analysis of oxygen and carbon in carbon dioxide: Journal of Scientific Instruments, v. 42, p. 689–692.

Shankai, Z., Conzemius, R.J., and Svec, H.J., 1984, Determination of carbon, nitrogen and oxygen in solids by laser mass spectrometry: Analytical Chemistry, v. 56, p. 382–385.

Sommer, M.A., Yonover, R.N., Bourcier, W.L., and Gibson, E.K., 1985, Determination of H_2O and CO_2 concentrations in fluid inclusions in minerals using laser decrepitation and capacitance manometer analysis: Analytical Chemistry, v. 57, p. 449–453.

Stacey, J.S., Sherrill, N.D., Dalrymple, G.B., Lanphere, M.A., and Carpenter, N.V., 1981, A five-collector system for the simultaneous measurement of argon isotope ratios in a static mass spectrometer: International Journal of Mass Spectrometry and Ion Physics, v. 39, p. 167–180.

Stewart, K.K., 1981, Flow-injection analysis: A review of its early history: Talanta, v. 28, p. 789–797.

Swart, P.K., Grady, M.M., and Pillinger, C.T., 1982, Isotopically distinguishable carbon phases in the Allende meteorite: Nature, v. 297, p. 381–383.

———1983a, A method for the identification and elimination of contamination during carbon isotopic analyses of extraterrestrial samples: Meteoritics, v. 18, p. 137–154.

Swart, P.K., Grady, M.M., Pillinger, C.T., Lewis, R.S., and Anders, E., 1983b, Interstellar carbon in meteorites: Science, v. 220, p. 406–410.

Swart, P.K., Pillinger, C.T., Milledge, H.J., and Seal, M., 1983c, Carbon isotopic variation within individual diamonds: Nature, v. 303, p. 793–795.

Tang, M., Lewis, R.S., Anders, E., Grady, M.M., Wright, I.P., and Pillinger, C.T., 1988, Isotopic anomalies of Ne, Xe and C in meteorites, pt. I, Separation of carriers by density and chemical resistance: Geochimica et Cosmochimica Acta, v. 52, p. 1221–1234.

Trott, G.W., and Beynon, J.H., 1979, A comment on smoothing of experimental ion kinetic energy data collected by computer: International Journal of Mass Spectrometry and Ion Physics, v. 31, p. 37–49.

Valley, J.W., Taylor, H.P., and O'Neil, J.R., 1986, eds., Stable isotopes in high temperature geological processes: Mineralogical Society of America, Reviews in Mineralogy, 570 p.

Wada, H., 1988, Microscale isotopic zoning in calcite and graphite crystals in marble: Nature, v. 331, p. 61–63.

Wada, H., Niitsuma, N., and Saito, T., 1982, Carbon and oxygen isotopic measurements of ultra-small samples: Shizouka University, Geoscience Reports, v. 7, p. 35–50.

Weast, R.C., ed., 1984, CRC Handbook of Chemistry and Physics: Boca Raton, Florida, CRC Press.

Wright, I.P., 1984, $\delta^{13}C$ measurements of smaller samples: Trends in Analytical Chemistry, v. 3, p. 210–215.

Wright, I.P., and Pillinger, C.T., 1983, Deuterium enrichments in Renazzo revealed by static mass spectrometry: Meteoritics, v. 18, p. 425–426.

Wright, I.P., McNaughton, N.J., Fallick, A.E., Gardiner, L.R., and Pillinger, C.T., 1983, A high-precision mass spectrometer for stable carbon isotope analysis at the nanogram level: Journal of Physics E: Scientific Instruments, v. 16, p. 497–504.

Wright, I.P., Swart, P.K., Grady, M.M., Pillinger, C.T., Lewis, R.S., and Anders, E., 1984, Isotopically anomalous carbon and nitrogen components in the Allende (CV3) and Murchison (CM2) carbonaceous chondrites: Associations with CCFXe, s–Xe and Ne-E(l): Planetary Sciences Unit Internal Report No. 1, Milton Keynes, England, 25 p.

Wright, I.P., Boyd, S.R., Franchi, I.A., and Pillinger, C.T., 1988, High-precision determination of nitrogen stable isotope ratios at the sub-nanomole level: Journal of Physics E: Scientific Instruments, v. 21, p. 865–875.

Zinner, E., and Epstein, S., 1987, Heavy carbon in individual oxide grains from the Murchison meteorite: Earth and Planetary Science Letters, v. 84, p. 359–368.

Zinner, E., Tang, M., and Anders, E., 1987, Large isotopic anomalies of Si, C, N and noble gases in interstellar silicon carbide from the Murray meteorite: Nature, v. 330, p. 730–732.

Laser Microprobe–Quadrupole Mass Spectrometer System for the Analysis of Gases and Volatiles from Geologic Materials

By Everett K. Gibson, Jr.,[1] *and* Robert H. Carr[2]

Abstract

A laser microprobe connected to a computer-controlled benchtop quadrupole mass spectrometer is capable of extracting gases and volatiles from a wide variety of geologic materials. The released gases are identified by mass spectrometry. A capacitance manometer is used to quantify the yield of released gases. Reference minerals have been analyzed in order to determine the nature of volatiles released by laser interaction with the surfaces. Minerals analyzed include carbonates (calcite, magnesite, dolomite, and azurite), a sulfate (barite), a sulfide (pyrite), and diamond. Two separate studies have been carried out to show the utility of the newly developed analysis system: (1) analysis of a weathering product associated with glass in an SNC meteorite and (2) analysis of different types of fluid inclusions in an Archean barite.

INTRODUCTION

The abundance, distribution, and chemical forms of the light volatile elements present in geologic materials can provide valuable information concerning the nature, origin, and subsequent evolutionary history of individual samples. For example, the ratio of carbon dioxide to water in many fluid inclusions can be used to infer the nature of mineralizing solutions and, from phase relations, to indicate the pressure/depth regime in which the host mineral formed (Roedder, 1972, 1984; Roedder and Bodnar, 1980). Mineral identification also can be enhanced by the determination of gases liberated upon breakdown of the sample by pyrolysis, combustion, or acid dissolution.

Many of the macroscopic methods used in the determination of volatile species essentially have been nonselective, with the possible multiplicity of origin of the extracted gases often presenting an insurmountable limitation to interpretation (Harris, 1981; Sommer and Schramm, 1983). "Probe" methods are becoming increasingly popular in a large range of scientific studies, because more detailed experimental data often can be obtained by using more localized analyses. The ability to selectively extract and analyze areas 10 to 40 μm in diameter offers great potential for study of important problems associated with the identification, origin, and elemental and isotopic composition of the materials. Laser extraction of gases from geologic samples has been undertaken in a variety of circumstances to facilitate this finer scale approach (Tsui and Holland, 1979; York and others, 1981; Kotra and Gibson, 1982). Laser-microprobe extraction of carbon, nitrogen, and oxygen from samples for stable isotopic measurements has been shown by Franchi and others (1986; this volume) to be a viable technique, but further refinements are required.

In this paper we describe an instrumental system that combines the ability of a laser probe to interact selectively with a small, predetermined locality in a sample with the analytical capability of a benchtop quadrupole mass spectrometer. The quadrupole mass spectrometer permits qualitative information to be obtained on the volatiles released from the samples. A capacitance manometer is included in the system to allow direct quantitation of the gases extracted (Sommer and others, 1985).

EXPERIMENTATION

Apparatus

The laser microprobe–quadrupole mass spectrometer computer system is shown in figure 1, and a schematic diagram of this system is shown in figure 2. The main sections are (1) the quadrupole mass spectrometer, (2) a vacuum valve and capacitance manometer section, (3) a vacuum pumping system, and (4) the sample chamber. Not shown in figure 2 are the laser and the sample-viewing microscope. A more detailed diagram of the sample chamber is given in figure 3.

Mass Spectrometer

The quadrupole mass spectrometer is an HP–5970B Mass Selective Detector (Hewlett Packard, Ltd., Palo Alto, Calif.) designed primarily for use with gas chromatographic systems. The electron-impact ionization source, hyperbolic mass filter, electron multiplier, power supply, drive electronics, and air-cooled turbomolecular pump are contained

[1] SN2, Planetary Sciences Branch, NASA Johnson Space Center, Houston, TX 77058.

[2] SN4, Experimental Planetology Branch, NASA Johnson Space Center, Houston, TX 77058. Present address: ICI Europa Ltd., Everslaan 45, B-3078 Kortenberg, Belgium.

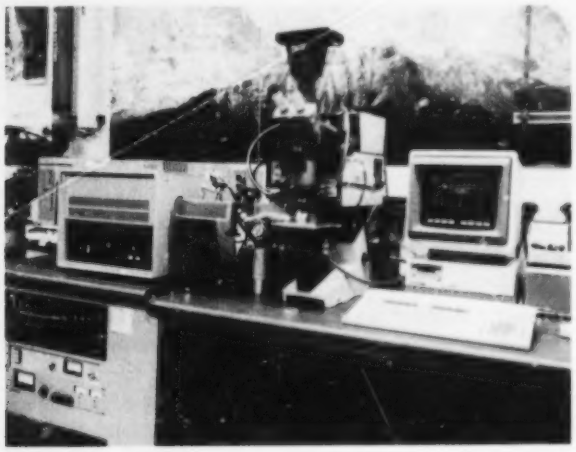

Figure 1. Laser microprobe–quadrupole mass spectrometer with the computer that controls the system (located on the right). The laser microprobe, along with its associated sample chamber, lighting, and photographic system, is shown in the center. The benchtop quadrupole mass spectrometer, along with its heated inlet line, is to the left of the laser microprobe. In the lower left are the control system for the vacuum system and the capacitance manometer readout units for quantifying the amounts of gases released during analysis.

in a single, compact (54-kg) unit, and an external two-stage direct-drive mechanical pump provides the backing vacuum.

Ionization of the neutral gas species entering the mass spectrometer is achieved by impact of electrons, with an energy of 70 eV, from either of two filaments that are user selectable by means of an external switch. The quadrupole mass filter consists of four molybdenum rods, 203 mm long, precisely formed to a hyperbolic shape. Detection of the positive ions extracted by the mass filter is accomplished by a continuous dynode electron multiplier, which has a maximum voltage setting of 3,000 V. The analyzer chamber is heated by means of heating tape that is covered by insulating material held in place by an aluminum shroud. During normal operation, the ion source end is held at about 280 °C, while the detector end is appreciably cooler, about 75 °C. The pumping system evacuates the analyzer to a background pressure of about 2×10^{-7} torr, as measured by an ion gauge located on the rear of the analyzer flange. Water is the major contaminant, with minor atmospheric gases and traces of pump oil.

Realtime control of the mass spectrometer is accomplished via the drive electronics located in the main unit. Operating parameters are entered via the data system (HP–59970 ChemStation), which also runs software for the automatic adjustment of voltages in the ion source, calibration, and mass assignment and scanning control of the mass spectrometer. An Autotune program is available to optimize instrument parameters automatically by comparing a library spectrum of perfluorotributylamine (PFTBA) with spectra of the PFTBA released from a small cylinder attached to the analyzer flange. Data acquisition programs control the operating mode of the instrument, while editing software allows plotting and tabulating mass spectra, background subtractions, and so on. Peripherals attached to the ChemStation are a combined fixed- and floppy-disc unit (HP–9133H), a graphics plotter (HP–7475A), and a printer (HP–2930).

Vacuum Valve System and Capacitance Manometer

The mass selective detector is normally used with an interfaced gas chromatograph. For the laser microprobe to be interfaced to the mass spectrometer, several modifications must be made to the sample inlet portion of the system. When not intended for use with chromatographic systems, the inlet of the HP–5970 mass spectrometer is supplied with a blank gasketed vacuum fitting (VCR, Cajon, Macedonia, Ohio). This fitting has been adapted by having a 22-cm length of 6-mm (outside diameter) by 4-mm (inside diameter) stainless steel tube welded through it such that the tubing terminates close to the mass spectrometer's ion source. The other end of the tube is welded to a high-vacuum bellows valve (Nupro, Willoughby, Ohio) that acts as the inlet valve (V_1, fig. 2). An aliquoter formed from two other valves (V_2 and V_3) allows a small (1.6 cm^3) volume of gas to be isolated from the larger (11.2 cm^3) volume, which contains a capacitance manometer and cold finger and is isolated, in turn, from the pumping system by a valve (V_4). The valve system can be heated above room temperature. Thermocouples are positioned strategically within the oven to monitor temperatures via a digital thermometer (11KC, Omega Engineering, Inc., Stamford, Conn.).

The sensitivity of the capacitance manometer for determining absolute pressures with extreme linearity has been described by Sommer and others (1985). The capacitance manometer employed has a bakable unit with a 1 to 10^{-6} torr range (315BHS Baratron, MKS Instruments, Burlington, Mass.), housed in an individual oven that is operated via a control unit (MKS–273). Output from the sensor head is passed, via a nonbakable transducer, to a multiplexor unit (MKS–274) for temperature compensation and, hence, to a high-accuracy electronic display unit (MKS–270B). A 0- to 10-V output from the display unit can be connected to a chart recorder so pressure changes may be visualized more easily.

Vacuum Pumping System

In addition to the mass spectrometer pumps, an auxiliary pumping system is provided to evacuate the sample chamber after samples are loaded. The auxiliary pumping system allows a high vacuum to be maintained

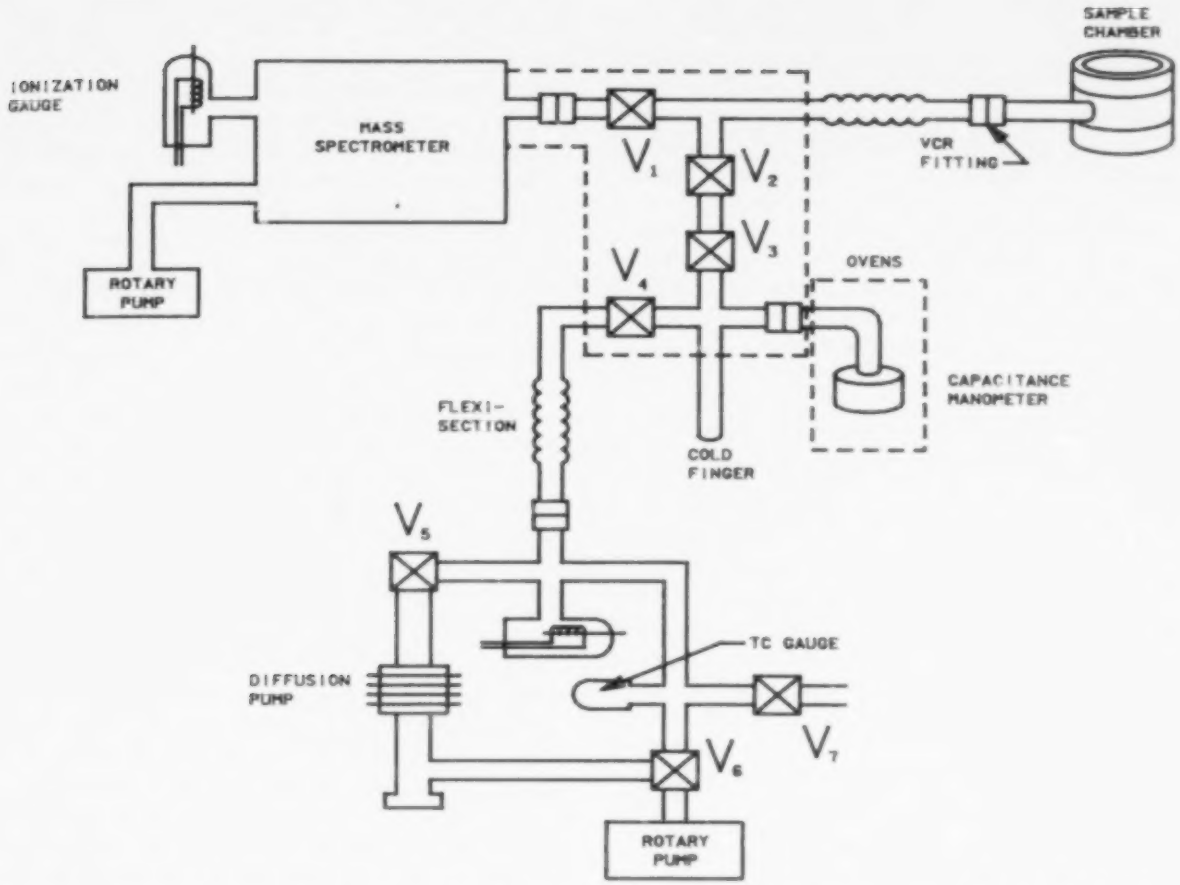

Figure 2. Schematic diagram of the laser microprobe–mass spectrometer system. The laser enters the sample chamber through an optical window. Valves V_1–V_7 and components are discussed in the text.

within portions of the system that are not on line to the mass spectrometer. An air-cooled oil-vapor diffusion pump (EO40/55, Edwards High Vacuum, Crawley, England) backed by a rotary pump (E2M2, Edwards) provides the vacuum, while a pipeline valve (fig. 2, V_5) (PVK40, Edwards) and a backing/roughing valve (V_6) (BRV10, Edwards) enable the diffusion pump to be isolated during initial pump down. Ionization and thermocouple gauges, operating from a controller (Type 843, Varian, Lexington, Mass.), monitor the vacuum. Another Nupro valve (V_7) can be used to admit purified air to the system for venting.

Laser Microprobe

The microprobe employed for gas extraction is an industrial-grade laser system that is normally used for excitation in spectrochemical analysis (Laser Mark III, Jarrell-Ash, Waltham, Mass.). A pulse of 1.06-μm light is generated by a Q-switched xenon-pumped neodymium glass laser and directed onto the sample by means of a trinocular metallurgical microscope (K16–10–801, American Optical Scientific Instruments, Buffalo, N.Y.). The energy output of the laser pulse is controllable in the range 0.1 to 1 J. There are five aperture settings available for the mechanical adjustment of the final diameter of the laser beam. Beam diameters range from 10 to 200 μm. A 35-mm camera is permanently mounted on the microscope to document analyses, while a Polaroid camera can be interchanged with one of the eyepieces to take "instant working pictures" of the sample under examination.

The microscope objectives used must be "air-spaced" objectives. Should ordinary microscope objectives that are not air spaced be used, catastropic rupture of the lens within the objectives can occur. Caution must be observed with the objectives during the pulsing of the laser, or serious injury might occur to the system's operators if the objectives "explode" and spray glass throughout the laboratory. The use of air-spaced objectives, however, has several disadvantages for the laser-microprobe studies. Magnification

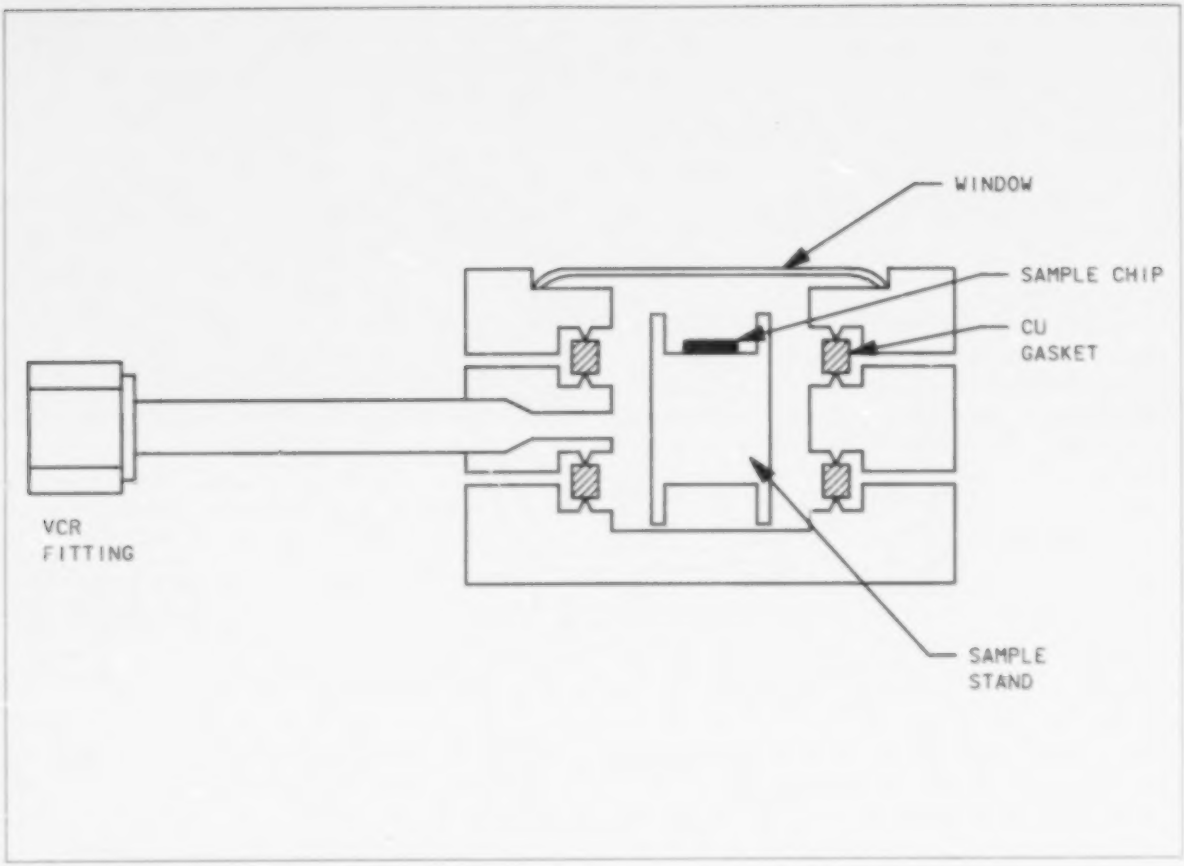

Figure 3. Diagram of the sample chamber used with the laser microprobe.

levels above 15 × cannot be obtained when air-spaced objectives are used (no known commercial source exists for such objectives). If higher magnification objectives were available, the working distance would be so small that focusing on the sample inside a sample chamber through an optical window could not be achieved. Should the laser be accidentally focused on the optical window and fired, a rupture of the sample chamber's window may occur, and glass might be blown around the laboratory. Use of any industrial-grade laser for sample studies requires extreme caution, and only qualified operators should use such equipment.

Sample Chamber

The sample chamber (fig. 3) is constructed from three stainless steel, copper-gasketed vacuum flanges (MDC, Hayward, Calif.) 33 mm in diameter and 6 mm thick that are attached to the mechanical stage of the laser microprobe. A 60-mm length of 6-mm-diameter stainless steel tubing connects the central flange to the valve systems by means of a VCR fitting (Cajon). A length of flexible tubing on the valve system allows for movement of the sample chamber under the laser-probe microscope. The top flange of the chamber has a quartz window (optical grade) 20 mm in diameter sealed to it, through which the sample may be viewed. The optical window must be constructed of materials that permit essentially all of the laser's energy to pass without any absorption. Optical-grade quartz or sapphire is the typical window material used for the 1.06-μm wavelengths obtained with neodymium glass lasers. Other window materials may be required for different wavelengths available with other types of lasers. The bottom flange may also have a window or may be all metal, depending upon whether transmitted or reflected light is used to illuminate, respectively, thin sections or optically thick samples. If a second windowed flange is used, a spacer is required to protect the glass from the microscope stage. The chamber and connecting tubing may be wrapped with heating tape if required.

Sample chips are supported in the chamber in a "cup" in the end of a piece of brass rod 12 mm in diameter. If required, the sample may be embedded in a low-vapor-pressure epoxy resin (for example, TorrSeal, Varian, Palo Alto, Calif.). Thin sections are supported on a drilled-through stand. Details of the preparation of thin sections have been given previously (Sommer and others, 1985).

In order to stop the inside of the optical window from being coated with material sprayed upward from the sample during the laser's pulse, a shield can be employed. A microscope slide's cover slip can be stationed immediately below the optical window of the sample chamber to receive the sample spray. After numerous laser pulses, the cover slip will be coated with material and should be changed. If material is allowed to be deposited on the optical window of the sample chamber, the laser's energy will be dissipated and difficulty will develop in observing and focusing on the sample. Light for illumination of samples is provided by incandescent sources via fiber optic cables and lenses, and various filters and polarizers may be used as required.

Procedures for Analysis

Preparation procedures for the samples depend largely on the nature of the sample and the type of analysis to be undertaken. Thin sections are prepared by extensive polishing followed by decontamination (Sommer and others, 1985), while rock fragments may be analyzed with essentially no pretreatment, as is the case with most samples described here. For thin-section studies, sections as thick as 100 to 150 μm are preferred so that the laser beam does not drill through the sample and into the embedding medium. Our studies have shown that, should the laser beam penetrate into the embedding medium (epoxy), molecular species are released that make the interpretation of the mass spectra difficult. It is possible to subtract spectra of the embedding medium from the sample spectra (should the beam penetrate through the thin section) to give a "corrected" spectrum, although this is not completely satisfactory.

In order to characterize the interactions of the laser probe's 1.06-μm wavelength beam with geologic materials, known minerals have been used as standards. Where possible, single crystals about 2 mm across have been used. In some cases, clusters of smaller crystals have been employed. Samples were embedded in vacuum sealant in the brass sample holder and left for several hours while the epoxy hardened. The sample holder was placed in the vacuum chamber, which was then sealed by being bolted to the microscope stage. The sample chamber was connected to the vacuum system with the VCR fitting, and heating tape was wrapped around exposed parts of the system. The vacuum chamber was allowed to pump down for about 30 min, via the auxiliary pumping system, to a pressure of about 10^{-5} torr before being left pumping through the mass spectrometer overnight.

Samples were viewed through the microscope, and the areas chosen for analysis were centered under the laser's focal point by movement of the stage. Mass spectrometer acquisition parameters were set via software, normally scanning the mass to charge (m/z) range of 3 to 100 at 2 Hz with the electron multiplier voltage set at 2,000 V. Background spectra were obtained for a short time (30 s), and then the laser was fired. Gases produced in the chamber by the laser's interaction with the sample expanded directly into the mass spectrometer to be ionized and detected. Once the gases had been pumped away, more background spectra were obtained while the sample was repositioned and the microscope refocused. The laser was then fired again. The laser could be fired every 15 s once its capacitor bank had been recharged. However, with repositioning the sample and refocusing, the time interval between laser shots was typically 1 min.

Upon completion of data acquisition, the editing software was used to examine the analytical results. Average background spectra were calculated from mass scans preceding the laser shot and subtracted from the spectra of sample gases. Individual ion profiles (ion abundances versus time) were examined to establish whether low-abundance species were genuinely released by the laser shot or whether they could be accounted for by variations in the system's background.

DISCUSSION AND RESULTS OF EXPERIMENTATION

Types of Lasers

Depending upon the type of lasing system, lasers can be operated in either a continuous or a pulsed mode. Pulsed lasers having narrow pulse widths offer the best possibility for sample decrepitation or gas release from solid samples, since they give a very rapid release of the gases, and minimal interaction of the volatiles with the laser's beam occurs. Some of the different types of lasers available for use are listed in table 1. Lasers occur in a wide variety and have many different characteristics. The wavelength and operating parameters are characteristic to each type. The wavelengths of lasers available range from the ultraviolet through the visible and near infrared out to many hundreds of micrometers for some devices in the far infrared. Characteristics of some of the different types of lasers available are shown in table 1, which also demonstrates that not all the optimum characteristics can be obtained in a single laser. For example, to obtain highest peak pulse power, one may have to sacrifice some other optimum

Table 1. Laser characteristics (after Ready (1971) and Lasers and Applications (1986))

[–, unknown; CW, continuous wavelength]

Laser	Wavelength (μm)	CW power (W)	Peak pulse power (W)	Pulse energy (J)	Pulse rep. rate (pulses/s)	Beam angle (mrad)
He-Ne	0.6328	0.001–0.1	–	rarely used pulsed	–	0.2–1
Ar^+	.4880	1–10	20	mJ	60	.5–1
	.5145					
Ar ion	.457	.002–25	25	–	Continuous	.4–2.68
	.530					
Kr^+	.6471	.5	2	mJ	60	.5–1
	.5681					
	.5208					
	.4762					
CO_2	10.6	10–5,000	10^5	0.1–5	~100	~1–4
N_2	.3371	not CW	10^5	–	1–100	2 × 20
Ruby	.6943	1	to 10^6	1–500	60	1–10
Nd glass	1.06	–	to 4×10^9	1–5000	1–10	.5–10
Nd YAG	1.06	1–250	to 10^5	.01–1	to 10,000	2–20
GaAs	.84–.9	1–10	1–100	<1 mJ	100–1,000	20 × 400
Excimer	.157	.4–250	–	.02–1,500	1/60–750	.05–10
	.193					
	.222					
	.248					
	.308					
	.351					

properties, such as high beam divergence angle or high pulse repetition rate.

An example of the variability of the effects of laser interaction with samples has been seen with a Q-switched neodymium glass laser and a neodymium glass power laser (Franchi and others, 1986; this volume; unpub. data, 1988). The Q-switched laser operating at 1 J energy output produced craters in calcite ranging up to 200 μm in size, whereas the power laser operating at the same energy output produced only a surface discoloration with the same samples. The Q-switched laser delivered the same amount of energy at the sample surface in a shorter time interval than the power laser. A summary of specifications that can be useful for determining the type of laser to be chosen for a particular study is given in table 2. It is obvious that the mode of laser operation, the power, pulse length, and repetition rates are important parameters that must be considered.

Laser Interactions with Geologic Samples

The interaction of laser beams with geologic materials needs to be researched more in order for a full understanding of what happens to the sample to be gained. The absorption or transmission of radiation by the target materials determines the type of process (ablation, mechanical disruption, cratering, or melting) that occurs within the sample. For example, if the target is pure optical-quality quartz, the laser beam (from a neodymium glass laser) will be transmitted through the material and leave no noticeable effects on the sample. However, should the quartz contain microscopic dislocations or defects, the portion of the radiation absorbed by the target would cause mechanical disruption of the surface of the sample because of fracturing or spalling in the region where the beam impinges on the sample. An example of such an interaction can be seen in figure 4*A*. Alternatively, if radiation from the laser beam is strongly absorbed within the sample, melting can occur. Olivine is a silicate that has a large mafic component that strongly absorbs the 1.06-μm wavelength from a neodymium glass laser and thus produces extensive melting (fig. 4*B*).

In order to understand the effects of lasers on geologic samples, a program to characterize laser interactions with various materials should be carried out, especially for those materials and laser energies in which the proposed studies are to be made. Examples of the neodymium glass laser (operating at 0.4 J) interactions with a variety of minerals can be seen in figure 5. The laser interactions produce fracturing and spalling with the quartz samples. With carbonates, the laser pits vary, depending upon the number of absorbing components present. With calcite (fig. 5*A*), very slight melting may occur, whereas with dolomite (fig. 5*B*), greater melting occurs. In the case of barite (fig. 5*C*), no noticeable melting occurs in the target area. Mafic minerals such as olivine typically absorb the laser energy, so melting within the laser pit results. However, should

Table 2. Lasers useful for high-power effects (after Ready (1971) and Lasers and Applications (1986))

Laser	Mode of operation	Power (W)	Pulse length	Pulse repetition rate
Ruby	Normal pulse	2×10^5 peak	0.2–10 ms	Low
Ruby	Q-switched	10^9	5–30 ns	Low
Ruby	Picosecond pulse	High	10 ps	Low
Nd glass	Normal pulse	$\sim 10^6$ peak	.5–10 ms	Low
Nd glass	Q-switched	to 4×10^9 peak	6–50 ns	Low
Nd glass	Picosecond pulse	to 10^{12} peak	10 ps	Low
Nd YAG	Continuous	to 250		
Nd YAG	Continuously pumped, repetitively Q-switched	10^4 peak, 10 average	200 ns	to 5,000 pulses/s
CO_2	Continuous	10–5,000		
CO_2	Repetitively pulsed	10^5 peak, 100 average	10–100 μs	100 pulses/s
CO_2	Repetitively Q-switched	10^5 peak, 1.5 average	200 ns	400 pulses/s
Ar ion	Continuous	to 25		
Excimer	Normal pulse	to 250	.03–80	to 750 pulses/s

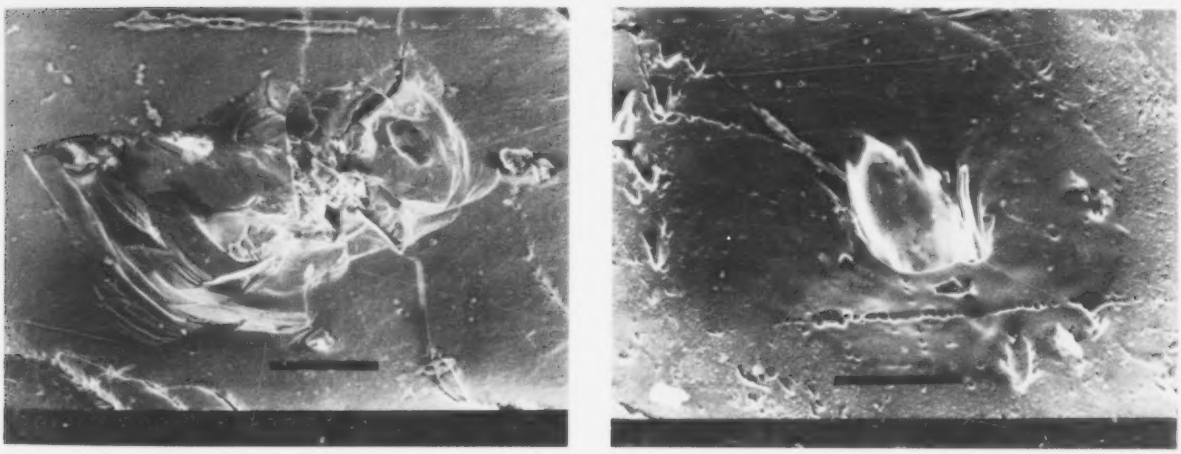

A *B*

Figure 4. Scanning electron microscope photographs of craters obtained by use of a Q-switched neodymium glass laser operating at 0.4-J energy level. Scale bars are 100 μm. *A*, Laser-pitted quartz sample showing evidence of mechanical spalling and disruption of the target. *B*, Laser-pitted olivine sample showing extensive evidence of melting of the silicates because of absorption of the laser's energy.

minerals contain numerous fractures and dislocations, melting along with fracturing results (figs. 5A,*C*). Sulfide minerals such as pyrite show extensive melting within the laser pit (fig. 5*D*).

The laser is extremely selective, but care must be used to avoid a significant contribution of volatiles from omnipresent microinclusions and other contaminants. Even in minerals that do not show significant melting (quartz, calcite, and so on), the laser can heat the surrounding minerals, and decrepitation of other inclusions or release of volatiles from the crystal (in sites other than fluid inclusions) would seem likely. To avoid this, exercise caution and determine "inclusion-free" mineral blanks for every sample.

Carbonates

To establish the level of reproducibility of the laser-extraction technique, a single crystal of azurite ($2CuCO_3 \cdot Cu(OH)_2$) was subjected to repeated laser shots. A ratio of the peak area of an individual species to the peak area of all species in a scan (total ion current) appears to have less scatter than the areas of a single mass observed after replicate shots into a material. The reproducibility of gas abundances released from the laser ablation of the

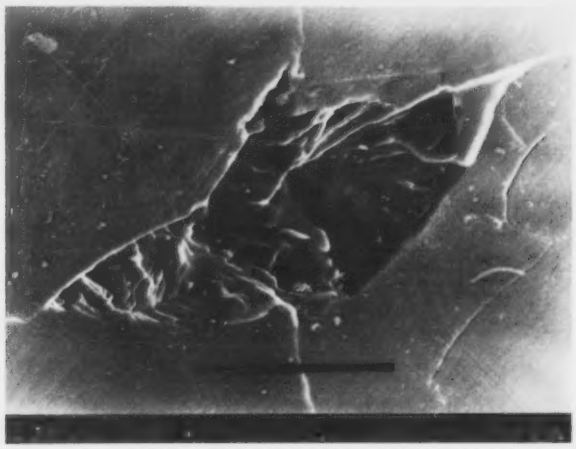

A

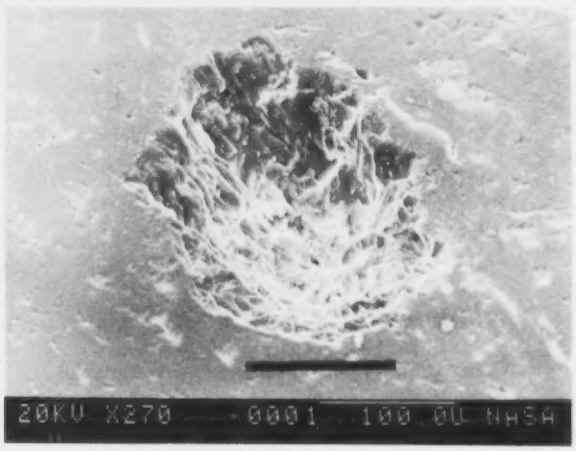

B

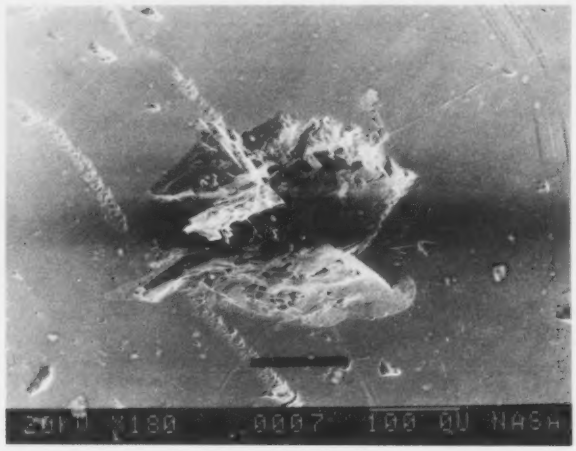

C

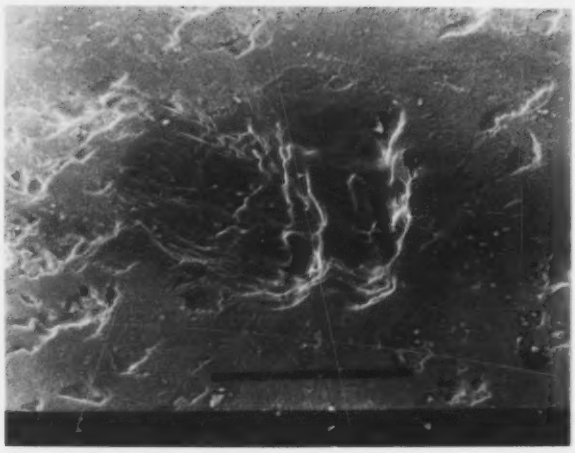

D

Figure 5. Scanning electron microscope photographs of laser pits in a variety of minerals. Scale bar in photographs is 100 μm. The operating power of the Q-switched neodymium glass laser used to produced the laser pits was 0.4 J. *A*, Calcite target showing evidence of melting in the bottom of the crater. Disruption and fracturing of the calcite appears to be assisted by the crystallographic boundaries of the target. *B*, Dolomite target showing a greater degree of melting because of absorption of the laser's energy. *C*, Barite target showing evidence of fracture of the crystal. *D*, Pyrite target showing extensive melting of the crystal because of absorption of the laser's energy. Peaks have been produced in the center of the crater.

crystal is usually within 10 to 15 percent for replicate analysis. This degree of reproducibility might be expected, considering possible differences within a naturally formed crystal and slight variations in the crystal orientation with respect to incident radiation.

Typical spectra from the laser-microprobe analysis of four different carbonates—calcite ($CaCO_3$), dolomite ($CaCO_3 \cdot MgCO_3$), magnesite ($MgCO_3$), and azurite—are given in figure 6. The four carbonates were analyzed by use of the same identical laser power settings; thus, the analysis conditions were identical. In all cases, the most abundant species occur at m/z values of 44 and 28, which correspond to the ions CO_2^+ and CO^+. The ratios of these two ions in the different spectra vary, however, with m/z of CO being more abundant than that of CO_2 in the calcite and dolomite analyses, while the reverse is true of the azurite data. The CO and CO_2 ion abundances from the magnesite analysis are almost equal. With further detailed work, it may be possible to distinguish different carbonates by their laser-microprobe-volatilized mass spectra. The variations of m/z 28 to m/z 44 ratios are indeed interesting. It is clear that more work is needed to determine the relative contributions of the following two phenomena to the intensity of m/z 28: (1) the laser-produced CO from the carbonate and (2) the

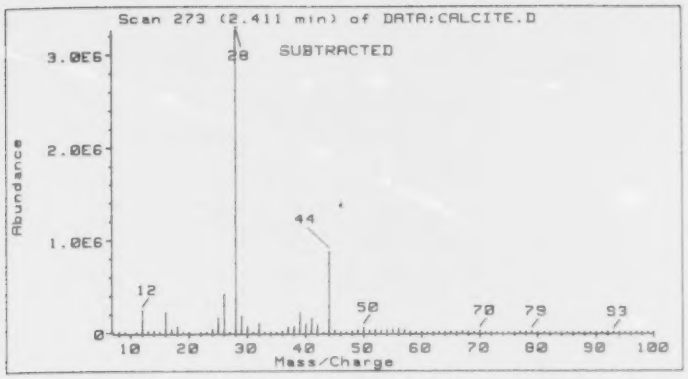

A

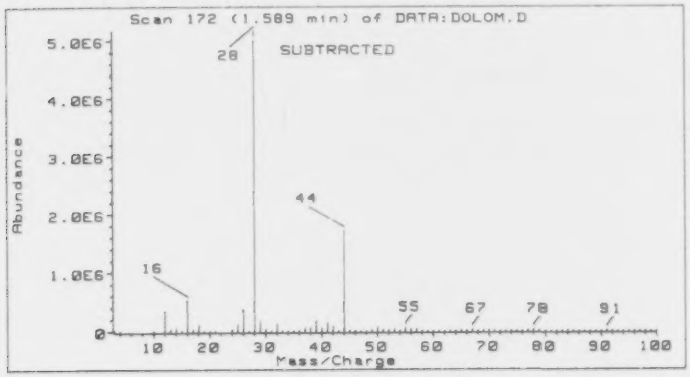

B

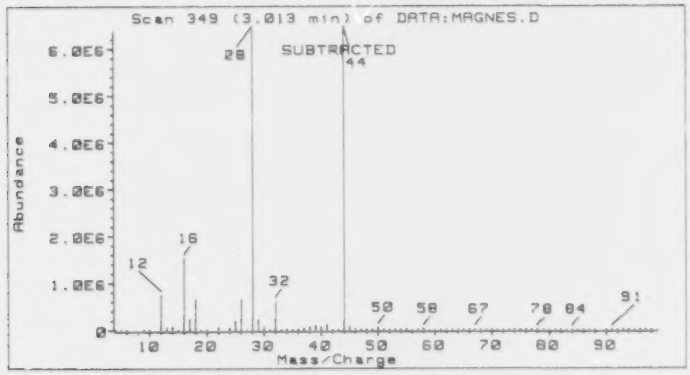

C

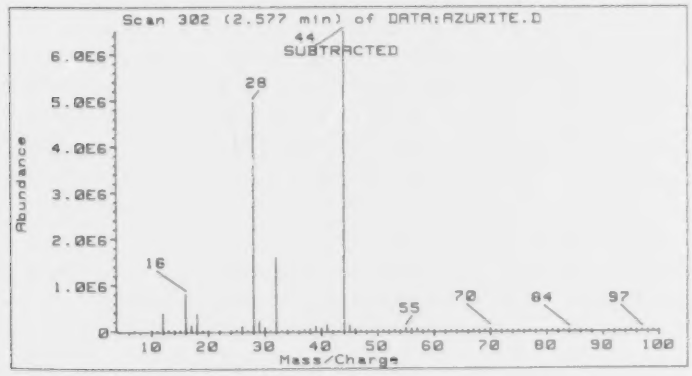

D

Figure 6. Background-subtracted mass spectra produced by interactions of laser microprobe with four different carbonates: (*A*) calcite, (*B*) dolomite, (*C*) magnesite, and (*D*) azurite. Note the increase in m/z 44 between calcite and azurite. The laser's energy is sufficiently strong to disrupt the bonding in the carbonates and produce a major contribution of CO (m/z 28). Laser operating conditions are the same as those given in figure 5.

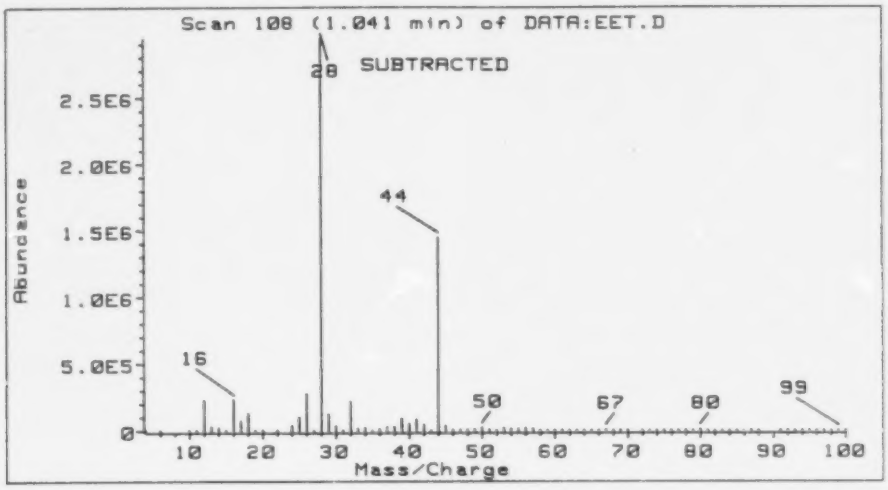

Figure 7. Background-subtracted spectrum of gases released by laser study of alteration product associated with EETA79001 meteorite. Note that the relative abundance of the m/z 28 and 44 peaks is identical to that seen from the calcite data in figure 6*A*.

mass-spectrometer-ion-source-produced CO from the carbon dioxide released by the laser irradiation of the carbonate. Therefore, the variations in the data (fig. 6) from different carbonates may reflect differences in the laser interaction with different minerals, possibly being a function of the amount of energy absorbed by the target and the binding energies of the carbonate ions in the host mineral's lattices.

Identification of Carbonate Weathering Product

One of the meteorites found in Antarctica (EETA79001) is believed, largely as a result of the discovery of trapped gases closely matching Viking spacecraft data (Bogard and Johnson, 1983; Becker and Pepin, 1984; Carr and others, 1985), to have originated on Mars. Interest has recently focused on the secondary minerals to see if Martian weathering products can be identified. White crystalline material surrounding glassy inclusions in the interior of EETA79001 had been tentatively identified as calcium carbonate on the basis of energy dispersive X-ray spectrometry (Wentworth and Gooding, 1986). As part of a detailed study of this material, the laser microprobe was used to determine the nature of the volatile species released from both the putative carbonate and exposed parts of the underlying groundmass. The major ions are CO and CO_2 (fig. 7), consistent with the identification of the unknown material as carbonate. The proportions of these two ions are also similar to the calcite data in figure 6*A*. It was initially believed that the unknown carbonate might be a hydrocarbonate mineral; however, the spectra obtained failed to show the presence of m/z 18 that would be indicative of the presence of a hydrated mineral. No gases could be detected at these masses after the laser was fired into the groundmass glass, which was the host for the carbonate phase. The results showed that the alteration product was a simple carbonate and not a hydrocarbonate phase.

Barite Study

Samples of fluid-inclusion-free barite crystals were subjected to laser microprobe–gas analysis to determine what gases were released from barite. Figure 8*A* shows the total ion current (TIC) versus time profile from the analysis of a single crystal of barite ($BaSO_4$). The three peaks in the profile are of different sizes (despite being produced with the same laser power settings) and show the different quantities of gases within three different inclusions within the barite crystal. Figure 8*B* is the background-subtracted spectrum from the final shot at 1.5 min after the start of data acquisition. Sulfur-bearing species are observed at m/z values of 64 (SO_2^+), 48 (SO^+), and 32 (S^+ or O_2^+), together with abundant m/z values for 28 and 44, presumably from trapped CO and CO_2 or coexisting carbonate within the barite along with m/z value of 18 from H_2O^+. Minor peaks at m/z values of 60 and 76 indicate the likely presence of COS and CS_2, while peaks possibly from the less abundant ^{34}S-isotope species can also be observed at m/z values of 34, 50, and 66.

Volatiles in 3.4-b.y.-old North Pole Barites

Examination of fluid inclusions within the 3.4-b.y.-old barites from the North Pole deposit from the Warrawoona Group of Northwestern Australia reveal a complex morphology and array of fluid inclusions. This study, along

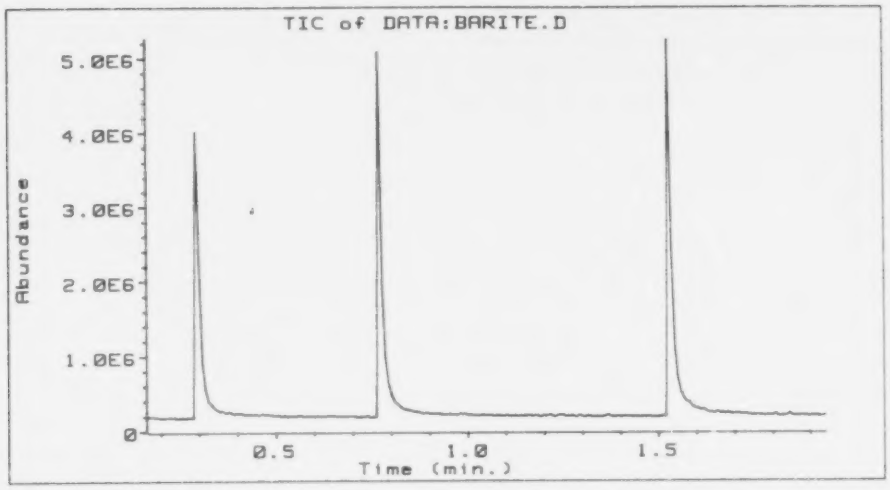

A

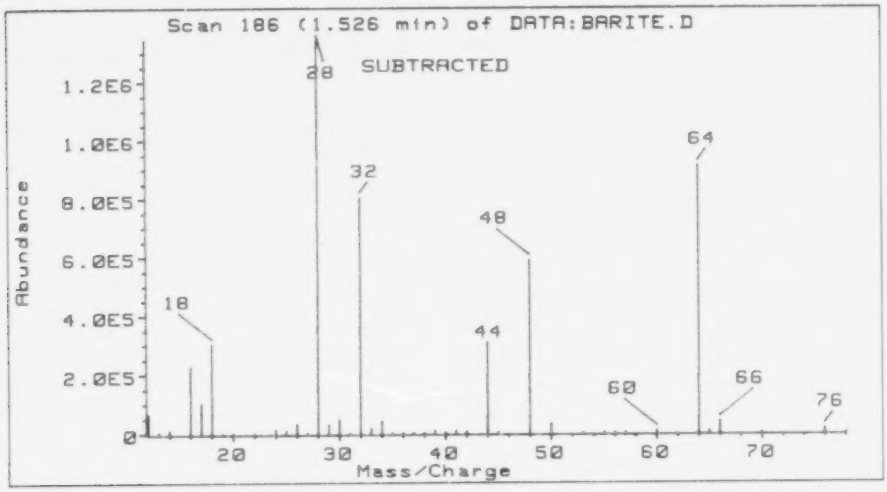

B

Figure 8. Laser microprobe–gas analysis study of barites. *A*, Total ion current (TIC) versus time profile for the analysis of a single barite crystal. The three peaks represent the three laser shots. *B*, Background-subtracted spectrum for the final laser shot. In addition to the sulfur ions (m/z 64, 48, 32) evidence of trapped carbonate within the barite can be seen from the m/z 44 and 28 ions. Other values are 18, H_2O^+; 60, COS; 76, CS_2; 34, 50, and 66, the less abundant ^{34}S-isotope species.

with previous work (Rankin and Shepherd, 1978; Bourcier and others, 1984), has identified at least four generations of inclusions. The inclusion types are (I) large (20–40 μm) intergrain inclusions having variable-sized vapor bubbles with one, two, or three phases, but which may also include carbon dioxide fluids or even a single phase; (II) smaller (10–30 μm) inclusions concentrated near grain boundaries containing three, or less commonly, two, vapor phases, aqueous and carbon-dioxide liquid, and a pale yellow daughter crystal; (III) small (1–5 μm) highly reflective carbon-dioxide-rich secondary and other small daughter crystal-bearing fluid inclusions; and (IV) very small (<1–5 μm), numerous aqueous inclusions evenly distributed throughout the grain interiors. Inclusions distributed within the interior of large grains are types I, III, and IV, with type II inclusions in or near grain boundaries. It has been assumed (Bourcier and others, 1984) that the type I and IV inclusions primarily relate to the formation of the barite and that the type II and III inclusions are secondary or were produced during later tectonic events that include a lower greenschist regional metamorphism about 2.95 b.y. ago (Hickman, 1981) and an event about 2.7 b.y. ago (Marston

and Grover, 1981). While the morphological distinctions of the inclusions are readily apparent, any attempt to correlate these inclusion types with primary mineral formation or secondary mineralization has been hampered by a lack of compositional data on volatiles from the individual inclusions.

Laser-microprobe and bulk (vacuum crushing) determinations were made of released volatiles from the fluid inclusions. Standard minerals yield reproducibilities of about ±5 percent. Minimum detection limits were found to be about 10^{-11} mol of gas.

Individual inclusions of types I, II, and III were analyzed by the laser microprobe (type IV inclusions were not analyzed because of their small size). Figure 9 is a C–H–O elemental plot of the data with the CO, CO_2, CH_4, and H_2O fields indicated. (This elemental plot is used to avoid the uncertainties of expressing individual volatile species after extraction and mass-spectrometric analysis.) The type I large intergrain inclusions yield C–O compositions of about 18, 40, and 42 percent, respectively (fig. 9). Only a slight trace of SO_2 was detected in type I inclusions. Type II and III (grain boundary and highly reflective intergrain inclusions) yield C–H–O compositions of about 25, 30, and 45 percent, respectively (fig. 9). These inclusions typically have SO_2 and H_2S present in their spectra. For comparison, the C–H–O of the bulk inclusions (obtained by crushing) yield compositions of 3, 63, and 34 percent, respectively.

The results indicate that the type I inclusions have volatile compositions distinct from the type II and III inclusions. In addition, the type I, II, and III inclusions are significantly richer in carbon and sulfur gases relative to the bulk inclusions (assumed to be predominantly type IV). Type I, II, and III inclusions are enriched in carbon phases and require that some form of decarbonation occurred during the various metamorphic events that have affected these rocks. The presence of both H_2S and SO_2 indicates that some inclusions have undergone volatile loss or addition since entrapment or during the replacement of gypsum by barite. The bulk-inclusion composition indicates a large aqueous contribution that cannot at this time be related to either primary or secondary mineral genesis. Addition of water may have occurred during some later process.

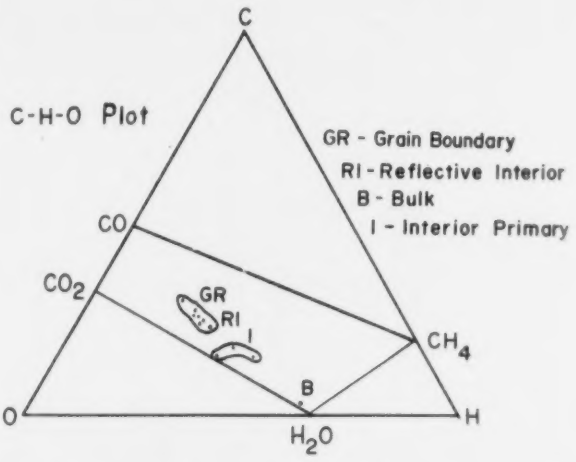

Figure 9. C–H–O plot of gases released from 3.4-b.y.-old barite from North Pole deposit from the Warrawoona Group of Northwestern Australia. The CO, CO_2, CH_4, and H_2O fields are indicated. GR, RI, and I refer to types II, III, and I fluid inclusions, respectively, discussed in the text. B refers to fluid-inclusion determinations made from bulk crushing of the barite. Only type I inclusions are believed to be primary. Note that the bulk crushing of the barite released volatiles having substantially different characteristics than the primary inclusions that could be selectively opened with the laser microprobe.

Sulfides

Several sulfide minerals have been subjected to the laser microprobe–mass spectrometer study in order to determine the gaseous species released during laser interactions. Figure 10 shows a spectrum from the analysis of pyrite (FeS_2). The main species observed is CS_2, the carbon possibly originating as the ubiquitous organic contamination found on all kinds of samples (Carr and others, 1985). Other abundant peaks can be attributed to H_2O, CO, S, CO_2, SO, and SO_2. Several sulfide minerals, including galena (PbS), cinnabar (HgS), chalcocite (CuS_2), chalcopyrite ($CuFeS_2$), and sphalerite (ZnS), have been studied, and all show the formation of species similar to those observed for pyrite.

Diamonds

The genesis of diamond is receiving increasing attention because an understanding of how and where they are formed could provide information on mantle processes and the composition of the early Earth. The volatile species trapped in inclusions in some diamonds may give vital clues in this regard (Bibby, 1982). Experiments where diamonds have been crushed have, apparently, shown the presence of methane in many samples (Roedder, 1984), but it is known that methane can be formed in crushing devices from the action of one metallic surface against another (Gibson and Andrawes, 1978). Thus, controversy still surrounds the validity of some of these results. Laser extraction of the gases is potentially a very clean technique; hence, using the laser probe to attempt to fracture or cleave a diamond might yield important information on the genesis of diamonds.

A type I diamond from the Koidu kimberlite formation in Sierra Leone, Africa, containing two graphite

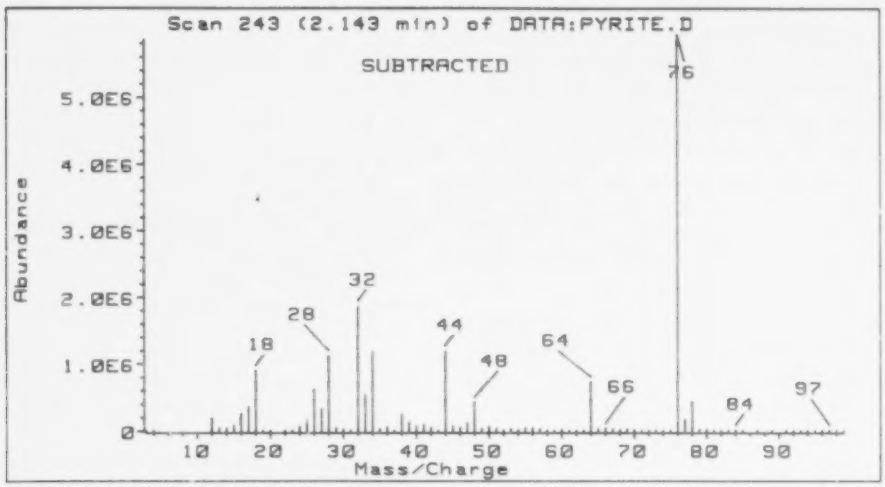

Figure 10. Background-subtracted spectrum of gas released from laser interactions with pyrite. Carbon disulfide (CS_2) is the major volatile released from the sulfide. The carbon source is from residual carbon species present within the vacuum system.

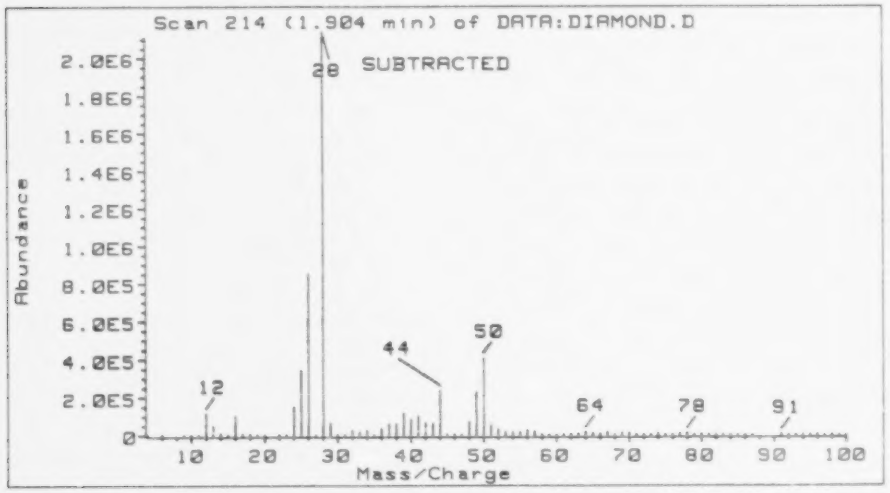

Figure 11. Background-subtracted spectrum of gases released from type I diamond during cleaving of diamond in area of graphite inclusion. Carbon monoxide and carbon dioxide were major gases released upon cleaving diamond. The m/z 50 ions (CF_2) result from the previous HF etch of the sample to remove adhering silicates. Note the absence of a peak at m/z 14 (N^+).

inclusions, was used for the initial experiment. Focusing on the surface of the diamond produced only a very shallow crater (approximately 30 μm in size), and no gases could be detected by the mass spectrometer. When the laser was directed at one of the inclusions, the diamond fractured and gases were released. Figure 11 shows a background-corrected spectrum. The main peak can be identified as CO, since daughter m/z 12 (C^+) and 16 (O^+) peaks are present, but there is no m/z 14 peak (N^+), which would be present if the m/z 28 peak was caused by N_2. Franchi and others (this volume) noted the presence of nitrogen in diamond. Our study of gases within diamonds was related only to the voids or inclusions in the diamond and did not measure nitrogen dissolved within the crystal structure of diamond. Franchi and others' study involved oxygen combustion of the diamond that resulted in the total destruction of the crystal. It is understandable that we did not note the presence of nitrogen within the inclusions that were opened.

The peaks at m/z values 24 to 26 may be due to C_2^+ species, and the small peak at m/z 44 is most likely from traces of CO_2. No methane was detected, as revealed by the absence of a m/z 15 peak (m/z 15 is the major peak produced by methane within the mass spectrometer). An unusually large peak at m/z 50 is present in the spectrum. However, this diamond had been treated with hydrofluoric acid to remove adhering silicates; thus, the m/z 50 contribution results from CF_2. Laser-microprobe studies of additional diamonds that had not been treated with HF acid failed to show the presence of m/z 50. Further work is necessary to determine gas populations of diamonds from a variety of occurrences, but the successful laser fracturing of this sample indicates that detailed analyses of trapped volatiles in diamonds will be possible in the future.

SUMMARY

The laser microprobe–quadrupole mass spectrometer analyzer has been successfully used to analyze volatiles and trapped fluids and vapors in a wide variety of materials. The microfocusing capabilities of the laser microprobe, coupled with a quadrupole mass spectrometer, result in a powerful analytical tool for analysis of volatiles in materials. This technique has been applied to a variety of geologically interesting materials and also has applications for the study of volatiles associated with synthetic materials. The laser microprobe–quadrupole mass spectrometer analysis technique is an important weapon in the arsenal of methods available for studying the abundances and distributions of low-molecular-weight compounds in small samples.

ACKNOWLEDGMENTS

Samples were provided by James L. Gooding, Stephen Haggerty, and the American Museum of Natural History, New York. Special thanks go to William Davidson (LEMSCO) for skilled technical assistance. Robert H. Carr was an NRC Research Associate at the NASA Johnson Space Center. Funding for this work was from NASA's Planetary Materials and Planetary Biology Program Offices.

REFERENCES CITED

Becker, R.H., and Pepin, R.O., 1984, The case for a martian origin of the shergottites: Nitrogen and noble gases in EETA79001: Earth and Planetary Science Letters, v. 69, p. 225–242.

Bibby, D.M., 1982, Impurities in natural diamond: Chemistry and Physics of Carbon, v. 18, p. 1–91.

Bogard, D.D., and Johnson, P., 1983, Martian gases in an Antarctic meteorite?: Science, v. 221, p. 651–654.

Bourcier, W.L., Gibson, E.K., Jr., and Kotra, R.K., 1984, Characterization and gas analysis of fluid inclusions in Archean barites from the Warrawoona Group, Northwestern Australia: Abstracts of Papers Submitted to the Lunar and Planetary Science Conference, no. 15, March 12–16, Houston, Texas, p. 82–83.

Carr, R.H., Grady, M.M., Wright, I.P., and Pillinger, C.T., 1985, Martian atmospheric carbon dioxide and weathering products in SNC meteorites: Nature, v. 314, p. 248–250.

Franchi, I.A., Wright, I.P., Gibson, E.K., Jr., and Pillinger, C.T., 1986, The laser microprobe: A technique for extracting carbon, nitrogen and oxygen from solid samples for isotopic measurements: Proceedings of the 16th Lunar and Planetary Science Conference, Journal of Geophysical Research, Supplement 91, no. B4, p. D514–D524.

Gibson, E.K., Jr., and Andrawes, F.F., 1978, Nature of the gases released from lunar rocks and soils upon crushing, *in* Merrill, R.B., ed., Lunar and planetary surfaces: Proceedings of the 9th Lunar and Planetary Science Conference, v. 2, March 13–17, Houston, Texas, p. 2433–2450.

Harris, D.M., 1981, The microdetermination of H_2O, CO_2, and SO_2 in glass using a 1280 °C microscope vacuum heating stage, cryopumping, and vapor pressure measurements from 77 to 273 K: Geochimica et Cosmochimica Acta, v. 45, p. 2023–2036.

Hickman, A.H., 1981, Crustal evolution of the Pilbara Block, Western Australia, *in* Glover, J.E., and Groves, D.I., eds., Archaean geology: Special Publication No. 7, Geological Society of Australia, p. 57–69.

Kotra, R.K., and Gibson, E.K. Jr., 1982, Direct analysis of fluid and vapor inclusions using laser microprobe-gas chromatography: EOS, Transactions of the American Geophysical Union, v. 63, p. 450.

Lasers and Applications, 1986, 1987 buying guide technical handbook and industry directory: Torrance, California, Lasers and Applications, 660 p.

Marston, R.J., and Grover, D.I., 1981, The metallogenesis of Archaean base-metal deposits in Western Australia, *in* Glover, J.E., and Groves, D.I., eds., Archaean geology: Special Publication No. 7, Geological Society of Australia, p. 409–420.

Rankin, A.H., and Shepherd, T.J., 1978, H_2S-bearing fluid inclusions in baryte from the North Pole deposit, Western Australia: Mineralogical Magazine, v. 42, p. 408–410.

Ready, J.F., 1971, Effects of high-power laser radiation: Academic Press, 433 p.

Roedder, E., 1972, Composition of fluid inclusions, *in* Fleischer, M., ed., Data of geochemistry, 6th ed.: U.S. Geological Survey Professional Paper 440–JJ, p. JJ1–JJ164.

———1984, Fluid inclusions: Reviews in Mineralogy, v. 12, 644 p.

Roedder, E., and Bodnar, R.J., 1980, Geologic pressure determinations from fluid inclusion studies: Annual Reviews of Earth and Planetary Science, v. 8, p. 263–301.

Sommer, M.A., and Schramm, L.S., 1983, An analysis of the water concentrations in silicate melt inclusions in quartz phenocrysts from the Bandelier Tuff, Jemez Mountains, New Mexico: Bulletin of Volcanology, v. 46, p. 299–320.

Sommer, M.A., Yonover, R.N., Bourcier, W.L., and Gibson, E.K., Jr., 1985, Determination of H_2O and CO_2 concentrations in fluid inclusions in minerals using laser decrepitation and capacitance manometer analysis: Analytical Chemistry, v. 57, p. 449–453.

Tsui, T.F., and Holland, H.D., 1979, The analysis of fluid inclusions by laser microprobe: Economic Geology, v. 74, p. 1647–1653.

Wentworth, S.J., and Gooding, J.L., 1986, Shergottite EETA79001: Petrologic heterogeneity and secondary alteration in lithology C: Meteoritics, v. 21, p. 536–537.

York, D., Hall, C.M., Yanase, Y., Hanes, J.A., and Kenyon, W.J., 1981, $^{40}Ar/^{39}Ar$ dating of terrestrial minerals with a continuous laser: Geophysical Research Letters, v. 11, p. 1136–1138.

Application of Lasers in Small-Sample Stable Isotopic Analysis

By I.A. Franchi,[1] S.R. Boyd,[1] I.P. Wright,[1] *and* C.T. Pillinger[1]

Abstract

Two techniques, both employing lasers, have been developed to sample geological materials for light-element stable isotopic analysis. Both techniques offer advantages in sample characterization and spatial resolution over conventional techniques. The first technique is laser sectioning and is primarily limited to diamonds. Thin wafers of diamond are precisely sectioned into ~100-microgram blocks that can then be analyzed on a high sensitivity mass spectrometer. This technique has been successfully used to investigate isotopic variation of carbon and nitrogen, as well as nitrogen concentration, in coated diamonds.

The second technique involves a laser microprobe that is used to melt or vaporize small areas (<100 micrometers in diameter) of a sample to liberate gases that can then be analyzed in the mass spectrometer. This technique has been evaluated for determining the isotopic composition of carbon, nitrogen, and oxygen. The results have shown that useful $\delta^{15}N$ measurements can be obtained with the laser microprobe and that $\delta^{13}C$ values can be determined to within ±3 per mil. However, $\delta^{18}O$ measurements are currently unreliable.

A laser microprobe study of the meteoritic polymict breccia Bencubbin confirms that isotopically heavy nitrogen ($\delta^{15}N$=995 per mil) is distributed throughout metal and silicate clast and matrix and thus must have been incorporated prior to brecciation.

INTRODUCTION

The complex evolution and polymineralic nature of many geological materials result in a heterogeneous elemental, and often isotopic, distribution throughout a sample, and it is well known that information on this internal variation can reveal much about the origin and history of a rock. Although individual components can be separated from a sample and analyzed by conventional whole-rock techniques, this is a time-consuming procedure requiring relatively large amounts of sample. Better characterization of the sample can be achieved if components can be analyzed in situ. To this end, a number of analytical techniques have been developed for geological studies, such as the electron microprobe for elemental abundance determinations, the ion probe, which has the added capability of determining isotopic compositions, and the laser microprobe for the study of noble gases. However, the application of such techniques to the study of the light elements (primarily H, C, N, and O) is currently rather limited because of analytical problems.

The determination of C, N, and O elemental abundances by use of the electron microprobe suffers from problems associated with the detection of weak secondary X rays, while isotopic analyses with the ion probe suffer from problems of resolving interfering species; because of these problems, both methods result in large uncertainties. In the case of nitrogen, the ion probe also suffers from the additional problem in that it is necessary to analyze nitrogen as CN^-, the result being that only samples containing appreciable quantities of carbon can be studied (Zinner and others, 1987).

The large gains in sensitivity that have been achieved with the use of static-vacuum mass spectrometry in the analysis of the light elements (Carr and others, 1986; Wright and others, 1988; Wright and Pillinger, this volume) have allowed the development of two techniques (both employing lasers) that offer good sample characterization and spatial resolution for stable isotopic measurements of C, N, and O. In the first technique, a laser is used to dissect a sample into small blocks that can then be analyzed by conventional techniques. In the second technique, a laser microprobe is used, one similar in design to that employed in the study of noble gases (Megrue, 1967; Plieninger and Schaeffer, 1976, Böhlke and others, this volume).

LASER SECTIONING

Natural diamonds can exhibit serial zoning with respect to carbon and nitrogen isotopic composition, nitrogen concentration, and nitrogen aggregation state (Boyd and others, 1987). The nitrogen in diamond may be present within a variety of structures (single nitrogen, nitrogen pairs, and higher aggregates) that give rise to characteristic absorption spectra in the infrared. Other structures that can develop in diamond, termed platelets, may also contain nitrogen (see Davies, 1984, for recent review). The causes of the zoning include multistage growth from isotopically distinct reservoirs and isotope fractionation processes operating within a single growth step. The zoning can be used to deduce a simple history for a given diamond sample. Synthetically produced diamonds can be sector zoned with

[1] Planetary Sciences Unit, Department of Earth Sciences, The Open University, Milton Keynes, MK7 6AA, England.

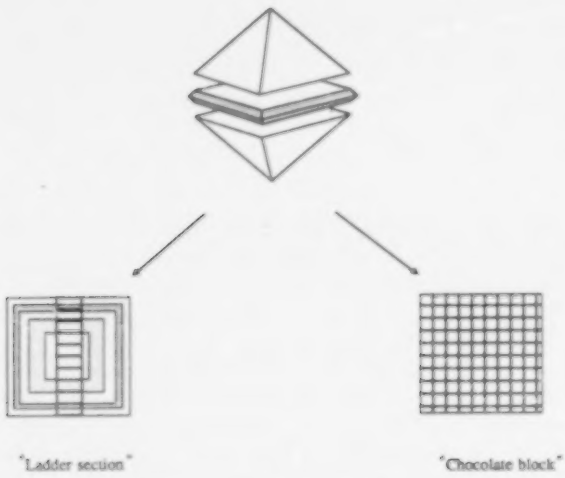

Figure 1. Sketches showing laser sectioning of diamond plates. A plate (about 5×5×0.3 mm) is cut from the center of the stone by a diamond saw. This plate is then laser sectioned in one of two patterns to produce either a "ladder section" or a "chocolate block."

respect to nitrogen concentration, nitrogen isotopic composition (Boyd and others, 1988a), and possibly carbon isotopic composition. This zoning is due to physical/chemical differences between the various growing facets.

In order to study the growth zoning present within a diamond, the sample is first prepared in the following way. A plate, usually about 5 mm in diameter, 300 to 500 μm thick is cut from the diamond by a diamond saw (fig. 1). When removed, the plate has a polished surface and is immediately amenable to study by both infrared (IR) and cathodoluminescence (CL) techniques, the latter being used to investigate zoning of impurities within the diamond. Both of these techniques can be used as a guide for the next stage of preparation of the plate, although for practical purposes the IR and CL techniques are usually applied after final preparation. The last stage of preparation involves mounting the plate upon a computer-controlled stage and dissecting it with a Q-switched 12 mW neodymium YAG laser. The two dissection patterns that have been most used ("ladder sections" and "chocolate blocks") are indicated in figure 1, and in both cases the sections are cut parallel to <111>.

The block sizes from ladder sections are cubes about 400 to 500 μm on a side that weigh between 300 and 500 μg. During sectioning, each block is individually labeled by the laser to prevent misidentification once the samples are removed from the stage. The size of block ensures ease of handling. This type of preparation has been used for the analysis of natural diamonds where the growth zones are both serial and symmetrical.

Chocolate blocks are smaller than those from ladder sections, being typically 250 × 250 × 500 μm and having a mass of about 100 μg. Although it is possible to label the individual blocks with the laser, this practice has been abandoned because there is no way of knowing before the IR and CL results are obtained which blocks are going to be analyzed. Instead, as the cutting pattern is in the form of a grid, each block is mapped and given a unique grid reference. If CL and IR indicate that a single block will contain insufficient nitrogen for a precise nitrogen isotopic measurement, then adjacent blocks can be taken and a composite analyzed. This technique is applicable when the zoning within the diamond is either sectored or asymmetrical. Although the laser can cut smaller block sizes, cutting them this size is impractical, as even with the 250-μm grid pattern, in excess of 400 blocks may result from a single diamond plate.

Certain diamonds (termed "coated diamonds") consist of an octahedral "core" surrounded by a fibrous "coat" that may have cube faces (Kamiya and Lang, 1965). Figure 2 shows the results obtained from a coated diamond (see Boyd and others, 1987) that was dissected into a ladder section of 500-μm cubes. $\delta^{13}C$ values obtained from the coat (exterior) were between −6.7 and −7.1 ‰, whereas the core of the diamond was lighter ($\delta^{13}C = -8.7$ ‰). Nitrogen isotopic measurements were anticorrelated with carbon, the lowest $\delta^{15}N$ values being within the coat (−3.9 to −5.5 ‰) and the highest occurring within the core (+4.7 to +5.1 ‰). The coat contained between 1,180 and 1,400 ppm nitrogen, present as A-feature nitrogen (pairs of atoms), whereas the core contained more nitrogen (1,640 to 1,810 ppm), and, although the A-feature IR-absorption spectra dominated, platelet absorptions were also detected.

THE LASER MICROPROBE

The laser-microprobe technique employs a neodymium glass, non-Q-switched pulsed laser (maximum output 5 J) to melt and (or) vaporize small areas of sample to liberate the gases of interest. The sample is loaded in a demountable stainless steel turret composed of two 70-mm flanges (fig. 3) connected to a glass extraction line (fig. 4). The uppermost flange contains a quartz window through which the sample can be viewed in reflected light and the laser beam focused on the sample surface (both with the same microscope). An arrangement of three flanges with quartz windows in the top and bottom flanges allows thick sections to be viewed in transmitted light. One important feature of the sample turret is the glass cover slip placed above the sample to protect the underside of the quartz window from molten material that can be ejected from laser-produced pits. The sample turret, complete with sample, is evacuated to 10^{-6} torr (normally 2–3 days) at ≤300 °C.

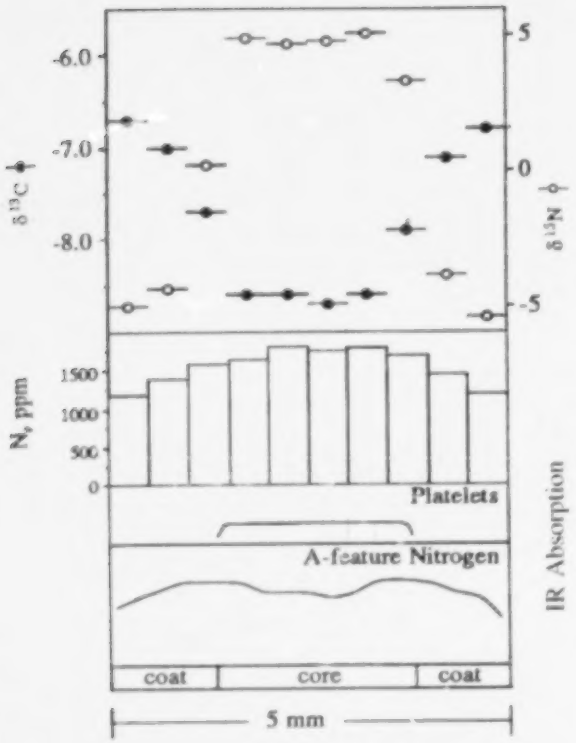

Figure 2. Typical results of $\delta^{13}C$, $\delta^{15}N$, and nitrogen concentration measurements from a ladder section of a coated diamond. The variation in the infrared (IR) absorption spectra characteristic of platelet and A-feature nitrogen (pairs of atoms) is also shown. Data from Boyd and others (1987). Open circle, $\delta^{15}N$ (right axis); filled circle, $\delta^{13}C$ (left axis).

To extract gases, the sample turret is isolated from the pumps and the laser (already focused on the surface) is fired at the sample. Manipulation of the sample turret under the fixed laser beam is achieved by three micrometers that allow movement in the *x*, *y*, and *z* directions. Connection to the glass purification section is achieved through two stainless steel flexible sections and a pyrex glass to metal seal. The gases evolved from the laser-produced pits (roughly cylindrical in shape and typically 50 to 100 μm wide by up to 150 μm deep) are purified by chemical processing, and interfering species are cryogenically separated before being analyzed in one of two online high-sensitivity static-vacuum mass spectrometers, one dedicated to CO_2 (see Carr and others, 1986) and the other to nitrogen (see Wright and others, 1988). The laser-microprobe extraction technique has been evaluated for a number of different materials by Franchi and others (1986a). The following is a summary of the observations of that study and their main conclusions.

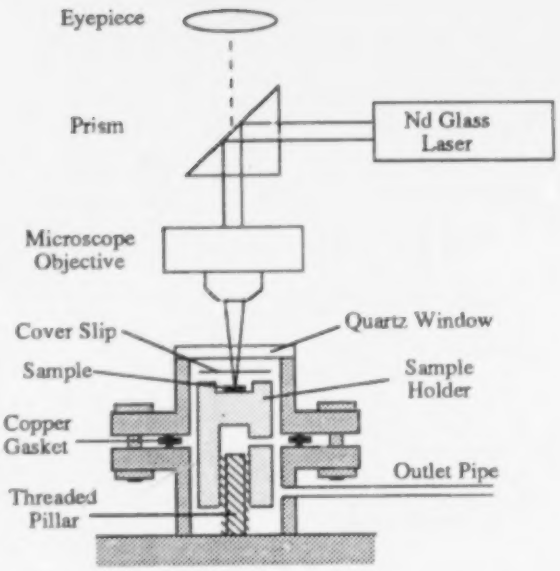

Figure 3. Schematic diagram of a sample turret, the laser, and the viewing optics.

Carbon and Oxygen

Carbonates would seemingly offer the least number of problems for the laser microprobe, given their high concentrations of carbon and oxygen and the fact that the carbon is already present in an oxidized form. However, experiments to date have not yielded results within the precision of the mass spectrometer. Figure 5 is a summary of the results from a number of laser-microprobe analyses of calcite relative to the true $\delta^{13}C$ and $\delta^{18}O$ values of the sample. The carbon data are mostly within ±3 ‰ of the expected values, and with the exception of one obviously anomalous point, all the measured values are slightly light. This enrichment in ^{12}C is probably due to an admixture of light carbon from either trapped atmospheric CO_2 ($\delta^{13}C \simeq -8$ ‰) and (or) organic material on or within the sample ($\delta^{13}C \simeq -25$ ‰) or from the system blank ($\delta^{13}C \simeq -30$ ‰). Unfortunately, because of its variability, it was impossible to correct for the system blank.

The $\delta^{18}O$ value of the CO_2 liberated from the calcite is 10 to 25 ‰ lighter than the true value (fig. 5). The obvious sources of contaminating oxygen are atmospheric O_2 and CO_2, but as can be seen from figure 5, it is impossible to produce the observed results from an admixture of sample and atmospheric gases. Another possibility is that the offset in $\delta^{18}O$ values may be due to an effect normally observed when CO_2 is generated from carbonates by pyrolysis as a result of the variable fractionation observed when only two of the three oxygen atoms in the carbonate group are converted to CO_2. However, McCrea

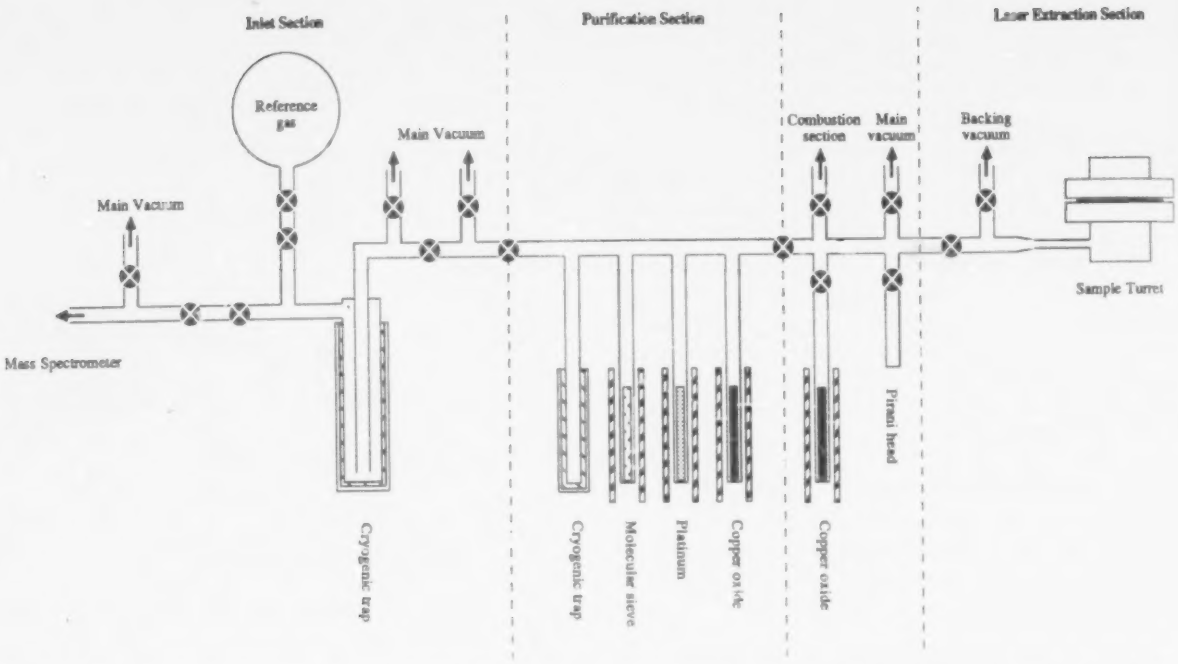

Figure 4. Schematic diagram of glass extraction line used for laser-microprobe analyses for nitrogen. The extraction line is made of pyrex glass, with quartz used when high temperatures are required. Most valves are of a special construction that allows an independent backing vacuum to be maintained between the atmosphere and sections along which sample gas flows. Details can be found in Boyd and others (1988b). The system employed for carbon analyses is very similar, the only difference being in the arrangement of valves and volumes in the inlet section.

(1950) has shown that this effect is small (approximately 4 ‰) and produces a fractionation in the opposite direction to that required to explain the laser microprobe results. Water vapor, which can have a light isotopic composition, is also an unlikely source of ^{16}O because of the small amounts present and the short time scale for equilibration. The fact that the walls of the sample chamber are metal and relatively cool also rules out the possibility of any isotopic exchange reactions. At present, it is not known why the measured $\delta^{18}O$ values are lighter than the true values, and more work is required in order to understand the source of the light oxygen.

Oxidation of graphitic carbon in an atmosphere of oxygen (≈250 torr) by use of the laser microprobe was less successful than the experiments with the calcite. Only small amounts of oxidized carbon (CO plus CO_2) were generated, and the $\delta^{13}C$ values were 3 to 8 ‰ lighter than the true value. However, because of the small amounts of gas being generated, it was impossible to determine whether this was due to isotopic fractionation during oxidation or simply was a blank contribution (Franchi and others, 1986a). Recently, a mass spectrometer has been developed that has better precision and smaller sample capability than that employed in this study. With a dedicated laser-microprobe extraction system, progress is expected in the measurement of high-precision $\delta^{13}C$ values of carbonates and in understanding the problems of $\delta^{18}O$ measurement, as well as the possibility of developing laser-induced oxidation of materials such as graphite, diamonds, carbides, and kerogen.

Nitrogen

The laser microprobe was also evaluated for nitrogen isotopic analysis by Franchi and others (1986a) by use of a number of materials having a range of nitrogen concentrations. In general, the results were very favorable, particularly with the more nitrogen-rich materials. The range in $\delta^{15}N$ values and nitrogen concentrations from analyses of artificial titanium nitride (table 1) illustrates a number of features of this technique. Variation in $\delta^{15}N$ value is due to different target areas being sampled, the results from repeated analyses in the same target area (target area 3) being reproducible within the precision of the mass spectrometer. Because the mean $\delta^{15}N$ value of the three target areas (−4.6 ‰) is close to the value obtained (−3.8 ‰) by stepped heating of a relatively large sample of this material, it is suggested that there is no discernible isotopic fractionation of the nitrogen during extraction and that the variations observed reflect isotopic heterogeneity within the material.

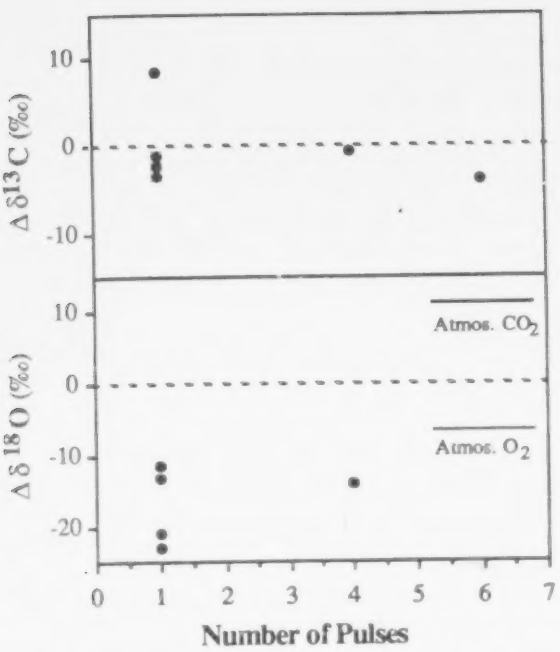

Figure 5. Results of laser-microprobe analyses for $\delta^{13}C$ and $\delta^{18}O$ values of calcite. The results are shown as $\Delta\delta$ values ($\delta_{TRUE} - \delta_{MEASURED}$) against the number of pulses used to liberate the gas analyzed. Laser output energy was 5 J. Analyses are of CO_2 only, as no CO above blank levels was detected. Apart from one apparently anomalous point, all the $\delta^{13}C$ values are slightly lighter than expected. No correction for the blank was performed ($\delta^{13}C = -30$ ‰) and therefore may account for the small shift. The cause of the large shift to light $\delta^{18}O$ values has not yet been identified.

Table 1. Results of laser-microprobe analysis of artificial titanium nitride

[Laser output energy was 5 J. The $\delta^{15}N$ value of the TiN obtained from stepped combustion is −3.8 ‰]

Target area	No. of pulses	Yield (ng N)	Yield (weight percent N)	$\delta^{15}N$ (per mil)
1	1	153.9	15.4	−4.7
2	1	156.2	15.6	−2.0
3	1	147.4	14.7	−7.5
3	1	64.5	6.4	−6.5
3	1	22.9	2.3	−7.5

The yield from the first pulse at each target area is also reproducible within the uncertainties of the mass spectrometer, and it is only when repeated analyses of the same target area are attempted that the yields become progressively lower. It appears that a number of factors combine to produce this effect. Nitrogen-poor titanium metal produced from the first pulse may collect in the bottom of the pit; therefore, some energy from subsequent pulses could be expended in heating this material. Focusing on the bottom of the pit is also more difficult, particularly because ejected material coats the underside of the cover slip. This coating may also attenuate subsequent pulses of the laser beam. These problems can be avoided by always focusing the laser beam on a fresh piece of sample surface free from ejected material. The concentration of nitrogen (=15 weight percent) is low compared to the expected value of 23 weight percent. Possibly, the pit volume was overestimated or perhaps some of the titanium nitride ejected from the pit was ejected without decomposing.

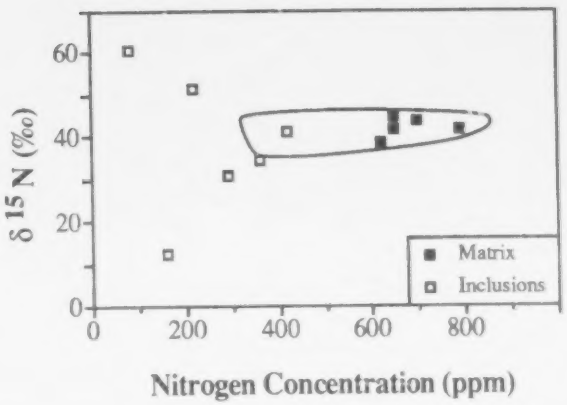

Figure 6. Results of laser-microprobe analyses for $\delta^{15}N$ of the Murchison meteorite. The data envelope shows the range of values obtained from whole-rock samples of Murchison in other laboratories employing more conventional techniques (Kerridge, 1985). Laser-microprobe analyses of the matrix lie within this envelope, but most of the analyses of small, individual, light-colored inclusions display lower nitrogen concentrations and more variable $\delta^{15}N$ values. Laser output energy for matrix was 5 J, but for inclusions ranged from 1 to 5 J, depending on the size of the inclusion. Between 5 and 10 pulses were necessary for each isotopic measurement of the matrix and up to 18 pulses for each inclusion.

The results from a study of the carbonaceous chondrite Murchison (fig. 6) also indicate that the laser microprobe is a useful tool for nitrogen analyses. Five analyses of the matrix define a narrow range of nitrogen concentration (620 to 790 ppm) and $\delta^{15}N$ values (+38.5 to +44.7 ‰) that are in excellent agreement with whole-rock determinations by other laboratories employing more conventional techniques. However, the results from a number of light-colored inclusions reveal a much wider range of $\delta^{15}N$ values (+12.4 to +60.6 ‰), as well as lower nitrogen concentrations (fig. 6). That the inclusions having the highest nitrogen concentrations have $\delta^{15}N$ values closest to those obtained from the matrix suggests that these inclusions were completely penetrated by the laser and that underlying matrix was sampled. Care must be taken to

Table 2. Results of laser-microprobe analysis of the iron meteorite Uwet

[Laser output energy was 5J; nm, not measured]

Target phase	No. of pulses	Yield (ng N)	Yield (ppm N)	$\delta^{15}N$ (per mil)
Schreibersite	12	3.4	62	−66
Schreibersite	21	1.6	17	−67
Schreibersite	25	1.6	14	−76
Kamacite	30	.6	3	nm
Kamacite	25	.7	4	nm

ensure that the laser is focused on areas of interest that are thicker than the depth of a laser-produced pit, typically 100 to 150 μm.

Although it appears to have been possible to obtain high nitrogen yields from the Murchison meteorite, problems were encountered when the iron meteorite Uwet was analyzed. Stepped heating of a whole-rock sample and an acid residue of this meteorite (employing a revised version of the technique used by Franchi and others (1986a)) have shown that the iron-nickel metal phase (kamacite) contains approximately 12 ppm nitrogen and the phosphide crystals (schreibersite) 165 ppm (Franchi, 1988), both with a $\delta^{15}N$ value of −96 ‰. However, the laser microprobe could extract only small amounts of nitrogen from this meteorite (table 2), with yields of only 3 or 4 ppm from the kamacite and up to 62 ppm from the schreibersite. Even these yields may be high, as the heavy $\delta^{15}N$ values of the nitrogen extracted from the schreibersite (−66 to −76 ‰) indicate that up to 30 percent of the nitrogen analyzed may represent terrestrial contamination. Therefore, as little as 25 percent of the indigenous nitrogen in this meteorite may have been liberated by the laser microprobe, probably due to incomplete degassing of molten metal or even the formation of nitrides as the ejecta cooled. Low recovery rates of gases from laser-induced melting or vaporization of geological materials is well recorded; for example, Kirschbaum (1988) reported yields of only 25 percent for argon and 13 percent for xenon from inclusions in the Allende meteorite. The results of Franchi and others (1986a) indicate that for some materials nitrogen also suffers from low yields.

A LASER-MICROPROBE STUDY OF BENCUBBIN

The laser microprobe has been used to investigate the distribution of isotopically heavy nitrogen in the Bencubbin meteorite. This meteorite is a mixture of iron-nickel metal and achondritic silicate clasts (plus a few chondritic clasts) welded together in a shock-produced glassy matrix (McCall, 1968; Newsom and Drake, 1979). The presence of primitive trace-element abundances in both the metal and silicate clasts indicates minimal planetary processing (Kallemeyn and others, 1978; Newsom and Drake, 1979). The silicate clasts also have an unusual oxygen isotopic

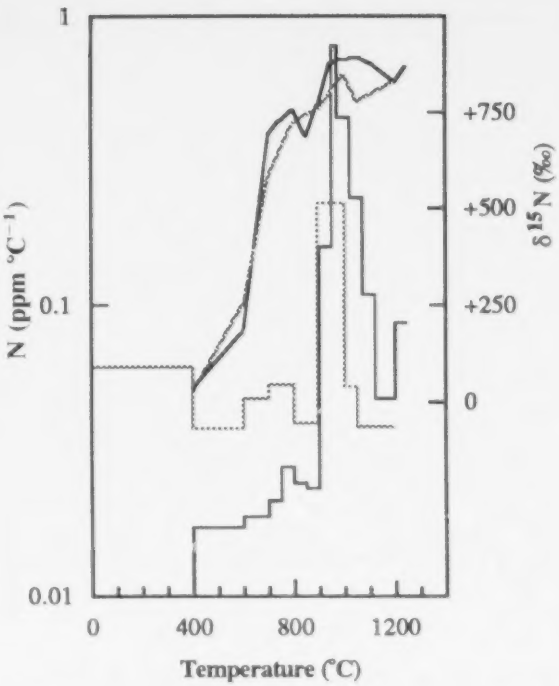

Figure 7. Stepped-heating release profiles of samples of a metal and silicate clast from the Bencubbin meteorite. Solid lines, metal clast; broken lines, silicate clast. The histogram displays the yield of nitrogen per degree centigrade (note log scale), the angled lines the $\delta^{15}N$ value from each step. Both samples produce a major release of heavy nitrogen over the temperature range 900 to 1,100 °C and a small release between 600 and 800 °C. The $\delta^{15}N$ values of gas released from both samples are very similar at all temperatures. Diagram after Franchi and others (1986b).

composition (Clayton and Mayeda, 1978). However, perhaps the most intriguing feature of this meteorite is that whole-rock samples contain nitrogen (around 50 ppm) highly enriched in ^{15}N, with $\delta^{15}N$ values up to +973 ‰ (Prombo and Clayton, 1985). Similar nitrogen-release profiles from high-resolution stepped heating of samples of metal and silicate clasts (fig. 7) indicate that there may be a single source for the heavy nitrogen, possibly a minor phase common to both types of clast (Franchi and others, 1986b). Therefore, determining the location of the heavy nitrogen within the meteorite is important, as this would help constrain the mechanism by which the nitrogen was incorporated into the meteorite and thus constrain possible origins of the ^{15}N enrichment.

The only phase that has been identified in both types of clasts is the glassy matrix material, which surrounds all the clasts and, in places, forms penetrating veins. It is considered that only 10 percent, or possibly 20 percent at

the very most, of the metal and silicate clast samples could have been matrix material that had been inadvertently sampled. Therefore, as the metal clast contained 82 ppm nitrogen ($\delta^{15}N = +868$ ‰) and the silicate clast 45 ppm ($\delta^{15}N = +789$ ‰), the matrix must contain several hundred parts per million if it is the carrier phase. Unfortunately, obtaining samples of the matrix is difficult because of the very hard, yet ductile nature of the meteorite. Stepped-heating extractions of two matrix samples liberated nitrogen having concentrations of 14 and 94 ppm and $\delta^{15}N$ values of +878 and +888 ‰, respectively (Franchi, 1988). These results were rather inconclusive, being the lowest and highest nitrogen concentrations found in this study and reflecting the very heterogeneous nature of the matrix.

Further information on the location of the heavy nitrogen yielded by high-resolution stepped heating of acid residues of the meteorite established that the nitrogen is concentrated in a minor phase with a uniform $\delta^{15}N$ value of about +995 ‰ (Franchi and others, 1986b). Analytical transmission electron microscopy has indicated that the only possible carriers are submicron chromium-rich sulfide grains. As yet, these very small grains have not been identified in whole-rock specimens of Bencubbin. Therefore, direct analysis of the nitrogen was considered to be the best means of determining its distribution. Rather than by acquisition of more, or larger, samples of the matrix for further stepped-heating experiments, it was hoped that the distribution of nitrogen within the meteorite could be determined by laser-microprobe analysis.

Twenty-one different target areas (metal clasts, silicate clasts, or matrix) have been analyzed by use of the laser microprobe. The results are presented in figure 8. To minimize errors on the yield calculations, the pit volumes were estimated from scanning electron microscope photographs of the sample after analysis. Whereas stepped heating revealed a degree of similarity in the nitrogen release profile from the various clasts, the laser microprobe appears to distinguish considerable $\delta^{15}N$ variations between the metal ($\delta^{15}N = +420$ to +958 ‰) and silicate ($\delta^{15}N = +190$ to +253 ‰) clasts. However, as the heavy nitrogen is known to have a uniform isotopic composition ($\delta^{15}N = +995$ ‰), the range in $\delta^{15}N$ values must be due to sampling of a second component that has a much lighter $\delta^{15}N$ value. The only isotopically light nitrogen observed during the stepped-heating extraction was that released below 600 °C (fig. 7) and is believed to be terrestrial contamination. It is therefore probable that the isotopically light nitrogen component sampled during the laser analyses is also terrestrial contamination.

The similar ranges of $\delta^{15}N$ values for the metal clasts and matrix (fig. 8) imply that they suffered similar degrees of contamination. However, the much lighter $\delta^{15}N$ values from the silicate clasts indicate more severe contamination. As the contamination is most probably concentrated on the sample surface as adsorbed atmospheric gases and organic materials, it is expected that the contamination would be degassed or volatilized where it interacts with the laser beam and also where the hot molten ejecta blanket falls on the sample surface. Figure 9 shows that the pit sizes and ejecta blankets in the metal clasts and matrix are similar but that the ejecta blankets around pits in the silicate clasts are approximately twice the width (four times the area) of those in the material and matrix. Therefore, if a uniform layer of adsorbed gases and organic materials is assumed, the range in $\delta^{15}N$ values obtained from the laser microprobe can be explained by adding variable amounts of surface contamination having a low $\delta^{15}N$ value to the isotopically heavy nitrogen indigenous to the sample.

To obtain an estimate of the concentration of the heavy nitrogen in the various materials liberated by the laser microprobe, mixing lines have been plotted on figure 8. The contamination component was assumed to have a $\delta^{15}N$ value of 0 ‰ (not unreasonable) and an abundance equivalent to a concentration of 50 ppm. The indigenous nitrogen is known to have a $\delta^{15}N$ value of +995 ‰ (Franchi and others, 1986b), and the lines for three different concentrations (5, 10, and 15 ppm) have been calculated. As can be seen in figure 8, the data from the metal clasts fall around the mixing line that has an assumed concentration of

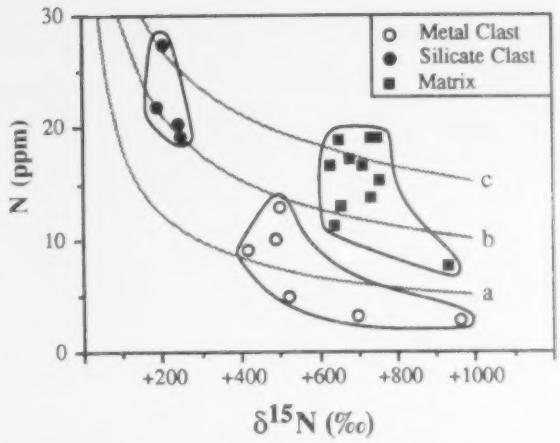

Figure 8. Results of laser-microprobe analyses of the Bencubbin meteorite. Laser output energy was 5 J. Between 6 and 20 laser pulses were employed for each analysis. The laser microprobe appears to resolve the different types of target areas on the basis of their $\delta^{15}N$ value and nitrogen content. However, to be consistent with the stepped-heating extractions, the data can be interpreted in terms of mixing an indigenous component ($\delta^{15}N = \approx 995$ ‰) with a contaminant component (about 50 ppm) with a $\delta^{15}N$ value of 0 ‰. The metal clasts scatter along the curve having an assumed 5 ppm of heavy nitrogen (line a), whereas the silicate clasts and matrix require higher heavy-nitrogen concentrations of between 10 ppm (line b) and 15 ppm (line c).

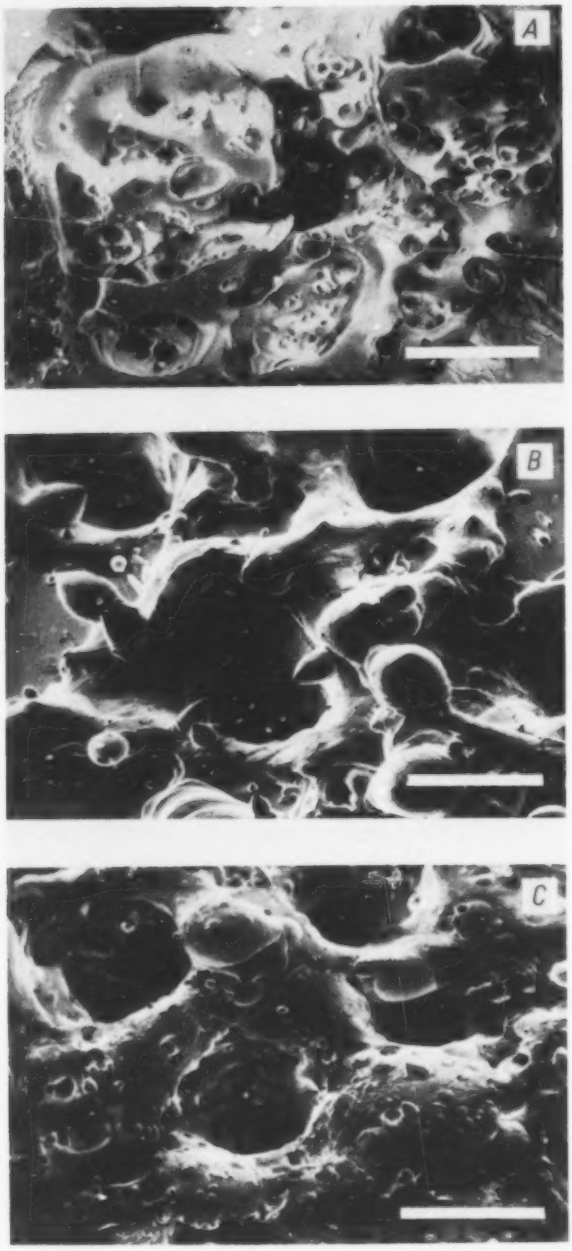

Figure 9. Laser-produced pits in different parts of the Bencubbin meteorite. A, Silicate clast. B, Metal clast. C, Matrix. Laser output energy was 5 J. The pits produced in each material are all similar, approximately 150 μm deep and ranging from about 80 μm across in the silicate clasts to 100 μm across in the metal clasts. However, the diameter of the ejecta blankets around the pits in the silicate clasts (around 500 μm) are much larger than those around pits in the metal clasts and matrix (200 to 300 μm). Scale bars all 100 μm.

heavy nitrogen of 5 ppm, whereas the silicate clasts and the matrix require higher concentrations of between 10 and 15 ppm. These results clearly indicate that the matrix is not the source, or carrier, of the heavy nitrogen but that the heavy nitrogen is distributed throughout the meteorite.

Curiously, the apparent concentration of isotopically heavy nitrogen in the clasts and matrix sampled by the laser is considerably lower than the concentrations determined by stepped heating. It was noted that the nitrogen concentrations in the iron meteorite Uwet determined by the laser microprobe were also considerably lower than the values obtained by stepped heating, with, at most, 30 percent of the nitrogen being recovered. That the metal clasts in Bencubbin have lower heavy-nitrogen concentrations than the silicate clasts and matrix, in contrast to the values obtained by stepped heating (fig. 2), suggests that the recovery rates from the metal were lower than from the matrix and silicate clasts. There are two possible effects that could influence the recovery rate. The first is the thickness of the ejecta blanket; the relatively thin blanket produced from the silicate clasts (fig. 9*A*) would presumably degas more readily than the thicker blankets obtained from the metal clasts and matrix (figs. 9*B* and *C*). The second effect is that as the metal cools it reacts with some of the free nitrogen to form nitrides, similar to the process that may have been responsible for the low yields from the iron meteorite Uwet. Such a problem is unlikely to arise during laser interaction with the matrix target areas, as large amounts of oxygen, produced from the breaking of the silicon-oxygen bonds in the silicate portions of the matrix, would be more likely to react with any hot metal to form metal oxides. Thus, the results from the laser-microprobe study corroborate the interpretation of the stepped-heating experiments that the heavy nitrogen is distributed throughout the metal and silicate clasts as well as the matrix. The implication of such a distribution is that the heavy nitrogen was present within the clasts prior to the brecciation and was not the result of late-stage in situ nuclear reactions or implantation processes occurring in a regolith environment.

CONCLUSIONS

The results from these preliminary experiments show that lasers are of considerable value in the study of light-element stable isotopic compositions. The laser's sectioning technique has produced excellent results in the study of diamonds, and the technique is currently being evaluated for other types of geological materials. The results from the laser microprobe indicate that this may prove to be a very powerful tool in stable isotope geochemistry. At the present time, useful $\delta^{15}N$ measurements can be made on various materials, but $\delta^{13}C$ and $\delta^{18}O$ determinations are less reliable. However, development of mass spectrometers capable of measuring $\delta^{15}N$ or $\delta^{13}C$ and $\delta^{18}O$ values with even greater analytical sensitivity and the development of the

appropriate gas-handling techniques, currently in progress, are required before analysis of a wide range of geological materials from a single laser pulse can be realized.

ACKNOWLEDGMENTS

Financial support for this work by the Science and Engineering Research Council and the Natural Environment Research Council is gratefully acknowledged. Laser sectioning of diamonds by Michael Seal of D. Drukker and Zn., Amsterdam, is also most gratefully appreciated. Helpful reviews by Pat Shanks, Bob Criss, and Everett Gibson have led to a much-improved manuscript.

REFERENCES CITED

Boyd, S.R., Mattey, D.P., Pillinger, C.T., Milledge, H.J., Mendelssohn, M.J., and Seal, M., 1987, Multiple growth events during diamond genesis: An integrated study of carbon and nitrogen isotopes and nitrogen aggregation state in coated stones: Earth and Planetary Science Letters, v. 86, p. 341–353.

Boyd, S.R., Pillinger, C.T., Milledge, H.J , Mendelssohn, M.J., and Seal, M., 1988a, Fractionation of nitrogen isotopes in a synthetic diamond of mixed crystal habit: Nature, v. 331, p. 604–607.

Boyd, S.R., Wright, I.P., Franchi, I.A., and Pillinger, C.T., 1988b, Preparation of sub-nanomole quantities of nitrogen gas for stable isotopic analysis: Journal of Physics E: Scientific Instruments, v. 21, p. 876–885.

Carr, R.H., Wright, I.P., Joines, A.W., and Pillinger, C.T., 1986, Measurement of carbon stable isotopes at the nanomole level: A static mass spectrometer and sample preparation technique: Journal of Physics E: Scientific Instruments, v. 19, p. 798–808.

Clayton, R.N., and Mayeda, T.K., 1978, Multiple parent bodies of polymict brecciated meteorites: Geochimica et Cosmochimica Acta, v. 42, p. 325–327.

Davies, G., 1984, Diamond: Bristol, Adam Hilger, 255 p.

Franchi, I.A., 1988, Nitrogen isotopic variation in irons and other Fe-Ni rich meteorites: Ph.D. thesis, The Open University, 272 p.

Franchi, I.A., Wright, I.P., Gibson, E.K., and Pillinger, C.T., 1986a, The laser microprobe: A technique for extracting carbon, nitrogen, and oxygen from solid materials for isotopic measurement: Journal of Geophysical Research Supplement, v. 16, p. 514–524.

Franchi, I.A., Wright, I.P., and Pillinger, C.T., 1986b, Heavy nitrogen in Bencubbin—A light-element isotopic anomaly in a stony-iron meteorite: Nature, v. 323, p. 138–140.

Kallemeyn, G.W., Boynton, W.V., Wills, J., and Wasson, J.T., 1978, Formation of the Bencubbin polymict meteorite breccia: Geochimica et Cosmochimica Acta, v. 42, p. 507–515.

Kamiya, Y., and Lang, A.R., 1965, On the structure of coated diamonds: Philosophical Magazine, v. 11, p. 347–356.

Kerridge, J.F., 1985, Carbon, hydrogen and nitrogen in carbonaceous chondrites: Abundances and isotopic compositions in bulk samples: Geochimica et Cosmochimica Acta, v. 49, p. 1707–1714.

Kirschbaum, C., 1988, Carrier phases for iodine in the Allende meteorite and their associated $^{129}Xe_r/^{127}I$ ratios: A laser microprobe study: Geochimica et Cosmochimica Acta, v. 52, p. 679–699.

McCall, G.J.H., 1968, The Bencubbin meteorite: Further details, including microscopic character of host material and two chondrite enclaves: Mineralogical Magazine, v. 36, p. 726–739.

McCrea, J.M., 1950, On the isotopic chemistry of carbonates and a paleotemperature scale: Journal of Chemical Physics, v. 18, p. 849–857.

Megrue, G.H., 1967, Isotopic analysis of rare gases with a laser microprobe: Science, v. 157, p. 1555–1556.

Newsom, H.E., and Drake, M.J., 1979, The origin of metal clasts in the Bencubbin meteoritic breccia: Geochimica et Cosmochimica Acta, v. 43, p. 689–707.

Plieninger, T., and Schaeffer, O.A., 1976, Laser probe ^{39}Ar-^{40}Ar ages of individual mineral grains in lunar basalt 15607 and lunar breccia 15465: Geochimica et Cosmochimica Acta Supplement 7, v. 40, p. 2055–2066.

Prombo, C.A., and Clayton, R.N., 1985, A striking nitrogen isotopic anomaly in the Bencubbin and Weatherford meteorites: Science, v. 230, p. 935–937.

Wright, I.P., Boyd, S.R., Franchi, I.A., and Pillinger, C.T., 1988, High-precision determination of nitrogen stable isotope ratios at the sub-nanomole level: Journal of Physics E: Scientific Instruments, v. 21, p. 865–875.

Zinner, E., Tang, M., and Anders, E., 1987, Large isotopic anomalies of Si, C, N and noble gases in interstellar silicon carbide from the Murray meteorite: Nature, v. 330, p. 730–732.

Simultaneous Analyses of Noble-Gas Isotopes and Halogens in Fluid Inclusions in Neutron-Irradiated Quartz Veins by Use of a Laser-Microprobe Noble-Gas Mass Spectrometer

By J.K. Böhlke,[1] C. Kirschbaum,[2] *and* J. Irwin[3]

Abstract

Simultaneous analyses of halogens and noble-gas isotopes in preselected fluid inclusions in minerals can provide unique information useful for (1) defining and delineating fluid reservoirs in ancient hydrothermal and metamorphic systems, (2) determining the sources of fluids and dissolved salts and determining some characteristics of rocks along fluid flow paths, and (3) documenting and quantifying mixing, boiling, and (or) unmixing of fluids in relation to mineral precipitation. In this study, a high-sensitivity noble-gas mass spectrometer combined with a laser sampler was adapted to analyze natural and neutron-induced Ar, Kr, and Xe isotopes released from fluid inclusions in minerals. Mineral samples were neutron irradiated prior to analysis to produce Ar, Kr, and Xe isotopes from Cl, K, Ca, Se, Br, Te, I, Ba, and U. Preliminary results indicate that natural abundances of Ar, Kr, and Xe isotopes, as well as products of Cl, K, Br, and I, can be measured simultaneously in less than 10^{-9} liter of dilute fluid released from hydrothermal quartz by laser decrepitation.

Aqueous fluid inclusions in Cretaceous vein quartz from Alleghany, in the Sierra Nevada, California, contain variable amounts of CO_2 (<1 to 6 molal) and small amounts of chlorine (≤0.2 molal). Fluid inclusions having intermediate CO_2 contents in three vug quartz chips from the Oriental mine have several similarities to high-temperature meteoric geothermal ground waters: atmospheric isotope ratios of Kr and Xe, moderately elevated $^{40}Ar/^{36}Ar$ ratios (~345–535), and absolute ^{36}Ar concentrations between approximately 25 and 100 percent of air-saturated water values. These data are consistent with at least two interpretations of the origin of gold quartz veins: (1) the veins formed from ascending dilute fluids that originated at the Earth's surface, equilibrated with air, and subsequently acquired CO_2 at greater depths in the crust either by participating in prograde metamorphic reactions or by dissolving deep magmatic gas fluxes or (2) the veins formed within a broad zone of mixing between ascending magmatic or metamorphic fluids and descending meteoric waters, such that neither endmember is represented by the analyzed samples. Fluid inclusions in two other quartz chips yield linear arrays (mixing lines?) in plots of $^{132}Xe/^{36}Ar$, $^{84}Kr/^{36}Ar$, and $Cl/^{36}Ar$ between (1) a chlorine-bearing component relatively enriched in the heavier noble gases and (2) a chlorine-free component relatively enriched in argon. These data, mostly from milky microfractured quartz, may indicate either that (1) mixtures of two fluid types (vapor + liquid?) were trapped as fluid inclusions or (2) milky quartz contains large amounts of contaminant gases.

All of the Alleghany fluid inclusions have high I/Cl ratios (~10^3 times seawater), and many appear to be relatively enriched in Xe, possibly because the fluids acquired I and Xe from organic-rich marine sedimentary rocks along flow paths. The chlorine concentrations of the fluid inclusions are significantly less than that of seawater, and the Br/Cl ratios are typical of low-salinity ground waters that have not interacted with strongly fractionated residual evaporite brines or salt deposits. Absence of significant marine and evaporitic salt sources within the metamorphic belt may be partly responsible for some of the chemical transport properties of the Cretaceous hydrothermal system that have led to gold ore deposition.

INTRODUCTION

Performing simultaneous analyses of noble-gas isotopes (Ar, Kr, and Xe) and halogens (Cl, Br, and I) in fluid inclusions could greatly increase our ability to define past fluid reservoirs and characterize their interactions in ancient hydrothermal systems. Ratios among these components may be used to determine likely sources of fluids and dissolved salts and to distinguish among processes such as fluid mixing or boiling. Furthermore, analyses of fluid inclusions in various igneous and metamorphic materials are essential for characterizing otherwise inaccessible reservoirs of volatiles in the Earth. In this paper, we report preliminary analyses of noble-gas isotopes and halogens in

[1] CMT-205, Argonne National Laboratory, Argonne, IL 60439; now at the U.S. Geological Survey, National Center, MS 954, Reston, VA 22092.

[2] Charles Evans and Associates, 301 Chesapeake Dr., Redwood City, CA 94063.

[3] Department of Physics, University of California, Berkeley, CA 94720.

fluid inclusions in gold-bearing quartz veins from the Sierra Nevada metamorphic belt, California. The data were obtained by use of a high-sensitivity noble-gas mass spectrometer combined with a laser sampling system. Simultaneous analyses of both gases and electrolyte species were made possible by neutron irradiation, which produced isotopes of Ar, Kr, and Xe from K, Ca, Cl, Br, Se, Ba, Te, U, and I (see table 1). By use of the laser sampling system, small preselected areas of crystals containing as little as 10^{-10} to 10^{-9} L of fluid inclusions were analyzed.

Gold quartz veins occur in deformed metamorphic belts of diverse ages worldwide. Many of the chemical and isotopic characteristics of the hydrothermal fluids responsible for veins of this type (for example, high CO_2, high $\delta^{18}O$) were similar to those expected of "metamorphic" fluids (Kerrich and Fyfe, 1981; Phillips and Groves, 1983). However, it is not known for certain whether the fluids originated predominantly as (1) highly exchanged deeply circulating meteoric waters, (2) expelled pore fluids, or (3) fluids degassed from hydrous minerals or magmas (Fyfe and Kerrich, 1984; Burrows and others, 1986; Nesbitt and others, 1986). Many of the chemical and light stable-isotopic characteristics of these fluid types converge because of fluid-rock interactions at low fluid to rock ratios. Oxygen and hydrogen isotopic analyses of fluids and minerals may be diagnostic of seawater or meteoric-water participation in hydrothermal systems, depending on the altitude and latitude of the recharge area (Craig, 1961, 1963; Taylor, 1974; White, 1974; Criss and Taylor, 1983; Wickham and Taylor, 1985); however, these isotope systems can yield ambiguous results, and they have not yet satisfactorily determined the ultimate origin of CO_2-rich gold quartz vein fluids (Nesbitt and others, 1986; Pickthorn and others, 1987; Böhlke and others, 1988). Ratios of noble-gas isotopes and halogens provide numerous alternative or complementary indicators of different fluid types and their sources. Also, analyses of noble gases and halogens can provide critical data for determining whether vein mineralization occurred in response to either (1) unmixing of CO_2-rich and H_2O-rich fluids during ascent (Robert and Kelly, 1987) or (2) mixing of ascending fluids with shallower reservoirs. The laser sampling system is important in this context because secondary fluid inclusions unrelated to mineralization may be abundant in large samples and because mixing and unmixing of fluids at the time of trapping are most convincingly documented at the level of individual inclusions or small groups of inclusions (Roedder, 1984).

The analyses reported here were performed both to test the technique and to provide preliminary answers to fundamental questions about the sources of fluids and mechanisms of mineralization in gold quartz veins. Further work is currently in progress to refine the technique, to extend the Sierran vein study, and to apply the technique in studies of other hydrothermal systems.

BACKGROUND

Noble Gases and Halogens in Ground Waters and Fluid Inclusions

The published record contains numerous data on halogens (especially Cl and Br) in ground waters, relatively few on noble gases (mostly He and Ar) in crustal fluids, and very few on either halogens or noble gases in fluid inclusions. The following brief selective survey of some of the causes and observed effects of halogen and noble-gas fractionations in natural fluids is presented to indicate some of the potential applications and to provide a basis for comparison for data obtained by the new multicomponent fluid-inclusion analyses described below.

The solubilities of the heavy noble gases in water increase with mass in the sequence Ar < Kr < Xe; both the relative and absolute solubilities are functions of salinity, temperature, and pressure (Smith and Kennedy, 1983; Shock and others, in press). Adsorption coefficients for these gases on solid surfaces also increase with mass (Ozima and Podosek, 1983), whereas the opposite appears to be true for solution in silicate melts (Lux, 1987). The concentrations and isotopic compositions of Ar, Kr, and Xe in many natural ground waters indicate that a large component of these noble gases dissolved in approximate equilibrium with the gases in air at ambient temperatures (Mazor and Wasserburg, 1965; Mazor, 1972, 1976; Herzberg and Mazor, 1979; Kennedy and others, 1985). Systematic variations in the absolute and relative abundances of Ar, Kr, and Xe, ranging over as much as one order of magnitude, have been observed in many surface-derived (meteoric) geothermal fluids. These variations have been interpreted in part as results of subsurface boiling, incorporation of fractionated gases from various aquifer rocks, and subsequent mixing (Mazor, 1976; Kennedy and others, 1985; Smith and Kennedy, 1985). The isotopic compositions of Ar, Kr, and Xe probably are not fractionated by more than a few percent by equilibrium vapor-liquid exchange (Ozima and Podosek, 1983). However, many waters that originated at the Earth's surface contain significant amounts of "excess" radiogenic ^{40}Ar acquired during water-rock interactions (Mazor, 1976; Kennedy and others, 1985; Smith and Kennedy, 1985; Zaikowski and others, 1987); the $^{40}Ar/^{36}Ar$ ratios of such fluids are functions of fluid residence time and the age and composition of the rocks. The noble-gas compositions of fluids exsolved from magmas or metamorphic rocks at depth in the Earth's crust have not been completely characterized, but they may deviate significantly from those of surface-derived fluids (Ozima and Podosek, 1983; Allegre and others, 1987; Fisher, 1985). The $^{40}Ar/^{36}Ar$ ratios of mantle-derived magmatic rocks range from approximately atmospheric (296) to greater than 20,000, presumably depending in part on the

mantle source region and degree of crustal contamination. Kennedy and others (1985) suggest that a "magmatic" component of argon having $^{40}Ar/^{36}Ar \geq 500$ may be present in Yellowstone spring waters. Excess ^{40}Ar amounting to as much as 90 to 99 percent of the total argon content has been detected in fluid inclusions from crystals in metamorphic quartz veins and igneous pegmatites (Rama and others, 1965; Naydenov and others, 1972). $^{3}He/^{4}He$ ratios have been interpreted widely as indicators of mantle volatiles, water-rock interactions, and crustal gas fluxes in aqueous systems (Craig and others, 1978; Kennedy and others, 1985; Torgersen and Clarke, 1985; Simmons and others, 1987) but will not be discussed further because the laser microprobe has not yet been adapted to measure helium isotope ratios.

The relative and absolute abundances of halogens (Cl, Br, and I) differ by orders of magnitude in waters from different sources (White, 1957; White and others, 1963; Collins and Egleson, 1967; Rittenhouse, 1967; Whittemore, 1984). For example, Br/Cl ratios of concentrated subsurface brines range from $<10^{-1}$ to $>10^{1}$ times that of seawater, depending in part on whether they are "neoformed" (from salt dissolution) or "residual" (from salt crystallization), respectively (Holser, 1979). I/Cl ratios of ground waters are almost always greater than that of seawater, and they are greatest ($\geq 10^{3}$ times that of seawater) in relatively dilute waters associated with organic matter. Previous halogen analyses of fluid-inclusion-bearing hydrothermal minerals, obtained by neutron activation (Wickman and Khattab, 1972; Luckscheiter and Parekh, 1979; Behr and Gerler, 1987) and by chemical analysis of leachates (Kozlowski and Karwowski, 1974), have yielded a wide range of Br/Cl ratios (~0.001 to 0.03), most of which are significantly greater than that of seawater (~0.0015). Nordstrom and others (1985) state that dilute ground waters and saline fluid-inclusion leachates in granitic rocks at Stripa, Sweden, have indistinguishable halogen ratios (Br/Cl = 0.004; I/Cl = 0.0001) and infer that fluid inclusions are the source of ground-water salts. Ratios of Br/Cl and I/Cl are not likely to change significantly during boiling or fluid unmixing, but their utility in detecting mixing of distinct fluid reservoirs has been documented (Whittemore, 1984).

In a study of natural and neutron-induced argon isotopes released from irradiated samples of quartz veins from granite-hosted tungsten deposits by stepwise heating and crushing, Kelley and others (1986) identified (1) a potassium-correlated component, presumed to have been released from solid mica inclusions, (2) a chlorine-correlated component, similar to air-saturated water, having a small amount of excess ^{40}Ar, attributed to fluid inclusions, and (3) a calcium-correlated component having a large amount of excess ^{40}Ar. This study established the importance of analyzing simultaneously natural and neutron-induced components of argon, which could be related to other independent information on the electrolyte chemistry of fluid inclusions (see also Turner, 1988). Irwin and others (unpub. data, 1988) have found evidence for several distinct sources of argon isotopes in irradiated metamorphic minerals analyzed by use of a laser-microprobe sampling system coupled with a high-sensitivity mass spectrometer (Kirschbaum, 1988). The current study represents an initial attempt to use the laser microprobe for analyzing Ar, Kr, and Xe isotopes in fluid inclusions in irradiated hydrothermal vein quartz (Böhlke and others, 1987; Kirschbaum and others, 1987). The multicomponent noble-gas mass spectrometric approach for simultaneously analyzing Ar, Kr, Xe, Cl, K, Ca, Br, Se, Te, U, and I (table 1) was first used by Turner (1965) for meteorite studies but has not previously been used in fluid inclusion studies.

Gold Quartz Veins in the Sierra Nevada

Gold quartz veins were deposited in previously deformed and metamorphosed rocks in the Cretaceous Sierran forearc approximately 110 to 140 m.y. ago (Böhlke and Kistler, 1986). The Sierran veins resemble "mesothermal-," "greenstone belt-," or "metamorphic-" type gold quartz veins that occur in other deformed metamorphic belts worldwide (Lindgren, 1933; Kerrich, 1981; Groves and others, 1985). The veins are distributed along fault zones at both regional and local scales, they occur in a variety of host rocks, and they typically are enveloped by carbonatized metasomatic wall rocks (Ferguson and Gannett, 1932; Coveney, 1981; Böhlke, 1986). The veins consist mainly of massive white ("milky") quartz in which there are scattered open cavities lined with relatively clear euhedrally terminated ("vug") quartz crystals. The veins probably were formed by repeated episodes of deformation and precipitation of quartz in fluid-filled open spaces. Wall-rock alteration is dominated by retrograde carbonatization reactions that were probably caused by ascending fluids that acquired CO_2 at greater depths (Böhlke, 1986).

Stable isotope data and phase equilibria for minerals in veins and altered wall rocks in the Alleghany district indicate that the metasomatic hydrothermal fluids (at 325±50 °C and 2±1 kbar) were isotopically heavy ($\delta^{18}O$ = +9 to +14 ‰; δD = −50 to −10 ‰) and CO_2 rich (~10 mole percent CO_2) (Marshall and Taylor, 1981; Böhlke and Kistler, 1986; Böhlke, in press). Many of the fluid inclusions observed in vein quartz from Alleghany have relatively high homogenization temperatures (approximately 180 to 250 °C), and a small proportion of them contain as much as 10 mole percent CO_2 (Coveney, 1981; Weir and Kerrick, 1987; Böhlke, unpub. data, 1988), consistent with the fluid properties estimated from phase equilibria. However, many of the fluid inclusions have significantly lower CO_2 contents and lower homogenization temperatures (as low as 110 °C). Also, most analyzed fluids obtained from bulk samples of decrepitated or crushed vein

Table 1. Neutron reactions, production rates, and approximate detection limits

[(x, y) = add x, lose y in a nuclear reaction; −β = lose a beta particle; E.C. = electron capture]

Reaction	Rate of production[a]	Limit of detection[b]	Detectable concentration in 10^{-6} g fluid[c]
	atoms product / atoms reactant	atoms reactant	ppm reactant
$^{37}Cl \xrightarrow{(n,\gamma)} {}^{38}Cl \xrightarrow{-\beta} {}^{38}Ar^{d}$	$^{38}Ar_{Cl}/Cl^{e} = 21.5 * 10^{-9}$	$8.3 * 10^{12}$	490
$^{39}K \xrightarrow{(n^{f},p)} {}^{39}Ar$	$^{39}Ar_{K}/K^{e} = 12.0 * 10^{-9}$	$5.4 * 10^{12}$	350
$^{40}Ca \xrightarrow{(n^{f},\alpha)} {}^{37}Ar$	$^{37}Ar_{Ca}/Ca^{e} = 6.04 * 10^{-9}$	$120 * 10^{12}$[g]	8300[g]
$^{82}Se \xrightarrow{(n,\gamma)} {}^{83}Se \xrightarrow{-\beta} {}^{83}Br \xrightarrow{-\beta} {}^{83}Kr^{d}$	$^{83}Kr_{Se}/Se = .860 * 10^{-9}$	$8.0 * 10^{12}$	1050
$^{81}Br \xrightarrow{(n,\gamma)} {}^{82}Br \xrightarrow{-\beta} {}^{82}Kr^{d}$	$^{82}Kr_{Br}/Br = 272. * 10^{-9}$	$.040 * 10^{12}$	5.3
$^{130}Te \xrightarrow{(n,\gamma)} {}^{131}Te \xrightarrow{-\beta} {}^{131}I \xrightarrow{-\beta} {}^{131}Xe^{d}$	$^{131}Xe_{Te}/Te = 16.8 * 10^{-9}$	$.59 * 10^{12}$[h,i]	130[h,i]
$^{127}I \xrightarrow{(n,\gamma)} {}^{128}I \xrightarrow{-\beta} {}^{128}Xe^{d}$	$^{128}Xe_{I}/I = 1283 * 10^{-9}$	$.0089 * 10^{12}$	1.9
$^{130}Ba \xrightarrow{(n,\gamma)} {}^{131}Ba \xrightarrow{E.C.} {}^{131}Cs \xrightarrow{E.C.} {}^{131}Xe^{d}$	$^{131}Xe_{Ba}/Ba = 2.52 * 10^{-9}$	$4.0 * 10^{12}$[h,i]	900[h,i]
$^{235}U \xrightarrow{(n,fission)} {}^{131}Xe^{d}, {}^{132}Xe^{d}, {}^{134}Xe^{d}, {}^{136}Xe^{d}, {}^{83}Kr^{d}, {}^{84}Kr^{d}$	$^{136}Xe_{U}/U = 56.2 * 10^{-9}$	$.076 * 10^{12}$[i]	30[i]
^{36}Ar	^{36}Ar —	$470 * 10^{3}$	$31 * 10^{-6}$
^{84}Kr	^{84}Kr —	$14 * 10^{3}$	$1.9 * 10^{-6}$
^{132}Xe	^{132}Xe —	$4.6 * 10^{3}$	$1.0 * 10^{-6}$

a = thermal neutron fluence = $2.07 * 10^{17}$ n/cm^2; "reactant" refers to the sum of all naturally occurring isotopes of the element.
b = corresponds to 2 times the average propagated uncertainties, after subtraction of blanks and extrapolation to time zero.
c = equivalent to a cubic aqueous inclusion 100 μm on a side.
d = some stable natural abundance also present.
e = monitored reactions.
f = fast neutrons (all others are thermal neutrons).
g = detection limit increases from this value with time owing to the 35-day half-life of ^{37}Ar.
h = detection limits are higher initially and approach these values as intermediate products decay with half-lives of 8 days (^{131}I) to 12 days (^{131}Ba).
i = Te, Ba, U detection limits are calculated assuming they are mutually exclusive (no mutual ^{131}Xe interference).

quartz from Alleghany have δD values that are too low (−100 to −50 ‰) to have been in equilibrium with hydrothermal sericite (Marshall and Taylor, 1981; Böhlke and Kistler, 1986; Böhlke and others, 1988). Massive milky vein quartz appears to yield more negative δD values than euhedral vug quartz, possibly because the milky quartz contains a larger proportion of late (modern?) secondary fluid inclusions (Böhlke and others, 1988). Because the Cretaceous paleolatitude and altitude of the Sierra Nevada metamorphic belt are not precisely known, it is not clear what the δD values of contemporary meteoric waters were at the time the veins formed.

Occurrences of low-grade disseminated gold mineralization within altered wall rocks at Alleghany have been attributed in part to lithologically controlled metasomatic reactions between wall rocks and the relatively CO_2-rich

fluid (Böhlke, in press), whereas occurrences of high-grade gold mineralization within the massive quartz veins commonly appear to be associated with relatively low temperature, CO_2-poor fluid inclusions (Coveney, 1981). No firm petrographic evidence has yet been found for CO_2–H_2O immiscibility in the Sierran veins, nor has it been demonstrated whether or not fluid mixing contributed to vein mineralization.

Fluid inclusions in vein quartz at Alleghany occur in growth bands parallel to euhedral crystal faces (primary inclusions?) and in crossing healed fractures (pseudosecondary and secondary inclusions). The inclusions tend to be larger (up to several hundred microns across) in vug crystals but smaller (a few microns or less) and indistinct in milky quartz. In a few large vug crystals, it has been observed that inclusions in outer growth bands have lower homogenization temperatures and higher ice melting temperatures than those farther inward; however, primary and pseudosecondary inclusions commonly have fairly uniform characteristics within centimeter-sized chips. All fluid inclusions from Alleghany appear to have chlorinities less than that of seawater (Coveney, 1981; Weir and Kerrick, 1987; Böhlke, unpub. data, 1988).

METHOD OF INVESTIGATION

Samples Studied

Analyses were performed on four chips of vein quartz from the Oriental mine that were selected to represent three different elevations and two contrasting quartz textures (euhedral vug quartz, massive milky quartz) and on one heterogeneous chip of vein quartz from the Gold Crown mine. All of the samples are from mineralized veins that have carbonatized metasomatic halos.

Samples 578–9v (65 level, Drain vein split), 553v (500 level near Oriental shaft), and 643v (1300 level, east of Granite Stope) are euhedral quartz crystals from vugs at different levels of the Oriental mine. Previous studies indicate that vug quartz crystals from the Oriental mine contain fluids that have relatively high δD values (-54 ± 14 ‰; Böhlke and others, 1988). Dense populations of irregular to equant fluid inclusions (mostly pseudosecondary) near the bases of these crystals contain two or three visible fluid phases and trace amounts of fibrous birefringent daughter minerals at room temperature (see Coveney, 1981). Liquid CO_2 was observed in many of the larger (50 to 200 μm) inclusions in 553v and 643v. CO_2–H_2O clathrate melting behavior was observed in many of the inclusions that did not have visible liquid CO_2 in all three of the vug samples. The majority of the fluid inclusions analyzed with the laser microprobe contained little or no visible liquid CO_2 at room temperature, but most of them probably contained on the order of 1 to 5 mole percent CO_2. Fibrous daughter minerals were observed in approximately half of the fluid inclusions in 553v and 643v but are relatively rare in 578–9v. The daughter minerals are tentatively identified as phyllosilicates and (or) carbonates (Coveney, 1981). Most of the fluid inclusions in splits of the analyzed vug crystals homogenize between 135 and 200 °C; higher temperatures typically correspond to higher CO_2 contents. CO_2 clathrate melting temperatures in 553v and 643v range from 8.8 to 9.8 °C (consistent with ~0.1–0.4 *m* NaCl equivalent), with a pronounced mode between 9.0 and 9.4 °C (~0.3 *m* NaCl equivalent). CO_2 melting temperatures in the same samples are between −57.5 and −56.5 °C and indicate that CO_2 is much more abundant than CH_4. Preliminary analyses of salts from decrepitated CO_2-bearing fluid inclusions in 553v and 643v by energy-dispersive X-ray analysis in a scanning electron microscope (SEM/EDX) yield alkali to chloride ratios between 1 and 6. These data indicate that bicarbonate may be the dominant anion in many of the fluids. If dilute $NaHCO_3$ and NaCl have the same effect on clathrate melting temperatures, then the melting temperatures and SEM/EDX data indicate that most of these inclusions have approximately 0.05 to 0.20 *m* Cl (that is, 0.1 to 0.4 times that of seawater). Inclusions in which clathrate was not observed have ice melting temperatures ≥−3.1 °C, consistent with ≤0.9 *m* Cl if NaCl is the only solute (not likely), or ≤0.4 *m* Cl if NaCl and CO_2 are the only solutes, or ≤0.1 *m* Cl if NaCl, CO_2, and $NaHCO_3$ are solutes with Na/Cl equal to 3. All of the available data indicate that the majority of fluid inclusions in 553v and 643v contain approximately 0.05 to 0.2 *m* chlorine and that 0.1 *m* chlorine probably is equal to the average within a factor of 2.

Sample 643m (adjacent to 643v in the Oriental vein) is a chip of massive milky white quartz. Previous studies indicate that massive milky quartz from the Oriental mine commonly contains fluids that have relatively low δD values (-90 ± 9 ‰; Böhlke and others, 1988). Fluid inclusions in 643m are abundant but generally small (a few micrometers or less). Most of the inclusions contain one or two visible fluid phases at room temperature, and they are too small to provide reliable melting or homogenization data. The massive quartz is highly fractured, and many of its fluid inclusions are clearly secondary or pseudosecondary; nevertheless, liquid CO_2 appears to be present in some of them.

Sample 671 (adit level near winze) is a euhedrally terminated quartz crystal with milky quartz at the base from a vug in the Gold Crown mine. The larger fluid inclusions in the clearer parts of this sample are generally similar in appearance and melting behavior to those in 553v and 643v, except that slightly lower clathrate melting temperatures (8.6–9.4 °C) of the 671 inclusions indicate slightly higher apparent salinities.

Because the Oriental vein mineralization had not been dated previously, the laser microprobe also was used to sample argon isotopes from hydrothermal phengitic micas

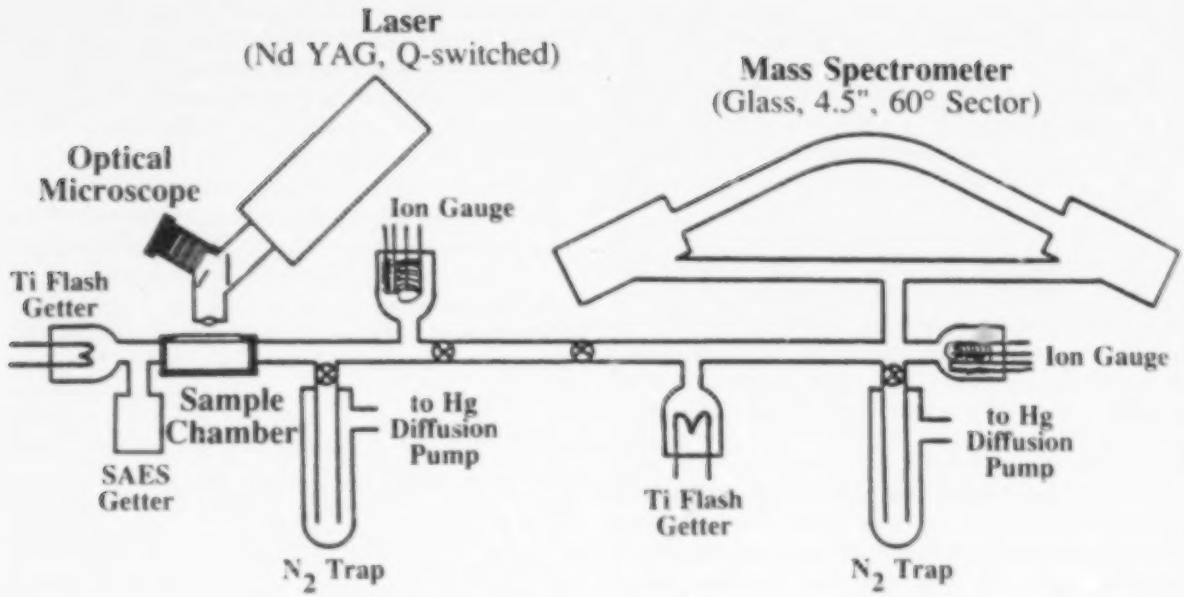

Figure 1. Schematic diagram of the laser-microprobe noble-gas mass spectrometer (from Kirschbaum, 1988).

for ^{40}Ar–^{39}Ar age determinations. The analyzed micas are green chromium-rich mariposites in a chip of dolomitized serpentinite from the wall of the Oriental vein at the west end of the 1300 level (Sample 611 in Böhlke, 1986).

Analytical Procedure

The apparatus used for the laser-microprobe extraction and mass-spectrometric analyses of Ar, Kr, and Xe isotopes is depicted in figure 1. Descriptions of the instrumentation and general analytical procedures are given in Kirschbaum (1986, 1988). The system includes a 4.5-inch radius 60°-sector glass mass spectrometer with a Bauer-Signer GS–98 source and a Johnston multiplier coupled to a pulse-counting detector optimized for low count rates (Kirschbaum, 1988). Fluid inclusions were decrepitated with a Jarrel-Ash 45–604 laser microprobe focused through a petrographic microscope.

For the present study, small (~5 mm diameter) unmounted quartz chips containing fluid inclusions were ground and polished with silicon carbide grit paper in distilled water in order to minimize sources of contamination. The polished chips were sealed in evacuated quartz tubes along with a standard hornblende flux monitor (MMHb–1) (Alexander and others, 1978) and irradiated in the University of California, Berkeley, TRIGA Mark III reactor for 3 megawatt hours (MWh). The irradiated chips were photographed, mapped, and then mounted in the mass spectrometer sample chamber with drops of high-vacuum sealant (Vac-seal). The chamber was then evacuated and baked at ~100 °C.

Fluid inclusions were sampled by 1 to 2-μs Q-switched laser pulses at an energy setting of 1 J. Each analysis consisted of between 2 and 50 laser pulses focused on a small area of the surface of a polished quartz chip where one or more fluid inclusions (~50 to 200 μm diameter) had been identified within 50 to 100 μm of the surface. Multiple laser shots produced excavated pits that are approximately 100 to 500 μm in diameter and depth and have conchoidal surfaces and no microscopic evidence of melting. Examination of chips after several analyses indicates that deeper fluid inclusions also may have been sampled by cracks that formed around the excavated pits. In some cases, the sampled volume appears to have been as deep as 1 to 2 mm. The exact mechanism by which the deeper inclusions were degassed is not known, but it is possible that multiple laser shots heated the fluid inclusions sufficiently to decrepitate them. In order to characterize potential contaminants within the quartz or on the surfaces of the samples, several analyses were made in areas of chips far from fluid inclusions. Laser-excavated pits in inclusion-free areas appear to be similar to those in inclusion-bearing areas.

Released gases were held in the sample chamber for 10 to 15 min in contact with a clean titanium surface and a Zr-Al alloy (SAES) getter and then were equilibrated with the mass spectrometer for 10 min before ionization and analysis. Sixteen mass numbers were counted in eight

cycles over a period of approximately 2 h. The counting sequence for one cycle was 100 s each for 132, 136, 131, 129, 128, and 127; 10 s each for 35, 36, 37, 38, 39, and 40; and 50 s each for 84, 83, 82, and 81. Masses 35, 37, 81, and 127 were monitored for Cl, Br, and I contamination in the mass spectrometer. Br and I contaminations were insignificant; Cl contamination was significant but stable and was included in the blank corrections. Blanks (no laser shots) were run before each analysis and averaged over a period of several days (corresponding to approximately 5 to 10 determinations). A single average blank value was then subtracted from each sample analysis performed within the same time period. Typical blanks were in the order of 10^3 to 10^4 atoms for masses 81–136 (Kr and Xe from air), 10^5 atoms for mass 38 (mainly HCl), 10^6 atoms for masses 36 and 37 (mainly HCl and Cl, respectively), and 10^8 atoms for mass 40 (Ar from air?).

Blank-corrected Ar, Kr, and Xe isotope data for fluid-inclusion-bearing and inclusion-free quartz, along with two sets of typical blank values, are listed in table 2. Blank-corrected argon isotope data for the hornblende standard are given in table 3. Data for all Ar isotopes, ^{84}Kr, and ^{132}Xe are given in counts per second (cps); data for all other Kr and Xe isotopes are given as ratios with ^{84}Kr or ^{132}Xe. ^{40}Ar data are not reported for analyses with large gas yields because of excessive detector deadtime corrections for count rates greater than ~150,000. The sensitivity of the instrument is such that 1 cps Xe = 14,000 atoms Xe (Kirschbaum, 1988). Sensitivities for Ar (1 cps = 18,000 atoms) and Kr (1 cps = 16,000 atoms) were assigned to be consistent with their relative ionization potentials. The sensitivity ratios derived from these values are within ±10 percent of those determined independently for the RARGA mass spectrometer with a similar Bauer-Signer ion source (Smith and Kennedy, 1985; B.M. Kennedy, personal commun., 1988). All ratios reported or discussed in this paper refer to atomic (or molar) proportions, whereas ppm refers to parts per million by weight.

Irradiation Parameters

Irradiation reactions, production rates, and approximate limits of detection for the quartz analyses are listed in table 1. Noble-gas products of neutron reactions are designated by subscripts identifying the primary reactants (e.g., $^{38}Ar_{Cl}$ refers to ^{38}Ar produced from Cl). All neutron irradiation reactions used to calculate the abundances of dissolved salts in the fluid inclusions were calibrated by use of hornblende (MMHb–1) as a standard for neutron flux monitoring. The production rates for $^{38}Ar_{Cl}$, $^{39}Ar_K$, and $^{37}Ar_{Ca}$ were calculated from the hornblende data in table 3 and the ratios among Cl, K, Ca, and ^{40}Ar (radiogenic) in MMHb–1 given by Roddick (1983). Corrections were made for the interfering isotopes $^{36}Ar_{Ca}$, $^{38}Ar_{Ca}$, $^{39}Ar_{Ca}$, $^{37}Ar_K$, $^{38}Ar_K$, and $^{40}Ar_K$ by use of the correction factors listed by Dalrymple and others (1981) for the U.S. Geological Survey TRIGA reactor. These corrections were found to be insignificant (≤0.5 percent) for all but $^{38}Ar_K$, which amounts to approximately 10 to 15 percent of total ^{38}Ar released from the hornblende. Independently determined correction factors for $^{36}Ar_{Ca}$, $^{39}Ar_{Ca}$, and $^{40}Ar_K$ for the Berkeley TRIGA reactor (G. Curtis, personal commun., 1988) yield practically identical results.

The mica ages and associated errors were calculated from equations given in Dalrymple and others (1981). The average J value used to calculate ^{40}Ar–^{39}Ar ages is 9.85×10^{-4}, with a population standard deviation of 0.33×10^{-4} (table 3).

The thermal neutron fluence (Φ) for this irradiation, calculated from

$$\Phi=\frac{(^{38}Ar_{Cl}/Cl)_{MMHb-1}}{0.2423\times\sigma^{37}_{Cl}} \qquad (1)$$

where $\sigma^{37}Cl$ is the thermal neutron cross section for ^{37}Cl and 0.2423 is the ratio $^{37}Cl/Cl$, was 2.07×10^{17} n/cm^2. Production rates of Kr and Xe isotopes from Br, Se, Ba, Te, U, and I were calculated from analogs of equation 1 by use of thermal neutron reaction cross sections and isotopic abundances of the reactants from Walker and others (1984).

Uncertainties

The uncertainties quoted in the tables and illustrated in the following figures are based on (1) the population standard deviation for the set of approximately 5 to 10 blank determinations used to correct a group of analyses and (2) the standard deviation of data about the line used to extrapolate count rates (or ratios) to time zero. Several potential sources of systematic or random errors are not reflected in the uncertainties assigned to individual analyses. These include sample contamination, selective release of gases from fluid inclusions, and errors in the assumed irradiation parameters and mass spectrometer sensitivities, for example.

The relative sensitivities and transmission efficiencies of the mass spectrometer for Ar, Kr, and Xe are not precisely known and could be in error by as much as ±20 percent or more (Kirschbaum, 1986; B.M. Kennedy, personal commun., 1988). Also, because neutron reaction cross sections depend on the neutron energy spectrum, the calculated noble-gas production rates for unmonitored thermal neutron reactions may be incorrect by varying amounts. For example, the ratio $(^{128}Xe_I/I):(^{38}Ar_{Cl}/Cl)$ from table 1 is approximately 20 to 40 percent smaller than those reported by Kirschbaum (1988) for several monitors irradiated in the University of Missouri Research Reactor facility, whereas the ratios $(^{128}Xe_I/I):(^{38}Ar_{Cl}/Cl)$, $(^{131}Xe_{Ba}/Ba):(^{38}Ar_{Cl}/Cl)$,

Table 2. Count rates (counts per second) and some calculated quantities for blanks and blank-corrected quartz analyses

Data for mass numbers 35–40, 84, and 132 are given in counts per second (cps). Other data are given as ratios (as indicated in the left-hand column). For each mass number or ratio, the first row indicates the value, and the second row indicates 1 standard deviation, calculated from uncertainties in the blank and in the extrapolation of count rates to time zero. F values (lower rows) are defined in the text. 1 cps Ar = 18,000 atoms Ar, 1 cps Kr = 16,000 atoms Kr, and 1 cps Xe = approximately 14,000 atoms Xe. Blank1 and Blank2 are typical averages of 5 to 10 determinations; all other analyses are blank corrected. Asterisks designate analyses that do not appear in the figures and were not used in calculations because of small yields and (or) large uncertainties.

ANALYSIS	BLANK1*	BLANK2*	1508	1510*	1551	1553	1555	1556	1558	1560	1562*	1565	1567*	1569
SHOTS	0	0			50	10	45	20	2	6	3	50	15	20
SYMBOL			D	T	S	S	X	Y	Y	Y	Z	X	T	T
35	867.50	864.60	83.20	51.80	46.60	65.00	68.86	-14.87	-15.80	88.78	86.20	150.50	-18.29	-19.05
	54.10	13.10	38.40	37.60	58.48	58.32	58.44	65.81	58.65	58.60	58.55	60.21	58.43	58.23
36	61.52	51.90	327.70	124.20	1392.00	245.50	50.76	664.70	381.80	781.00	292.20	131.90	41.95	1071.00
	12.48	7.26	18.30	18.02	19.57	13.17	16.57	14.12	14.77	13.34	14.56	14.53	14.83	15.81
37	226.30	241.80	46.16	20.05	27.29	29.17	30.32	4.63	3.40	23.40	32.33	58.09	0.47	12.81
	21.80	10.60	12.65	16.86	29.19	28.75	29.01	30.93	30.14	28.71	28.36	27.87	28.67	28.91
38	14.94	13.00	98.84	35.38	350.60	65.15	10.91	201.30	98.17	211.20	66.55	35.88	19.14	313.50
	3.30	1.16	9.74	9.22	5.78	3.96	4.27	3.81	3.92	4.68	5.71	3.69	4.06	6.43
39	2.22	2.90	7.23	12.21	15.33	3.19	3.93	7.90	3.01	9.57	4.98	16.27	1.65	17.79
	0.44	0.91	8.19	8.25	1.76	1.70	1.84	1.86	1.73	1.79	1.81	1.84	1.76	2.03
40	10767.00	9154.00	134900.00	41868.00	0.00	90495.00	14401.00	0.00	131915.00	0.00	89751.00	41161.00	24804.00	0.00
	2651.00	782.80	9346.00	6530.00	0.00	4808.00	3987.00	0.00	5766.00	0.00	5148.00	4812.00	3697.00	0.00
81/84	0.10	0.05	0.02	-0.03	-0.01	-0.03	-0.10	0.03	0.05	-0.03	-0.03	-0.04	-0.04	0.00
	0.03	0.06	0.01	0.03	0.00	0.02	0.12	0.01	0.02	0.02	0.02	0.05	0.12	0.02
82/84	0.23	0.21	0.31	0.26	0.24	0.24	0.17	0.29	0.34	0.25	0.26	0.25	1.04	0.29
	0.02	0.06	0.02	0.01	0.00	0.01	0.03	0.02	0.01	0.01	0.02	0.02	0.24	0.01
83/84	0.16	0.16	0.20	0.20	0.20	0.20	0.20	0.22	0.20	0.23	0.19	0.21	0.18	0.20
	0.06	0.04	0.01	0.02	0.00	0.01	0.03	0.01	0.02	0.00	0.01	0.01	0.03	0.01
84	0.52	0.39	10.28	3.96	54.87	12.19	1.56	23.81	11.99	28.32	8.05	3.33	1.46	41.14
	0.12	0.16	0.42	0.44	0.89	0.28	0.35	0.52	0.54	0.75	0.35	0.25	0.30	0.96
127/132	0.27	0.22	0.09	0.50	0.02	0.02	0.20	0.01	-0.06	0.00	0.11	0.05	0.32	0.01
	0.06	0.12	0.22	0.27	0.03	0.05	0.22	0.04	0.05	0.06	0.11	0.06	0.48	0.02
128/132	0.13	0.15	2.30	1.27	0.90	0.87	0.16	1.24	0.77	0.81	0.88	0.10	2.86	1.31
	0.04	0.07	0.30	0.33	0.03	0.10	0.04	0.05	0.10	0.04	0.09	0.01	1.42	0.03
129/132	1.11	1.05	1.06	1.15	1.00	0.94	0.92	0.93	0.94	0.98	1.02	0.98	1.21	1.00
	0.05	0.08	0.21	0.35	0.01	0.03	0.07	0.03	0.03	0.02	0.05	0.02	0.25	0.02
131/132	0.89	0.93	1.17	1.16	0.75	0.77	0.78	0.82	0.80	0.79	0.82	0.83	0.97	0.80
	0.09	0.12	0.20	0.30	0.01	0.04	0.08	0.03	0.02	0.02	0.04	0.04	0.23	0.02
132	0.48	0.31	0.88	0.54	9.67	2.30	0.77	3.79	2.35	5.42	1.15	2.44	0.21	6.22
	0.07	0.11	0.15	0.13	0.26	0.16	0.17	0.14	0.14	0.21	0.14	0.15	0.12	0.23
136/132	0.33	0.33	0.38	0.66	0.31	0.33	0.34	0.31	0.34	0.32	0.34	0.31	0.25	0.34
	0.05	0.06	0.10	0.18	0.01	0.01	0.04	0.01	0.03	0.01	0.03	0.02	0.09	0.01
K/CL	1.17	1.60	0.35	1.82	0.31	0.30	5.13	0.19	0.20	0.27	0.77	2.63	0.26	0.28
40/36	175.02	176.38	411.66	337.10	0.00	368.62	283.71	0.00	345.51	0.00	307.16	312.06	591.28	0.00
F84	0.37	0.32	1.35	1.37	1.69	2.13	1.32	1.54	1.35	1.56	1.18	1.09	1.50	1.65
F132	8.07	6.25	2.79	4.53	7.25	9.79	15.76	5.96	6.42	7.25	4.13	19.31	5.22	6.06
FBR	0.23	0.05	1.34	0.85	0.99	1.22	-1.60	1.26	2.82	0.99	1.93	0.67	5.02	1.41
FI	128.20	113.97	813.63	830.20	1406.73	1498.09	778.50	901.55	968.88	961.11	1251.63	103.20	808.30	1066.53
CL/36	0.256E+07	0.291E+07	0.529E+07	0.451E+07	0.298E+07	0.360E+07	0.126E+07	0.535E+07	0.322E+07	0.384E+07	0.185E+07	0.391E+07	0.125E+08	0.488E+07

($^{131}Xe_{Te}/Te$):($^{38}Ar_{Cl}/Cl$), and ($^{128}Xe_{I}/I$):($^{82}Kr_{Br}/Br$) from table 1 are within approximately ±10 percent of the values reported by Turner (1965) and Hohenberg and others (1981) for monitors irradiated in the Brookhaven and Missouri reactors, respectively. In combination, the potential errors listed above may be taken to imply that calculated ratios between different noble gases (Ar:Kr:Xe) or halogens (Cl:Br:I) could be systematically in error by as much as 50+ percent. However, these particular uncertainties should have relatively little effect on ratios such as Cl/^{36}Ar, K/Cl, ^{40}Ar/^{36}Ar, ^{129}Xe/^{132}Xe, and ^{83}Kr/^{84}Kr. It is expected that these sources of error will be reduced in future analyses by use of synthetic fluid inclusions as neutron reaction monitors and gas ratio standards. The analytical isotopic fractionation is estimated to be less than 0.5 percent/amu for Xe (B.M. Kennedy, personal commun., 1988).

It is possible that daughter minerals containing some of the analyzed components were not completely degassed when fluids were released from the fluid inclusions. For example, if significant amounts of K, Ca, and Ba were incorporated into carbonate or phyllosilicate daughter minerals after a fluid inclusion was trapped, and if these daughter minerals retained neutron-induced noble gases during an analysis, then the concentrations of these three elements in the original trapped fluid may have been higher than indicated by the analysis. Nevertheless, independent evidence indicates that potassium-bearing daughter minerals did release a significant fraction of neutron-induced ^{39}Ar (see below). Furthermore, significant quantities of the

Mass 37 count rates are not corrected for 37 Ar decay, as they are indistinguishable from Cl blanks. 0.0 cps is reported for mass 40 when the count rate was too high (>150,000 cps) for reliable deadtime correction. Symbols listed in the table and plotted in the figures (see fig. 2) are as follows: D (diamond), vug quartz 578–9v (Drain vein split of Oriental vein, 65 level);Y (inverted triangle), vug quartz 553v (Oriental vein, 500 level); T (triangle), vug quartz 643v (Oriental vein, 1300 level); S (square), massive milky quartz 643m (Oriental vein, 1300 level); C (circle), vug quartz 671 (Gold Crown vein, adit level); X (star), inclusion-free quartz (samples 553v and 671)

ANALYSIS	1571*	1842	1845	1847	1849	1851	1853	1855	1857	1859	1861	1863	1865
SHOTS	5	10	10	10	10	10	20	20	20	12	15	20	10
SYMBOL	C	S	S	S	S	S	C	C	C	T	T	T	T
35	-39.92	27.78	-28.92	12.97	-1.10	8.49	-9.16	27.15	12.30	18.64	5.09	42.15	-10.27
	58.35	54.88	54.47	14.03	14.70	13.60	14.33	13.53	14.77	13.39	13.24	13.67	13.52
36	20.32	750.80	173.30	437.60	220.60	727.00	107.80	1799.00	334.90	138.50	842.90	1406.00	673.90
	14.55	17.58	13.38	11.74	8.83	9.72	8.61	14.41	7.79	9.61	10.26	9.41	12.00
37	-17.50	25.15	-5.44	-1.32	7.73	48.96	-22.99	22.17	0.18	6.16	50.22	37.22	0.67
	28.74	22.23	22.59	12.55	14.43	11.44	14.44	12.09	13.79	15.22	22.17	13.31	16.78
38	3.98	171.00	41.89	103.30	55.39	162.00	27.37	342.60	68.31	38.54	221.80	354.40	190.00
	3.57	4.26	3.67	6.19	1.63	1.99	2.70	6.55	1.48	2.22	5.04	3.25	4.80
39	3.07	12.27	4.97	9.52	3.60	12.26	3.10	15.21	6.10	5.30	13.74	30.23	11.77
	1.76	0.51	0.63	1.60	1.49	2.36	0.98	1.17	0.92	1.41	0.95	1.50	1.57
40	9583.00	0.00	64655.00	0.00	117159.00	0.00	44337.00	0.00	0.00	74221.00	0.00	0.00	0.00
	3944.00	0.00	3012.00	0.00	6515.00	0.00	1736.00	0.00	0.00	2563.00	0.00	0.00	0.00
81/84	0.20	-0.01	0.00	0.02	0.01	0.00	0.00	0.00	0.08	-0.02	-0.02	0.00	0.00
	0.64	0.01	0.01	0.01	0.02	0.01	0.01	0.00	0.03	0.01	0.00	0.00	0.01
82/84	-0.05	0.23	0.26	0.50	0.68	0.25	0.28	0.24	0.26	0.25	0.30	0.29	0.25
	0.24	0.01	0.01	0.03	0.14	0.01	0.03	0.01	0.01	0.02	0.01	0.01	0.01
83/84	0.18	0.22	0.32	0.19	0.24	0.19	0.21	0.20	0.22	0.20	0.14	0.21	0.21
	0.09	0.00	0.03	0.01	0.02	0.01	0.01	0.01	0.02	0.02	0.00	0.01	0.01
84	0.33	20.71	5.68	15.36	7.03	21.79	3.02	22.95	5.74	5.10	30.42	47.44	24.71
	0.29	0.35	0.23	0.67	0.35	0.27	0.20	0.28	0.33	0.17	0.29	0.27	0.69
127/132	0.28	0.01	0.20	0.04	0.02	0.05	0.14	0.16	0.29	0.18	0.04	0.03	0.15
	0.29	0.03	0.08	0.06	0.04	0.03	0.15	0.10	0.15	0.10	0.01	0.02	0.03
128/132	1.11	0.88	1.04	0.79	1.05	0.78	0.61	0.40	1.03	1.11	0.94	0.80	1.42
	0.56	0.03	0.12	0.07	0.14	0.04	0.19	0.05	0.21	0.16	0.07	0.01	0.05
129/132	1.03	0.95	0.98	0.99	1.12	1.03	0.69	1.14	1.01	0.99	0.98	0.91	1.01
	0.18	0.02	0.08	0.02	0.05	0.02	0.13	0.08	0.08	0.05	0.01	0.03	0.02
131/132	1.10	0.86	1.02	0.87	0.88	0.85	0.89	0.95	0.85	0.81	0.85	0.81	0.88
	0.20	0.04	0.10	0.03	0.05	0.03	0.12	0.09	0.10	0.08	0.02	0.02	0.02
132	0.28	2.99	0.88	2.38	1.29	3.51	0.46	0.93	0.52	0.79	5.83	8.48	3.08
	0.21	0.11	0.12	0.15	0.13	0.17	0.12	0.13	0.11	0.14	0.25	0.22	0.17
136/132	0.34	0.32	0.69	0.38	0.33	0.29	0.19	0.37	0.22	0.38	0.32	0.31	0.35
	0.09	0.03	0.15	0.02	0.02	0.02	0.09	0.14	0.05	0.08	0.01	0.01	0.02
K/CL	33.33	0.73	0.95	0.81	0.46	0.86	0.78	5.97	2.03	0.76	0.39	0.60	0.33
40/36	471.60	0.00	373.08	0.00	531.09	0.00	411.29	0.00	0.00	535.89	0.00	0.00	0.00
F84	0.70	1.19	1.41	1.51	1.37	1.29	1.20	0.55	0.74	1.58	1.55	1.45	1.56
F132	14.20	4.16	5.31	5.68	6.09	5.04	4.42	0.54	1.62	5.97	7.23	6.30	4.77
F38	-23.06	0.93	1.76	10.02	11.16	1.74	1.60	8.13	2.83	0.87	2.16	2.02	0.83
FI	26957.07	1253.67	1427.57	1255.15	1408.17	1514.16	539.60	1033.05	1445.95	1023.14	1243.77	1067.02	1015.06
CL/36	0.377E+06	0.185E+07	0.250E+07	0.224E+07	0.294E+07	0.162E+07	0.307E+07	0.118E+06	0.748E+06	0.420E+07	0.350E+07	0.298E+07	0.437E+07

halogens (Cl, Br, and I) are not likely to be incorporated into daughter minerals except in fluid inclusions that have much higher salinities than those described here.

RESULTS

Argon Isotopes

Laser-microprobe analyses of fluid-inclusion-bearing quartz from Alleghany yielded approximately 5 to 20 times as much ^{36}Ar, ^{38}Ar, ^{39}Ar, and ^{40}Ar as did blank runs or analyses of inclusion-free quartz. Ratios among these isotopes indicate that small populations of fluid inclusions contained measurable amounts of Ar, K, and Cl.

Corrections for all interfering Ar isotopes were found to be insignificant in the calculation of K, Cl, and Ca abundances from the quartz analyses (<0.1 percent of the total count rates) when the correction factors listed in Dalrymple and others (1981) were used. This result was not changed when production data from other sources (Saito and Ozima, 1977; G. Curtis, personal commun., 1988) were used in the calculations.

The relatively small amounts of argon released from inclusion-free quartz have $^{40}Ar/^{36}Ar$ ratios indistinguishable from that of air, some of which was probably adsorbed on the sample surfaces or in cracks. Seven analyses of fluid-inclusion-bearing quartz (all available data) yield $^{40}Ar/^{36}Ar$ ratios between 345 and 535. These elevated $^{40}Ar/^{36}Ar$ ratios are associated with ^{38}Ar produced from chlorine during irradiation, but there is not a clear correlation

Table 3. Argon isotope data for hornblende monitor (MMHb–1)

[Data are in counts per second (blank corrected); ^{37}Ar count rates are corrected for decay; $^{40}Ar^*$ = radiogenic (nonatmospheric) ^{40}Ar. σ = 1 standard deviation, based on uncertainties in the blanks and in the extrapolation of count rates to time zero.

$$J=\frac{(e^{\lambda\tau}-1)}{(^{40}Ar^*/^{39}Ar_K)},$$

where $\lambda = 5.543\times10^{-10}$ and $\tau = 518.9$ m.a. (Steiger and Jäger, 1977, Roddick, 1983)]

Isotope or ratio	Analysis				
	1514	1528	1654	1745	1747
^{36}Ar	3.69	15.29	13.42	5.88	2.44
σ	9.85	9.36	5.18	4.49	4.89
^{37}Ar	142.5	622.7	347.6	767.4	406.4
σ	35.9	58.5	109.7	237.6	249.5
^{38}Ar	6.72	19.49	18.20	26.20	14.83
σ	1.02	2.39	2.74	1.75	1.74
^{39}Ar	68.5	207.6	175.0	293.8	193.9
σ	9.7	4.3	2.3	5.0	1.7
^{40}Ar	23,855	72,717	64,421	106,878	64,365
σ	3,709	2,545	3,624	9,352	3,438
$^{40}Ar^*/^{39}Ar_K$	332.9	329.2	346.1	358.3	328.4
$^{40}Ar^*/^{37}Ar_{Ca}$	159.8	109.8	174.2	137.2	156.7
$^{40}Ar^*/^{38}Ar_{Cl}$	4,453	4,929	4,534	4,969	5,406
J ($\times10^6$)	1,002	1,013	964	931	1,016

between the apparent relative abundances of "excess" ^{40}Ar and chlorine (fig. 2).

$^{39}Ar/^{36}Ar$ and $^{38}Ar/^{36}Ar$ ratios for fluid inclusions are shown in figure 3. The relative amounts of neutron-induced $^{39}Ar_K$ and $^{38}Ar_{Cl}$ indicate that most of the fluid inclusions have K/Cl ratios between 0.1 and 1.0, with milky quartz 643m values generally higher (0.6±0.2) than vug quartz 553v and 643v values (0.4±0.2). K/Cl ratios of decrepitated salts analyzed by SEM/EDX also are higher for milky quartz 643m (0.2±0.1) than for vug quartz 553v and 643v (<0.1), but the SEM/EDX values are systematically lower than those indicated by the corresponding argon isotope data. The differences between apparent K/Cl ratios determined by the two techniques may be rationalized if it is assumed that (1) significant amounts of potassium are present in daughter minerals, (2) neutron-induced $^{39}Ar_K$ produced in the daughter minerals was released with laser decrepitated gases, and (3) potassium in daughter minerals was not released with thermally decrepitated salts. ^{39}Ar could have been released to the fluid during irradiation by recoil from fine-grained fibrous daughter minerals, or it could have been released by laser heating during the analysis. The average K/Cl ratio of the vug quartz fluids determined from the argon isotopes (0.4) is approximately consistent with an independent estimate of the CO_2-bearing hydrothermal fluid composition in which K/Na ≈0.1 (calculated from mica-feldspar phase equilibria in altered vein wall rocks, Böhlke, in press), if Na/Cl ≈4.0 (within the range of SEM/EDX analyses of decrepitated salts).

The fact that analyses of inclusion-free quartz and other analyses having low $^{38}Ar/^{36}Ar$ ratios (that is, low Cl) yield relatively high K/Cl ratios (fig. 3) indicates that there may be a small amount of potassium in the quartz that is not in fluid inclusions. It is not known whether this excess potassium resides within the quartz matrix, possibly as minute solid inclusions of mica, or represents some surface contamination. Although the uncertainties are large, it appears that the analyses of inclusion-free quartz also may contain a small chlorine component, either from surface contamination or from small fluid inclusions in adjacent areas.

The yields of ^{37}Ar were not significantly different from the blank values; thus, calcium was not present in measurable concentrations. From the data in tables 1 and 2 it is estimated that the Ca/Cl ratio in the dissolved component of the fluid inclusions is less than approximately 3. SEM/EDX analyses of decrepitated salts indicate that the Ca/Cl ratio may be as small as 0.01 or less; however, it is possible that both techniques failed to detect small amounts of calcium that may be present in carbonate daughter minerals.

Krypton and Xenon Isotopes

Fluid-inclusion-bearing quartz yielded approximately 5 to 20 times as much krypton and xenon as inclusion-free quartz. With a few anomalous exceptions, all analyses of quartz, with or without fluid inclusions, yielded $^{83}Kr/^{84}Kr$, $^{129}Xe/^{132}Xe$, and $^{136}Xe/^{132}Xe$ ratios statistically indistinguishable from those of air, consistent with the interpretation that U, Se, Te, and Ba were not present in amounts sufficient to produce detectable noble gas isotopes during the irradiation. From the data in tables 1 and 2, it is estimated that U/Cl≤0.001, Se/Cl≤0.2, Te/Cl≤0.01, and Ba/Cl≤0.07 in the fluid phases of the inclusions. There is no clear evidence of natural "excess" xenon or krypton isotopes that, if present, might have been acquired by the hydrothermal fluids during reactions with uranium-bearing rocks before the fluids were trapped or might have come from isotopically anomalous (mantle?) source regions.

In contrast, almost all fluid-inclusion analyses yielded $^{82}Kr/^{84}Kr$ and $^{128}Xe/^{132}Xe$ ratios significantly greater than those of air. The data, summarized in figure 4, indicate that measurable amounts of ^{82}Kr and ^{128}Xe were produced by neutron reactions with bromine and iodine and that there are significant variations in the I/Br ratios of the sampled fluids.

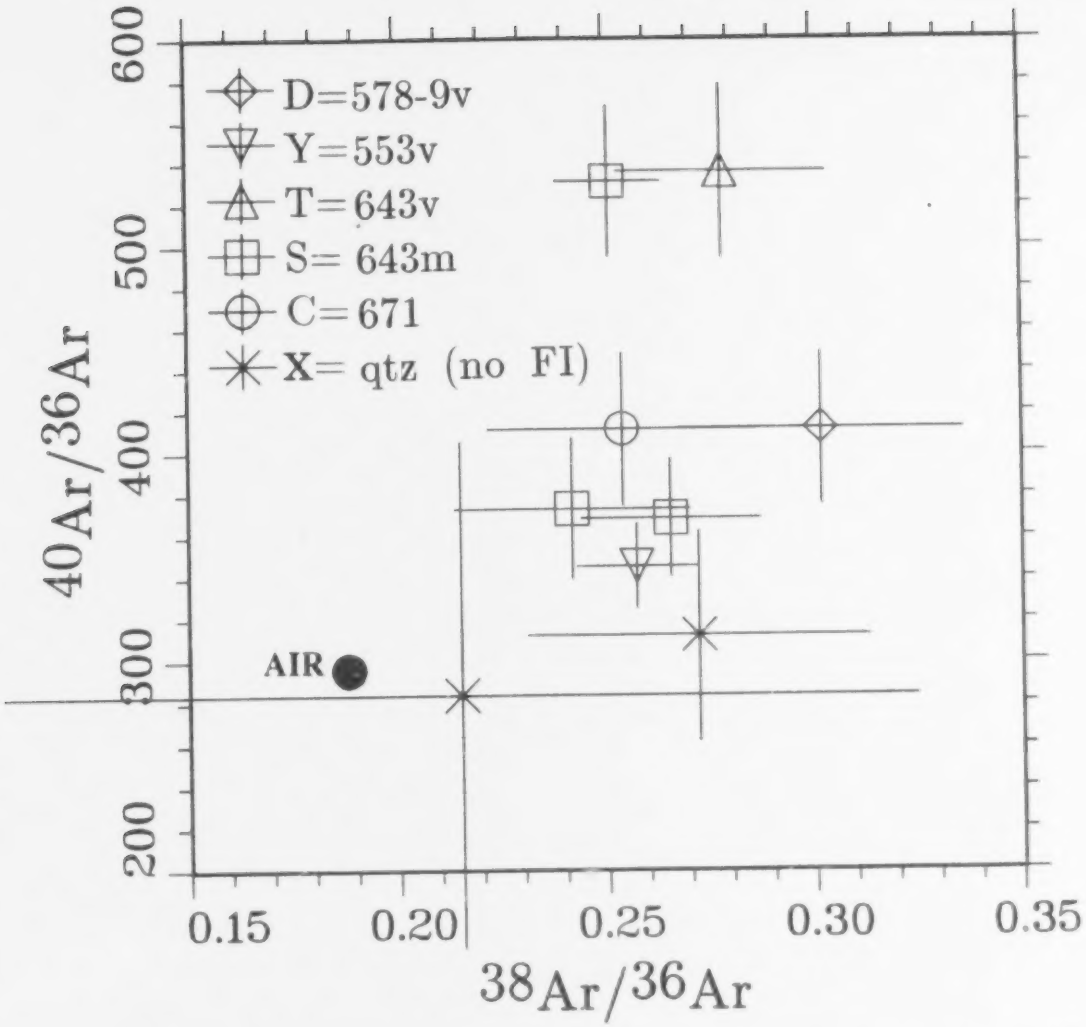

Figure 2. $^{40}Ar/^{36}Ar$ versus $^{38}Ar/^{36}Ar$ for fluid-inclusion-bearing and fluid-inclusion-free quartz from Alleghany, Calif. Each data point represents one laser-microprobe analysis. The error bars represent 1 standard deviation in the blanks and in the extrapolated count rates at time zero. The symbols for this and subsequent figures are as follows: D (diamond), vug quartz 578–9v (Drain vein split of Oriental vein, 65 level); Y (inverted triangle), vug quartz 553v (Oriental vein, 500 level); T (triangle), vug quartz 643v (Oriental vein, 1300 level); S (square), massive milky quartz 643 m (Oriental vein, 1300 level); C (circle), vug quartz 671 (Gold Crown vein, adit level); X (star), inclusion-free (no FI) quartz (samples 553v and 671). Fluid-inclusion-bearing quartz analyses yield $^{40}Ar/^{36}Ar$ ratios greater than that of air, but there is no apparent correlation between $^{40}Ar/^{36}Ar$ and $^{38}Ar_{Cl}$. Inclusion-free quartz analyses yield $^{40}Ar/^{36}Ar$ ratios indistinguishable from that of air, possibly from small amounts of adsorbed gas.

Absolute Abundances

From microthermometric cooling and heating analyses, the majority of fluid inclusions in vug quartz 553v and 643v are estimated to contain between 0.05 and 0.2 *m* Cl and to average approximately 0.1 *m* Cl (~3,600 ppm Cl by weight). This average chlorine concentration may be used to estimate the quantities of fluid that were sampled and the absolute concentrations of the other analyzed components (all calculations based on the average chlorine value are estimated to be uncertain by a factor of 2). Gases extracted by six laser shots aimed at a group of fluid inclusions in sample 553v (Analysis 1560) indicate that 5.4×10^{13} atoms (9.0×10^{-11} mol) of Cl were present in the sampled fluid.

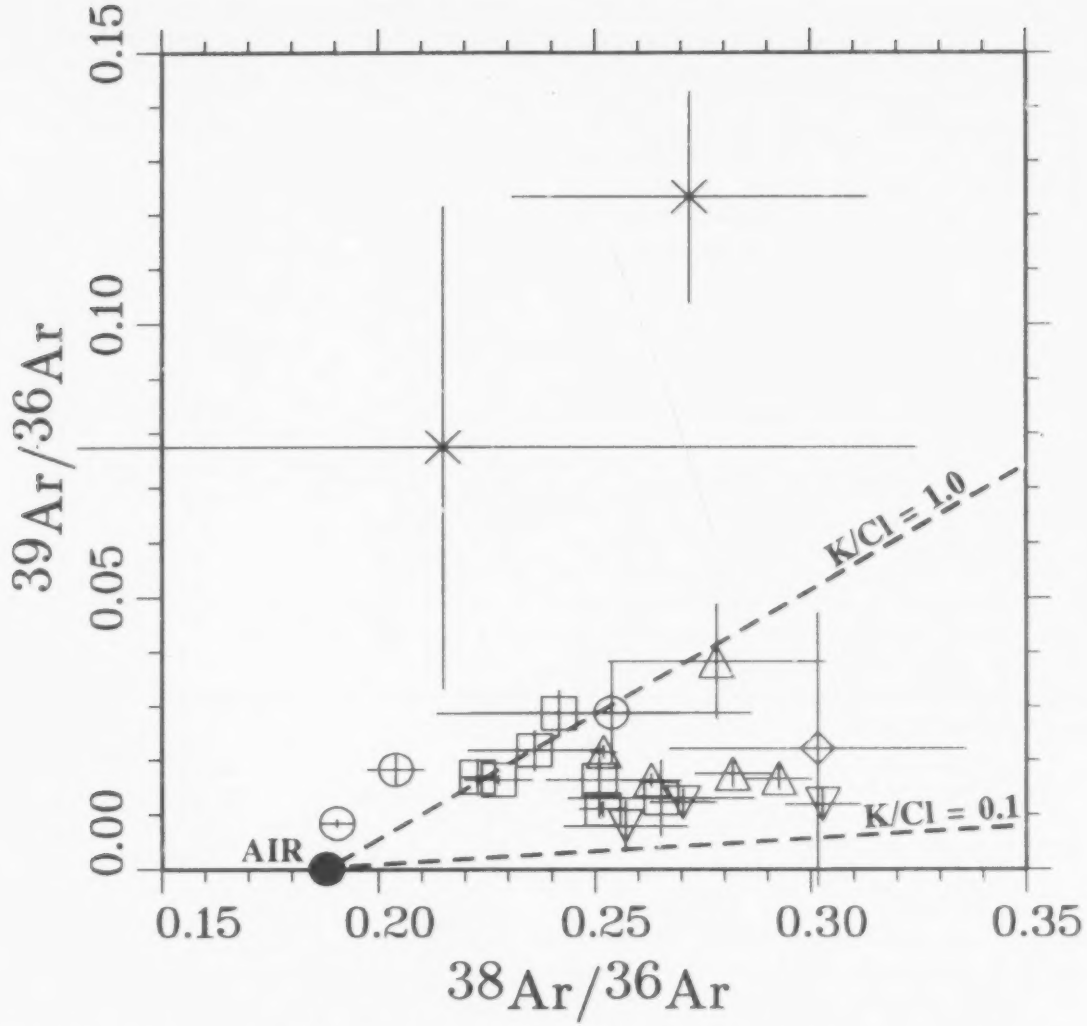

Figure 3. $^{37}Ar/^{36}Ar$ versus $^{38}Ar/^{36}Ar$. See figure 2 for key to symbols. The calculated K/Cl ratios are based on the relative production rates of $^{39}Ar_K$ and $^{38}Ar_{Cl}$ listed in table 1. The apparent K/Cl ratios generally are smaller in fluid-inclusion-bearing vug quartz 553v and 643v and are larger in inclusion-free quartz and other samples with relatively low $^{38}Ar/^{36}Ar$. A small amount of potassium not in fluid inclusions may be present on the sample surfaces or within the quartz.

This chlorine could have been dissolved in 0.9×10^{-9} L of water, if the water contained 0.1 *m* Cl. This quantity of water is equivalent to the contents of 1 cubic inclusion measuring approximately 97 μm on a side, or 10 cubic inclusions measuring 45 μm on a side. This is not unreasonable for the microfractured volume sampled during the run, although the amount of fluid actually sampled is not precisely known. In contrast, 45 laser shots into an inclusion-free area of the same quartz chip (Analysis 1555) yielded less than one-tenth as much ^{38}Ar and could not have sampled more than 2×10^{-11} L of water with the same chlorine concentration.

From the data in tables 1 and 2, the average Oriental mine vug quartz fluid from 553v and 643v (eight analyses), assuming 0.1 *m* Cl (~3,600 ppm Cl), is found to contain in the order of 2.3×10^{-4} *m* Br (~19 ppm Br) and 0.9×10^{-4} *m* I (~11 ppm I). The Cl and Br concentrations are roughly one-fifth those of seawater, while the I concentration is about 200 times that of seawater. The same fluid apparently contains ~1,400 ppm K, ≤9,000 ppm Ca, ≤1,200 ppm Se, ≤1,000 ppm Ba, ≤140 ppm Te, and ≤40 ppm U.

The average $Cl/^{36}Ar$ ratio of this fluid (4.0×10^{6}) corresponds to 2.5×10^{-8} *m* ^{36}Ar. Air-saturated water contains approximately 4.6×10^{-8} *m* ^{36}Ar at 20 °C (calcu-

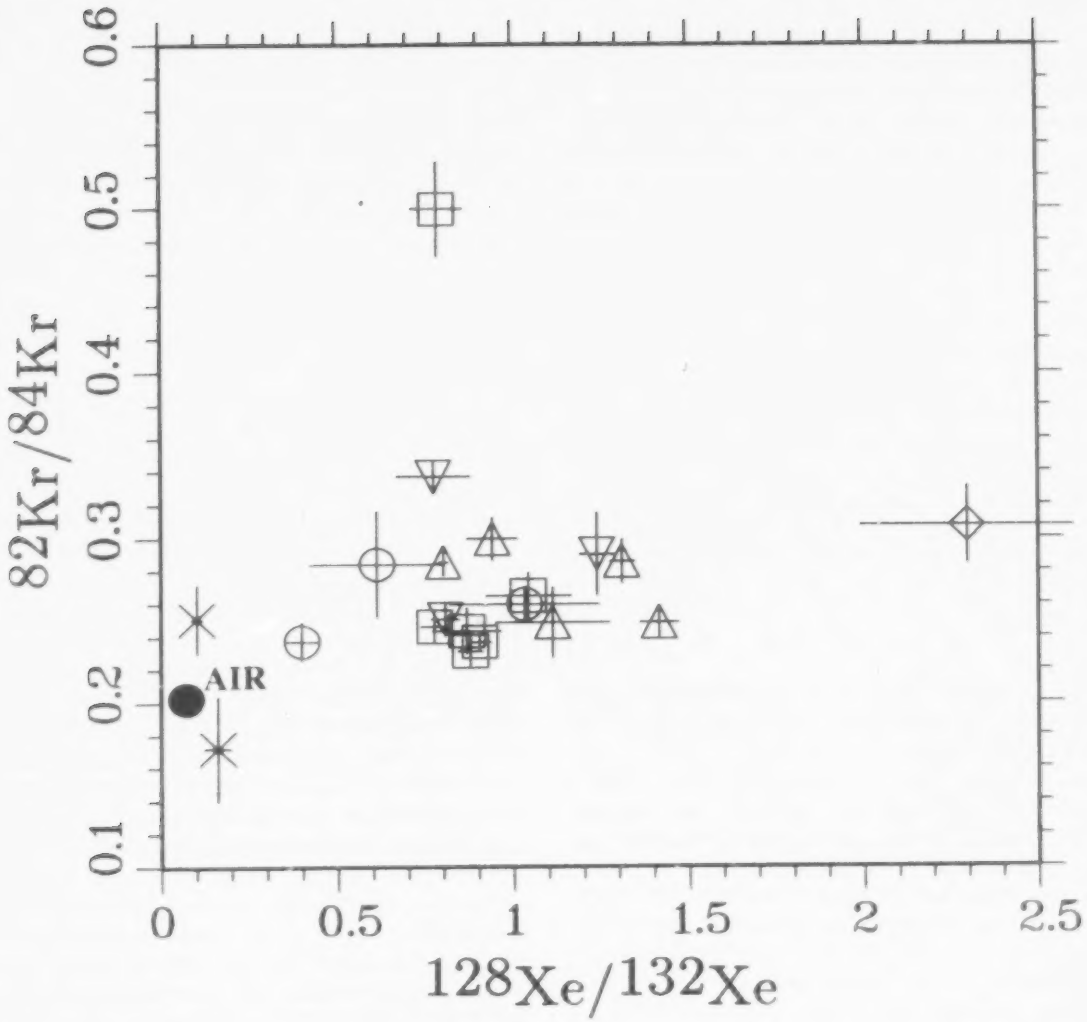

Figure 4. $^{82}Kr/^{84}Kr$ versus $^{128}Xe/^{132}Xe$. See figure 2 for key to symbols. Fluid-inclusion-bearing quartz contains significant amounts of neutron-induced $^{82}Kr_{Br}$ and $^{126}Xe_{I}$, whereas inclusion-free quartz does not.

lated from data in Shock and others, in press). The presence of 0.1 *m* NaCl in the recharging water would lower the argon solubility by less than 5 percent (Smith and Kennedy, 1983). Because of the uncertainties and possible real variability in the chlorine contents of these fluid inclusions, it may be concluded that the ^{36}Ar concentrations are equal to or somewhat less than air-saturated water but probably not substantially greater (that is, approximately 25 to 100 percent of air-saturated water concentrations). The same conclusion holds approximately for the absolute concentrations of ^{84}Kr and ^{132}Xe, although the apparent $^{132}Xe/^{36}Ar$ ratios are somewhat higher than expected for air-saturated water (see below).

DISCUSSION

Contamination

There are numerous potential sources of contamination, including gases adsorbed on the quartz chips, water or gases trapped in cracks during sample preparation, and fingerprints. Nevertheless, several observations indicate that the bulk of both natural and neutron-induced noble gases were sampled mainly from fluid inclusions, at least in vug quartz samples 578–9v, 553v, and 643v from the Oriental mine.

1. Yields of both natural and neutron-induced noble-gas isotopes from laser shots into fluid inclusions were much larger than blanks and much larger than yields from laser shots into inclusion-free areas of the same quartz chips. This is true even though the inclusion-free areas were hit with the maximum numbers of laser shots (see table 2).
2. Inclusion-bearing quartz yielded significantly smaller $^{132}Xe/^{36}Ar$, $^{132}Xe/Cl$, $^{132}Xe/I$, and K/Cl, and larger I/Cl and Br/Cl ratios than inclusion-free quartz. These differences indicate that a source of gas compositionally distinct from adsorbed gas or quartz matrix gas was present where fluid inclusions were present.
3. Halogen ratios of fluid-inclusion-bearing quartz ($Br/Cl = 1–3 \times 10^{-3}$, $I/Cl = 7–13 \times 10^{-4}$) are distinct from those of human sweat ($Br/Cl = 1 \times 10^{-4}$, $I/Cl = 2 \times 10^{-6}$) (ICRP, 1975).
4. Total chlorine yields are reasonable compared to rough estimates of sampled inclusion volumes and salinities.
5. The available $^{40}Ar/^{36}Ar$ ratios from the fluid-inclusion-bearing quartz are greater than those of air or inclusion-free quartz. Thus, argon from inclusion-bearing quartz was not the same as argon in adsorbed air, trapped air, or trapped laboratory water.
6. Calculated argon concentrations are less than or equal to experimentally determined 1-bar air saturation values and are well within the range encountered in thermal ground waters. Also, the majority of $Cl/^{36}Ar$, $^{84}Kr/Cl$, and $^{132}Xe/Cl$ ratios are fairly uniform (most are within a factor of 2 to 3). These observations indicate that large proportions of trapped contaminant air were not sampled in most cases. Rather, it is concluded that the bulk of the natural noble gases from inclusion-bearing vug quartz, including ^{36}Ar, were present as dissolved components of aqueous fluid inclusions of relatively uniform compositions.

The latter criteria (in 6) are not completely satisfied for milky quartz 643m from the Oriental mine or for vug quartz 671 from the Gold Crown mine. Analyses of these samples yield more variable, and in some cases much smaller, $Cl/^{36}Ar$ ratios. Some of these data indicate that an anomalous gas-rich component is present in addition to the liquid-rich fluid inclusion component.

Dissolved Atmospheric Gases

The measured isotopic ratios of krypton and xenon and the calculated ^{36}Ar concentrations for fluid inclusions in vug quartz 578–9v, 553v, and 643v from the Oriental mine appear to be consistent with the interpretation that the sampled fluids originated at the Earth's surface. The $^{40}Ar/^{36}Ar$ ratios of the Alleghany fluid inclusions, though higher than atmospheric, are similar to those of modern meteoric hydrothermal waters. In an earlier study, Kelley and others (1986) concluded that meteoric hydrothermal fluids trapped in some Paleozoic quartz veins approximately retained their initial low-temperature air-saturated-water argon concentrations while participating in 400 °C reactions at depth and acquiring moderate amounts of excess ^{40}Ar. Similar Ar, Kr, and Xe isotopic ratios might be acquired by nonmeteoric fluids from rocks that adsorbed atmospheric noble gases previously at low temperature, or possibly from other (mantle?) sources, but it would be fortuitous if the absolute concentrations of desorbed or deep-source gases were near air-saturated water values.

Most of the sampled fluid inclusions contained significantly less than the maximum observed CO_2 concentration observed at Alleghany, and it is possible that the noble-gas data do not accurately represent the CO_2-rich endmember fluids. Nevertheless, all of the fluid inclusions observed in the vug quartz samples clearly were trapped at high temperatures and pressures, they appear to have roughly uniform salinities and K/Cl ratios, and a large proportion of them either contain liquid CO_2 at room temperature or form clathrate on cooling. Thus, although they may represent mixtures of CO_2-rich and CO_2-poor fluids, they probably were trapped at or near the time of vein formation and wall-rock metasomatism. If the analyzed fluids were indeed largely meteoric in origin, there remain at least two possible explanations for the origin of the veins: (1) if the noble gases in the analyzed fluids are essentially the same as those in the CO_2-rich endmember, then it is possible that meteoric water circulated to depths below which the veins were formed, acquired CO_2 from prograde devolatilization reactions or other (mantle?) sources, and then formed the veins while ascending; (2) if the noble gases in the analyzed fluids are somewhat different from those in the CO_2-rich endmember, then it is possible that meteoric water circulated only as deep as the veins were formed. In the latter case, the veins could represent vertically extensive zones of mixing between descending surface waters and ascending magmatic or metamorphic fluids. In either case, the noble gas data permit the interpretation that surface waters reached depths of at least 5 to 10 km in fault zones within the Sierran forearc metamorphic terrane. This interpretation is consistent with O and H isotopic evidence for deep meteoric water circulation elsewhere in the Cordillera of western North America (Criss and Taylor, 1983; Nesbitt and others, 1986; Murowchick and others, 1987), whereas O and H isotopic data from the Sierran veins themselves are not conclusive (Böhlke and Kistler, 1986; Böhlke and others, 1988). The Alleghany fluids do not resemble seawater or trapped marine pore fluids, because most of the fluid inclusions appear to be significantly less saline than seawater.

Table 4. Argon isotopic data for hydrothermal sericite

[Data are in counts per second (blank corrected). ^{37}Ar count rates are not corrected for decay, as they are indistinguishable from the blank values. $^{40}Ar^*$, radiogenic (nonatmospheric) ^{40}Ar. Ages were calculated from equations summarized in Dalrymple and others (1981) and decay constants from Steiger and Jäger (1977). σ = standard deviation based on uncertainties in blanks and in extrapolation of count rate to time zero]

Isotope	Analysis		
	1534	1536	1538
^{36}Ar	−6.96	14.45	5.66
σ	9.08	9.26	8.49
^{37}Ar	14.0	−5.1	7.7
σ	19.4	22.2	18.3
^{38}Ar	1.06	8.69	5.91
σ	2.39	2.37	2.33
^{39}Ar	191.1	438.5	494.8
σ	3.7	4.2	6.7
^{40}Ar	11,054	30,674	33,738
σ	1,747	1,858	1,833
$^{40}Ar^*/^{39}Ar_K$	68.6	60.2	64.8
Age (m.y.)	118.0	104.0	111.7

Natural Radiogenic Gases

$^{40}Ar/^{36}Ar$ ratios between 345 and 535 (fig. 2) indicate that the fluid inclusions contain significant amounts of nonatmospheric ^{40}Ar that was (1) present in the fluids when they were trapped and (or) (2) produced by potassium decay within the fluid inclusions since they were trapped. Laser-microprobe argon isotopic analyses of hydrothermal sericites in altered serpentinite adjacent to the Oriental vein (table 4) yield an average $^{40}Ar/^{39}Ar$ age of 111 million years, indistinguishable from Rb/Sr and K/Ar ages of sericites from other veins in the Alleghany district (Böhlke and Kistler, 1986). The dated sericites are believed to have formed during wall-rock carbonatization reactions in equilibrium with fluids with approximately 10 mole percent CO_2 (Böhlke, in press), similar to the highest concentrations observed in some of the vug quartz fluid inclusions.

A ^{40}Ar–^{39}Ar isochron for the approximate age of the veins (110 Ma) is shown in figure 5. The fluid inclusion data (fig. 5) plot well above the 110 Ma isochron and indicate that unsupported "excess" radiogenic ^{40}Ar is present. In the 110 million years since the formation of the veins, production of ^{40}Ar from decay of potassium within the inclusions will have increased the $^{40}Ar/^{36}Ar$ ratios by less than 1 percent. The measured ratios therefore are indistinguishable from the initial ratios at the time of trapping, which appear to have been somewhat variable. If one component of the dissolved gas in each fluid sample had an atmospheric $^{40}Ar/^{36}Ar$ ratio and contained all of the ^{36}Ar, then the concentrations of excess ^{40}Ar were approximately $2–8\times10^{-6}$ *m* (assuming 0.1 *m* Cl), or approximately 15 to 45 percent of the total ^{40}Ar concentrations.

The $^{40}Ar/^{36}Ar$ ratios of the Alleghany hydrothermal fluids at the time of trapping were higher than those of many low-temperature ground waters and hot springs, which commonly are between 295 and 320 (Mazor, 1976; Mazor and Truesdell, 1981; Mazor and others, 1988), but similar to those measured in some hot springs and well waters from the Yellowstone, Wyoming (~295–650), and Valles, New Mexico (~320–665), geothermal areas (Kennedy and others, 1985; Smith and Kennedy, 1985). These values also are similar to those determined by Kelley and others (1986) for meteoric fluids trapped in granite-hosted quartz veins associated with tungsten mineralization at Carrock Fell (≥715) and Hemerdon Ball (≥385), England. Thus, the Alleghany $^{40}Ar/^{36}Ar$ data are consistent with the hypothesis that the analyzed quartz trapped high-temperature meteoric fluids that circulated at depth. The measured $^{40}Ar/^{36}Ar$ ratios are not as high as those reported or implied for some Paleozoic basin brines (up to 2,100, Zaikowski and others, 1987), for fluid inclusions in a "metamorphic" quartz vein ~7,500?, Rama and others, 1965), and for fluid inclusions in igneous pegmatites (3,000–30,000?, Naydenov and others, 1972).

Because several Kr and Xe isotopes are produced by natural fission of ^{238}U, it is likely that some "excess" quantities of radiogenic Kr and Xe are present in subsurface waters that have "excess" radiogenic ^{40}Ar produced by natural decay of ^{40}K. In the same way that ratios of excess $^{40}Ar/^{4}He$ in basin brines reflect the K/U ratios of aquifer rocks, so might the ratios of excess $^{40}Ar/^{136}Xe$. To test this possibility, and to check the consistency of the argon and xenon isotope data, we have plotted $^{40}Ar/^{36}Ar$ versus $^{136}Xe/^{129}Xe$ in figure 6. The calculated slopes in figure 6 are based on the assumption that the elemental and isotopic ratios were fixed initially by equilibrium with air between 0 and 25 °C. These slopes indicate that for $K/U\geq10^4$ (a value typical of rocks in the Earth's crust, Zartman and others, 1961), little change may be expected in $^{136}Xe/^{129}Xe$ because of uranium fission for the range of $^{40}Ar/^{36}Ar$ ratios observed in the Alleghany quartz. The Alleghany quartz data do not indicate a correlation between excess ^{40}Ar and excess ^{136}Xe, as almost all analyses yield $^{136}Xe/^{129}Xe$ ratios indistinguishable from that of air. Natural excess radiogenic ^{136}Xe may be detected in meteoric fluids with higher $^{40}Ar/^{36}Ar$ ratios or in other fluid types with lower $^{129}Xe/^{36}Ar$ ratios. The relatively high apparent $^{136}Xe/^{36}Ar$ ratio of one analysis in figure 6 could indicate that some neutron-induced gas from uranium was sampled, but the significance of this datum in questionable, as it is clearly anomalous (see table 2).

Halogen Ratios

Halogen data for the Alleghany fluid inclusions are summarized in figure 7 and are compared to other data in

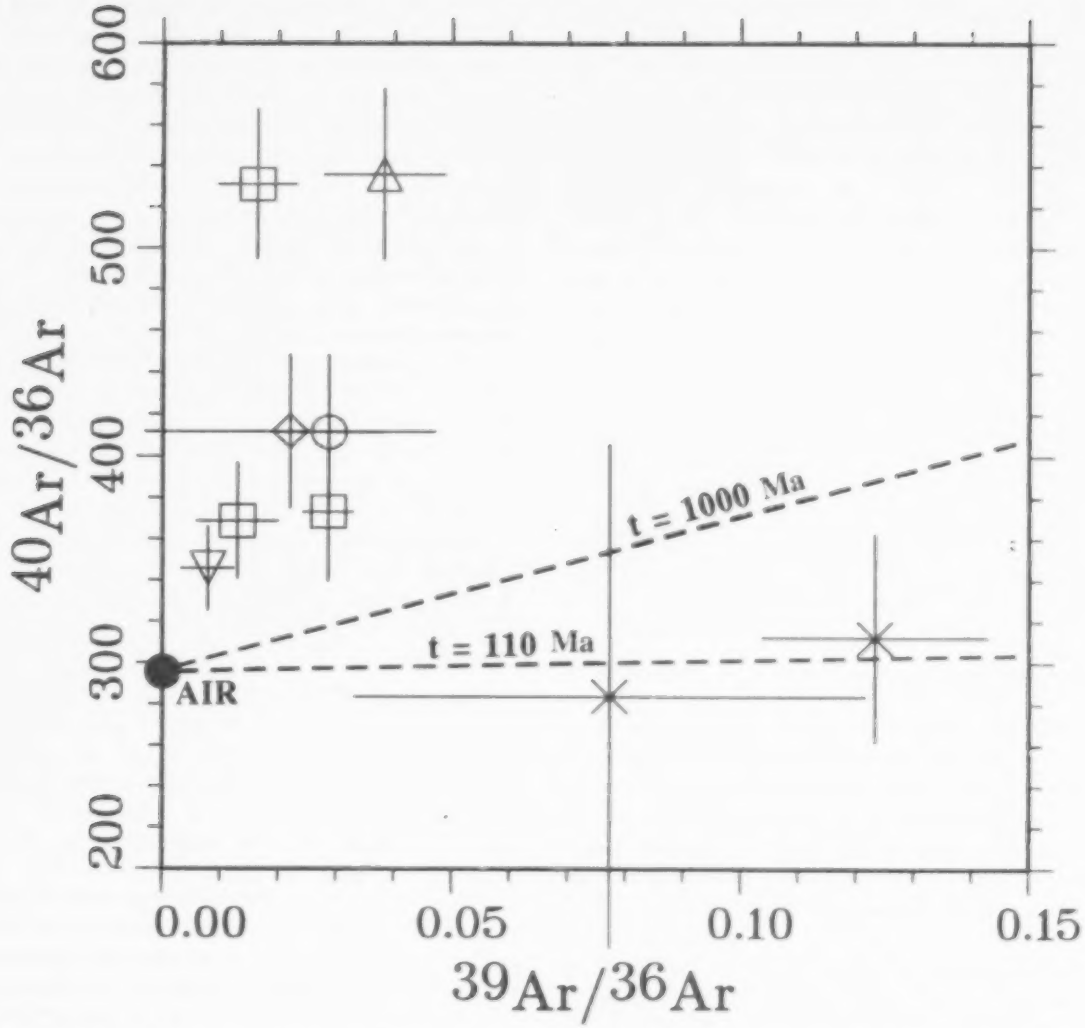

Figure 5. ^{40}Ar–^{39}Ar isochron plot with fluid inclusion data. See figure 2 for key to symbols. ^{40}Ar–^{39}Ar isochrons are based on the production rate of $^{39}Ar_K$ listed in table 1 (corresponding to $J = 9.85\times10^{-4}$). The approximate age of the veins (and likely maximum (t) time since trapping of the fluid inclusions) is 110 Ma. Fluid inclusions contain ^{40}Ar in excess of that which could have been produced by in situ decay of potassium since entrapment, whereas inclusion-free quartz does not.

figure 8. The fractionation factor F_1^{sw} is a convenient expression of halogen ratios relative to the composition of the largest and most uniform near-surface reservoir (seawater):

$$F_1^{sw} = \frac{(i/Cl)_{sample}}{(i/Cl)_{sw}} \qquad (2)$$

where $(Br/Cl)_{sw} = 1.52\times10^{-3}$ and $(I/Cl)_{sw} = 8.38\times10^{-7}$ (Sverdrup and others, 1942; Fuge and Johnson, 1986).

There is a small but systematic difference between F_1^{sw} values in massive milky quartz 643m (1,400±100) and those in vug quartz 553v and 643v (1,030±100). The uncertainties in the calculated Br/Cl ratios are relatively large, and there are no distinct differences in F_{Br}^{sw} among the different quartz samples. Two analyses of milky quartz 643m yield anomalously high F_{Br}^{sw} values, but the significance of these data is uncertain.

Most of the analyzed Alleghany fluid inclusions have chlorine concentrations significantly less than that of seawater, and F_{Br}^{sw} values near those of seawater and most other low-salinity fluids, including geothermal waters in volcanic

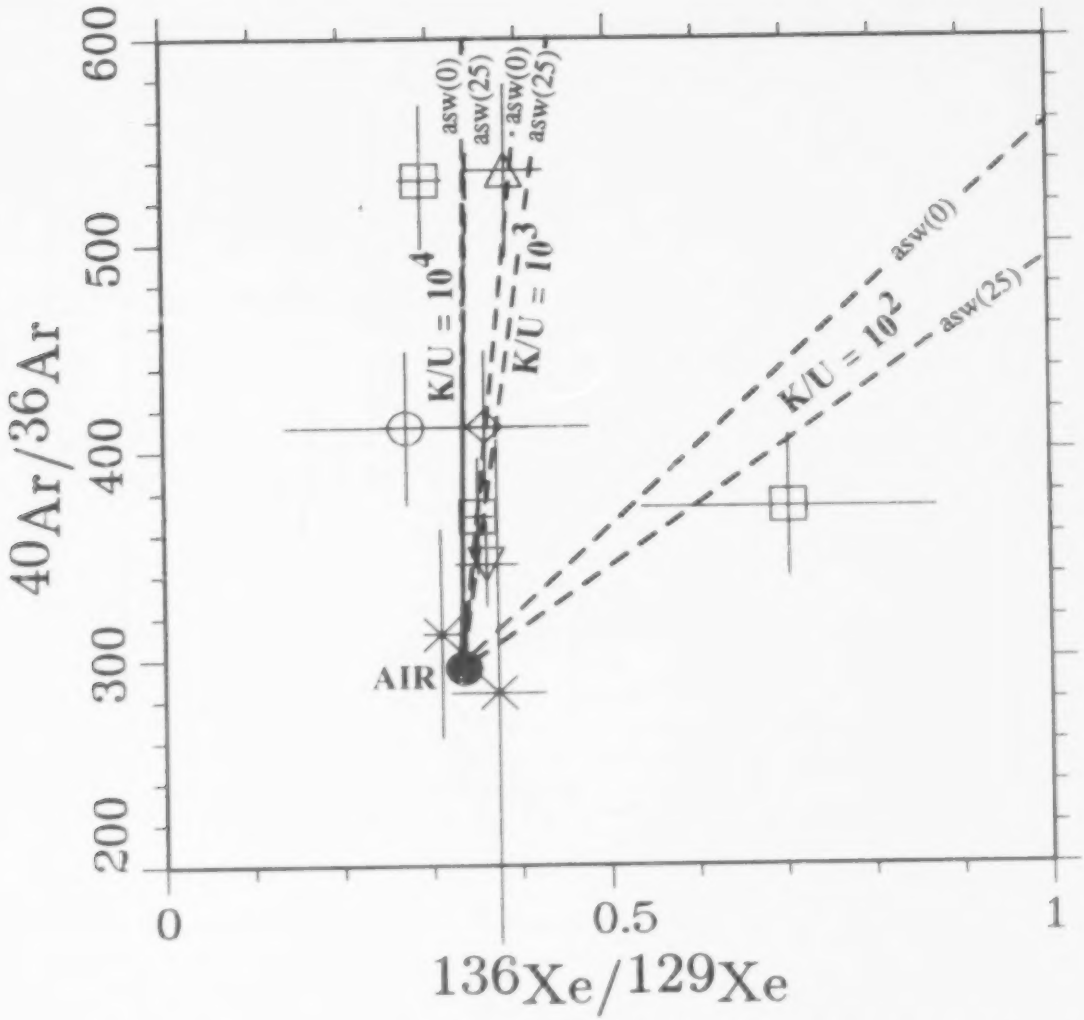

Figure 6. Relative abundances of radiogenic ^{40}Ar and ^{136}Xe. See figure 2 for key to symbols. Natural production curves are based on data from Ozima and Podosek (1983) and the assumption that all isotopes in the fluid initially were in equilibrium with air (asw(0) = air-saturated water at 0 °C). Most crustal rocks have K/U between 10^{-3} and 10^{-5} (for example, Zartman and others, 1961). The general lack of evidence for excess radiogenic ^{136}Xe is consistent with the relatively low amounts of excess radiogenic ^{40}Ar in the Alleghany quartz fluids.

terranes (fig. 8). The hydrothermal fluids trapped in these inclusions do not resemble marine pore fluids and apparently did not obtain strongly fractionated salts from either residual (high Br/Cl) or neoformed (low Br/Cl) evaporite brines (fig. 8; Holser, 1979). These results are consistent with the lack of evidence for evaporite deposits within the Sierra Nevada metamorphic belt and may be characteristic of low-salinity fluids responsible for gold mineralization. Absence of marine and evaporite salt sources may be critical for determining the chemical transport properties of hydrothermal fluids responsible for gold ores deficient in base metals (see Hedenquist and Henley, 1985; Henley, 1985). The bulk of the Alleghany data contrast with the results of several previous analyses of hydrothermal fluid inclusions, which yielded generally higher Br/Cl ratios (Wickman and Khattab, 1972; Kozlowski and Karwowski, 1974; Luckscheiter and Parekh, 1979; Behr and Gerler, 1987). At least a few of the earlier analyses pertained to saline (residual?) brine inclusions in minerals associated with base-metal (Pb, Zn) deposits (Behr and Gerler, 1987).

The Alleghany fluids have I/Cl ratios approximately 1,000 times that of seawater, significantly higher than most

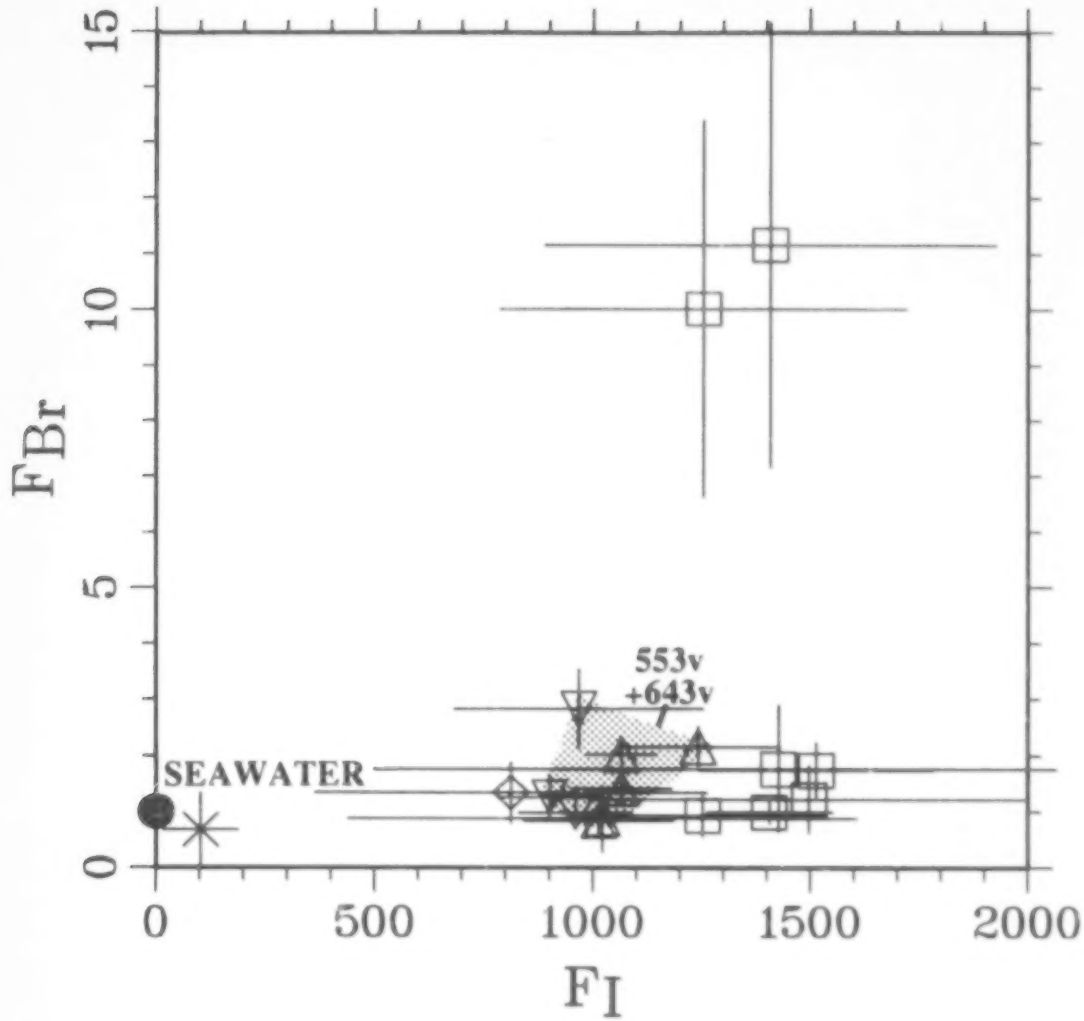

Figure 7. Halogen ratios (F^{SW}_{Br} versus F^{SW}_{I}) for the Alleghany fluid inclusions. See figure 2 for key to symbols. F^{SW}_{Br} and F^{SW}_{I} are defined by equation 2. Data for 671 are not shown because they have large uncertainties. Fluid-inclusion-bearing quartz data are distinct from inclusion-free quartz data and sweat (for example, fingerprints) and indicate that $(Br/Cl)_{FI} \geq (Br/Cl)_{SW}$ and $(I/Cl)_{FI} >> (I/Cl)_{SW}$.

saline brines and geothermal waters but similar to some low-salinity oil-field brines and to thermal springs associated with mercury deposits in the California Coast Ranges (fig. 8). High iodine contents in some natural subsurface waters may result from reactions with iodine-rich marine organic matter in sedimentary rocks (White, 1957; Collins and Egleson, 1967). The mechanism and timing of iodine transfer from the organic components of sediments to pore waters is not well understood. Nevertheless, the high I/Cl ratios of the Alleghany fluid inclusions may indicate that the hydrothermal fluids responsible for vein mineralization extracted iodine from organic-rich marine sediments or metasedimentary rocks.

Noble-Gas Ratios

Ratios of natural noble-gas isotopes for the Alleghany fluid inclusions are summarized in figure 9 and are compared to other data in figure 10. The noble-gas fractionation factor F^{air}_{i} (Smith and Kennedy, 1983) is analogous to that used to describe halogen ratios, but with air as the normalizing reservoir:

$$F^{air}_{i} = \frac{(i/^{36}Ar)_{sample}}{(i/^{36}Ar)_{air}} \quad (3)$$

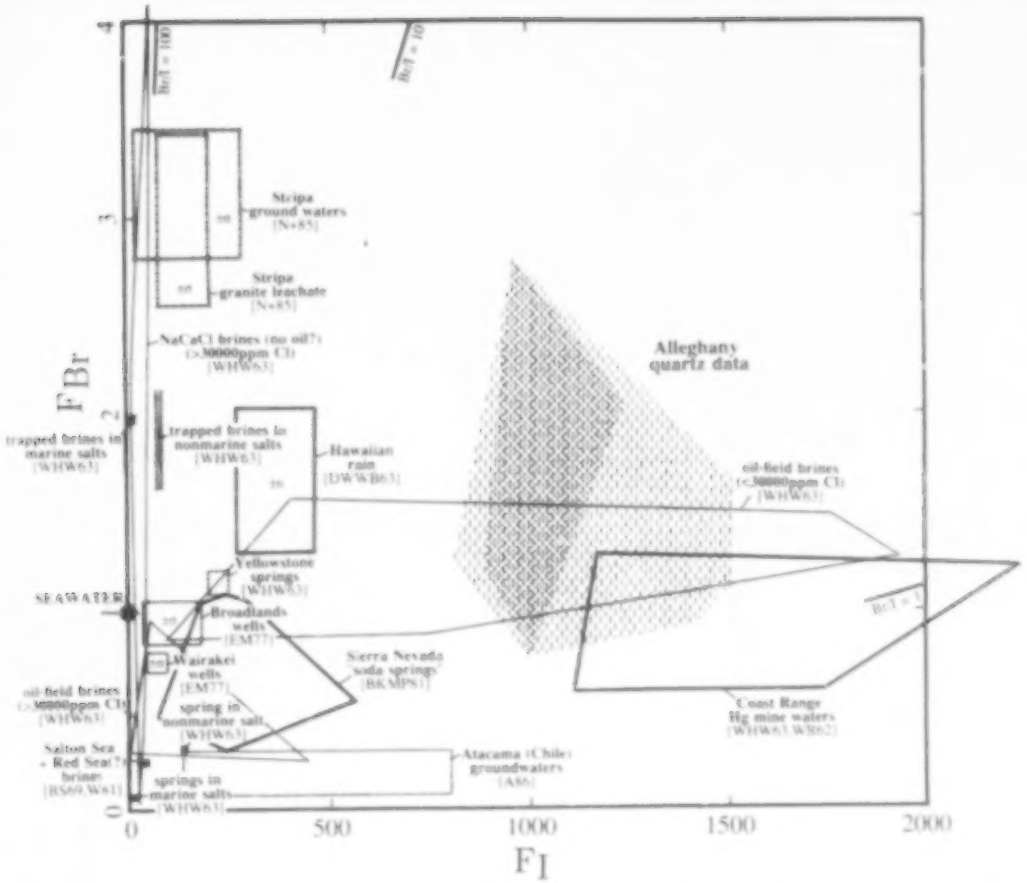

Figure 8. Halogen ratios (F^{sw}_{Br} versus F^{sw}_{I}) for Alleghany quartz compared to other data for natural waters. Sources of data: A86, C.N. Alpers (personal commun., 1987); BKMP81, Barnes and others (1981); BS69, Brewer and Spencer (1969); DWWB63, Duce and others (1963); EM77, Ellis and Mahon (1977); N+85, Nordstrom and others (1985); W81, White (1981); WR62, White and Roberson (1962); WHW63, White and others (1963). $\pm\sigma$ represents ± 1 standard deviation for a group of analyses. The area shaded with vertical lines encloses all of the data points shown in figure 7, except for two analyses with high Br/Cl; the area shaded with dots corresponds to vug quartz 553v and 643v. The Alleghany quartz data resemble those of other low-salinity fluids associated with organic-rich marine sedimentary rocks.

where $(^{84}Kr/^{36}Ar)_{air} = 2.068\times10^{-2}$ and $(^{132}Xe/^{36}Ar)_{air} = 7.446\times10^{-4}$ (Ozima and Podosek, 1983).

The relative abundances of Xe, Kr, and Ar have distinctive patterns in the different sample types: (1) analyses of fluid inclusions in Oriental mine vug quartz 553v and 643v cluster near average values of F^{air}_{84} (1.53±.09) and F^{air}_{132} (6.25±.74); (2) analyses of Oriental mine milky quartz 643m define a linear array approximately centered on the vug quartz cluster; and (3) analyses of Gold Crown mine quartz 671 define an apparent extension of the 643m array to lower values of F^{air}_{84} and F^{air}_{132} (both to less than 1.0).

Most of the Oriental mine fluid inclusions have apparent F^{air}_{84} values between those of air and low-temperature air-saturated waters (fig. 9). The roughly similar F^{air}_{84} values (fig. 10) of geothermal-water analyses reflect the fact that air is a major source of noble gases in many thermal springs and ground waters (Mazor, 1976; Kennedy and others, 1985). However, the Oriental mine fluid inclusions differ from most geothermal waters or gases in their relatively high apparent $^{132}Xe/^{84}Kr$ ratios and F^{air}_{132} values (fig. 10). Some excess xenon could be present on the sample surfaces, as xenon is the most readily adsorbed from air and the most difficult to desorb under vacuum, except perhaps with the laser. Some excess xenon also could be present in the interiors of the quartz crystals, possibly because it was selectively adsorbed and trapped during crystal growth (Ozima and Podosek, 1983; Matsubara and others, 1988). Analyses of inclusion-free quartz yield the

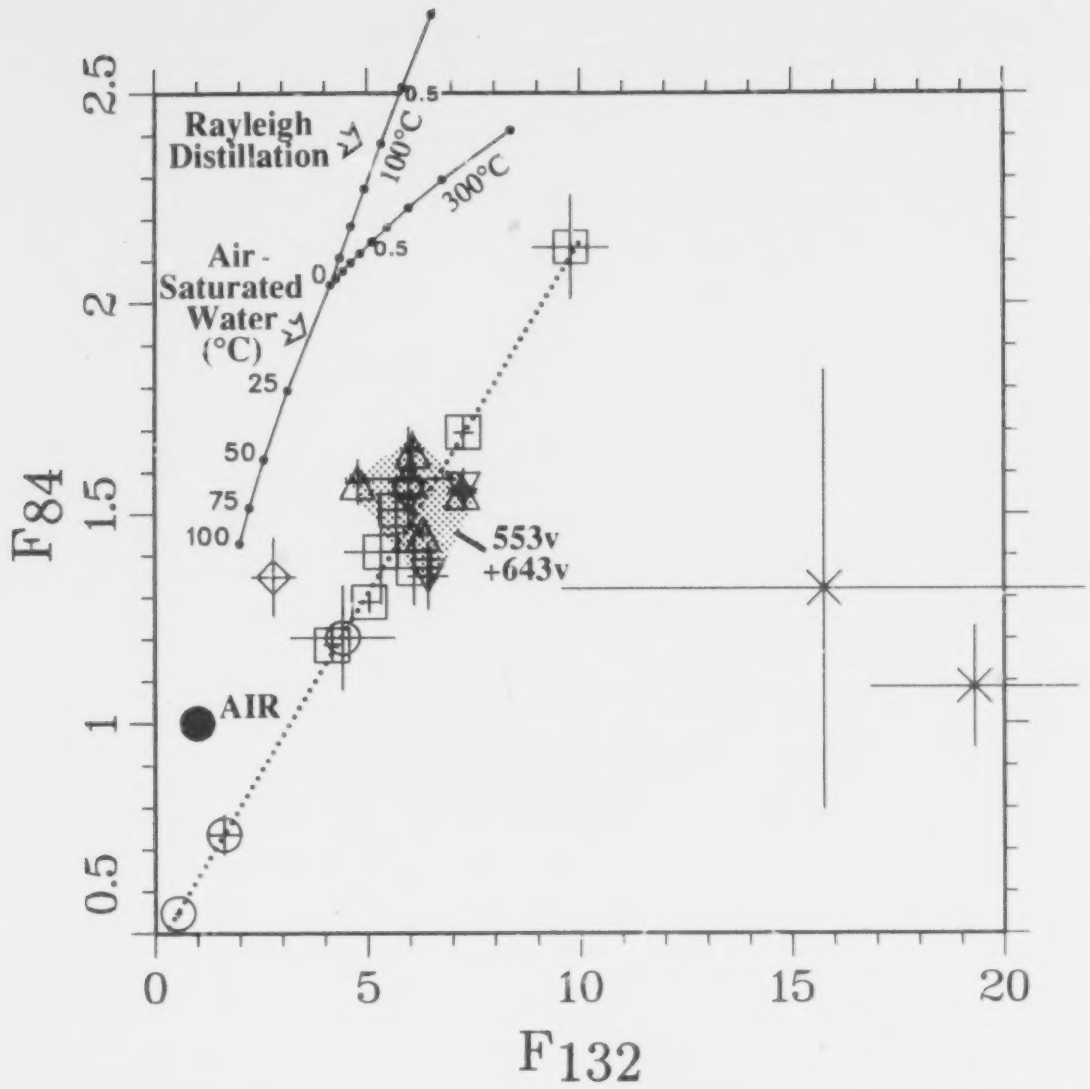

Figure 9. Noble gas ratios (F_{84}^{air} versus F_{132}^{air}). See figure 2 for key to symbols. F_{84}^{air} and F_{132}^{air} are defined by equation 3. The reference curve for air-saturated water at various temperatures was calculated from data in Shock and others (in press) and is approximately consistent with data in Smith and Kennedy (1983); reference curves for Rayleigh (open-system) distiliation were calculated from data in Shock and others (in press) with an assumed initial composition corresponding to air-saturated water at 0 °C. The points on the distillation curves refer to the fraction of the original dissolved argon remaining in the liquid (Ar/Ar^{o} = 0.5 is labeled). Data from 553v and 643v, falling in a tight cluster, indicate relatively little gas fractionation. Data from 643m and 671 define a linear trend (dotted line) roughly parallel to that defined by air, air-saturated water, and boiling water, but shifted to higher F_{132} and (or) lower F_{84}.

highest F_{132}^{air} values (see fig. 9) and are qualitatively consistent with some form of xenon contamination; however, the gas yields from inclusion-free quartz are probably too small to account for all of the apparent fluid-inclusion enrichments. For example, the amount of xenon-rich gas released by inclusion-free quartz in sample 553v, analysis 1555 (9.1×10^{5} atoms of ^{36}Ar, F_{132}^{air}=15.8), subtracted from the gas released from inclusion-bearing quartz in the same chip, analysis 1560 (1.4×10^{7} atoms of ^{36}Ar, F_{132}^{air}= 7.3), would yield F_{132}^{air}= 6.6, which would not greatly alter its position

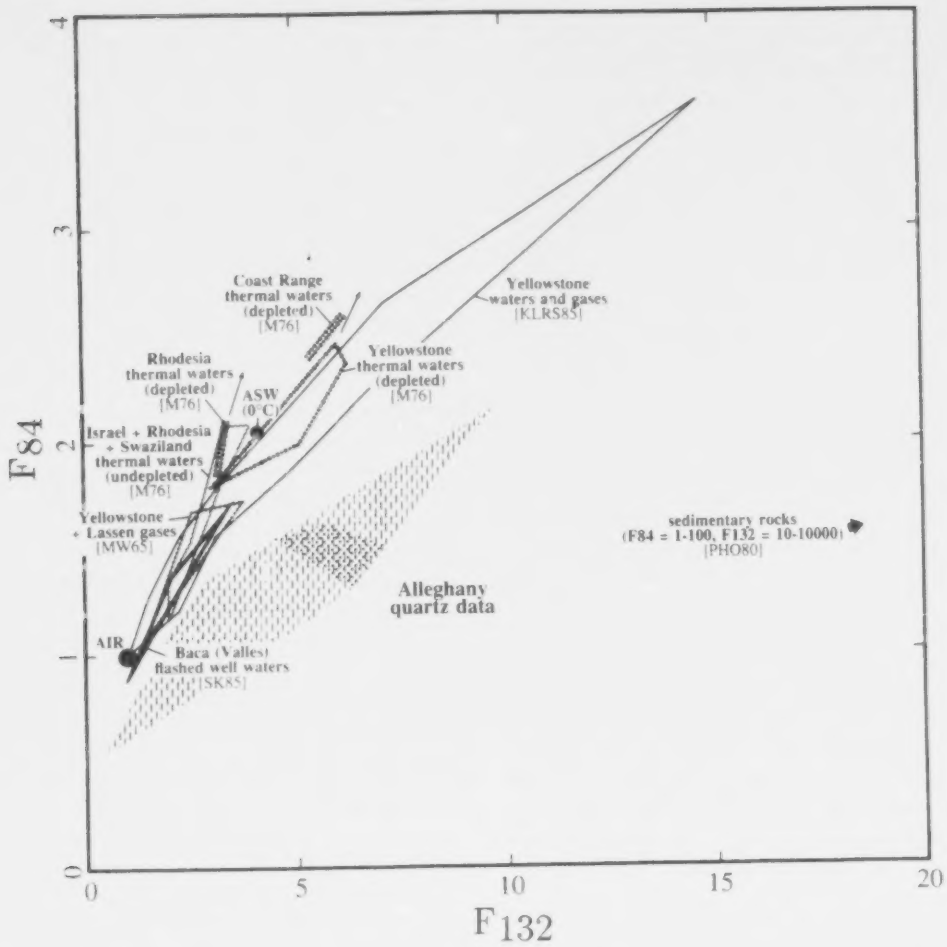

Figure 10. Noble-gas ratios (F_{84}^{air} versus F_{132}^{air}) for Alleghany quartz compared with other data for natural waters. Sources of data are KLRS85, Kennedy and others (1985); M76, Mazor (1976, assuming $^{40}Ar/^{36}Ar=295.5$—arrow indicates correction for 10 percent excess radiogenic ^{40}Ar); MW65, Mazor and Wasserburg (1965, as in M76); PHO80, Podosek and others (1980); SK85, Smith and Kennedy (1985). "Depleted" waters have ≤25 percent of 20 °C air-saturated argon concentrations. The area shaded with vertical lines encloses all of the data points for fluid-inclusion-bearing quartz shown in figure 9; the area shaded with dots corresponds to vug quartz 553v and 643v. ASW, air-saturated water.

in figure 9. Selective adsorption of gases released from the fluid inclusions during analysis presumably would cause the measured Xe/Ar ratios to be too low.

If excess ^{132}Xe is present in some of the fluid inclusions, then it must have been present in the hydrothermal fluids at the time of trapping, as the other xenon isotopes generally do not indicate that significant amounts of uranium fission products are present. Many sedimentary rocks have high Xe/Ar and Xe/Kr ratios, owing to selective adsorption of xenon from ground water or seawater, such that $F_{132}^{air} \simeq 10^1$–$10^4$ and $F_{84}^{air} \simeq 10^0$–10^2 in a variety of argillaceous and siliceous sedimentary rocks and carbonaceous materials (Podosek and others, 1980; Ozima and Podosek, 1983; Matsuda and Nagao, 1986). Although the behavior of noble gases in rock-water systems at high temperatures and pressures is not well known, it is possible that the Alleghany fluids acquired excess xenon with approximately atmospheric isotopic ratios by desorption or recrystallization of xenon-rich sedimentary rocks along their flow paths. This xenon enrichment could take place with relatively little change in the F_{84}^{air} value of the fluid because the initial Kr/Xe ratio of the fluid would have been much greater than that of the gas desorbed from the rocks. An excess xenon component from organic-rich marine

best copy available

argillaceous sedimentary rocks also would be consistent with the high observed I/Cl ratios in the fluid inclusions.

The correlation between F_{84}^{air} and F_{132}^{air} displayed by the 643m and 671 data is roughly parallel to the fractionation produced by vapor phase separation at <300 °C. Two reference curves for Rayleigh (open-system) distillation of noble gases from boiling fluids at low pressures are shown in figure 9. The overall slope of the linear trend defined by analyses of 643m and 671 could indicate that the fluid inclusions contained mixtures of fluids (liquids ± vapors) that boiled or unmixed either before or as they were trapped. However, as there is no independent evidence for phase separation, it is difficult to explain F_{84}^{air} and F_{132}^{air} values less than 1.0 by such processes involving meteoric water, and the data array is remarkably linear, in contrast to the Rayleigh curves. These data may therefore represent mixtures of gases from two (or more) distinct sources. One endmember appears to be slightly enriched in ^{84}Kr and ^{132}Xe relative to the vug quartz fluids; the other endmember is relatively enriched in ^{36}Ar. Low F_{84}^{air} and F_{132}^{air} values (≤ 1.0) are not common in geothermal waters but have been reported for well water from Valles, New Mexico, where argon-rich gases may have been acquired by fluids from glassy volcanic rocks (Smith and Kennedy, 1985). Experiments indicate that silicate liquids exposed to air during eruption may contain noble-gas components with low F values (Lux, 1987), which presumably could be leached later by hydrothermal fluids. The possibility remains that the Xe/Ar sensitivity or transmission ratios assumed for the mass spectrometer are significantly in error; however, we cannot yet rationalize an error of the direction and magnitude required to produce the apparent shift in the array of fluid inclusion data relative to the shallow meteoric water data (fig. 10).

Halogen and Noble-Gas Correlations

Processes such as phase separation and fluid mixing are most likely to be distinguishable on plots relating noble gases to halogens, as in figures 11 and 12. For example, vapor phase separation at <300 °C would be expected to cause significant changes in the noble-gas ratios of the residual liquid (see fig. 9) but would not alter its halogen ratios. Fluid inclusions that trapped boiling or unmixing fluids, or fluids that had boiled or unmixed just prior to trapping, would therefore tend to plot in horizontal arrays in figure 11. In contrast, mixing of fluids from different sources could result in arrays having a wide variety of slopes, depending on the past history of each fluid. The systematic difference in F_1^{sw} between analyses of vug quartz (553v and 643v) and milky quartz (643m) indicates that the fluid inclusions in these two groups of samples from the Oriental mine are not simply related by vapor-phase separation. However, each quartz sample considered separately could have trapped fluids that had undergone small amounts of phase separation.

Analyses of vug quartz 553v and 643v yield relatively high $Cl/^{36}Ar$ ratios and no positive correlation between $Cl/^{36}Ar$ and either F_{84}^{air} or F_{132}^{air} (fig. 12). Because the solubilities of Ar, Kr, and Xe converge at high temperatures, it is possible that, at the temperatures estimated for carbonate metasomatism along the veins (T>300 °C), separation of a vapor phase (CO_2?) could remove a portion of the noble gases without fractionating them significantly. Fluid inclusions containing such fluids would define nearly vertical arrays in figures 12 *A* and *B*. The vug quartz data are permissive of a small amount of vapor separation, but the restricted range of $Cl/^{36}Ar$ ratios is consistent with the general lack of petrographic evidence of such a process.

Analyses of milky quartz 643m and Gold Crown quartz 671 yield relatively low $Cl/^{36}Ar$ ratios and exhibit linear positive correlations between $Cl/^{36}Ar$ and both F_{84}^{air} and F_{132}^{air}. The slopes of the data arrays defined by 643m alone are approximately consistent with the effects of vapor loss at relatively low temperatures (see also fig. 9); however, the colinearities of 643m and 671 data in figures 9 and 12 may be more plausibly interpreted as mixing lines between two endmembers, one gas-rich or essentially chlorine free ($Cl/^{36}Ar \simeq 0.0$; $F_{84}^{air} = 0.50$; $F_{132}^{air} = 0.25$) and the other a chlorine-bearing fluid ($Cl/^{36}Ar \geq 4.2 \times 10^6$; $F_{84} \geq 2.15$; $F_{132}^{air} \geq 10.0$). Mixtures of these two components are indicated by dotted lines in figures 9, 11, and 12. The significance of the low $Cl/^{36}Ar$ endmember is not known, as it was detected only in a single sample from the Gold Crown mine. If it is assumed that all of the analyzed gases came predominantly from fluid inclusions with the measured chlorine concentrations, then some of the aqueous 671 fluids must have been greatly enriched in noble gases (preferentially argon) relative to air-saturated water. Alternatively, the low $Cl/^{36}Ar$ component could represent unobserved (small?) vapor-phase inclusions or some form of unidentified contamination, either of which may be present mainly in the massive milky forms of quartz. Work is in progress to determine if these apparent mixing lines may be analytical artifacts or if they reflect multistage hydrothermal processes involving, for example, acquisition of various gas ratios from rocks, vapor-liquid separation, and subsequent mixing (see Smith and Kennedy, 1985).

CONCLUSIONS

The abundances of Ar, Kr, and Xe isotopes naturally dissolved in hydrothermal waters, and of Ar, Kr, and Xe isotopes produced by neutron irradiation of dissolved K, Cl, Br, I, and possibly Ca, Ba, U(?), Te(?), and Se(?) are sufficient to be detected in individual large fluid inclusions or clusters of small inclusions by use of the laser-

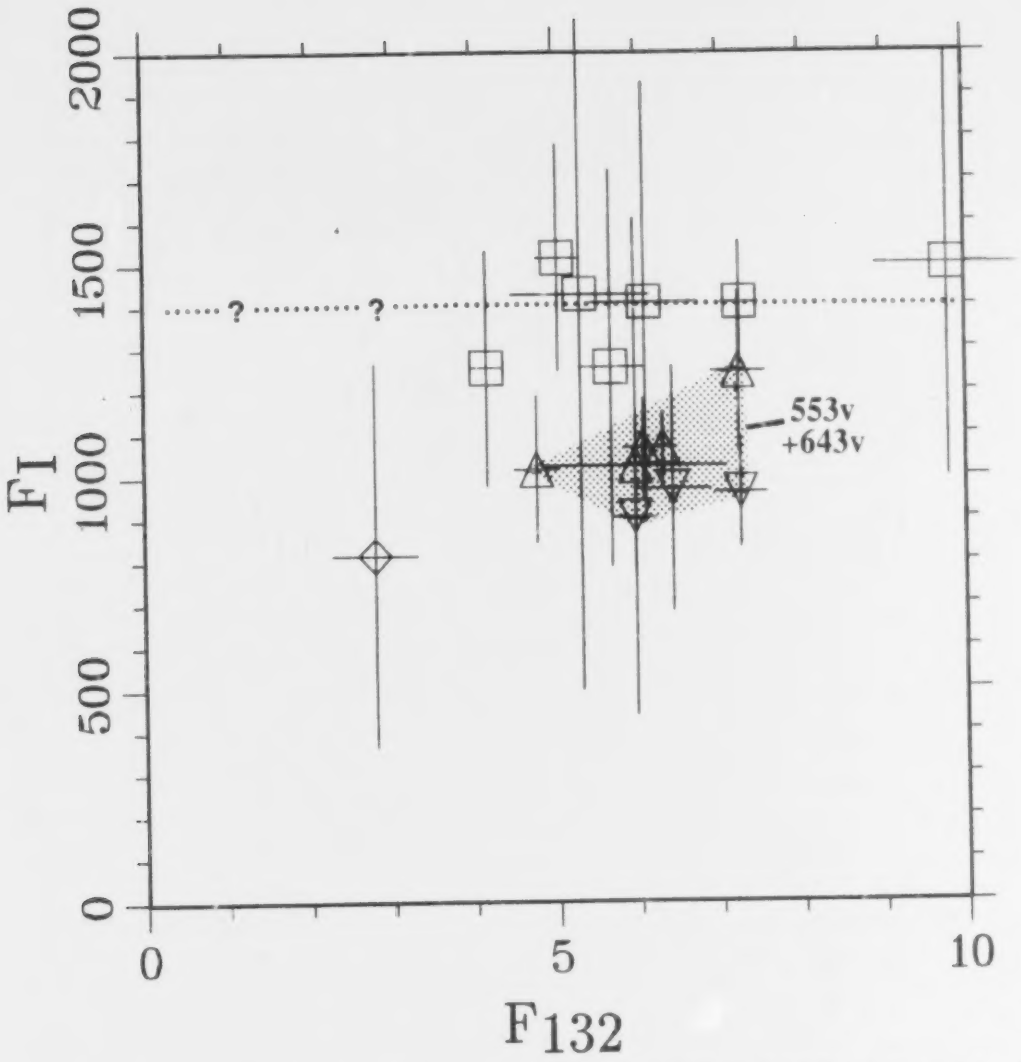

Figure 11. F_1^{sw} versus F_{132}^{air}. See figure 2 for key to symbols. F_{132}^{air} and F_1^{sw} are defined by equations 2 and 3. Data for 671 are not shown because they have large uncertainties in F_1^{sw}. Data from different samples are relatively distinct in F_1 but exhibit considerable overlap in F_{132}. Horizontal arrays on this plot would be consistent with progressive vapor-phase separation before or during fluid trapping or with mixtures of fluids with constant I/Cl (for example, the dotted line).

microprobe noble-gas mass spectrometer. The relative abundances of Ar, Kr, and Xe isotopes, and K, Cl, Br, and I have been successfully measured simultaneously in 10^{-10} to 10^{-9} L of *dilute* CO_2-bearing aqueous fluid inclusions in irradiated vein quartz from Alleghany, California.

Fluid inclusions in euhedral quartz crystals from vugs in the Oriental mine have relatively uniform ratios of halogens and noble gases. The absolute and relative concentrations of chlorine and bromine indicate that the fluids were not undiluted seawater, nor did they obtain salts from strongly fractionated evaporite brines. Absence of salinity sources such as these within the metamorphic belt may have helped to determine the metal transport properties of the Sierran hydrothermal system. The fluid inclusions are greatly enriched in iodine, possibly acquired from organic-rich sediments. There is some evidence that vug quartz and milky quartz from the same sample site contained different fluids, distinguished by slightly different I/Cl ratios; however, the data do not indicate whether these fluids mixed at the time of vein mineralization. The isotopic compositions of krypton and xenon, and the absolute concentrations of ^{36}Ar, indicate that the CO_2-bearing dilute fluid inclusions in

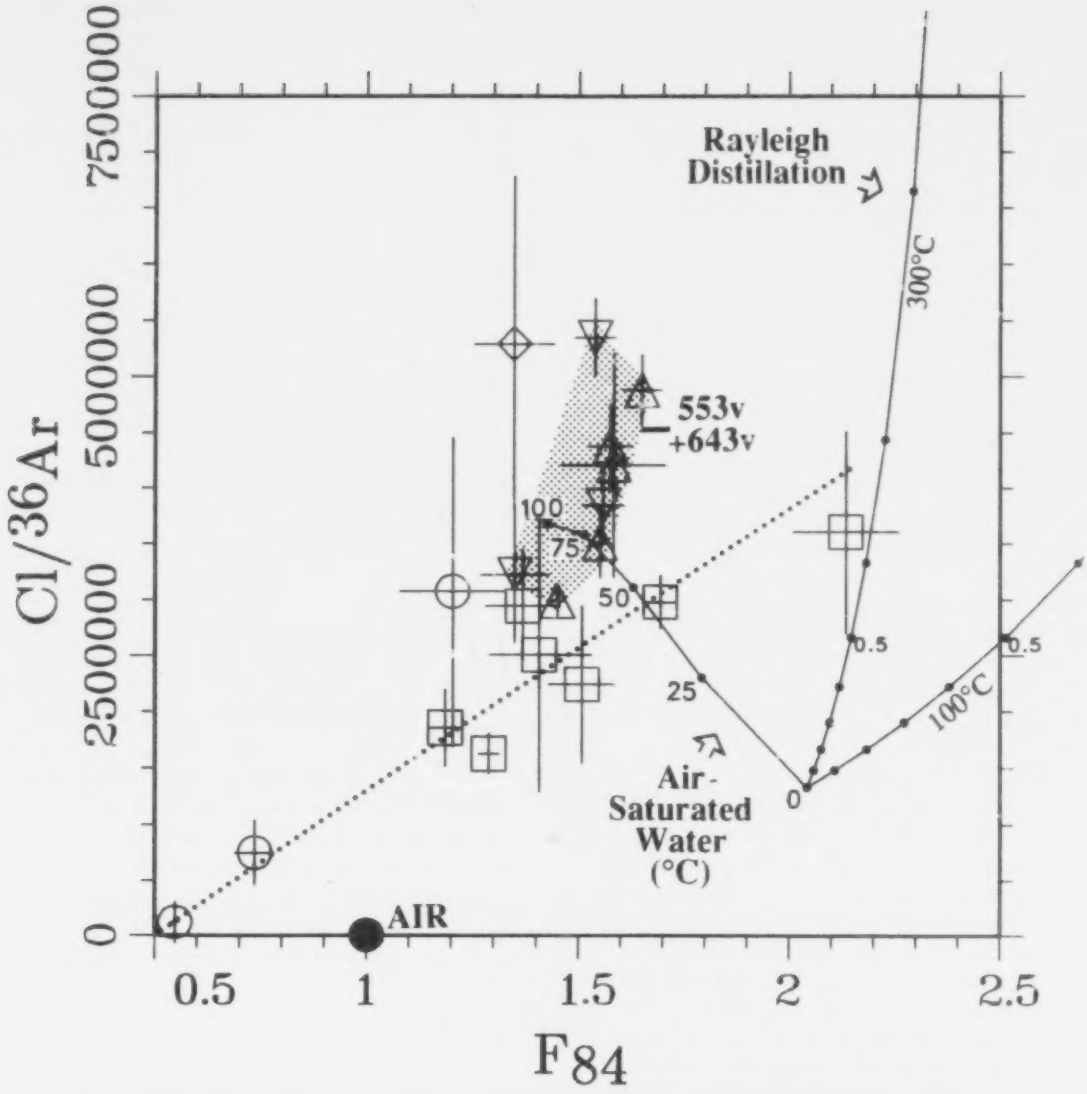

Figure 12. $Cl/^{36}Ar$ versus F_{84}^{air} (*A*) and F_{132}^{air} (*B*). See figure 2 for key to symbols. F_{84}^{air} and F_{132}^{air} are defined by equation 3. Reference curves for Rayleigh (open-system) distillation were calculated from data in Shock and others (in press) with an assumed initial composition corresponding to air-saturated water at 0 °C with 0.1 *m* Cl. The labels on the distillation curves refer to the fraction of original dissolved argon remaining in the liquid (Ar/Ar° = 0.5 is labeled). Data from vug quartz 553v and 643v could be consistent with small amounts of vapor loss at high temperatures. Data from 643m and 671 define a linear trend (dotted line) consistent with mixing of two distinct gas components of uncertain origin (see also figs. 9 and 11).

vug quartz could contain a significant component of meteoric water, which obtained noble gases from air. Moderately elevated $^{40}Ar/^{36}Ar$ ratios in the fluid inclusions cannot be due to in situ potassium decay but are consistent with exchange between meteoric thermal waters and potassium-bearing rocks before trapping. These data indicate that meteoric water was present at least as deep as the veins were forming, but they do not rule out the presence of another deeper CO_2-rich fluid source.

Fluid inclusions in massive milky quartz from the Oriental mine and a heterogeneous crystal from the Gold Crown mine define common linear arrays in noble-gas correlation diagrams. These correlations may be interpreted as mixing lines between two noble-gas components, one of

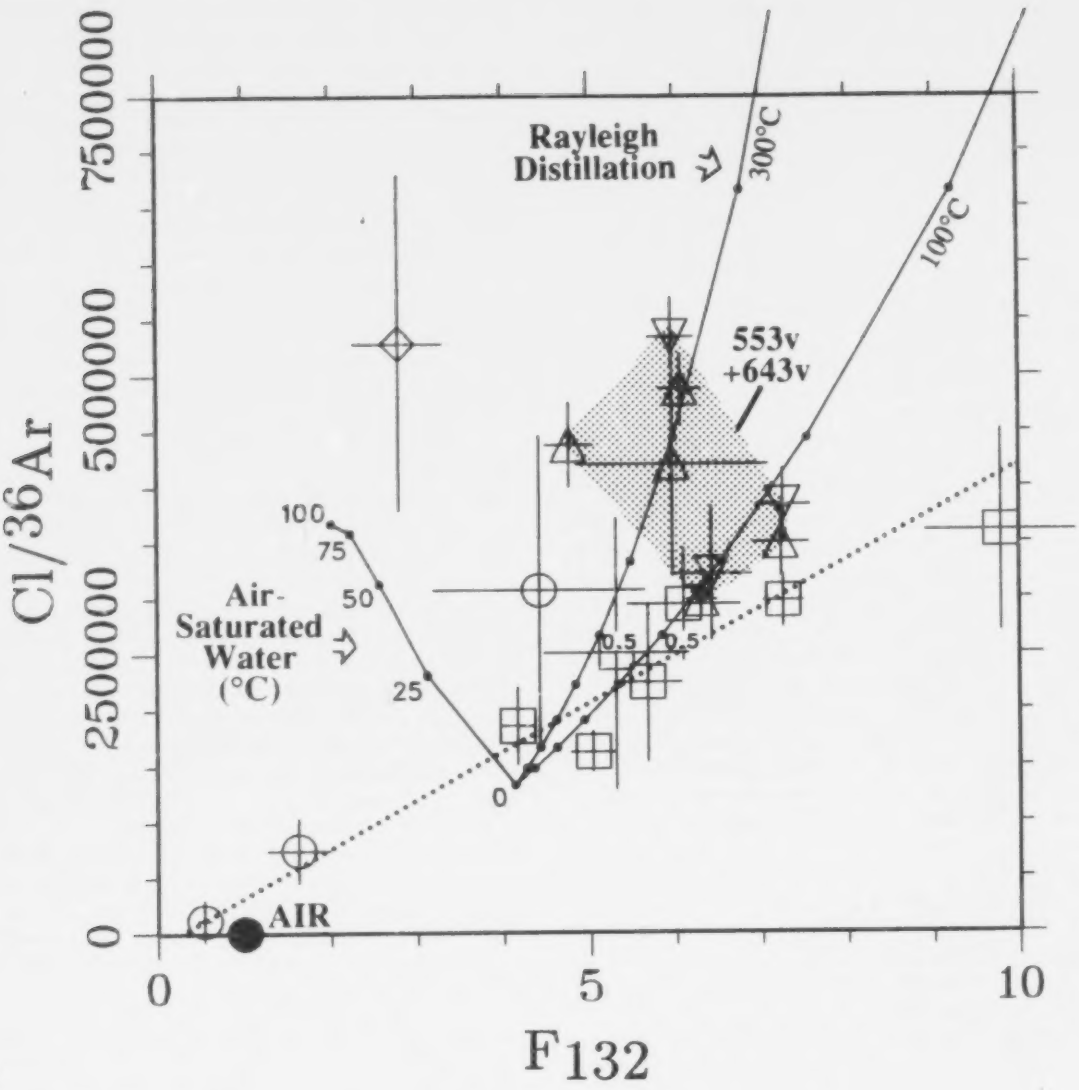

B

Figure 12.—Continued.

which has unusually low Kr/Ar and Xe/Ar ratios and may not be associated with chlorine. The significance of these apparent mixtures is currently under investigation.

Summaries of data in the literature indicate that ratios among dissolved Ar, Kr, and Xe in ground waters vary by factors of at least 3 (Kr/Ar) to 10 (Xe/Ar), whereas ratios among Cl, Br, and I vary by factors of more than 10 (Br/Cl) to 1,000 (I/Cl). Because these elements and the noble-gas isotopic ratios exhibit contrasting behavior with respect to fluid-rock interactions, phase separation, and source characteristics, simultaneous halogen and noble-gas analyses of fluid inclusions are expected to provide unique resolving power for (1) determining the sources of fluids and dissolved salts and (2) distinguishing processes such as mixing, boiling, and unmixing in a variety of fossil and evolving active hydrothermal systems.

ACKNOWLEDGMENTS

The noble-gas analyses were performed in the laboratory of J.H. Reynolds (University of California, Berkeley), who directed the construction of the instrument and supported our attempts to use it on terrestrial materials. W.E. Glassley helped to broaden the scope of the terrestrial investigations. Laboratory and computing facilities at Argonne National Laboratory were provided under the

supervision of N.C. Sturchio. E. Shock assisted with calculations of noble-gas solubilities. We thank D.R. Dickey (Oriental mine) for generous assistance in the field. This study was funded in part by the U.S. Department of Energy, Office of Basic Energy Sciences, under Contract W–31–109–Eng–38, by the National Aeronautic and Space Administration under Contract NAG 9–34, and by the Department of Energy under Contract DE–AC03–76SF00098. J.H. Reynolds, B.M. Kennedy, S.P. Smith, R.E. Criss, W.C. Shanks, J. Abrajano, and N.C. Sturchio made numerous suggestions for improving the interpretation and presentation of the data.

REFERENCES CITED

Alexander, E.C., Jr., Michelson, G.M., and Lanphere, M.A., 1978, MMHb–1: A new ^{40}Ar–^{39}Ar dating standard, *in* Zartman, R.E., ed., Fourth international conference on geochronology, cosmochronology, and isotope geology: U.S. Geological Survey Open-File Report 78–701, p. 6–8.

Allegre, C.J., Staudacher, T., and Sarda, P., 1987, Rare gas systematics: Formation of the atmosphere, evolution and structure of the Earth's mantle: Earth and Planetary Science Letters, v. 81, p. 127–150.

Barnes, I., Kistler, R.W., Mariner, R.H., and Presser, T.S., 1981, Geochemical evidence on the nature of the basement rocks of the Sierra Nevada, California: U.S. Geological Survey Water-Supply Paper 2181, 13 p.

Behr, H.-J., and Gerler, J., 1987, Inclusions of sedimentary brines in post-Variscan mineralizations in the Federal Republic of Germany—A study by neutron activation analysis: Chemical Geology, v. 61, p. 65–77.

Böhlke, J.K., 1986, Local wall rock control of alteration and mineralization reactions along discordant gold quartz veins at Alleghany, California: Ph.D. dissertation, University of California, Berkeley, 308 p.

———in press, Comparison of metasomatic reactions between a common CO_2-rich vein fluid and diverse wall rocks: Intensive variables, mass transfer, and Au mineralization of Alleghany, California: Economic Geology.

Böhlke, J.K., and Kistler, R.W., 1986, Rb-Sr, K-Ar, and stable isotope evidence for the ages and sources of fluid components of gold quartz veins in the northern Sierra Nevada foothills metamorphic belt: Economic Geology, v. 81, p. 296–322.

Böhlke, J.K., Kirschbaum, C., Irwin, J.J., and Glassley, W.E., 1987, Laser microprobe analyses of noble gas isotopes in fluid inclusions in neutron-irradiated quartz veins: Geological Society of America Abstracts with Programs, v. 19, p. 594.

Böhlke, J.K., Coveney, R.M., Jr., Rye, R.O., and Barnes, I., 1988, Stable isotope investigation of gold quartz veins at the Oriental mine, Alleghany district, California: U.S. Geological Survey Open-File Report 88–279, 24 p.

Brewer, P.G., and Spencer, D.W., 1969, A note on the chemical composition of the Red Sea brines, *in* Degens, E.T., and Ross, D.A., eds., Hot brines and heavy metal deposits in the Red Sea: New York, Springer-Verlag, p. 174–179.

Burrows, D.R., Wood, P.C., and Spooner, E.T.C., 1986, Carbon isotope evidence for a magmatic origin for Archaean gold-quartz vein ore deposits: Nature, v. 321, p. 851–854.

Collins, A.G., and Egleson, G.C., 1967, Iodide abundance in oilfield brines in Oklahoma: Science, v. 156, p. 934–935.

Coveney, R.M., Jr., 1981, Gold quartz veins and auriferous granite at the Oriental mine, Alleghany district, California: Economic Geology, v. 76, p. 2176–2199.

Craig, H., 1961, Isotopic variations in meteoric waters: Science, v. 133, p. 1702–1703.

———1963, The isotopic geochemistry of water and carbon in geothermal areas, *in* Tongiorgi, E., ed., Nuclear geology on geothermal areas: Consiglio Nazionale della Ricerche, Laboratorio de Geologia Nucleare, p. 17–53.

Craig, H., Lupton, J.E., Welhan, J.A., and Poreda, R., 1978, Helium isotope ratios in Yellowstone and Lassen Parks volcanic gases: Geophysical Research Letters, v. 5, p. 897–900.

Criss, R.E., and Taylor, H.P., Jr., 1983, An $^{18}O/^{16}O$ and D/H study of Tertiary hydrothermal systems in the southern half of the Idaho batholith: Geological Society of America Bulletin, v. 94, p. 640–663.

Dalrymple, G.B., Alexander, E.C., Lanphere, M.A., and Kraker, G.P., 1981, Irradiation of samples for ^{40}Ar–^{39}Ar dating using the Geological Survey TRIGA reactor: U.S. Geological Survey Professional Paper 1176, 55 p.

Duce, R.A., Wasson, J.T., Winchester, J.W., and Burns, F., 1963, Atmospheric iodine, bromine, and chlorine: Journal of Geophysical Research, v. 68, p. 3943–3947.

Ellis, A.J., and Mahon, W.A.J., 1977, Chemistry and geothermal systems: New York, Academic Press, 392 p.

Ferguson, H.G., and Gannett, R.W., 1932, Gold quartz veins of the Alleghany district, California: U.S. Geological Survey Professional Paper 172, 139 p.

Fisher, D.E., 1985, Radiogenic rare gases and the evolutionary history of the depleted mantle: Journal of Geophysical Research, v. 90, p. 1801–1807.

Fuge, R., and Johnson, C.C., 1986, The geochemistry of iodine—A review: Environmental Geochemisry and Health, v. 8, p. 31–54.

Fyfe, W.S., and Kerrich, R., 1984, Gold: Natural concentration processes, *in* Foster, R.P., ed., Gold '82: The geology, geochemistry and genesis of gold deposits: Rotterdam, A.A. Balkema, p. 99–127.

Groves, D.I., Phillips, G.N., Ho, S.E., and Houstoun, S.M., 1985, The nature, genesis and regional controls of gold mineralization in Archaean greestone belts of the western Australian shield: A brief review: Geological Society of South Africa Transactions, v. 88, p. 135–148.

Hedenquist, J.W., and Henley, R.W., 1985, The importance of CO_2 on freezing point measurements of fluid inclusions: Evidence from active geothermal systems and implications for epithermal ore deposition: Economic Geology, v. 80, p. 1379–1406.

Henley, R.W., 1985, The geothermal framework of epithermal deposits, *in* Berger, B.R., and Bethke, P.M., eds., Geology and geochemistry of epithermal systems: Society of Economic Geologists, Reviews in Economic Geology, v. 2, p. 1–24.

Herzberg, O., and Mazor, E., 1979, Hydrological applications of noble gases and temperature measurements in underground water systems: Examples from Israel: Journal of Hydrology, v. 41, p. 217–231.

Hohenberg, C.M., Hudson, B., Kennedy, B.M., and Podosek, F.A., 1981, Noble gas retention chronologies for the St. Severin meteorite: Geochimica et Cosmochimica Acta, v. 45, p. 535–546.

Holser, W.T., 1979, Trace elements and isotopes in evaporites, *in* Burns, R.G., ed., Marine minerals: Mineralogical Society of America, Reviews in Mineralogy, v. 6, p. 295–346.

ICRP, 1975, Report of the task group on reference man: International Commission on Radiological Protection, no. 23, 480 p.

Kelley, S., Turner, G., Butterfield, A.W., and Shepherd, T.J., 1986, The source and significance of argon isotopes in fluid inclusions from areas of mineralization: Earth and Planetary Science Letters, v. 79, p. 303–318.

Kelly, W.C., Rye, R.O., and Livnat, A., 1986, Saline mine-waters of the Keweenaw Peninsula, northern Michigan: Their nature, origin, and relation to similar deep waters in Precambrian crystalline rocks of the Canadian shield: American Journal of Science, v. 286, p. 281–308.

Kennedy, B.M., Lynch, M.A., Reynolds, J.H., and Smith, S.P., 1985, Intensive sampling of noble gases in fluids at Yellowstone, pt. I, Early overview of the data; regional patterns: Geochimica et Cosmochimica Acta, v. 49, p. 1251–1261.

Kerrich, R., 1981, Archean gold-bearing chemical sedimentary rocks and veins: A synthesis of stable isotope and geochemical relations: Ontario Geological Survey Miscellaneous Paper 97, p. 144–175.

Kerrich, R., and Fyfe, W.S., 1981, The gold-carbonate association: Source of CO_2, and CO_2 fixation reactions in Archean lode deposits: Chemical Geology, v. 33, p. 265–294.

Kirschbaum, C.L., 1986, Laser microprobe studies of rare gas isotopes in meteorites: Ph.D. dissertation, U. of California, Berkeley, 107 p.

———1988, Carrier phases for iodine in the Allende meteorite and their associated $^{129}Xer/^{127}I$ ratios: A laser microprobe study: Geochimica et Cosmochimica Acta, v. 52, p. 679–699.

Kirschbaum, C., Irwin, J.J., Böhlke, J.K., and Glassley, W.E., 1987, Simultaneous analysis of halogens and noble gases in neutron-irradiated quartz veins: A laser microprobe study: EOS, Transactions of the American Geophysical Union, v. 68, p. 1514.

Kozłowski, A., and Karwowski, L., 1974, Chlorine/bromine ratio in fluid inclusions: Economic Geology, v. 69, p. 268–271.

Lindgren, W., 1933, Mineral deposits: New York, McGraw-Hill, Inc., 930 p.

Luckscheiter, B., and Parekh, P.P., 1979, A new method for the determination of dissolved elements in fluid inclusions: Neues Jahrbuch für Mineralogie, v. 3, p. 135–144.

Lux, G., 1987, The behavior of noble gases in silicate liquids: Solution, diffusion, bubbles, and surface effects, with applications to natural samples: Geochimica et Cosmochimica Acta, v. 51, p. 1549–1560.

Marshall, B., and Taylor, B.E., 1981, Origin of hydrothermal fluids responsible for gold deposition, Alleghany district, Sierra County, California, *in* Silberman, M., and others, Proceedings of the symposium on mineral deposits of the Pacific Northwest: U.S. Geological Survey Open-File Report 81–355, p. 280–293.

Matsubara, K., Matsuda, J., Nagao, K., Kita, I., and Taguchi, S., 1988, Xe in amorphous silica: A new thermometer in geothermal systems: Geophysical Research Letters, v. 15, p. 657–660.

Matsuda, J., and Nagao, K., 1986, Noble gas abundances in a deep-sea sediment core from eastern equatorial Pacific: Geochemical Journal, v. 20, p. 71–80.

Mazor, E., 1972, Paleotemperatures and other hydrological parameters deduced from noble gases dissolved in groundwaters; Jordan Rift Valley, Israel: Geochimica et Cosmochimica Acta, v. 36, p. 1321–1336.

———1976, Atmospheric and radiogenic noble gases in thermal waters: Their potential application to prospecting and steam production studies: Proceedings of the Second United Nations Symposium on the Development and Use of Geothermal Resources, v. 1, p. 793–802.

Mazor, E., and Truesdell, A.H., 1981, Dynamics of a geothermal field traced by noble gases: Cerro Prieto, Mexico, *in* Proceedings of the Third Symposium on the Cerro Prieto Geothermal Field, Baja California, Mexico: p. 163–173.

Mazor, E., and Wasserburg, G.J., 1965, Helium, neon, argon, krypton, and xenon in gas emanations from Yellowstone and Lassen volcanic National Parks: Geochimica et Cosmochimica Acta, v. 29, p. 443–454.

Mazor, E., Dubois, J.D., Fluck, J., and Jaffe, F.C., 1988, Noble gases as tracers identifying geothermal components in regions devoid of surface geothermal manifestations: A case study in the Baden Springs area, Switzerland: Chemical Geology, v. 72, p. 47–61.

Murowchick, J.B., Muehlenbachs, K., and Nesbitt, B.E., 1987, Nature of ore fluids in the Coquihalla gold belt, British Columbia, *in* Elliott, I.L., and Smee, B.W., eds., Geoexpo/86: Exploration in the North American Cordillera: Association of Exploration Geochemists, p. 160–167.

Naydenov, B.M., Bogolepov, V.G., Polyvyannyy, E.Ya., and Zakharchenko, A.I., 1972, Behavior of argon isotopes in pegmatite mineralizing solutions: Geochemistry International, v. 9, p. 471–473.

Nesbitt, B.E., Murowchick, J.B., and Muehlenbachs, K., 1986, Dual origins of lode gold deposits in the Canadian Cordillera: Geology, v. 14, p. 506–509.

Nordstrom, D.K., Andrews, J.N., Carlsson, L., Fontes, J.-C., Fritz, P., Moser, H., and Olsson, T., 1985, Hydrogeological and hydrogeochemical investigations in boreholes—Final report of the phase I geochemical investigations of the Stripa groundwaters: Swedish Nuclear Fuel and Waste Management Co., Technical Report 85–06.

Ozima, M., and Podosek, F.A., 1983, Noble gas geochemistry: Cambridge, Cambridge University Press, 367 p.

Phillips, G.N., and Groves, D.I., 1983, The nature of Archaean gold-bearing fluids as deduced from gold deposits of Western Australia: Geological Society of Australia Journal, v. 30, p. 25–39.

Pickthorn, W.J., Goldfarb, R.J., and Leach, D.L., 1987, Comment on "Dual origins of lode gold deposits in the Canadian Cordillera": Geology, v. 15, p. 471–472.

Podosek, F.A., Honda, M., and Ozima, M., 1980, Sedimentary noble gases: Geochimica et Cosmochimica Acta, v. 44, p. 1875–1884.

Rama, S.N.I., Hart, S.R., and Roedder, E., 1965, Excess radiogenic argon in fluid inclusions: Journal of Geophysical Research, v. 70, p. 509–511.

Rittenhouse, G., 1967, Bromine in oil-field waters and its use in determining possibilities of origin of these waters: American Association of Petroleum Geologists Bulletin, v. 51, p. 2430–2440.

Robert, F., and Kelly, W.C., 1987, Ore-forming fluids in Archean gold-quartz veins at the Sigma mine, Abitibi greenstone belt, Quebec, Canada: Economic Geology, v. 82, p. 1464–1482.

Roddick, J.C., 1983, High precision intercalibration of ^{40}Ar–^{39}Ar standards: Geochimica et Cosmochimica Acta, v. 47, p. 887–898.

Roedder, E., 1984, Fluid inclusions: Mineralogical Society of America Reviews in Mineralogy, v. 12, 644 p.

Saito, K., and Ozima, M., 1977, ^{40}Ar–^{39}Ar geochronological studies on submarine rocks from the western Pacific Ocean: Earth and Planetary Science Letters, v. 33, p. 353–369.

Shock, E.L., Helgeson, H.C., and Sverjensky, D.A., in press, Calculation of the thermodynamic and transport properties of aqueous species at high pressures and temperatures: Standard state properties of inorganic neutral species: Geochimica et Cosmochimica Acta.

Simmons, S.F., Sawkins, F.J., and Schlutter, D.J., 1987, Mantle-derived helium in two Peruvian hydrothermal ore deposits: Nature, v. 329, p. 429–432.

Smith, S.P., and Kennedy, B.M., 1983, The solubility of noble gases in water and in NaCl brine: Geochimica et Cosmochimica Acta, v. 47, p. 503–515.

———1985, Noble gas evidence for two fluids in the Baca (Valles Caldera) geothermal reservoir: Geochimica et Cosmochimica Acta, v. 49, p. 893–902.

Steiger, R.H., and Jäger, E., 1977, Subcommission on geochronology: Convention on the use of decay constants in geo- and cosmochronology: Earth and Planetary Science Letters, v. 36, p. 359–362.

Sverdrup, H.U., Johnson, M.W., and Fleming, R.H., 1942, The Oceans: New York, Prentice-Hall, Inc., 1087 p.

Taylor, H.P., 1974, The application of oxygen and hydrogen isotope studies to problems of hydrothermal alteration and ore deposition: Economic Geology, v. 69, p. 843–883.

Torgersen, T., and Clarke, W.B., 1985, Helium accumulation in groundwater, pt. I, An evaluation of sources and the continental flux of crustal ^{4}He in the Great Artesian Basin, Australia: Geochimica et Cosmochimica Acta, v. 49, p. 1211–1218.

Turner, G., 1965, Extinct iodine 129 and trace elements in chondrites: Journal of Geophysical Research, v. 70, p. 5433–5445.

———1988, Hydrothermal fluids and argon isotopes in quartz veins and cherts: Geochimica et Cosmochimica Acta, v. 52, p. 1443–1448.

Walker, F.W., Miller, D.G., and Feiner, F., 1984, Chart of the nuclides, 13th ed.: San Jose, California, General Electric Co.

Weir, R.H., Jr., and Kerrick, D.M., 1987, Mineralogic, fluid inclusion, and stable isotope studies of several gold mines in the Mother Lode, Tuolumne and Mariposa Counties, California: Economic Geology, v. 82, p. 328–344.

White, D.E., 1957, Magmatic, connate, and metamorphic waters: Geological Society of America Bulletin, v. 68, p. 1659–1682.

———1974, Diverse origins of hydrothermal ore fluids: Economic Geology, v. 69, p. 954–973.

———1981, Active geothermal systems and hydrothermal ore deposits: Economic Geology, 75th Anniversary Volume, p. 392–423.

White, D.E., and Roberson, C.E., 1962, Sulphur Bank, California, a major hot spring quicksilver deposit, *in* Petrologic studies: Geological Society of America Buddington Volume, p. 397–428.

White, D.E., Hem, J.D., and Waring, G.A., 1963, Chemical composition of subsurface waters: U.S. Geological Survey Professional Paper 440-F, p. F1–F67.

Whittemore, D.O., 1984, Geochemical identification of salinity sources, *in* French, R.H., ed., Salinity in watercourses and reservoirs: Boston, Butterworth Publishers, p. 505–514.

Wickham, S.M., and Taylor, H.P., Jr., 1985, Stable isotopic evidence for large-scale seawater infiltration in a regional metamorphic terrane; the Trois Seigneurs Massif, Pyrenees, France: Contributions to Mineralogy and Petrology, v. 91, p. 122–137.

Wickman, F.E., and Khattab, K.M., 1972, Non-destructive activation analysis of fluid inclusions in fluorite: Economic Geology, v. 67, p. 236–239.

Zaikowski, A., Kosanke, B.J., and Hubbard, N., 1987, Noble gas composition of deep brines from the Palo Duro Basin, Texas: Geochimica et Cosmochimica Acta, v. 51, p. 73–84.

Zartman, R.E., Wasserburg, G.J., and Reynolds, J.H., 1961, Helium, argon, and carbon in some natural gases: Journal of Geophysical Research, v. 66, p. 277–306.

The GLM Continuous Laser System for $^{40}Ar/^{39}Ar$ Dating: Description and Performance Characteristics

By G. Brent Dalrymple

Abstract

The GLM is a laser system designed for $^{40}Ar/^{39}Ar$ dating of single mineral grains of mass as little as 1 microgram. The instrument consists of a continuous argon-ion laser for sample heating and fusion, laser optics, a small extraction/cleanup system, and an ultrasensitive, ultralow-background rare-gas mass spectrometer. Radiogenic ^{40}Ar yields commonly exceed 99 percent, and the precision of the ages measured with the GLM is typically 0.2 to 0.5 percent for homogeneous samples. The GLM may be used for total fusion dating of single- and multiple-grain samples, for age spectrum analysis of single grains, and as a microprobe to determine apparent ages from small areas within single grains.

INTRODUCTION

In the $^{40}Ar/^{39}Ar$ method of K-Ar dating, the sample is irradiated with fast neutrons to induce the reaction $^{39}K(n,p)^{39}Ar$. The age of the sample is then calculated from the $^{40}Ar/^{39}Ar$ ratio after appropriate corrections for interfering Ar isotopes from the atmosphere and from undesirable neutron reactions with Ca and K.

$$t=\frac{1}{\lambda}\log_e\left(1+J\times\frac{^{40}Ar}{^{39}Ar}\right)$$

where λ is the decay constant of ^{40}K ($=5.534\times10^{-10}yr^{-1}$). The conversion factor, J, for the reaction $^{39}K(n,p)^{39}Ar$ is determined by irradiating a monitor mineral of known age with the samples whose age is to be determined (Merrihue and Turner, 1966; Brereton, 1970; Dalrymple and Lanphere, 1969, 1971; Lanphere and Dalrymple, 1971; Dalrymple and others, 1981).

The method can be used in two different ways. If all of the argon is released by fusing the mineral in a single heating, the result is a *total fusion age*. If the argon is released from the sample in steps by incrementally heating the sample to progressively higher temperatures, the result is a series of ages known as an *age spectrum*.

The $^{40}Ar/^{39}Ar$ method, which only requires the measurement of isotope ratios rather than abundances, has several advantages over the conventional method, wherein the argon is measured by isotope dilution and the potassium is measured on a different sample aliquant by one of several techniques, most commonly flame photometry. These advantages include (1) higher precision, (2) smaller sample size, (3) elimination of problems caused by sample inhomogeneity, and (4) the ability to recover age and thermal history information from age spectra. Disadvantages of the $^{40}Ar/^{39}Ar$ method include (1) the necessity of access to a nuclear reactor, (2) shipping and handling radioactive materials, (3) normalization of results to a monitor mineral of known age, and (4) interferences from neutron reactions that produce undesirable argon isotopes. These disadvantages, however, are easily dealt with and are outweighed by the above-mentioned advantages.

Most commonly, the argon analysis for $^{40}Ar/^{39}Ar$ dating is done with the same or similar equipment and techniques used for the conventional (isotope dilution) method of analysis. The sample is fused in ultrahigh vacuum by either induction heating or an internal resistance furnace, the reactive gases are removed by some combination of molecular sieve and hot metal and metal-oxide getters, and the mass analysis is done with a rare-gas mass spectrometer (Dalrymple and Lanphere, 1969). These procedures usually require sample weights in the range of 0.01–1.0 g, depending on the age and potassium content of the sample.

A laser was first used for rare-gas isotopic analysis by Megrue (1967), who volatilized small volumes of meteoritic material with a pulsed laser and analyzed the helium and neon isotopes released. Later, Megrue (1973) applied this method to the $^{40}Ar/^{39}Ar$ dating of a lunar breccia. The pulsed laser probe can produce $^{40}Ar/^{39}Ar$ total fusion ages from a small area (typically 20 to 200 μm diameter) within a single crystal (for example, Müller and others, 1977; Sutter and Hartung, 1984) but lacks the capability of producing age spectra or of analyzing whole, single mineral grains. Because of these disadvantages, the pulsed laser probe has been used only minimally for dating terrestrial materials.

York and others (1981) were the first to demonstrate that a continuous laser could be used not only to produce $^{40}Ar/^{39}Ar$ ages from single crystals but also to determine age spectra. Since then, continuous laser probes at the University of Toronto, Princeton University, and the U.S. Geological Survey at Menlo Park have been used to date tektites and illites (Glass and others, 1986; Bray and others, 1987), to determine the distribution of apparent ages within single crystals (York and Hall, 1986; Phillips and Onstott,

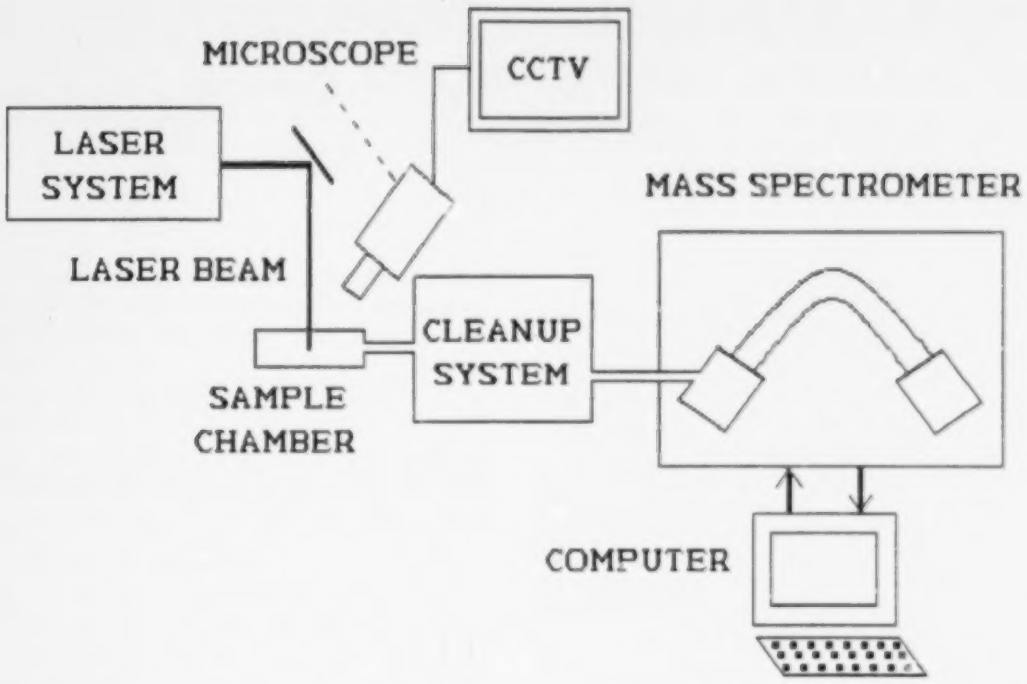

Figure 1. Block diagram of the GLM, a continuous laser system for $^{40}Ar/^{39}Ar$ dating of single mineral grains.

1986), to produce age spectra from single grains of biotite and hornblende (Layer and others, 1987), to circumvent xenocrystic contamination in volcanic rocks (LoBello and others, 1987), and to determine highly precise ages by the use of sanidine crystals from Oligocene rhyolite flows (Dalrymple and Duffield, 1988). These laser probes consist of a continuous laser for sample fusion, a small-volume extraction/cleanup system, and an ultraclean, ultrasensitive rare-gas mass spectrometer. Not only can the instruments produce both total fusion and incremental heating data, they yield $^{40}Ar/^{39}Ar$ ages with precisions as good or better than any other method of $^{40}Ar/^{39}Ar$ dating from samples that weigh as little as 1 μg.

The purpose of this paper is to describe the GLM (Great Little Machine), the U.S. Geological Survey continuous laser probe, and its performance characteristics.

DESCRIPTION OF THE GLM

The GLM (fig. 1) consists of a laser system, a sample chamber monitored by a microscope and closed-circuit television, a cleanup system, and an ultrasensitive, ultralow-background rare-gas mass spectrometer controlled by a computer. The cleanup system, sample chamber, and laser system were designed for full computer control, but the hardware necessary for implementing this feature is presently lacking.

The Laser System

The laser system (fig. 2) consists of a continuous laser, beam expander, beam steerers, beam switch, power meter, and neutral density filters. The laser is a 5-W argon-ion laser (Coherent Innova 90–5) with principal wavelengths at 488 nm and 514 nm and a maximum all-lines output of 7.5 W. The output is continuously variable from about 25 mW to 7.5 W and is regulated to about 0.2 percent (RMS) in light regulation mode. The laser is equipped with a wavelength selector for minimizing laser spot diameter when necessary, an internal aperture for controlling the transverse mode, an internal shutter that interrupts lasing for safety, and a RS232 interface for computer control.

The laser beam, which exits the laser with a diameter of 1.5 mm at the $1/e^2$ points, is passed through a 10 × Galillean beam expander (Oriel model 15600) that is used to focus the beam onto the sample. The beam expander has an aperture of 23 mm, a fused silica diverging input lense with a focal length of −8 mm, and an output lens with a focal length of +80 mm. The output lens is an achromatic cemented doublet with negligible spherical aberration and very low wavefront distortion. Even though it is a cemented doublet, there is no damage to the output lens because the power density of the expanded beam is only about 0.04

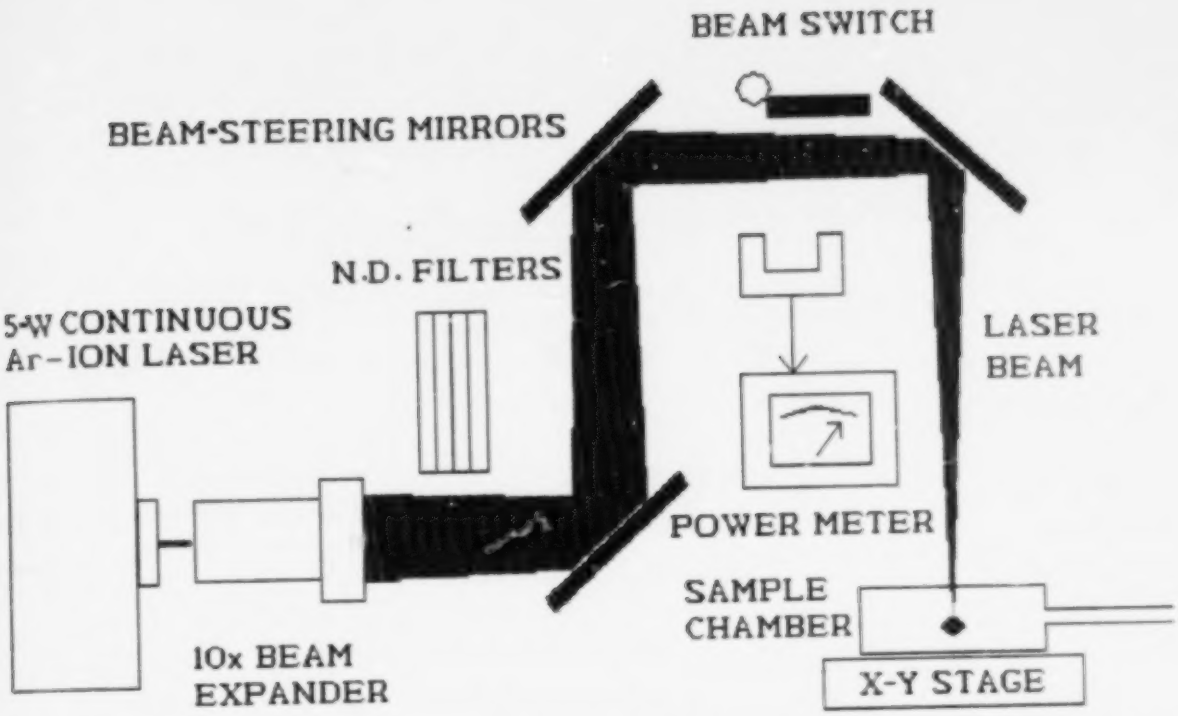

Figure 2. Schematic diagram of the laser system of the GLM. The neutral density (N.D.) filters are inserted into the light path during focusing and alignment of the laser beam.

W/mm^2. Both the input and output lenses are coated with a multilayer, antireflection coating that reduces the combined surface reflection, scatter, and absorption losses to less than 0.8 percent for wavelengths from 400 to 700 nm and thus minimizes power loss within the expander.

The laser beam is directed vertically into the sample chamber by first-surface beam-steering mirrors held on adjustable mounts attached to vibration-damped rods (Newport model 675). Rotational and angular adjustment of the mirrors, by micrometers, permits easy and precise alignment of the focused laser beam with the crosshairs of the microscope. The mirrors are specifically coated (Newport DM.5) for efficient reflection (>99 percent) of wavelengths from the argon-ion laser. A beam switch (Advanced Kinetics LSW–25–L, modified with mirror for argon-ion wavelengths) installed in the beam path is used to switch the beam away from the sample chamber and into the detector of a power meter, which also serves as a beam dump. The switch is a safety feature but also permits monitoring of the laser beam power independent of the internal laser power meter. For visually focusing the beam and aligning the beam with the microscope crosshairs, neutral density filters that decrease the beam intensity by 1/1000 are temporarily inserted into the beam path.

The Sample Chamber

The sample chamber (fig. 3) consists of two 2.75-in stainless steel vacuum flanges (Varian Conflat). The bottom of the chamber is a bored out blank flange into which a short inlet tube is welded. The end of the inlet tube is fitted with a 1.33-in mini-Conflat Flange that is attached to a 0.375-in flexible stainless steel hose leading to the remainder of the extraction/cleanup system. All welds are internal to the vacuum system to prevent virtual leaks. The upper part of the sample chamber is an unmodified, 1.5-in, zero-length viewport with 7056 glass (Varian 954–5127).

The sample planchette, which sits upon a stainless steel platform to minimize the distance to the vacuum viewport and improve the viewing angle of the microscope, is made of copper. It has 21 machined and numbered sample wells 1.04 mm deep and 3.5 mm in diameter into which loose sample grains are placed. The planchette is covered with a 1.6 mm-thick pyrex coverplate to prevent fused material from being deposited onto the vacuum viewport and to retain mineral grains, particularly biotite and hornblende, in their sample wells.

The sample chamber is attached to an *x-y* stage, which permits motion of the chamber under the laser beam.

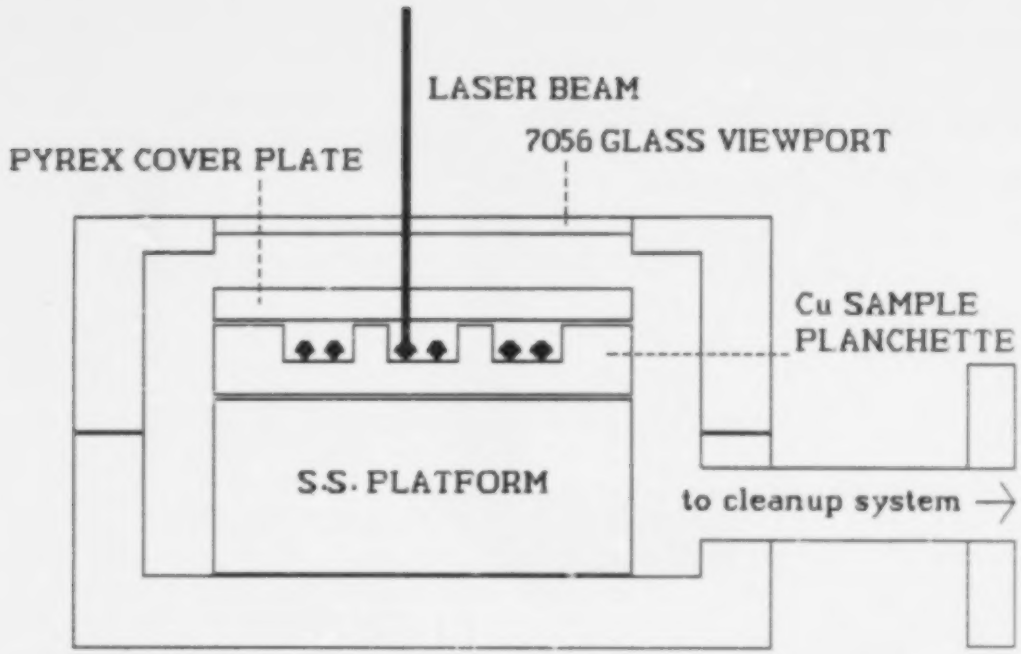

Figure 3. Schematic diagram of the sample chamber of the GLM. The body of the chamber is made from two 2.75-in Varian Conflat flanges. S.S., stainless steel.

Once the beam is aligned with the microscope crosshairs, then any grain can be brought coincident with the crosshairs, and hence the laser beam, by manipulation of the stage.

A stereo microscope is used to align the laser beam with the individual mineral grains by use of the ocular crosshairs and to view the samples when the laser beam is not directed into the sample chamber. The microscope is fitted with a solid state color closed circuit television camera (Panasonic WV–CD120) attached to a 13-in monitor (Panasonic CT–1330M) and a video cassette recorder (Panasonic NV–8950) that are used to monitor and record the fusion process. The microscope is equipped with a long-pass filter between the objective lenses and the sample chamber. The filter is of colored glass with 50 percent transmission at 550 nm and a transmission of approximately 10^{-5} for wavelengths less than 520 nm.

The Extraction/Cleanup System

The extraction/cleanup system (fig. 4) is constructed primarily of type 304 stainless steel and has a volume of approximately 175 cm^3, which includes the sample chamber and the flexible stainless steel hose. The small volume permits admission of 90 percent of the sample gas into the mass spectrometer by expansion and obviates the need for gas transfer by the use of activated charcoal. The system consists of a Zr-V-Fe getter (SAES St172/H1/16–10/300C) operated at room temperature to remove primarily hydrogen, a Zr-Al getter (SAES AP10–GP) operated at 450 °C to crack hydrocarbons and remove other reactive gases, and a pyrex LN_2 finger to isolate condensibles. The system is pumped by a 20-L/s vacion pump (Varian 911–5030) and a 50-L/s turbomolecular pumping system (Balzers TSU–050), both equipped with bakeable valves (Varian 951–5014) so that they can be isolated from the system. The entire system, including the sample chamber, which can be removed from the *x-y* stage and placed in the oven, can be baked at 300 °C.

The Mass Spectrometer

The mass spectrometer is a 90° sector direction-focusing instrument with a radius of 15 cm (Mass Analyser Products model 216) and a Baur-Signer ion source (model GS–98). It is equipped with a Zr-Al getter (SAES GP–50W) operated at room temperature and a 30 L/s vacion pump (Varian 911–5032) and is bakeable to 350 °C. The analyzer was manufactured and assembled by means of techniques designed to provide the lowest possible background and desorption.

The magnetic field is switched under digital computer control by a Hall probe for feedback. Resolution of the field control system is 15 ppm in mass per digital step. The

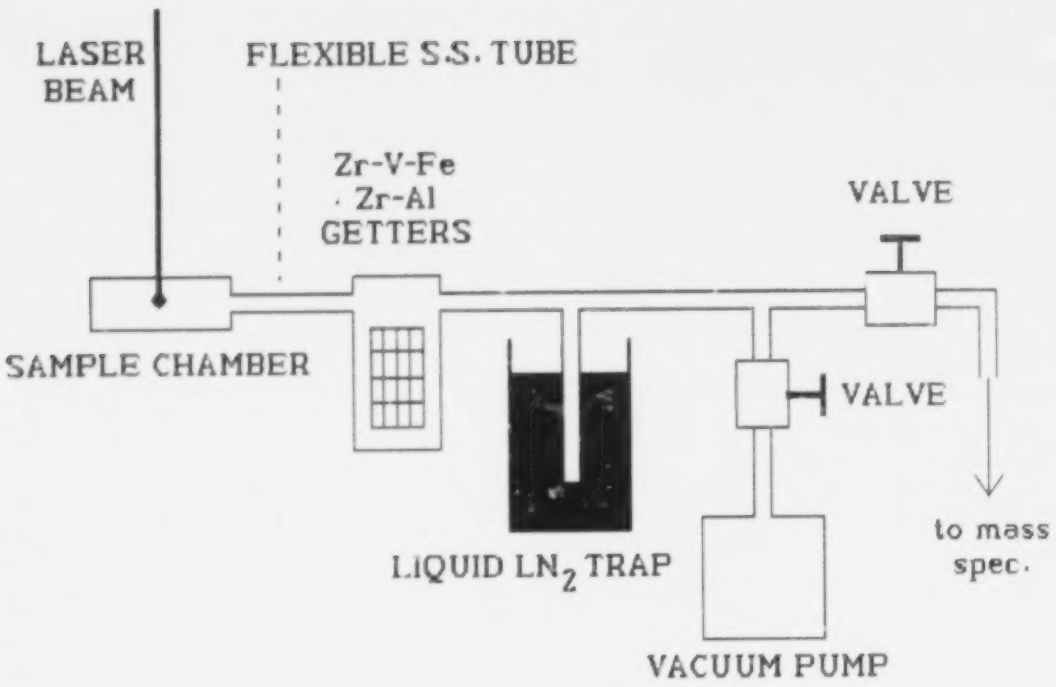

Figure 4. Schematic diagram of the extraction/cleanup system of the GLM. Only one of the two vacuum pumping systems is shown, for simplicity. S.S., stainless steel.

magnet has curved-entrance pole faces to correct for α^2R aberrations. With the source defining slit 0.4 mm wide and the collector entrance slit 1.44 mm wide, the flat-topped peak to half-width ratio is approximately 0.7 at a resolution of 80.

The instrument has tandem ion collectors: a retractable Faraday cup mounted on a linear-motion feedthrough and a fixed 18-stage electron multiplier (Thorn EMI 9642/3A). Each collector has an independent amplifier, the outputs from which are fed to a Solartron (model 7060) integrating digital voltmeter (IDVM). In normal operation only the electron multiplier is used. Mass spectrometer operation is completely controlled by computer (Zenith 241) via an IEEE–488 buss controller. The total volume of the analyzer is less than 1,500 cm^3.

OPERATION

Operation of the GLM is relatively simple (fig. 5). First, the extraction line is isolated from the vacuum pumps by closing the valves, and the line is left static for 5 min. The getters and LN_2 trap are active, so the accumulating "blank" is also cleaned during the isolation. Next, the mass spectrometer is isolated from its vacuum pump, and the blank is admitted to the spectrometer and analyzed. For the blank analysis, four sets of data are taken. Each set consists of

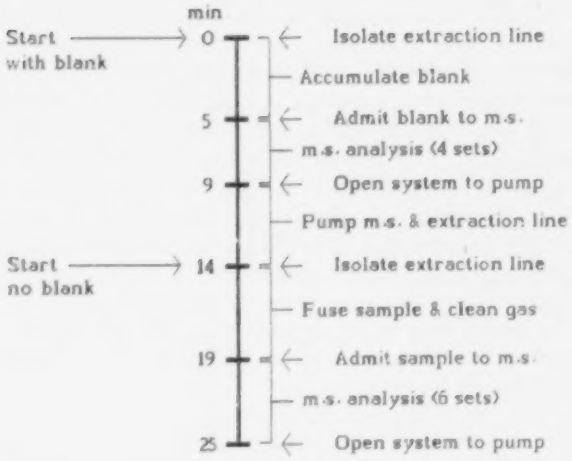

Figure 5. Schematic diagram of procedure for the GLM. Without the background measurement, a $^{40}Ar/^{39}Ar$ age analysis takes less than 10 min. m.s., mass spectrometer.

four 1.28-s integrations for each of the masses 36, 37, 38, 39, and 40 as well as the baselines between each mass. After the blank analysis, the extraction line and mass spectrometer are pumped for 5 min, then the extraction line is again isolated for 5 min. During this isolation period, the sample

Table 1. Typical results of $^{40}Ar/^{39}Ar$ total fusion age analyses by use of the GLM continuous laser system

[$^{40}Ar_r$, radiogenic ^{40}Ar]

Sample no.	Mineral (grain size)	No. of grains	Sample wt.[1] (micrograms)	$^{40}Ar_r$		Age[2] (Ma)
				10^{-14} mol	percent	
85G001	sanidine	10–11	100	2.07	98.4	28.17 ± .32
	(180–250 μm)	12–14	–	4.27	99.1	28.21 ± .21
		10–14	190	4.53	99.0	28.24 ± .21
		10–14	–	5.95	98.8	28.11 ± .19
		20–25	–	10.00	99.1	28.21 ± .17
		10–12	–	6.34	99.5	28.27 ± .19
					mean =	28.20 ± .06
MMHb–1	hornblende	1	22	3.59	99.9	520.2 ± 3.7
	(180–250 μm)	3	72	7.77	99.7	515.5 ± 2.9
		3	–	4.68	99.8	521.2 ± 3.3
		3	35	5.70	99.9	521.7 ± 3.1
		2	–	2.54	99.8	516.1 ± 4.5
		4–5	137	14.18	99.3	521.6 ± 2.7
					mean =	519.4 ± 2.8
SB–3	biotite	1	15	2.81	98.5	164.3 ± 1.5
	(180–250 μm)	4	15	3.21	99.7	164.1 ± 1.4
		3	–	1.73	97.7	161.2 ± 2.1
		4	17	3.69	97.5	163.0 ± 1.3
		2	18	4.25	98.3	164.8 ± 1.2
		4	–	3.03	97.7	161.4 ± 1.4
					mean =	163.1 ± 1.5

[1] Estimated from the diameter of the glass sphere that often forms on fusion.

[2] Decay constants: $\lambda_\epsilon = 0.581 \times 10^{-10}\ yr^{-1}$, $\lambda_\beta = 4.692 \times 10^{-10} yr^{-1}$. Errors are estimates of the standard deviation of precision (Dalrymple and Lanphere, 1971).

is fused or heated (for an incremental heating experiment), and the sample gas is cleaned by exposure to the getters and LN_2 trap. At the end of the 5-min period, the mass spectrometer is isolated from its pump and the sample gas is admitted to the spectrometer and analyzed, taking six sets of data. The entire procedure takes approximately 25 min. After the analysis, the extraction line and mass spectrometer are pumped for 10 min, during which time the data from the analysis are reduced, and the procedure then may be repeated. During data reduction, the blank for each isotope is subtracted from the sample values after appropriate adjustments for baselines.

Because the blank is relatively constant during the day, it is not necessary to measure it before each sample analysis; thus, the time for an analysis is reduced to less than 10 min (fig. 5), and 20 to 30 age measurements are allowed during a single day. Complete automation of the system will eliminate operator error and permit unattended operation but will not shorten the time for a single analysis.

PERFORMANCE CHARACTERISTICS

Mineral grains are fused easily and in a few seconds with the GLM laser. The power required to fuse a mineral grain of given mass is primarily a function of the power density, which varies inversely as the square of the focused beam radius and the ability of the mineral grain to absorb laser light of 488-nm and 514-nm wavelength. The dark minerals, biotite and hornblende, for example, require only 100 to 200 mW for complete fusion. Muscovite and plagioclase typically require 1 to 2 W. In contrast sanidine, which is relatively transparent to the argon-ion laser beam, commonly requires 5 to 7 W and once fused into a transparent glass sphere cannot be refused with the power available.

In addition to single grains, multiple grains can be fused simultaneously, provided the grains are in proximity to one another in the sample pan. For multiple-grain fusion, which is sometimes desirable to increase sample mass and hence precision, the laser is focused on a single grain. When that grain melts, the surface tension of the silicate melt "pulls in" the surrounding grains, which are incorporated into the melt. As many as 30 grains of 300-μm diameter have been fused in less than 2 s by this method.

The mass spectrometer has a fundamental sensitivity of 1.3 mA/torr with the ion source operated at an emission current of 250 μA. The electron multiplier, which is operated at 2.25 kV, provides a gain of about 4.2×10^4 and

a realized sensitivity of about 3.5×10^{-14} mol/V of signal to the IDVM. The data system has a dynamic range of 10^6 and a lower measurement limit of 0.00001 V, so that it is possible to determine argon-isotope ratios to within ±0.1 percent even for isotope concentrations less than 1×10^{-14} mol. The sensitivity of the instrument could be increased by a factor or two or three by increasing the emission current of the ion source, and perhaps another factor of two or so (relative to multiplier noise) by increasing the voltage to the multipler, but so far this has not proved necessary.

The background in the mass spectrometer is typically 1.5×10^{-18} mol (9×10^5 atoms) for m/z=36, 1×10^{-17} mol for m/z=37, 2×10^{-18} mol for m/z=39, and 1.5×10^{-16} mol for m/z=40. A typical blank, which includes the mass spectrometer background, consists of about 2×10^{-18} mol of m/z=36, 1×10^{-17} mol of m/z=37, 4×10^{-18} mol of m/z=39, and 4×10^{-16} mol of m/z=40. The blank varies somewhat from day to day but is relatively constant throughout the day. For example, the mean blank for 27 January 1988 consisted of $(4.38\pm0.14)\times10^{-16}$ mol of m/z=40, $(4.16\pm0.35)\times10^{-18}$ mol of m/z=39, $(9.72\pm0.35)\times10^{-18}$ of m/z=37, and $(1.74\pm0.69)\times10^{-18}$ of m/z=36, where the errors are the calculated standard deviations of seven blank runs taken during the day.

The precision of age measurements made with the GLM is as good or better than can be obtained by any other analytical method, even though the masses of sample analyzed are typically three to four orders of magnitude smaller than required by other analytical techniques. Table 1 shows some representative results for three different minerals. The precision of the results for the sanidine and the hornblende are typical. The biotite, however, is from a quartz diorite that has suffered some postcrystallization heating, and the poorer precision for that mineral is probably due to inhomogeneity among the individual grains.

Because the GLM system is so clean, the atmospheric contamination is very low, and radiogenic ^{40}Ar percentages commonly exceed 99 percent. The very low atmospheric contamination is at least partly responsible for the excellent precision obtained by the GLM.

The Toronto continuous laser probe has been successfully used to date single potassium feldspar grains as young as 0.5 Ma (LoBello and others, 1987). The results obtained to date with the GLM indicate that the system is capable of producing ^{40}Ar/^{39}Ar ages of good precision for samples having high ratios of K/Ca as young as 0.1 Ma and has the potential of resolving differences in apparent age of as little as 0.2 percent for high K/Ca samples as young as a few Ma (Dalrymple and Duffield, 1988).

FUTURE IMPROVEMENTS

The following improvements are planned for the GLM.

1. Improved beam expander that will allow precise focusing and beam alignment.
2. Motor-driven valves that will allow computer control of the extraction line and mass spectrometer isolation and pumping cycles, as well as the introduction of the sample gas into the mass spectrometer.
3. Infrared microscope that will permit temperature measurement of individual grains for incremental heating and permit complete computer control of the heating/fusion process.
4. Motor drives for the *x*-*y* stage that will allow computer control of the sample positioning.

ACKNOWLEDGMENTS

I am grateful to Derek York, Chris Hall, and Tullis Onstott, who generously shared their thoughts on continuous laser probes and the designs of the Toronto and Princeton instruments. I also thank R.E. Criss, M.A. Lanphere, W.C. Shanks, and N.D. Sherrill, who reviewed the manuscript and offered several suggestions for improvement.

REFERENCES CITED

Bray, C.J., Spooner, E.T.C., Hall, C.M., York, D., Bilis, T.M., and Krueger, H.W., 1987, Laser probe ^{40}Ar/^{39}Ar and conventional K/Ar dating of illites associated with the McClean unconformity-related uranium deposits, north Saskatchewan, Canada: Canadian Journal of Earth Science, v. 24, p. 10–23.

Brereton, N.R., 1970, Corrections for interfering isotopes in the ^{40}Ar/^{39}Ar dating method: Earth and Planetary Science Letters, v. 8, p. 427–433.

Dalrymple, G.B., and Duffield, W.A., 1988, High precision ^{40}Ar/^{39}Ar dating of Oligocene rhyolites from the Mogollon-Datil volcanic field using a continuous laser system: Geophysical Research Letters, v. 15, p. 463–466.

Dalrymple, G.B., and Lanphere, M.A., 1969, Potassium-argon dating: San Francisco, W.H. Freeman and Co., 258 p.

———1971, ^{40}Ar/^{39}Ar technique of K-Ar dating: A comparison with the conventional technique: Earth and Planetary Science Letters, v. 12, p. 300–308.

Dalrymple, G.B., Alexander, E.C., Jr., Lanphere, M.A., and Kraker, G.P., 1981, Irradiation of samples for ^{40}Ar/^{39}Ar dating using the Geological Survey TRIGA reactor: U.S. Geological Survey Professional Paper 1176, 55 p.

Glass, B.P., Hall, C.M., and York, D., 1986, ^{40}Ar/^{39}Ar laser-probe dating of North American tektite fragments from Barbados and the age of the Eocene-Oligocene boundary: Chemical Geology (Isotope Geosciences Section), v. 59, p. 181–186.

Lanphere, M.A., and Dalrymple, G.B., 1971, A test of the ^{40}Ar/^{39}Ar age spectrum technique on some terrestrial materials: Earth and Planetary Science Letters, v. 12, p. 359–372.

Layer, P.W., Hall, C.M., and York, D., 1987, The derivation of ^{40}Ar/^{39}Ar age spectra of single grains of hornblende and biotite by laser step-heating: Geophysical Research Letters, v. 14, p. 757–760.

LoBello, Ph., Feraud, G., Hall, C.M., York, D., Lavina, P., and Bernat, M., 1987, $^{40}Ar/^{39}Ar$ step-heating and laser fusion dating of a Quaternary pumice from Neschers, Massif Central, France: The defeat of xenocrystic contamination: Chemical Geology (Isotope Geoscience Section), v. 66, p. 61–71.

Megrue, G.H., 1967, Isotopic analysis of rare gases with a laser microprobe: Science, v. 157, p. 1555–1556.

———1973, Spatial distribution of $^{40}Ar/^{39}Ar$ ages in lunar breccia 14301: Journal of Geophysical Research, v. 78, p. 3216–3221.

Merrihue, C., and Turner, G., 1966, Potassium-argon dating by activation with fast neutrons: Journal of Geophysical Research, v. 71, p. 2852–2857.

Müller, H.W., Plieninger, T., James, O.B., and Schaeffer, O.A., 1977, Laser probe ^{39}Ar-^{40}Ar dating of material from consortium breccia 73215: Proceedings of the 8th Lunar Science Conference, p. 1489–1499.

Phillips, D., and Onstott, T.C., 1986, Argon diffusion profiles in mantle derived phlogopite: A laser probe study [abs.]: EOS, Transactions of the American Geophysical Union, v. 67, p. 1248.

Sutter, J.F., and Hartung, J.B., 1984, Laser microprobe $^{40}Ar/^{39}Ar$ dating of mineral grains in situ: Scanning Electron Microscopy, v. 4, p. 1525–1529.

York, D., and Hall, C.M., 1986, Continuous-laser probe thin section chrontouring of sediments [abs.]: TERRA cognita, v. 6, p. 117.

York, D., Hall, C.M., Yanase, Y., Hanes, J.A., and Kenyon, W.J., 1981, $^{40}Ar/^{39}Ar$ dating of terrestrial minerals with a continuous laser: Geophysical Research Letters, v. 8, p. 1136–1138.

Application of the Laser Microprobe (LAMMA 1000) to the Microanalysis of Coal Constituents

By Paul C. Lyons, John J. Morelli,[1,2] and David M. Hercules[1]

Abstract

The laser microprobe mass analyzer (LAMMA 1000) was used to detect trace and minor elements in coal components. Laser micro mass spectrometry (LAMMS) signatures were obtained easily on the maceral and mineral components in coal. Macerals in the same coal sample show major differences with respect to partitioning of many elements such as Li, K, Ca, Ti, Fe, Sr, Y, and Ba. The elemental partitioning differences are explained as being due primarily to varying amounts of illite, kaolinite, phosphate minerals, and other minerals occurring as microscopic and submicroscopic inclusions in the macerals. Other elements, such as Cr, V, and Ga, which were commonly detected in vitrinites, appear to be mainly of organic origin.

This microprobe can be applied to semiquantitative microanalysis of some elements detected in coal, but development of this capability will probably require the use of maceral standards that are of maximum purity and that have uniform concentrations of the elements to be analyzed. Early indications from our group's experience with LAMMS are that it has potential for elemental mapping of minerals and macerals in coal and for organic analysis of coal macerals but needs more development. Stable isotopic ratios such as $^{40}Ca/^{88}Sr$, $^{40}Ca/^{138}Ba$, $^{23}Na/^{40}Ca$, $^{88}Sr/^{24}Mg$, and $^{56}Fe/^{40}Ca$, obtained by LAMMS across maceral and mineral interfaces, could be related to marine, terrestrial, and diagenetic geochemistry.

INTRODUCTION

Coal is a mixture of minerals and discrete morphological organic components called macerals. Chemically, coal is composed of inorganic compounds (minerals) and complex macromolecular organic compounds. Microprobe techniques have been applied to the microchemical analysis of coal. These techniques include the (1) electron microprobe (Dutcher and others, 1964; Minkin and others, 1979; Denoyer and others, 1982; and Lyons and others, 1984a), (2) scanning transmission electron microscope (STEM; Minkin and others, 1983; Palmer and Wandless, 1985), (3) scanning electron microscope/energy-dispersive X-ray analysis (SEM/EDX; Augustyn and others, 1976; Boateng and Phillips, 1976; Finkelman and others, 1976; Stanton and Finkelman, 1979; Finkelman, 1981; Lyons and others, 1982; Makjanic and others, 1983; Thorne and others, 1983), (4) proton-induced X-ray emission (PIXE: Chen and others, 1981; Minkin and others, 1982, 1987), and (5) secondary ion mass spectrometry (SIMS; Gaines and Paige, 1983; Wolf and others, 1983; McIntyre and others, 1985; Martin and McIntyre, 1985; Martin and others, 1986). These techniques were applied principally to elemental analysis of the inorganic (mineral) components and, to a lesser extent, to the elements in the maceral components of coal. Traditionally, microchemical techniques have been used for elements with atomic number (Z) = 11 to 92.

The application of laser micro mass spectrometry (LAMMS; Morelli and others, 1988) to the microanalysis of coal offers the advantage of both inorganic and organic analysis. Pioneering work on the application of the laser to coal analysis was done in the middle and late 1960's (Vastola and Pirone, 1966; Joy and others, 1968; Karn and Sharkey, 1968; Vastola and others, 1970). This work is summarized in Vastola and McGahan (1983). Early problems with the technique were due to poor beam resolution (optimum 50 μm) and the lack of high-speed computer techniques for data acquisition, reduction, and analysis. Nevertheless, early laser spectral data were obtained for the microlithotype vitrite from different rank coals (Vastola and Pirone, 1966). However, the early work of Vastola and Pirone (1966) indicated that a laser surface microprobe that had fine spatial resolution was needed for maceral microanalysis; this need was fulfilled by the development of LAMMA (LAser Microprobe Mass Analyzer) 1000 in the early 1980's (Heinen and others, 1983; Hercules, 1984).

This paper illustrates some of the work accomplished in the laser microanalysis of coal, a team effort by the U.S. Geological Survey and the University of Pittsburgh, Department of Chemistry. This work has resulted in LAMMS spectra of common macerals and minerals found in bituminous coal. The potential of LAMMS for stable isotopic geochemistry of coal is briefly addressed.

COAL MACERAL TERMINOLOGY

The fundamental organic constituents of coal are called macerals, which are comparable to minerals in inorganic rocks. Macerals are classified on the basis of optical reflectance into three groups: the liptinite, vitrinite, and inertinite maceral groups, in order of increasing reflec-

[1] University of Pittsburgh, Department of Chemistry, Pittsburgh, PA 15260.

[2] Present address: McDonnell Douglas Research Laboratories, P.O. Box 516, St. Louis, MO 63166.

tance. However, reflectance is rank dependent, so this order of reflectance is not applicable in low-volatile bituminous and higher rank coals.

Macerals are distinguished in reflected or fluorescent light on the basis of morphology, size, degree of cellularity, fluorescent properties, and botanical origin (Stach and others, 1982). In Euramerican bituminous and anthracitic coals, macerals of the vitrinite group are the major macerals and typically occur in bands. Three distinct macerals of this group are telinite (cellular), collinite (noncellular), and vitrodetrinite (small, angular, transported vitrinite). Generally, both vitrinite and inertinite macerals in Euramerican bituminous coals are nonfluorescent, so they can be readily distinguished from liptinite macerals. Thus, an oval-shaped fluorescent body with a lumen would be called sporinite, a maceral of the liptinite maceral group. Fusinite, like telinite, is cellular but has a higher reflectance like other inertinite macerals.

The Advantages of the LAMMA System

There are several compelling reasons for considering the application of the LAMMA 1000 (Leybold-Heraeus GMBH) to the microanalysis of coal constituents. It is basically a surface analytical system that has a depth of penetration of 0.1 to several micrometers (Leybold-Heraeus GMBH, undated). LAMMS can be performed on the same polished surface that is analyzed by standard optical petrographic procedures (Stach and others, 1982). Also, the LAMMS has the capability to analyze most elements, including the light elements ($Z < 11$), such as H, Li, Be, and B, and it has parts-per-million sensitivity for many elements (Hercules, 1984). The LAMMA 1000 can function as both an organic and inorganic microprobe, unlike most microprobes. It is capable of detecting in coal elemental ions and organic and inorganic molecular ions up to a mass of 500 amu. Also, after a vacuum is obtained, this system can analyze coal constituents rapidly, and many spectra can be stored in 1 min. An adequate vacuum normally takes about 10 to 20 min to obtain for small coal samples. Another advantage of the LAMMA 1000 is that relatively large samples, up to 10 cm across, can be mounted on the sample holder so that large areas of the coal surface containing many macerals and minerals can be analyzed. It is therefore possible to map the distribution of large macerals and minerals (Wilk and Hercules, 1987; Morelli and others, 1987) and to determine the spatial distribution of elements or compounds. This capability is particularly useful near mineral and maceral interfaces. The rapid LAMMS ionization (15 ns) also reduces the likelihood of extensive ion recombination (Balasanmugan and others, 1981). Another advantage is that that the shallow depth of penetration of the laser beam reduces the possibility of analyzing material not seen on the surface by optical techniques. SIMS (Blattner and Evans, 1980) is limited by sample roughness and surface contamination that are not problems with LAMMS; preliminary laser bursts using LAMMA can eliminate surface contaminants.

There are other advantages to microanalysis when the LAMMA 1000 is used. First and foremost is its capability to analyze areas as small as 5 μm in diameter. Thus, macerals, maceral inclusions, cell walls, mineral matter, and even intracellular inclusions can be analyzed for both their inorganic and organic constituents. LAMMS can analyze hydrocarbon components that cannot be analyzed by most other microprobes. Because data can be obtained readily on both cations and anions by reversing polarity, both positive and negative LAMMS spectra can be obtained. Also, LAMMS ionization can be varied over a range of ionization conditions by the use of variable laser power density (Denoyer and others, 1982; Leybold-Heraeus GMBH, 1983). Thus, complex organic components can be ionized under conditions that promote parent-ion formation without causing extensive fragmentation and possible molecular rearrangement.

THE LAMMA 1000 SYSTEM

A schematic of the LAMMA 1000 system is shown in figure 1. Details of this system can be found in Hercules (1984), Lyons and others (1984b, 1987), and Morelli and others (1988).

The LAMMA 1000 can be used in either an observation or analysis mode. The laser, ionization, and products can be observed in the analysis mode under 100 × total magnification. A 250 × total magnification is used in the observation mode to pinpoint the target with *x*-*y*-*z* manipulators having movements of 70, 50, and 50 mm, respectively.

A Q-switched, high-power Nd YAG (Yttrium Aluminum Garnet) laser is used for analysis. The fundamental mode is $\lambda = 1{,}060$ nm, but the LAMMA is normally used in the frequency-quadrupled mode of $\lambda = 265$ nm. The laser pulse is 20 ns. The intensity of the laser can be continuously varied with crossed polarizers so that optimum ionization can be obtained by trial-and-error procedures. A time-of-flight mass spectrometer having a drift tube of 1.8 m is used for separation of the ions that are always singly charged, either negatively or positively, in coal microanalysis. Either negative or positive ions can be analyzed by the LAMMA system.

The electronics of the LAMMA 1000 system consist of an open 17-dynode copper-beryllium multiplier that has good signal-to-noise characteristics, as shown in LAMMS spectra of this paper. The signal is preamplified (10 ×) and fed into a Biomation 8100 transient recorder that has 2 kilobytes of memory (Morelli and others, 1988). The data can be transferred in digital form from the transient

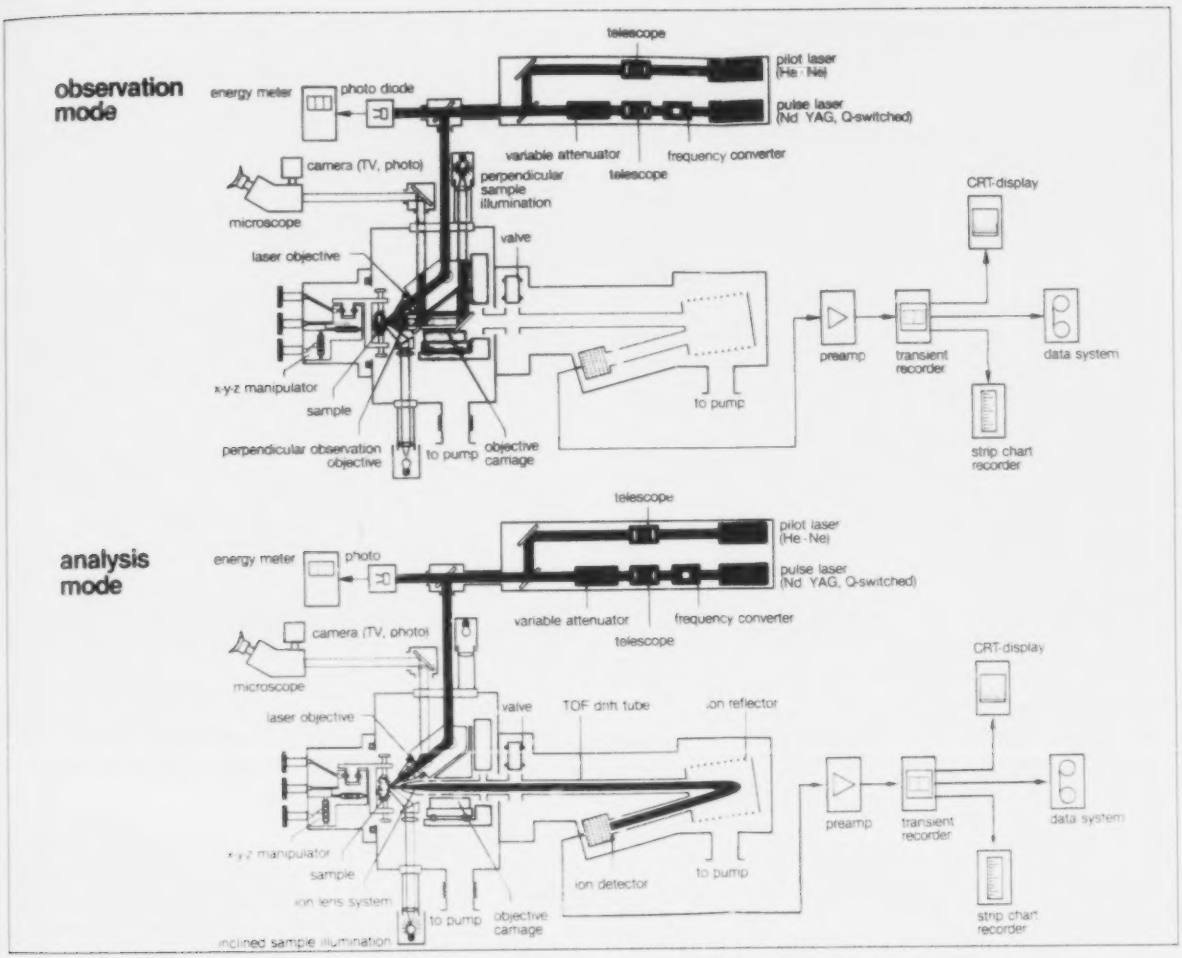

Figure 1. Schematic of the LAMMA 1000. Courtesy of Leybold-Heraeus GMBH.

recorder to a Hewlett Packard 1000E Series computer. Under ideal conditions, the spectral resolution of the LAMMA instrument is approximately 800 ($m/\Delta m$) at mass 350. Data can be transferred from the computer to a graphics terminal where hard copies of individual or averaged spectrum can be plotted in about 5 min. The spectra can also be observed or monitored on an oscilloscope during analysis. A maximum of 60 LAMMS spectra can be obtained on the same target during 1 min of analysis.

Detection Limits

The detection limits for selected metals analyzed by the LAMMA 1000 system are usually in the range 0.1 to 1.0 ppm (Hercules, 1984). For the alkali metals (Li, Na, K, Rb, Cs), the detection limits are 0.1 to 0.5 ppm, and for the alkaline earth elements (Mg, Ca, Sr, Ba), the detection limits are 0.4 to 1.0 ppm. The detection limits for Al, Pb, Ag, and U are 0.2, 0.3, 1.0, and 2.0 ppm, respectively.

These limits were determined in a noncoal matrix and may represent optimum detection limits. However, from quantitative data (Lyons and others, in press a), it is known that gallium, in the range 1 to 10 ppm, can be detected by LAMMS in a vitrinite (coal) matrix. Thus, it is assumed on the basis of relative ionization potential that the detection limits for the alkali metals in a vitrinite matrix are this good or better.

The LAMMS detection limits for some elements are relatively poor. Hercules (1984) reported a detection limit of 20 ppm for copper. The detection limit for silicon in the positive spectrum is much less. For example, Lyons and others (in press b) show that LAMMS spectra of clays, which contain major amounts of Si, show only weak peaks for Si but intense peaks for Al. This same study shows that

Figure 2. SEM micrograph of a microcrater (melt type) produced by the LAMMA 1000 in a coal maceral. Note the micron and submicron mineral grains in and around the microcrater. Scale 10 μm. Micrograph courtesy of John Evans, U.S. Geological Survey.

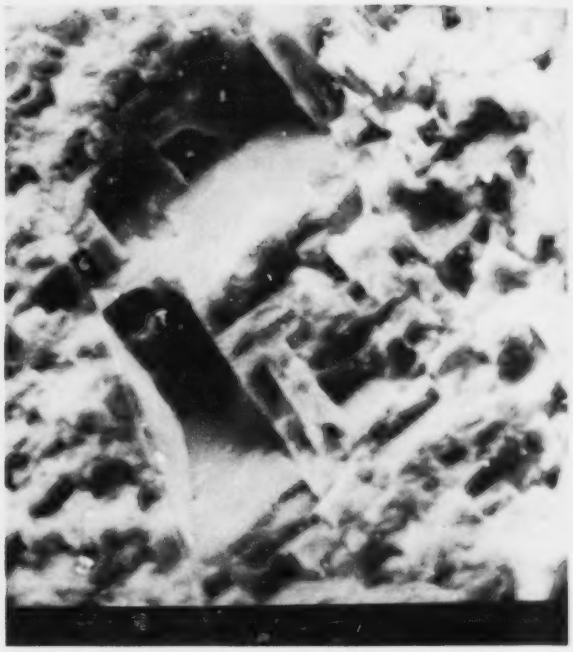

Figure 3. Photomicrograph of the microcraters (shock type) produced by the LAMMA 1000 in the mineral magnesite. Scale 10 μm. Micrograph courtesy of Johann Gieb, Institut für Geologie und Paleontologie, Lahnberge, Federal Republic of Germany.

the common appearance of silicon in clays as SiO_2^- and SiO_3^- ions in negative LAMMS spectra perhaps explains silicon's lack of detection in LAMMS positive spectra. Apparently, silicon does not readily form stable Si^+ ions during LAMMS ionization but forms mainly oxygen-containing anions.

Crater Characteristics

The optimum LAMMA crater is subcircular and about 1 μm in diameter (Hercules, 1984). In a coal matrix, the crater is elliptical, about 5 μm in shortest dimension and 20 μm in longest dimension, and has a maximum depth estimated to be 5 μm but may be considerably less when lower laser power densities are used. This type of crater, here called a melt crater (fig. 2), is different from the crater produced in some minerals where the cleavage appears to have influenced the crater characteristics. The latter type of crater, here called a shock crater (fig. 3), appears to show the characteristics of a shock impact, although there was probably also melting, ionization, and devolatilization near the center of the crater. In some minerals such as spodumene, the depth of the laser crater produced by the LAMMA 1000 has been determined optically to be about 0.1 μm (E. Roedder, U.S. Geological Survey, retired, personal commun., 1986). After each laser burst on the same target, the crater size appears to enlarge slightly in diameter but less significantly in depth. Thus, the LAMMA 1000 is *not* useful for depth profiling in coal.

Relationship of LAMMA to Other Microprobes

Although most microprobes have beam spatial resolution of <10 μm, the depth of penetration of the various microprobe beams varies considerably. For example, PIXE has a minimum depth of penetration of 50 μm or more (Minkin and others, 1982), whereas SIMS has an penetrative depth of 0.1 μm or less (McIntyre and others, 1985). Thus, SIMS is surface sensitive and LAMMS is not except at lower power densities. Also, both SIMS and LAMMS can detect the entire range of elements from hydrogen to uranium.

The nature of the beam varies among most microprobes. In the SEM/EDX, PIXE, and SIMS, charged particles are used: electrons; protons; and Ar, He, Cs, and O ions, respectively. Alternatively, LAMMS uses a neutral beam, normally ultraviolet light (λ = 265 nm), for microanalysis.

These differences have some analytical consequences. Typically, if charged particles are used for anal-

ysis, there are charging problems encountered during the analysis. The charging problem is circumvented by coating the analyte with some conductor such as graphite or gold. Although LAMMS has some minor charging problems, the surface does *not* require coating because a change in the electrostatic potential can usually eliminate any charge that may build up.

Another difference among the microprobes is the method of detection of the atoms or ions. The SEM/EDX and PIXE use X-ray spectrometers for detection of the atoms, whereas LAMMS and SIMS use mass spectrometers, which are based on the mass/charge (m/z) differences among the ions.

Preliminary collaborative work on the same samples by use of PIXE, SIMS, and LAMMA, in cooperation with J.A. Minkin, (U.S. Geological Survey) and R.R. Martin (University of Western Ontario), indicates that SIMS and LAMMS yield similar mass spectra. Thus, SIMS and LAMMS spectra can be compared easily.

Procedures Used in LAMMA Coal Microanalysis

The procedures used in LAMMS analysis of coal constitutents are given in Lyons and others (1987). First, coal macerals are observed on polished surfaces through a petrographic microscope, and circles (250 to 500 μm in diameter) are inscribed so that the general micro-area can be found easily with the LAMMA 1000 optical subsystem. Photomicrographs are used as maps to help align the laser optics on the target.

Both positive and negative LAMMS spectra are normally obtained in separate analysis steps. However, most of the elemental signals, excluding the halogens (F, Cl, and Br), are seen in the positive-ion mode, which is the mode most frequently used in the microanalysis of coal constituents. The optimum laser energy is determined by trial-and-error techniques outside of the target area or on a similar maceral or mineral. Normally, a laser energy at the source equivalent to about twice the threshold of ionization is used. The sample-stage manipulators are used to align the laser on the target. One or more single preliminary spectra are obtained to optimize laser energy conditions; subsequently, 12 additional spectra are obtained and averaged. The data for the individual and averaged spectra are stored in digital form in the computer.

In coal microanalysis, unit mass calibration of the LAMMA 1000 is easily accomplished by use of commonly occurring coal isotopic signals having known m/z values at 23 (^{23}Na), 39 (^{39}K), and 56 (^{56}Fe) in the lower mass range and the organic peaks at m/z 61 (C_5H), 85 (C_7H), and 109 (C_9H) in the higher mass range. Peaks at m/z up to about 500 have been observed occasionally in LAMMS coal analysis, but generally the signals are below m/z 200.

LAMMA SIGNATURES AND THEIR INTERPRETATIONS

Because LAMMS is fundamentally, at present, a qualitative tool with parts-per-million sensitivity for most elements (Hercules, 1984), it is ideally suited to the detection of elements in minerals and macerals in coal (see Lyons and others, 1984b, 1987; Morelli and others, 1988). These suites of elements and occasional molecular peaks in particular macerals or minerals have been referred to as LAMMA "fingerprints" (that is, signatures, Lyons and others, 1987). The reproducibility of major isotopic peaks is ±8 percent (at best), which gives LAMMS the potential for semiquantitative analysis (Morelli and others, 1988).

It has been shown that two types of vitrinite (telocollinite and corpocollinite) in the same coal can be distinguished by LAMMS (Lyons and others, 1987). On the basis of Li, Ca (m/z 40 and 44), Ti, Sr, Ba, F, Cl, and a peak at m/z 65, which were lacking or absent in the nonbanded vitrinite (corpocollinite), these authors demonstrated the potential of LAMMS as a "fingerprinting" system. In addition, they showed that the mineral pyrite (FeS_2), identified on the basis of chemistry and crystal habit, is readily "fingerprinted" with LAMMS peaks at m/z 32, 56, 88, 112, 120, 144, and 176, which correspond to S^+, Fe^+, FeS^+, Fe_2^+, FeS_2^+, Fe_2S^+, and $Fe_2S_2^+$, respectively.

Other LAMMS spectra of vitrinites are shown in figures 4 and 5. Figure 4 is the positive LAMMS spectrum of vitrinite from the Indiana V coal bed (Middle Pennsylvanian, Late Carboniferous), which shows an intense vanadium signal at m/z 51 and a weaker signal at m/z 39 (potassium). These are contrasted with the vitrinite from the Liddell coal bed (Permian) of the Sydney Basin, Australia (fig. 5), which shows peaks at m/z 90 (zirconium) and 161–164 (dysprosium). These two elements are rarely observed in the LAMMS spectra of coal macerals. However, the similarity of the spectra in most other respects may indicate that similar soil conditions or geochemical processes, rather than different plant precursors (Carboniferous tropical plants as opposed to Permian temperate Gondwana plants), exercised the major control over the microchemistry of the vitrinites.

The signal at m/z 65 in positive spectra of vitrinite and inertinite macerals has not been unequivocally identified. It is a molecular signal, not an elemental signal, because there is no major isotopic peak at m/z 65; typically it is relatively intense in high-sulfur coals (fig. 4) and in some intertinite macerals (fig. 6). Where m/z 65 is extremely intense, as in figure 6, an inertinite maceral from the Wilgus coal bed, Ohio, it is associated with peaks at m/z 64 and 66. That these three peaks also occur when there is little or no iron indicates that they are *not* due to pyritic sulfur. S_2 and compound ions SO_2, SO_3, and so on, would normally be expected in negative spectra and not in positive

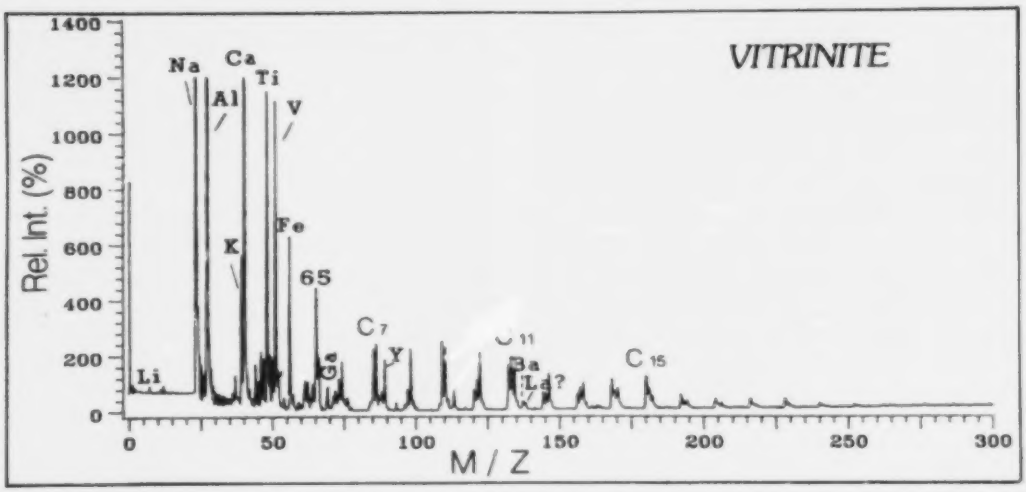

Figure 4. LAMMS positive spectrum of vitrinite from the Indiana V coal bed (Middle Pennsylvanian), Lynnville mine, Warwick County, Indiana. Peaks at C_7, C_{11}, and C_{15} are part of a C_{odd} series; m/z 65 = HS_2(?). Rel. Int., relative intensity.

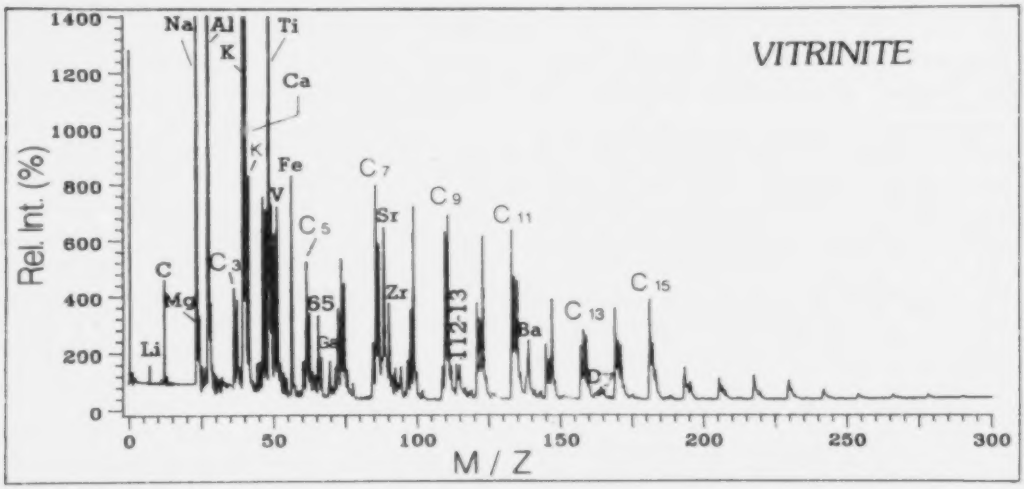

Figure 5. LAMMS positive spectrum of vitrinite from the Liddell coal bed (Permian), Sydney Basin, Australia. Peaks at C_3–C_{15} are C_{odd} series; m/z 65 = HS_2(?); m/z 112–113 = cadmium(?). Rel. Int., relative intensity.

spectra. We speculate here that the peaks at m/z 64, 65, and 66 are due to S_2^+, HS_2^+, and $H_2S_2^+$ of probable organic origin. LAMMS characterization of organosulfur compounds is necessary to support this assertion. Note also in figure 6 in the LAMMS spectrum that the peak at m/z 77 is interpreted as a benzene derivative (C_6H_5), which would be expected from pyrolysis of aromatic compounds. Also, note in the LAMMS signature of this maceral the relatively intense peaks for Mg, Ca, Co, Sr, Y, Ba, and La.

Negative LAMMS spectra usually are not informative in the microanalysis of coal macerals. However, the spectrum of vitrinite from the Appalachian basin (fig. 7) shows the presence of O (m/z 16), OH (m/z 17), F (m/z 19), and Cl (m/z 35 and 37). The O, OH, F, and Cl could be derived from clays in the vitrinite (see Lyons and others, 1987). However, these elements could also be a part of organic molecules composing the vitrinite.

Some examples of positive-ion LAMMS spectra of minerals from coals are shown in figures 8 through 11. Sphalerite from the Herrin (No. 6) coal bed of the Illinois basin (fig. 8) shows the principal Zn isotopic signals at m/z 64, 66, and 68, as well as the signals at m/z 56 and 58,

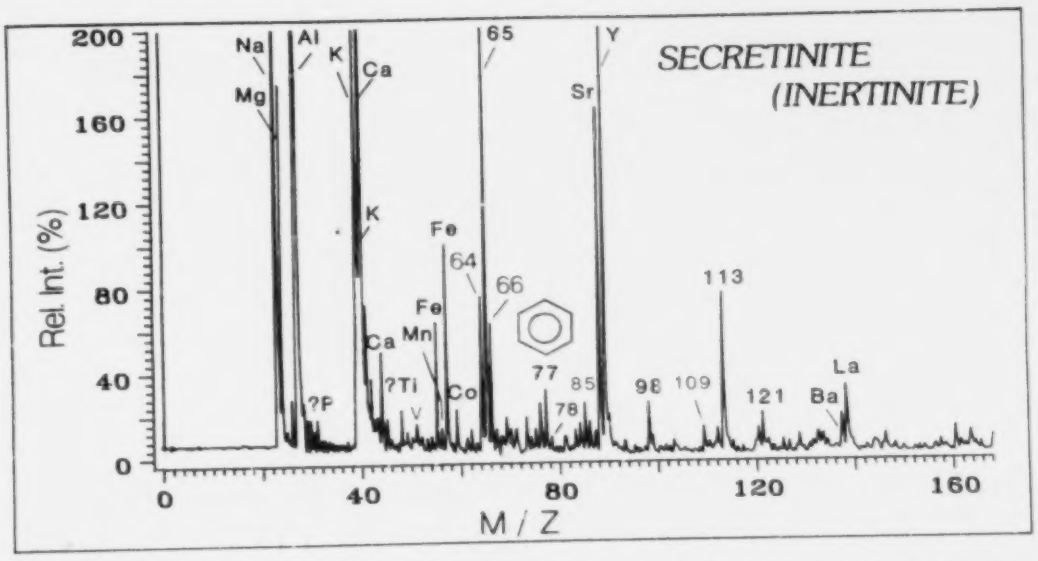

Figure 6. LAMMS positive spectrum of the inertinite maceral secretinite (see Lyons and others, 1986) from the Wilgus coal bed (Upper Pennsylvanian), Lawrence County, Ohio. Coal sample courtesy of G.K. Merrill, University of Houston. Interpretations of numbered mass to charge peaks are 64 = S_2(?); 65 = HS_2; 78 = C_6H_6 (benzene); 85 = C_7H; 98 = C_8H_2; 109 = C_9H; 113 = not identified; 121 = $C_{10}H$. Rel. Int., relative intensity.

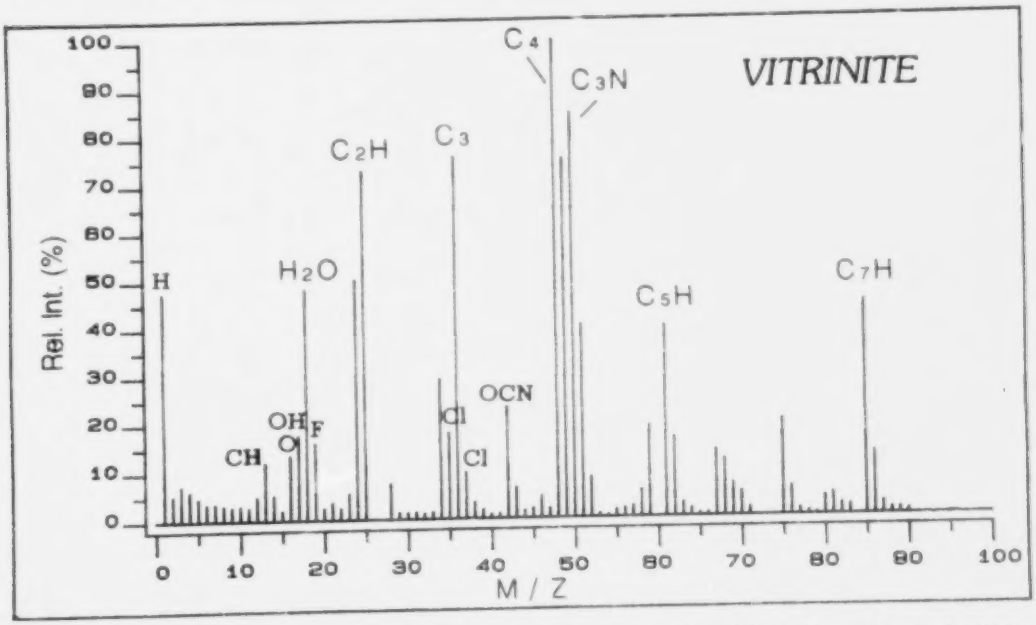

Figure 7. LAMMS negative spectrum of vitrinite from the Raymond coal bed (Upper Pennsylvanian), Kanawha County, West Virginia. Rel. Int., relative intensity.

corresponding to Fe and Ni, respectively. Peaks at m/z 69 and 71 are probably attributable to gallium. A LAMMS spectra of cleat calcite (calcite filling a microfracture) with associated impurities is shown on figure 9. The signals at m/z 40, 42, and 44 indicate high concentrations of calcium. The peaks at m/z 27 (due to Al) and at 54 and 56 (due to Fe) perhaps indicate some aluminum-bearing mineral impurities and, perhaps, Fe in the calcite structure. Figure 10 is a LAMMS spectrum interpreted as "illite" associated with the inertinite maceral of figure 6. The signals at m/z 27, 39 and

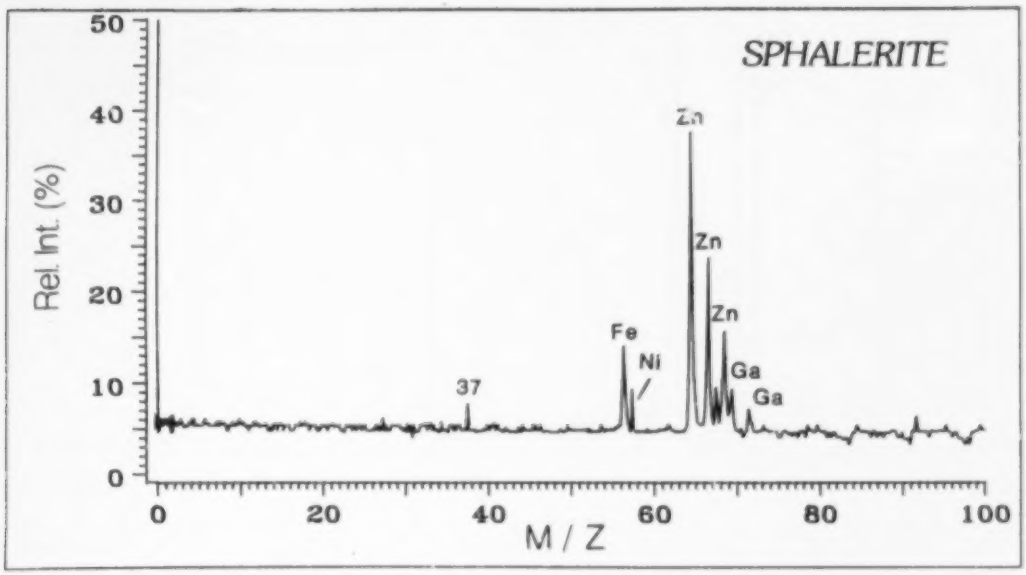

Figure 8. LAMMS positive spectrum of sphalerite from the Herrin (No. 6) coal bed (Middle Pennsylvanian), Peoria County, Illinois. Interpretation of peak at m/z 37 = C_3H. Rel. Int., relative intensity. Specimen courtesy of James C. Cobb, Kentucky Geological Survey.

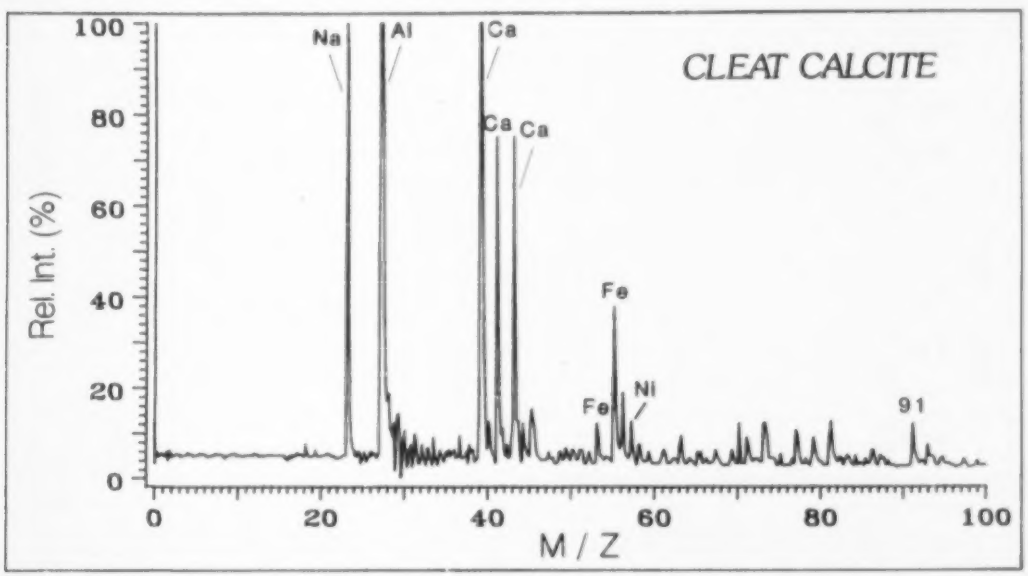

Figure 9. LAMMS positive spectrum of cleat calcite with aluminum-bearing mineral impurities and, perhaps, iron in the calcite structure. The sample is from the Wilgus coal bed (Upper Pennsylvanian), Lawrence County, Ohio. Rel. Int., relative intensity.

41, and 54 and 56 correspond to Al, K, and Fe, respectively, which are the major LAMMS signals characteristic of illite (Lyons and others, in press b). The titanium signal at m/z 48 may have the same mineralogical origin. The alkaline earth peaks at m/z 24, 40 and 44, 88, and 138, which correspond to Mg, Ca, Sr, and Ba, respectively, are interpreted as being due to one or more associated minerals (for example, calcite or other carbonate minerals, phosphates, barite, and so on). An arsenic-bearing pyrite in the cell walls of the Lower Bakerstown coal bed, Maryland (fig. 11) may imply the derivation of arsenic (as well as sulfur) from degradation of organic matter in the cell walls. Minkin and others (1984) previously noted arsenic in pyrite in coal by microprobe techniques.

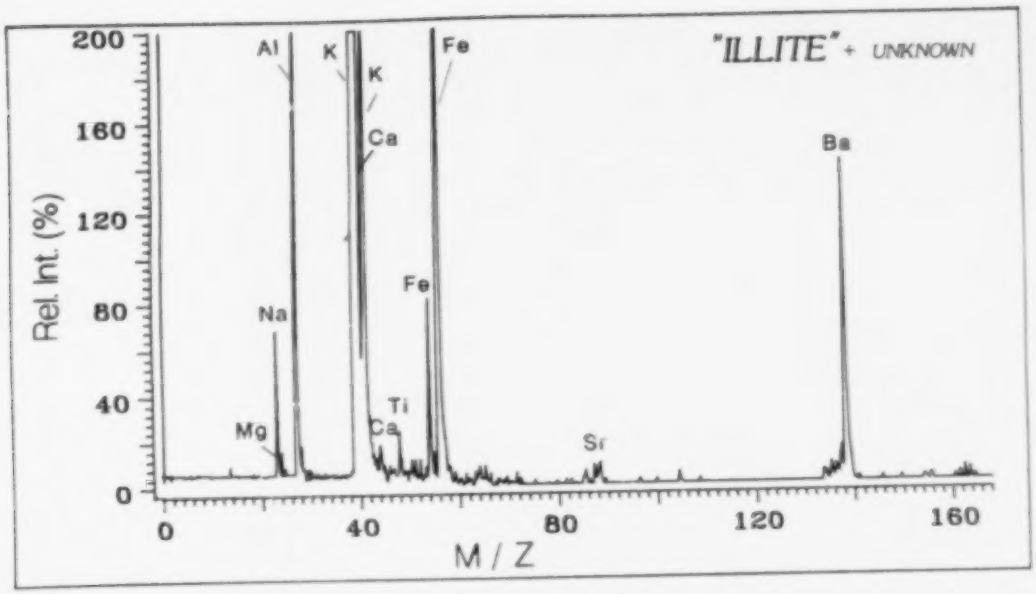

Figure 10. LAMMS positive spectrum of "illite" from the Wilgus coal bed (Upper Pennsylvanian), Lawrence County, Ohio. Coal sample courtesy of G.K. Merrill, University of Houston. Rel. Int., relative intensity.

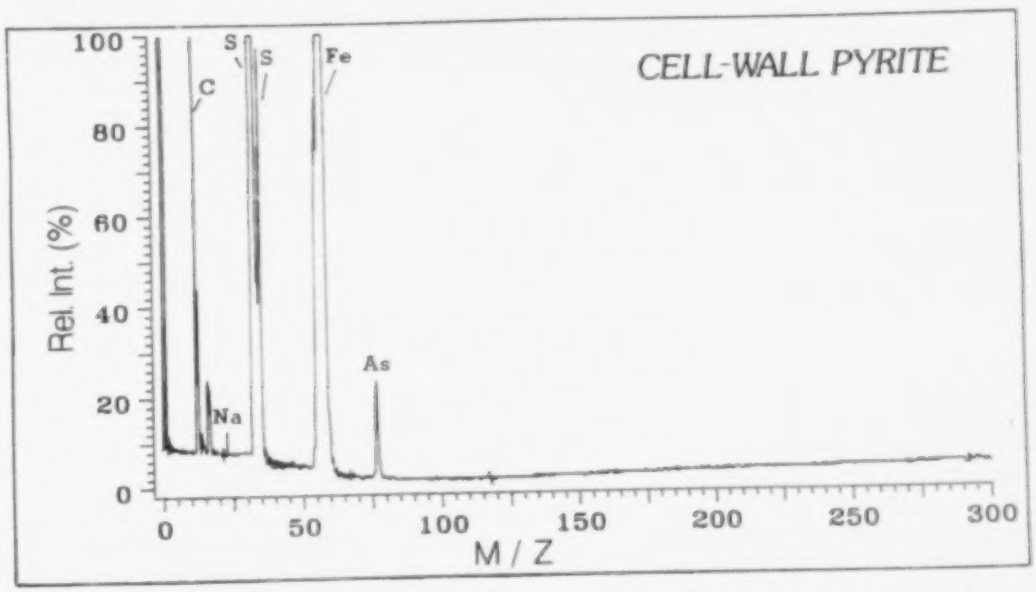

Figure 11. LAMMS positive spectrum of arsenic-bearing pyrite in the cell wall of a pyrite coal ball, Lower Bakerstown coal bed (Upper Pennsylvanian), Garrett County, Maryland. Rel. Int., relative intensity.

Potential of LAMMA for Organic Microanalysis of Macerals

LAMMS has already been applied to the "fingerprinting" of organic polymers. For example, epoxy and paraffin (Nitsche and others, 1978), polyethylene, polystyrene, and phenoxl resin (Dutta and Talmi, 1982) and other organic polymers (Gardella and others, 1986, Hercules and others, 1982; Hercules, 1983) have been successfully "fingerprinted" by LAMMS techniques. Their work therefore opens up the possibility that macerals also can be "fingerprinted" by LAMMS, because organic polymers are homogeneous

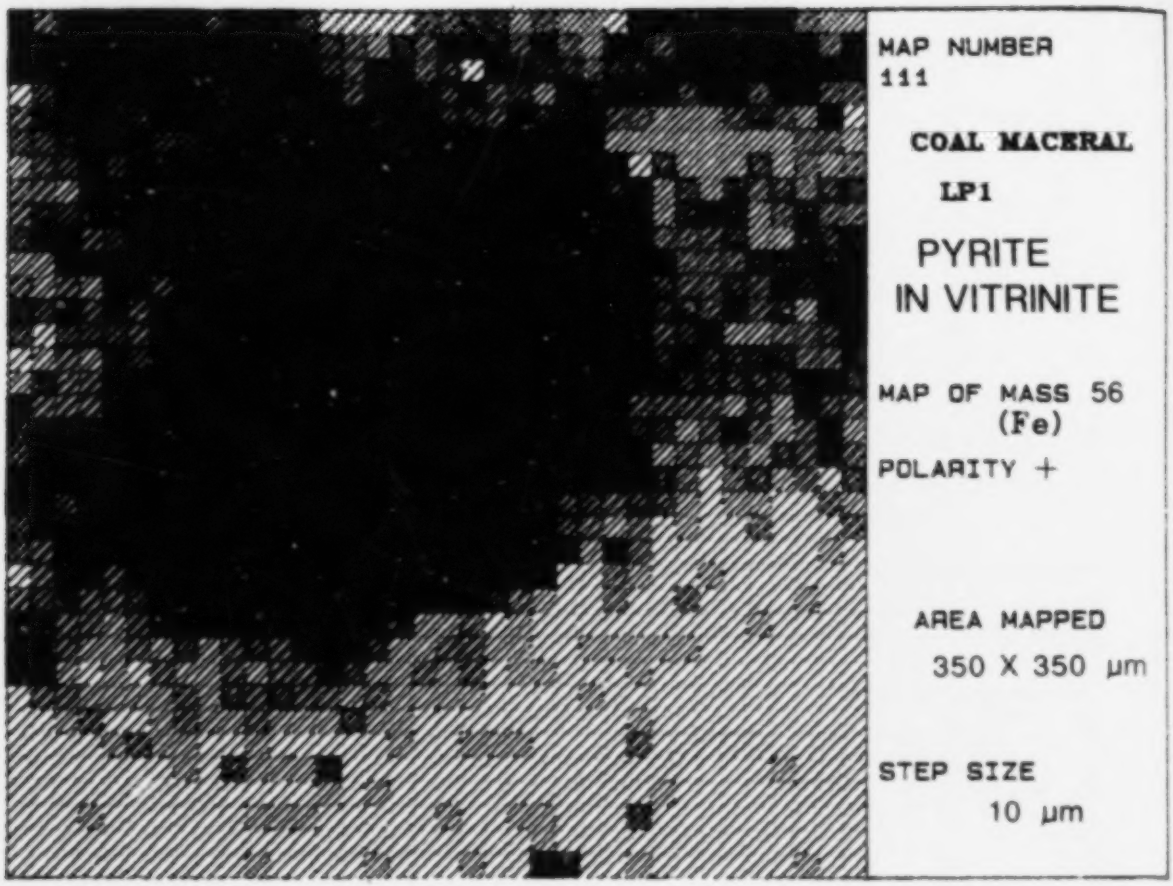

Figure 12. LAMMS map of pyrite (black) in a vitrinite matrix (light), unnamed coal bed (Middle Pennsylvanian), Narragansett basin, Massachusetts. The map is of m/z 56 (Fe^+). From Wilk and Hercules (1987) and Morelli and others (1987). The 350-µm by 350-µm area covered in the figure represents 1,225 LAMMS analyses at 10-µm intervals. The map essentially shows a pyrite grain (~250 µm across) surrounded by vitrinite.

substances somewhat like macerals. More experimentation with different laser energies and microchemical surface techniques is necessary to test this possibility.

POTENTIAL OF LAMMA FOR QUANTITATIVE WORK IN COAL MICROCHEMISTRY

Preliminary work indicates that LAMMS has some semiquantitative potential for the microchemical analysis of coal macerals (Morelli and others, 1988). Reproducibility of the laser energy is ±8 percent at best; therefore, averaging of multiple LAMMS shots (as shown for mixtures of benzalkonium chloride) is necessary for quantitive analysis (Hercules, 1984). Calibration plots for lithium and lead in standard samples indicate a linear relationship (Kaufmann and Hillenkamp, 1979; Wechsung and others, undated) in which standard deviations are less than 5 percent at concentrations greater than 10 ppm (Kaufmann and Hillenkamp, 1979). However, reproducibilities in practical analyses are generally ±15 percent (relative standard deviation) at best. Hercules (1984) has shown, using average LAMMS data, that there is a good correlation with high-performance liquid chromatography for the quantitative analysis of some organic compounds. Positive correlation of analytical results were also obtained between ^{19}F NMR (Nuclear Magnetic Resonance) and LAMMS in analyses of polyvinylidine fluoride (Hercules, 1983).

LAMMA "MAPPING"

Illustrations of LAMMS for mapping of the distribution of elements in a vitrinite matrix are given in figures 12 and 13. Figure 12 shows the distribution of Fe^+ (m/z 56) from pyrite in a vitrinite matrix (Wilk and Hercules, 1987;

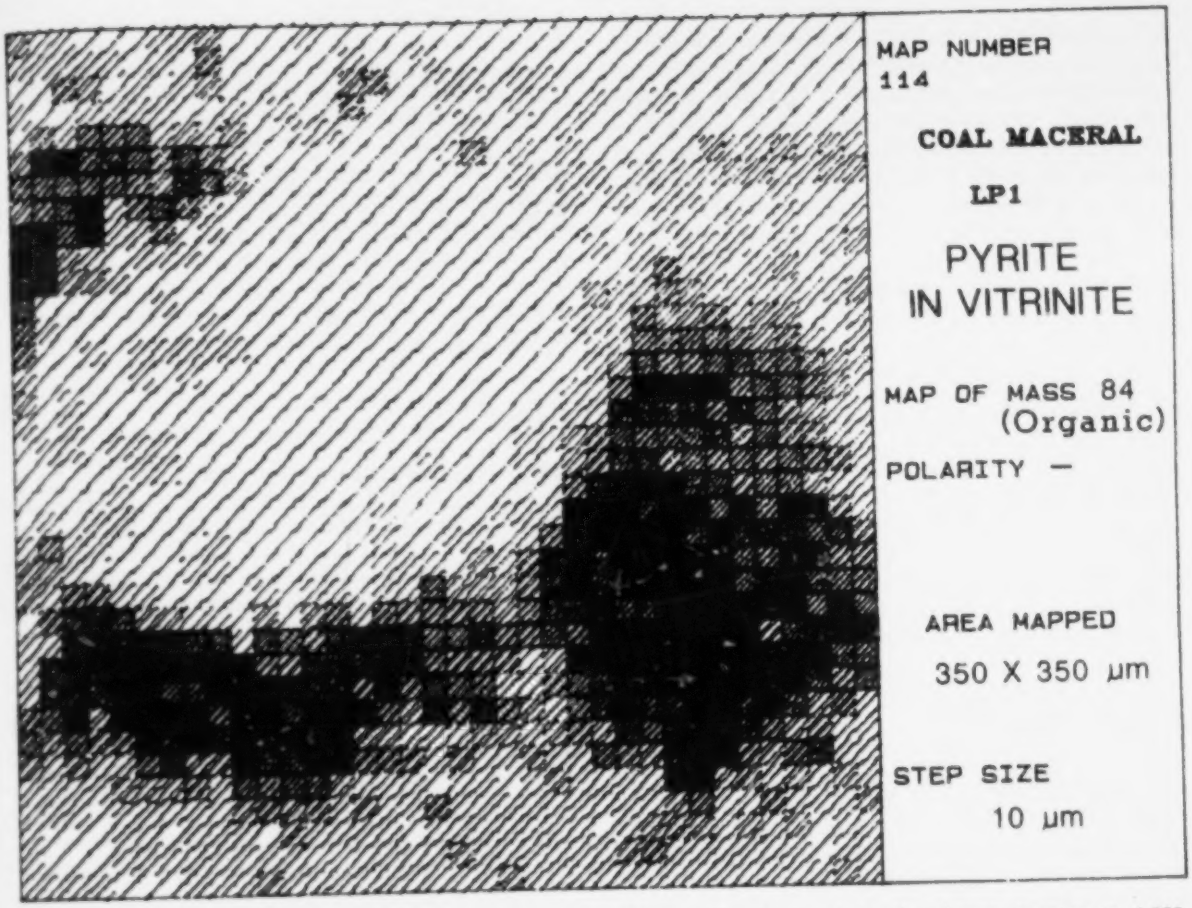

Figure 13. LAMMS map of pyrite (light area left of center) surrounded by vitrinite (darker areas), unnamed coal bed (Middle Pennsylvanian), Narragansett basin, Massachusetts. Map is of m/z 84 (C_7^-), negative spectra, same area as figure 12. From Wilk and Hercules (1987). The 350-µm by 350-µm area covered in the figure represents 1,225 LAMMS analyses at 10-µm intervals. The map essentially shows a pyrite grain (~250 µm across) surrounded by vitrinite.

Morelli and others, 1987). Figure 13 shows the same area at m/z 84 (C_7^-). The 350 µm × 350 µm area covered in figures 12 and 13 represents 1,225 LAMMS analyses at 10-µm intervals. The "maps" (figs. 12 and 13) essentially show a pyrite grain (~250 µm across) surrounded by vitrinite. Although SIMS is clearly superior to LAMMS in mapping (McIntyre and others, 1985, Martin and others, 1986), both have ion-imaging capability for imaging of the same microareas. However, charging problems with SIMS (Wilk and Hercules, 1987) may make it less superior in this respect for automated mapping of microsurfaces of coal.

POTENTIAL OF LAMMS FOR STABLE ISOTOPIC GEOCHEMISTRY OF COAL

The application of stable isotopic geochemistry has focused on the elements H, C, N, O, and S (Anderson and Arthur, 1983), all abundant in coal. Although LAMMS has sufficient mass resolution to detect the more abundant isotopes such as ^{12}C, ^{13}C, ^{16}O, ^{18}O, and ^{32}S and ^{34}S, the natural variation in abundance of the isotopes is too small for LAMMS, at present, to be a viable technique for measuring fractionation of the isotopes because the reproducibility of the major isotopic signal in LAMMS is ±8 percent. With averaging of many isotopic ratios, reproducibility might be improved to a few percent, at best, which is still too imprecise for useful isotopic ratio determination.

One of the limitations of the LAMMA system is that, at present, it has only unit mass resolution. For element identification and determination of concentration, the masses of interest must be free of interference by other elements or molecules, such as hydrocarbons (C_xH_y), having the same nominal mass to charge ratio. An example is m/z 27, the same nominal mass to charge for Al and C_2H_3.

Multiply charged ions used in spark-source mass spectrometry to verify the presence of many elements are not available from the laser source. Two techniques can be used to produce interference-free peaks: (1) removal of the carbonaceous material by pretreatment or (2) use of a mass spectrometer of sufficiently high resolving power to "split off" interfering ions in a multiplet spectrum. The combination of a laser ion source and a high-resolution mass-to-charge analyzer would have this capability.

The greatest potential of LAMMS for stable isotopic geochemistry is mapping of common elements found in coal across mineral and maceral interfaces. Thus, $^{40}Ca/^{88}Sr$, $^{40}Ca/^{138}Ba$, $^{23}Na/^{40}Ca$, $^{88}Sr/^{24}Mg$, $^{56}Fe/^{40}Ca$, and other elemental ratios from carbonates, clays, phosphates, barite, and other minerals possibly could be related to saltwater, terrestrial, and diagenetic influences on the peat. Such mapping could be related to $^{34}S/^{32}S$ and $^{16}O/^{18}O$ ratios obtained by conventional techniques from samples from the same bands in the coal. Lyons and others (in press c) have shown that sulfate, probably from marine water, was introduced after the peat was laid down; bacterial sulfate reduction caused a fractionation of sulfur so that the pyrite shows a regular increase of ^{34}S with depth in the peat (coal).

CONCLUSIONS

Recent results (Lyons and others, 1984b, 1987; Morelli and others, 1987) show that the LAMMA 1000 has the capability for qualitative microprobe analysis of trace or minor elements in macerals or minerals in coal. LAMMS signatures can be obtained easily on minerals and on vitrinite and inertinite macerals. The partitioning of elements among closely associated macerals can be studied by use of LAMMS by normalizing isotopic signal intensities to the intensity of the m/z 85^+ organic peak (C_7H) (Morelli and others, 1988).

These studies indicate that some elements, such as Al, K, Ca, Ti, Fe, Sr, and Ba in coal macerals, can be explained as being due to microscopic and submicroscopic mineral matter (fig. 2; see also Minkin and others, 1983; Palmer and Filby, 1984) dispersed in the macerals. Other elements, such as Cr, V, and Ga, which have rather uniform intensities relative to m/z 85^+, appear to be partly or mainly complexed in organic compounds. One challenge for LAMMS is to develop a semiquantitative capability for the microanalyses of coal components, which will probably require the use of maceral elemental standards that have rather uniform elemental concentrations. LAMMS has some potential for mapping isotopic ratios such as $^{40}Ca/^{88}Sr$, $^{40}Ca/^{138}Ba$, $^{23}Na/^{40}Ca$, $^{88}Sr/^{24}Mg$, and $^{56}Fe/^{40}Ca$ across mineral and maceral interfaces in coal. These ratios could be related to $^{16}O/^{18}O$ and $^{32}S/^{34}S$ ratios obtained by conventional techniques and to marine, terrestrial, and diagenetic geochemistry.

ACKNOWLEDGMENTS

The authors thank Z.A. Wilk, formerly of the Chemistry Department, University of Pittsburgh, for supplying the LAMMA maps (figs. 12 and 13); John Evans, U.S. Geological Survey, for allowing us to use his SEM micrograph (fig. 2); Johann Gieb, Institut für Geologie und Paleontologie, Lahnberge, Federal Republic of Germany, for supplying an SEM micrograph (fig. 3); J. Sharkey, University of Pittsburgh, for supplying information on the potential of LAMMS; and C.A. Palmer and R.B. Finkelman, U.S. Geological Survey, for reviewing the paper.

REFERENCES CITED

Anderson, T.F., and Arthur, M.A., 1983, Stable isotopes of oxygen and carbon, and their application to sedimentologic and paleoenvironmental problems, *in* Arthur, M.A., Anderson, T.F., Kaplan, I.R., Veizer, J., and Land, L.S., eds., Stable isotopes in sedimentary geology: SEPM Short Course No. 10, Society of Economic Paleontologists and Mineralogists, p. 1–151.

Augustyn, D., Iley, M., and Marsh, H., 1976, Optical and scanning electron microscopy of brown coals: Fuel, v. 55, no. 1, p. 25–28.

Balasanmugan, K., Tuan, A.D., Day, R.J., and Hercules, D.M., 1981, Some cation and anion attachment reactions in laser desorption mass spectrometry: Analytical Chemistry, v. 53, p. 2296–2298.

Blattner, R.J., and Evans, C.A., Jr., 1980, High-performance secondary ion mass spectrometry: Scanning Electron Microscopy, 1980/IV, p. 55–68.

Boateng, D.A.D., and Phillips, C.R., 1976, Examination of coal surfaces by microscopy and the electron microscope: Fuel, v. 55, no. 4, p. 381–322.

Chen, J.R., Kneis, H., Martin, B., Nobiling, R., Traxel, K., Chao, E.C.T., and Minkin, J.A., 1981, Trace elemental analysis of bituminous coals using the Heidelberg proton microprobe: Nuclear Instruments and Methods, 1/81, p. 151-157.

Denoyer, E., Van Grieken, R., Adams, F., and Natusch, D.F.S., 1982, Laser microprobe mass spectrometry 1: Basic principles and performance characteristics: Analytical Chemistry, v. 54, p. 26A–41A.

Dutcher, R.R., White, E.W., and Spackman, W., 1964, Elemental ash distribution in coal components—Use of the electron probe: Proceedings of the 22d Ironmaking Conference, Iron and Steel Division, The Metallurgical Society of the American Institute of Mining and Metallurgical Engineers, p. 463–483.

Dutta, P.K., and Talmi, Y., 1982, Compositional and structural study of a coal surface using a laser microprobe mass detector: Fuel, v. 61, p. 1241–1244.

Finkelman, R.B., 1981, Modes of occurrence of trace elements in coal: U.S. Geological Survey Open-File Report 81-99, 322 p.

Finkelman, R.B., Stanton, R.W., and Breger, I.A., 1976, Energy dispersive analysis of in situ minerals in coal: Geological

Society of America, Abstracts with Programs, v. 8, no. 6, p. 865–866.

Gaines, A.F., and Paige, F.M., 1983, Comparison of fast atom bombardment, secondary ion, and laser microprobe mass spectrometry as techniques for determining coal structure: Fuel, v. 62, p. 1041–45.

Gardella, J.A., Jr., Hercules, D.M., and Heinen, H.J., 1980, Mass spectrometry of molecular solids: Laser Microprobe Mass Analysis (LAMMA) of selected polymers: Spectroscopy Letters, v. 13, no. 6, p. 347–360.

Heinen, J.J., Meier, S., Vogt, H., Wechsung, R., 1983, LAMMA 1000, a new laser microprobe mass analyzer for bulk samples: International Journal of Mass Spectrometry and Ion Physics, v. 47, p. 19–22.

Hercules, D.M., 1983, Organic mass spectrometry using the laser microprobe: Pure and Applied Chemistry, v. 55, p. 1869–1887.

———1984, Solid state mass spectrometry using a laser microprobe, *in* Voorhees, K.J., ed., Analytical pyrolysis: London, Butterworths, p. 1–41.

Hercules, D.M., Day, R.J., Balasanmugan, K., Dang, T.A., and Li, C.P., 1982, Laser microprobe mass spectrometry 2: Applications to structural analysis: Analytical Chemistry, v. 54, p. 280A–290A.

Joy, W.K., Ladner, W.R. and Pritchard, E., 1968, Laser heating of coal particles in the source of "Time-of-Flight" mass spectrometer: Nature, v. 217, p. 640–641.

Karn, F.S., and Sharkey, A.G., Jr., 1968, Pyrolysis of coal macerals by laser irradiation: Fuel, v. 47, p. 193–195.

Kaufmann, R., and Hillenkamp, F., 1979, LAMMA and its applications: Industrial Research/Development, April 1979, p. 145–152.

Leybold-Heraeus GMBH, 1983, Applications -LAMMA 1000 analysis of steel: Leybold-Heraeus GMBH 190–4000.2, new ed., print 09/82, no. 10, 2 p.

———undated, LAMMA 1000 Laser Microprobe: Leybold-Heraeus GMBH (information brochure), 8 p.

Lyons, P.C., Finkelman, R.B., Thompson, C.L., Brown, F.W., and Hatcher, P.G., 1982, Properties, origin, and nomenclature of rodlets of the inertinite maceral group in coals of the central Appalachian Basin, U.S.A.: International Journal of Coal Geology, v. 1, p. 313–346.

Lyons, P.C., Hatcher, P.G., Minkin, J.A., Thompson, C.L., Larson, R.R., Hamlin, Z.A., and Pheifer, R.N., 1984a, Resin rodlets in shale and coal (Lower Cretaceous), Baltimore Canyon Trough: International Journal of Coal Geology, v. 3, p. 257–278.

Lyons, P.C., Hercules, D.M., Mattern, D., Sellers, G.M., Brown, F.W., Simon, F.O., and Hatcher, P.G., 1984b, Laser microprobe characterization of coal macerals: 1984 International Chemical Congress of Pacific Basin Societies, Honolulu, Hawaii, December 16–21, 1984, Abstracts of Papers, No. 07C14.

Lyons, P.C., Hatcher, P.G., Brown, F.W., 1986, Secretinite: A proposed new maceral of the inertinite maceral group: Fuel, v. 65, p. 1094–1098.

Lyons, P.C., Hercules, D.M., Morelli, J.J., Sellers, G.A., Mattern, D., Thompson-Rizer, C.L., Brown, F.W., and Millay, M.A., 1987, Application of laser microprobe (LAMMA 1000) to "fingerprinting" of coal constituents in bituminous coal: International Journal of Coal Geology, v. 7, p. 185–194.

Lyons, P.C., Palmer, C.A., Bostick, N.H., Fletcher, J.D., Brown, F.W., Brown, Z.A., Krasnow, M.R., and Romankiw, L.A., in press a, Chemistry and origin of minor and trace elements in vitrinite concentrates in a rank series from the Eastern United States, England, and Australia, *in* Lyons, P.C., and Alpern, B., eds., Peat and coal, 2, Coal: Classification, coalification, mineralogy, trace-element chemistry, and oil and gas potential of coal: International Journal of Coal Geology, v. 13.

Lyons, P.C., Hosterman, J.W., Lineman, D., Morelli, J.J., and Hercules, D.M., in press b, Laser microprobe (LAMMA 1000) chemical analysis of clay minerals: Potential application to in situ analysis of clay minerals in coal: XI International Congress of Carboniferous Stratigraphy and Geology, Beijing, China, August 31–September 4, 1987, Compte Rendu.

Lyons, P.C., Whelan, J.C., and Dulong, F.T., in press c, Marine origin of pyritic sulfur in the Lower Bakerstown coal bed, Castleman coal field, Maryland (U.S.A.), *in* Lyons, P.C., and Alpern, B., eds., Peat and coal, 1: Origin, facies, and depositional models: International Journal of Coal Geology, v. 12.

Makjanic, J., Orlic, I., Jasic, M., Marijanovic, P., Raos, D., Rendic, D., and Valkovic, V., 1983, Elemental analysis of coal using X-ray spectroscopy: Fuel, v. 62, no. 11, p. 1247–1249.

Martin, R.R., and McIntyre, N.S., 1985, An investigation of coal using Secondary Ion Mass Spectrometry (SIMS): 1985 International Conference on Coal Science, Proceedings, p. 796–799.

Martin, R.R., Wiems, B., McIntyre, N.S., Kronberg, B.I., and MacPhee, J.A., 1986, SIMS imaging in the study of coal surfaces: Fuel, v. 65, p. 1024–1028.

McIntyre, N.S., Martin, R.R., Chauvin, W.J., Winder, C.G., Brown, J.R., and MacPhee, J.A., 1985, Studies of elemental distributions within discrete coal macerals: Fuel, v. 64, p. 1705–1712.

Minkin, J.A., Chao, E.C.T., and Thompson, C.L., 1979, Distribution of elements in coal macerals and minerals: Determination by electron microprobe: American Chemical Society, Division of Fuel Chemistry, April 1979, Preprints (papers presented at Honolulu), v. 24, no. 1, p. 242–249.

Minkin, J.A., Chao, E.C.T., Thompson, C.L., Nobiling, R., and Blank, H., 1982, Proton microprobe determination of elemental concentrations in coal macerals: Scanning Electron Microscopy, 1982/I, p. 175–184.

Minkin, J.A., Chao, E.C.T., Thompson, C.L., Wandless, M.V., Dulong, F.T., Larson, R.R., and Neuzil, S.G., 1983, Submicroscopic (<1 μm) mineral contents of vitrinites in selected bituminous coal beds, *in* Gooley, R., ed., Microbeam analysis—1983: San Francisco Press, p. 27–30.

Minkin, J.A., Finkelman, R.B., Thompson, C.L., Chao, E.C.T., Ruppert, L.F., Blank, H., and Cecil, C.B., 1984, Microcharacterization of arsenic- and selenium-bearing pyrite in Upper Freeport coal, Indiana County, Pennsylvania: Scanning Electron Microscopy, 1984/IV, p. 1515–1524.

Minkin, J.A., Chao, E.C.T., Blank, H., and Dulong, F.T., 1987, Proton microprobe analysis of trace-element variations in vitrinites in the same and different coal beds: Scanning Electron Microscopy, v. 1, no. 2, p. 503–513.

Morelli, J.J., Wilk, Z.A., Hercules, D.M., Lyons, P.C., Palmer, C.A., and Fletcher, J.D., 1987, Direct analysis of coal macerals using laser micro mass spectrometry: 4th Annual Pittsburgh Coal Conference, September 28–October 2, 1987, Pittsburgh, Proceedings, p. 166–177.

Morelli, J.J., Hercules, D.M., Lyons, P.C., Palmer, C.A., and Fletcher, J.D., 1988, Monitoring relative elemental concentrations in vitrinite using Laser Micro Mass Spectrometry with the LAMMA instrument: Mikrochimica Acta, 1988, III, p. 105–118.

Nitsche, R., Kaufmann, R., Killenkamp, F., Unsold, E., Vogt, H., and Wechung, R., 1978, Mass spectrometric analysis of laser induced microplasmas from organic samples: Israel Journal of Chemistry, v. 17, p. 181–184.

Palmer, C.A., and Filby, R.H., 1984, Distribution of trace elements in coal from the Powhatan No. 6 mine, Ohio: Fuel, v. 63, p. 318–328.

Palmer, C.A., and Wandless, M.V., 1985, Distribution of trace elements in coal minerals of selected eastern United States coal: 1985 International Conference on Coal Science, Proceedings, p. 792–795.

Stach, E., Mackowsky, M.-Th., Teichmüller, M., Taylor, G.H., Chandra, D., and Teichmüller, R., 1982, Stach's textbook of coal petrology, 3d revision: Berlin, Stuggart Borntraeger, 535 p.

Stanton, R.W., and Finkelman, R.B., 1979, Petrographic analysis of bituminous coal: Optical and SEM identification of its constituents: Scanning Electron Microscopy, 1979/I, p. 465–471.

Thorne, L., McCormick, G., Downing, B., and Price, B., 1983, Some aspects of the analysis of coal by X-ray fluorescence spectroscopy: Fuel, v. 62, no. 9, p. 1053–1057.

Vastola, F.J., and McGahan, L.J., 1983, Laser micropyrolysis of coal macerals: Pennsylvania State University, Final report to the Gas Research Institute (Contract No. 5014–363–0237), 148 p.

Vastola, F.J., and Pirone, A.J., 1966, Use of the laser-micropyrolysis-mass spectrometer in studying the pyrolysis of coal: American Chemical Society, 151st Meeting, Division of Fuel Chemistry, Symposium on Pyrolysis Reactions of Fossil Fuels, Pittsburgh, March 1966 Preprints, v. 10, no. 2, p. C53–C58.

Vastola, F.J., Pirone, A.J., Given, P.H., and Dutcher, R.B., 1970, *in* Friedel, R.A., ed., Spectrometry of fuels, New York, Plenum Press, 344 p.

Wechsung, R., Heinen, H.J., Meier, S., Vogt, H., Hillenkamp, F., and Kaufmann, R., undated, Recent results of organic and inorganic analysis with laser microprobe mass analysis: Leybold-Heraeus GMBH, 14 p.

Wilk, Z.A., and Hercules, D.M., 1987, Organic and elemental ion mapping using laser mass spectrometry: Analytical Chemistry, v. 59, no. 14, p. 1819–1825.

Wolf, M., Migeon, H.N., Butterworth, M., Gaines, A.F., Owen, N., and Page, F.M., 1983, SIMS of organic molecules: International Journal of Mass Spectrometry and Ion Physics, v. 46, p. 487–490.

Quantitative Separation of Authigenic Overgrowths from Mineral Grains by Air-Abrasion and Gravity Settling Techniques

By Paul P. Hearn, Jr., Jerry D. Gandy, John N. Aleinikoff, *and* Raymond W. Werre

Abstract

Techniques that permit the removal and isolation of secondary overgrowths on sand-sized mineral grains are described. The surface layers of sized mineral separates are removed as micron-sized flakes by tangential collisions with the ceramic walls of an air-driven abrasion mill. The abraded surface material is subsequently separated and concentrated by suspension in water and collection on acetone-soluble filters. These simple techniques facilitate the physical separation of samples of authigenic overgrowths or reaction rims on mineral grains for a wide variety of analytical determinations.

INTRODUCTION

In a variety of current problems in applied and experimental geochemistry, it is desirable either to remove or to obtain physical samples of surface layers or coatings on mineral grains. Some examples include (1) separation of secondary overgrowths on feldspar and quartz grains in sedimentary rocks for $^{40}Ar/^{39}Ar$ age determinations, oxygen isotopic analyses, and structural state determinations, (2) separation of inherited components in zircon samples for improved uranium-lead age determinations, (3) removal of glass from sanidine grains in volcanic rocks for more accurate age determinations, (4) removal of secondary generations of chlorite and actinolite from hornblende grains that have undergone retrograde metamorphism, and (5) separation of reaction products developed on grain surfaces during mineral-water reaction experiments. We describe here a simple and relatively inexpensive air-driven abrasion device that is useful in a number of applications of this nature.

The air-driven abrasion mill was modified from a design developed by one of the authors (Aleinikoff) for use in uranium-lead analyses of zircon. The mill differs from earlier designs (Bandyopadhyay, 1976; Krogh, 1982) by having increased sample capacity and by employing sintered alumina as the abrasive medium.

METHODS

Mill Construction and Operating Conditions

The abrasion mill consists of a ceramic abrasion chamber and a stainless steel head assembly that are held together with a simple aluminum frame (fig. 1). The abrasion chambers were machined from pressed blocks of powdered alumina (99.5 percent Al_2O_3) and then sintered at high temperature by a commercial ceramics company (R&W Products, Inc.).

The air inlet port (see fig. 1) is connected to a regulated supply of compressed air, which enters the abrasion chamber through four angled slots on the base of the head assembly and creates a circular flow pattern. Abrasion occurs by tangential collisions between grains and the walls of the abrasion chamber (fig. 2*A–C*). Most of the abraded material is trapped on the stainless steel screens covering the outlet port. Particles that pass through the screens are collected in a simple trap consisting of a graduated cylinder filled to about one-third capacity with water. Most of the coarser particles (the cores of the original grains) remain in the bottom of the mill.

Two different versions of the abrasion mill were constructed—one having an internal diameter of 2 in. and a larger version having an internal diameter of 4 in (fig. 3). The smaller mill is suitable for samples weighing up to 600 mg, while the larger version will accept up to 3 g of sample. Typical inlet air pressures are 2 to 10 psi and 20 to 50 psi (dynamic) for the small and large version, respectively. The 2-in mill uses tygon tubing with simple pipe-to-tubing friction fittings; the higher operating pressures of the 4-in mill necessitate the use of high-pressure hose and fittings on the inlet side, but tygon tubing can still be used for the exhaust line. A trap capable of removing contaminating particulate matter, water, and oil should be placed upstream of the inlet port for both mills.

In general, the speed of the abrasion process is determined by air-flow velocity (controlled by inlet air pressure) and the mass of sample in the mill. Typical run times for separation of overgrowths on potassium feldspar grains range from 2 to 4 hours for maximum sample loads. In cases where less sample is required, as in the removal of overgrowths from zircon, considerably less run time is necessary. In any case, optimum air pressure and run times are best determined by trial and error for specific sample types. In cases where separates of overgrowths or grain coatings are being produced, it is important not to continue the run for too long so as to avoid contamination of the separate. In contrast, when surface layers are being removed to produce clean "cores," longer run times will be necessary.

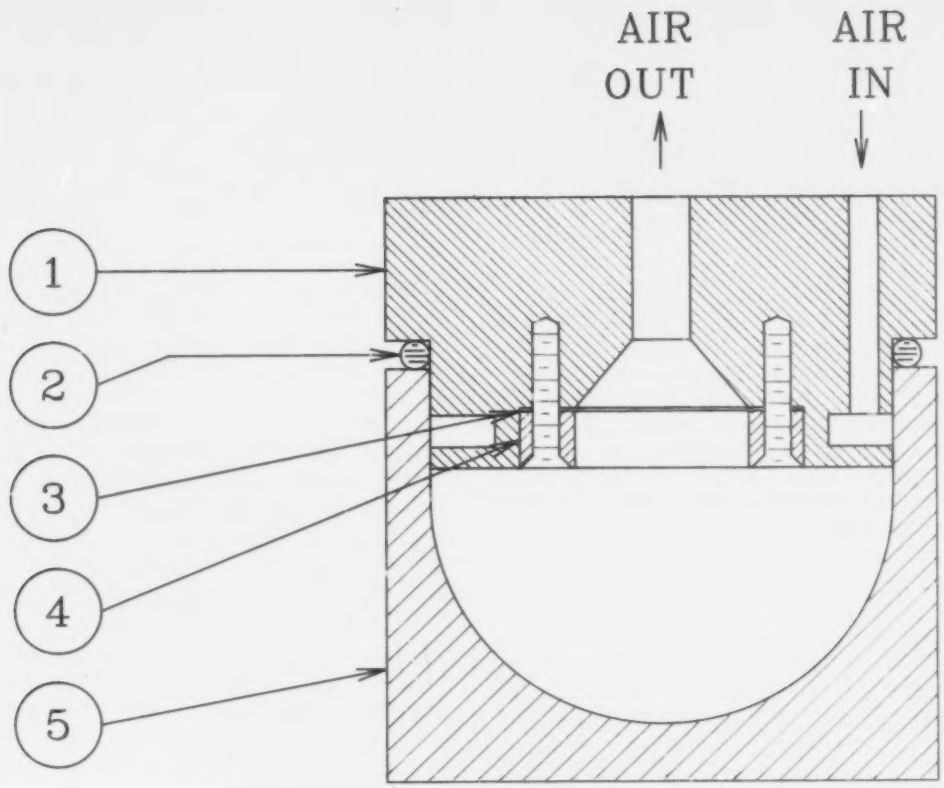

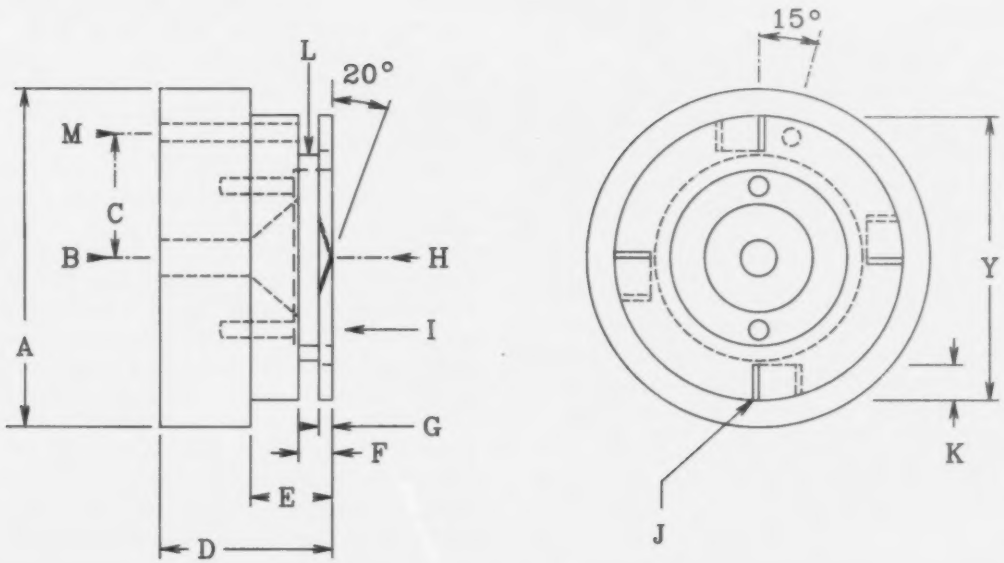

Piece 1

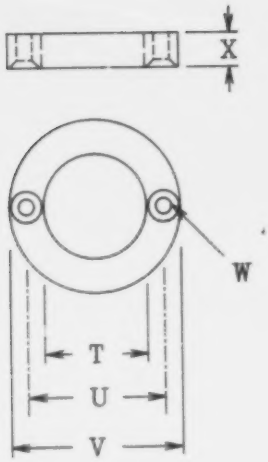

Piece 4

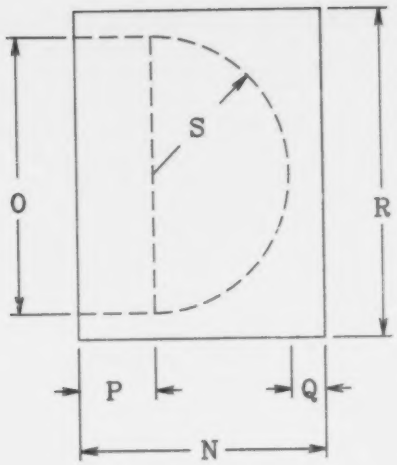

Piece 5

Figure 1. Schematic diagram showing construction of air-driven abrasion mill. Specifications for small (2-in I.D.) and large (4-in I.D.) versions are indicated in the listing below the figure. All dimensions are given in inches. Dimensions in parentheses refer to large mill.

1 – Head assembly (stainless steel)
2 – O-ring (note: O-ring groove should be cut in large mill)
3 – Outlet-port screen (stainless steel)
4 – Machine screws
5 – Abrasion chamber (sintered alumina)

Letter	Small mill	Large mill
A	diameter 2.375	diameter 4.750
B	Drill through 0.250 (0.500) in on centerline and machine to fit tubing	
C	0.875	1.750
D	1.187	2.125
E	0.562 ±.005	1.125 ±.005
F	0.233	0.280
G	0.093	0.093
H	On centerline bore to 1.225 ±.005 in (1.630 ±.005 in) to 0.265-in depth, then countersink 82° to 0.750-in diameter	
I	Drill and tap 2 holes for 4–40 (6–32) machine screws, 3/8 in deep, 180° apart on 1.000-in (1.312 in) bolt circle	
J	Cut 4 slots at 20° to face, .015 in wide, 0.250 (0.437) in deep (K), 90° apart	
K	0.250	0.437
L	1.437 diameter	3.000 diameter
M	Drill 0.125-in hole through body but not flange, machine to fit tube fitting	
N	1.812	3.500
O	2.000 ±.002	4.000 ±.002
P	0.562 ±.005	1.125 ±.005
Q	0.250	0.437
R	2.375	4.800
S	radius 1	radius 2
T	0.750	1.000
U	1.000	1.312
V	1.246 ±.002	1.622 ±.002
W	Drill #31 (#26) holes, 180° apart on 1.000- (1.312) in bolt circle, countersink for 4–40 (6–32) machine screw	
X	0.250	0.250
Y	1.995 ±.001	3.996 ±.001

A

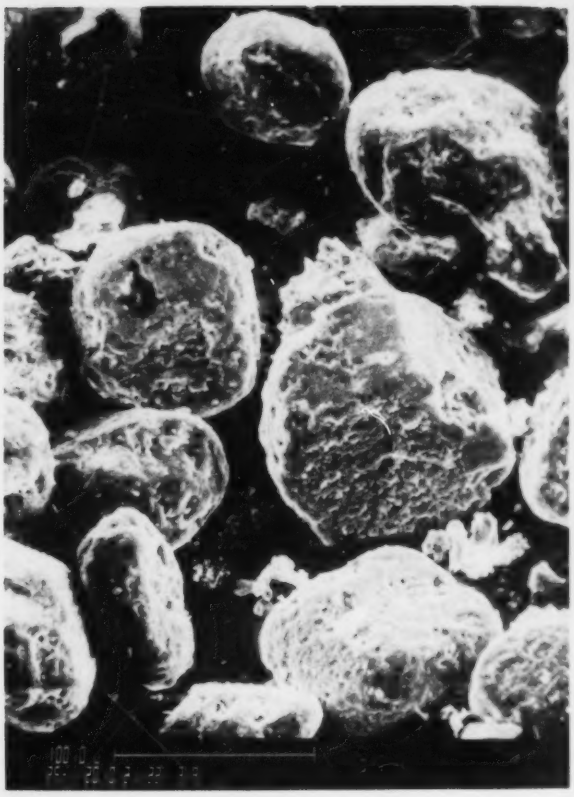

B

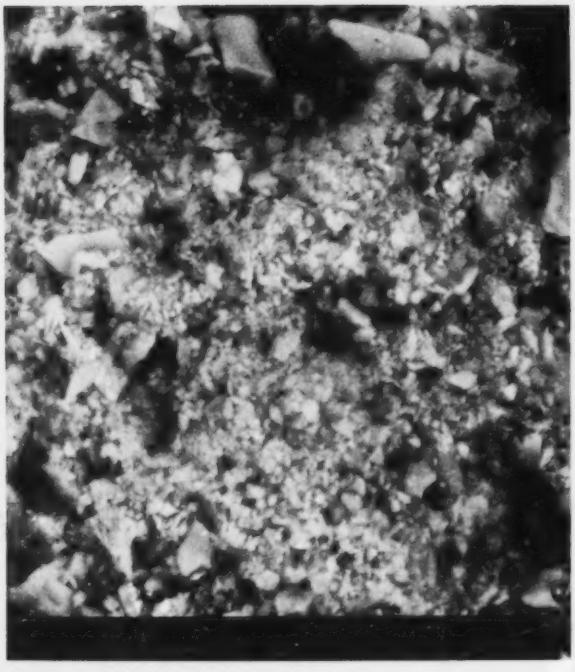

C

D

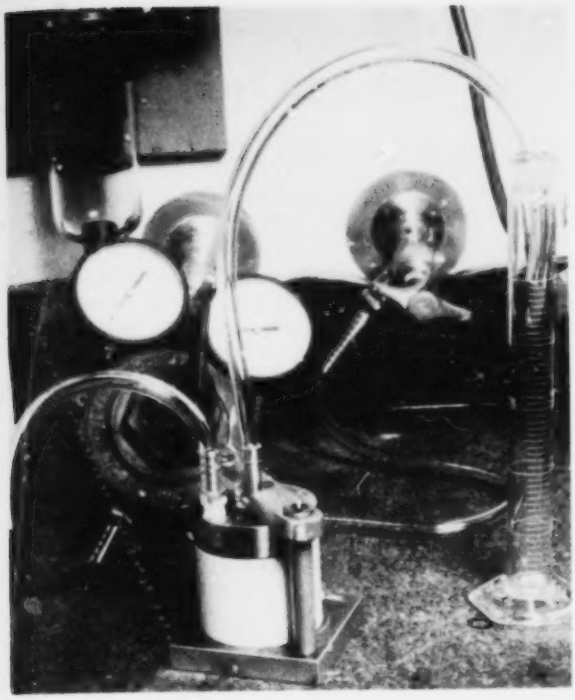

A

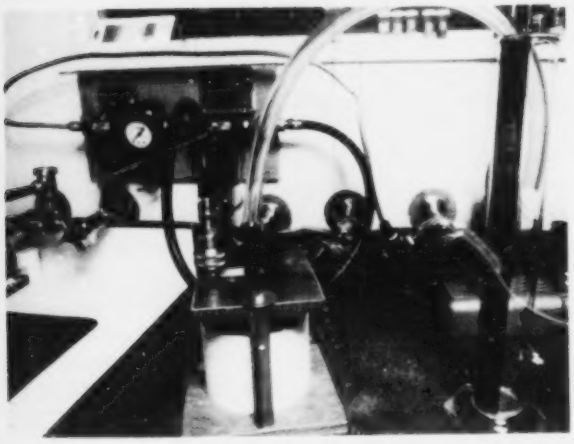

B

Figure 3. *A*, Photograph of 2-in I.D. abrasion mill showing configuration of inlet air supply, regulator, and water trap. *B*, Photograph of 4-in I.D. abrasion mill showing regulator (mounted on wall), high-pressure inlet-air hose and quick-snap fittings, and scaled-up water trap.

◀ **Figure 2.** *A*, Scanning electron micrograph of a sized separate of detrital potassium feldspar grains that have well-developed authigenic overgrowths. Source rock: Butterly Dolomite (Lower Ordovician), near Davis, Okla. *B*, Micrograph of the above sample after 4 hours in small abrasion mill at inlet pressure of 10 psi. *C*, Micrograph of abraded overgrowth material. *D*, Micrograph of same field as in *C* seen with cathodoluminescence detector; note luminescing contaminant grain of high-temperature potassium feldspar.

Separation of Abraded Surface Material

Surface material that is separated from abraded cores is recovered in the following manner. The mill is disassembled, and, with distilled water, the abraded dust is carefully rinsed from the outlet port screens and the transfer tube into a teflon beaker. While a few larger fragments containing core material often will be included with the fine fraction, these can be separated if they are allowed to settle and the finer fraction is suctioned off with a pipette. Alternatively, for small samples this separation can be done by centrifugation. In both cases the appropriate settling times can be computed for specific phases by the Stokes equation (see appropriate sections in Folk, 1968, and Jackson, 1975). The particle size of the abraded surface material will vary somewhat according to the physical properties of each sample (hardness, cleavage, and so on) and the microtopography of grain surfaces. However, our experience with abrasion of potassium feldspar, quartz, and zircon indicates an average particle size of 1 to 5 μm.

The final separate of abraded surface material is most easily concentrated by filtration through a cellulose nitrate membrane filter, which may then be dissolved by repeated acetone rinses. The purity of the final separate should be assessed with a petrographic microscope, or better still, with a scanning electron microscope. In the case of authigenic overgrowths on detrital potassium feldspar, separates should be evaluated by use of a luminoscope or a scanning electron microscope that has a cathodoluminescence detector (see fig. 2*D*). Fragments of detrital potassium feldspar luminesce with a bright blue color and are easily distinguishable from authigenic particles, which do not luminesce (Nickel, 1978; Kastner and Siever, 1979).

REFERENCES CITED

Bandyopadhyay, T., 1976, A grinder-polisher for fabricating minispheres: Indian Journal of Earth Sciences 3, p. 109–112.

Folk, R.L., 1968, Petrology of sedimentary rocks: Austin, Hemphill's, 170 p.

Jackson, M.L., 1975, Soil chemical analysis—Advanced course, 2d ed., 10th printing: Published by the author, Madison, WI 53705, 895 p.

Kastner, M., and Siever, R., 1979, Low temperature feldspars in sedimentary rocks: American Journal of Science, v. 279, p. 435–479.

Krogh, T.E., 1982, Improved accuracy of U-Pb zircon ages by the creation of more concordant systems using an air abrasion technique: Geochimica et Cosmochimica Acta, v. 46, p. 637–649.

Nickel, E., 1978, The present status of cathode luminescence as a tool in sedimentology: Minerals Science Engineering, v. 10, p. 73–100.

Resonance Ionization Spectroscopy and its Potential Application in Geosciences

By Robert D. Willis,[1] Norbert Thonnard,[1] *and* David R. Cole[2]

Abstract

Resonance ionization spectroscopy (RIS) provides the basis for several new analytical techniques that have outstanding potential in the geosciences. The RIS-based methods feature high sensitivity (parts-per-million to parts-per-trillion range), elemental selectivity (10^3 to 10^9), and generality (applicable to all elements except helium and neon). We discuss the RIS process and describe the application of RIS to the analysis of chemically processed samples, noble-gas samples, and to in situ analysis of solids. Applications of RIS in the geosciences include quantitative major, minor, and trace analysis, isotopic analysis, microprobe and depth-profiling analysis, and ultrasensitive noble-gas analysis.

INTRODUCTION

This paper provides a brief overview of resonance ionization and examines the potential of RIS techniques in the geosciences. Resonance ionization spectroscopy is a laser-based multistep photon-absorption process ending with the ionization of an atom. As a method of ionization that is both highly selective and very efficient, RIS provides the basis for several new analytical techniques that have demonstrated impressive, and in many cases unique, capabilities in the analysis of solids, liquids, and gases.

The concept of RIS was introduced by Hurst and co-workers (Hurst and others, 1975; Payne and others, 1975) at the Oak Ridge National Laboratory, who used RIS to detect a single atom of cesium in a background of 10^{19} argon atoms and 10^{18} CH_4 molecules (Hurst and others, 1977). The concept was subsequently generalized (Hurst and others, 1979) to include all elements of the periodic table except for helium and neon, which were excluded for practical reasons.

Applications of RIS are being developed at a number of university and government laboratories worldwide as well as in the commercial sector. The areas of application include basic research into sputtering processes (Winograd and others, 1982; Kimock and others, 1984), spectroscopy of atoms and molecules (Rempe and Walther, 1987; Agostini and others, 1987; Berry, 1987), materials analysis and surface analysis (Pellin and others, 1984; Gruen and others, 1986; Parks and others, 1983, 1985), medical and environmental applications (Moore and others, 1987; Rimke and others, 1987), ultrasensitive noble-gas measurements (Thonnard and others, 1987b), and elementary particle physics (Fairbank and others, 1987).

One can point to several demonstrations of RIS techniques in the geosciences: the recent measurement of rhodium concentrations at the Cretaceous-Tertiary boundary by Bekov and others (1988), isotopic measurement of subnanogram quantities of rhenium and osmium by Walker and Fassett (1986) and Walker and others (1988), and the measurement of ^{81}Kr in ground water by Willis and others (1989). In general, however, the RIS-based techniques are relatively unknown to the geoscience community, primarily because of the newness of the methods, some of which are still undergoing fairly rapid development, and because the techniques are largely confined to research laboratories. The situation is changing, however, as the RIS techniques mature, and we believe that the RIS methods will contribute increasingly to the geosciences.

THE RIS PROCESS

In nonresonant photoionization (fig. 1*A*) atoms can be ionized by the simultaneous absorption of several photons whose total combined energy exceeds the ionization potential or by the absorption of a single photon of sufficiently high energy. Either process is inefficient, as photon-absorption cross sections are low, and only a small fraction of the atoms in the laser beam is ionized. If the laser beam is focused to increase the photon flux, the reaction rate can be raised, but due to the decreased ionization volume, the overall efficiency remains low. In addition, the process is nonselective and ionizes any element within the laser beam.

In the RIS process (fig. 1*B*) the photon energy is matched to the energy difference between energy levels that are unique to a specific element (resonance). As photon-absorption cross sections are many orders of magnitude larger for resonant transitions than for nonresonant transitions, the photon flux from available lasers is therefore sufficient to saturate the bound-bound transitions without focusing. In a three-photon RIS scheme (fig. 1*B*), finding a second excited state that is within 1.16 eV of the ionization potential is usually possible and thereby allows saturated ionization from the second excited state with a large flux of 1.064-nm-wavelength infrared photons. These photons have insufficient energy to be a source of interference that

[1] Atom Sciences, Inc., 114 Ridgeway Center, Oak Ridge, TN 37830.

[2] Geosciences Group, Chemistry Division, Oak Ridge National Laboratory, Oak Ridge, TN 37831.

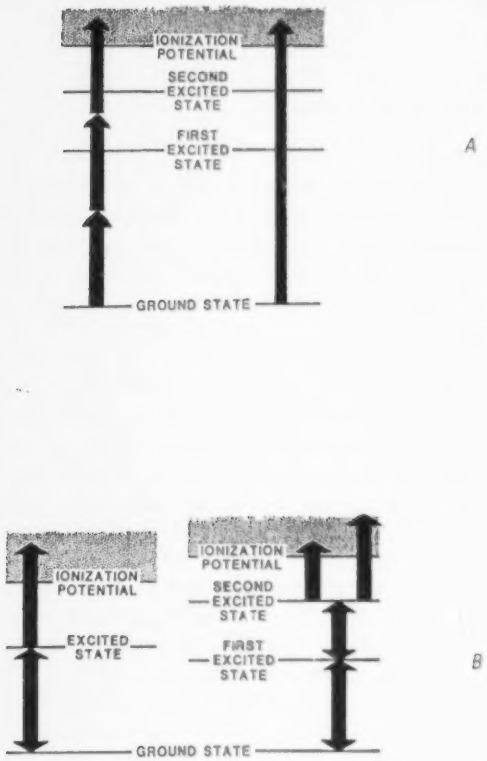

Figure 1. Comparison of nonresonant photoionization (*A*) with resonance ionization spectroscopy (*B*). Because discrete transitions unique to a selected element are used in *B*, the ionization process is element specific and much more efficient than *A*.

results from nonresonant multiphoton ionization. It is therefore possible to saturate the ionization process for a selected element with essentially no ionization of other elements. With properly chosen laser schemes, the ionization efficiency of the selected element can be as much as 10^9 times higher than for other elements (Fassett and others, 1983; Beekman and Thonnard, 1989).

The properties of saturated ionization for most elements make single atom counting feasible with the RIS process. With RIS, all atoms of the selected element within the laser beam (which can be several millimeters in diameter) will be ionized and hence counted with almost unit probability, while very few interfering counts will be generated. In addition, the RIS process is very general, as illustrated in figure 2. By use of lasers that are commercially available and frequency-converting optical elements, together with published spectroscopic data, three-color RIS schemes have been developed that allow saturated ionization of 68 elements. By use of more elaborate techniques to generate tunable vacuum ultraviolet (VUV) photons (Tompkins and Mahon, 1981; Kramer and others, 1983; Herman and others, 1985), it is possible to ionize the noble gases Ar, Kr, and Xe and also some of the other elements on the right-hand side of the periodic table with this preferred RIS scheme. An additional 13 elements can be ionized with this same apparatus if a two-photon transition to the first excited state is used, though with some loss in sensitivity and selectivity.

In our discussion of the RIS process, we assume the existence of a source of free atoms in their ground state (the population that is generally of most interest). Thus, gaseous samples can be probed directly with the RIS lasers, solids are typically analyzed by a sputtering ion beam to convert bound atoms of the solid into the (predominantly) neutral, bound state atoms in the gas phase, and liquid samples can be deposited on a filament for thermal atomization or can be dried on a substrate and sputtered as a solid.

In table 1, we have classified the periodic table from the RIS user's point of view. For purposes of comparison, we indicate, for the different groups of elements, "ballpark" sensitivities that are presently achieved or can be expected reasonably with SIRIS (sputter-initiated resonance ionization spectroscopy), the solids analysis instrument at Atom Sciences employing sputter atomization. Elements within groups A and B (table 1) can be ionized with the preferred three-color scheme with sensitivities at the parts-per-billion level and selectivities greater than 10^4. All elements of group A have resonance wavelengths that are available from a single dye combination: DCM in the first dye laser and R590 in the second, if required. Analysis of elements in group B requires changing dyes in the dye lasers, a 15- to 30-min procedure. Analysis of elements in group C by a two-photon transition to the first excited state yields sensitivities of 0.1 to 1 ppm and selectivities of 10^3 and 10^6. The loss in sensitivity is due to the reduced ionization volume (as the laser beam is often focused to a 0.1-mm diameter) and decreased ionization efficiency because two-photon transitions are difficult to saturate, while selectivity is reduced because of the increased multiphoton nonresonant ionization from the intense (focused) ultraviolet (UV) laser beam. However, if tunable VUV radiation is generated—a difficult step, but already implemented for krypton and xenon—the sensitivity for elements in groups C and D can be similar to that for groups A and B. (Atom Sciences is presently working on VUV generation for As, C, H, N, O, P, Se, and Ar.) Once spectroscopic data become available, elements in group E will probably fall into groups A and B.

Although RIS can be achieved for many elements by use of continuous-wave lasers, the generality illustrated in figure 2 presently can be achieved only with pulsed lasers. The very high peak power of pulsed lasers enables efficient generation of UV and VUV radiation in nonlinear processes, so the entire periodic table is accessible. In addition, the high peak power assures saturation of the RIS process, possible only for a few elements with use of continuous-

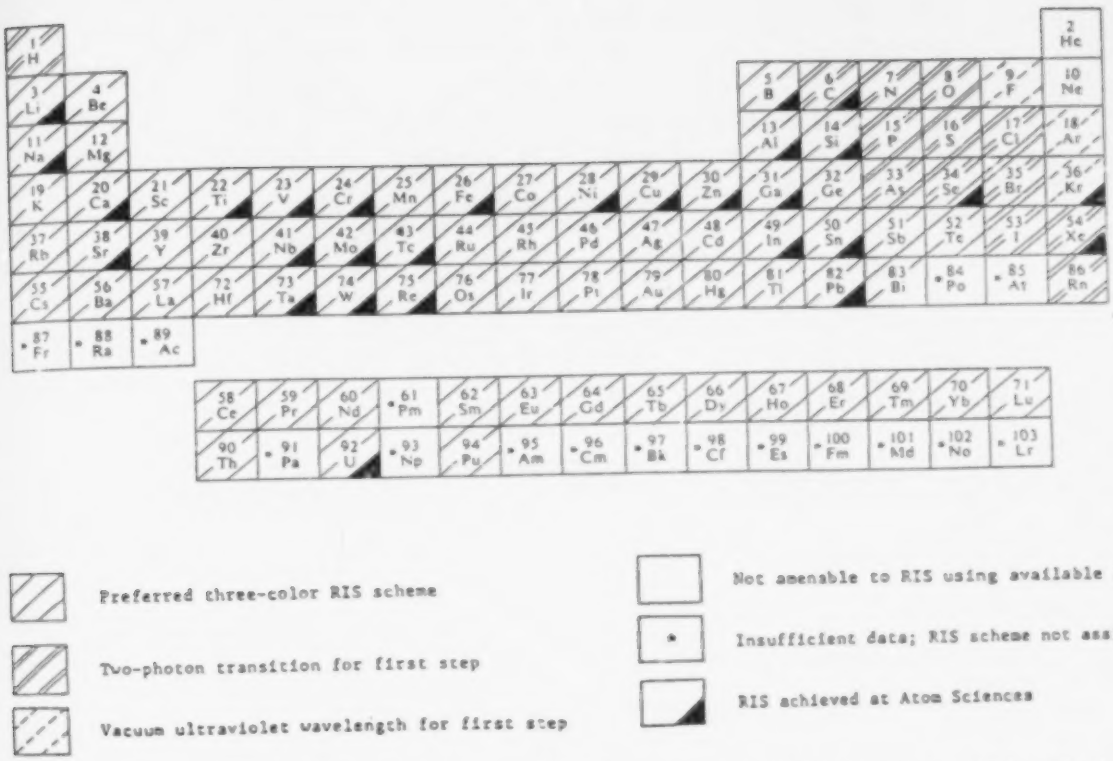
Preferred three-color RIS scheme
Two-photon transition for first step
Vacuum ultraviolet wavelength for first step
Not amenable to RIS using available lasers
Insufficient data; RIS scheme not assigned
RIS achieved at Atom Sciences

Figure 2. Periodic table identifying those elements for which practical RIS schemes have been identified. Commercially available laser systems can ionize 68 elements by use of a three-color scheme to achieve saturated ionization with very low interference. An additional 13 elements can be ionized by the use of two-photon transitions to the first excited state. To date, RIS has been achieved for most elements by researchers around the world.

wave lasers. The pulsed neodymium YAG (yttrium aluminum garnet) laser system, because of its high peak power and convenient and reliable operation, is used frequently for the RIS process. The repetition rate of this system, however, is limited to tens of hertz. Higher repetition rates can be achieved with excimer (hundreds of hertz) and copper vapor (thousands of hertz) lasers, but at considerable loss of peak power and flexibility.

The use of pulsed lasers in the RIS process has important consequences in terms of sample utilization and the effective duty cycle of the technique. With pulsed atomization sources, it is possible to achieve very efficient sample utilization by properly matching the atomization and ionization duty cycles (Kimock and others, 1984). However, the sensitivity of the RIS-based techniques as measured in ions detected per second is fundamentally limited by the repetition rate of the laser system, as discussed later in the paper.

RIS-BASED METHODS AND APPLICATIONS

The high ionization efficiency, element specificity, and applicability to all elements (except helium and neon) make RIS an ideal ultrasensitive analysis tool. The RIS method requires free atoms, and as the ionizing laser beams are usually only several millimeters in diameter, it is desirable for these free atoms to be concentrated in the laser beams. For many applications, isotopic information is also of interest. For elements with an atomic number greater than 5, the RIS technique does not readily provide isotopic selectivity; therefore, a mass-analysis step is desirable in the detection system. But, a mass-analysis step is not always necessary; the first demonstration of single atom counting when using RIS was achieved in a proportional counter in which single cesium atoms were detected in a background of 10^{19} argon atoms and 10^{18} CH_4 molecules (Hurst and others, 1977), while recent work by Niemax (1985) has demonstrated ultratrace isotopically resolved element detection at the picogram level when using resonance excitation and collisional ionization in a thermionic diode detector.

The following sections describe in a general way the implementation of RIS in techniques now being applied to the analysis of chemically processed samples, noble-gas samples, and solid samples. We shall also discuss specific applications of RIS that demonstrate the potential of these techniques to problems in the geosciences.

Table 1. Classification of RIS schemes

Group		Element	Number of elements
A.	DCM dye for first laser; R590 for second laser (if needed)	Al, B, Ba, Bi, Ca, Co, Cs, Cu, Dy, Er, Fe, Ga, Gd, Ge, Hf, Ho, In, K, La, Mo, Na, Ni, Pu, Rb, Re, Sc, Si, Sn, Ta, Tb, Tc, Th, Ti, Tl, Tm, U, V, W, Zr	39
B.	Other dye combinations	Ag, Au, Be, Cd, Ce, Cr, Eu, Hg, Ir, Li, Lu, Mg, Mn, Nb, Nd, Os, Pb, Pd, Pr, Pt, Rh, Ru, Sb, Sm, Sr, Te, Y, Yb, Zn	29
C.	Two-photon transition for the first step	As, Br, C+Cl, H, I, N, O, P, Rn, S, Se, Xe	13
D.	Vacuum ultraviolet (VUV) for the first step	Ar, F, Kr	3
E.	Insufficient data	Ac, Am, At, Bk, Cf, Cm, Es, Fm, Fr, Lr, Md, No, Np, Pa, Pm, Po, Ra	17
Not currently amenable to RIS:		Ne, He	2
Total			103

Analysis of Chemically Processed Samples

Figure 3 shows the RIS enhancement of solid-source thermal-ionization mass spectrometry, called resonance ionization mass spectrometry (RIMS). In this analytical technique, the sample, be it biological tissue or fluid, a mineral or other solid, or an environmental water sample, is chemically processed to separate and concentrate the analyte and deposit it on a filament. Quantitation is typically achieved with the isotope dilution technique. Heating of the filament vaporizes the sample, while the RIS laser beams ionize the vapor cloud. Because of the pulsed ionization, time of flight (TOF) can be used for mass analysis. Poor sample utilization resulting from the low duty cycle of the laser has been improved considerably by pulsing the current to the vaporization filament (Fassett and others, 1984).

The RIMS technique has already made a number of valuable contributions to the field of geoscience. For example, Walker and Fassett (1986) used RIMS to measure the isotopic compositions of microgram and picogram quantities of rhenium and osmium. The reported precisions and accuracies were ~1 percent and 1 to 5 percent for microgram and picogram quantities, respectively. The selectivity of RIMS was valuable in eliminating Re/Os isobaric interferences but even more crucial in enabling the authors to correct accurately for hydrocarbon interferences. In a more recent study, Walker and others (1988) measured $^{187}Re/^{186}Os$ and $^{187}Os/^{186}Os$ isotopic ratios in a series of komatiite flows and obtained precisions of ~2 percent (essentially controlled by counting statistics). Bekov and others (1988) used a variation of RIMS to provide the first data on rhodium concentrations at the Cretaceous-Tertiary boundary. A mass analyzer was used to improve the selectivity. The quoted detection limits for rhodium in chemically pretreated samples were 3 parts per trillion (ppt), and the authors claim detection limits as low as 1 ppt for the platinum-group elements and, in principle, their isotopes. Such sensitivity could be useful in geochemical prospecting and in studying the origin of the noble metals (Bekov, 1989; Chen and others, 1987).

Most of the lanthanide- and actinide-group elements can be ionized by use of the preferred three-color scheme (fig. 2), for which the sensitivities are at the parts-per-billion level. This region of the periodic table is also rich in isotopic systems that have isobaric overlaps—Pu/U, Nd/Sm, Tc/Mo, and Lu/Yb—and provides opportunities to demonstrate the elemental selectivity of RIS. Donohue and others (1982), for example, used RIMS to measure neodymium and samarium isotopic ratios in binary mixtures in which there had been no chemical separation. The elimination of isobaric interferences was demonstrated, and the authors concluded that precisions of ±0.5 percent for isotopic ratio measurements could be achieved reasonably with an improved laser system and proper data-collection scheme.

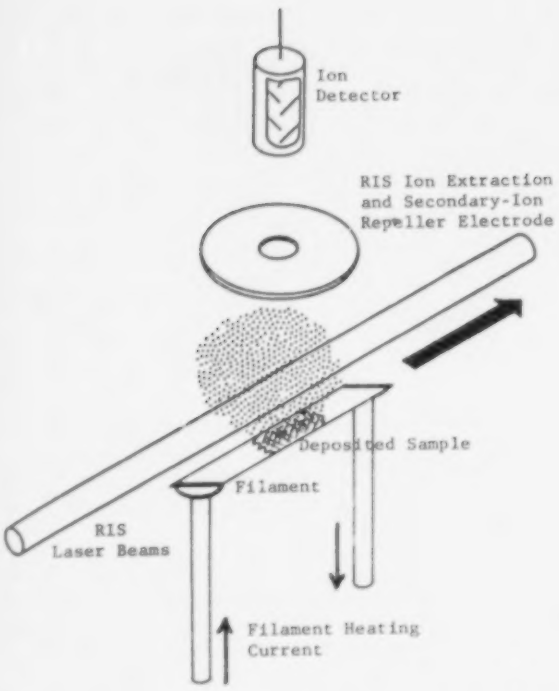

Figure 3. Schematic drawing of the resonance ionization mass spectrometer (RIMS) technique. The sample, which is processed chemically, is deposited on a filament for vaporization. The RIS laser beams ionize only the selected element.

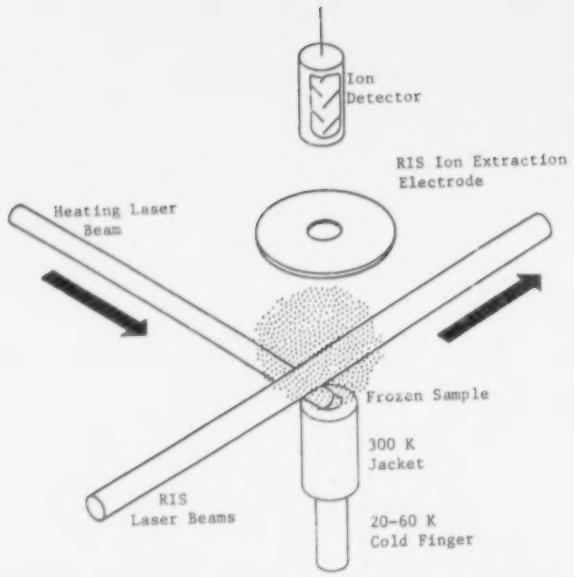

Figure 4. RIS analysis of noble-gas samples. The sample is introduced into the static mass spectrometer, frozen onto the cold finger, and subsequently released by a pulsed, heating laser a few microseconds before the RIS lasers are fired, thereby concentrating the atoms in the RIS laser beams.

Ultrasensitive Noble-Gas Measurements

A technique for the analysis of noble-gas samples, first developed at Oak Ridge National Laboratory (Hurst and others, 1985), is illustrated in figure 4. Typical diameters of RIS laser beams are only several millimeters, while mass spectrometer volumes are several liters; thus, for noble-gas samples containing fewer than 1,000 atoms, the probability of even a single noble-gas atom being in the RIS laser beam would be small. Unacceptably long analysis times would be required. It is possible to concentrate the noble-gas atoms in the RIS laser beams by employing a cold finger (Hurst and others, 1984) that freezes the noble gas onto a small spot. A pulsed, heating laser releases the noble-gas atoms into the ionization region just before the RIS lasers are fired. Combining this "atom bunching" with the high ionization efficiency and selectivity of RIS has made it possible to detect selected isotopes of krypton with fewer than 1,000 atoms in a 6-L mass spectrometer, even in the presence of 2×10^{8} residual gas atoms (10^{-9} torr vacuum).

The pioneering work of Hurst's group at Oak Ridge National Laboratory is being carried forward at Atom Sciences, where efforts are presently under way to extend the method to any isotope of the heavy noble gases (Ar, Kr, Xe, Rn). One application being developed at Atom Sciences is to date ground water by measuring the concentration of the cosmogenic radioisotope ^{81}Kr (half-life = 210,000 years). An example of this work is shown in figure 5. The figure is a TOF spectrum of a processed krypton sample extracted from approximately 50 L of ground water showing the detection of 6,200 atoms of ^{81}Kr in the TOF apparatus. Details of the sample processing and analysis are given by Thonnard and others (1987a,b). The same approach can be used in dating polar ice, a key step toward interpreting the atmospheric record preserved in the ice.

Other radioisotopes of interest that are difficult to detect by decay counting are ^{39}Ar (half-life = 269 years) and ^{85}Kr (half-life = 10.7 years), which are valuable "clocks" for measuring the rates of deep-ocean circulation (^{39}Ar) and new ocean-water formation (^{85}Kr). Although an RIS scheme for argon has not yet been demonstrated, it should be possible. In the area of cosmochemistry, much has been learned about the evolution of the solar system from isotopic analysis of small noble-gas samples extracted from meteorites. These measurements demand high sensitivity and selectivity, especially against hydrocarbon backgrounds in the mass spectrometer. Turner's group at Sheffield (Turner, 1987) is using RIS to study xenon anomalies

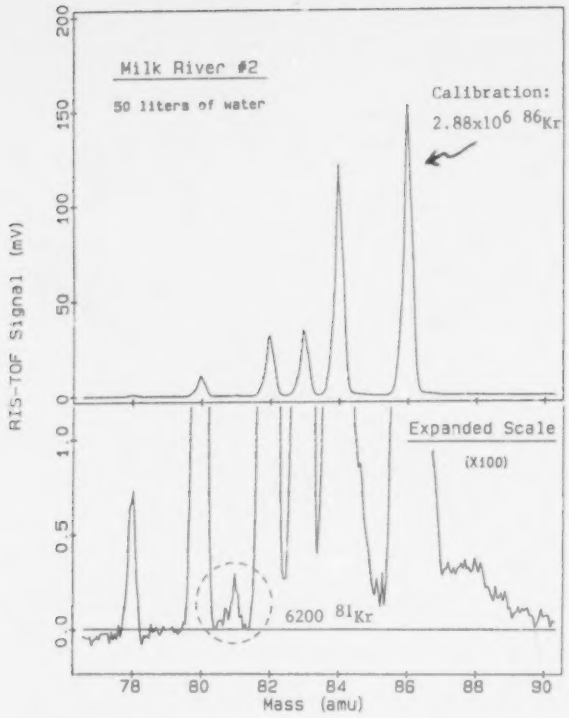

Figure 5. Krypton mass spectrum for sample extracted from 50 L of water from the Milk River aquifer in Canada. The time-of-flight (TOF) apparatus detected 6,200 atoms of ^{81}Kr. Because the magnitude of the ^{81}Kr signal was only slightly less than that of modern water, an age of less than 100,000 years is indicated. Decay counting would have required processing 100,000 L of water. amu, atomic mass units.

in meteorites. Another application of ultrasensitive noble-gas measurements is ^{81}Kr-Kr dating in which radioactive ^{81}Kr and stable spallation krypton are measured to determine cosmic-ray exposure ages of chondritic meteorites and lunar samples (Marti, 1982; Eugster, 1989).

Direct Analysis of Solids

For direct analysis of solid surfaces, two techniques are showing great promise. Material can be removed from the sample surface with either an atomizing laser pulse (Beekman and others, 1980) or a sputtering ion beam (Parks and others, 1983), with subsequent ionization of the expanding cloud of neutral atoms by RIS laser beams (fig. 6). The former is called LARIS (laser atomization RIS), while the latter is called SIRIS (sputter-initiated RIS). When the atomizing laser or sputtering ion beam is focused, regions in the micrometer or submicrometer size regime can be analyzed with high sensitivity. Imaging can be achieved

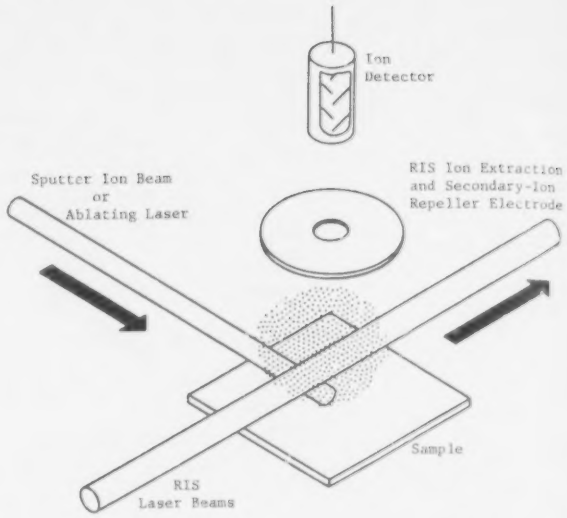

Figure 6. Direct analysis of solid samples by the use of sputter-initiated RIS (SIRIS) or laser-atomization RIS (LARIS). Because resonance ionization acts on the preponderance of the neutral atoms evolved from the sample, sensitivity is increased and matrix effects are reduced.

by rastering the beam over the surface, while depth profiling is possible by collecting data as the sample is eroded during the analysis. The two techniques will probably become complementary. SIRIS, utilizing the well-controlled linear sputtering process, is developing into a precise analytical technique that has high lateral and depth resolution, while LARIS, perhaps less quantitative, promises lower ultimate detection limits by several orders of magnitude.

Both techniques rely on resonance ionization of the neutral atoms removed from the sample. This process offers two distinct advantages over secondary ion mass spectrometry (SIMS). First, the neutral fraction of ejected particles is often 99 percent or greater, so SIRIS and LARIS should be capable of achieving lower detection limits for most elements. Secondly, because the neutral flux is analyzed, SIRIS and LARIS measurements are potentially much less matrix dependent than SIMS and should be more quantitative. Because the RIS methods virtually eliminate isobaric interferences, the mass-resolution requirements of the detector are in general greatly reduced compared to the SIMS technique. A low-resolution TOF detector suffices for many applications and offers nearly 100 percent transmission efficiency.

Figures 7 and 8 illustrate some of the salient features of SIRIS and LARIS by use of results obtained at Atom Sciences. Figure 7 shows LARIS TOF spectra of a silicon sample containing 58 ppm gallium (Beekman and Thonnard, 1989). The lower spectrum (lasers tuned to gallium resonance) shows the simplicity of the TOF spec-

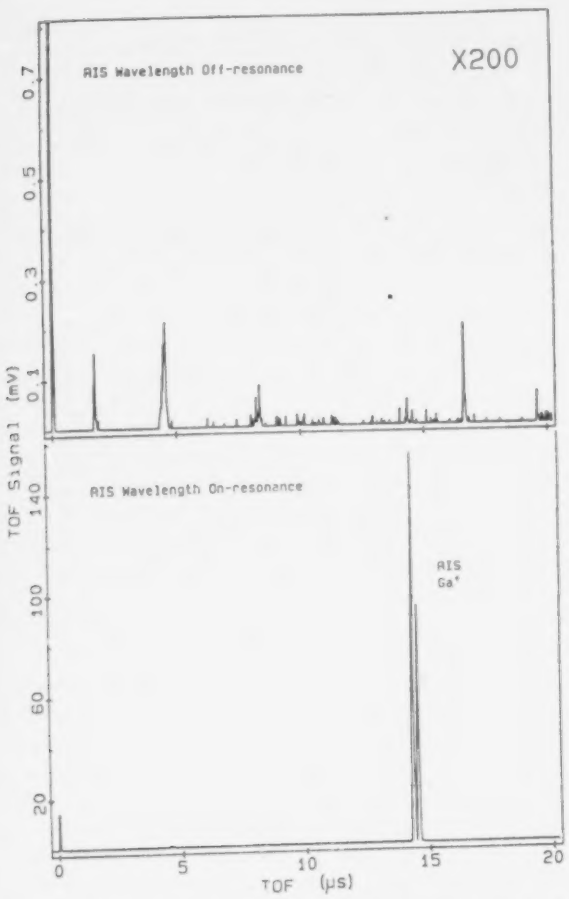

Figure 7. Laser-atomization resonance ionization time-of-flight (TOF) mass spectrum of a silicon sample containing 58 ppm gallium (lower plot). Total mass range is 0 to 133 amu. The simplicity of the spectrum, which has only a hint of a signal at 4.6 μs, results from direct ionization of silicon from the atomization laser, which was adjusted to deliver 4×10^7 W/cm^2. With the RIS laser detuned by only 0.07 nm, some signals are seen in the 200 × expanded scale view (upper plot). Comparison of the resonant ^{69}Ga signal with the nonresonant mass 28 signal indicates 3×10^8 greater gallium resonance ionization than nonresonant silicon ionization and thus demonstrates the remarkable selectivity of RIS.

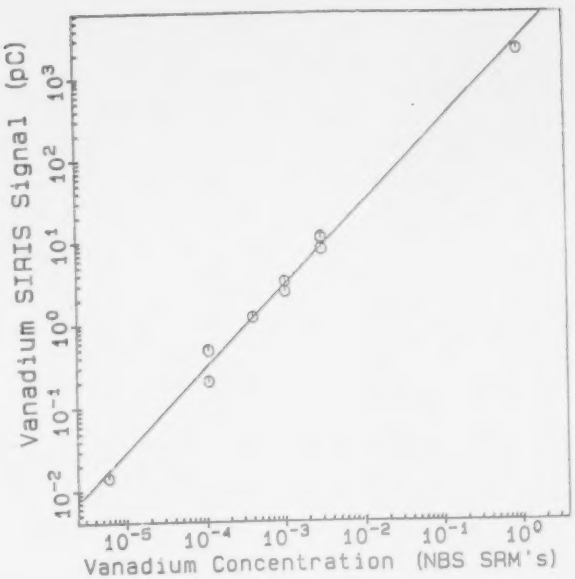

Figure 8. Correlation of vanadium SIRIS signal versus accepted National Bureau of Standards concentration values. Excellent agreement is obtained over nearly six decades even though three different matrix materials were used (pure vanadium at 10°, stainless steel at 10^{-2} to 10^{-4}, and "pure" iron at 7×10^{-6}). Because the data for pure vanadium were obtained with 1/200th of the sputtering ion current used for the remaining samples, the indication is that sputtering is a linear process, which is important for quantitation. pc, picocoulomb; SRM's, standard reference materials.

trum. The remarkable selectivity of RIS is illustrated by comparing the on-resonance gallium signal to the off-resonance silicon signal (upper spectrum). Figure 8 shows the correlation of the SIRIS signal for vanadium versus the certified National Bureau of Standards (NBS) values for a suite of standards spanning almost six orders of magnitude in vanadium concentration. The fact that these measurements comprised three different matrix materials (pure vanadium, stainless steel, and "pure" iron) is of importance because it illustrates the matrix-independence of the method.

A schematic diagram of the SIRIS apparatus developed at Atom Sciences is shown in figure 9 and is described in more detail by Parks and others (1983; 1985). Briefly, the sample is sputtered by use of a pulsed (30 Hz) argon ion beam produced in a duoplasmatron microbeam ion gun. Typical parameters for the sputtering beam are 5 μA of current in a 1-μs pulse, ion energy of 10 keV, and a spot size of 100 μm (reducible to 5 μm with reduced current). The laser system comprises two tunable dye lasers pumped by a 30-Hz neodymium YAG laser and can generate any wavelength between about 220 and 1,064 nm. Mass analysis is provided by either a TOF analyzer or a magnetic sector. SIMS ions constitute background in the SIRIS data and are rejected by means of an energy analyzer. SIRIS ions are detected by an electron multiplier with a conversion dynode operated in the analog or single-ion-counting mode. The target chamber maintains a base pressure of 4×10^{-9} torr.

The sensitivity of SIRIS-type instruments has been studied at Atom Sciences and elsewhere. At Atom Sciences, a detection limit of 2 ppb for gallium in silicon has been reported (Parks and others, 1984), and at Argonne National Laboratory, Pellin and co-workers (Young and

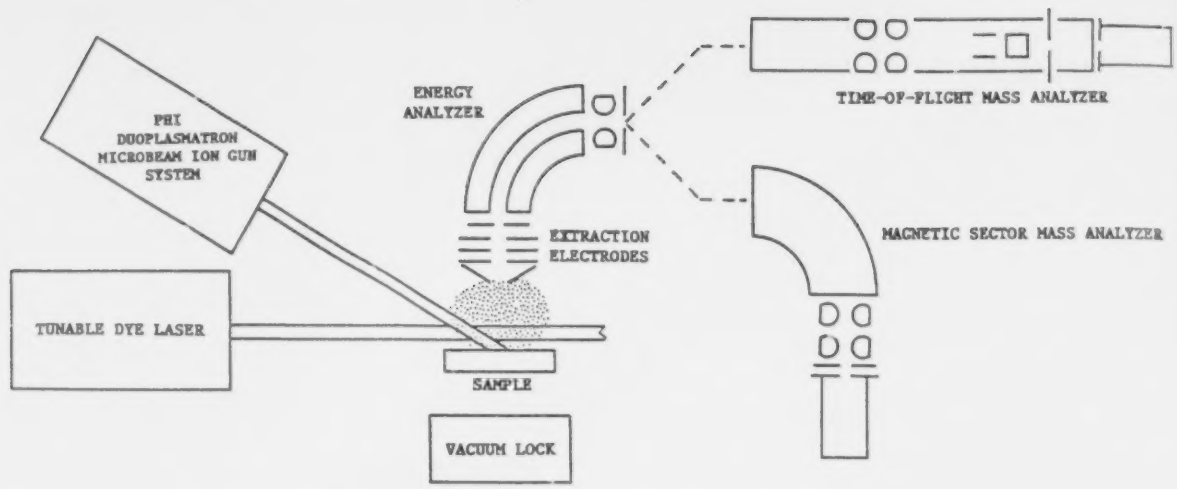

Figure 9. Schematic diagram of SIRIS apparatus, which consists of a pulsed-ion source, tunable laser system, ultrahigh vacuum system, extraction electrodes, and either a double-focusing magnetic sector mass spectrometer or a time-of-flight mass analyzer. Secondary ions generated in the sputtering process constitute a background noise in SIRIS and are eliminated with the use of time and energy discrimination.

others, 1987; Pellin and others, 1986) reported detection limits of 0.5 ppb for ^{54}Fe in silicon and 2 ppb for ^{56}Fe in silicon. This last result is a particularly impressive demonstration of the elemental selectivity of RIS; without this selectivity, the ^{56}Fe signal would be overwhelmed by the signal from the $^{28}Si_2$ dimer.

Development of the LARIS technique is not as far along as SIRIS, but a detection limit of 10 ppb for gallium in silicon was recently demonstrated (Beekman and Thonnard, 1989) in a very simple system after only 500 laser shots (50- s analysis time). Simple operational changes could lower the detection limit to below 0.1 ppb, while the potential of achieving sub-parts-per-trillion sensitivity is realistic.

As an analytical tool, SIRIS has much in common with SIMS and the ion microprobe, and a list of potential applications of SIRIS in geochemistry would look very familiar to users of SIMS techniques. The broad generality of RIS as illustrated in figure 2, the sub-parts-per million to parts-per-trillion sensitivites for much of the periodic table, and the low matrix dependence provide SIRIS with a tremendous potential for quantitative in situ trace analysis of solids. It is well known that the SIMS spectra of geological samples are overwhelmingly complicated by the presence of molecular ion species. While these can be eliminated by energy filtering of the secondary ions or by using spectrometers that have very high mass resolution, the loss in signal intensity is substantial (Shimizu and Hart, 1982), and the elemental isobaric interferences remain. The remarkable selectivity of RIS (particularly for those elements in groups A and B of table 1) affords tremendous simplification of the mass spectra of complex samples.

The SIRIS system at Atom Sciences has demonstrated a lateral resolution down to 5 to 10 μm and a depth profiling resolution of ~30 Å and thus potentially enabled studies of (1) the distribution of major, minor, and trace elements in minerals, (2) elemental diffusion gradients, (3) the magnitude of isotopic zoning or inhomogeneities in individual mineral grains, (4) the extent of isotopic variation that is due to changes in fluid type, fluid source region, and temperature as preserved in growth zones of hydrothermal and authigenic minerals, and (5) the degree of isotopic equilibration between individual grains of different phases. When VUV laser schemes become available, it may be possible to study the light stable isotopes (C, H, N, O, S, P, and others in group C of table 1) in different mineralogical settings where these elements are present at the trace level. Such studies could provide insight, for example, into the nature of solid solution of these elements in oxides and silicates (see Freund, 1987). Because of interferences from the major elements, or poor sensitivity as in the case of nitrogen, these studies would be difficult or impossible with SIMS.

Zinner (this volume) has pointed out that the limited sample size and relatively large isotopic anomalies make extraterrestrial samples ideal subjects for ion-microprobe analysis. Both primitive meteorites and interplanetary dust particles (IDP's) contain considerable evidence for the existence of preserved interstellar material that was formed prior to the formation of the solar system. Neutron-rich isotopes such as ^{48}Ca, ^{50}Ti, ^{54}Cr, and ^{64}Ni are of interest, as they provide evidence of supernova events in the presolar system (Andrew Davis, James Frank Inst., University of Chicago, personal commun., 1986). The iron group of

elements are among the group A and B elements (table 1) that can be detected by SIRIS with high sensitivity, and the expected high selectivity should eliminate isobaric interferences that complicate the SIMS data. The existence of hydrocarbons in Comet Halley dust particles has stimulated interest in the abundances and distribution of biogenically important elements including H, C, N, O, P, and S. As discussed earlier, ionization of these elements by a two-photon transition for the first excitation step results in reduced sensitivity (in the few parts-per-million range) and selectivity. Even so, the present SIRIS technique may offer advantages over SIMS in some applications. For example, the direct determination of nitrogen concentrations in extraterrestrial samples is not feasible with SIMS because of the low ion yields for nitrogen. Instead, nitrogen concentrations are inferred by the measure of the yield of CN ions. Isobaric interferences complicate this measurement, and the CN yields are influenced by the carbon content of the matrix (Zinner, this volume). In this particular application, the SIRIS technique probably offers unique capabilities. For example, nitrogen contents and isotopic compositions in diamonds could be investigated on a much finer scale than described by Boyd and others (1988), who observed large isotopic fractionations that were due to the influence of crystal structure. With improved techniques for generating VUV light for the first excitation step, the ultimate sensitivity and selectivity of the SIRIS technique can be approached for this important set of elements.

The previous paragraphs have emphasized potential advantages of the SIRIS and LARIS techniques and possible applications of these techniques in the geosciences. We must balance this discussion by stating that the SIRIS and LARIS techniques have not yet, to our knowledge, been demonstrated on complete geological samples. The added complexity of these samples will undoubtedly pose new problems for these techniques as it did in the case of the microprobe. Indeed, the present situation is perhaps analogous to that confronting the SIMS technique when its capabilities were first being extended to the fields of geochemistry and cosmochemistry. SIRIS and LARIS are still suffering some of the "growing pains" of a new technique. Researchers have begun only recently to address key analytical concerns such as matrix effects and fractionation effects in relatively simple matrices. Limits to SIRIS and LARIS sensitivity that are due to the duty cycle of these techniques is another area of concern. In the remaining paragraphs, we would like to briefly discuss the issues of matrix effects, fractionation effects, and duty cycle.

Figure 8, discussed earlier, suggests that matrix effects with SIRIS are minimal. Parks and others (1985) investigated the SIRIS yield for silicon and boron in various matrices, and the results are presented in table 2. The maximum matrix effect observed in this limited study was approximately a factor of 4 for boron in BPSG. This matrix is a type of glass (boron phosphide silica glass), and the poor relative yield is probably due to charge buildup in the target. Our experience is that factors of 3 or 4 in the relative yield from different matrices are the exception rather than the rule; in SIMS measurements, matrix effects can be as high as several orders of magnitude. Matrix effects are expected to be small for two reasons: (1) the yield of sputtered neutrals does not depend strongly on the properties of the surface and (2) the ionization process takes place in the gas phase, decoupled from surface effects. This relative matrix independence should greatly improve the prospects for quantitative analysis.

Table 2. Relative SIRIS response for silicon and boron in various matrices

Matrix	Element	Relative SIRIS response
Si	Si	1.00
Al	Si	.96
$PdSi_2$	^{28}Si	.96
$PdSi_2$	^{30}Si	.96
$TiSi_2$	Si	3.60
GaAs	Si	3.65
Si	B	1.00
GaAs	B	.77
BPSG[1]	B	.23

[1] Boron phosphide silica glass.

Stable isotopic measurements are basic to geochemistry, and it is important to assess the ability of SIRIS to measure isotopic ratios. To date, efforts have focused by and large on quantitative trace analysis rather than on isotopic measurements, so data are sparse. In the case of SIRIS, fractionation effects will occur both in the sputtering process and in the ionization step. However, with proper choices of the sputtering-beam pulse width, the laser pulse width, and the time delay between the sputtering-beam pulse and the ionization laser, the ionization probability of the ejected neutrals (in the absence of isotopic effects in the RIS process itself) will be independent of the particle velocity (or mass) (Kimock and others, 1984). Our experience at Atom Sciences indicates that fractionation effects are dominated by the RIS process itself. In isolated cases we have observed fractionation effects between odd- and even-mass isotopes of about 10 percent, whereas for odd or even isotopes taken separately, the maximum error in the ratios is typically 2 percent. The odd-even effect is presumably caused by a dependence of the ionization probability on the polarization of the photons used in the excitation step(s) (Fairbank and others, 1989). Figure 10 shows a SIRIS TOF spectrum of pure molybdenum. Integration of the individual peak areas yielded natural molybdenum abundance ratios within 2 to 3 percent with no corrections applied to the raw data.

We believe that with careful attention to saturation of the RIS process, polarization of the lasers, and by running

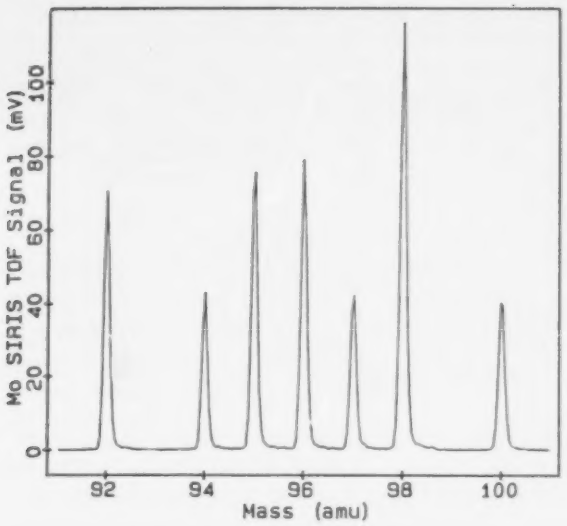

Figure 10. SIRIS time-of-flight (TOF) spectrum of pure molybdenum. The resolution m/Δm of the TOF detector was approximately 500, and the analysis time was 1 min (600 shots). The measured isotopic ratios agreed with the natural abundance ratios within 2 to 3 percent. amu, atomic mass units.

standards next to samples, isotopic ratios can be measured with precisions and accuracies better than 0.5 percent. In fact, analysis of calibration spectra used in the krypton work described earlier shows precision of 0.25 percent and accuracies ranging between 0.5 and 1.5 percent for the major isotopes.

Factors limiting the sensitivity of SIRIS, as discussed by Kimock and others (1984), are the low duty cycle, which is due to use of pulsed lasers, and the brightness of the primary ion beam. For the typical case of a repetition rate of 30 Hz and ion-beam pulse width of 1 μs, the duty cycle is 3×10^{-5}. This low duty cycle can be offset partly by the higher yield of ejected neutrals compared to secondary ions for specific cases. In analysis for elements having very poor secondary ion yields (10^{-5} or less, for example), the SIRIS signal level can be significantly higher for SIRIS than for SIMS and thus allow access to analysis for elements not previously detectable. Nevertheless, for those elements having good SIMS sensitivity, the signal intensity (ions detected per second) may be two orders of magnitude smaller than for SIMS. One should note, however, that the sample utilization, that is, the amount of sample consumed during the analysis, is very low since the sputtering beam is pulsed and is frequently much less than in SIMS because of the higher overall efficiency.

The duty cycle problem can be improved by using brighter ion beam sources delivering a few milliamps of current in a spot size of several millimeters and using the higher repetition rate or continuous-wave lasers discussed earlier. For microprobe analyses, however, the present microbeam ion guns are already space-charge limited and cannot be made brighter. Analysis for some elements, especially those having high secondary ion yields and few potential isobaric or molecular interferences, will probably continue being done advantageously with SIMS. But, the accessibility to almost all elements of the periodic table with high sensitivity, good quantitation, and virtually no interferences will make the SIRIS technique valuable.

SUMMARY AND CONCLUSIONS

Resonance ionization spectroscopy (RIS) is a method of ionization in which narrow-band lasers are used to ionize elements selectively and efficiently. It is the basis for several ultrasensitive elemental analysis techniques including, but not limited to, (1) analysis of chemically processed samples deposited on a filament for vaporization (RIMS), (2) ultrasensitive noble-gas measurements, and (3) direct analysis of solid samples by the use of either sputter-initiated RIS (SIRIS) or laser-atomization RIS (LARIS). In the latter methods, pulsed-ion sputtering or pulsed-laser atomization is used to vaporize atoms from a solid sample, and the RIS laser(s) then ionize(s) atoms of a selected element that are detected and counted. Because the neutral flux is analyzed, SIRIS and LARIS measurements are potentially much less matrix dependent than SIMS and should be more quantitative. These two surface-analysis techniques can analyze impurities in a variety of materials (minerals, glasses, semiconductors, metals) with sensitivities in the low parts-per-million to low parts-per-billion range. The absence of isobaric interferences that are due to the selectivity of the RIS process greatly simplifies the analysis of complex samples. In addition to elemental analysis, isotopic information is obtained by use of either a TOF analyzer or a magnetic-sector energy analyzer. Both the SIRIS and LARIS techniques are capable of microprobe analyses if one focuses the sputtering beam (SIRIS) or the atomization laser (LARIS). With recent development in liquid-metal ion sources, spatial resolutions of 1,000 Å are possible with SIRIS.

Applications of RIS in the geosciences have been relatively limited to date, owing to the newness of the methods. However, we expect a growing interest in these techniques as their capabilities continue to improve and become better known.

ACKNOWLEDGMENTS

The authors gratefully acknowledge Ceci Steele for typing this paper. D.R. Cole would like to thank David Wesolowski for his careful review of this paper. Support of D.R. Cole was provided by the Division of Engineering and Geosciences, Office of Basic Energy Sciences, U.S.

Department of Energy, under contract DE–AC05–840R21400 with Martin Marietta Energy Systems, Inc.

REFERENCES CITED

Agostini, P., L'Huillier, A., Petite, G., Tang, X., and Lambropoulos, P., 1987, Multiphoton spectroscopy of autoionizing states and AC Stark shifts in strontium atoms, *in* Hurst, G.S. and Morgan, C.G., eds., Resonance ionization spectroscopy 1986: Institute of Physics Conference Series Number 84, Bristol, England, p. 39–44.

Beekman, D.W., and Thonnard, N., 1989, Laser ablation as an atomization source for ultrasensitive element analysis using resonance ionization time-of-flight mass spectrometry, *in* Lucatorto, T.B., and Parks, J.E., eds., Resonance ionization spectroscopy 1988: Institute of Physics Conference Series No. 94, Bristol, England, p. 163–166.

Beekman, D.W., Callcott, T.A., Kramer, S.D., Arakawa, E.T., and Hurst, G.S., 1980, Resonance ionization source for mass spectroscopy: International Journal of Mass Spectrometry and Ion Physics, v. 34, p. 89–97.

Bekov, G.I., 1989, Ultrasensitive laser photoionization analysis in oceanology, geochemistry, and geology, *in* Lucatorto, T.B., and Parks, J.E., eds., Resonance ionization spectroscopy 1988: Institute of Physics Conference Series No. 94, Bristol, England, p. 331–336.

Bekov, G.I., Letokhov, V.S., Radaev, V.N., Badykov, D.D., and Nazarov, M.A., 1988, Rhodium distribution at the Cretaceous/Tertiary boundary analyzed by ultrasensitive photoionization: Nature, v. 332, p. 146–148.

Berry, R.S., 1987, Angular distributions and electron correlation from resonance ionization spectroscopy of barium atoms, *in* Hurst, G.S., and Morgan, C.G., eds., Resonance ionization spectroscopy 1986: Institute of Physics Conference Series Number 84, Bristol, England, p. 203–208.

Boyd, S.R., Pillinger, C.T., Milledge, H.J., Mendelssohn, M.J., and Seal, M., 1988, Fractionation of nitrogen isotopes in a synthetic diamond of mixed crystal habit: Nature, v. 331, p. 604–607.

Chen, D.Y., Xiao, G.Y., and Wen, K.L., 1987, The development of a SIRIS system for exploration in China, *in* Hurst, G.S., and Morgan, C.G., eds., Resonance ionization spectroscopy 1986: Institute of Physics Conference Series Number 84, Bristol, England, p. 175–178.

Donohue, D.L., Young, J.P., and Smith, D.H., 1982, Determination of rare-earth isotope ratios by resonance ionization mass spectrometry: International Journal of Mass Spectrometry and Ion Physics, v. 43, p. 293–307.

Eugster, O., 1989, ^{81}Kr in meteorites and lunar rocks as a clue for the cosmic-ray exposure history of solar system material and the terrestrial age of meteorites, *in* Lucatorto, T.B., and Parks, J.E., eds., Resonance ionization spectroscopy 1988: Institute of Physics Conference Series No. 94, Bristol, England, p. 343–350.

Fairbank, W.M., Jr., Riis, E., LaBelle, R.D., Parks, J.E., Spaar, M.T.,and Hurst, G.S., 1987, A search for new elementary particles using sputter-initiated resonance ionization spectroscopy, *in* Hurst, G.S., and Morgan, C.G., eds., Resonance ionization spectroscopy 1986: Institute of Physics Conference Series Number 84, Bristol, England, p. 275–280.

Fairbank, W.M., Jr., Hutchinson, J.M.R., Parks, J.E., and Spaar, M.T., 1989, Observation of anomalous isotope ratios in SIRIS measurements of molybdenum, *in* Lucatorto, T.B., and Parks, J.E., eds., Resonance ionization spectroscopy 1988: Institute of Physics Conference Series No. 94, Bristol, England, p. 293–296.

Fassett, J.D., Travis, J.C., Moore, L.J., and Lytle, F.E., 1983, Atomic ion formation and measurement with resonance ionization mass spectrometry: Analytical Chemistry, v. 55, p. 765–770.

Fassett, J.D., Moore, L.R., Shideler, R.W., and Travis, J.C., 1984, Pulsed thermal atom source for resonance ionization mass spectrometry: Analytical Chemistry, v. 56, p. 203–206.

Freund, F., 1987, Hydrogen and carbon in solid solution in oxides and silicates: Physics and Chemistry of Minerals, v. 15, p. 1–18.

Gruen, D.M., Pellin, M.J., Young, C.E., and Calaway, W.F., 1986, Laser spectroscopy of sputtered atoms: Journal of Vacuum Science and Technology, v. A4, no. 3, p. 1779–1785.

Herman, P.R., LaRocque, P.E., Lipson, R.H., Jamruz, W., and Stoicheff, B.P., 1985, Vacuum ultraviolet laser spectroscopy III: Laboratory sources of coherent radiation tunable from 105 to 175 nm using Mg, Zn, and Hg vapors: Canadian Journal of Physics, v. 63, p. 1581–1588.

Hurst, G.S., Payne, M.G., Nayfeh, M.H., Judish, J.P., and Wagner, E.B., 1975, Saturated two-photon resonance ionization of He (2^1S): Physics Review Letters, v. 35, p. 82–85.

Hurst, G.S., Nayfeh, M.H., and Young, J.P., 1977, A demonstration of one-atom detection: Applied Physics Letters, v. 30, p. 229–231.

Hurst, G.S., Payne, M.G., Kramer, S.D., and Young, J.P., 1979, Resonance ionization spectroscopy and one-atom detection: Reviews of Modern Physics, v. 51, p. 767–819.

Hurst, G.S., Payne, M.G., Phillips, R.C., Dabbs, J.W.T., and Lehmann, B.E., 1984, Development of an atom buncher: Journal of Applied Physics, v. 55, p. 1278–1284.

Hurst, G.S., Payne, M.G., Kramer, S.D., Chen, C.H., Phillips, R.C., Allman, S.L., Alton, G.D., Dabbs, J.W.T., Willis, R.D., and Lehmann, B.E., 1985, Method for counting noble gas atoms with isotopic selectivity: Reports on Progress in Physics, v. 48, p. 1333–1370.

Kimock, F.M., Baxter, J.P., Pappas, D.L., Kobrin, P.H., and Winograd, N., 1984, Solids analysis using energetic ion bombardment and multiphoton resonance ionization with time-of-flight detection: Analytical Chemistry, v. 56, p. 2782–2791.

Kramer, S.D., Chen, C.H., Payne, M.G., Hurst, G.S., and Lehmann, B.E., 1983, Tunable VUV light generation for the low-level resonant ionization detection of krypton: Applied Optics, v. 22, p. 3271–3275.

Marti, K., 1982, Krypton-81-krypton dating by mass spectrometry, *in* Currie, L.A., ed., Nuclear and chemical dating techniques: Interpreting the environmental record: American Chemical Society Symposium Series, v. 176, p. 129–137.

Moore, L.J., Parks, J.E., Taylor, E.H., Beekman, D.W., and Spaar, M.T., 1987, Medical and biological applications of resonance ionization spectroscopy, *in* Hurst, G.S., and Mor-

gan, C.G., eds., Resonance ionization spectroscopy 1986: Institute of Physics Conference Series Number 84, Bristol, England, p. 239–244.

Niemax, K., 1985, Spectroscopy using thermionic diode detectors: Applied Physics, v. B38, p. 147–157.

Parks, J.E., Schmitt, H.W., Hurst, G.S., and Fairbank, W.M., Jr., 1983, Sputter-initiated resonance ionization spectroscopy: Thin solid films: v. 108, p. 69–78.

———1984, Sputter initiated RIS (SIRIS) for analysis of semiconductor impurities, *in* Hurst, G.S., and Payne, M.G., eds., Resonance ionization spectroscopy 1984: Boston, The Institute of Physics Conference Series Number 71, p. 167–174.

Parks, J.E., Beekman, D.W., Schmitt, H.W., and Spaar, M.T., 1985, Ultrasensitive elemental analysis of materials using sputter initiated resonance ionization spectroscopy, *in* Katz, W., and Williams, P., eds., Applied material characterization: Pittsburgh, Materials Research Society Symposium, Materials Research Society, v. 48, p. 309–317.

Payne, M.G., Hurst, G.S., Nayfeh, M.H., Judish, J.P., Chen, C.H., Wagner, E.B., and Young, J.P., 1975, Kinetics of He(2^1S) using resonance ionization spectroscopy: Physics Review Letters, v. 35, p. 1154–1156.

Pellin, M.J., Young, C.E., Calaway, W.F., and Gruen, D.M., 1984, Trace surface analysis with pico-coulomb ion fluences: Direct detection of multiphoton ionized iron atoms from iron-doped silicon targets: Surface Science, v. 144, p. 619–637.

———1986, Trace surface analysis: 30 ppb analysis with removal of less than a monolayer, Fe and Ti impurities in the first atomic layer of Si wafers: Nuclear Instruments and Methods in Physics Research, v. B13, p. 653–657.

Rempe, G., and Walther, H., 1987, Experiments with the single-atom laser, *in* Hurst, G.S., and Morgan, C.G., eds., Resonance ionization spectroscopy 1986: Institute of Physics Conference Series Number 84, Bristol, England, p. 11–19.

Rimke, H., Peuser, P., Sattelberger, P., Trautmann, N., Herrmann, G., Ruster, W., Ames, F., Kluge, H-J., and Otten, E.W., 1987, Detection of trace amounts of actinides and technetium by resonance ionization mass spectrometry, *in* Hurst, G.S., and Morgan, C.G., eds., Resonance ionization spectroscopy 1986: Institute of Physics Conference Series Number 84, Bristol, England, p. 235–238.

Shimizu, N., and Hart, S.R., 1982, Applications of the ion microprobe to geochemistry and cosmochemistry: Annual Review of Earth and Planetary Sciences, v. 10, p. 483–526.

Thonnard, N., Willis, R.D., Wright, M.C., and Davis, W.A., 1987a, Noble gas atom counting using RIS and TOF mass spectrometry II: First results, *in* Hurst, G.S., and Morgan, C.G., eds., Resonance ionization spectroscopy 1986: Institute of Physics Conference Series Number 84, Bristol, England, p. 75–80.

———1987b, Resonance ionization spectroscopy and the detection of ^{81}Kr: Nuclear Instruments and Methods in Physics Research, v. B29, p. 398–406.

Tompkins, F.S., and Mahon, R., 1981, High-efficiency four-wave sum and difference mixing in Hg vapor: Optics Letters, v. 6, p. 179–181.

Turner, G., 1987, Application of RIMS to the study of noble gases in meteorites, *in* Hurst, G.S., and Morgan, C.G., eds., Resonance ionization spectroscopy 1986: Institute of Physics Conference Series No. 84, Bristol, England, p. 51–58.

Walker, R.J., and Fassett, J.D., 1986, Isotopic measurements of subnanogram quantities of rhenium and osmium by resonance ionization mass spectrometry: Analytical Chemistry, v. 58, p. 2923–2927.

Walker, R.J., Shirey, S.B., and Stecher, O., 1988, Comparative Re-Os, Sm-Nd and Rb-Sr isotope and trace element systematics for Archaen komatiite flows from Munro Township, Abitibi Belt, Ontario: Earth and Planetary Science Letters, v. 87, p. 1–12.

Willis, R.D., Thonnard, N., Wright, M.C., Lehmann, B.E., and Rauber, D., 1989, Counting ^{81}Kr atoms in groundwater using RIS-TOF, *in* Lucatorto, T.B., and Parks, J.E., eds., Resonance ionization spectroscopy 1988: Institute of Physics Conference Series No. 94, Bristol, England, p. 213–216.

Winograd, N., Baxter, J.P., and Kimock, F.M., 1982, Multiphoton resonance ionization of sputtered neutrals: A novel approach to materials characterization: Chemical Physics Letters, v. 88, p. 581–584.

Young, C.E., Pellin, M.J., Calaway, W.F., Jorgensen, B., Schweitzer, E.L., and Gruen, D.M., 1987, Trace surface analysis via RIS/TOF mass spectrometry, *in* Hurst, G.S., and Morgan, C.G., eds., Resonance ionization spectroscopy 1986: Institute of Physics Conference Series Number 84, Bristol, England, p. 163–168.

Use of the Ion Microprobe to Measure Natural Abundances of Oxygen Isotopes in Minerals

By Bruno J. Giletti[1] *and* Nobu Shimizu[2]

Abstract

Ion microprobe analysis with the Cameca model 4f permits determination of oxygen isotopic compositions in crystal surfaces in volumes as small as 1 micrometer on a side, although larger volumes are needed to reduce analytical uncertainties to less than 1 per mil. Analyses of a plagioclase feldspar yielded blocks of data of 100 mass spectrometer cycles that had standard deviations of the mean of approximately 0.7 per mil for 1 σ. A succession of such blocks of data on the same specimen yielded maximum differences on the order of 1.1 per mil. The ability to reproduce differences between specimens of different $\delta^{18}O$ values and to obtain such data for different minerals, however, remains to be determined through testing.

DESIRABLE CONDITIONS FOR ^{18}O ANALYSIS

The principal advantage of using an ion microprobe (or secondary ion mass spectrometer, SIMS) (Slodzian, 1980) to measure oxygen isotopic compositions in minerals is that a very small area (and volume) is analyzed, so detailed studies of inhomogeneous particles as well as of very small particles are permitted. This capability opens up the possibility of answering questions that were not previously solvable with the use of the standard extraction (employing BrF_5, ClF_3, or F_2) and mass spectrometric analysis.

Before examining the performance of an ion microprobe, it is useful to consider some of the problems and goals of such analyses in order to assess the specific needs of the analyst. Examples of the problems would include (1) determination of the $\delta^{18}O$ values of coexisting minerals in normal, closed-system, rapidly cooled igneous rocks to assess the degree of equilibration, (2) a similar determination for slowly cooled igneous or metamorphic rocks, where gradients will be found in most minerals, with the objective of measuring the cooling rate (see Giletti, 1986), (3) measurement of $\delta^{18}O$ values of fossil shells to determine changes in the environment of the organism during its life cycle, and (4) measurement of $\delta^{18}O$ values of ore and gangue minerals to assess the nature of the ore fluid over the time of the deposition. A different category of problem, concerning the relative abundances of all three oxygen isotopes (16, 17, and 18) and the interpretation of early solar system history, is discussed by Zinner (this volume).

Examples of more complex geological processes include multiple metamorphic episodes or open system behavior where fluids enter and (or) leave the rock specimen in question. In these cases, chemical reactions or recrystallization may affect some minerals and not others (for example, alteration, metasomatism, solution-precipitation). Figure 1 shows a cartoon example of an igneous rock that has had a history that is somewhat more complex than simple cooling. The minerals are generally normal in appearance, but the fine-grained band labeled "Other" is suggestive of a later history, which may be fracturing and vein filling, a small shear zone, or another event. The mineral grains are not intended to depict the results of particular events, so their shape is not intended to appear diagnostic.

It clearly would be desirable to analyze the small mineral particles as well as to measure $\delta^{18}O$ values in traverses across the various larger mineral particles. In addition, given our present knowledge of diffusional anisotropies in quartz (Giletti and Yund, 1984) and hornblende (Farver and Giletti, 1985), such traverses should also be measured in different directions.

In the example of figure 1, an area for analysis should be on the order of <50 μm. If detail is sought in the tiny grains, then <10 μm is preferable. In addition, the depth of the analyzed area should be small, preferably <1 μm. It is possible to imagine fine-grained rocks where the volume analyzed is a few micrometers across in all dimensions. This volume should be contrasted with the normal oxygen extraction and mass spectrometer analysis, where sample volumes are 2 to 5 mm^3.

A cube of quartz, 1 μm on a side yields 10^8 ^{18}O atoms. A reasonable useful yield of ions of 0.3 percent would result in counting 3×10^5 ^{18}O atoms, with a counting uncertainty of 2 ‰ (1 σ). By increasing the size to 2 μm on a side, the uncertainty would be lowered to 0.7 ‰. Consequently, the ion probe analysis represents a potential improvement of approximately 3 orders of magnitude in volume of sample, or approximately 2 orders of magnitude if a comparable precision of 0.1 to 0.2 ‰, comparable to normal mass spectrometer analysis, can be attained.

Oxygen isotopic compositions and their variations in nonhomogeneous minerals have been measured routinely, by using ion microprobes, when very large variations have

[1] Department of Geological Sciences, Brown University, Providence, RI 02912.

[2] Department of Earth Atmospheric and Planetary Sciences, Massachusetts Institute of Technology, Cambridge, MA 02139.

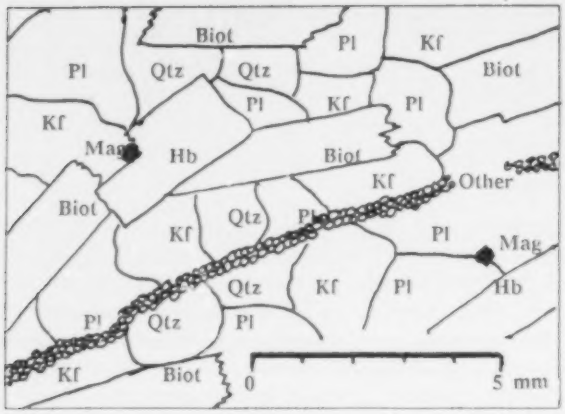

Figure 1. Hypothetical thin section of a granite illustrating scale on which analyses are needed. Minerals are Qtz, quartz; Pl, plagioclase; Kf, microcline; Hb, hornblende; Biot, biotite; Mag, magnetite; and the fine-grained band labeled "Other," some fine-grained material that may be the result of later deformation, recrystallization, or fracturing and deposition.

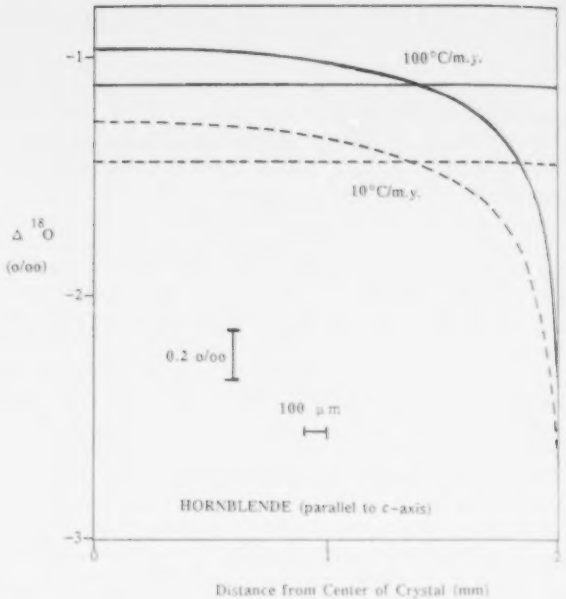

Figure 2. Difference in ^{18}O concentration between a hornblende crystal and an adjacent homogeneous reservoir of plagioclase as a function of distance from the center of the hornblende crystal to its edge. Variation is due to variation of isotopic fractionation factor during cooling in the vicinity of the closure temperature and is also due to the slowing down of the oxygen diffusion rate as the rock cooled at a rate of 10 or 100 °C per million years (m.y.). Horizontal straight lines show mean $\Delta^{18}O$ value for the entire crystal. o/oo, per mil.

resulted from doping the mineral with isotopically enriched oxygen (Giletti and others, 1978; Giletti and Yund, 1984). The objective of the present discussion is to focus on measuring naturally occurring, and thus very small, variations in oxygen isotopic composition in these extremely small volumes of material. These have not yet been reported.

Needless to say, such analyses should give a high degree of precision. For cases in which there is compositional zoning in the $\delta^{18}O$ values, this zoning may be several per mil, but it might also be only 1 or 2 o/oo, or even less. This zoning may reflect late-stage changes in ambient fluids, late-stage growth of the crystal, or late-stage alteration.

If the rock had a simple history, it may still have $\delta^{18}O$ zoning resulting from diffusional exchange during cooling (Dodson, 1986). The Dodson model, together with oxygen diffusion data in hornblende (Farver and Giletti, 1985) and plagioclase (Giletti and others, 1978), were used to compute the compositional gradient of $\delta^{18}O$, parallel to the *c* axis, in a hornblende crystal that was in contact with plagioclase and cooled at 10 or 100 °C per million years (see fig. 2). The ordinate is taken as the difference from the value in the adjacent plagioclase. Analyses that give uncertainties of 0.2 o/oo or better are needed if the cooling rate is to be determined.

ION MICROPROBE FEATURES AND OPERATION

Most ion microprobe studies have used the Cameca IMS 3f or earlier versions of the ion probe produced by various companies. We shall be reporting on the newer model of the Cameca, the IMS 4f. It is useful to treat this in terms of the earlier model, however, so that the other papers (Hervig and others, this volume; Zinner, this volume) can refer to the description given here. Some of the new features of the 4f will then be introduced.

Figure 3 shows a schematic drawing of the Cameca IMS 3f ion microprobe as published by the Cameca Company. Its operation is straightforward in principle, and a very brief description will be given to illustrate ion probe characteristics and operation in general.

An ion microprobe consists of two parts: (1) the source and ion optics of a primary beam and (2) the ion optics of the mass analyzer of the secondary beam. The sample surface is the object that is common to the two parts. The purpose of the primary beam is to direct ions of moderately high energy at the sample surface in order to knock (sputter) sample atoms from the surface. These sample atoms will include positively or negatively charged ions, and these can be accelerated into the mass analyzer part as a secondary beam. The mass analyzer then separates the ions according to mass and either measures the abundance of a given mass or displays an image of the sample.

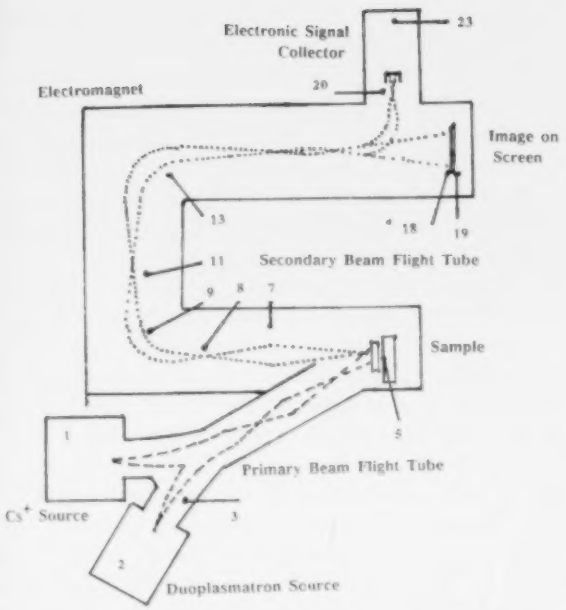

Figure 3. Schematic drawing of the Cameca IMS 3f ion microprobe, with primary beam at bottom and secondary ion optics at center and top. See text for description. Modification of a figure from the Cameca Company, Courbevoie, France.

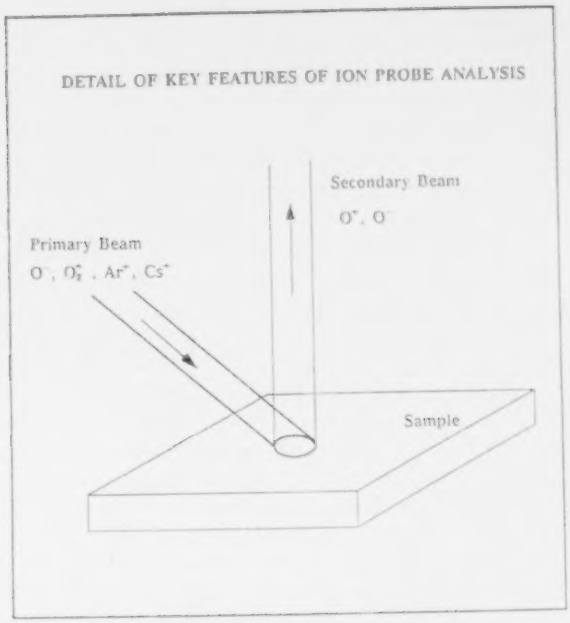

Figure 4. Schematic drawing of local geometric relations of primary and secondary ion beams with relation to sample in Cameca ion microprobe. Scale is such that the area of sample struck by the primary beam may be in the range of 1 to a few hundred micrometers in diameter.

showing where the given mass ions derive (creating a "map" of the abundance distribution of that mass in the sample surface).

The operation of the ion probe can now be considered in more detail (see fig. 3). A primary ion beam, created in the source regions 1 or 2, can be atoms of Cs^+, O^-, O_2^+, Ar^+, or other gases (see Hervig and others, this volume). The cesium ions are produced by heating molten cesium metal so as to evaporate cesium atoms and having these come into contact with very hot metal so the atoms are ionized to Cs^+. The gas ions are created by introducing oxygen, argon, or another gas into a duoplasmatron, where the applied high voltage causes the atoms to ionize into a plasma. In either case, the ions are accelerated by several thousand volts (usually 10 kV) toward the sample. The polarity of the applied potential will select the sign of the charge on the ions being accelerated. The beam is cleaned up by means of a magnetic sector "mass spectrometer" to give ions of a single mass at region 3, then the beam is focused and shaped to impinge on the sample at 5. The cleanup by the mass spectrometer at 3 results in a primary beam that consists of one mass of the gas being used. Where the ion is a single atom, only one isotope of the gas is accelerated to the sample. The primary beam is focused into a small cross-sectional area as it arrives at the sample. This focusing occurs in the primary beam column (between 3 and 5) and results in a beam of circular cross section whose diameter can be chosen. Generally, the beam can be given a diameter between less than 1 to a few hundred micrometers. In addition, the beam can be swept over a rectangular area, much as in a cathode ray oscilloscope or TV tube. This action is called rastering. The size of the rastered area can be chosen and may be 0 to 400 μm across, where these dimensions refer to the area swept by the center of the primary beam.

The atoms in the sample surface are sputtered off by the cascades of collisions induced by the primary beam ions when they strike the surface (fig. 4). The sputtered material consists of several different species: neutral atoms, positively or negatively charged atoms, or clusters of atoms. The charged ions are predominantly singly charged, although multiply charged ions are observed also. The multi-atom fragments consist mostly of two atoms, though larger groupings are observed, with the abundances dropping by orders of magnitude for each additional atom above two. These multi-atom fragments need not follow simple rules of chemistry but may be made up of any two atoms in the sample. In silicates, the common pair is the metal oxide (KO, SiO, NdO, and so on), again, with no relevance to the valence properties. The vast majority of the atoms do come off as single atoms or ions.

The multi-atom fragments of single charge act much as do the single-atom ions. If such a fragment has the same

"molecular" weight as the atomic weight of a single atom being analyzed, the fragment will augment the signal received for that mass and give a greater apparent abundance to the isotope being studied.

These sputtered ions are then accelerated by a 4,500-V potential, as the secondary beam, in the direction of areas 7 and 8 in figure 3. Normally, less than 1 percent of the sputtered atoms are ions of the appropriate charge to be accelerated as the secondary beam and measured. The beam is bent by the electrostatic analyzer at 9 and the magnet at 13, which produces the mass separations commonly encountered in a mass spectrometer. The electrostatic deflection of the beam at 9 results in a small dispersion (region 11) of the ions, depending on their energies.

The Cameca instrument takes advantage of this effect to remove some of the multi-atom fragments from the secondary beam. It was observed that the energy distributions of the single-atom ions differ from those of the multi-atom fragments. More of the single-atom ions have higher energy. If a slit is placed at region 11, only atoms of higher energy can be selected to enter the magnet. The result is that atoms of the isotope being analyzed will be reduced in number by the slit, but multi-atom fragments will be far more reduced, thereby "purifying" the secondary beam. This technique is called energy filtering. An alternative way to effect this filtering is to keep everything else the same and reduce the accelerating voltage from 4,500 V. This technique is called a voltage offset. The voltage offset is often in the range 30 to 100 V. Less offset voltage will not produce much effect, and more will often reduce the signal received so drastically that the sacrifice in counting statistics of the signal is considered too great.

An alternative to energy filtering to remove the extraneous multi-atom fragments is to distinguish them from the single-atom ions on the basis of mass. The interfering fragment will have the same nominal mass as the isotope being studied, but there will be a very small difference in the masses. By using the mass spectrometer of the ion probe under conditions of high mass resolution, it is sometimes possible to separate the beams of the fragment ions from the single-atom ions and to measure only the desired isotope. As in the case of energy filtering, the price paid for the higher mass resolution is a decrease in signal intensity. Consequently, although mass resolutions in excess of 15,000 are attainable with the Cameca ion probes, the signals become highly attenuated, so that precise abundance measurements are difficult for low-concentration species.

Once the beam leaves the magnet at 13 (fig. 3), it can be collected for study in different ways. It is then either imaged at 19 or is measured by use of either a Faraday cup or an electron multiplier in region 20–23. The imaging at 19 occurs on a phosphorescent screen viewed with a microscope or on a cathode ray oscilloscope display. The ion optics are designed to produce a focused image of the ion beam at the detector at 18 so that an image of the sample surface is seen. Regions of high concentration of the isotope being imaged will appear as bright areas on the image.

Quantitative measurement of the ion beam is effected by deflecting the beam into the region 20–23, where an electron multiplier or DC amplifier is used. Oxygen isotopic analysis performed with this instrument, with some modifications, is discussed by Hervig and others (this volume) and by Zinner (this volume).

The Cameca 4f model is different from the 3f in several respects, but we shall consider only two, which are important to the ^{18}O analyses. The principal innovation is the normal-incidence electron gun (Slodzian and others, 1987). As discussed also by Hervig and others and by Zinner (this volume), a serious problem arises in the analysis of electrical insulators. If a Cs^+ primary beam is used, charging of the sample surface takes place, which alters the net accelerating potential of the secondary beam and distorts the local field at the sample surface where the ions are collected for their trip through the analyzer optics. The result is drastic reduction of the secondary beam signal (2 or 3 orders of magnitude).

The solution to this problem in the case of the 4f is shown in figure 5. Electrons are generated by an electron gun mounted partway along the flight tube of the secondary beam (in the vicinity of regions 7 and 8 of figure 3, which depicts the Cameca 3f) and are accelerated and then deflected "upstream" toward the sample surface. The accelerating potential is identical to that applied to accelerate the O^- ions of the secondary beam, approximately 4,500 V, but in the opposite sense. The result is that, if the sample acquires a positive charge owing to the Cs^+ primary beam, the electrons will neutralize it. If there is no charge buildup, a weak magnet deflects the electrons from the surface of the sample. As a result, charge neutralization will occur as though "on demand," and signal intensity is maintained at a high level. Additional focusing is required for the secondary beam because distortion is introduced in the course of controlling the electron beam. This adjustment is made as shown on the right-hand side of figure 5.

The second modification in the 4f enables peaks to be switched electrostatically. This capability permits rapid alternation between masses 16 and 18, without the delays inherent in driving the mass spectrometer electromagnet to the appropriate field strengths for the different masses. The result is that modest variations in the signal intensity with time can be offset by reducing the time spent on one mass during such variations. Data collection times can be made quite short (we used 100 ms for mass 16 in some of our measurements). Such short counting times and rapid switching are possible if the electron multiplier is used. Owing to the slower reponse time of the amplifier of the Faraday cup collector, peak switching is not normally used.

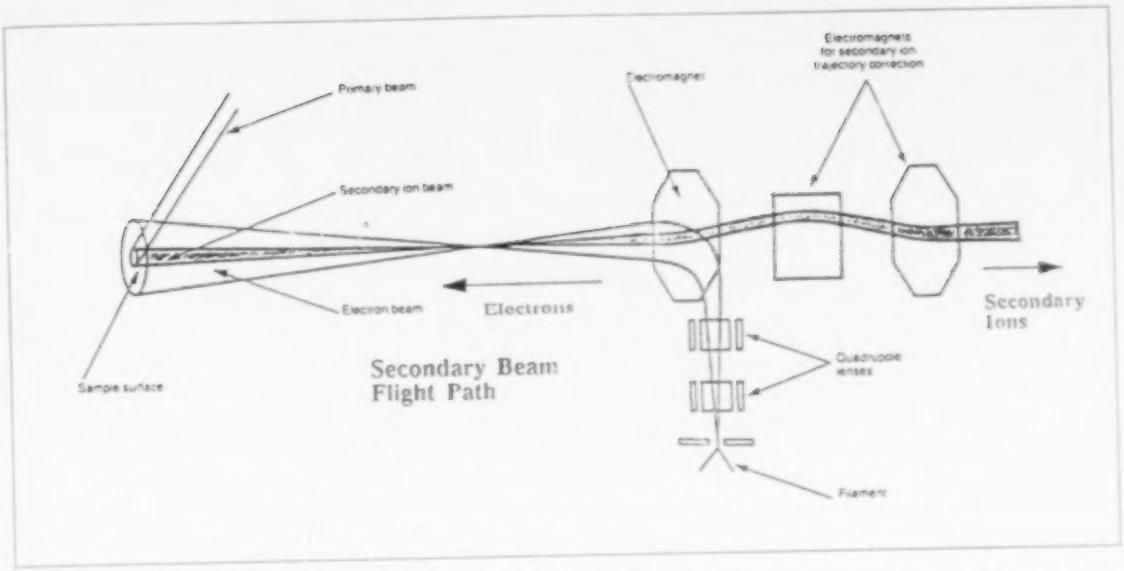

Figure 5. Schematic drawing of the charge neutralization device used on the Cameca 4f ion microprobe. Left-hand end of diagram shows same geometry as in figure 4 except inverted left-to-right. Remainder of diagram is part of flight tube for secondary beam. Filament is source of electron beam that is deflected "upstream" in the secondary beam, back to the sample surface. Modification of a drawing from the Cameca Company, Courbevoie, France.

Strong oxygen signals (mass 16 approximately 5×10^5 counts per second (cps)) were obtained by use of an 8-pA primary beam of somewhat uncertain size on the order of 0.5 to 1 μm in diameter.

RESULTS

The results presented were obtained on the demonstrator instrument at the Cameca factory in Courbevoie, France. The sample was a plagioclase from a Lake County, Oregon, basalt, chosen in the hope that a plagioclase quenched in a lava would be homogeneous. Specific operating conditions used with the Cameca IMS 4f to measure $^{18}O/^{16}O$ ratios are delineated in the following list.

Lake County plagioclase is from a basalt (therefore quenched so as to avoid gradients)
Primary beam = Cs^+ ions
Spot size of primary beam = 1 μm
Primary beam current = ~10 pA
Secondary beam = O^- ions
Normal-incidence electron gun employed (to neutralize sample charge)
Mass resolution = approximately 1,500
Electrostatic peak switching, count 16 for 0.1 s and 18 for 5 s
Each data set is 10 blocks of 10 scans each (100 ratios)
When rastered, used 50- by 50-μm area to start off, then reduced to 15- by 15-μm area for data collection
Mass 18 counts per scan = (0.5 to 1) × 10^4

The analyses consisted of sets of data obtained by finding the ratio of mass 18 abundance to mass 16 abundance. A given ratio was found by taking the ratio of the signal at mass 18 relative to that for mass 16, where the latter is the weighted mean of the two mass 16 values measured just before and just after the mass 18. The weighting is based on the time intervals between the collection of the mass 18 and the two mass 16's, as these are not symmetrically disposed in time about the 18. Background counts as well as monitoring of the ^{30}Si signal were also part of the mass spectrometer cycle. Blocks of data consisting of 100 such ratios were taken.

Table 1 shows the results of a single day of analyses and includes a single analysis in which a small rastered area was used instead of no rastering by the primary beam. The data are presented in the order they were taken. Each entry is the mean of the 100 cycles described above. Spacing occurs to indicate where the sample was moved to begin sputtering in a new spot on the crystal. The uncertainties are given as standard deviations of the mean, in per mil.

Table 1. Reproducibility of ^{18}O analyses by use of the Cameca IMS 4f ion microprobe

[All data were run continuously in 1 day. Sample is a plagioclase from Lake County, Oregon. Extra spacing between run numbers indicates a change to a new spot on crystal surface]

Run	$^{18}O/^{16}O$ ($\times 10^3$)	+/− 1σ (o/oo)	Mean ($\times 10^3$)	Stand. dev. from mean (o/oo)	Stand. dev. from A[1] (o/oo)
32	1.979	0.7		0.8	
33	1.977	.35		.2	
34	1.9764	.63	1.97747	.5	1.0
35	1.9722	.78		2.5	
36	1.9821	.76	1.97715	2.5	1.1
37	1.9729	.6		3.3	
38	1.9794	.57		.1	
39	1.9835	.52		2.1	
40	1.9817	.64	1.9794	1.2	0=A[1]
41	1.9784	.67		.4	
42	1.9801	.60		1.2	
43	1.9747	.59	1.9777	1.5	.8
44 (miniraster)	1.9972	.8		3.4	
45 (miniraster)	1.9887	.69	1.9938	2.6	7.3

[1] Arbitrary value against which the others will be compared.

DISCUSSION

It can be seen from table 1 that these are preliminary data given as a progress report. While the Cameca Company was quite generous in allocating 5 days to this study (following another briefer visit 6 months earlier), the time was too short to indicate the quality of the data that ultimately can be obtained from this instrument.

Before discussing the results further, it is useful to consider the key factors that control the determination of high-precision $\delta^{18}O$ data. One of these is the statistics of the measurement. The primary ion beam can be made quite intense and thereby produce a strong secondary beam signal. Use of a Cs^+ primary beam and O^- secondary ions is no exception. It is relatively easy to obtain a mass 16 signal that is 1 million cps, which means that the mass 18 signal in oxygen is 2,000 cps. If counted for 5 s, this rate would give a mass 18 standard deviation of 1 percent for one such count.

A problem with such count rates lies in the dead time of the electron multiplier used to measure the counts. Dead time is the interval from the acceptance of a count by the counter until the counter is ready to accept the next count. Dead times on the order of 25 ns are common in the multipliers used on Cameca ion probes. For high count rates, the electron multiplier will not be able to keep up, and a correction must be made for those counts that it misses. Such a correction is not accurate enough for the oxygen work if the rates are on the order of millions of counts per second.

The relative abundances of the oxygen mass 16 to mass 18 are 500 to 1. The choice is either to increase the count rate so that the mass 18 can be counted with better precision, with consequent loss of precision in the huge mass 16 signal, or to reduce the count rate for mass 16 to approximately 500,000 cps, with a loss in the mass 18 precision.

Consider a specific case of dead-time correction. For a 25-ns dead time and a count rate of 500,000 cps, the multiplier would fail to record 1.25 percent of the counts, and the apparent rate would need to be increased by that amount. If the count rate were 600,000 cps, the multiplier would miss 1.5 percent of the counts. Suppose that the dead time should really be 30 ns; then, the corrections would need to be 1.5 and 1.8 percent, respectively. Clearly, the measured ratio of mass 18 to 16, for instance, depends directly on the correction for the dead time. If a correction is made, however, the two count rates would still be in the ratio of 1.2 to 1.

Our experience is too limited to permit us to make a definitive statement, but it appears that the measured ratio will vary from day to day by as much as several per mil. Further, the absolute ratio is not known well. As a result, it appears desirable to measure the ratio and compare it to that for a standard that is mounted in the same sample mount and is measured on the same day. If this is done, and the same dead-time correction is used for all the measurements, the relative values of the ratios ($\Delta^{18}O$'s) could still be correct. The problem would arise again, however, if the correction became large (say >10 percent), because uncertainties are inherent in the way the correction can be made. If the same, relatively low, count rate is used for all measurements, then there is less chance for discrepancies.

The logical solution is to count mass 18 for a long time, but this solution permits greater variations in the signal intensity that are due to a slight drift as well as small fluctuation in the signal intensity. Alternatively, an electron multiplier that has a shorter dead time might be sought.

A second factor in obtaining high precision is the fractionation of the isotopes during the analysis. By that we mean the steady-state measurement of a different isotopic ratio in the ion probe from that of the sample. If sputtering causes fractionation, the result is that a different composition is left on the sample surface. This process will, in turn, affect the composition of the sputtered material until a steady state is reached that yields a sputtered sampling that is the same as the sample itself. Despite this, however, the fraction of sputtered atoms that is ionized needs not have the same isotopic composition as the sputtered material (see Shimizu and Hart, 1982). These authors also found that where the sputtered ions were sampled, relative to the aligned optic axes of the primary and secondary beams, was critical to the degree of fractionation that occurred. Consequently, careful alignment and maintenance of the same

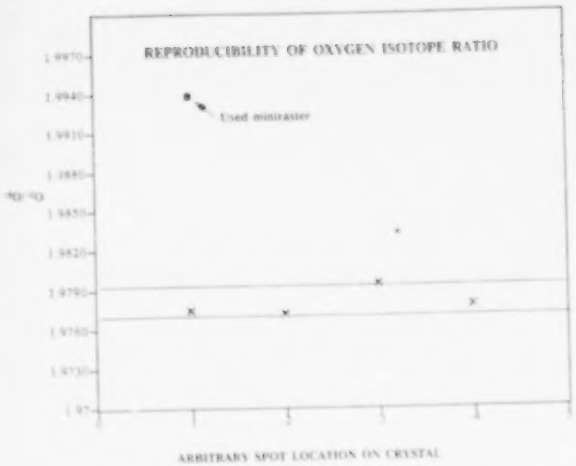

Figure 6. $^{18}O/^{16}O$ ratio measured on different places of a single crystal of Lake County, Oregon, plagioclase. Spacing between the two lines is 1 ‰ and is given to assist in assessing reproducibility. Note data point where rastering was employed.

conditions of operation may prove essential to optimum ^{18}O analysis.

Another possible cause of fractionation is if not all the ions produced and accelerated into the secondary beam are allowed to travel to the collector. The technique of energy filtering, used to reduce interferences by multi-atom fragments, may also transmit different masses selectively. It may be best to operate without energy filtering.

Figure 6 shows the data from table 1. The results of all the analyses fall within 1.1 ‰ of each other. This fact is encouraging but not definitive. It is necessary to assess the performance of the instrument in two other critical ways. The first is to be able to compare the results of measurements taken on two different specimens, with different $\delta^{18}O$ values, and obtain the correct value of this difference.

The second is to be able to measure the same two specimens at a significantly later date (days or weeks) and still obtain the same difference. It would be even more desirable if the same $^{18}O/^{16}O$ ratios were obtained on the same specimen on different days. Preliminary data taken on days different from the day when the values of table 1 were obtained suggest that the last may not be possible (see also Hervig and others, this volume). Note how important the modest change in operating conditions, namely the use of rastering, is to the data. It remains to be seen if rastering will give reliable, though different absolute, values.

It will be necessary to make numerous additional measurements before the uncertainty in the measured $^{18}O/^{16}O$ ratios can be known. The measurements show considerable promise but are a beginning at best. The absolute values of the ratios are quite different (see table 1) from the expected values, where the ^{18}O might be expected to be 0.203 percent of the total oxygen. This difference is probably due to fractionation at the sputtering site. The absolute value is not a critical constraint, however, if differences in the $^{18}O/^{16}O$ ratios can be measured well. In that sense, this system would be no different from standard mass spectrometry, where the ratio is determined relative to a standard. A standard could be mounted alongside the unknown and the $\Delta^{18}O$ between them determined. The same standard could then be used to compare with other specimens also, much as in the case of standard mass spectrometry.

A great deal remains to be done. First is to reproduce the same $\Delta^{18}O$ between two specimens on different days. Second is to determine the optimum operating conditions to achieve the smallest uncertainty in this reproducibility test. Third, the difference in $\Delta^{18}O$ should be varied between different specimens, and the correct difference should be obtained in all cases. Finally, the assessment of the effect of the crystal matrix remains to be made. Can a feldspar be compared to a quartz, to a mica, or to a nonsilicate such as magnetite (see Hervig and others, this volume)? Will multiple standards be needed? It should be clear from these questions that a more detailed treatment of the data presented is not warranted at this point. The data need to be compared with other results of the sort just described before a proper assessment of the capabilities of the Cameca 4f can be made. It should be noted that closer scrutiny may lead to larger or smaller uncertainties than are shown here.

CONCLUSIONS

Preliminary measurements have been made of $^{18}O/^{16}O$ ratios by use of the Cameca IMS 4f ion microprobe. The normal-incidence electron gun makes for considerable stability and a high secondary O^- beam intensity. Rapid electrostatic peak switching permits avoidance of drift and some variation problems that arise from a fluctuating beam. Replicate measurements on a single crystal of plagioclase fall within a range of 1.1 ‰. It is not yet known if replication of differences between two specimens can be achieved over long time periods of days to months. It is also necessary to determine the effects of comparing the $^{18}O/^{16}O$ ratios of different minerals. While promising results were obtained, the definitive assessments of the Cameca 4f for $^{18}O/^{16}O$ analysis remain to be performed.

ACKNOWLEDGMENTS

The authors wish to thank the Cameca Company for making time available on their demonstrator model, IMS 4f. Particular thanks are due to H.N. Migeon and J.-J. Le Goux for their generous cooperation in helping us to run the

tests. We also wish to thank Bob Criss and Pat Shanks for organizing this workshop and for their efforts, together with those of Ernst Zinner, for reviewing this manuscript.

REFERENCES CITED

Dodson, M.H., 1986, Closure profiles in cooling systems: Material Sciences Forum, v. 7, p. 145–154.

Farver, J.R., and Giletti, B.J., 1985, Oxygen diffusion in amphiboles: Geochimica et Cosmochimica Acta, v. 49, p. 1403–1411.

Giletti, B.J., 1986, Diffusion effects on oxygen isotope temperatures of slowly cooled igneous and metamorphic rocks: Earth and Planetary Science Letters, v. 77, p. 218–228.

Giletti, B.J., and Yund, R.A., 1984, Oxygen diffusion in quartz: Journal of Geophysical Research, v. 89, p. 4039–4046.

Giletti, B.J., Semet, M.P., and Yund, R.A., 1978, Studies in diffusion, pt. III, Oxygen in feldspars, an ion microprobe determination: Geochimica et Cosmochimica Acta, v. 42, p. 45–57.

Shimizu, N., and Hart, S.R., 1982, Isotope fractionation in secondary ion mass spectrometry: Journal of Applied Physics, v. 53, p. 1303–1311.

Slodzian, G., 1980, Microanalyzers using secondary ion emission: Advances in electronics and electron physics, supplement 138: Academic Press, p. 1–44.

Slodzian, G., Chaintreau, M.P., and Dennebouy, R.C., 1987, Self-regulated potential at insulating surfaces in presence of a strong electrostatic extraction field: Cameca News, May 1987, p. 1–6.

Charge Neutralization and Oxygen Isotopic Analysis of Insulators with the Ion Microprobe

By Richard L. Hervig,[1] Robert M. Thomas,[2] *and* Peter Williams[2]

Abstract

The Cameca IMS 3f ion microprobe at Arizona State University has been modified to allow the analysis of $^{18}O/^{16}O$ ratios on 10- to 20-micrometer spots in insulating minerals in thin section. A primary beam of K^+ or Cs^+ is used, and charge is neutralized by an electron flood gun operating at −7.5 kilovolts. Negative secondary ions are accelerated to −4.5 kiloelectronvolts into the mass spectrometer, where $^{18}O^-$ is detected on the electron multiplier by pulse counting, and $^{16}O^-$ is detected on the electron multiplier or directly measured by an electrometer. In either configuration, internal precisions of 1.2 to 1.7 per mil (1 standard error of the mean) in $^{18}O/^{16}O$ ratios can be achieved. Preliminary analyses, showing quartz to be 10 to 15 per mil lighter than hydrothermally altered plagioclase, suggest that matrix effects are important.

INTRODUCTION

The microanalysis of minerals in thin section for stable isotopic ratios is a desirable goal for researchers working on the ion microprobe (secondary ion mass spectrometer). A major impediment is charge buildup on minerals during analysis. The ion microprobe uses an energetic ion beam to strike a selected mineral. Because most rock-forming minerals are insulators, different degrees of local charge are bound to build up on the sample surface. This charging acts like an electrostatic lens at the sample, deflecting the secondary-ion beam away from the mass spectrometer and commonly reducing the secondary-ion current to the level of instrumental noise. Great strides in overcoming this problem for isotopic measurements have been made by the research group at Washington University in St. Louis under the leadership of Ernst Zinner. In measuring δD, $\delta^{13}C$, $\delta^{15}N$, and $\delta^{18}O$ in extraterrestrial samples, they have avoided the problem of charging by pressing small (~10 μm) particles into a conducting matrix of gold foil. When the primary-ion beam overlaps the particle and the metal, excess charge on the particle "leaks" off to the foil (Zinner, this volume). Although this technique has produced results of fundamental importance in the study of the solar system, it cannot be applied to the study of minerals in thin section, so mineral zoning studies are inaccessible.

Recent technological developments (new normal-incidence electron guns) may provide a means of effective charge neutralization that will enable microanalysis of thin sections (Slodzian and others, 1986; Giletti and Shimizu, this volume), but the technique has not been adequately tested. This contribution reviews various techniques that may provide some means of charge neutralization and shows the results of preliminary oxygen isotopic microanalyses of minerals in thin section.

Statement of the Problem

Historically, ion-microprobe analyses of insulating phases have used a negatively charged primary-ion beam of oxygen directed toward samples coated with a thin conducting layer of carbon or noble metal (Lovering, 1975). Most commonly, a positive potential is applied to the sample to drive positive secondary ions into the mass spectrometer (see fig. 1 of Eldridge and others, this volume). Although the sample is at high positive potential, a net negative charge builds up in the crater formed as the impacting primary beam erodes the conducting film. This charge on the sample is approximately compensated when the abundant secondary electrons that are produced hop to the conducting coat around the crater. At worst, the crater becomes biased to slightly negative values relative to the rest of the sample surface. If this charging increases to high enough values, the secondary-ion beam will become unstable and the intensity will drop because it will be partially deflected from the mass spectrometer slits.

In the case of analysis for oxygen isotopes, two problems that arise from the above approach are immediately apparent: (1) an oxygen primary beam will contaminate the sample and (2) the positive secondary-ion yield of oxygen is very small. The latter can be addressed by changing the polarities on the extraction optics of the ion probe so that negative ions are collected and analyzed; the negative secondary-ion spectrum of oxides shows very intense signals for oxygen and other electronegative elements. Achieving a change in the primary ion species from oxygen to another element is more difficult. If a positive primary ion impacts an insulator while negative ions and secondary electrons are extracted, the sample charges to high, positive values (see fig. 2 of Eldridge and others, this volume).

[1] Center for Solid State Science, Arizona State University, Tempe, AZ 85287.

[2] Department of Chemistry, Arizona State University, Tempe, AZ 85287.

Because of the above difficulties, our initial efforts to analyze minerals for oxygen isotopes were aimed toward developing non-oxygen negative primary-ion beams (Hervig and Williams, 1986). Later, alternative methods of negative secondary-ion analysis in insulators by the use of positive primary beams and auxiliary high-energy electron flood guns were developed. The results of these experiments are described below and are followed by discussion of some preliminary isotopic determinations on natural samples and laboratory standards made in experiments in which primary K^+ and Cs^+ beams were used.

EXPERIMENTATION

This work was carried out in a Cameca IMS 3f ion microprobe analyzer equipped with a standard duoplasmatron ion source, an alkali-metal ion source (constructed in-house), and a primary beam mass filter. The duoplasmatron was modified by eliminating the plasma expansion cup and restricting the intermediate electrode aperture to a diameter of 1/16 in (with a channel length of 1/8 in). All primary ion currents were measured with the Cameca Faraday cup assembly and corrected for secondary electron errors by calibration against a Faraday cup installed at the sample position. All samples were sputter coated with a thin (100–200 Å) conducting layer of Au-Pd alloy prior to insertion into the sample chamber.

Alternative Non-Oxygen Negative Primary Ion Beams

Fluorine

We first investigated the feasibility of generating a F^- primary-ion beam in the Cameca duoplasmatron. Reuter (1984) reported that high primary currents of CF_3^+ could be generated in the same model ion probe by attaching a tank of an O_2–CF_4 mix to the duoplasmatron. Oxygen was used as the support gas instead of argon because with the latter, CF_4 was observed to polymerize on one of the electrodes and thus accelerate the degradation of the duoplasmatron. When we fed a similar gas into the duoplasmatron and extracted negative ions, we found large signals for $^{16}O^-$ (>200nA) and $^{19}F^-$ (>40 nA). The fluorine beam was stable for several hours at a time and generated a similar normalized count rate for $^{18}O^-$ from a standard quartz as a $^{16}O^-$ primary beam. Corrosion of the duoplasmatron was accelerated relative to use of pure oxygen, but only by a factor of about four. Unfortunately, the signal for $^{18}O^-$ relative to $^{16}O^-$ increased with time during a single analysis. The most likely reason for this is contamination of $^{19}F^-$ by $^{18}OH^-$. The mass-resolving capacity of the Cameca primary column is not sufficient to resolve these two ion species. We concluded that F^- is not acceptable for the analysis of $^{18}O/^{16}O$ ratios. A.O. Nier (University of Minnesota, personal commun., 1988) has recently suggested mixing CF_4 with a tank of isotopically pure $^{16}O_2$. Presumably, $^{16}OH_3^-$ would be of negligible intensity.

Cyanide

The $^{12}C^{14}N^-$ ion is known to be very readily formed. For safety reasons, HCN was ruled out as a feed gas. Instead, we used a mixture of 25 percent CO_2: 75 percent air. This mixture gave a maximum of 300 nA CN^-, although 50 to 100 nA was more common. At the same time, an abundant $^{16}O^-$ signal was obtained (maximum of 800 nA), so conventional analyses could use this species without changing the feed gas to the duoplasmatron. Initially, we had problems with primary-beam stability. By testing several mixtures, we found that the most stable CN^- beams were achieved with relatively high ratios of N_2 to CO_2. Secondary-ion count rates for $^{18}O^-$ on quartz normalized to primary-beam intensity were higher than obtained by use of $^{16}O^-$ by approximately the ratio of the masses of the primary beams (26/16). At 8 keV impact energy, count rates (counts per second) were $>10^7$ cps/nA for $^{16}O^-$ and $>2 \times 10^4$ cps/nA for $^{18}O^-$.

A serious problem developed when CN^- generation resulted in severe corrosion of the duoplasmatron. Operation for 24 hours eroded the aperture in the intermediate electrode to more than twice its initial diameter and large whiskers grew from the electrode to the anode. The corrosion problem was solved by designing a new intermediate electrode. A mild steel electrode was machined with a large aperture (1/8-in diameter), and a Macor machinable ceramic insert with a 1/16-in aperture was pressed inside this. This magnetic electrode, having an insulating, nonmagnetic insert, thus had a large magnetic aperture but the optimum physical aperture. This design has worked well for routine operation with Ar^+ and O_2^+ primary beams, and we have used this design exclusively since mid-1985. Enlargement of the intermediate electrode aperture during operation with routine gases has been nearly absent, so our intermediate electrodes no longer wear out.

Although this development was favorable, whiskers continued to grow rapidly from the cathode during operation with cyanide. At best, a stable CN^- beam would last for about 8 hours, but eventually, the drift would be too large for data to be taken. In the stable part of one of these sessions, we analyzed a mantle-derived olivine (Fo_{90}) four times, obtaining good internal precision (1 standard error of the mean ranged from 1 to 1.5 ‰). The arithmetic mean of the four analyses on different points had a standard deviation of 3 ‰. Although somewhat encouraging, the erratic behavior of the CN^- primary beam forced us eventually to abandon this approach.

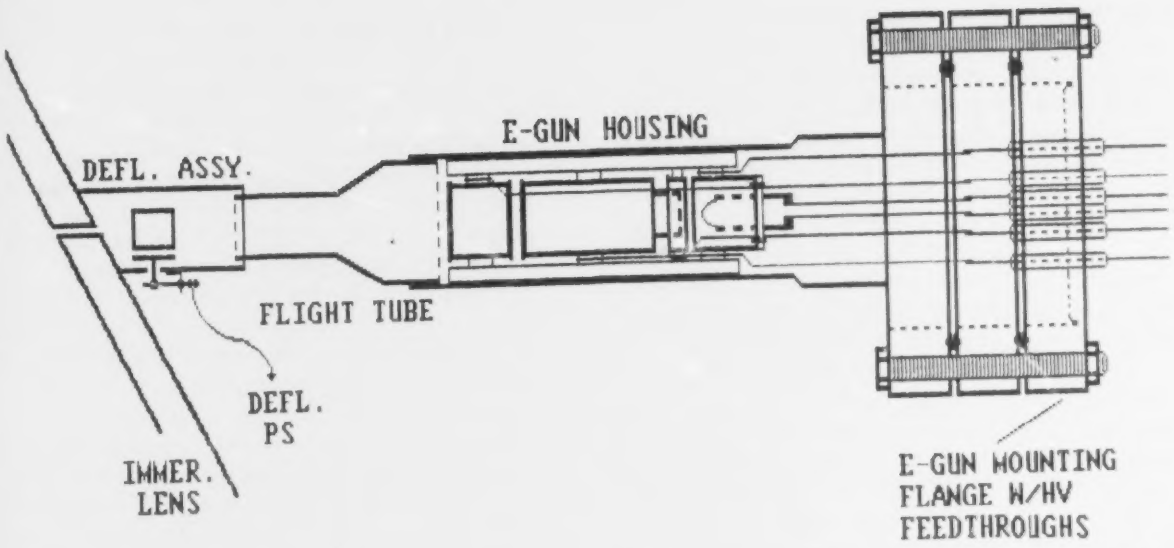

Figure 1. Schematic drawing of the electron flood gun assembly. As received, the gun was mounted on a 2¾-in Conflat flange. An adapter tube was constructed with a Cephalex flange for mating to the Cameca sample chamber. The four boxes shown in the electron gun housing represent the four lenses supplied with the gun, but only the first and last lenses were energized. A deflector assembly (DEFL. ASSY.) and flight tube were attached to the immersion lens (IMMER. LENS), which defines a plane parallel to, and 5 mm away from, the sample surface. Typical operating conditions were (1) filament voltage of −7.5 kV, (2) filament current of 5 A, (3) first lens voltage of −1.2 kV, and (4) last lens voltage of −3.4 kV. HV, high voltage; DEFL. PS, deflector power supply.

Positive Alkali Metal Primary Beams with an Electron Flood Gun

While oxygen primary beams (positive or negative) enhance positive secondary-ion count rates (relative to an Ar^+ primary beam), a primary beam of Cs^+ greatly enhances negative secondary-ion count rates (relative to Ar^+). Routine use of cesium ion sources in ion microprobe analyses obviates the need for exotic (and corrosive) feed gases for the duoplasmatron. Our cesium source was made at Arizona State University (Lareau and Williams, 1986). The problem, as stated earlier, is that the input of positive primary ions and the extraction of negative secondary ions and secondary electrons lead to severe positive charge buildup in the analysis crater on insulating samples. We approached this problem by using an electron flood gun to supply additional electrons to the sample surface.

Successfulness of this technique hinges upon three requirements: (1) a high-energy electron gun is needed to permit electrons to reach the sample, which is at a potential of −4,500 V, (2) the impact energy of the electrons must be selected such that the yield of secondary electrons is less than 1, and (3) proof of charge neutralization rests on obtaining stable secondary-ion signals from samples for indefinite periods and (or) generating sharp images of negative secondary ions from insulating materials.

Electron Flood Gun

A 10-keV electron gun (Model No. CE–537) was purchased from Cliftronics, Inc., of New Jersey. The gun is a high current, four-lens design with a tungsten filament. It was mounted on an auxiliary port on the Cameca sample chamber so that the electron beam struck the sample at an angle ~30° to the sample normal (fig. 1). Although the diameter of the port is only slightly larger than the electron gun diameter, operation of the potentials up to 9 kV is possible routinely without arcing. A grounded flight tube between the gun and the immersion lens housing prevents charge buildup on insulators near the electron trajectory; the einzel lens nearest the sample must also be well screened from stray electrons. The flight tube incorporated deflectors for beam steering, but usually these were not needed. Electron currents (measured at the sample) up to several hundred microamperes have been obtained and used for studies in electron-stimulated desorption (Gillen and Williams, 1986; Williams and Gillen, 1987). For charge neutralization, we reduced the current to 0.5 to 1.5 μA.

The choice of an appropriate electron accelerating potential was extremely important because the secondary electron yield of many oxides is a function of electron impact and angle and can be greater than unity at particular electron energies. For example, the secondary electron yield of ~500 eV electrons on MgO is much greater than 5

(Dekker, 1958). Because secondary electrons will be accelerated away from the sample, an electron gun providing electrons at such energies causes the sample to charge more positively, opposite to the desired effect. Secondary electron yields peak at energies of a few hundred electronvolts (Kanaya and others, 1978) and fall below unity at very low and very high energies. Thus, effective neutralization of positive charge can be achieved by delivering to the sample either very low-energy electrons, as in the new normal-incidence Cameca electron gun (Slodzian and others, 1986; Giletti and Shimizu, this volume) or very high-energy electrons ($E_{impact} \geq 3keV$) as in this work.

We originally felt that the secondary electron problem could be avoided by installing permanent magnets near the sample to produce a weak magnetic field (100–200 G) parallel to the sample surface and return the low-energy secondary electrons to the sample. Although this approach seemed to work, we later discovered that the magnets were not needed if an appropriate electron energy were used. Additional concerns arose about possible mass fractionation related to the magnets, so this approach was abandoned.

The best evidence for the absence of sample charging is the ability to obtain well-resolved negative secondary-ion images of insulating samples when using a *defocused* primary beam (Slodzian and others, 1987). We have been able to obtain such images from certain samples but not from others, and the success or failure of imaging attempts does not depend on the presence of the electron gun. Rather, it appears that certain minerals are more conducive to imaging than others. Biotites give clear negative secondary-ion images, but quartz and plagioclase do not. A simple explanation is that the cleavage traces in biotite retain residues of the noble-metal coating that originally covered the surface. These residues in the traces provide a leakage path for excess charge to the conducting coat, while a 1-nA, ~150-μm diameter, defocused Cs^+ beam completely removed the coat from polished quartz and plagioclase crystals.

The *focused* alkali-metal primary beam has been imaged clearly imaged by $^{16}O^-$ secondary ions on mineral grains at beam diameters ≤50 μm. In this case, the electron gun is absolutely required; switching off the filament voltage eliminates the image. In addition, we have developed techniques to generate stable and intense O^- secondary-ion count rates for long periods of time.

Detection of Secondary Ions

The natural abundance ratio of ^{18}O to ^{16}O, being 1:500, conflicts with the dynamic range of the electron multiplier, as count rates for $^{18}O^-$ must be kept below $\sim 10^3$ counts per second (cps) in order to keep count losses on the $^{16}O^-$ signal below 1 percent. Analysis times are quite long at these conditions, but at higher count rates, the error in determining the counting system dead time becomes significant. The alternative of using an electrometer to measure both isotopes is much more attractive, but up to now we have not been able to obtain stable signals for $^{18}O^- > 1 \times 10^6$ cps ($^{16}O^- = 5 \times 10^8$ cps). The Cameca electrometer has a variable offset current that corresponds to a count rate of $\sim 10^5$ cps, so signals of $\sim 10^6$ cps cannot be measured accurately. A situation arises where we must either give up a factor of 10^2 to 10^3 in secondary-ion intensity (and analysis speed) or measure one isotope on the electrometer and the other with the electron multiplier. McKeegan (1987) has successfully analyzed oxygen isotopes by using only the electron multiplier, but analyses require ~45 min and precision is rarely better than ±2 ‰. We have tested the analysis of ^{16}O on both detectors, finding that ratios can be precisely measured either way, but errors in the absolute ratios are very large when two different detection devices are used. The advantage to such a technique is in searching for mineral zoning. As each analysis requires only ~20 min, internal precision of <1 ‰ can be achieved, and absolute ratios are not so important. Important parameters include the settling time and offset current of the Faraday cup electrometer, the dead time on the electron multiplier, and the degree of charging on the sample.

Analytical Conditions

Primary Beam.—During most analyses reported here, a Cs^+ beam was generated from a General Ionex ion source assembled at Arizona State University. As part of a separate study, this source was loaded with Na, K, and Rb, as well as Cs, to test the relative effectiveness of different alkali beams in ion-microprobe analysis (Lareau and Williams, 1986). On some occasions, analyses for oxygen isotopes were made with K^- as the analyzing beam. At all times, the beam was mass analyzed (for $^{133}Cs^+$ or $^{39}K^+$). Primary currents ranged from 0.1 nA to 5 nA (best results at 0.1 nA) with a corresponding range in beam diameter from 10 to 30 μm.

Secondary Beam.—The sample was held at −4.5 kV and negative ions were accepted into the mass spectrometer from a circular area 20 μm in diameter defined by a combination of electrostatic lenses and physical apertures.

Analysis.—The analysis was begun by sputtering a crater for 10 min to reach stable levels of charging and constant secondary-ion counts. A 10- to 15-min analysis would follow, during which <1 ng of sample would be consumed at primary currents of ~1 nA. The energy window was wide open (energy bandpass of 130 eV) and translated to discriminate against ions with <0 eV excess energy (those formed above the sample in the gas phase). Each cycle of measurements began by ramping the sample voltage to values ±100 V from the initial value of 4,500 V while monitoring the secondary-ion intensity of $^{18}O^-$. The sample voltage was then returned to the centroid of the voltage-intensity peak as a means to compensate for sample

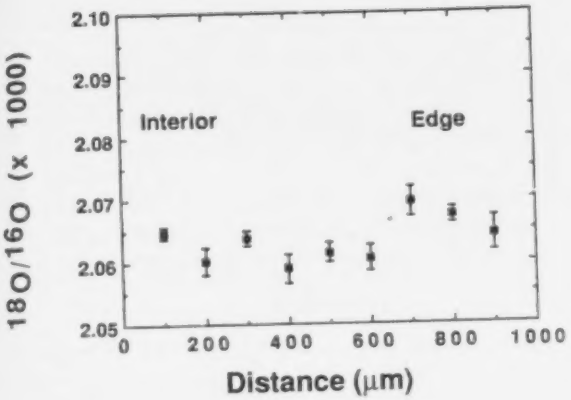

Figure 2. Step scan of oxygen isotopic ratios across a plagioclase crystal in a hydrothermally altered granite from the Isle of Skye, Scotland. K^+ primary beam was at 5 nA and 30 μm in diameter and rastered over a 50 μm × 50 μm area. Secondary ions were collected from a circular area 20 μm in diameter in the center of the crater. $^{16}O^-$ intensity was measured on a Faraday cup, and $^{18}O^-$ was measured on an electron multiplier. Errors are given as 1 standard error of the mean. The reported $^{18}O/^{16}O$ ratios are approximately 30 ‰ too high, probably as a result of using two different detectors for the different isotopes and (or) the result of electronic effects. No clear-cut spatial trend in $^{18}O/^{16}O$ is apparent in this sample.

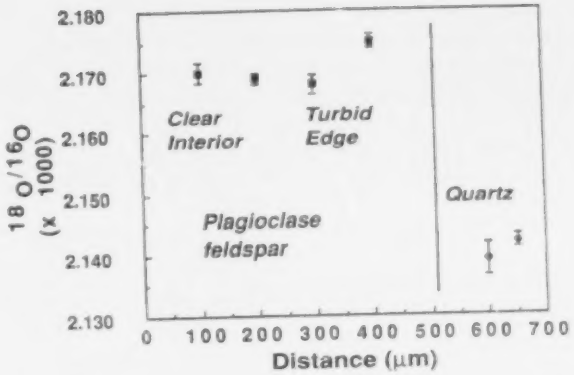

Figure 3. Step scan of oxygen isotopic ratios across same plagioclase crystal as in figure 2. Analytical conditions were identical except that the primary beam was Cs^+ at 1 nA focused to a 25-μm diameter and rastered over a 50 μm × 50 μm square. Note that the two analyses of an adjacent quartz crystal appear to have a significantly lower $^{18}O/^{16}O$ ratio than the plagioclase, an unreasonable situation that probably arises from large (>10 ‰) matrix effects.

charging. This procedure showed that the sample charged to −50 to −80 V. Intensities were measured on masses 18, 17, 16.5 (when the electrometer offset signal was determined), and 16.

Other Variables.—At this time, we are experimenting with different operating conditions. Keeping the field aperture constant at 750 μm, we compared analyses by using different transfer optic lens settings. Analyses with transfer optics set to give an analyzed area 20 μm in diameter gave slightly higher ion intensities, but errors in isotopic ratios were identical to those when transfer optics gave an area 60 μm in diameter. There is an advantage to using the larger analyzed area in that aligning the secondary beam on the ion optical axis is easier.

RESULTS AND DISCUSSION

There are two questions we want to answer in developing this technique. Can we obtain the same $^{18}O/^{16}O$ ratio several times on the same crystal, and how much does chemical composition affect the relative yield of the two oxygen isotopes (that is, how serious are matrix effects)?

The results of nine analyses spaced at ~100-μm intervals are shown in figure 2 for a crystal of plagioclase in a thin section of granite from the Isle of Skye, Scotland, supplied by John Ferry of Johns Hopkins University. This sample was selected because large ^{18}O depletions caused by interaction of rocks with low-^{18}O meteoric-hydrothermal fluids are known to be widespread in this region (Forester and Taylor, 1977). This crystal has homogeneous major-element chemistry in its clear core (left side of the figure) but has a "turbid" rim produced during a hydrothermal event. Errors in each analysis were calculated as 1 standard error of the mean and range from 0.4 ‰ to 1.4 ‰. Even though there are some textural differences associated with the last two analyses as the turbid zone on the right side of the figure is approached, it appears that, to the precision of the ion-microprobe analyses (~1 ‰), the crystal is homogeneous.

The absolute ratios are higher than expected by roughly 30 ‰. These high values may be due to a poorly calibrated feedback resistor (10^{10} Ω) in the electrometer. Such problems are inevitable when two detection modes are used, and we have not yet tried to improve this performance but have instead concentrated on obtaining reproducible *relative* ratios that have good internal precision.

Not shown in figure 2 is an analysis of a quartz grain adjacent to the plagioclase. The measured ratio was 7.5 ‰ *lighter* than the mean value for plagioclase. Because texturally clean quartz in a granite would be expected to be isotopically heavier (typically by 2 to 20 ‰) than feldspar altered by meteoric hydrothermal fluids (Forester and Taylor, 1977; Criss and Taylor, 1983), our results show that matrix effects are important in ion-microprobe analyses of minerals for oxygen isotopes.

One year later, we returned to this same grain and performed another traverse from the clear interior to the turbid rim. These data are shown on figure 3 with two

analyses of an adjacent quartz grain. The ^{18}O signal is relatively high again, this time by ~80 ‰. Subsequent failure of the electron multiplier preamplifier confirmed that electronics probably contribute to the high ratio. Errors (1 standard error of the mean) are less than ±2 ‰. Once again, the plagioclase appears to be isotopically homogeneous. Quartz shows low $^{18}O/^{16}O$ ratios again, this time by ~15 ‰.

At the present time, we are encouraged by several recent developments. As we have not been able to increase $^{18}O^-$ count rates to levels at which the Cameca Faraday cup can be used, we have lowered the primary beam intensity from 1–5 nA to 0.1–0.5 nA. Because this change caused the primary beam spot size to decrease to ~10 μm, we shifted to a stationary beam (~10 μm), and the observed count rates (10^8 cps for $^{16}O^-$ and 5×10^5 cps for $^{18}O^-$) were slightly lower than those observed with the rastered beam at the higher primary currents. The energy window has been closed down to a bandpass of 40 eV. Degree of charging, which had been ~50 to 80 V, is now 10 to 12 V. Stability of the secondary-ion signal is much improved, and internal precisions (1 standard error of the mean) for 15-min analyses are routinely between 1 and 2 ‰. We have tested whether it is important to maintain a small analyzed area (20-μm diameter) or shift to a lesser magnification (60-μm diameter). No improvement has been seen, but the ease of alignment of the secondary-ion beam on the optic axis at the latter conditions may be critical for later analyses of small samples (for example, Fahey and others, 1987). We have tested whether high precisions are achievable with both isotopes on the electron multiplier. Count rates were reduced by offsetting the sample voltage by 100 eV so that ^{16}O intensities were $<5 \times 10^5$ cps. Although analyses take 45 min, internal precisions of ±1.4 ‰ have been obtained (fig. 4). Matrix effects are often reduced when high-energy ions are used. We have not yet tested whether this is true in oxygen isotopic analyses.

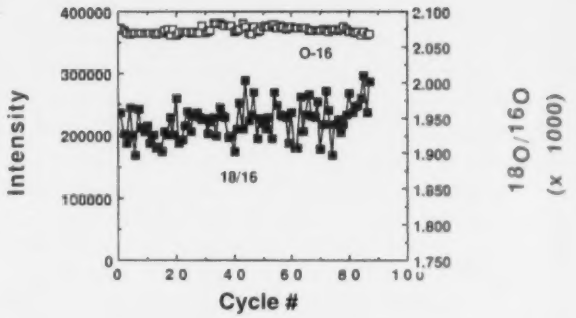

Figure 4. Recent analysis for ^{18}O and ^{16}O in NBS 610 silicate glass. Both isotopes were measured on the electron multiplier, and ^{16}O is reported as counts per second (open squares, left scale). Each cycle represents a measurement of ^{16}O and ^{18}O. Also shown is the dimensionless $^{18}O/^{16}O$ ratio (solid squares, right scale). The upward drift of the ratio at the end of the analysis represents a decrease in ^{16}O (caused by minor instrument instability), while ^{18}O remained constant. One standard error of the mean was 1.4 ‰. Analysis time was 45 min.

FUTURE STUDIES

If recent improvements in the technique can be maintained, we will be working with various collaborators on determining the extent of zoning of minerals in hydrothermally altered granites and mylonites. Analysis of authigenic and detrital quartz is an obvious application, and available bulk-analyzed samples of coexisting quartz and magnetite will enable us to test matrix effects.

We face several problems in determining absolute and precise oxygen-isotopic ratios. We do not understand the contribution of the electron multiplier electronics to the measured isotopic ratios, and if we continue to analyze isotopes on two different detectors, determination of absolute ratios may not be feasible. In addition, absolute calibration of the isotopic ratios requires comparison with appropriate homogeneous, bulk-analyzed standards. Although careful bulk analyses show very good estimates of error, the degree of isotopic variation in individual grains contained in any mass spectrometer run is unknown, so microanalysis of standard grains from a bulk-analyzed batch will be somewhat uncertain.

Concerning precision, if we keep count rates low so that the electron multiplier can be used for both oxygen isotopes, the problem arises that over 8 hours is required to collect 10^7 counts for ^{18}O (0.3 ‰ precision). Although many problems can be studied at the currrent precisions of 1 to 2 ‰ (1 standard error of the mean), analyzing both isotopes at higher intensities on a Faraday cup is very desirable. Thus, we are currently rebuilding the Cameca secondary-ion Faraday cup in the hopes of measuring $^{18}O-$ at intensities in the range of 10^5 to 10^6 cps (10^{-14} to 10^{-13} A) without significant noise. One other problem that may become significant is that because of the high currents we use on the electron gun, certain beam-sensitive phases may not be amenable to our technique.

CONCLUSIONS

Use of an alkali-metal ion source and a high energy electron flood gun can control charge buildup to the point of allowing $^{18}O/^{16}O$ ratios of 10- to 20-μm spots in insulating phases to be determined to a precision of 1 ‰. Matrix effects between quartz and plagioclase feldspar probably exceed 10 ‰. The degree of isotopic homogeneity we should expect in a mineral showing homogeneous major-element chemistry remains unknown.

ACKNOWLEDGMENTS

Research to support our development of techniques for oxygen-isotopic analysis with the ion microprobe has been supported by a grant from the Petroleum Research Fund (# 18512–AC5 to Peter Williams). Helpful comments from Ian Hutcheon, Bob Criss, Pat Shanks, and Bruno Giletti were appreciated. The Department of Physics machine shop at Arizona State University has played an integral role in producing these results.

REFERENCES CITED

Criss, R.E., and Taylor, H.P., Jr, 1983, An $^{18}O/^{16}O$ and D/H study of Tertiary hydrothermal systems in the southern half of the Idaho batholith: Geological Society of America Bulletin, v. 94, p. 640–663.

Dekker, A.J., 1958, Secondary electron emission: Solid State Physics, v. 6, p. 251–311.

Fahey, A.J., Goswami, J.N., McKeegan, K.D., and Zinner, E., 1987, ^{26}Al, ^{244}Pu, ^{50}Ti, REE and trace element abundances in hibonite grains from CM and CV meteorites: Geochimica et Cosmochimica Acta, v. 51, p. 329–350.

Forester, R.W., and Taylor, H.P., Jr., 1977, $^{18}O/^{16}O$, D/H, and $^{13}C/^{12}C$ studies of the Tertiary igneous complex of Skye, Scotland: American Journal of Science, v. 277, p. 136–177.

Gillen, J.G., and Williams, P. 1986, Electron-stimulated desorption microscopy, *in* Romig, A.D., Jr., and Chambers, W.F., eds., Microbeam analysis—1986: San Francisco, San Francisco Press, p. 109–112.

Hervig, R.L., and Williams, P., 1986, Non-oxygen negative ion beams for oxygen isotopic analysis in insulators, *in* Benninghoven, A., Colton, R.J., Simons, D.S., and Werner, H.W., eds., Secondary ion mass spectrometry, SIMS V: Berlin, Springer Series in Chemical Physics, v. 44, p. 152–154.

Kanaya, K., Ono, S., and Ishigaki, F., 1978, Secondary electron emission from insulators: Journal of Physics D: Applied Physics, v. 11, p. 2425–2437.

Lareau, R.T., and Williams, P. 1986, Survey of alkali primary ion sources for SIMS, *in* Benninghoven, A., Colton, R.J., Simons, D.S., and Werner, H.W., eds., Secondary ion mass spectrometry, SIMS V: Berlin, Springer Series in Chemical Physics, v. 44, p. 149–151.

Lovering, J.F., 1975, Application of SIMS microanalysis techniques to trace element and isotopic studies in geochemistry and cosmochemistry: National Bureau of Standards Special Publication 427, p. 135–178.

McKeegan, K.D., 1987, Oxygen isotopes in refractory stratospheric dust particles: Proof of extraterrestrial origin: Science, v. 237, p. 1468–1471.

Reuter, W., 1984, CF_3^+: An alternative primary beam source for the sensitive detection of electropositive elements, *in* Benninghoven, A., Okano, J., Shimizu, R., and Werner, H.W., eds., Secondary ion mass spectrometry, SIMS IV [illegible] Springer Series in Chemical Physics, v. 36, p. 54–[illegible]

Slodzian, G., Chaintreau, M., and Dennebouy, R., 1986, Self-regulated potential at insulating surfaces in the presence of a strong electrostatic extraction field, *in* Romig, A.D., Jr., and Chambers, W.F., eds., Microbeam analysis—1986, San Francisco, San Francisco Press, p. 78.

———1987, SIMS: Self-regulated potential at insulating surfaces in presence of a strong electrostatic extraction field: Cameca News, May 1987, p. 1–6.

Williams, P., and Gillen, J.G., 1987, Direct evidence for coulombic ejection of electron-desorbed ions: Surface Science, v. 180, p. L109–L112.

Isotopic Measurements with the Ion Microprobe

By Ernst Zinner[1]

Abstract

The principles and applications of isotopic ratic measurements by microprobe secondary ion mass spectrometry (SIMS) are reviewed. After a discussion of general instrumental aspects and measurement techniques for isotopic analysis, a more detailed treatment is given for the elements H, C, N, O, Mg, Si, S, Ca, Ti, and Pb. Examples include measurements of D/H ratios in interplanetary dust particles; of C, N, and Si isotopes in presolar SiC; of Ca, Ti, and O isotopes in meteoritic hibonites; and of U-Pb dating of terrestrial and extraterrestrial zircons.

INTRODUCTION

Isotope geology has been dominated by two techniques: gas mass spectrometry and thermal ionization mass spectrometry (see White and Wood, 1986). These two traditional branches of mass spectrometry are distinguished by the physical mechanism of ion production. In the last decade secondary ion mass spectrometry (SIMS) has become an increasingly important tool for the geoscientist. The main two applications are measurements of trace elements and isotopic ratios on a small spatial scale (Shimizu and Hart, 1982a).

In the ion microprobe, secondary ions are produced by ion bombardment of the sample to be analyzed. The focusing of the bombarding ions into a fine beam allows the in situ analysis of individual mineral phases. The main advantages of the technique are

1. High sensitivity. Detection limits for certain elements are as low as 1 ppb even in complex geological samples.
2. Small sample size. Meaningful analyses have been reported on subpicogram ($<10^{-12}$ g) amounts of total sample, involving in extreme cases the measurement of less than 1 femtogram ($<10^{-15}$ g) of a specific element.
3. Measurement of elements that are difficult to analyze by other techniques. These include isotopic measurements of iron and osmium.

These advantages are to be compared with problems that are inherent in the technique:

1. The sputtering process produces a large variety of molecular secondary ions along with atomic ions. These molecular ions interfere with the atomic ions of interest. In geological samples, the problem of interfering molecular species depends on the composition of the analyzed mineral, so the analysis of each element is a special problem.
2. The ionization efficiencies of different elements vary by many orders of magnitude. Certain elements are easily ionized and can be measured fairly readily, while other elements (such as noble gases) practically cannot be measured at all.
3. In addition to the variation of the ionization efficiency between different elements, the ionization efficiency of a given element depends strongly on the chemical composition of the sample from which the element is sputtered. This so-called "matrix effect" is one of the major problems of quantitative elemental analysis by SIMS.

The ion microprobe has been hailed as the ultimate weapon of the geoscientist for more than 20 years (Lovering, 1975), but its emergence as a practical instrument has been tied to the advent of a second generation of ion microprobes that include the Cameca IMS 3f (Lepareur, 1980) and the Sensitive High mass Resolution Ion MicroProbe (SHRIMP) at the Australian National University at Canberra (Clement and others, 1977). These instruments have technical features such as high mass-resolving power and energy filtering that help to overcome the problems of the presence of molecular isobaric interferences and the matrix dependence of secondary-ion yields.

While SIMS has been applied to the trace-element analysis of geological samples of both terrestrial and extraterrestrial origin (Shimizu and Hart, 1982a; Crozaz and Zinner, 1986; Veizer and others, 1987), the majority of isotopic measurements have been performed on extraterrestrial material. The reason is that the isotopic variations discovered in interplanetary dust particles (IDP's) and primitive meteorites are much larger than those found in terrestrial geological materials (for example, Clayton and others, 1973, 1988; Begemann, 1980; Wasserburg and Papanastassiou, 1982; Anders, 1988). However, important isotopic measurements have been made on terrestrial rocks and include prominently U-Pb dating of individual zircons and the study of the distribution of S and Pb isotopes in ore minerals (Hart and others, 1981; Froude and others, 1983; Williams and others, 1984; Eldridge and others, this volume).

Although the field of SIMS isotopic measurements is still in a state of vigorous development, it has reached a degree of maturity that makes an overview desirable. The present paper has this general objective but will emphasize

[1] McDonnell Center for the Space Sciences and Physics Department, Washington University, St. Louis, MO 63130.

the practical aspects of isotopic analysis with the ion microprobe at the expense of a detailed historical account of all studies reported in the literature. It will concentrate on measurements made with the Cameca IMS 3f ion microprobe and on analysis techniques developed for this instrument at the Washington University ion microprobe laboratory. At the same time, it will review the work of other experimenters either with the Cameca IMS 3f or with other instruments. The next section provides a general discussion of the techniques and problems of isotopic analysis by SIMS. This discussion is followed by more detailed treatments of the isotopic measurement of a series of elements ranging from hydrogen to lead.

GENERAL ASPECTS OF ISOTOPIC ANALYSIS BY SIMS

Instrumentation

This section is restricted to the discussion of practically important questions of isotopic measurements by SIMS. For an introduction to SIMS, the reader is referred to the more general literature on that subject (Slodzian, 1980; Williams, 1983; Benninghoven and others, 1987) and to Giletti and Shimizu (this volume). A wealth of extremely useful details on isotopic measurements with the Cameca IMS 3f ion microprobe can be found in the Ph.D. theses of McKeegan (1987a) and Fahey (1988).

The ion microprobe is a mass spectrometer in which the ions are produced through sputtering by a finely focused primary-ion beam. Two ion sources are available: a duoplasmatron capable of delivering beams of oxygen or argon ions, and a cesium source. Primary oxygen ions are used for the analysis of positive secondary ions because the presence of oxygen on the sample surface significantly enhances positive ion yields. The presence of cesium enhances the yield of negative secondary ions. A duoplasmatron can generate O^- and O_2^+ ions, but the negative beam is preferred for insulating samples because it minimizes sample charging. Additional discussion of primary beam generation and of the sputtering process is given by Hervig and others (this volume).

Sample Preparation

Since the sample surface is part of the secondary-ion extraction system (Slodzian, 1980), the sample surface has to be flat and conducting. For the analysis of positive secondary ions, polished sections of geological samples are coated with 200 to 1,000 Å of carbon or gold. For isotopic analysis, the primary beam sputters a small (3–20 μm) hole through this coating. In all practical cases, charging of the analyzed area under the O^- beam is less than 20 V and can be compensated for.

On the other hand, bombardment with Cs^+ ions and extraction of negative secondaries result in intolerable charging conditions on polished surfaces of insulating samples, even if they are metal coated. In order to avoid this problem, samples to be analyzed in the negative secondary ion mode under a Cs^+ primary beam are pressed into gold foil (McKeegan and others, 1985; McKeegan, 1987a). This method works well as long as individual grains of samples are smaller than 20 to 30 μm and has been employed for isotopic measurements of H^-, C^-, O^-, CN^-, and Si^-. Recently, Slodzian and others (1987) designed a charge compensation device for the negative ion mode that is reported to make negative secondary-ion analysis from insulating samples possible (also see Hervig and others, this volume). This device is now standard equipment on the Cameca IMS 4f instruments.

Mass Spectrometer

In both the Cameca IMS 3f and the SHRIMP, the mass spectrometer is of the double focusing magnetic type (Clement and others, 1977; Lepareur, 1980). Because of the wide energy distribution of sputtered secondary ions, only a double focusing mass spectrometer gives the high mass-resolving power (MRP) found in these instruments without a significant loss of transmission. With few exceptions, all isotopic measurements discussed in the present paper rely on the use of high mass resolution for the elimination of molecular isobaric interferences. While the suppression of molecular ions by energy filtering has been successfully applied for the measurement of trace elements (Shimizu and Hart, 1982a; Zinner and Crozaz, 1986), for isotopic ratio measurements the use of high mass resolution has several advantages:

1. Certain interferences such as hydrides cannot be suppressed very efficiently by energy filtering. For example, the presence of an ^{28}SiH signal might present a substantial interference for Si isotopic measurement, whereas the Si concentration can be obtained from the ^{28}Si signal, which is more likely to be free of interferences (signals from N_2^+ and CO^+ are usually negligible for the analysis of Si).
2. The loss of signal incurred by the selection of only high-energy ions (energy filtering) is usually much more severe than that accompanying analysis at high mass resolution.
3. The precision requirements for isotopic analysis are normally much higher than those for elemental abundance measurements and make it of prime importance to maximize the secondary-ion signal.

The Cameca IMS 3f/4f is an ion microscope that produces a direct image of the sample surface by mass-selected secondary ions. Although for isotopic measurements the primary beam is focused into a small spot on the

sample, the imaging capability is extremely helpful for inspection of the analyzed area for the presence of inclusions, for the tuning of the secondary beam to high-mass-resolution conditions, and for maintaining reproducible tuning conditions, an important function for the measurement of intrinsic mass fractionation effects (Fahey and others, 1987a,b).

Both the Cameca IMS 3f/4f and the SHRIMP employ a mass spectrometric geometry of electrostatic analyzer followed by magnet. This arrangement provides dispersion in ion energy and, with the aid of an energy slit, the possibility of energy selection (Lepareur, 1980; Slodzian, 1980). Restriction to a limited energy window (typically 25–50 V) of low-energy ions helps in tuning to high MRP conditions.

Detection System

Mass-analyzed secondary ions either are counted individually in an electron multiplier or their current is measured in a Faraday cup. The vast majority of isotopic measurements reported so far have been made by ion counting in the electron multiplier. Several problems are associated with ion counting:

1. The detection efficiency is a function of the ion species (element, molecule, charge). For a given element the detection efficiency varies with isotopic mass (Zinner and others, 1986a).
2. For precise isotopic measurements, the dead time of the detection system must be known with high accuracy, but the dead time depends on the detected ion species (Zinner and others, 1986a).

The isotopic mass dependence of the detection efficiency mimics a linear mass fractionation that is, however, smaller than the isotopic mass fractionation produced in the sputter-ionization process. Both fractionation effects can be treated together as "instrumental mass fractionation." The determination of the counting system dead time is best achieved by isotopic measurements of a standard of known isotopic composition. Such a standard should have at least three isotopes of varying and well-known abundances, and the element should lend itself to ion probe analysis. The number of elements having these characteristics is limited. The most favorable example is titanium (Fahey and others, 1987a). The dependence of the dead time on the ion species might present a limit to the precision of isotopic measurements by single ion counting.

Only few isotopic measurements employing current measuring techniques have been published (Ireland and others, 1986a; Chaussidon and others, 1987). This is still a field to be worked at, since subsequent measurements by Ireland (1988) indicated that the Faraday cup results of Ireland and others (1986a) probably were in error.

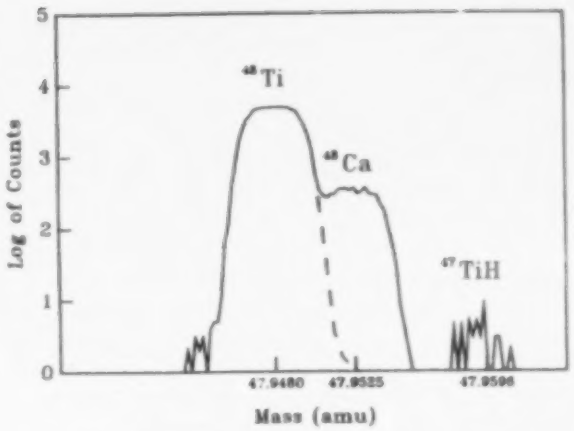

Figure 1. High-mass-resolution spectrum of the mass 48 region that shows the structure of the $^{48}Ti^+$ and $^{48}Ca^+$ peaks and was obtained from meteoritic hibonite in the Cameca IMS 3f ion microprobe. The peaks are resolved without interference even though no valley separates ^{48}Ti and ^{48}Ca. Separation of ^{48}Ti and ^{48}Ca requires a mass-resolving power (MRP) in excess of 10,500. Also shown is ^{47}TiH, which is clearly resolved under these high MRP conditions. amu, atomic mass units.

Isotopic Measurement Techniques

Isotopic analysis of a given element requires a careful evaluation of the molecular and atomic isobaric interferences encountered at the masses of the measured isotopes. These interferences determine the MRP needed to resolve them or, if they cannot be resolved, the procedures to be used to correct for their contribution to the measured signal.

Mass-Resolving Power

There is no completely satisfactory definition of the MRP, because the requirements for mass resolution depend not only on the mass difference and relative intensities of the peaks to be resolved but also on the detailed shape of the peaks in question.

We define the mass-resolving power as MRP = $m/\Delta m$ where Δm is the 10-percent width of a given peak at mass m. This is an arbitrary operational definition that differs from other definitions, which typically define MRP by a 1-percent valley separation between peaks (for example, Ireland and others, 1985). However, in many cases the signal of a given peak can be measured virtually without interference even if it is not separated by a valley from a neighboring peak. This fact is demonstrated by figure 1, which shows a high-mass-resolution spectrum of mass 48 with the peaks of $^{48}Ti^+$ and $^{48}Ca^+$. Although the two peaks are not well separated, the contribution of the low-mass tail of ^{48}Ca at the center of the $^{48}Ti^+$ peak is less than 10^{-4} and

thus negligible within the precision of typical ion microprobe titanium isotopic measurements (Fahey and others, 1985, 1987a).

The MRP required for the elimination of isobaric interferences in many cases exceeds the capabilities of present-day instruments. The practical maximum of the MRP for isotopic measurements is ~15,000 counts per second (cps) in the Cameca IMS 3f/4f, approximately the same as that in the SHRIMP (Ireland, 1988). The mass separation between ^{48}Ti and ^{48}Ca corresponds to an MRP of 10,500. Examples of isobaric interferences of smaller mass separations are ^{46}Ca with ^{46}Ti, and ^{50}V and ^{50}Cr with ^{50}Ti, with the mass difference between ^{50}Cr and ^{50}Ti corresponding to an MRP of 40,000. An even more important example to geochronologists is the separation between ^{87}Rb (mass = 86.909188 amu) and ^{87}Sr (mass = 86.908884 amu), which would require a currently unattainable MRP of 2.9×10^5. In some of these cases the contributions of interfering isobars can be subtracted if other isotopes of the interfering species can be measured. An example of this "peak stripping" technique is the correction of $^{48}Ca^{++}$ for magnesium isotopic measurements (Hutcheon, 1982). The correction procedures for ^{46}Ca, ^{50}V, and ^{50}Cr interferences in the case of titanium isotopic measurements have been discussed in detail by Fahey and others (1987a).

Peak Jumping

In the absence of multiple collector systems, ion probe isotopic measurements are made by peak jumping. Under computer control the magnetic field is stepped to values corresponding to the centers of the peak tops. These values can be located reliably as long as the magnetic field is cycled through the same sequence of values and the peaks are centered periodically (Huneke and others, 1983; Fahey and others, 1987a). Dwelling times at peak tops can be adjusted, depending on the signal intensity of different isotopes. Counts from many cycles are averaged to minimize the effects of both random and systematic changes in the secondary-ion signals. Because of a finite settling time of the magnet, dwelling times of much less than 1 s are not practical.

Much faster cycling can be achieved by electrostatic peak switching as implemented in the Cameca IMS 4f. This method has the potential advantage that signal fluctuations can be averaged out more effectively. However, no systematic isotopic studies by electrostatic peak switching have been reported to date. Furthermore, a true advantage is achieved only under a limited set of circumstances. Isotopic measurements in this laboratory indicate that for count rates of up to ~20,000 cps a precision commensurate with counting statistics can be obtained by magnetic peak switching. More rapid switching would be of advantage only if the count rate of the least abundant isotope were substantially higher while that of the most abundant isotope were still low enough as to not lead to a loss of precision because of limited knowledge of the dead time of the pulse-counting system.

Instrumental Mass Fractionation

For precise isotopic measurements, the signal ratios measured in the detection system have to be related to the true isotopic abundance ratios in the analyzed sample. There are two effects that change the original isotopic ratios of the sample: one is the instrumental mass fractionation, and the other is the response of the detection system. The latter has already been discussed for an electron multiplier pulse-counting system. The instrumental mass fractionation is a combination of the ionization probability as function of isotopic mass during sputtering and the selection effects imposed on the secondary ions between emission from the sample surface and collection in the detector. This effect has been studied by a number of experimenters (Slodzian and others, 1980; Jull, 1982; Shimizu and Hart, 1982b; Gnaser and Hutcheon, 1987, 1988) who found that generally the light isotopes are ionized preferentially relative to the heavier ones. The magnitude of this isotopic mass fractionation varies from element to element and is inversely related to the ionization efficiency. For a given element, mass fractionation is a function of the secondary-ion emission angle and velocity as well as the chemical composition of the sample (matrix effect).

Since we are still far from a detailed understanding of the basic phenomenon of ion emission by sputtering and since transmission conditions of secondary ions in a SIMS instrument are too complex to be taken into account theoretically, in practice a correction for the instrumental mass fractionation is based on either external or internal calibration.

External Calibration.—In this method, the isotopic ratios measured in the unknown sample are compared with those measured in an external standard that has a known isotopic composition. Standard and sample should have the same chemical composition, and the measurements must be made under identical conditions. Since the instrumental mass fractionation strongly depends on the energy of the secondary ions (Slodzian and others, 1980; Gnaser and Hutcheon, 1987), it is important to select identical energy windows and to compensate for shifts in the selected energy because of sample charging (Fahey and others, 1987a,b).

For elements such as H, Li, B, C, and N that have only two stable isotopes, the instrumental mass-fractionation correction necessarily must rely on external standards. However, also for elements having more than two stable isotopes, such as oxygen and silicon, SIMS isotopic measurements have been reported as deviations from the ratios measured in standards (Fahey and others, 1987c; McKeegan, 1987a; Zinner and others, 1987). In certain cases, when models for the production of isotopic

effects in the sample are available, the observed corrected deviations in elements having more than two isotopes can be split into contributions that can be attributed to different mechanisms. A prime example are the magnesium isotopic results obtained from refractory inclusions in meteorites that show evidence for ^{26}Mg enrichments resulting from the decay of primordial ^{26}Al. In these cases, the intrinsic (that is, corrected for instrumental mass fractionation) magnesium isotopic effects are divided into a contribution from natural mass-dependent fractionation processes and ^{26}Mg excesses attributed to the decay of primordial ^{26}Al (Macdougall and Phinney, 1979; Hutcheon, 1982; Huneke and others, 1983; Hinton and Bischoff, 1984; Fahey and others, 1987b). The same decomposition of isotopic effects has been made for titanium and calcium SIMS isotopic measurements (Fahey and others, 1987a; Hinton and others, 1987a).

Traditionally, the deviations of isotopic ratios from those of terrestrial standards are expressed as δ values in per mil (‰), where for the isotope i of element E

$$\delta E_i = 1{,}000\left[\frac{(E_i/E_j)_{\text{measured}}}{(E_i/E_j)_{\text{standard}}} - 1\right].$$

E_j is the reference isotope. For example, $\delta^{17}O_{SMOW}$ and $\delta^{18}O_{SMOW}$ are the per-mil deviations of the $^{17}O/^{16}O$ and $^{18}O/^{16}O$ ratios from those of SMOW (standard mean ocean water). However, for elements having three and more isotopes, if the intrinsic isotopic effects are decomposed into mass-dependent fractionation (F), due to physicochemical processes, and into non-mass-dependent (also called nonlinear) effects, due to other mechanisms (for example, radioactive decay, nucleosynthetic processes), δE_i denotes only the non-mass-dependent deviation. Thus, in the above example of meteoritic inclusions that have ^{26}Mg excesses, $\delta^{26}Mg$ would stand for only the ^{26}Mg excess after a correction for mass-dependent fractionation effects (intrinsic and instrumental).

Internal Calibration.—For elements that have three or more stable isotopes, if one is interested in only non-mass-dependent effects and if one has convincing arguments that such effects are present in only *some* of the isotopes, one can eschew the use of external standards and make an internal mass fractionation correction by normalizing the measured isotopic ratios to an isotope pair. By definition, the two selected isotopes should be free of non-mass-dependent effects but in many cases this situation is far from certain. The ambiguity resulting from the choice of the normalizing isotope pair has been discussed in the literature (Niederer and others, 1985).

For ion microprobe analysis, the internal calibration approach has the advantage that a higher precision can be achieved by it than by external calibration. Furthermore, in many cases, no suitable standards that have matching chemical compositions are available. Still, there is a basic problem associated with internal calibration as well as with the decomposition of isotopic anomalies into mass-dependent and non-mass-dependent effects: the mass dependence of the isotopic fractionation has to be known. For the internal calibration this involves the instrumental fractionation as well as the intrinsic fractionation of the sample studied. In principle, the fractionation laws can be different for these two effects.

There is good evidence that the instrumental isotopic fractionation (α) in the ion probe follows an "exponential" law that was originally found for thermal ionization mass spectrometric (TIMS) instruments through measurements of doubly spiked calcium samples (Russell and others, 1978),

$$\frac{(E_i/E_j)_{\text{measured}}}{(E_i/E_j)_{\text{sample}}} = \left[\frac{m_i}{m_j}\right]^{\alpha},$$

where m_i and m_j are the atomic masses of isotopes i and j. This law has been clearly demonstrated for measurements on titanium and calcium (Zinner and others, 1986b; Fahey and others, 1987a). Figure 2 shows titanium measurements on terrestrial and lunar standards after internal normalization to the ^{46}Ti–^{48}Ti isotope pair under the assumption of a linear and an exponential mass-fractionation law. The divergence between the two normalizations depends on the size of the fractionation. In the case of calcite, which shows the largest instrumental fractionation for calcium (19.2 ‰/amu), the difference between the $\delta^{48}Ca$ values computed after a ^{40}Ca–^{44}Ca normalization according to the two laws is 11.5 ‰.

For other elements, either the instrumental mass fractionation is not large enough or the absolute isotopic ratios of the sample are not known well enough to test the form of the fractionation law. For example, the typical instrumental mass fractionation for Mg is 8 ‰/amu, so there is a difference of only 0.25 ‰ for $\delta^{26}Mg$ between the exponential and linear law. On the other hand, the discrepancy between $^{26}Mg/^{24}Mg$ ratios reported for terrestrial samples (see Ireland and others, 1986a) is much larger than this difference.

Precision

It has been repeatedly stated that ion microprobe isotopic measurements are intrinsically less precise than measurements by other mass spectrometric methods. This statement is certainly true for measurements that require external calibration for elements such as H, C, and N. For magnesium, a precision of <1 ‰ (2σ) can be achieved (Brigham and others, 1986; Ireland and others, 1986a; Fahey and others, 1987b; Hinton and others, 1988a), and for potassium, Hinton and others (1987b, 1988b) reported a precision of better than 0.2 ‰ (2σ).

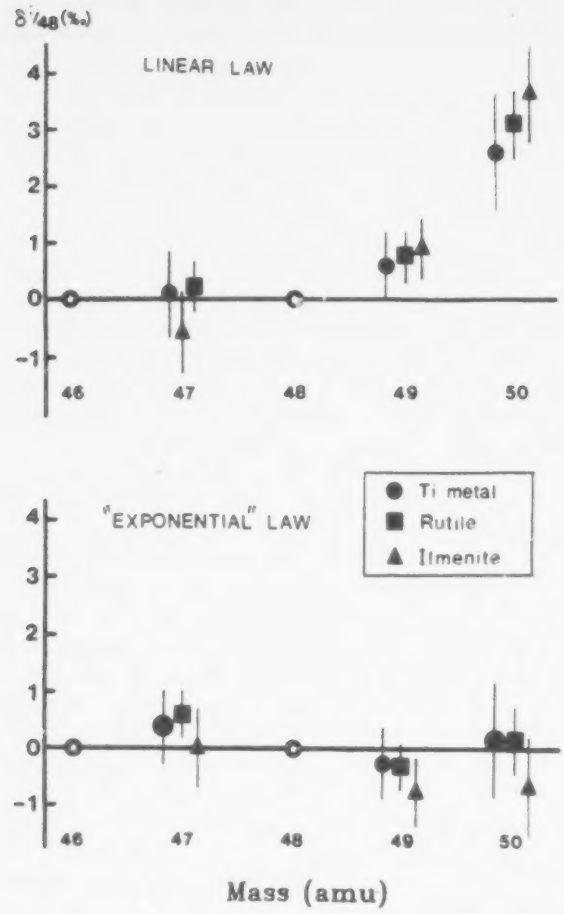

Figure 2. Plotted are $\delta(^{i}Ti/^{48}Ti)$ values of titanium ratios measured in different standards after normalization to the ^{46}Ti–^{48}Ti pair (stars), where the superscript i refers to the isotope of interest. An "exponential" law better describes the instrumental mass fractionation in the ion probe than a linear law. A linear fractionation law was used for the upper graph, an "exponential" law for the lower one. Note that the apparent excesses of ~1 ‰ for $\delta^{49}Ti$ and ~3 ‰ for $\delta^{50}Ti$ in the upper graph are clearly shown in the lower graph to be artifacts of the inappropriate correction procedure (from Fahey and others, 1987a).

For internal calibration measurements, the answer as to the ultimate precision of SIMS isotopic measurements has not been obtained yet. Limiting factors are the knowledge of the exact form of the instrumental mass-fractionation law and, for an ion counting system, the accuracy with which its dead time is known. Measurements of current charge in a Faraday cup currently suffer from inadequate designs both in the Cameca IMS 3f/4f (unpub. data from this laboratory) and the SHRIMP (Ireland, 1988). The limitation in precision imposed by fluctuations in the secondary-ion signal due to instabilities in the primary-ion beam and sample heterogeneity will be overcome only by multiple collection systems. Such a system is presently being tested for the SHRIMP.

The relationship between statistical precision and amount of sample consumed during analysis is straightforward. If V is the volume of the consumed sample, σ its density, and A its average atomic weight, the number of atoms of a given isotope collected during isotopic analysis is

$$\frac{V\sigma}{A} N C_a I \eta T d.$$

Here, N is Avogadro's number, C_a the atomic concentration of the element measured, I the isotopic abundance, η the ionization efficiency, T the fraction of emitted ions that are detected, and d the duty cycle of the measurement.

To illustrate this relationship, we consider the carbon isotopic analysis of a 1-μm SiC grain (Zinner and others, 1987; Tang and others, 1988). Such a grain contains ~3×10^{10} carbon atoms and 3×10^{8} ^{13}C atoms. With a useful ion yield S (product of ηI) of ~3×10^{-4} and a duty cycle of 50 percent, 45,000 ^{13}C atoms are counted, and a statistical precision of 4.7 ‰ (1σ) results. From a 0.1-μm grain only 45 ^{13}C atoms will be counted. The situation is worse for minor and trace elements as well as for elements that have low-abundance isotopes. As a consequence, a 1 ‰ precision cannot be achieved for oxygen isotopic measurements on a 1-μm spatial scale.

ISOTOPIC MEASUREMENTS OF INDIVIDUAL ELEMENTS

There are essentially three factors that affect the feasibility of isotopic analysis of a given element in the ion microprobe: ionization efficiency, isobaric interferences, and isotopic abundances.

As a general rule, elements on the left side of the periodic table readily form positive secondary ions, and elements on the right side form negative secondary ions. There are, however, exceptions to this simple picture. For example, in spite of the fact that C and O as well as P have relatively high yields of negative secondary ions, N does not form stable negative ions at all.

The presence and intensity of isobaric interferences depend on the chemical composition of the sample. Because of the shape of the mass defect curve (the mass defect is the difference between the mass of a given nucleus and the sum of its constituent nucleons), there is a systematic relationship between the atomic mass of a given element and the MRP required to separate the most common isobaric interferences (for example, Liebl, 1980). This situation is graphically displayed in figure 3, which shows a plot of the deviation of the nuclidic masses of the stable isotopes from

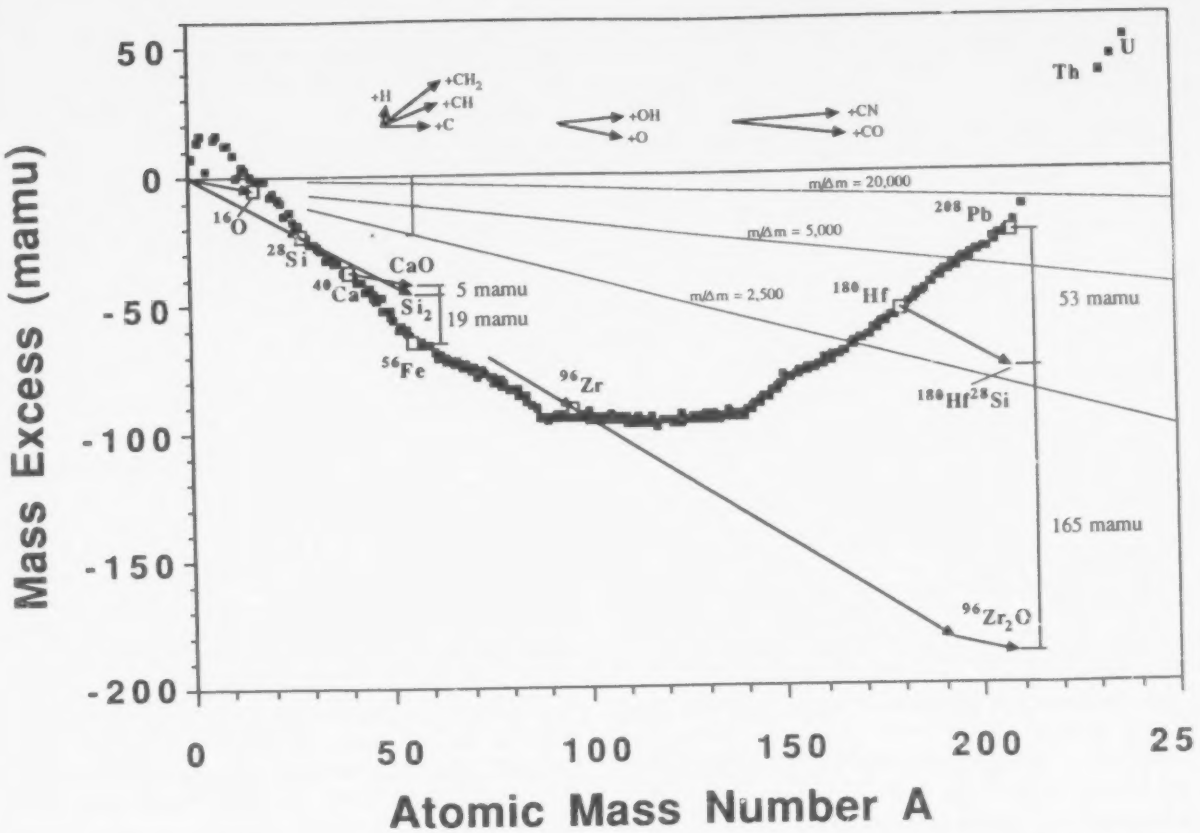

Figure 3. Mass excess (in milli-amu, mamu) of the nuclides plotted against atomic mass number A. The mass excess is defined as the difference between the mass of a given nucleus in atomic mass units (1 amu = 1/12 of the mass of ^{12}C) and the atomic mass number A (number of nucleons). This plot provides a simple graphical way to compute mass differences of isobaric interferences. Singly charged ions are represented by vectors from zero to the particular nuclide point. Mass excesses of molecular ions are obtained by vector additions. Doubly charged ions are represented by vectors having the same direction but half the length of singly charged ion vectors. The vertical distance between two vectors representing two isobaric species at a given mass number (for example, ^{56}Fe and $^{28}Si_2$) gives the mass difference, Δm. The MRP required to separate the two species is then A/Δm since A = m. Also shown are lines of constant MRP equal to m/Δm, indicating what mass differnce (Δm) is separated at any particular mass number for a given MRP (adapted from Liebl, 1980).

their respective atomic mass numbers (the unit of atomic masses is defined as 1/12 of the mass of ^{12}C). For example, for ^{56}Fe with atomic mass number A equal to 56 and a mass of 55.93494 amu, this deviation is −0.06506 amu. For atomic mass numbers A smaller than 100, most molecular isobaric interferences have larger atomic masses than those of the atoms, but the required m/Δm increases with A. Molecular species such as $^{28}Si_2$ or ^{40}CaO have larger masses than ^{56}Fe, as can be seen from figure 3. The situation is reversed for high atomic numbers. For example, molecular species (HfSi, Zr_2O) interfering with lead have smaller atomic masses than the lead isotopes (see fig. 3). As a consequence, elements having atomic masses up to 60 and lead are most suitable for SIMS isotopic analysis at high MRP.

Elements having low-abundance isotopes sometimes pose special problems. An example is the measurement of ^{17}O, whose abundance is only 0.04 percent of that of ^{16}O. Although the separation of ^{17}O and ^{16}OH requires only a moderate MRP of 4,700, the $^{16}OH^-$ signal from most samples is much higher than the $^{17}O^-$ signal, so special correction procedures are necessary (McKeegan, 1987a).

What follows is to a large extent based on the experience gained at the Washington University ion microprobe laboratory but includes also many results reported by other experimenters. Table 1 presents a list of parameters characterizing high-mass-resolution measurements with the Cameca IMS 3f ion microprobe for a series of selected elements. Column 2 gives the preferred mode of analysis. Positive secondary ions are produced by an O^- beam with

Table 1. Parameters for isotopic measurements when using the Cameca IMS 3f/4f

[MRP, mass-resolving power]

Element	Preferred mode	MRP (m/Δm)	Sensitivity (counts/nA/wt% of element)	Precision (2σ) (in per mil)	Problems
H	H^-, Cs^+	500	3×10^6	~30	Low deuterium abundance.
C	C^-, Cs^+	3,500	2×10^5	~5	
N	CN^-, Cs^+	6,000	$2\times10^{5*}$	?	Low ^{15}N; BO interference; need presence of C.
O	O^-, Cs^+	6,000	8×10^4	2	Low ^{17}O; OH interference.
Mg	Mg^+, O^-	3,000	$2–3\times10^5$	.5	
Si	Si^+, O^-	3,000	$1–2\times10^4$	.5	
	Si^-, Cs^+	3,000	10^5	.5	
Ca	Ca^+, O^-	12,000	2.5×10^4	1.0	^{48}Ti, $^{88}Sr^{++}$ interference; low ^{48}Ca abundance.
Ti	Ti^+, O^-	10,000	2×10^4	1.0	^{48}Ca, ^{50}Cr interferences.
Pb†	Pb^+, O^-	9,000			

† Measurements made with the SHRIMP.

* With 50 weight percent C present.

an energy of 17 keV, and negative secondary ions are produced with a Cs^+ beam of 14.5 keV energy. For the MRP (m/Δm) listed in column 3, Δm is the 10 percent peak width as defined previously. The sensitivity in column 4 is given as the number of ion counts per second per nanoampere of primary beam current per weight percent concentration of the analyzed element. Sensitivity depends on many conditions and can vary by as much as a factor of 2 to 3; the numbers given are typical values for practical applications. Except for H and Mg, all measurements were made at a magnification corresponding to a 150-μm imaged field (Lepareur, 1980); H and Mg were measured with magnification corresponding to 150-μm and 75-μm imaged fields (McKeegan, 1987a). Column 5 lists the precision that can be achieved in these measurements, albeit with some effort. In many practical cases the actual precision is much less than this, particularly in cases where it is sufficient for the purpose of the specific measurement. More detailed discussions follow.

Hydrogen

Hydrogen isotopes have been measured as positive secondary ions (Hinton and others, 1983) and negative secondary ions (Zinner and others, 1983; McKeegan and others, 1985). Negative secondaries have the advantage that the H_2^- interference is less than 0.5 percent of the D^- signal, whereas for positive ions the H_2^+ signal is greater than the D^+ signal by up to a factor of 100 (see fig. 1 of McKeegan and others, 1985). The precision of 30 ‰ is not that of single measurements, which can have much higher precision, but the typical variation between measurements of individual grains of a given standard. This variation may be the result of the lack of control of the ion emission geometry in the case of grains pressed into gold and may be smaller if measurements can be performed on polished surfaces. However, no systematic studies of this aspect have been made yet.

The most important result obtained by D/H measurements in the ion probe has been the discovery of large deuterium excesses in interplanetary dust particles (IDP's) (Zinner and others, 1983; McKeegan and others, 1985, 1987) and primitive meteorites (Hinton and others, 1983; McKeegan and Zinner, 1984). Figure 4 shows the ranges of δD values measured in different individual IDP's. The deuterium excesses are heterogeneously distributed on a micrometer scale, as the analysis of single fragments of certain IDP's gives large variations in δD, ranging in the most extreme case from −320 to +2,700 ‰. One analysis of such a fragment consumes only 10^{-11} g of sample. The carriers of deuterium excesses in IDP's and meteorites seem to be carbonaceous materials. Because of their small sizes, imaging of the deuterium distribution in the ion probe (McKeegan and others, 1987) appears to be a promising approach.

Carbon

The large interference of $^{12}CH^-$, whose signal is usually much higher than that of $^{13}C^-$, makes high mass resolution a necessity (see fig. 3 of McKeegan and others, 1985). Since carbon has only two isotopes, an external standard must be used. NBS–21 (graphite) has been used in this laboratory (McKeegan and others, 1985; Zinner and others, 1987). The instrumental mass fractionation for carbon is typically 45 to 50 ‰/amu but studies by McKeegan and others (1985) indicated that matrix effects between very different substances are smaller than 5 ‰,

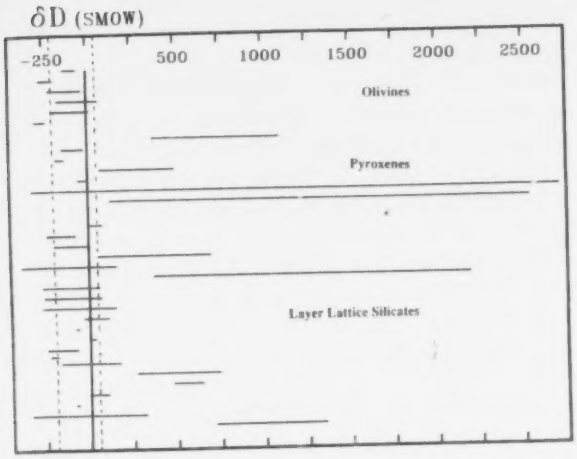

Figure 4. The hydrogen isotopic composition measured in 34 interplanetary dust particles (IDP's). Plotted is the range of δD values (normalized to standard mean ocean water (SMOW)) observed in individual fragments of the IDP's. Many of the IDP's show large deuterium excesses that, as indicated by the range spanned by individual measurements, vary on a micrometer scale (the IDP's are about 10 μm in size). "Olivines," "Pyroxenes," and "Layer Lattice Silicates" indicate the infrared classes of the IDP's established from Fourier transform infrared measurements. The fourth category comprises particles that do not fall into any of these classes. Vertical dashed lines denote the range of δD values observed in terrestrial rocks.

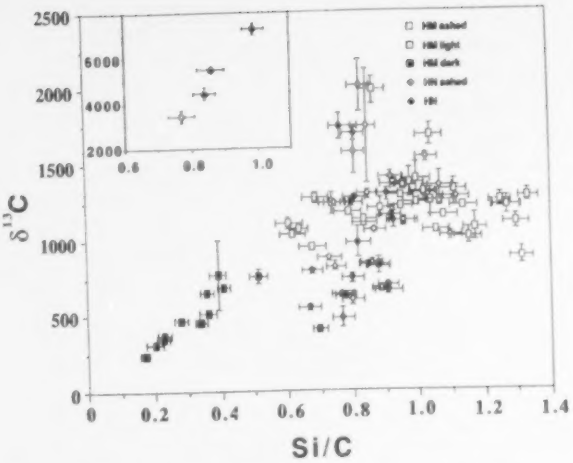

Figure 5. Plot of $\delta^{13}C$ versus Si/C measured in separates from the Murchison carbonaceous chondrite. The different symbols denote different size fractions of acid residues, some of which had also been oxidized in a plasma discharge ("ashed"). The correlation between $\delta^{13}C$ and Si/C provides evidence for multiple carbonaceous components, namely isotopically normal pure carbon and isotopically heavy SiC. The SiC in these separates shows large and variable ^{13}C excesses and is probably of presolar origin (from Tang and others, 1988). HM, residue of grains in size range of 0.03 to 0.2 μm; HN, residue of grains in size range of 0.2 to 2.0 μm.

which is the magnitude of the variation between measurements on different grains of a given substance.

Ion microprobe isotopic measurements have been made in IDP's and materials from primitive meteorites. While anomalies measured in IDP's are only of limited size (McKeegan and others, 1985), primitive meteorites contain SiC whose carbon isotopic composition differs from terrestrial material by up to 7,000 ‰ (Zinner and Epstein, 1987; Zinner and others, 1987; Tang and others, 1988). Figure 5 shows a plot of ^{13}C excesses measured in small agglomerates of separates from the Murchison carbonaceous chondrite (Tang and others, 1988). These separates are mixtures of isotopically heavy SiC and an isotopically normal pure carbon phase. The SiC shows large ^{13}C excesses, mostly between 500 and 2,000 ‰, with individual data points for $\delta^{13}C$ ranging up to 7,000 ‰. On the basis of this extremely anomalous isotopic composition and the fact that SiC cannot be formed from a gas of solar system composition, Zinner and others (1987) argued for a presolar origin of the SiC in the atmospheres of certain stars.

Nitrogen

Because nitrogen does not form negative ions and its positive secondary-ion yield is extremely low, nitrogen isotopes can be measured only in very special cases. In the presence of C, N yields a very intense CN^- signal, so it is possible to measure N isotopes in carbonaceous materials in the form of CN^- (Carey and others, 1987). Figure 6 shows high-mass-resolution spectra at the atomic masses 26 and 27 obtained from a Murchison separate containing mostly SiC (Tang and others, 1988). While an MRP of 4,300 is sufficient to separate $^{12}C^{15}N$ from $^{13}C^{14}N$ at mass 27, a higher MRP is required for the separation of $^{11}B^{16}O$ from $^{12}C^{15}N$ (boron is a contaminant apparently introduced during the chemical treatment that led to the separation of SiC).

Silicon carbide grains identified in the carbonaceous meteorites Murchison and Murray contain isotopically highly anomalous nitrogen, providing additional evidence for their extrasolar origin. Ion probe measurements (Zinner and others, 1987; Tang and others, 1988) revealed isotopically light as well as heavy nitrogen with $\delta^{15}N$ values ranging from −850 ‰ to +4,300 ‰. The variability of the nitrogen and the carbon isotopic compositions of meteoritic SiC indicate different stellar sources.

Oxygen

Oxygen-rich samples under Cs^+ bombardment have a high yield of O^- secondary ions. The main problems

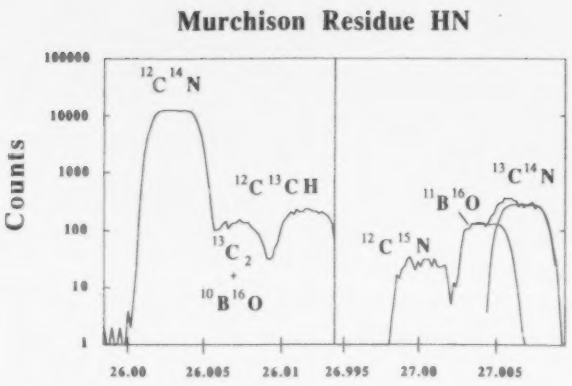

Figure 6. High-mass-resolution spectra of the mass 26 and mass 27 regions measured in a Murchison separate consisting mostly of SiC. The CN^- obtained from nitrogen-bearing carbonaceous samples is used to measure nitrogen isotopic ratios from the $^{12}C^{14}N$ and $^{12}C^{15}N$ peaks. The latter is resolved not only from $^{13}C^{14}N$ but also from the interfering $^{11}B^{16}O$. HN, residue of grains in size range of 0.2 to 2.0 μm.

associated with isotopic measurements of oxygen are the low abundances of ^{17}O and ^{18}O, and the presence of $^{16}OH^-$ (separated from ^{17}O by 3.6×10^{-3} amu, corresponding to an MRP of 4,710) that can be up to 100 times larger than the $^{17}O^-$ signal. If only the $^{18}O/^{16}O$ ratio is measured, the problem is less severe, since in the case where $^{16}OH^- = 100 \times {}^{17}O^-$, $^{17}OH^-$ would be only 0.7 percent of the $^{18}O^-$ signal. In addition, the $H_2{}^{16}O^-$ signal is usually negligible and furthermore is separated from ^{18}O by 11.4×10^{-3} amu, corresponding to an MRP of only 1,570. For a more detailed discussion of $^{18}O/^{16}O$ measurements, see Hervig and others (this volume).

For the measurement of all three oxygen isotopes, the $^{16}OH^-$ interference requires a careful evaluation and correction of the contribution of the tail of the $^{16}OH^-$ peak to the signal in the center of the $^{17}O^-$ peak. In the procedure developed by McKeegan (1987b) the tail of the $^{16}O^-$ peak is monitored at a distance from the $^{16}O^-$ peak center that corresponds to the mass difference between ^{17}O and ^{16}OH. The ^{16}O tail to ^{16}O peak ratio is then applied to the $^{16}OH^-$ signal to obtain the tail correction to $^{17}O^-$.

Measurements on different terrestrial oxide standards (spinel and hibonite) showed that their isotopic differences can be reproduced within 2 ‰ (2σ) if measurements on many individual grains are averaged (McKeegan, 1987b). However, individual measurements on different grains vary by typically 5 to 8 ‰ from the average. As already discussed for hydrogen isotopic measurements, these fluctuations might reflect variations in the local geometry of grains pressed into gold foil. Obtaining measurements on polished sections made by the Cameca IMS 4f and its charge compensation electron gun is highly desirable so it can be established whether better control of the local geometry can lead to a higher precision for individual measurements.

Ion microprobe isotopic measurements have provided important information on the distribution of an ^{16}O-rich component, first discovered by Clayton and others (1973), in early solar system materials. McKeegan (1987b) presented evidence for the extraterrestrial origin of refractory stratospheric dust particles on the basis of their ^{16}O-rich isotopic composition. Fahey and others (1987c) showed that hibonites exhibiting both excesses and depletions in ^{48}Ca and ^{50}Ti have ^{16}O excesses. These excesses range from 40 ‰ to 70 ‰, surpassing the value previously observed for the spinel fraction from CM and CV meteorites (Clayton and others, 1977; Clayton and Mayeda, 1984). Furthermore, the large variations in the oxygen isotopic compositions of individual spinel grains from Murchison and Murray (McKeegan, 1987b; Grossman and others, 1988; Zinner and Tang, 1988) indicate that several oxygen reservoirs were responsible for the distribution of oxygen isotopes in the early solar system.

It is worth mentioning that the "best" absolute value for the $^{17}O/^{16}O$ ratio has been obtained from SIMS measurements. Although oxygen isotopic measurements relative to SMOW can be made with exceedingly high precision, the $^{17}O/^{16}O$ ratio itself has been poorly known. Under the assumption that the $(^{18}O/^{16}O)_{SMOW}$ ratio is given by the value of Baertschi (1976), Fahey and others (1987c), from measurements on terrestrial spinel, obtained $(^{17}O/^{16}O)_{SMOW} = 0.00038288 \pm .00000028$ ($2\sigma_{mean}$).

Magnesium

By far, most ion microprobe isotopic measurements have been made for magnesium. The following provides only a limited list of papers reporting such measurements: Bradley and others (1978), Lorin and Christophe Michel-Levy (1978), Macdougall and Phinney (1979), Bar-Matthews and others (1982), Hutcheon (1982), Huneke and others (1983), Hutcheon and others (1983, 1987), Clayton and others (1984), Hinton and Bischoff (1984), Lorin and Havette (1984), McKeegan and others (1985), Brigham and others (1986), Ireland and others (1986a), Fahey and others (1987a,b), Hinton and others (1988a), Ireland (1988). The reason for this abundance of measurements is the fact that the ion microprobe is uniquely suited for in situ measurements of ^{26}Mg excesses believed to be due to the decay of live ^{26}Al in the early solar system (see Wasserburg and Papanastassiou, 1982).

Evidence for live ^{26}Al is given by the distribution of ^{26}Mg excesses that are proportional to the Al/Mg ratio. An example is shown in figure 7, where the $^{26}Mg/^{24}Mg$ ratios (after correction for instrumental and intrinsic mass frac-

tionation) measured in different mineral grains of a coarse-grained Allende refractory inclusion are plotted against the $Al/^{24}Mg$ ratios. Measurements were made in the ion microprobe that allows the measurement of both the Mg isotopes and the Al/Mg ratio in individual phases. All data points lie on a line having a slope of 3.9×10^{-5}. Interpreted as an isochron, this line corresponds to an $^{26}Al/^{27}Al$ ratio of 3.9×10^{-5} at the time of formation (isotopic closure) of this inclusion.

Magnesium isotopic measurements are among the simplest ones to be made by SIMS. At low MRP, the interference from $^{48}Ca^{++}$ can be corrected for by peak stripping (Hutcheon, 1982), but care must be taken that possible MgH interferences can be excluded safely. High-mass-resolution analysis is preferred (Huneke and others, 1983; McKeegan and others, 1985; Ireland and others, 1986a) where an MRP of 3,000 eliminates all significant interferences and still yields a high sensitivity (table 1). Measurements of the intrinsic mass fractionation of a sample with the use of an external standard can be made with a precision of ~0.5 ‰ (2σ) (Ireland and others, 1986a). Approximately the same precision can be achieved for internal calibration measurements of $\delta^{26}Mg$ after normalization to the ^{24}Mg–^{25}Mg pair (Hutcheon, 1982; Ireland and others, 1986a). Normalizations were made with an assumed linear instrumental mass-fractionation law and with a standard $^{26}Mg/^{24}Mg$ ratio. Although values for this ratio reported in the literature vary widely (see above), ion probe measurements on terrestrial materials from this laboratory (McKeegan and others, 1985; Fahey and others, 1987b) are consistent with the ratios of Catanzaro and others (1966) within 0.3 ‰ (2σ).

Evidence for ^{26}Mg excesses associated with ^{26}Al (half-life 7×10^5 years) has been found in 10 different meteorites, but it is still not clear how widely ^{26}Al was distributed in the early solar system. The most comprehensive ion probe study on refractory inclusions from the Allende carbonaceous chondrite was presented by Hutcheon (1982). He showed that only inclusions of one type had well-defined Al-Mg isochrons corresponding to an initial $^{26}Al/^{27}Al$ ratio of 4 to 5×10^{-5}. Other inclusions had isochrons of much smaller slopes or had ^{26}Mg excesses that failed to be correlated with the Al/Mg ratio. While such observations can be explained by invoking late formation or redistribution of Mg and Al after ^{26}Al decay, the distribution of ^{26}Al in hibonites from primitive meteorites is even more puzzling (Ireland and others, 1986a, 1988a; Fahey and others, 1987a; Ireland, 1988). Hibonite is among the first minerals believed to condense from a gas of solar composition (Davis and others, 1982; Kornacki and Fegley, 1984). Meteoritic hibonites exhibit the largest calcium and titanium isotopic anomalies found to date (see below). However, hibonites that have the largest Ca and Ti effects and trace element patterns indicating early formation do not show any evidence for ^{26}Al, while hibonites that have small

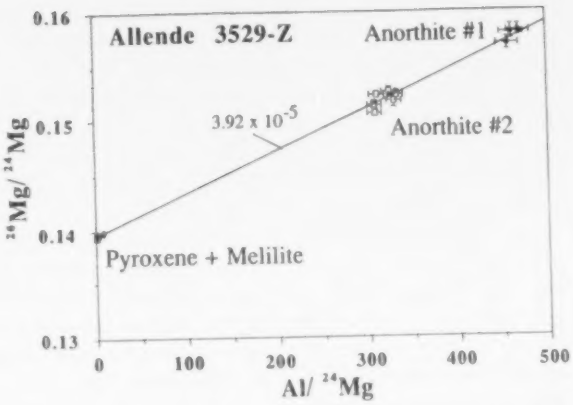

Figure 7. Plot of $^{26}Mg/^{24}Mg$ versus $Al/^{24}Mg$ measured in different minerals of a coarse-grained Ca-Al-rich inclusion (CAI), 3529–Z, from the carbonaceous meteorite Allende. The magnesium isotopes in this inclusion show ^{26}Mg excesses that are correlated with the $Al/^{24}Mg$ ratio and thus indicate that the ^{26}Mg excesses originate from the in situ decay of live ^{26}Al (half-life 7.2×10^5 years). If this were indeed the case, then the slope of the correlation line gives the $^{26}Al/^{27}Al$ ratio at the time of formation of this inclusion (from MacPherson and others, 1988).

or no Ca and Ti anomalies and trace element patterns indicating a complex formation history have $^{26}Mg^*$ (radiogenic) that are consistent with an initial $^{26}Al/^{27}Al$ ratio of 5×10^{-5} (Ireland, 1988; Ireland and others, 1988a).

Heterogeneity of ^{26}Al in the early solar system is a possible explanation for the above observations (Hutcheon, 1982). Also, Fahey and others (1987b) interpreted the observation that the $(^{26}Al/^{27}Al)_0$ in the rim of a refractory inclusion from Efremovka is larger than that in the interior as evidence for an inhomogeneous ^{26}Al distribution. Still, such an explanation for the hibonites is not really satisfying (Ireland and others, 1988a), and the truth may lie somewhere else.

A series of ion probe magnesium isotopic studies was concerned with the intrinsic isotopic fractionation in refractory meteoritic materials (Huneke and others, 1983; Clayton and others, 1984; Hinton and Bischoff, 1984; Hinton and others, 1985; Fahey and others, 1987b). The most intriguing observations were made by Macdougall and Phinney (1979) and Hutcheon and others (1983) who found extreme magnesium isotopic fractionations (up to 345 ‰/amu) that varied on a submicrometer scale in a hibonite-spinel sample from Murchison. No magnesium fractionation of comparable magnitude has ever been found in any other object.

Silicon

Silicon isotopes have been measured as positive (Huneke and others, 1983; Clayton and others, 1984;

McKeegan and others, 1985) and negative secondaries (Zinner and others, 1987). The silicon signal per primary beam current for a given sample is higher for negative secondary ions (see table 1), but since the sputter rate (number of sputtered atoms per incident ion) of Cs^+ is roughly 40 times that of O^-, the ionization efficiency (number of secondary ions per sputtered atom of a given species) is much higher for positive secondaries. The instrumental mass fractionation, however, is much larger for positive (−32 ‰/amu) than for negative ions (−8 ‰/amu). Comparison measurements in this laboratory for both ion polarities on silicon and SiC indicate that also for silicon the instrumental mass fractionation is best described by the "exponential" law. Ion probe measurements of silicon isotopes in terrestrial materials disagree with the values reported by Barnes and others (1975): if normalized to the ^{28}Si–^{29}Si pair with $(^{29}Si/^{28}Si)_{normal}=0.0506331$ (Barnes and others, 1975), the average for $^{30}Si/^{28}Si$ is 0.033474 ±.000014 ($2\sigma_{mean}$) rather than 0.0336214.

Ion probe isotopic measurements of silicon in IDP's did not detect any deviations from the terrestrial composition (McKeegan and others, 1985). Measurements in meteoritic materials revealed intrinsic mass-fractionation effects but no discernible non-mass-dependent effects (Huneke and others, 1983; Clayton and others, 1984) until Zinner and others (1987) and Tang and others (1988) found large anomalies in SiC from Murray and Murchison. Figure 8 displays their data in a three-isotope plot. Some data points are considerably displaced from the terrestrial composition along a slope ½ fractionation line, but many others lie far above or below the line. The distribution of the points in the plane indicates that at least three distinct isotopic components are needed to explain the silicon isotopic variability found in presolar SiC from primitive meteorites.

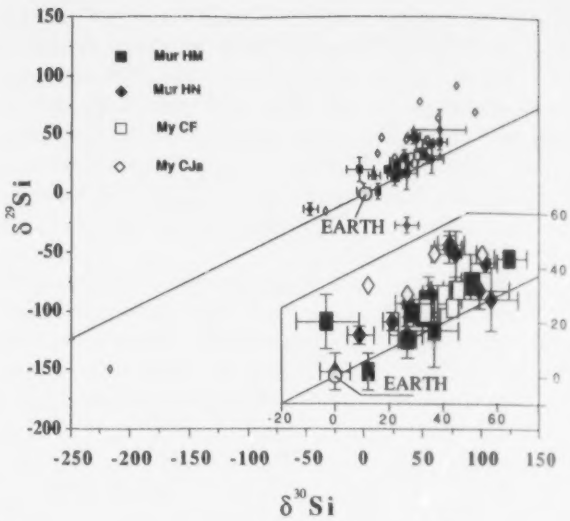

Figure 8. Three-isotope plot of $\delta(^{29}Si/^{28}Si)$ versus $\delta(^{30}Si/^{28}Si)$ measured in SiC samples from the Murray (My) and Murchison (Mur) carbonaceous chondrites. The squares and diamonds stand for different size fractions. Most data points are far from the terrestrial mass-fractionation line, which has a slope of ½ and passes through the mean terrestrial composition (labeled EARTH) that defines the origin (0,0). All ordinary ("mass-dependent") fractionation processes such as diffusion or equilibrium partitioning produce deviations that fall on this line; samples that do not conform to the terrestrial fractionation line bear witness for distinct primordial isotopic reservoirs. The extremely anomalous silicon isotopic compositions are further evidence for the presolar origin of the meteoritic SiC. Inset shows expanded plot in the vicinity of EARTH and the terrestrial fractionation line (from Tang and others, 1988). HM and CF, residue of grains in size range of 0.03 to 0.2 μm; HN, residue of grains in size range of 0.2 to 2.0 μm.

Sulfur

Sulfur isotopic measurements have been made with the Cameca IMS 3f (Chaussidon and others, 1987; N. Shimizu, personal commun., 1987) and the SHRIMP (Eldridge and others, this volume) ion microprobes. Both positive and negative secondary ions produced by O^- bombardments were used. No analyses with Cs^+ bombardment have been reported to date, but preliminary studies in this laboratory indicate that sulfides (galena, troilite) conduct well enough that negative ion analysis with a Cs^+ beam is feasible in these minerals. Analyses were restricted to measurements of ^{32}S and ^{34}S in terrestrial rocks. A detailed discussion of these studies can be found in Eldridge and others (this volume).

Potassium

Two types of potassium isotopic measurements have been reported: a study of the potassium isotopic mass fractionation in the Earth, the moon, and meteorites (Hinton and others, 1987b, 1988b) and the search for ^{41}K excesses that are due to the decay of ^{41}Ca (half-life 1.9×10^5 years) in refractory inclusions from primitive meteorites (Hutcheon and others, 1984). The first study involved measurements in high potassium phases at low MRP (AEI IM–20 ion probe) and, with the use of external standards, achieved a precision of 0.2 ‰ (2σ), better than that achieved by thermal ionization mass spectrometric analyses. The potassium isotopic composition was found to be light by approximately 1 ‰/amu both in lunar samples and meteorites relative to the Earth, in disagreement with fractionation models based on U/K ratios that predict heavy potassium for the moon. The second type of measurements were made with a Cameca IMS 3f in phases with extremely high Ca/K ratios at an MRP of ~5,000, which eliminates interferences for $^{41}K^+$ such as $^{40}CaH^+$, $^{25}Mg^{16}O^+$, and so forth, but not $^{40}Ca^{42}Ca^{++}$ and $^{26}Mg^{56}Fe^{++}$. These doubly charged ions pose an extremely serious problem. From

measurements in pyroxene from Allende inclusions, Hutcheon and others (1984) could set an upper limit of 8×10^{-9} on the $^{41}Ca/^{40}Ca$ ratio in these objects at the time of their formation. This low value would require an interval of $\sim 2 \times 10^6$ years between ^{41}Ca production and inclusion formation if the ^{41}Ca to ^{40}Ca production ratio was 10^{-4}.

Calcium and Titanium

Calcium and titanium isotopic ratios have been measured at low MRP with the AEI IM–20 ion probe at the University of Chicago (Hinton and others, 1985, 1987a). The calcium measurements were restricted to ^{40}Ca, ^{42}Ca, ^{44}Ca, and, while Hinton and others (1987a) measured all titanium isotopes, they had to make an interference correction for the contribution of $^{48}Ca^+$ to the $^{48}Ti^+$ signal. Since in refractory objects such as hibonites from primitive meteorites the ^{48}Ca shows the largest effect among the calcium isotopes, it is preferable to separate the $^{48}Ca^+$ and $^{48}Ti^+$ signals.

The necessary resolution can be achieved in the Cameca IMS 3f/4f (see fig. 1) and in the SHRIMP. Both instruments have been used to measure titanium isotopes under high MRP conditions (Fahey and others, 1985, 1987a; Ireland and others, 1985; Ireland, 1988). The SHRIMP has the advantage that at high MRP its ion transmission is higher than that of the Cameca IMS 3f/4f by a factor of 20 to 50. This advantage is a direct consequence of its larger dimensions and its higher extraction voltage for secondary ions. The technique for the measurement of titanium at high MRP has been described in detail by Fahey and others (1987a). They include a discussion of the interference correction for ^{46}Ca, ^{50}V, and ^{50}Cr that cannot be resolved from ^{46}Ti and ^{50}Ti.

Measurements of all calcium isotopes except ^{46}Ca have been made at an MRP similar to that of the titanium measurements (Zinner and others, 1986b; Fahey and others, 1987c). In most minerals measured so far, the $^{48}Ti^+$ signal is much more intense than the $^{48}Ca^+$ signal. In these cases, the $^{48}Ca^+$ signal is measured by first locating the center of the ^{48}Ti peak and then changing the magnetic field by an amount corresponding to the mass difference between ^{48}Ti and ^{48}Ca. Although a contribution from the tail of the $^{48}Ti^+$ peak to the $^{48}Ca^+$ signal cannot be completely avoided, a tail correction is made similar to that discussed for the ^{17}O peak.

Ion probe isotopic measurements of calcium and titanium in hibonites revealed large anomalies (fig. 9) that exceed those observed previously by thermal ionization mass spectrometry by more than an order of magnitude (Zinner and others, 1986b; Fahey and others, 1987c). The largest effects are found for ^{48}Ca and ^{50}Ti and are correlated in the sense that excesses of ^{48}Ca accompany excesses of ^{50}Ti and deficits of ^{48}Ca accompany deficits of ^{50}Ti. Since

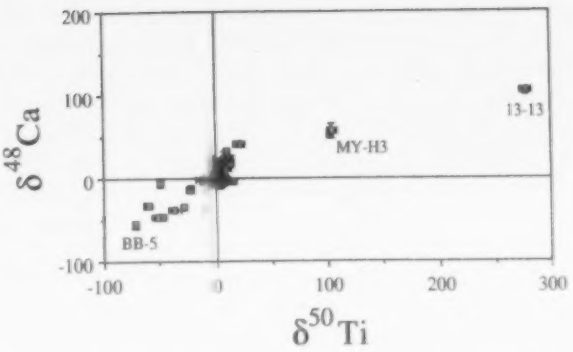

Figure 9. Calcium and titanium isotopes measured in meteoritic hibonite ($Ca\,[Al, Ti, Mg]_{12}O_{19}$) show correlated anomalies in ^{48}Ca and ^{50}Ti: both isotopes show either excesses or deficits. However, these ^{48}Ca and ^{50}Ti anomalies are completely decoupled from ^{16}O and ^{26}Mg anomalies in the same samples. The ^{48}Ca and ^{50}Ti correlated effects are evidence for the nucleosynthetic origin of the Ca-Ti isotopic anomalies. The excesses are thought to be produced by neutron-rich nuclear statistical equilibrium processes during supernova explosions. The compositions with deficits in the neutron-rich isotopes consist probably of several nucleosynthetic components. An appropriate mixture of these and the neutron-rich component resulted in the average solar system isotopic composition of calcium and titanium. Plotted are ion probe measurements of hibonites from the meteorites Murray, Murchison, and Lancé. Data for Murray MY–H3 are from Fahey and others (1987a) and Zinner and others (1986b), for Murchison BB-5 from Fahey and others (1987c), and for Murchison 13–13 from Ireland and others (1988b). (Courtesy of T. Ireland.)

different nucleosynthetic processes in different astrophysical sites are responsible for the production of different calcium and titanium isotopes (see, for example, Niederer and others, 1985), the isotopic variability in hibonites represents incomplete mixing of materials carrying different isotopic components in the early stages of the solar system. In case of the correlated ^{48}Ca and ^{50}Ti excesses, the nucleosynthetic process responsible can be identified as neutron-rich nuclear statistical equilibrium burning (Cameron, 1979; Hartmann and others, 1985). The ion microprobe, with its capability of small spot analysis, makes it possible to find large isotopic effects that provide a link to the nucleosynthetic sources of solar system materials.

Lead

The main application of lead isotopic measurements is the determination of U-Pb ages. Although the first efforts were made at low MRP with peak stripping (Andersen and Hinthorne, 1972; Hinthorne and others, 1979), U-Pb measurements are now exclusively made on the SHRIMP at high MRP (Compston and others, 1984). Aided by the high

ion transmission of the SHRIMP at high MRP, Compston and co-workers have made U-Th-Pb dating of zircons into a routine procedure. In addition to the measurement of lead isotopes, they have developed techniques for the quantitative measurements of Th/U and Pb/U ratios (Compston and others, 1984). An MRP of 9,000 (10 percent width definition) is used to resolve the lead isotopes from interferences such as Zr_2O, Zr_2OH, HfSi, HfSiH, and combinations of SiO and rare-earth elements. The determination of the Th/U and Pb/U ratios relies on corrections made from the measured ThO^+ and UO^+ signals. Ion microprobe dating of zircons has resulted in a large number of applications, including the identification of 4.2×10^9-year-old terrestrial zircons (Froude and others, 1983), evidence for unsupported radiogenic Pb in Antarctic zircons (Williams and others, 1984), U-Pb dating of lunar zircons (Compston and others, 1984), and the determination of U-Pb ages of meteoritic perovskite grains from the Murchison and Allende carbonaceous chondrites (Ireland and others, 1986b).

Hart and others (1981) used the Cameca IMS 3f operated at low MRP to study the zoning of the lead isotopic composition within a terrestrial galena crystal and found large variations in $^{208}Pb/^{206}Pb$ and $^{207}Pb/^{206}Pb$ ratios. Unfortunately, to date no correlated sulfur isotopic measurements were made on this sample. Such studies can provide important information on the genesis of ore deposits.

Other Elements

Ion probe isotopic measurements have been reported for a number of other elements. Although some of the applications of these measurements are potentially of high interest, none of them has become routine so far. Isotopic analyses of the elements listed in the following may require very different techniques and thus cannot be summarized in a simple way. The reader is referred to the original references.

Lithium isotopes in meteoritic inclusions have been measured by Hutcheon and others (1977) and Phinney and others (1979); the latter investigators also measured boron isotopes. No isotopic anomalies were found for these elements. A series of chromium isotopic measurements was made in a search for short-lived ^{53}Mn (half-life 3.7×10^6 years) in meteoritic material (Scatena-Wachel and others, 1984, 1985; Hutcheon and others, 1985). Although Hutcheon and others (1985) found some evidence of ^{53}Cr excesses in iron meteorites, the lack of a correlation with the $^{55}Mn/^{52}Cr$ ratio makes it doubtful that substantial amounts of ^{53}Mn were present in these objects.

Fahey and Zinner (1987) failed to find iron isotopic anomalies in a Lancé inclusion that has large ^{48}Ca and ^{50}Ti anomalies (Fahey and others, 1986). The neutron-rich nuclear statistical equilibrium process that produces ^{48}Ca, ^{50}Ti, and ^{54}Cr is predicted to produce also ^{60}Fe (half-life 1.5×10^6 years) (Cameron, 1979; Hartmann and others, 1985), but ion probe searches (Hinton and others, 1984; Scatena-Wachel and others, 1985) for evidence of ^{60}Ni excesses due to ^{60}Fe decay were negative. Hutcheon and others (1987) reported isotopic studies of Mg, Fe, Mo, Ru, and W in Fremdlinge from Allende refractory inclusions. While they found evidence for mass-dependent fractionation of molybdenum, they did not observe large non-mass-dependent isotopic anomalies.

Ion microprobe measurements of $^{87}Sr/^{86}Sr$ ratios in terrestrial carbonates have been reported by Exley (1983), Exley and Jones (1983), and Scatena-Wachel and others (1986). A prerequisite for such measurements are low rubidium concentrations. Because the separation of ^{87}Rb and ^{87}Sr requires an MRP of 2.9×10^5, in situ Rb-Sr dating by ion microprobe mass spectrometry is out of the question for present-day instruments. For osmium isotopic measurements, SIMS proved to be superior to previous techniques (Luck and others, 1980). SIMS allowed the determination of Re-Os ages of terrestrial samples (Allègre and Luck, 1980; Luck and Allègre, 1982) based on a new determination of the ^{187}Re half-life from the study of iron and carbonaceous meteorites (Luck and others, 1980; Luck and Allègre, 1983).

CONCLUSION AND OUTLOOK

Secondary ion mass spectrometry has been applied successfully to isotopic measurements of many different elements. Although most of the work reported so far has been done on extraterrestrial materials, ion microprobe measurements of sulfur and lead isotopes have been important developments for geochemistry and geochronology.

As for the future, improvements for SIMS isotopic analysis can be expected to be associated with increased selectivity and sensitivity. It is doubtful that future instruments will rely on substantial increases of mass spectrometer MRP for improvements in selectivity (separation of atomic ions of interest from interferences), although new concepts such as Fourier transform mass spectrometry should not be excluded. It is more likely that selection by laser resonance ionization will play a major role.

An important increase in sensitivity can be achieved by multiple collection systems. Furthermore, such systems would result in increased precision of isotopic ratio measurements at high count rates because effects from fluctuations in the secondary ion signal would be eliminated (for example, instabilities of the primary beam current, beam position, inhomogeneities in the analyzed sample).

Resonance ionization is also promising for improvements in sensitivity. Useful ion yields in present-day instruments are on the order of 10^{-4} to 10^{-3}. More

complete, selective ionization could lead to either the analysis of smaller samples (femtogram analysis) or to improvements in the precision of isotopic measurements (for example, complete ionization would eliminate instrumental mass-fractionation effects). However, such capabilities presently exist only in theory; their realization will require further developments in laser technology (for example, higher repetition rates and higher laser power densities).

ACKNOWLEDGMENTS

I gratefully acknowledge the important role of R.M. Walker in establishing the Washington University ion probe laboratory. A.J. Fahey and K.D. McKeegan made essential contributions to many of the isotopic measurement techniques discussed in this paper. I thank E.G. Koenig for her help with the preparation of the manuscript. This work was supported by NASA Grant NAG9–55 and NSF Grant EAR–8719528.

REFERENCES CITED

Allègre, C.J., and Luck, J.M., 1980, Osmium isotopes as petrogenetic and geological tracers: Earth and Planetary Science Letters, v. 48, p. 148–154.

Anders E., 1988, Circumstellar material in meteorites: Noble gases, carbon, and nitrogen, *in* Kerridge, J.F., ed., Meteorites and the early solar system, chap. 13.1: University of Arizona Press, p. 927–955.

Andersen, C.A., and Hinthorne, J.R., 1972, U, Th, Pb and REE abundances and $^{207}Pb/^{206}Pb$ ages of individual minerals in returned lunar material by ion microprobe mass analysis: Earth and Planetary Science Letters, v. 14, p. 195–200.

Baertschi, P., 1976, Absolute ^{18}O content of standard mean ocean water: Earth and Planetary Science Letters, v. 31, p. 341–344.

Bar-Matthews, M., Hutcheon, I.D., MacPherson, G.J., and Grossman, L., 1982, A corundum-rich inclusion in the Murchison carbonaceous chondrite: Geochimica et Cosmochimica Acta, v. 46, p. 31–41.

Barnes, I.L., Moore, L.J., Machlan, L.A., Murphy, T.J., and Shields, W.R., 1975, Absolute isotopic abundance ratios and atomic weight of a reference sample of silicon: Journal of Research of the National Bureau of Standards, v. 79A, p. 727–735.

Begemann, F., 1980, Isotopic anomalies in meteorites: Report on Progress in Physics, v. 43, p. 1309–1356.

Benninghoven, A., Rüdenauer, F.G., and Werner, H.W., 1987, Secondary Ion Mass Spectrometry: New York, Wiley & Sons, 1216 p.

Bradley, J.G., Huneke, J.C., and Wasserburg, G.J., 1978, Ion microprobe evidence for the presence of excess ^{26}Mg in an Allende anorthite crystal: Journal of Geophysical Research, v. 83, p. 244–254.

Brigham, C.A., Hutcheon, I.D., Papanastassiou, D.A., and Wasserburg, G.J., 1986, Evidence for ^{26}Al and Mg isotopic heterogeneity in a fined-grained CAI, *in* Lunar and Planetary Science XVII: Houston, Lunar and Planetary Institute, p. 85–86.

Cameron, A.G.W., 1979, The neutron-rich silicon-burning and equilibrium processes of nucleosynthesis: Astrophysical Journal Letters, v. 230, p. L53–L57.

Carey, W., Zinner, E., Fraundorf, P., and Lewis, R.S., 1987, Ion probe and TEM studies of a diamond bearing Allende residue: Meteoritics, v. 22, p. 349–350.

Catanzaro, E.J., Murphy, T.J., Garner, E.L., and Shields, W.R., 1966, Absolute isotopic abundance ratios and atomic weights of magnesium: Journal of Research of the National Bureau of Standards, v. 70A, p. 453–458.

Chaussidon, M., Albarede, F., and Sheppard, S.M.F., 1987, Sulphur isotope heterogeneity in the mantle from ion microprobe measurements of sulphide inclusions in diamonds: Nature, v. 330, p. 242–244.

Clayton, R.N., and Mayeda, T., 1984, The oxygen isotope record in Murchison and other carbonaceous chondrites: Earth and Planetary Science Letters, v. 67, p. 151–161.

Clayton, R.N., Grossman, L., and Mayeda, T.K., 1973, A component of primitive nuclear composition in carbonaceous meteorites: Science, v. 182, p. 485–488.

Clayton, R.N., Onuma, N., Grossman, L., and Mayeda, T.K., 1977, Distribution of the pre-solar component in Allende and other carbonaceous chondrites: Earth and Planetary Science Letters, v. 34, p. 209–224.

Clayton, R.N., MacPherson, G.J., Hutcheon, I.D., Davis, A.M., Grossman, L., Mayeda, T.K., Molini-Velsko, C., Allen, J.M., El Gonesy, A., 1984, Two forsterite-bearing FUN inclusions in the Allende meteorite: Geochimica et Cosmochimica Acta, v. 48, p. 535–548.

Clayton, R.N., Hinton, R.W., and Davis, A.M., 1988, Isotopic variations in the rock-forming elements in meteorites: Philosophical Transactions of the Royal Society of London A, v. 325, p. 483–501.

Clement, S.W.J., Compston, W., and Newstead, G., 1977, Design of a large, high resolution ion microprobe, *in* Benninghoven, A., ed., Proceedings of the International Secondary Ion Mass Spectroscopy Conference: Münster, Springer Verlag.

Compston, W., Williams, I.S., and Meyer, C., 1984, U-Pb geochronology of zircons from lunar breccia 73217 using a sensitive high mass-resolution ion microprobe, *in* Boynton, W.V., and others, eds., Proceedings of the Fourteenth Lunar and Planetary Science Conference, pt. 2: Journal of Geophysical Research, v. 89, p. B525–B534.

Crozaz, G., and Zinner, E., 1986, Quantitative ion microprobe analysis of the rare earth elements in minerals: Scanning Electron Microscopy, 1986/II, p. 369–376.

Davis, A.M., Tanaka, T., and Grossmann, L., 1982, Chemical composition of HAL, an isotopically-unusual Allende inclusion: Geochimica et Cosmochimica Acta, v. 46, p. 1627–1651.

Exley, R.A., 1983, Evaluation and application of the ion microprobe in the strontium isotope geochemistry of carbonates: Earth and Planetary Science Letters, v. 65, p. 303–310.

Exley, R.A., and Jones, A.P., 1983, $^{87}Sr/^{86}Sr$ in kimberlitic carbonates by ion microprobe: Hydrothermal alteration,

crustal contamination and relation to carbonatite: Contributions to Mineralogy and Petrology, v. 83, p. 288–292.

Fahey, A.J., 1988, Ion microprobe measurements of Mg, Ca, Ti and Fe isotopic ratios and trace element abundances in hibonite-bearing inclusions from primitive meteorites: unpublished Ph.D. dissertation, St. Louis, Missouri, Washington University, 206 p.

Fahey, A.J., and Zinner, E., 1987, Determination of the Fe isotopic ratios in terrestrial minerals and a Lancé hibonite-hercynite inclusion, *in* Lunar and Planetary Science XVIII: Houston, Lunar and Planetary Institute, p. 277–278.

Fahey, A.J., Goswami, J.N., McKeegan, K.D., and Zinner, E., 1985, Evidence for extreme ^{50}Ti enrichments in primitive meteorites: Astrophysical Journal, v. 296, p. L17–L20.

Fahey, A.J., Zinner, E., and Kurat, G., 1986, Anomalous Ca and Ti in a hercynite-hibonite inclusion from Lancé: Meteoritics, v. 21, p. 359–360.

Fahey, A., Goswami, J.N., McKeegan, K.D., and Zinner, E., 1987a, ^{26}Al, ^{244}Pu, ^{50}Ti, REE and trace element abundances in hibonite grains from CM and CV meteorites: Geochimica et Cosmochimica Acta, v. 51, p. 329–350.

Fahey, A.J., Zinner, E., Crozaz, G., and Kornacki, A.S., 1987b, Microdistributions of Mg isotopes and REE abundances in a Type A calcium-aluminum-rich inclusion from Efremovka: Geochimica et Cosmochimica Acta, v. 51, p. 3215–3229.

Fahey, A.J., Goswami, J.N., McKeegan, K.D., and Zinner, E., 1987c, ^{16}O excesses in Murchison and Murray hibonites: A case against a late supernova injection origin of isotopic anomalies in O, Mg, Ca and Ti: Astrophysical Journal Letters, v. 323, p. L91–L95.

Froude, D.O., Ireland, T.R., Kinny, P.D., Williams, I.S., Compston, W., Williams, I.R., and Myers, J.S., 1983, Ion microprobe identification of 4,100–4,200 Myr-old terrestrial zircons: Nature, v. 304, p. 616–618.

Gnaser, H., and Hutcheon, I.D., 1987, Velocity-dependent isotope fractionation in secondary-ion emission: Physical Review B, v. 35, p. 877–879.

———1988, Preferential emission of the lighter isotopes in the initial stage of sputtering: Surface Science, v. 195, p. 499–512.

Grossman, L., Fahey, A.J., and Zinner, E., 1988, Carbon and oxygen isotopic compositions of individual spinel crystals from the Murchison meteorite, *in* Lunar Planetary Science XIX: Houston, Lunar and Planetary Institute, p. 435–436.

Hart, S.R., Shimizu, N., and Sverjensky, D.A., 1981, Lead isotope zoning in galena: An ion microprobe study of a galena crystal from the Buick Mine, Southeast Missouri: Economic Geology, v. 76, p. 1873–1878.

Hartmann, D., Woosley, S.E., and El Eid, M.F., 1985, Nucleosynthesis in neutron-rich supernova ejecta: Astrophysical Journal, v. 297, p. 837–845.

Hinthorne, J.R., Andersen, C.A., Conrad, R.L., and Lovering, J., 1979, Single-grain ^{207}Pb/^{206}Pb and U/Pb age determinations with a 10-μm spatial resolution using the ion microprobe mass analyzer (IMMA): Chemical Geology, v. 25, p. 271–303.

Hinton, R.W., and Bischoff, A., 1984, Ion microprobe magnesium isotope analysis of plagioclase and hibonite from ordinary chondrites: Nature, v. 308, p. 169–172.

Hinton, R.W., Long, J.V.P., Fallick, A.E., and Pillinger, C.T., 1983, Ion microprobe measurement of D/H ratios in meteorites, *in* Lunar and Planetary Science, XIV: Houston, Lunar and Planetary Institute, Texas: p. 313–314.

Hinton, R.W., Grossman, L., and MacPherson, G.J., 1984, Magnesium and calcium isotopes in hibonite-bearing CAIs: Meteoritics, v. 19, p. 240–241.

Hinton, R.W., Davis, A.M., and Scatena-Wachel, D.E., 1985, Ion microprobe measurement of calcium and magnesium isotopic mass fractionation in refractory inclusions, *in* Lunar and Planetary Science XVI: Houston, Lunar and Planetary Institute, p. 354–355.

Hinton, R.W., Davis, A.M., and Scatena-Wachel, D.E., 1987a, Large negative ^{50}Ti anomalies in refractory inclusions from the Murchison carbonaceous chondrite—Evidence for incomplete mixing of neutron-rich supernova ejecta into the solar system: Astrophysical Journal, v. 313, p. 420–428.

Hinton, R.W., Clayton, R.N., Olsen, E.J., and Davis, A.M., 1987b, Isotopic mass fractionation of potassium in the Earth compared to the bulk solar system, *in* Lunar and Planetary Science XVIII: Houston, Lunar and Planetary Institute, p. 429–430.

Hinton, R.W., Davis, A.M., Scatena-Wachel, D.E., Grossman, L., and Draus, R.J., 1988a, A chemical and isotopic study of hibonite-rich refractory inclusions in primitive meteorites: Geochimica et Cosmochimica Acta, v. 52, p. 2573–2598.

Hinton, R.W., Clayton, R.N., Davis, A.M., and Olsen, E.J., 1988b, Isotopic mass fractionation of potassium in the Moon, *in* Lunar and Planetary Science XIX: Houston, Lunar and Planetary Institute, p. 497–498.

Huneke, J.C., Armstrong, J.T., and Wasserburg, G.J., 1983, FUN with PANURGE: High mass resolution ion microprobe measurements of Mg in Allende inclusions: Geochimica et Cosmochimica Acta, v. 47, p. 635–650.

Hutcheon, I.D., 1982, Ion probe magnesium isotopic measurements of Allende inclusions, *in* Curie, L.A., ed., Nuclear and chemical dating techniques: Interpreting the environmental record: American Chemical Society Symposium Series No. 176, p. 95–128.

Hutcheon, I.D., Steele, I.M., Solberg, T.N., Clayton, R.N., and Smith, J.V., 1977, Ion microprobe studies of lithium in Allende inclusions: Meteoritics, v. 13, p. 261.

Hutcheon, I.D., Steele, I.M., Scatena-Wachel, D.E., Macdougall, J.D., and Phinney, D., 1983, Extreme Mg fractionation and evidence of Ti isotopic variations in Murchison refractory inclusions, *in* Lunar and Planetary Science, XIV: Houston, Lunar and Planetary Institute, p. 339–340.

Hutcheon, I.D., Armstrong, J.T., and Wasserburg, G.J., 1984, Excess ^{41}K in allende CAI: A hint re-examined: Meteoritics, v. 19, p. 243–244.

Hutcheon, I.D., Teshima, J., Armstrong, J.T., and Wasserburg, G.J., 1985, The Cr isotopic composition of phosphates in IIIB iron meteorites: A search for ^{53}Mn: Meteoritics, v. 20, p. 668–669.

Hutcheon, I.D., Armstrong, J.T., and Wasserburg, G.J., 1987, Isotopic studies of Mg, Fe, Mo, Ru and W in Fremdlinge from Allende refractory inclusions: Geochimica et Cosmochimica Acta, v. 51, p. 3175–3192.

Ireland, T.R., 1988, Correlated morphological, chemical, and isotopic systematics of hibonites from the Murchison carbonaceous chondrite: Geochimica et Cosmochimica Acta, v. 52, p. 2827–2839.

Ireland, T.R., Compston, W., and Heydegger, H.R., 1985, Titanium isotopic anomalies in hibonites from the Murchison carbonaceous chondrite: Geochimica et Cosmochimica Acta, v. 49, p. 1989–1993.

Ireland, T.R., Compston, W., and Esat, T.M., 1986a, Magnesium isotopic compositions of olivine, spinel and hibonite from the Murchison carbonaceous chondrite: Geochimica et Cosmochimica Acta, v. 50, p. 1413–1421.

Ireland, T.R., Compston, W., and Williams, I.S., 1986b, U-Pb age determinations of meteoritic perovskites: TERRA cognita, v. 6, p. 174.

Ireland, T.R., Fahey, A.J., and Zinner, E.K., 1988a, High-temperature processes and trace-element abundances in hibonites from the Murchison carbonaceous chondrite: Constraints on high-temperature processes in the solar nebula: Geochimica et Cosmochimica Acta, v. 52, p. 2841–2854.

———1988b, Calcium and titanium isotopic systematics of hibonites, *in* Lunar and Planetary Science XIX: Houston, Lunar and Planetary Institute, p. 529–530.

Jull, A.J.T., 1982, Variations of isotopic discrimination in secondary ion mass spectrometry: International Journal of Mass Spectrometry and Ion Physics, v. 41, p. 135–141.

Kornacki, A.S., and Fegley, B., Jr., 1984, Origin of spinel-rich chondrules and inclusions in carbonaceous and ordinary chondrites, *in* Boynton, W.V., and others, eds., Proceedings of the Fourteenth Lunar and Planetary Science Conference, pt. 2: Journal of Geophysical Research, v. 89, p. B588–B596.

Lepareur, M., 1980, Le micro-analyseur ionique de seconde generation Cameca, modele 3F: Revue Technique Thomson-CSF, v. 12, p. 225–265.

Liebl, H., 1980, SIMS instrumentation and imaging techniques: Scanning, v. 3, p. 79–89.

Lorin, J.C., and Christophe Michel-Levy, M., 1978, Radiogenic ^{26}Mg fine-scale distribution in Ca-Al inclusions in the Allende and Leoville meteorites, *in* Zartman, R.E., ed., Fourth International Conference on Geochronology, Cosmochronology, and Isotope Geology: U.S. Geological Survey Open-File Report 78–701, p. 257–259.

Lorin, J.C., and Havette, A., 1984, Extreme magnesium isotope fractionation in the Leoville meteorite, *in* Isotopic ratios in the solar system: Toulouse, France, Cepadues-Editions, p. 43–69.

Lovering, J.F., 1975, Application of SIMS microanalysis techniques to trace element and isotopic studies in geochemistry and cosmochemistry: National Bureau of Standards Special Publication 427, p. 135–178.

Luck, J.M., and Allègre, C.J., 1982, The study of molybdenites through the ^{187}Re–^{187}Os chronometer: Earth and Planetary Science Letters, v. 61, p. 291–296.

———1983, ^{187}Re–^{187}Os systematics in meteorites and cosmochemical consequences: Nature, v. 302, p. 130–132.

Luck, J.M., Birck, J.L., and Allègre, C.J., 1980, ^{187}Re–^{187}Os systematics in meteorites: Early chronology of the solar system and age of the galaxy: Nature, v. 283, p. 256–259.

Macdougall, J.D., and Phinney, D., 1979, Magnesium isotopic variations in hibonite from the Murchison meteorite: An ion microprobe study: Geophysical Research Letters, v. 6, p. 215–218.

MacPherson, G.J., Fahey, A.J., Lundberg, L.L., and Zinner, E., 1988, Al-Mg isotopic systematics and metamorphism in five coarse-grained Allende CAIs: Meteoritics, v. 23, p. 286.

McKeegan, K.D., 1987a, Ion microprobe measurements of H, C, O, Mg, and Si isotopic abundances in individual interplanetary dust particles: Unpublished Ph.D. dissertation, St. Louis, Missouri, Washington University, 187 p.

———1987b, Oxygen isotopic abundances in refractory stratospheric dust particles: Proof of extraterrestrial origin: Science, v. 237, p. 1468–1471.

McKeegan, K.D., and Zinner, E., 1984, On the distribution of excess deuterium in Renazzo and Semarkona: An ion microprobe study: Lunar and Planetary Science XV: Houston, Lunar and Planetary Institute, p. 534–535.

McKeegan, K.D., Walker, R.M., and Zinner, E., 1985, Ion microprobe isotopic measurements of individual interplanetary dust particles: Geochimica et Cosmochimica Acta, v. 49, p. 1971–1987.

McKeegan, K.D., Swan, P., Walker, R.M., Wopenka, B., and Zinner, E., 1987, Hydrogen isotopic variations in interplanetary dust particles, *in* Lunar and Planetary Science XVIII: Houston, Lunar and Planetary Institute, p. 627–628.

Niederer, F.R., Papanastassiou, D.A., and Wasserburg, G.J., 1985, Absolute isotopic abundances of Ti in meteorites: Geochimica et Cosmochimica Acta, v. 49, p. 835–851.

Phinney, D., Whitehead, B., and Anderson, D., 1979, Li, Be, and B in minerals of a refractory-rich Allende inclusion, *in* Merrill, R.B., and others, eds., Meteorites and lunar rocks: Proceedings of the Lunar and Planetary Science Conference, No. 10, v. 1, March 19–23, Houston, Texas, p. 885–905.

Russell, W.A., Papanastassiou, D.A., and Tombrello, T.A., 1978, Ca isotope fractionation on the Earth and in other solar system materials: Geochimica et Cosmochimica Acta, v. 42, p. 1075–1090.

Scatena-Wachel, D.E., Hinton, R.W., and Davis, A.M., 1984, Preliminary ion microprobe study of chromium isotopes in Orgueil, Lunar and Planetary Science XV: Houston, Lunar and Planetary Institute, p. 718–719.

———1985, A search for extinct ^{53}Mn and ^{60}Fe in iron meteorites: Meteoritics, v. 20, p. 751–752.

Scatena-Wachel, D.E., Jones, A.P., Marian, A., Hinton, R.W., and Clayton, R.N., 1986, Strontium isotopes of kimberlites and carbonatites: TERRA cognita, v. 6, p. 202.

Shimizu, N., and Hart, S.R., 1982a, Applications of the microprobe to geochemistry and cosmochemistry: Annual Review, Earth and Planetary Science, v. 10, p. 483–526.

———1982b, Isotope fractionation in secondary ion mass spectrometry: Journal of Applied Physics, v. 53, p. 1303–1311.

Slodzian, G., 1980, Microanalyzers using secondary ion emission: Advances in electronics and electron physics, supplement 13B: Academic Press, p. 1–44.

Slodzian, G., Lorin, J.C., and Havette, A., 1980, Isotopic effect on the ionization probabilities in secondary ion emission: Journal of Physics, v. 23, p. 555–558.

Slodzian, G., Chaintreau, M.P., and Dennebouy, R.C., 1987, SIMS: Self-regulated potential at insulating surfaces in presence of a strong electrostatic extraction field: Cameca News, May 1987, p. 1–6.

Tang M., Anders, E., and Zinner, E., 1988, Noble gases, C, N and Si isotopes in interstellar SiC from the Murchison carbonaceous, *in* Lunar and Planetary Science XIX: Houston, Lunar and Planetary Institute, p. 1177–1178.

Veizer, J., Hinton, R.W., Clayton, R.N., and Lerman, A., 1987, Chemical diagenesis of carbonates in thin-sections: Ion microprobe as a trace element tool: Chemical Geology, v. 64, p. 225–237.

Wasserburg, G.J., and Papanastassiou, D.A., 1982, Some short-lived nuclides in the early solar system—A connection with the placental ISM, *in* Barnes, C.A., Clayton, D.D., and Schramm, D.N., eds., Essays in nuclear astrophysics: Cambridge University Press, p. 77–140.

White, F.A., and Wood, G.M., 1986, Mass spectrometry: New York, J. Wiley & Sons, 773 p.

Williams, I.S., Compston, W., Black, L.P., Ireland, T.R., and Foster, J.J., 1984, Unsupported radiogenic Pb in zircon: A cause of anomalously high Pb-Pb, U-Pb, and Th-Pb ages: Contributions to Mineralogy and Petrology, v. 88, p. 322–327.

Williams, P., 1983, Secondary Ion Mass Spectrometry: Applied Atomic Collision Physics, v. 4, p. 327–377.

Zinner, E., and Crozaz, G., 1986, A method for the quantitative measurement of rare earth elements in the ion microprobe: International Journal of Mass Spectrometry and Ion Processes, v. 69, p. 17–38.

Zinner, E., and Epstein, S., 1987, Heavy carbon in individual oxide grains from the Murchison meteorite: Earth and Planetary Science Letters, v. 84, p. 359–368.

Zinner, E., and Tang M., 1988, Anomalous oxygen in spinels from a Murray separate, *in* Lunar and Planetary Science XIX: Houston, Lunar and Planetary Institute, p. 1323–1324.

Zinner, E., McKeegan, K.D., and Walker, R.M., 1983, Laboratory measurements of D/H ratios in interplanetary dust: Nature, v. 305, p. 119–121.

Zinner, E., Fahey, A.J., and McKeegan, K.D., 1986a, Characterization of electron multipliers by charge distributions, *in* Benninghoven, A., Colton, R.J., Simons, D.S., and Werner, H.W., eds., Secondary ion mass spectrometry (SIMS V): New York, Springer-Verlag, p. 170–172.

Zinner, E., Fahey, A.J., Goswami, J.N., Ireland, T.R., and McKeegan, K.D., 1986b, Large ^{48}Ca anomalies are associated with ^{50}Ti anomalies in Murchison and Murray hibonites:Astrophysical Journal Letters, v. 311, p. L103–L107.

Zinner, E., Tang M., and Anders, E., 1987, Large isotopic anomalies of Si, C, N and noble gases in interstellar silicon carbide from the Murray meteorite: Nature, v. 330, p. 730–732.

Sulfur Isotopic Analyses on the SHRIMP Ion Microprobe

By C.S. Eldridge,[1, 2] W. Compston,[2] I.S. Williams,[2] *and* J.L. Walshe[1]

Abstract

The ion microprobe offers the user the advantages of high spatial resolution, in situ analytical capabilities, and respite from the tedium and hazards of sample preparation for conventional isotopic analyses. Because the only sample preparation needed is sample polishing, photographing, and carbon coating, the microprobe allows relatively rapid analyses of small samples as compared to selective abrasion or other physical means of isolating microsamples for conventional mass spectrometry. Like other mass spectrometers, however, each ion microprobe must be examined to quantify mass fractionation, demonstrate linearity, and discover if there are residual contamination, or memory, effects on measured isotopic ratios. Moreover, additional steps must be taken to ensure that appropriate standards are used and that standards are analyzed in the same analytical conditions as the unknown. Ion microprobe analyses are limited by instrumental analytical precision, commonly around 1 to 3 per mil (2σ), with accuracy equaling precision.

Of the stable isotopes, the sulfur isotopic system is the easiest to analyze precisely on the ion microprobe because of the abundance of the minor isotope (^{34}S). The ion microprobe SHRIMP has been used to study the sulfur isotopic systematics of sediment-hosted massive sulfide deposits, and important new data have been obtained from the McArthur River H.Y.C. and Mount Isa lead-zinc deposits, Australia, and the Rammelsberg deposits, West Germany, as well as the Salton Sea geothermal system, California. These studies have shown in some cases that the isotopic variability may actually be several times that found in conventional studies because of the averaging effects of conventional sample preparation, that mineralization in such deposits need not be syngenetic, and that biogenic sulfide may not have contributed sulfur to base-metal deposition at the site of ore precipitation.

The next step in ion microprobe analyses, the improvement of precision, is being pursued by several methods. Investigations of multiple collection and increase of secondary-ion yields through use of negatively charged ions or laser-enhanced positive secondary ions are under way or planned.

INTRODUCTION

Research performed on the light stable isotopes (sulfur, oxygen, carbon, and hydrogen) has had a major impact on many subdisciplines of the geosciences (Valley and others, 1986; Kyser, 1987). Analytical precisions of conventional analyses are such that many fundamental natural processes, both equilibrium and kinetic, can be examined by use of the light stable isotope ratios. Often, though, stable isotopic studies are limited by the amount of sample necessary for analyses. Typically, around 10 mg of pure mineral separate must be concentrated from the hand sample and converted to a purified gas for mass spectrometric analysis. Traditional methods of physical or chemical concentration of the chosen mineral are incapable of discriminating between various generations, and it is increasingly clear, through conventional studies involving careful dissecting of relatively coarse-grained materials or those enlisting microanalytical techniques, that rocks and individual mineral grains sometimes contain more information concerning their origins and subsequent modifications than can be obtained easily by bulk sampling and analytical means. While it is possible to lessen the amount of sample required for conventional analysis by holding the sample inlet system of a conventional mass spectrometer in a static mode and not sacrificing gas to the pumping system, this type of analysis offers no advantage in relating small samples to specific textural features. Therefore, sampling techniques have been developed for conventional isotopic measurements of single grains or parts of single grains, including crushing and abrasion, step heating of hand-picked crystals, and laser ablation. However, all of these sampling techniques are limited by labor-intensive steps involved in liberation, purification, and transfer of gas to the mass spectrometer. Furthermore, some of the methods mentioned above may produce data that are only average isotopic values for the sample and may sacrifice the sample's important textural information that is crucial to proper data interpretation. Alternatively, the ion microprobe offers sampling on a very fine scale (15 to 30 μm), eliminates the difficult and potentially hazardous aspects of sample preparation for conventional mass spectrometry, and provides largely nondestructive in situ analyses that can be related to the microtextural features of the sample.

ANALYTICAL METHOD

Analysis of the stable isotopic composition of solids in the ion microprobe requires little sample preparation. The sample must be cut to a size that will fit into the sample

[1] Geology Department, The Australian National University, GPO Box 4, Canberra, A.C.T. 2601, Australia.
[2] Research School of Earth Sciences, The Australian National University, GPO Box 4, Canberra, A.C.T. 2601, Australia.

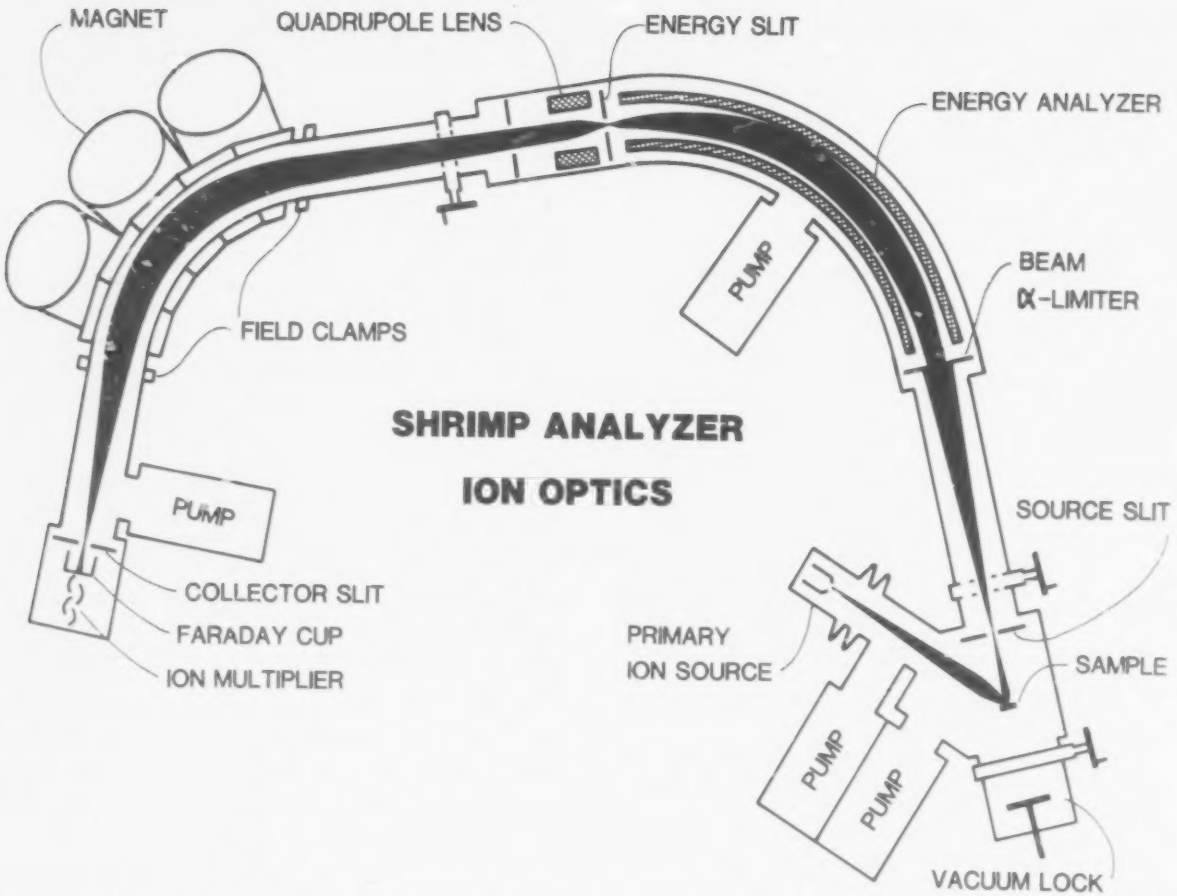

Figure 1A. Schematic drawing of the SHRIMP overall geometry. The major components are the primary column, where the primary beam is generated; the source chamber, site of secondary-ion formation and extraction; electrostatic sector analyzer (cylindrical, 85°) that allows transmission of ions within an energy bandpass of 150 eV in 25 keV; 72.5° nonnormal entry sector magnet for mass analysis with a dispersion of 773 mm × (Δm/m); and the collector, which has a detection system for simultaneous counting of eight masses. All major segments of the instrument are joined by bellows to allow movement and the best possible overall alignment. The collector housing is on rails and is wired to a computer-driven motor so that it can be located for the optimum peak shape position for each isotope. The housing is also on two independently movable plates and can be tilted left or right as well as nose up or down in order to best match the slits with the incoming ion beams.

holder and must also be polished. Typically, a polish finishing with 1-μm diamond abrasive is sufficient. The SHRIMP (Sensitive High mass Resolution Ion MicroProbe) sample holder is circular, has a diameter of 25.4 mm, and holds samples no thicker than 7 mm. Diverse materials, from appropriately trimmed thin sections to polished blocks to assemblages of grains, once oriented to allow space for the standard plug and mounted in epoxy, can be used. The epoxy prevents samples from acting as virtual leaks inside the vacuum chamber, and the mounts must be coated (typically with carbon, but copper or gold can be used) to dissipate charge during analyses. Once under vacuum in the source chamber, any portion of the mount can be analyzed by controlling drive motors attached to the sample-holding arm. Continuous viewing, in reflected light only, of the sample is permitted during analyses. Photomicrographs of relevant portions of these mounts, for navigational purposes, must be prepared prior to analytical sessions.

The ion microprobe obtains material for analysis by directing a primary-ion beam onto the sample surface. Impact of the primary ions dislodges material from the sample, a small portion of which is ionized, and these secondary ions are then directed into the mass analysis portion of the instrument (figs. 1, 2). Descriptions of the interaction of the primary beam with the sample and models of secondary ion formation can be found in several papers

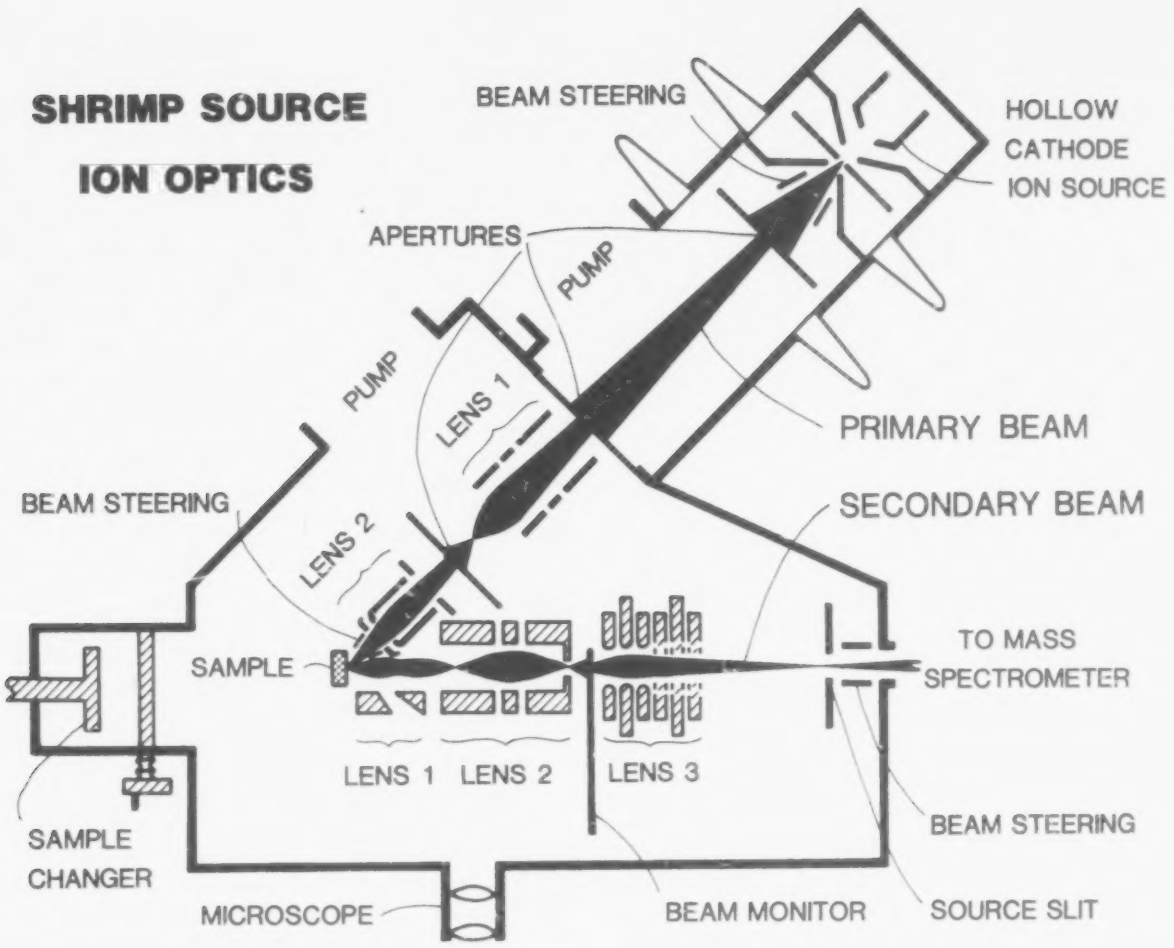

Figure 1*B*. Schematic drawing of the SHRIMP primary-ion source and secondary extraction ion optics. The primary-ion beam is generated in an IONEX duoplasmatron fitted with a cold, hollow, nickel cathode. The primary-ion beam can be operated, like most commercially available instruments, in critical illumination where the extraction aperture is imaged and the beam current is proportional to the primary-beam spot size on the target. However, Kohler illumination, where an aperture between the two primary column einzel lenses is imaged and the spot size is essentially fixed while the beam current (ion density) may be varied, is more commonly used. Different areas of the target are accessed when the sample is moved under the primary-ion beam by means of *x* and *y* positioners, and the target can be focused in the *z* dimension through a micrometer attached to the sample arm. Focusing in the *z* dimension is used essentially to compensate for surficial imperfections such as polishing relief. The primary beam impacts at 45° to the sample surface, and secondary ions are extracted normal to the plane of the sample, accelerated to ~11 kV across a 1-mm gap. Secondary ions are focused through three lens systems, passed through the source slit (commonly at 80 μm wide), and finally steered into the mass-analysis system. Approximately 10 percent (the exact amount is dependent on the target matrix) of the secondary-ion beam is trimmed by the secondary-beam monitor. Counts from the monitor are divided into the counts obtained for each isotope at the collector, and, in a manner similar to multiple collection, ratios are corrected for fluctuations in the intensity of the primary beam.

(for example, Schwarz and Helms, 1981; Williams, 1982; Shimizu, 1986, and references therein), and more detail of the operation of the SHRIMP ion microprobe is contained in papers by Clement and others (1977) and Ireland and others (1986). Primary ions are accelerated at 10 kV, and they can be focused onto the target by use of either critical or Kohler illumination to produce a minimum crater size of between 15 and 30 μm in diameter. The primary beam yields a current of 2 to 7 nA at the target. Because all of the atoms contained in that crater are removed and have the potential for entering the mass analyser, the mass spectrometer portion of the ion microprobe needs to be able to resolve

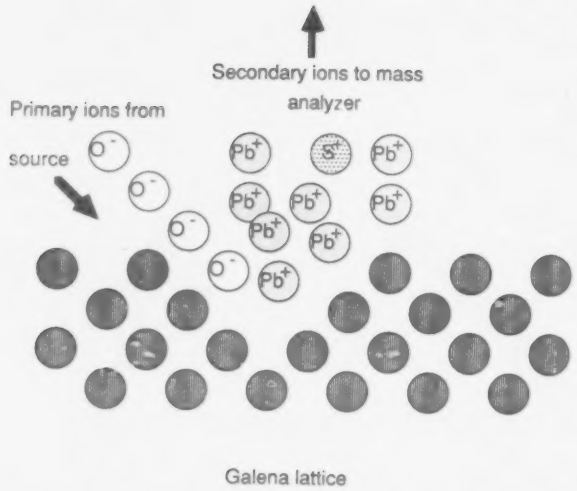

Figure 2. Schematic view of the sputtering event in which a primary beam of negatively charged oxygen ions is used and positively charged secondary ions of sulfur and lead from galena are produced. The high ratio of Pb^+ to S^+ illustrates the low ionization efficiency of sulfur in this analytical mode.

possible isobaric overlaps on the masses of interest (table 1). The mass spectrometer portion is double focusing, with the secondary ions, accelerated to 11 kV, initially being focused by the electrostatic analyser (a passive energy filter), which allows only ions of a selected energy to pass into the magnetic mass analyser, and then being focused into the collector by the magnetic sector.

SHRIMP was designed by S.W.J. Clement, W. Compston, and G. Newstead (Clement and others, 1977), who used equations for overall geometry from Matsuda (1974). It was constructed largely at the Research School of Earth Sciences of the Australian National University. Its primary constraints were that it have a mass resolution of 10,000 (m/Δm) and as high a sensitivity as possible. The sensitivity, a function of the width of divergence-limiting slits, increases with the length of the flight tube and size of the magnet. The magnet has a radius of 1 m, maximum field of 5 kG, has nonlaminated pole pieces, weighs 6 t, and is water cooled. The electrostatic sector, as demanded by the equations (Matsuda, 1974), has a radius of 1.27 m. To minimize stray magnetic fields acting on the secondary ions before they actually enter the magnetic sector, the electrostatic sector is surrounded by Mu metal shielding inside the vacuum and mild steel outside. The path traversed by the secondary ions through these two sectors to the collector is approximately 7.4 m long. High vacuum is maintained by three 400-L/s turbomolecular pumps, two pumping differentially on the source and one on the collector housing, and one 300-L/s oil diffusion pump on the electrostatic analyzer. Typically, a vacuum of approximately 4×10^{-8} torr is achieved throughout, except in the primary column, where it is of lower quality due to the gas needed for the primary beam.

Sulfur Isotopic Analyses

Sulfur isotopic analyses offer the best chance of precise measurements in the ion microprobe because of the relatively high ratio of heavy to light isotope (table 1). Currently, analyses of sulfur isotopes in SHRIMP utilize a negatively charged oxygen ion primary beam and extract positively charged ^{32}S and ^{34}S secondary ions. As sulfur ionizes more readily to form negatively charged ions, this is not the optimum system for sulfur isotopic analyses; however, the use of the negative oxygen ion beam causes the least disruption to the operation of the facility. The mass resolution required for stable isotopic analyses is not particularly great (table 1). For sulfur isotopic work, a mass resolution of 2,000 is sufficient to prevent $^{16}O_2^+$ (from the primary beam or from sulfates) from overlapping with $^{32}S^+$, but a mass resolution of 4,500 is needed to separate $^{64}Zn^{2+}$ from $^{32}S^+$. Little $^{64}Zn^{2+}$ reaches the collector, however, even during sulfur isotopic analyses of sphalerite (Eldridge and others, 1987b), so it may be safe to work at

Table 1. Some factors affecting stable isotopic analyses on the ion microprobe

Natural abundance ratios	Possible common isobaric overlaps	Δm (milli-amu)	Required resolution (m/Δm)
S ..... $^{32}S/^{34}S$ = 22:1	$^{16}O_2^+$; $^{64}Zn^{2+}$ on $^{32}S^+$	17.75; 7.52	1,800; 4,252
$^{32}S/^{33}S$ = 127:1	$H^{32}S^+$ on $^{33}S^+$	8.438	3,908
	$H^{33}S^+$ on $^{34}S^+$	11.416	2,976
C ..... $^{12}C/^{13}C$ = 90:1	$H^{12}C^+$ on $^{13}C^+$	4.470	2,910
	$^{24}Mg^{2+}$ on $^{12}C^+$	7.478	1,605
	$^{26}Mg^{2+}$ on $^{13}C^+$	12.057	1,078
O ..... $^{16}O/^{18}O$ = 489:1	$H_2{}^{16}O^+$ on $^{18}O^+$	11.405	1,578
H ..... H/D = 6,666:1	H_2^+ on D^+	1.548	1,301
	$^4He^{2+}$ on D^+	12.80	1,564

mass resolution of 2,000 for most sulfides and sulfates. SHRIMP sensitivity decreases so little with increasing resolution that analyses are often carried out at the same resolution needed for zircon analyses (mass resolution of 6,500) without detrimental effects. Because of the high sensitivity at this high mass resolution, no efforts are made at energy filtering on this instrument, in contrast to analyses done on other instruments (Shimizu, 1986).

Ions of the two sulfur masses are counted sequentially in an ETP (Australian manufacture) 10-stage ion multiplier, and the signals passed through two 10 × cascaded amplifiers to the discriminator. Mass 32 is counted for 3 s and then mass 34 for 10 s in computer-controlled cyclic magnetic field stepping. There is a 1-s delay, before each mass is counted, to let the magnet settle at the new field value. It has also been found that the optimum peak shape for each mass is obtained at slightly different collector positions, so the collector is moved toward the magnet for measuring mass 32 and away from the collector for mass 34 while the magnetic field value is altered and settled. The difference in position is usually on the order of 1 mm. The typical analysis comprises measurement of 30 $^{34}S/^{32}S$ ratios and takes approximately 30 min. During this period, a crater of nearly 30 μm in diameter and 5 μm deep is removed from the target. If pyrite is used, for example, this would correspond roughly to 4×10^{14} atoms. At typical count rates, because of all the measuring time lost to cycling, only 1 in $\sim10^7$ atoms is actually ionized, matches the acceptance of the mass analyser, and is counted.

Despite the inefficiency, SHRIMP performs sulfur isotopic measurements reliably in this analytical mode. Data from early experiments have demonstrated that the precision is approaching the limit imposed by counting statistics (approximately ±2 per mil (‰), 2σ). The analyses, corrected for sputtering-induced fractionation by use of standards, are accurate within this precision. Instrumental response is linear over a wide range in $\delta^{34}S$ values for many sulfur bearing minerals, there do not appear to be any effects that are due to charging of the sample, and there are no memory effects (Eldridge and others, 1987b). In SHRIMP analyses, it has been found that measured sulfur isotopic ratios are fractionated, relative to those measured conventionally, with the light isotope always enriched. Fractionation appears linear, and therefore correction of ion microprobe data to the Canyon Diablo scale is straightforward. However, two significant features of ion microprobe analysis must be closely monitored. First, the degree of enrichment varies in accordance with the mineral analyzed in a manner that parallels light isotopic enrichment in equilibrium isotopic partitioning experiments. Sulfates give ion microprobe ratios that are highly enriched (~6 percent/amu) in ^{32}S, while galena yields ratios less enriched in ^{32}S (~1.5 percent/amu), and the iron and copper-iron sulfides fall accordingly in between (Eldridge and others, 1987b). Second, while the relative order of this fractionation appears constant from one analytical session to the next, the absolute value may shift by several per mil even with just a sample change. Therefore, it is imperative to measure the isotopic compositions of unknown minerals relative to a standard of like matrix and to measure the compositions of the standard and unknowns in the same analytical session (Eldridge and others, 1987b). To accomplish this, a special method of casting epoxy mounts has been developed. Samples are placed on double-sided tape inside a 25.4-mm holder, and a 10-mm metal rod, with its circumference lightly coated with silicon grease, is placed beside the sample and perpendicular to the glass plate. When cured, the disks all have uniform hollows that allow a tight press-fit of an epoxy mount 10 mm in diameter, holding minerals of known isotopic composition, so that measurements of standards and unknowns can be interspersed in a given analytical session.

APPLICATIONS

The greatest advantages of ion microprobe determinations are their in situ analytical capabilities and their spatial resolution. One area that requires both of these features but tolerates low precision (±2 ‰) because of a naturally large range in isotopic composition is the study of sediment-hosted massive sulfide deposits. Such ores have been the subject of study for many years and have remained controversial because of the unresolved role of biogenic sulfide and questions as to the timing of formation relative to host rocks. Two Phanerozoic deposits (the H.Y.C. at McArthur River and the lead-zinc at Mount Isa, Australia), one Paleozoic (Rammelsberg, West Germany), and one possible modern analog (Salton Sea geothermal system, California) have been studied by use of SHRIMP.

H.Y.C. at McArthur River

The H.Y.C. deposit in the Northern Territory of Australia is one of the world's best examples of shale-hosted lead-zinc mineralization, and it has been studied over the past 20 years by several investigators (for example, Croxford, 1968; Williams, 1978a,b; Rye and Williams, 1981; Williams and Logan, 1986). The deposit comprises ~230 million metric tons of mineralization containing 9 percent zinc and 4 percent lead. Mineralization occurs over a vertical interval of 55 m on average, distributed concordantly (fig. 3A) in eight beds of dolomitic and carbonaceous siltstones that are thought to have been deposited in an emergent sabkha environment (Williams and Logan, 1986). The sulfide minerals in the H.Y.C. are noted for their fine grain size (<200 μm in diameter) and lack of any apparent metamorphic overprint. The host rocks for the mineralization are often found to be quite pyritic, and the relationship between the pyrite and base-metal sulfides has remained

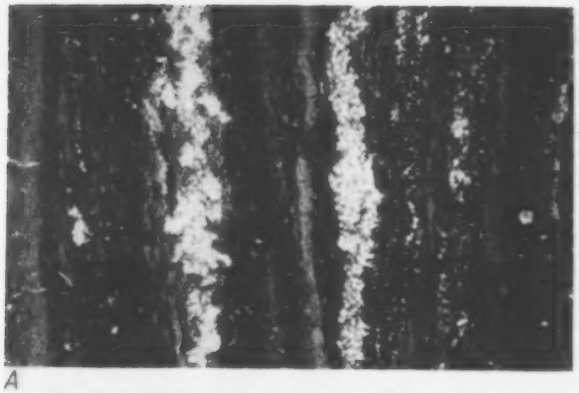

A

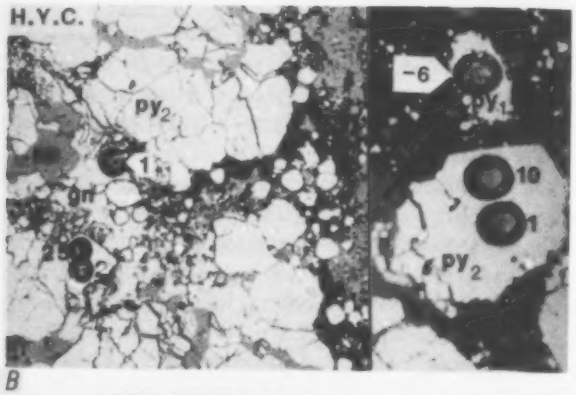
H.Y.C.
py2
1
gn
-6
py1
10
1
py2

B

C

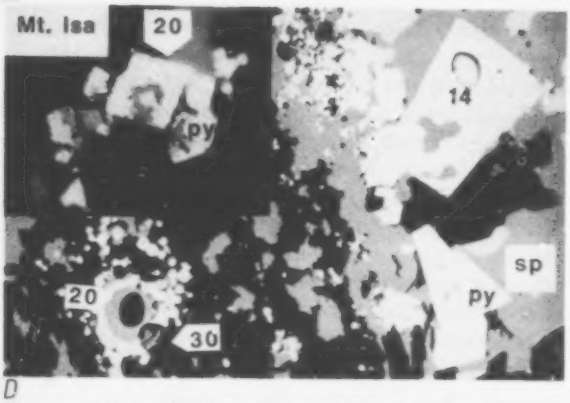
Mt. Isa
20
py
14
sp
20
30
py

D

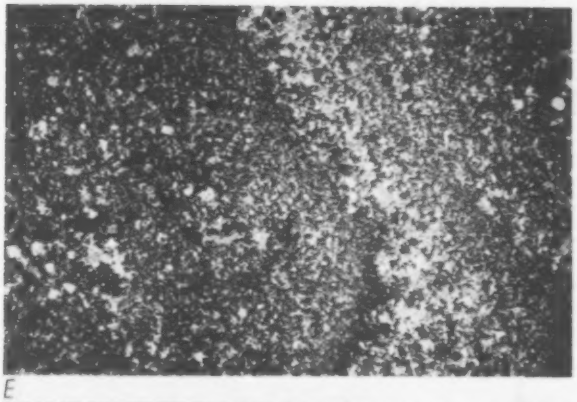

E

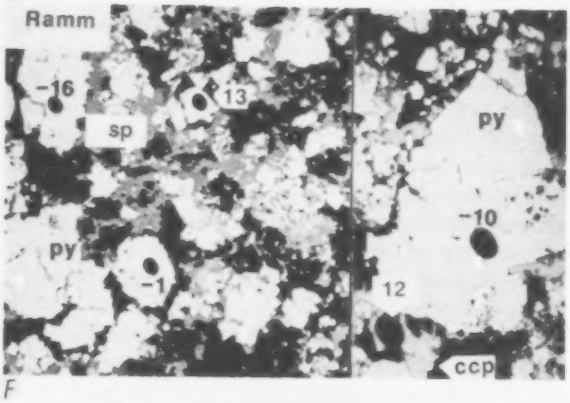
Ramm
-16
sp
13
py
-10
py
-1
12
ccp

F

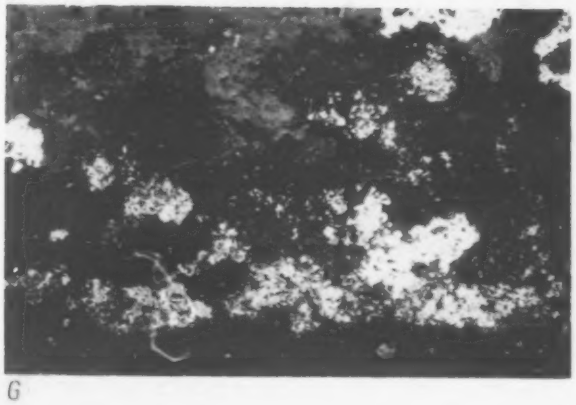

G

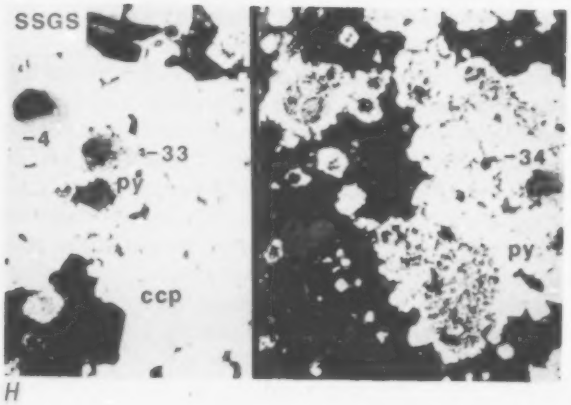
SSGS
-4
-33
py
-34
py
ccp

H

Figure 3. These pairs of photomicrographs are of samples used in each of the four applications of SHRIMP sulfur isotopic analyses described in the text. Photos on the left illustrate how the sulfides are distributed in the host rocks, and on the right actual analytical craters are shown with their $\delta^{34}S$ values, in per mil, relative to Canyon Diablo troilite. The scale for each of the rock photos is given in the caption, while the ~30-μm in diameter craters serve as scales for the detail pictures.

A, Mineralized dolosiltstone from the No.7 orebody of the H.Y.C. deposit at McArthur River. Sulfide minerals comprising pyrite, sphalerite, and galena are generally distributed parallel to the bedding of the host rock; however, there are some minor crosscutting veinlets of galena. In this sample the crosscutting galena is isotopically indistinguishable from that found along the bedding. The long dimension is approximately 12 mm.

B, The left photo shows typical textural relations between pyrite and base-metal sulfides of the H.Y.C. at McArthur River. Py_2 appears to be overgrown and crosscut by sphalerite (sp) and galena (gn). The py_2 is isotopically zoned (2 to 25 ‰), having a mean composition quite distinct from that of the base-metal sulfide. The 1 ‰ in the left-center of the photo is galena. The right photo was taken approximately 0.8 mm away from the left photo, and it shows the usual isotopic relationship between the fine-grained py_1 crystals and the coarse-grained py_2. The py_1 (−6 ‰) is considerably lighter than the adjacent, isotopically zoned py_2 (1–10 ‰) or the base-metal sulfide in the same sample.

C, This sample of Mount Isa ore from the No. 14 orebody contains bands of sulfides displaying the typical bimodal size distribution. The field of view is ~7 mm wide.

D, The larger photo shows adjacent coarse-grained and fine-grained pyrite from Mount Isa, both distributed parallel to the bedding of the host rock but having quite different isotopic compositions. The fine-grained, framboidal pyrite (py) is much heavier (~30 ‰) than the coarse-grained, cubic pyrite (~14 ‰) or associated base-metal sulfide(~20 ‰). Sphalerite is indicated by sp. The smaller photo (upper left corner) shows the temporal relationship between the coarse-grained, isotopically light pyrite and the fine-grained, isotopically heavy pyrite. This composite crystal, an overgrowth of cubic on framboidal pyrite, has an isotopic composition between that (20 ‰) of the two endmember pyrites.

E, A sample of copper-rich ore from Rammelsberg made up of graded beds of sulfide clasts having variable proportions of pyrite, chalcopyrite, sphalerite, and galena. The field of view is ~10 mm wide.

F, The left photo of Rammelsberg ore is an assemblage of cubic pyrite clasts, of drastically differing isotopic compositions, surrounded by sphalerite and minor galena (not visible). The right photo shows gross isotopic disequilibrium between pyrite (−10 ‰) and an overgrowth of chalcopyrite (12 ‰).

G, Fine-grained sediment from 4,029 ft (1,228 m) down the Salton Sea geothermal system State-2 well, with framboidal pyrite (light gray, mottled) occurring parallel to the bedding, crosscut in places by a vein of chalcopyrite (lightest gray, massive). The field of view is ~7 mm in the long dimension.

H, The photo on the left, from the Salton Sea geothermal system, shows some of the fine-grained pyrite (py), now engulfed in chalcopyrite (ccp), and the photo on the right shows some pristine framboidal pyrite several millimeters from the chalcopyrite. The pyrites are isotopically indistinguishable (~−33 ‰), regardless of their proximity to the chalcopyrite. The base-metal sulfide (−4 ‰) is quite distinct from the pyrite in isotopic composition despite the fact that it surrounded some of the pyrite crystals.

enigmatic because of the inability to obtain pure mineral separates for isotopic analysis. The situation is further complicated for the analyst in that the pyrite occurring with the base-metal sulfides comprises two forms: py_1, a bright yellowish-white, cubic, high-relief mineral typically overgrown by py_2, a brownish mineral that is often framboidal and is of low relief. Understanding which, if either, pyrite type was genetically related to the base-metal mineralization has proven impossible until investigation by ion microprobe.

In the SHRIMP investigation, no textural evidence has been found to counter the paragenetic sequence of sulfide deposition first described by Williams (1978a); however, isotopic systematics have been found to be more complicated than suggested from earlier conventional isotopic work (Smith and Croxford, 1973). Throughout the deposit, isotopic variation spans 60 ‰, with pyrite being the most heterogeneous mineral (py_1, −15 to 12 ‰; py_2, −1 to 45 ‰). Though both pyrite types may be heterogeneous within samples, py_1 varies less (that is, <10 ‰) than py_2 (<46 ‰). Within samples, py_1 and py_2 are usually quite distinct isotopically with the $\Delta_{py2-py1}$ typically around 10 ‰. Base-metal sulfides, with $\delta^{34}S$ values limited to the range −5 to 14 ‰, have considerably less variable isotopic compositions than either pyrite type. Base-metal sulfides can be less than, equal to, or greater than py_1 in $\delta^{34}S$ value but are usually less than py_2 (fig. 3*B*). It is possible to find single samples that contain nearly the entire range of isotopic variability of the deposit. For example, in a 1-cm^2 area of one sample from the No. 6 orebody, py_1 was −12 ‰, py_2 was 45 ‰, and sphalerite was 0 ‰. This variation alone is more than three times that found throughout the whole deposit by means of conventional isotopic study (Smith and Croxford, 1973).

The isotopic heterogeneity of py_1 and py_2 and the consistent enrichment of ^{34}S in py_2 as compared to py_1 suggest that these two pyrites may both have been formed through biogenic reduction of seawater sulfate such that the sediment was open to sulfate during the formation of py_1 and closed before py_2 began to precipitate. Isotopic disequilibrium between base-metal sulfides and pyrite is found throughout the deposit and implies that no sulfide from either pyrite was utilized in precipitating the lead or zinc sulfides. The isotopic heterogeneity between sphalerite and pyrite or galena and pyrite also indicates that little movement toward isotopic equilibration has occurred in 1.8 billion years since deposition (Eldridge and others, unpub. data, 1988).

Mount Isa Lead-Zinc

The ore deposit at Mount Isa has traditionally been divided into the lead-zinc and the copper orebodies, and each has been mined and milled separately (Bennet, 1965; Perkins, 1984). Lead-zinc ores comprise nearly 100 million metric tons at 7 percent lead and 6 percent zinc (Gustafson and Williams, 1981) and are largely conformable with the Urquhart shale, while the copper ore occurs in a highly recrystallized, often fractured, silica dolomite. The geologic setting for the Mount Isa lead-zinc ore is thought to be similar to that of the McArthur River deposit, as the Urquhart shale is dolomitic and has many features consistent with deposition in an intermittently emergent basin (Neudert and Russel, 1981). To date, SHRIMP analyses have been concentrated in the lead-zinc mineralization with the aims of identifying the sulfides that were part of the host rocks and those that may have been introduced, as well as what might have been formed as a part of the metamorphic events.

Like the mineralization at McArthur River, Mount Isa ore hosts two pyrite types (fig. 3*C*); however, they are found in a somewhat different style from McArthur River. There is fine-grained (often framboidal) pyrite that ranges in isotopic composition from 2 to 30 ‰ and a coarse-grained, cubic pyrite that varies only from ~10 to 27 ‰ (fig. 3*D*). This coarser pyrite generally occurs with the lead and zinc mineralization and can be found as overgrowths on the framboidal pyrite (fig. 3*D*). The coarse-grained pyrite to fine-grained pyrite isotopic relationships vary little within a sample but widely from sample to sample, where the coarse-grained pyrite may have $\delta^{34}S$ values lower than, equal to, or higher than the adjacent fine-grained pyrite. As at McArthur River, the fine-grained pyrite does not appear to have contributed sulfur at the site of base-metal precipitation. Moreover, isotopic disequilibrium between fine-grained pyrite and adjacent base-metal sulfides appears to have survived greenschist metamorphism of the deposit (Eldridge and others, 1985b; 1986b).

Rammelsberg

The Rammelsberg orebody, like the McArthur River and Mount Isa lead-zinc deposits, is hosted in and is generally conformable with sedimentary rock. It is considerably smaller than either of the previously mentioned orebodies, with only 25 million metric tons of ore at 20 percent zinc, 8 percent lead, and 1 percent copper. Though the ore is hosted in shale and may have formed in a rift environment (Sawkins and Burke, 1980) like the McArthur River and Mount Isa deposits, Rammelsberg ore has features that clearly distinguish it from that found at McArthur River or Mount Isa. In addition to the familiar sulfides interbedded with shale, Rammelsberg ore has graded beds of sulfide minerals (fig. 3*E*), and the orebody is mineralogically zoned ascending from pyritic to barite ore (Anger and others, 1966) as are the Japanese Kuroko deposits (Ohmoto and Skinner, 1983).

Only a few isotopic analyses from one sample of clastic Rammelsberg ore have been carried out, but within that 4-cm^2 area nearly the entire isotopic range from the whole orebody, as determined conventionally (Anger and others, 1966), was found by use of the ion microprobe. The magnitude of variation in $\delta^{34}S$ values is similar to that at Mount Isa lead-zinc (~30 ‰); however, the ore at Rammelsberg is a physical mixture where neighboring clasts of pyrite may differ in $\delta^{34}S$ value by the full 30 ‰ (fig. 3*F*), in contrast to Mount Isa lead-zinc ore, where heterogeneity is most notable from stratum to stratum. As at McArthur River and Mount Isa, the base-metal mineralization has a more restricted range in $\delta^{34}S$ values than does the pyrite. Chalcopyrite at Rammelsberg has been found to be ~13 ‰ regardless of whether it has overgrown isotopically light (−13 ‰) pyrite or isotopically heavy (13 ‰) pyrite. Thus it would appear that base-metal mineralization required no sulfur from preexisting iron sulfides. This isotopic heterogeneity has prevailed through greenschist metamorphism of the orebody (Eldridge and others, 1985a; 1986a; 1988).

Salton Sea

The Salton Sea geothermal system (SSGS) is located in a tectonically active continental rift zone where hot (up to 365 °C) and highly saline hydrothermal brines interact with Pliocene-Pleistocene fluvial and lacustrine sediments (McKibben and others, 1987). A modern continental rift setting where hydrothermal fluids encounter evaporitic sediments has been postulated as a modern analog for ancient sediment-hosted sulfide deposits such as McArthur River or Mount Isa lead-zinc (see discussion by Williams in Williams and Logan, 1986), so it is logical to study sulfide formation in the SSGS as a possible corollary to the ancient occurrences. SSGS sediments include evaporitic anhydrite and often contain diagenetic pyrite. Mineralization, characterized by fine-grained sulfides deposited in sediments and subvertical veins (fig. 3*G*), is apparently formed from fluids that are relatively sulfur poor (Skinner and others, 1967; McKibben and Elders, 1985), and it has been proposed that base-metal-sulfide precipitation involved recycling of biogenic sulfide stored in the sedimentary pyrite (White, 1968).

Cursory conventional isotopic studies have revealed only a narrow range in $\delta^{34}S$ values for the system (McKibben, 1986), while ion microprobe investigations have demonstrated a range of over 40 ‰ within a sample and as many as three generations of isotopically distinct sulfides within several samples (McKibben and Eldridge, in press). As in the three older deposits, described above, the hydrothermal base-metal sulfides have been found as overgrowths

on earlier pyrite, yet no evidence of sulfur recycling has been discovered (fig. 3*H*). Ion microprobe studies have also shown that disequilibrium between closely intergrown biogenic pyrite and continental evaporitic anhydrite has been preserved to depths in excess of 3,000 m and to metamorphic grades of lower amphibolite facies (Eldridge and McKibben, 1988; McKibben and Eldridge, in press). The ion microprobe data, combined with conventional analyses of aqueous H_2S and SO_4, have demonstrated that the sulfide used in precipitation of the base-metal sulfides has come largely from hydrothermal partial reduction of anhydrite sulfate and could not have involved diagenetic sulfide from the site of mineralization.

SUMMARY

Thus, by the use of SHRIMP, it has been found that all of these deposits share some characteristics. Individual samples have been found in each deposit that contain nearly the whole range or more isotopic heterogeneity than has been discovered throughout the entire orebody when conventional means have been used (fig. 4); isotopic heterogeneity has been preserved over very small distances (tens of micrometers to millimeters) for very long periods of time and through various degrees of metamorphism (from diagenesis to lower amphibolite grade), and no direct evidence has been found to suggest incorporation of locally derived biogenic sulfide at the site of ore precipitation. Moreover, isotopic compositions, together with the preserved textural settings of the minerals, can be used to constrain the timing of mineralization. For example, the fact that the deposits are hosted in sediments, and may be in part generally conformable with the sediments, is no guarantee that the formation of sulfides was contemporaneous with deposition of the host sediments. Clearly, the ongoing mineralization at the Salton Sea is largely epigenetic, and the combination of ore textural and isotopic data suggests that mineralization at McArthur River and Mount Isa were also epigenetic. Rammelsberg, on the other hand, was likely to have formed syngenetically.

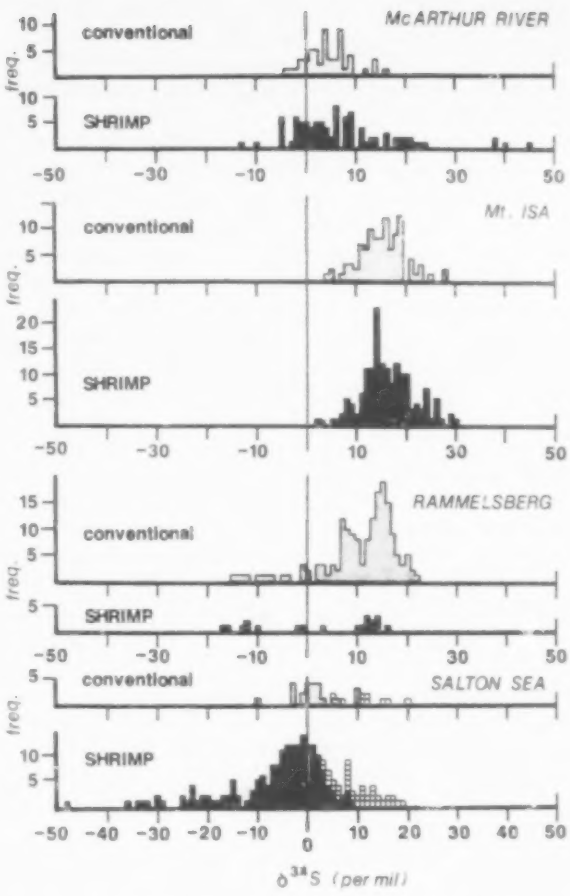

Figure 4. Comparison of conventional and SHRIMP sulfur isotopic data from four areas of sulfide mineralization. Black squares are data from sulfide minerals that may include, depending on the deposit, pyrite, pyrrhotite, sphalerite, galena, and chalcopyrite. The white squares are data from sulfate minerals, chiefly anhydrite, but may include gypsum. Conventional data sources: McArthur River, Smith and Croxford, 1973; Mount Isa lead-zinc, Solomon, 1965; Smith and others, 1978; Rammelsberg, Anger and others, 1966; Salton Sea, McKibben, 1986. SHRIMP data sources: McArthur River, Eldridge and others, unpub. data, 1988; Mount Isa lead-zinc, Eldridge and others, 1985b; Rammelsberg, Eldridge and others, 1988; Salton Sea, McKibben and Eldridge, in press.

FUTURE DEVELOPMENTS

Improvement of analytical precision would allow application of this powerful in situ analytical technique to a wide range of topics, and several avenues for better sulfur isotopic analyses are open. The ion counting system can be reconfigured for multiple collection, more efficiently using the ions produced in sputtering by eliminating the time wasted in magnetic field cycling. Compared to single collection, such a system could be used either to produce an increased number of analyses of a given precision in a given time or the same number of analyses, of increased precision, in a given time. Additionally, the method of production and extraction of secondary ions in the source chamber can be altered. A tunable laser can increase the ions produced per atom sputtered (Willis and others, this volume) and thus increase the secondary-ion count rate. Alternatively, negative secondary ions can be extracted and counted (fig. 5). In experiments with SHRIMP, it has been found that, with the change to extraction of negative secondary ions, count rates increase dramatically for galena, somewhat for other sulfides, and not at all for pyrite

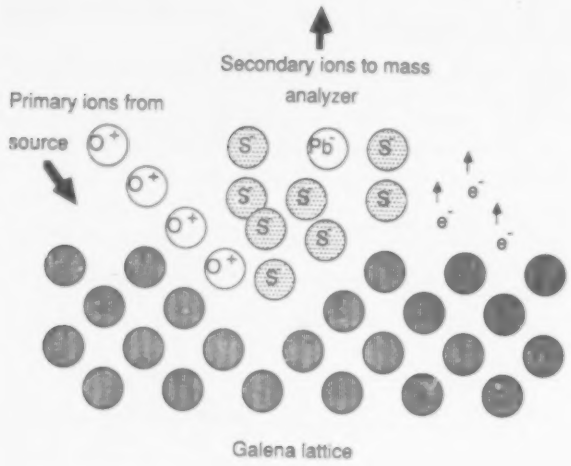

Figure 5. Schematic view of the sputtering event in which a primary beam of positively charged oxygen ions is used and negatively charged sulfur and lead ions are produced. Note the increased production of sulfur ions relative to lead as compared to figure 2, as well as the exit of electrons from the target surface.

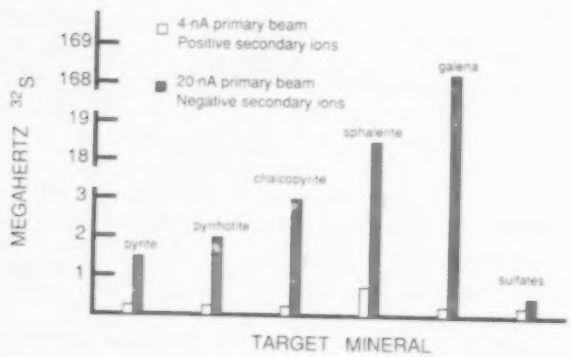

Figure 6. Comparitive secondary-ion yields for sulfide and sulfate minerals from use of positive and negative secondary ions. There is no compensation for charging effects in the negative-ion mode, and galena is the only mineral to benefit to the full extent possible. See Eldridge and others (1987a) for more details.

or sulfates (fig. 6). It is thought that charging of the sample surface, which is due to removal of electrons as well as negatively charged secondary ions, impedes this method of operation. It is not entirely clear why poor conductors like sphalerite give somewhat increased secondary-ion yields of negative ions, while better conductors, like pyrite, do not. However, charge compensation, by use of an electron flood gun (fig. 7), may raise all levels of secondary-ion output to similar values for all matrices (Hervig and others, this

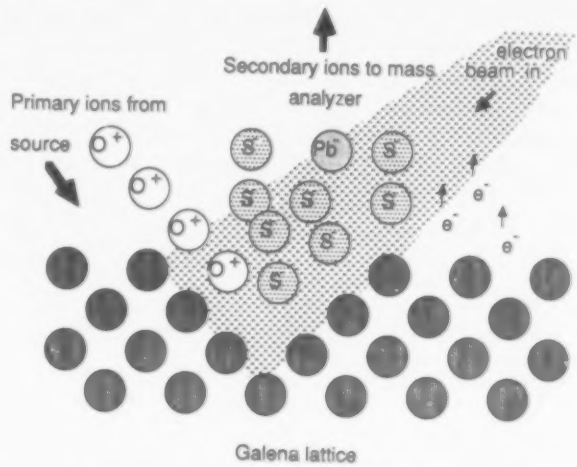

Figure 7. Schematic view of the sputtering event showing how an electron flood gun, bombarding a wide area, may replace the electrons lost to the secondary-ion extraction process and eliminate sample charging, which drastically reduces secondary-ion yields for most minerals.

volume; Giletti and Shimizu, this volume). Alternatively, pressing a very small sample into a block of gold and overlapping the primary beam onto the block may also work (Zinner, this volume). While no testing has been done to compare laser-enhanced emission of positively charged and charge-compensated emission of negatively charged secondary sulfur ions, multiple collection of secondary ions, with yields enhanced by either method, may allow the precision of ion microprobe analyses to equal that afforded by conventional analyses (± 0.1 ‰).

ACKNOWLEDGMENTS

We wish to thank Dr. J.J. Foster of the Research School of Earth Sciences for his unfailing assistance in keeping SHRIMP in tune. Advice on photography from R. Wilde-Brown and P. Willis of the Research School of Earth Sciences, The Australian National University, was quite helpful. The Australian Research Grants Scheme supported the efforts of the first author, and he was also granted a visiting fellowship by the Research School of Earth Sciences; support from both is gratefully acknowledged. We are grateful to Dr. N. Williams of Carpentaria Exploration Co. Pty., Ltd., and Dr. D.J. Patterson of Mount Isa Mines, Ltd., for their cooperation and assistance in the McArthur River and Mount Isa projects, respectively. The work on the Salton Sea geothermal system benefited from the support of Dr. M.A. McKibben of the University of California, Riverside, through National Science Foundation grant EAR 8617430 and Department of Energy grant DE FG03 85ER13408. Rammelsberg research was aided by Dr. H.

Sperling of Preussag Aktiengesellschaft and National Science Foundation grants EAR 8319402 and EAR 8319654 to Dr. H. Ohmoto of the Pennsylvania State University.

REFERENCES CITED

Anger, G., Nielsen, H., Puchelt, H., and Ricke, W., 1966, Sulfur isotopes in the Rammelsberg ore deposit (Germany): Economic Geology, v. 61, p. 511–536.

Bennet, E.M., 1965, Lead-zinc-silver and copper deposits of Mount Isa, *in* McAndrew, J., ed., 8th Commonwealth Mining and Metallurgy Congress Melbourne, Australian Institute of Mining and Metallurgy, p. 233–246.

Clement, S.W.J., Compston, W., and Newstead, G., 1977, Design of a large, high mass resolution ion microprobe: Proceedings of the International S.I.M.S. Conference, Muenster, 17 p.

Croxford, N.J.W., 1968, A mineralogical examination of the McArthur lead-zinc-silver deposit: Proceedings, Australian Institute of Mining and Metallurgy No. 226, pt. 2, p. 97–108.

Eldridge, C.S., and McKibben, M.A., 1988, Sulfur isotopic systematics in the Salton Sea geothermal system: A SHRIMP ion microprobe study of micro-scale $\delta^{34}S$ variations [abs.]: V.M. Goldschmidt Conference, May 11–13, Baltimore, Maryland, Program and abstracts, p. 40.

Eldridge, C.S., Compston, W., Williams, I.S., Ohmoto, H., Walshe, J.L., and Both, R.A., 1985a, Ion microprobe determination of sulfur isotopic variation in pyrite from a single sample of Rammelsberg ore [abs.]: Geological Society of America, Abstracts with Programs, v. 17, p. 573.

Eldridge, C.S., Compston, W., Williams, I.S., Patterson, D.J., Walshe, J.L., and Both, R.A., 1985b, Ion microprobe determination of sulfur isotopic compositions of sulfides from the Mt. Isa Pb/Zn orebody [abs.]: Geological Society of America, Abstracts with Programs, v. 17, p. 573.

Eldridge, C.S., Compston, W., Williams, I.S., Patterson, D.J., Ohmoto, H., Walshe, J.L., and Both, R.A., 1986a, SHRIMP ion microprobe determination of sulfur isotopic ratios in some sediment-hosted massive sulfide ores: Variability in their timing and formation [abs.]: TERRA cognita, v. 6 no. 2, p. 134.

Eldridge, C.S., Williams, N., Compston, W., and Walshe, J.L., 1986b, SHRIMP ion microprobe determination of the sulfur isotopic composition of sulfides from the McArthur River deposit, Northern Territory, Australia [abs.]: Geological Society of America, Abstracts with Programs, v. 18, p. 593.

Eldridge, C.S., Compston, W., Williams, I.S., and Walshe, J.L., 1987a, SHRIMP ion microprobe analyses of sulfur isotopes using multiple collection of negative secondary ions [abs.]: Geological Society of America, Abstracts with Programs, v. 19, p. 654.

Eldridge, C.S., Compston, W., Williams, I.S., Walshe, J.L., and Both, R.A., 1987b, In situ microanalysis for $^{34}S/^{32}S$ ratios using the ion microprobe SHRIMP: International Journal of Mass Spectrometry and Ion Processes, v. 54, p. 40–59.

Eldridge, C.S., Compston, W., Williams, I.S., Both, R.A., Walshe, J.L., and Ohmoto, H., 1988, Sulfur isotopic variability in sediment-hosted massive sulfide deposits as determined using the ion microprobe SHRIMP: I, An example from the Rammelsberg orebody: Economic Geology, v. 83, p. 443–449.

Gustafson, L.B., and Williams, N., 1981, Sediment-hosted stratiform deposits of copper, lead and zinc: Economic Geology 75th Anniversary Volume, p. 139–178.

Ireland, T.R., Compston, W., and Esat, T.M., 1986, Magnesium isotopic compositions of olivine, spinel, and hibonite from the Murchison carbonaceous chondrite: Geochimica et Cosmochima Acta, v. 50, p. 1413–1421.

Kyser, T.K., ed., 1987, Stable isotope geochemistry of low temperature processes: Mineralogical Association of Canada, v. 13, 451 p.

Matsuda, H., 1974, Double focusing mass spectrometers of second order: International Journal Mass Spectrometry and Ion Physics, v. 14, p. 219–233.

McKibben, M.A., 1986, Hydrothermal minerals in the Salton Sea geothermal system, *in* Turner, R.J.W., and Einaudi, M.T., eds., Conference on the Genesis of Stratiform Sediment Hosted Pb-Zn Deposits: Stanford University Publication Series in Geology, No. 20, p. 161–163.

McKibben, M.A., and Elders, W.A., 1985, Fe-Zn-Cu-Pb mineralization in the Salton Sea geothermal system, Imperial Valley, California: Economic Geology, v. 80, p. 539–578.

McKibben, M.A., and Eldridge, C.S., in press, Sulfur isotopic variations among minerals and aqueous species in the Salton Sea geothermal system, California: A SHRIMP ion microprobe and conventional study: American Journal of Science.

McKibben, M.A., Williams, A.E., Elders, W.A., and Eldridge, C.S., 1987, Saline brines and metallogenesis in a modern sediment-filled rift: The Salton Sea geothermal system, California, U.S.A.: Applied Geochemistry, v. 2, p. 563–578.

Neudert, M.K., and Russel, R.E., 1981, Shallow water and hypersaline features from the middle Proterozoic Mt. Isa sequence: Nature, v. 293, no. 5830, p. 284–286.

Ohmoto, H., and Skinner, B.J., eds., 1983, The Kuroko and related volcanogenic massive sulfide deposits: Economic Geology Monograph 5, 604 p.

Perkins, W.G., 1984, Mount Isa silica dolomite and copper orebodies: The result of a syntectonic hydrothermal alteration system: Economic Geology, v. 79, p. 601–637.

Rye, D.M., and Williams, N., 1981, Studies of the base metal sulfide deposits at McArthur River, Northern Territory, Australia: III, The stable isotope geochemistry of the H.Y.C., Ridge, and Cooley Deposits: Economic Geology, v. 76, p. 1–26.

Sawkins, F.J., and Burke, K., 1980, Extensional tectonics and mid-Paleozoic massive sulfide occurrences in Europe: Geologische Rundschau, v. 69, p. 349–360.

Schwarz, S.A., and Helms, C.R., 1981, An elementary model of neutral and ion sputtering yields: Surface Science, v. 102, p. 578–587.

Shimizu, N., 1986, Silicon-induced enhancement in secondary ion emission from silicates: International Journal Mass Spectrometry and Ion Processes, v. 69, p. 325–338.

Skinner, B.J., White, D.E., Rose, H.J., Jr., and Mays, R.E., 1967, Sulfides associated with the Salton Sea geothermal brine: Economic Geology, v. 62, p. 316–320.

Smith, J.W., and Croxford, N.J.W., 1973, Sulfur isotope ratios in the McArthur lead-zinc-silver deposit: Nature, Physical Science, v. 245 no. 140, p. 10–12.

Smith, J.W., Burns, M.S., and Croxford, N.J.W., 1978, Stable isotope studies of the origins of mineralization at Mt. Isa: Mineralium Deposita, v. 13, p. 369–381.

Solomon, P.J., 1965, Investigations into sulfide mineralization at Mount Isa, Queensland: Economic Geology, v. 60, p. 735–765.

Valley, J.W., Taylor, H.P., Jr., and O'Neil, J.R., eds., 1986, Stable isotopes in high temperature geological processes: Mineralogical Society of America, Reviews in Mineralogy, v. 16, 570 p.

White, D.E., 1968, Environments of generation of some base-metal ore deposits: Economic Geology, v. 63, p. 301–335.

Williams, N., 1978a, Studies of the base metal sulfide deposits at the McArthur River, Northern Territory, Australia: I, The Cooley and Ridge deposits: Economic Geology, v. 73, p. 1005–1035.

———1978b, Studies of the base metal sulfide deposits at the McArthur River, Northern Territory, Australia: II, The sulfide-S and organic-C relationships of the concordant deposits and their significance: Economic Geology, v. 73, p. 1036–1056.

Williams, N., and Logan, R.G., 1986, Geology and evolution of the H.Y.C. stratiform Pb-Zn orebodies, Australia, *in* Turner, R.J.W., and Einaudi, M.T., eds., Conference on the Genesis of Stratiform Sediment Hosted Pb-Zn Deposits: Stanford University Publication Series in Geology, No. 20, p. 57–60.

Williams, P., 1982, On mechanisms of sputtered ion emission: Applied Surface Science, v. 13, p. 241–259.